Outdoor Acoustic Green's Function Extraction

Max Denis, Sandra L. Collier, David A. Ligon, John M. Noble, W.C. Kirkpatrick Alberts II,
Leng K. Sim, Christian G. Reiff, and Deryck D. James

U.S. Army Research Laboratory

17th Long-Range Sound Propagation Symposium
12 – 14 June, Lyon, France

Motivation

- Green's function retrieval allows for outdoor remote sensing

Atmospheric tomography

- Estimate temperature and wind characteristics

Selected references:

- Godin et al. (Godin, Irisov et al. 2014)
- Ostashev et al. (Ostashev and Wilson 2015)

Localization and characterization of the acoustic environment

- Localizing acoustic sources and scatterers
- Estimate the dispersion characteristics of the environment

Selected references:

- Li et al. (JASA 2017)

Objectives

- Incorporate retrieved GF into acoustic imaging techniques
  - Plane wave beamforming
- Atmospheric tomography using radial basis functions

Cross-Correlation

- Consider the received signals at $\mathbf{r}_l^B$ and $\mathbf{r}_v^A$ from a source at $\mathbf{r}_0$

$$p(\mathbf{r}_v^A,\mathbf{r}_0;t) = G(\mathbf{r}_v^A,\mathbf{r}_0;t) * S(\mathbf{r}_0;t)$$

$$p(\mathbf{r}_l^B,\mathbf{r}_0;t) = G(\mathbf{r}_l^B,\mathbf{r}_0;t) * S(\mathbf{r}_0;t)$$

- Cross-correlation(CC) Green's function retrieval method[1,2]

Assumptions: Lossless medium and homogeneous illumination of all receivers

$$C(\mathbf{r}_l^B,\mathbf{r}_v^A;t) = \left\langle p(\mathbf{r}_l^B,\mathbf{r}_0;t) * p(\mathbf{r}_v^A,\mathbf{r}_0;-t) \right\rangle = \oint_\Omega \left[G(\mathbf{r}_l^B,\mathbf{r}_0;t) * G(\mathbf{r}_v^A,\mathbf{r}_0;-t) \right] * |S(\mathbf{r}_0;t)|^2 d\mathbf{r}_0$$

$\therefore$ when $S(t) \to \delta(t)$, CC yields

$$C(\mathbf{r}_l^B,\mathbf{r}_v^A;t) \approx G(\mathbf{r}_l^B,\mathbf{r}_v^A;t) = \oint_\Omega \left[G(\mathbf{r}_l^B,\mathbf{r}_0;t) * G(\mathbf{r}_v^A,\mathbf{r}_0;-t) \right] d\mathbf{r}_0$$

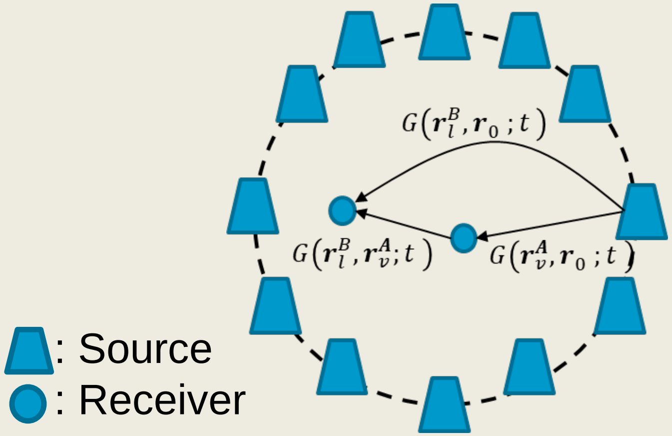

[1]Wapenaar 2004
[2]Wapenaar and Fokkema 2006

Multidimenstional Deconvolution

- Multidimensional deconvolution(MDD) Green's retrieval method[1,2]
  - Assume the received signal at $\mathbf{r}_l^B$ can be obtained by the following equation:

$$p(\mathbf{r}_l^B,\mathbf{r}_0;t)=\oint_{\Omega} G(\mathbf{r}_l^B,\mathbf{r}_v^A;t)*p(\mathbf{r}_v^A,\mathbf{r}_0;t)d\mathbf{r}_0$$

  - The cross-correlation $C(\mathbf{r}_l^B,\mathbf{r}_v^A;t)=\left\langle p(\mathbf{r}_l^B,\mathbf{r}_0;t)*p(\mathbf{r}_v^A,\mathbf{r}_0;-t)\right\rangle$ yields

$$C(\mathbf{r}_l^B,\mathbf{r}_k^A;t)=\int_{\Omega} G(\mathbf{r}_l^B,\mathbf{r}_v^A;t)*\Gamma(\mathbf{r}_v^A,\mathbf{r}_k^A;t)d\mathbf{r}_0$$

$\Gamma(\mathbf{r}_v^A,\mathbf{r}_k^A;t)$: Point Spread Function

  - System of equations of the cross-spectrum $C(\mathbf{r}_l^B,\mathbf{r}_k^A;\omega)$

$$\begin{bmatrix} C(\boldsymbol{r}_l^B,\boldsymbol{r}_1^A;\omega) \\ C(\boldsymbol{r}_l^B,\boldsymbol{r}_2^A;\omega) \\ \vdots \\ C(\boldsymbol{r}_l^B,\boldsymbol{r}_N^A;\omega) \end{bmatrix} = \begin{bmatrix} \Gamma(\boldsymbol{r}_1^B,\boldsymbol{r}_1^A;\omega) & \Gamma(\boldsymbol{r}_1^B,\boldsymbol{r}_2^A;\omega) & \cdots & \Gamma(\boldsymbol{r}_1^B,\boldsymbol{r}_N^A;\omega) \\ \Gamma(\boldsymbol{r}_2^B,\boldsymbol{r}_1^A;\omega) & \Gamma(\boldsymbol{r}_2^B,\boldsymbol{r}_2^A;\omega) & \cdots & \Gamma(\boldsymbol{r}_2^B,\boldsymbol{r}_N^A;\omega) \\ \vdots & \vdots & \ddots & \vdots \\ \Gamma(\boldsymbol{r}_N^B,\boldsymbol{r}_1^A;\omega) & \Gamma(\boldsymbol{r}_N^B,\boldsymbol{r}_2^A;\omega) & \cdots & \Gamma(\boldsymbol{r}_N^B,\boldsymbol{r}_N^A;\omega) \end{bmatrix} \begin{bmatrix} G(\boldsymbol{r}_l^B,\boldsymbol{r}_1^A;\omega) \\ G(\boldsymbol{r}_l^B,\boldsymbol{r}_2^A;\omega) \\ \vdots \\ G(\boldsymbol{r}_l^B,\boldsymbol{r}_N^A;\omega) \end{bmatrix}$$

  – Damped Least-square inversion

$$\mathbf{G}=\left[\boldsymbol{\Gamma}^{\dagger}\boldsymbol{\Gamma}+\varepsilon\mathbf{I}\right]^{-1}\boldsymbol{\Gamma}^{\dagger}\mathbf{C}$$

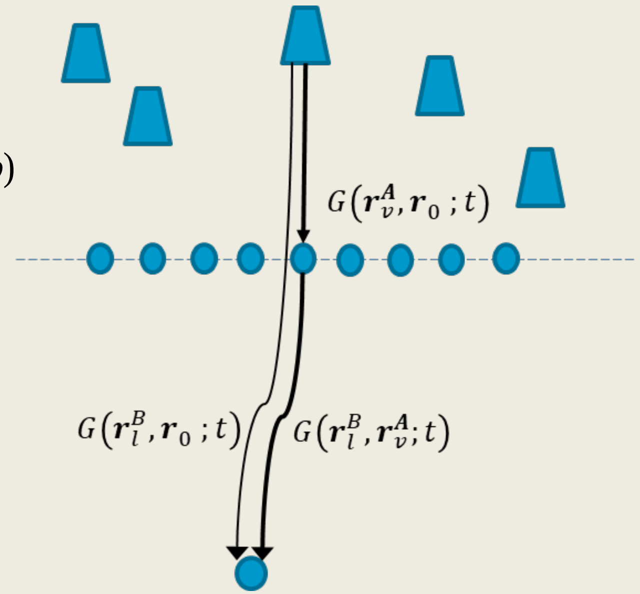

Materials

- Experiments conducted in southern Maryland
  - Sites: Open field and forested area
  - Sources
    - Propane cannon
    - Recorded signal
  - Tri-axial receiving microphone arrays
    - Element spacing: 0.05m
    - Source-receiver range: 100m-600m
    - Sampling frequency: 25 kHz
  - Airmar meteorological sensors:
    - Temperature, humidity, wind speed and direction
  - Lidar: Radial wind velocity

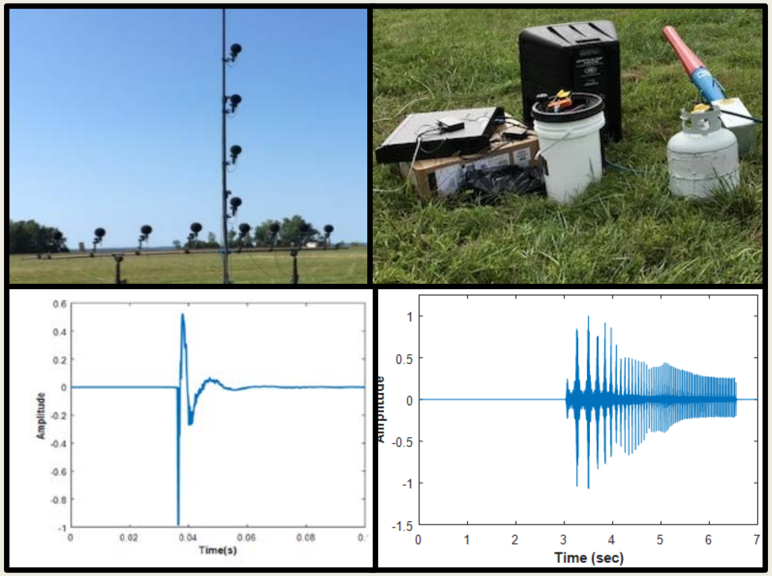

- Atmospheric conditions

Experimental Day	Temperature (C)	Humidity (%)	Wind speed (m/s)	Wind direction (deg)
14 Sep 2016 - Open field	23.0±0.1	77.5±0.7	2.6±0.4	273.0±19.3
15 Sep 2016 – Forest area	22.9±0.2	63.7±0.5	2.2±0.8	67.2±36.8
30 Aug 2017 – Open field	20.6±3.3	66.1±3.71	2.49±0.05	188±108
01 Sep 2017 – Open field	24.0±0.5	58.8±2.2	1.3±0.7	118.0±69.0

Experiment Sites

Plane Wave Beamforming

- Plane wave beamformer

$$\mathbf{b}(\gamma,\theta;\omega) = e^{2\pi i f q\,[\mathbf{x}\cos\theta + \mathbf{y}\sin\theta]}$$

$q = c^{-1}$: Slowness (c: sound speed)

θ : Azimuth angle

$(\mathbf{x},\mathbf{y})$: Cartesian oordinates

- Beam power

$$\mathbf{B}(\gamma,\theta;\omega) = \mathbf{b}^{*}(\gamma,\theta;\omega)\,\mathbf{K}(\mathbf{r}_j,\mathbf{r}_k;\omega)\,\mathbf{b}(\gamma,\theta;\omega)$$

  – Cross spectral density matrix

$$\mathbf{K}(\mathbf{r}_j,\mathbf{r}_k;\omega) = \left\langle \mathbf{p}(\mathbf{r}_j,\mathbf{r}_0;\omega)\,\mathbf{p}^{*}(\mathbf{r}_k,\mathbf{r}_0;\omega)\right\rangle$$

  – Received signal

$$\mathbf{p}(\mathbf{r}_j,\mathbf{r}_0;\omega) = [\,p(\mathbf{r}_1,\mathbf{r}_0;\omega), p(\mathbf{r}_2,\mathbf{r}_0;\omega),\ldots, p(\mathbf{r}_N,\mathbf{r}_0;\omega)]^{T}$$

  – Retrieved GF application

$$K(\mathbf{r}_j,\mathbf{r}_k;\omega) = \begin{cases} G(\mathbf{r}_j,\mathbf{r}_k;\omega) & j \neq k \\ 0 & j = k \end{cases}$$

Source localization: (x_o, y_o)= (300, -100)m

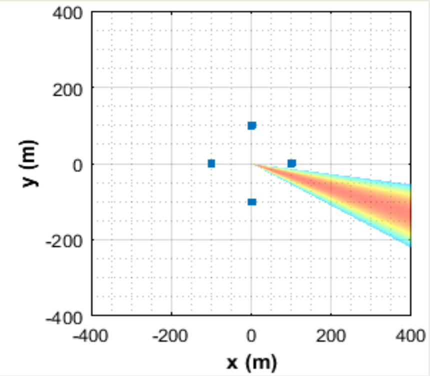

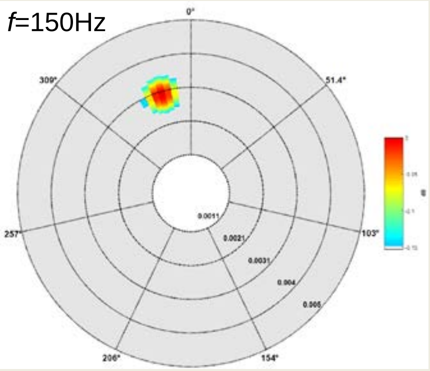

Dispersion relationship

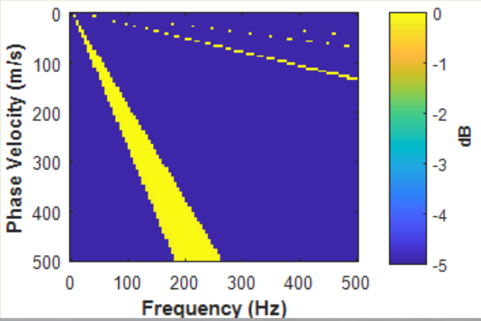

U.S. ARMY RDECOM

Radial Basis Function

ARL

- Forward tomography problem[1]

$$\Delta t_i = \frac{l_i}{c_o}\left(1 - \frac{\mathbf{U}_0 \bullet \mathbf{L}_i}{c_o}\right) - \int_{x_{i1}}^{x_{i2}} \left(\frac{\Delta T(x)}{2T_o c_o} + \frac{\Delta \mathbf{U}(x) \bullet \mathbf{L}_i}{c_o^2}\right) dl_i$$

$\mathbf{U} = (u_x, u_y)$: Wind velocity vector

T : Temperature

$\mathbf{L}_i$: Unit vector parallel to the sound ray

l_i : Length along the ray path

$(c_o, \mathbf{U}_0, T_o)$: Field mean values (Airmar)

  – Radial basis function[2]

$$\Delta T(x) = \mathbf{\Phi}_T(x)\mathbf{W}_T$$

$$\psi(x) = \mathbf{\Phi}_\psi(x)\mathbf{W}_\psi \Rightarrow \left(\Delta u_x = \frac{\partial \psi}{\partial x}, \Delta u_y = \frac{\partial \psi}{\partial y}\right)$$

  – RBF tomographic Inversion

$$\mathbf{d} = \mathbf{\Omega}_T \mathbf{W}_T + \mathbf{\Omega}_\psi \mathbf{W}_\psi$$

$$\mathbf{W} = (\mathbf{\Omega}^T \mathbf{\Omega})^{-1} \mathbf{\Omega}^T \mathbf{d}$$

Gaussian RBF: $\phi(r) = e^{-kr^2}$

Target $\Rightarrow$

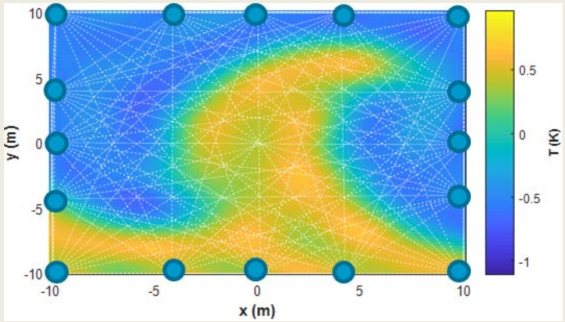

Reconstruc ted $\Rightarrow$

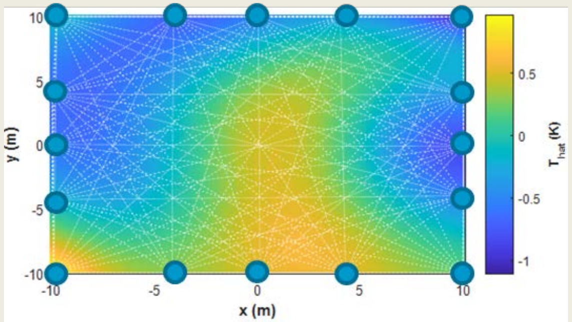

Wind velocity $\Rightarrow$

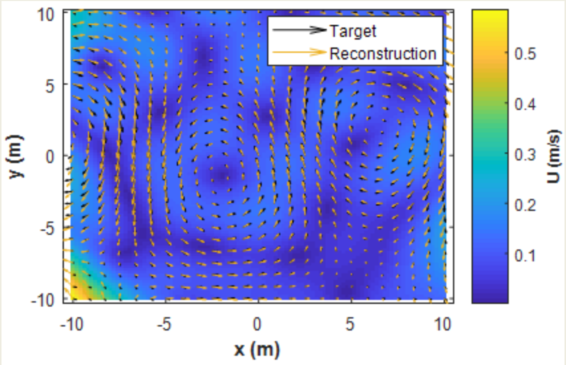

[1]Ostashev et al. (2008)

[2]Weins (2008)

Data Processing

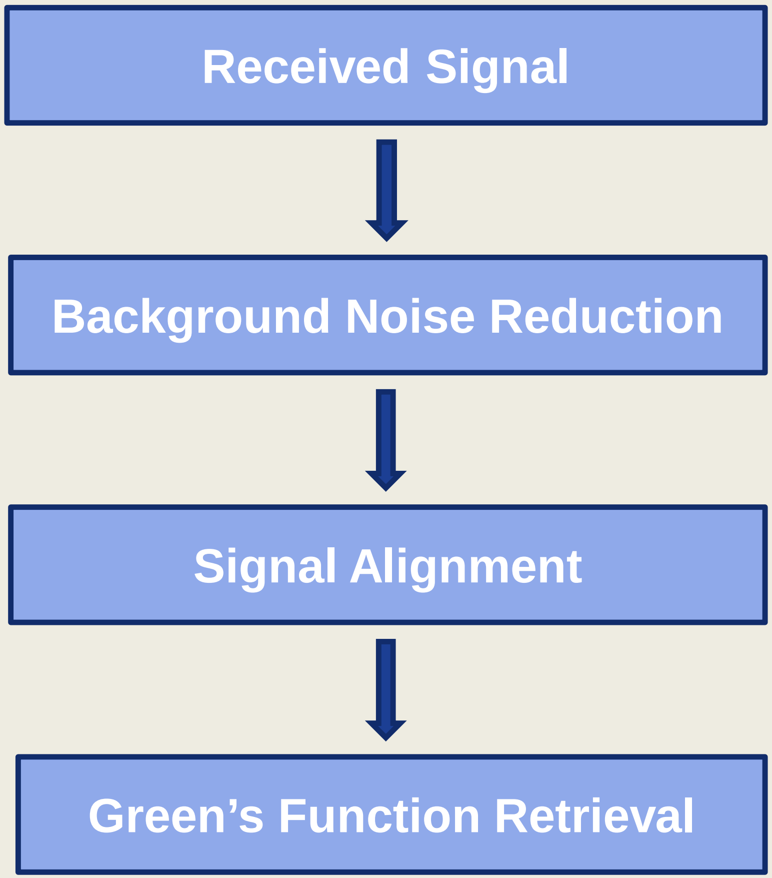

Data Processing:

- ***Calibration***
  - Recorded signal calibrated
- ***Background noise reduction***
  - Bandpass filter: 60Hz-3kHz
  - Weiner filter
- ***Signal alignment***
  - Matched filter with reference signal
  - Peak detection
- ***Green’s function retrieval***
  - CC method
  - MDD method

Open Field Experiment
14 September 2016

Estimated Green's Function Open Field, Propane Cannon

100 ⟷ 400

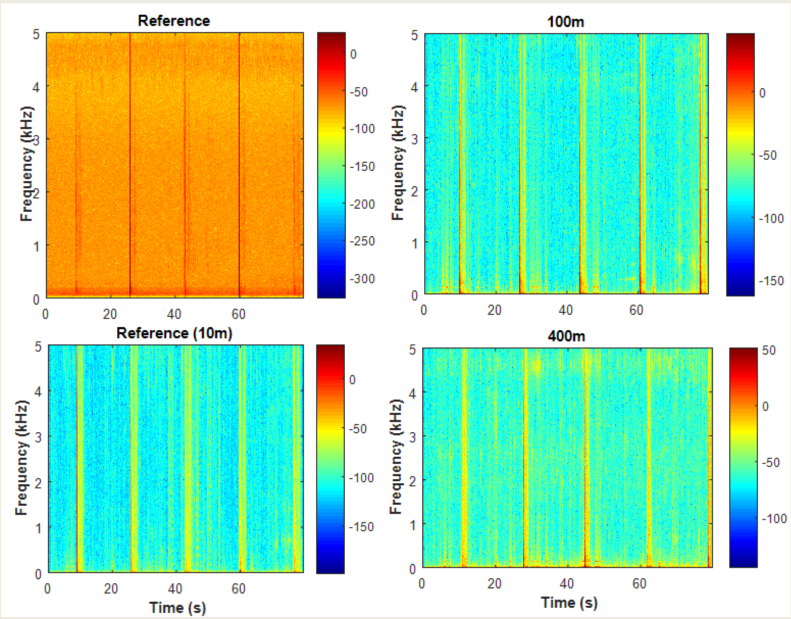

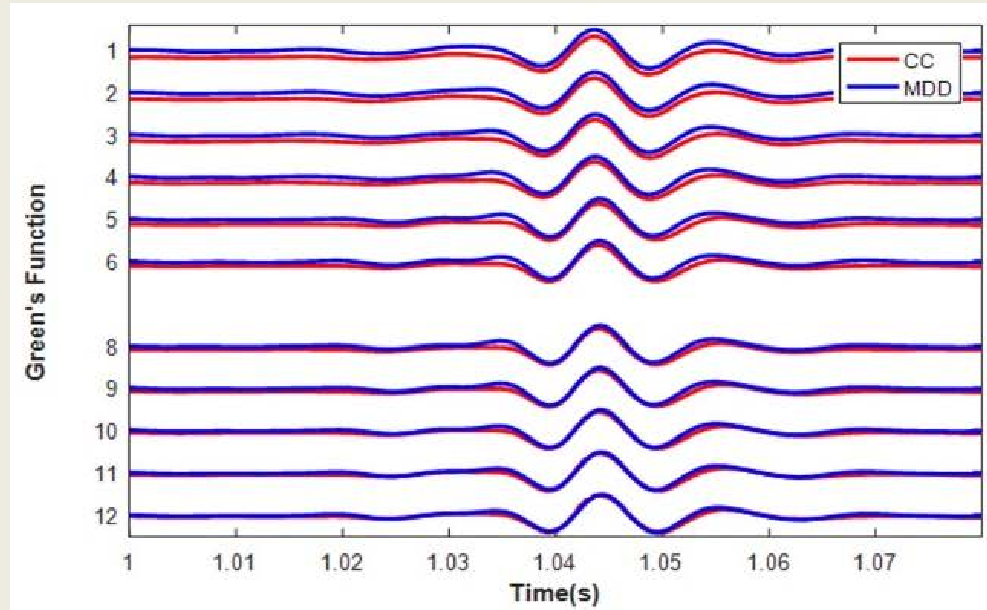

Beamforming Analysis

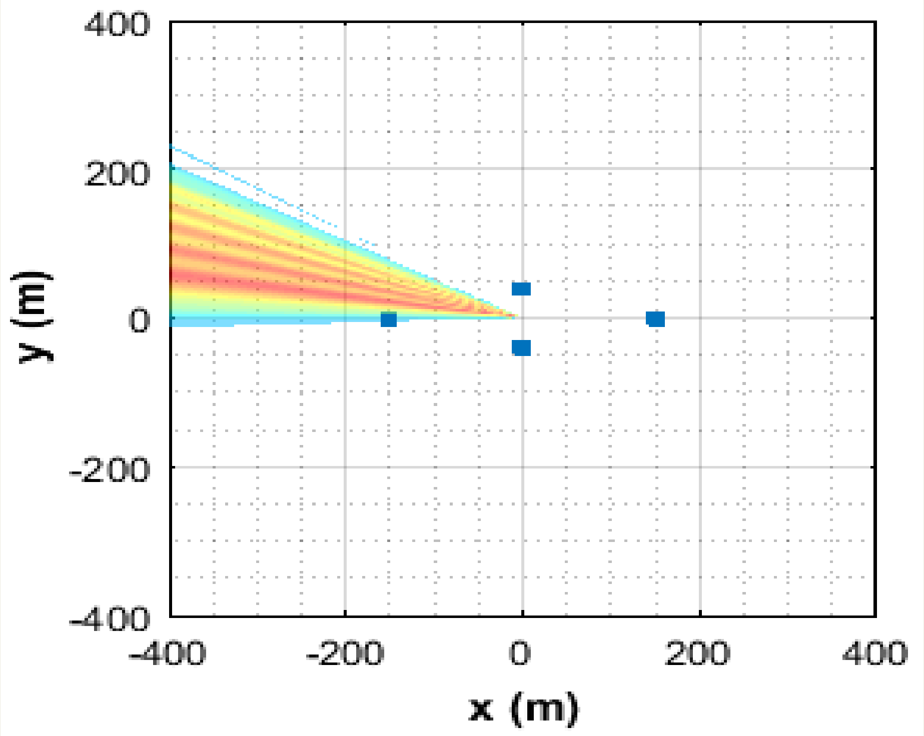

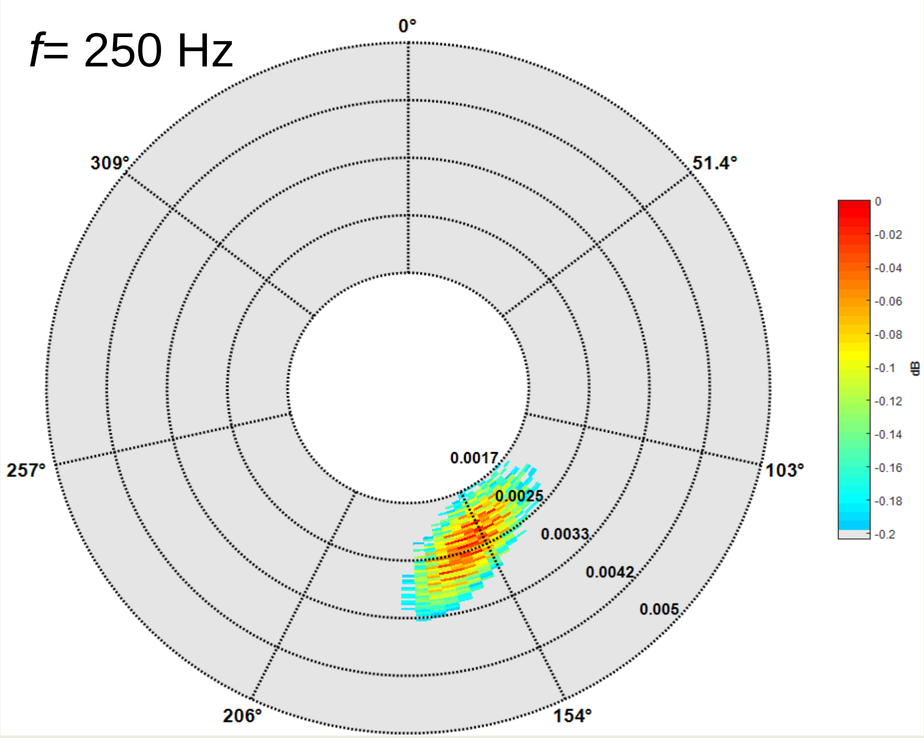

Dispersion Analysis

$c \sim 400\ m/s\ @\ 250\ Hz$

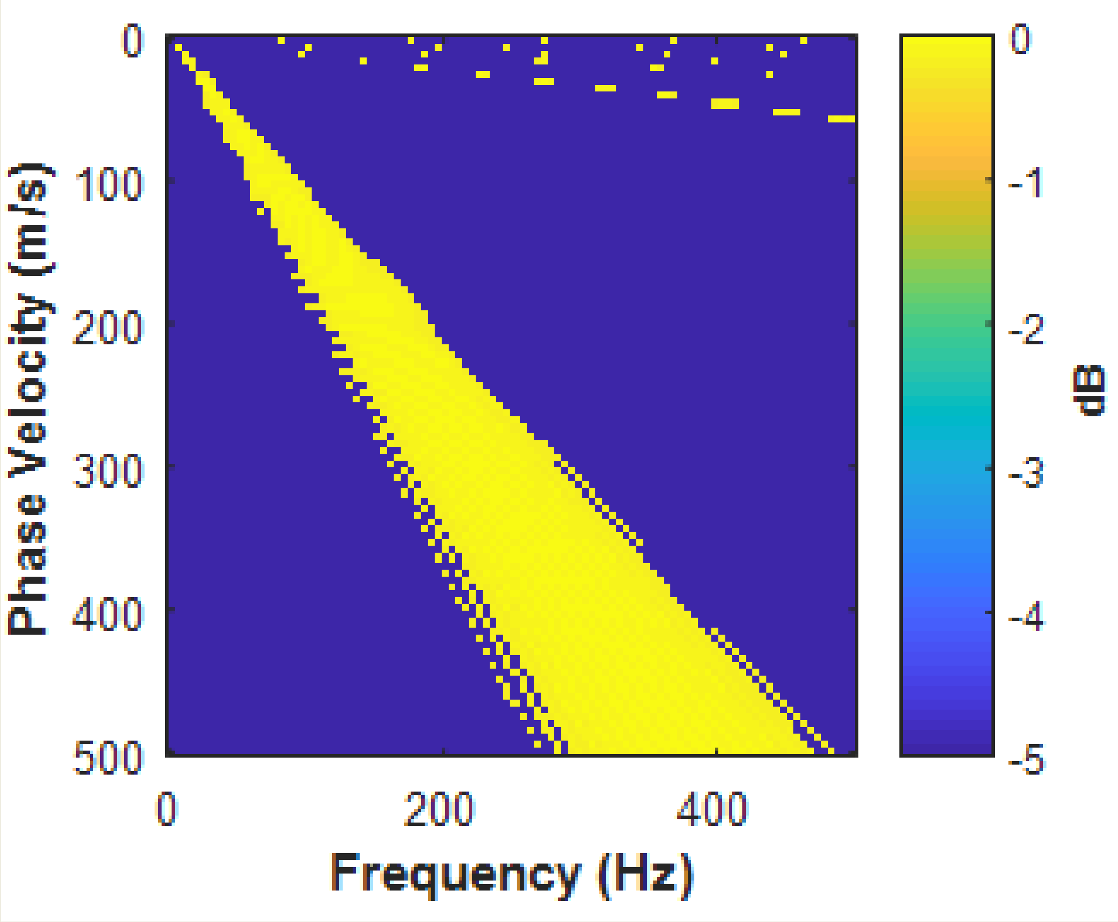

Forest Area Experiment
15 September 2016

Estimated Green's Function
Forest Area, Propane Cannon

100 ⟺ 300

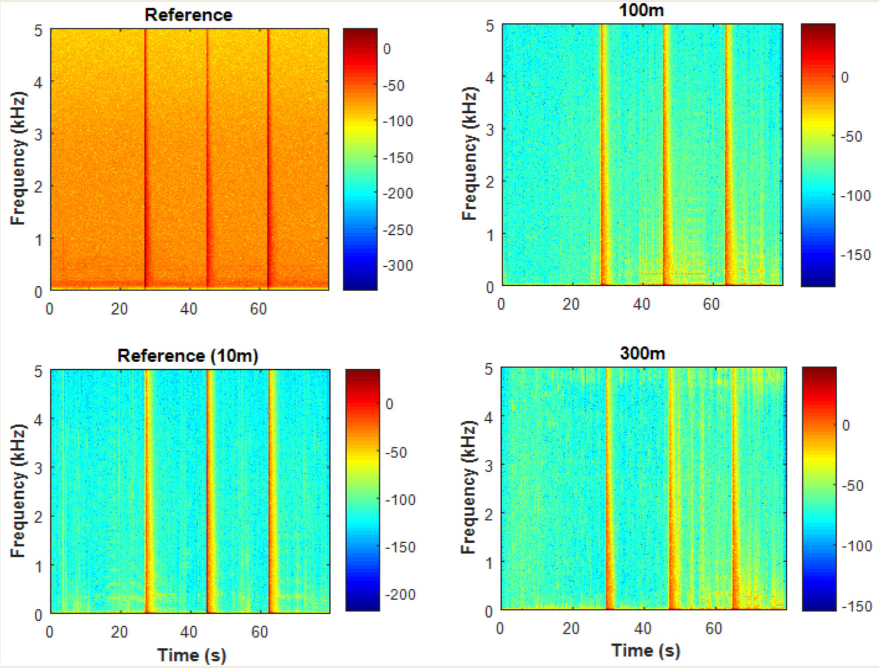

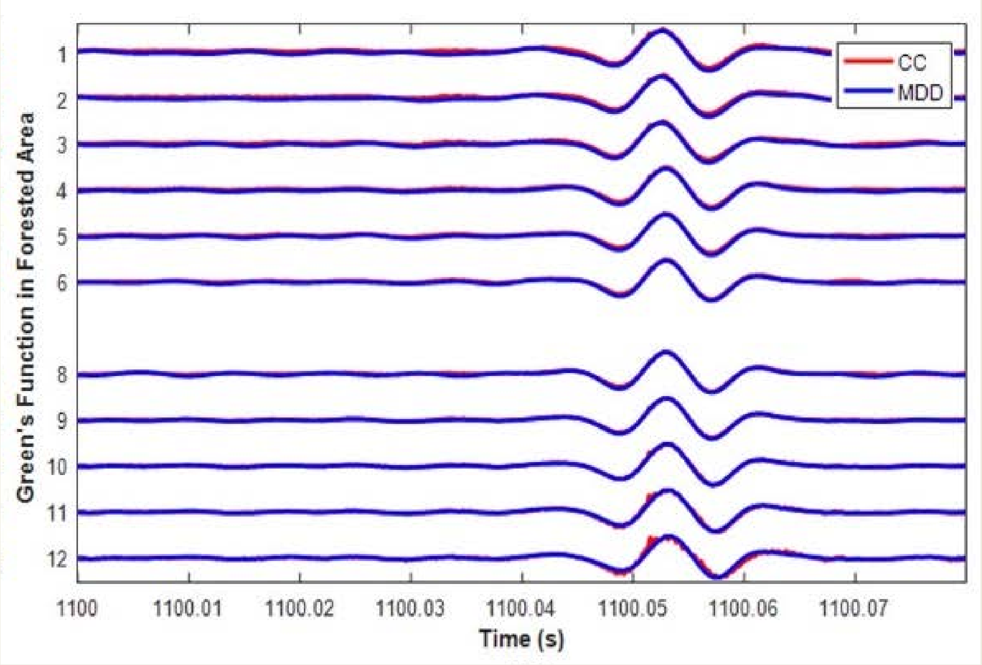

Beamforming Analysis

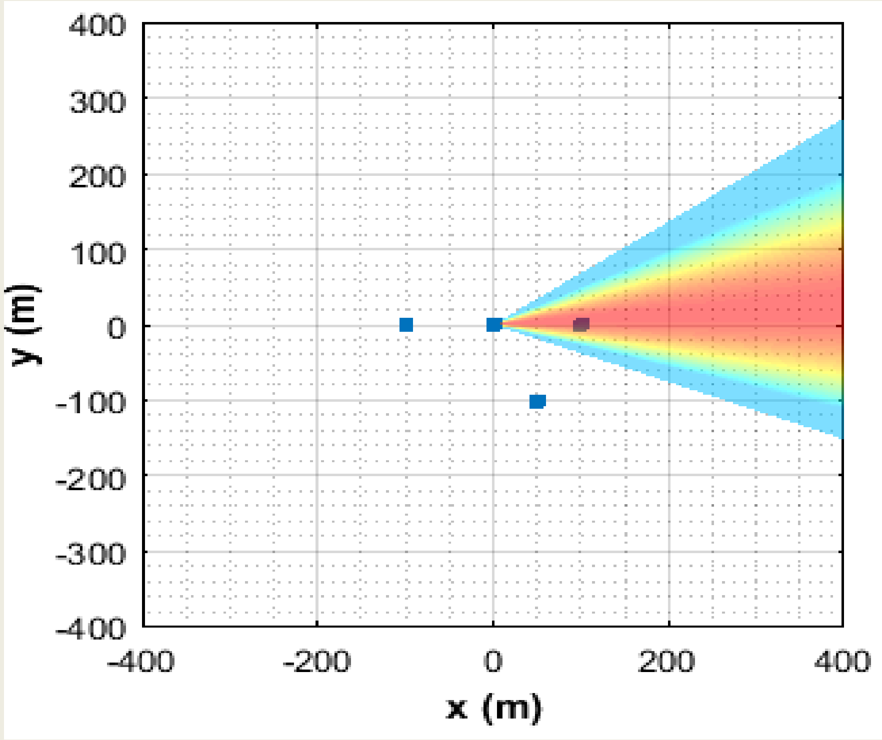

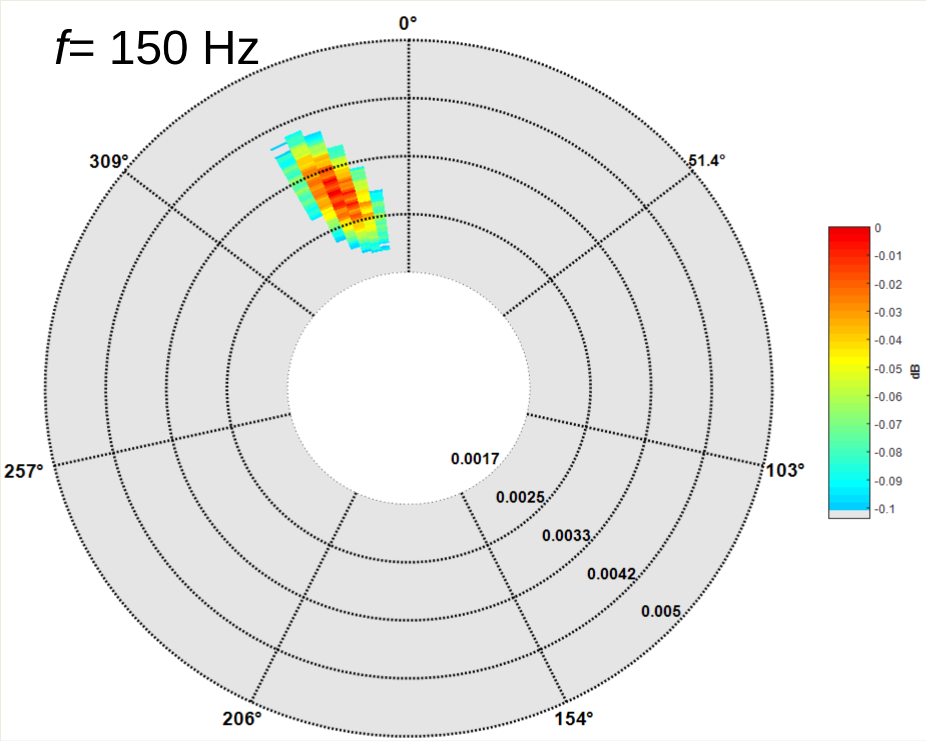

Dispersion Analysis

$c \sim 344\ m/s\ @\ 150\ Hz$

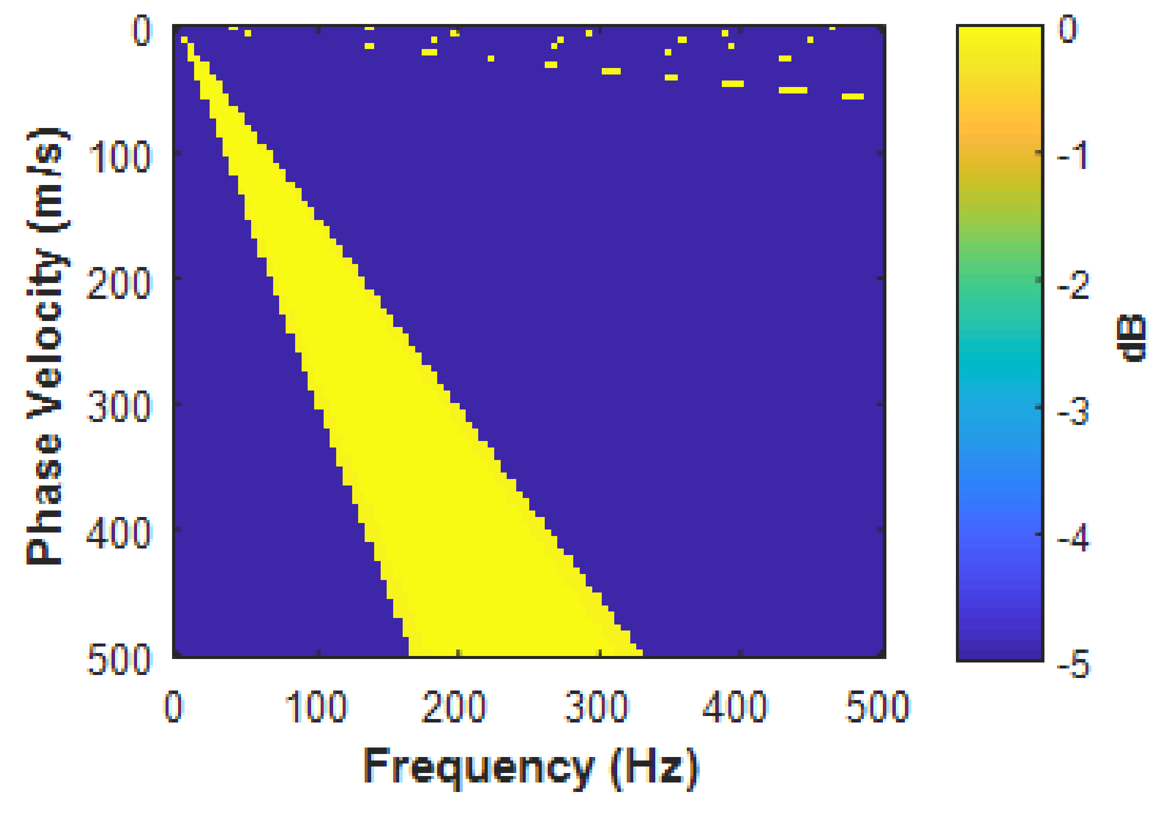

Open Field Experiment
30 August 2017

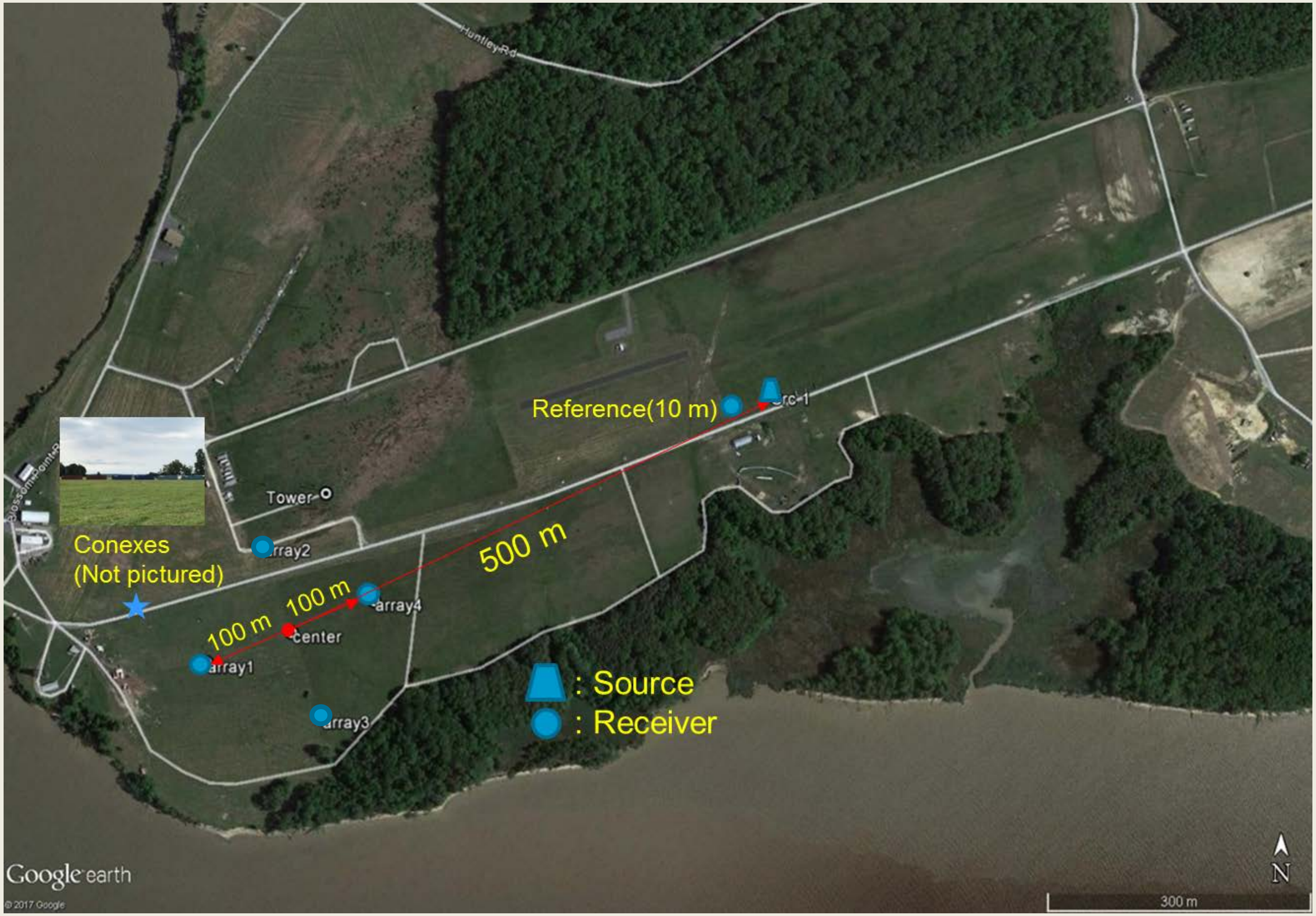

Estimated Green's Function
Open Field, Propane Cannon

400 ⟷ 600

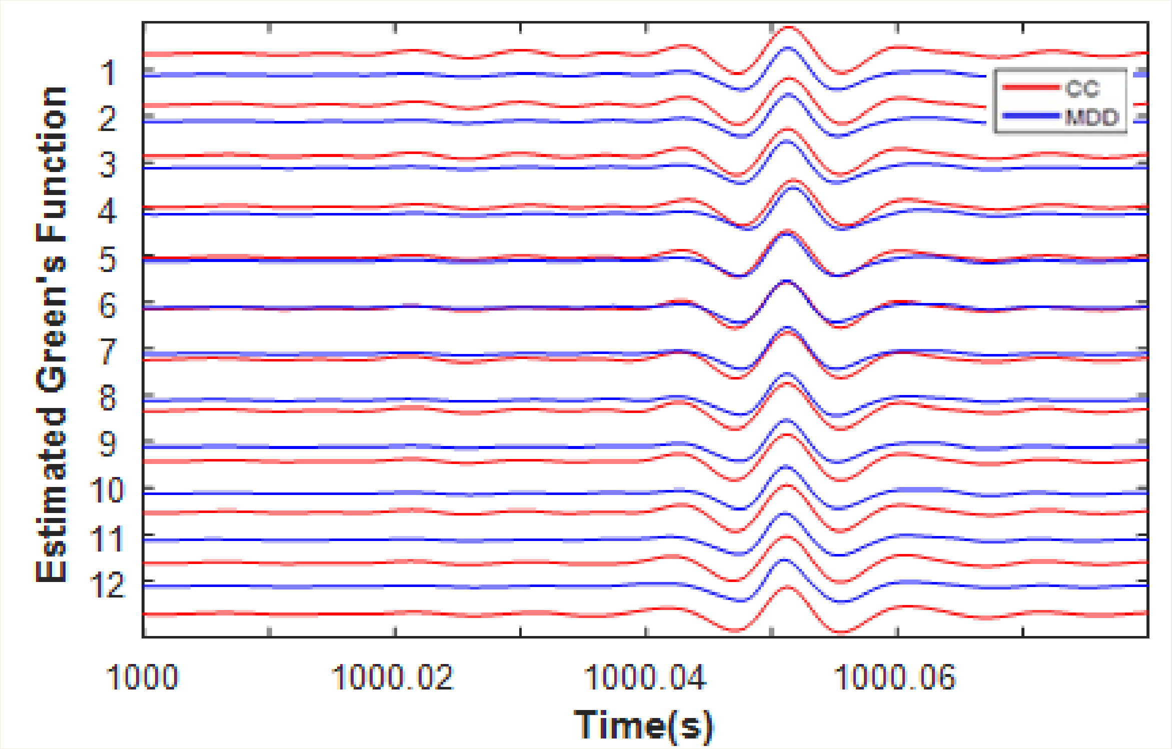

Beamforming Analysis

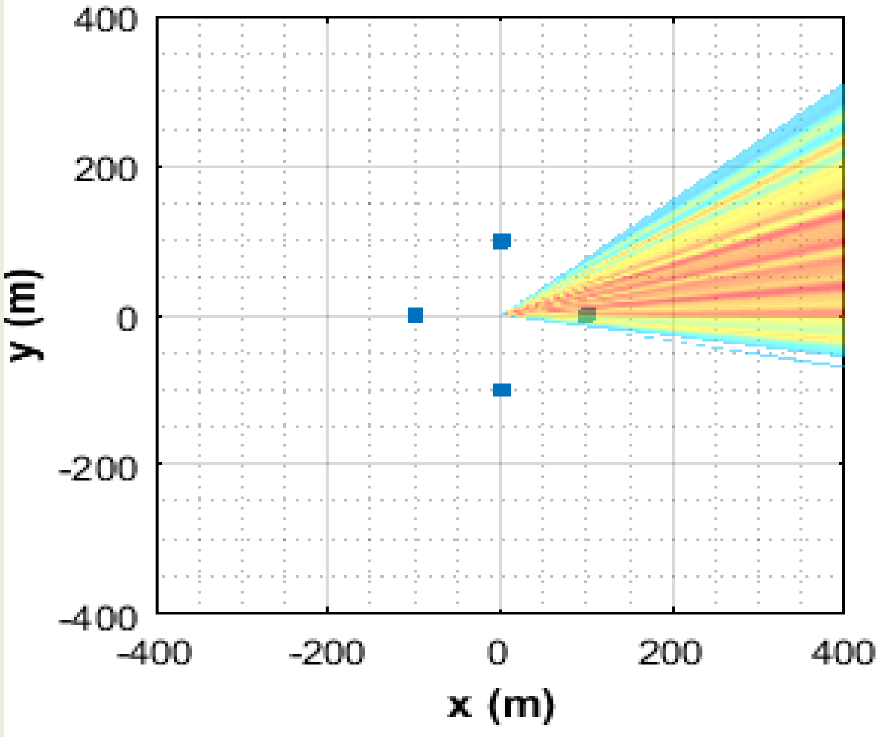

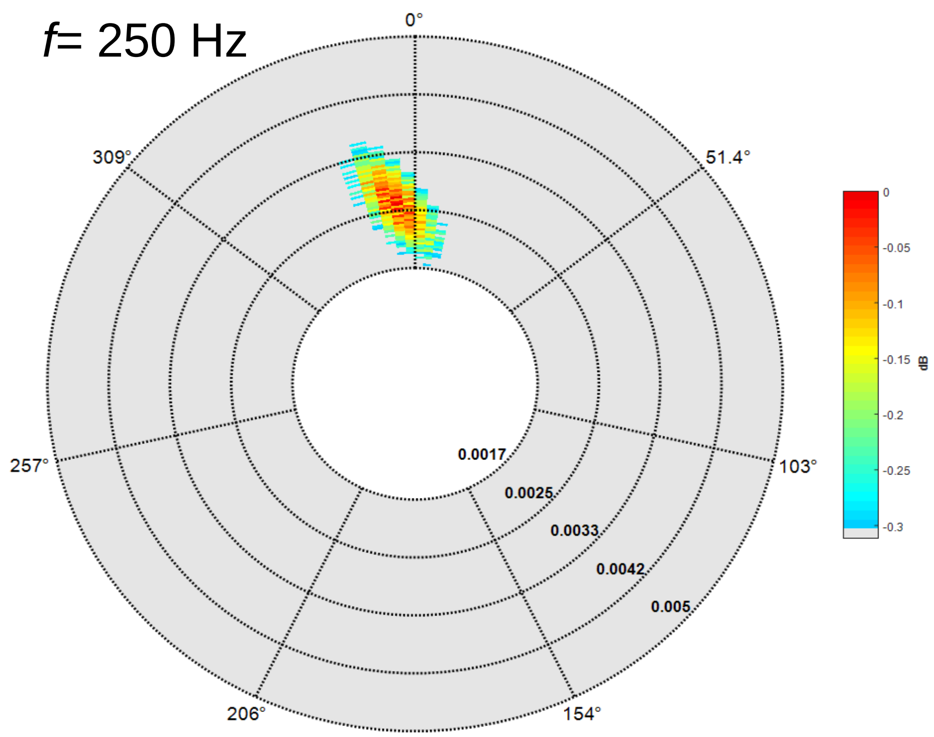

Dispersion Analysis

$c{\sim}400\ m/s\ @\ 250\ Hz$

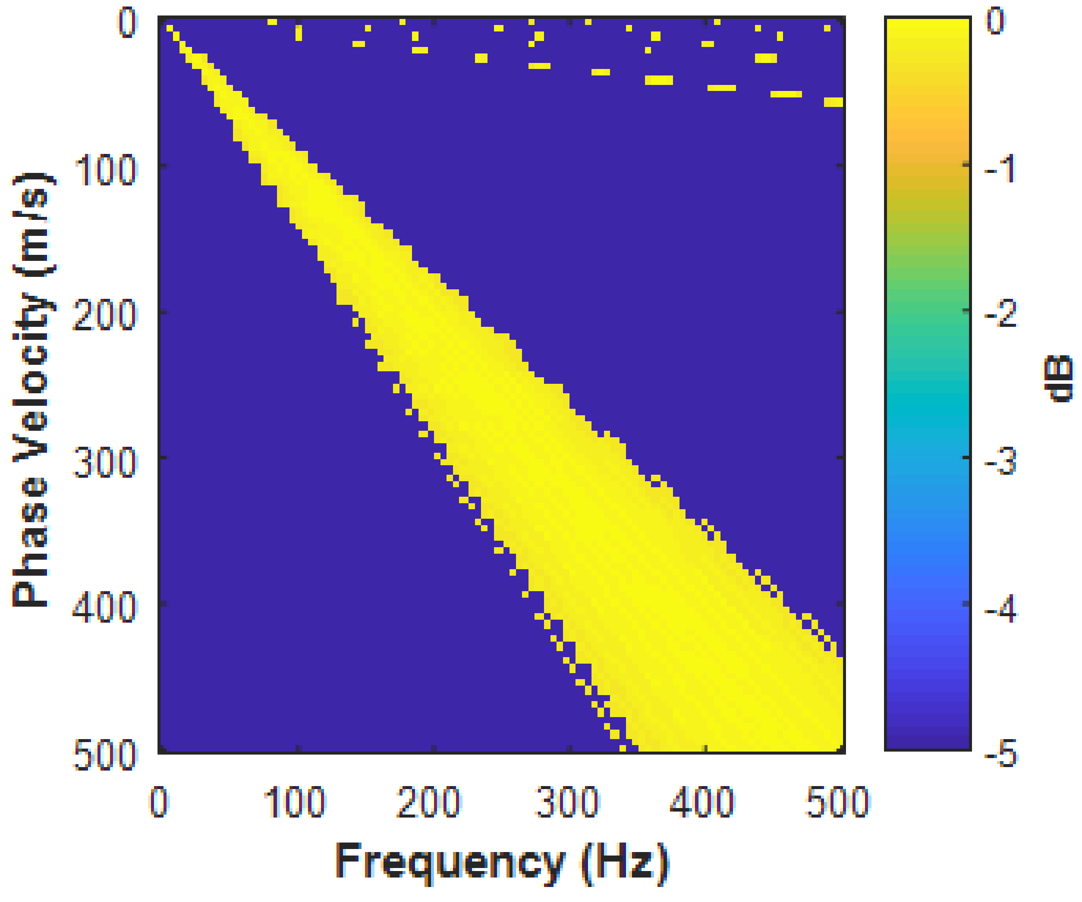

Beamforming Analysis
Open Field, 01 September 2017

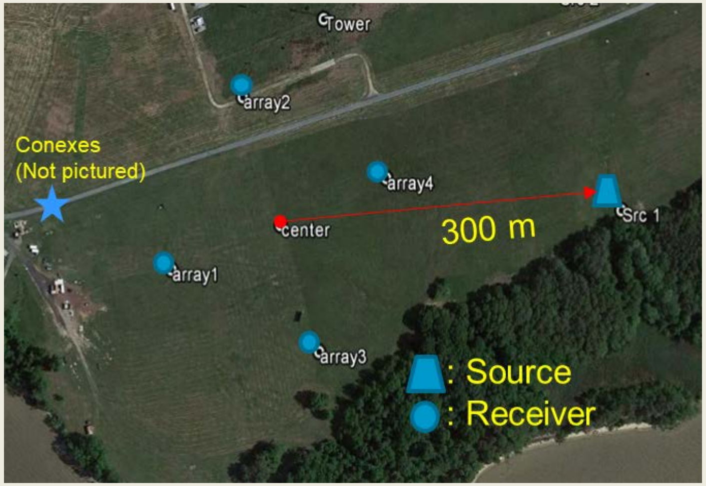

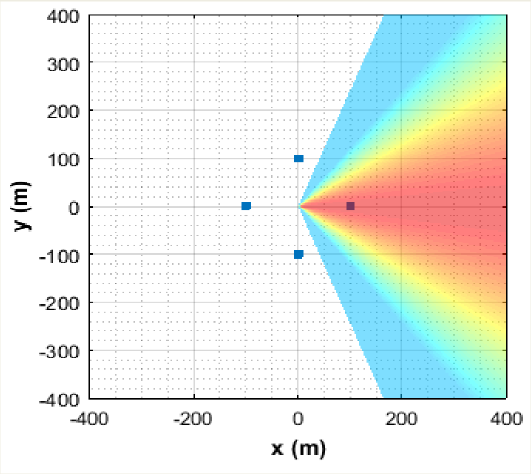

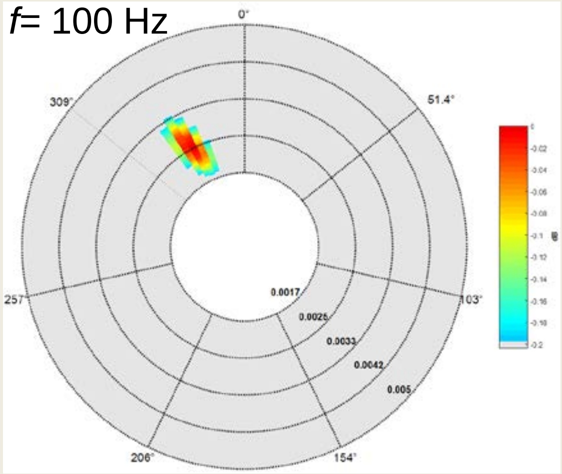

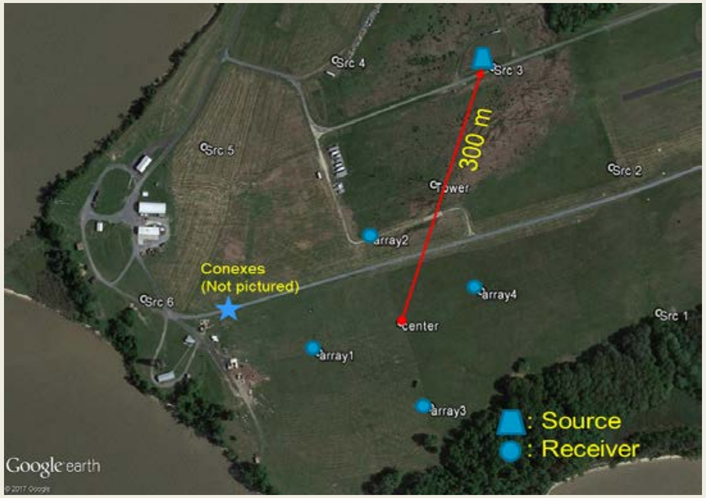

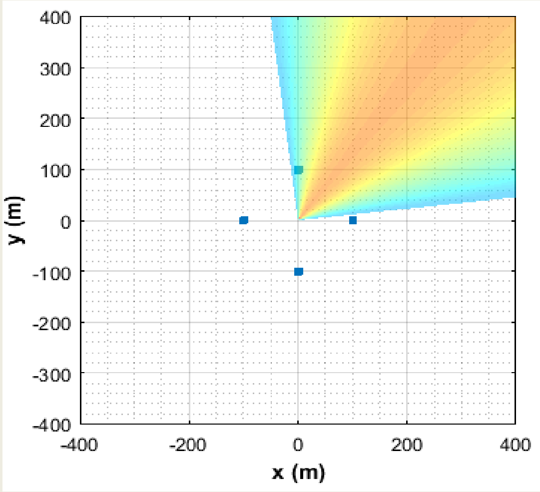

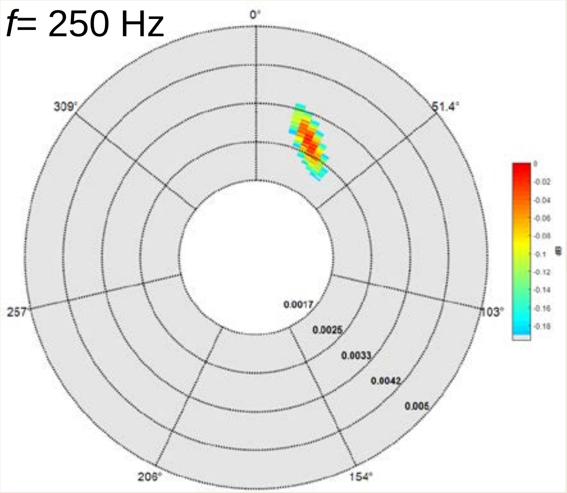

Dispersion Analysis

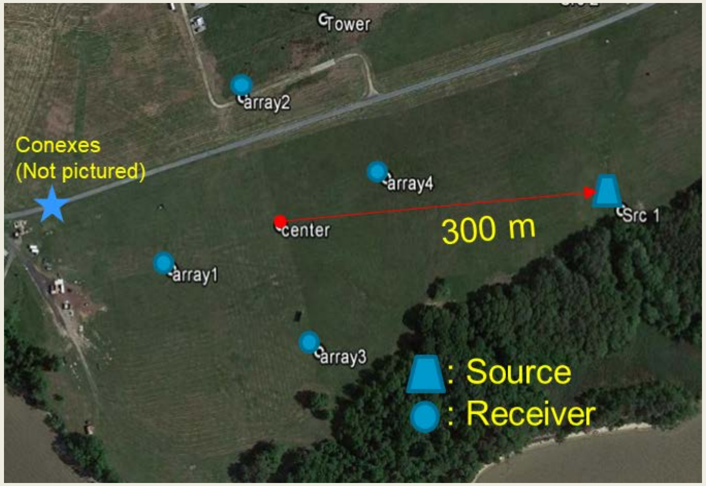

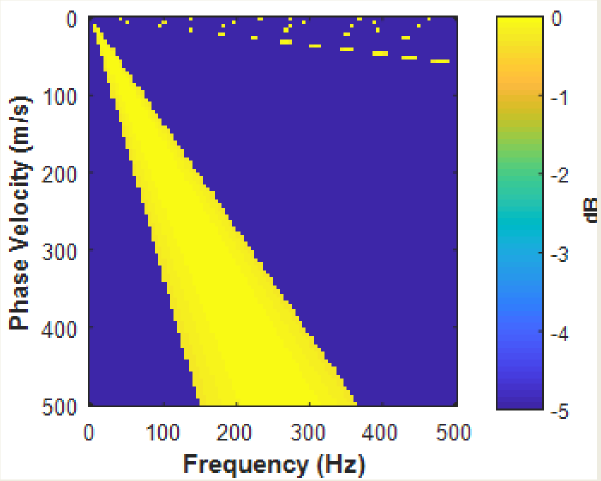

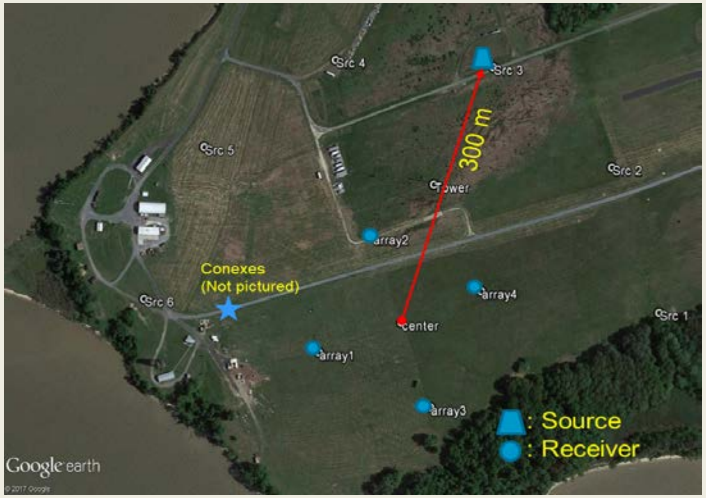

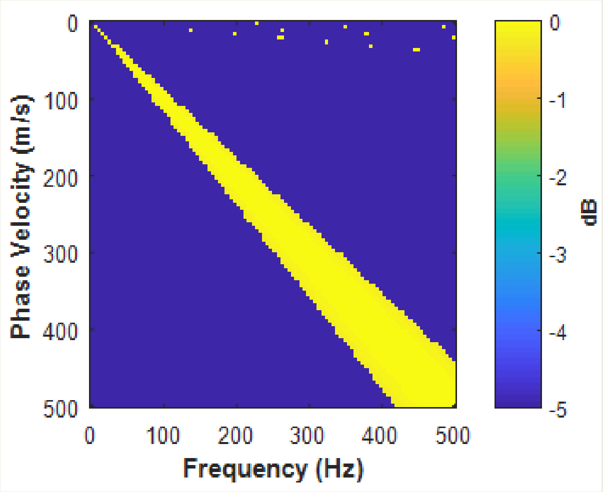

Beamforming Analysis
Open Field, 01 September 2017

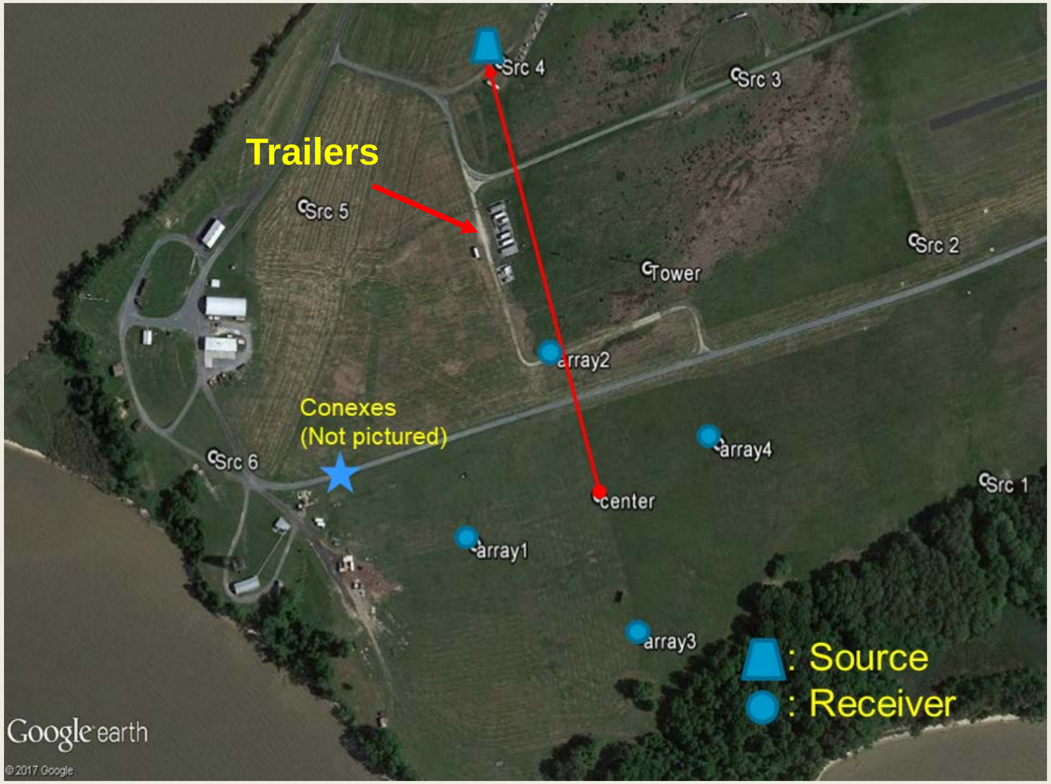

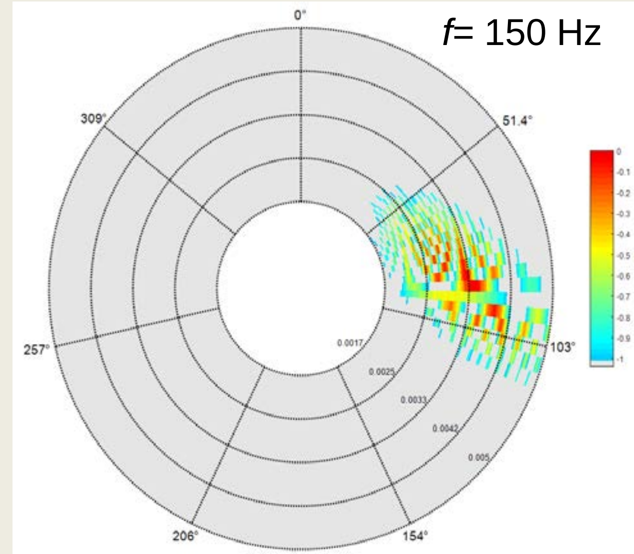

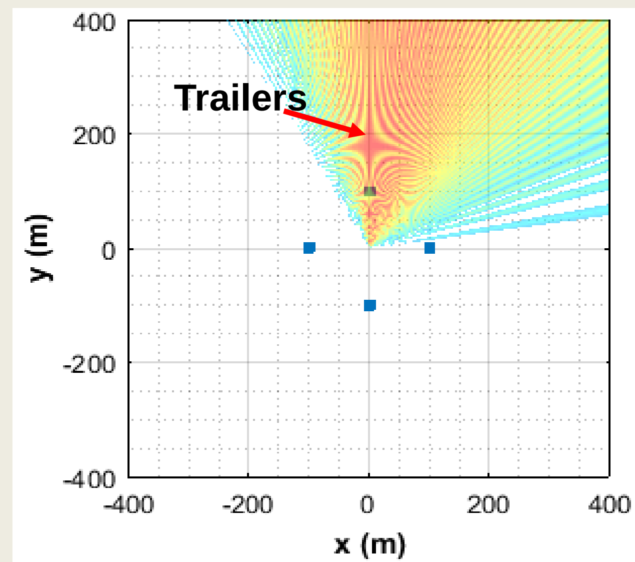

Dispersion Analysis

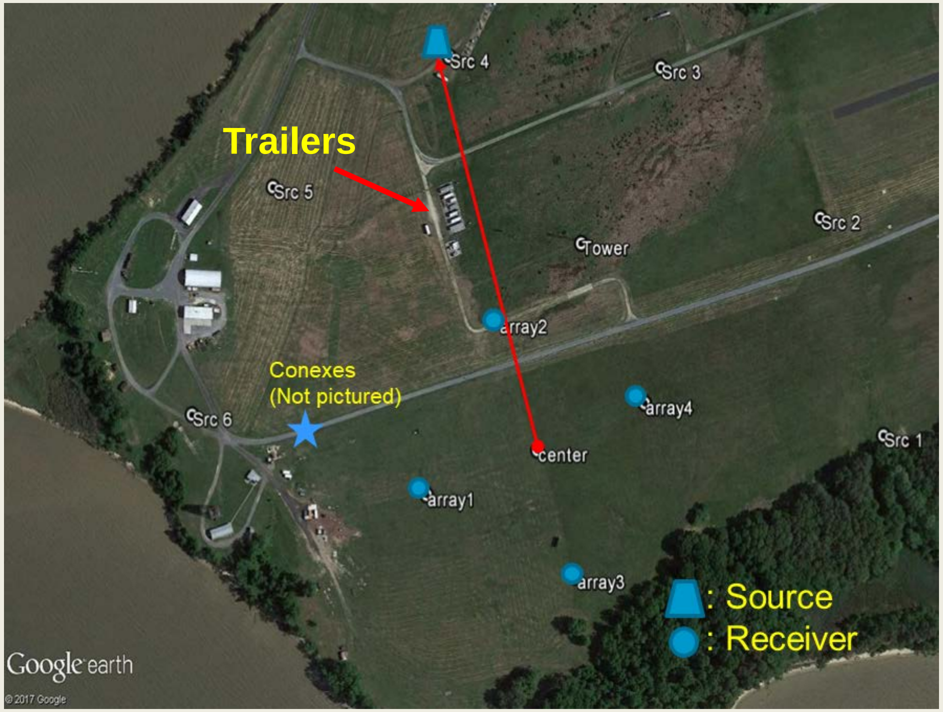

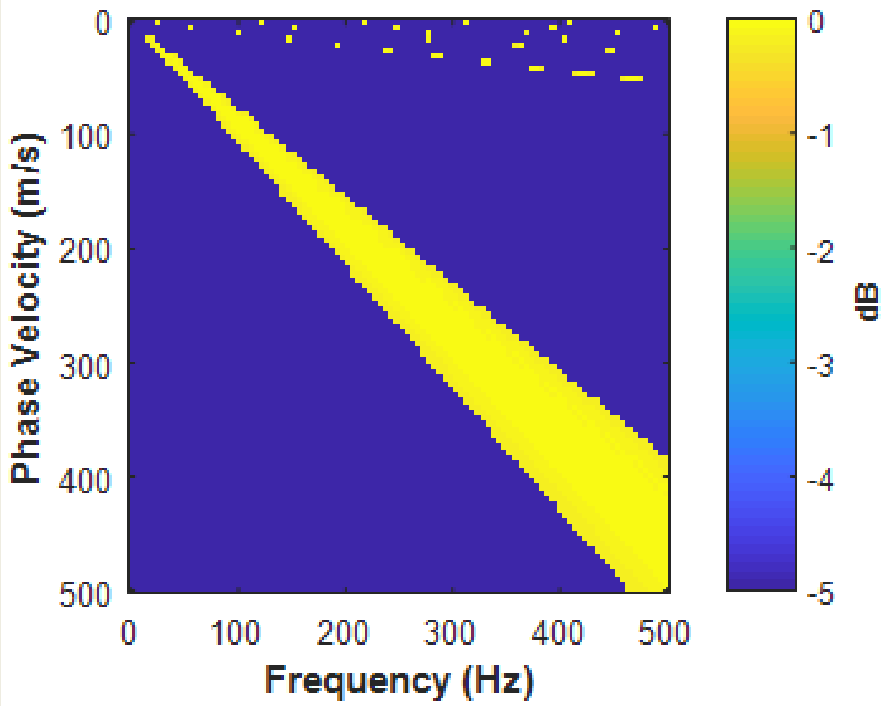

Beamforming Recorded Signal

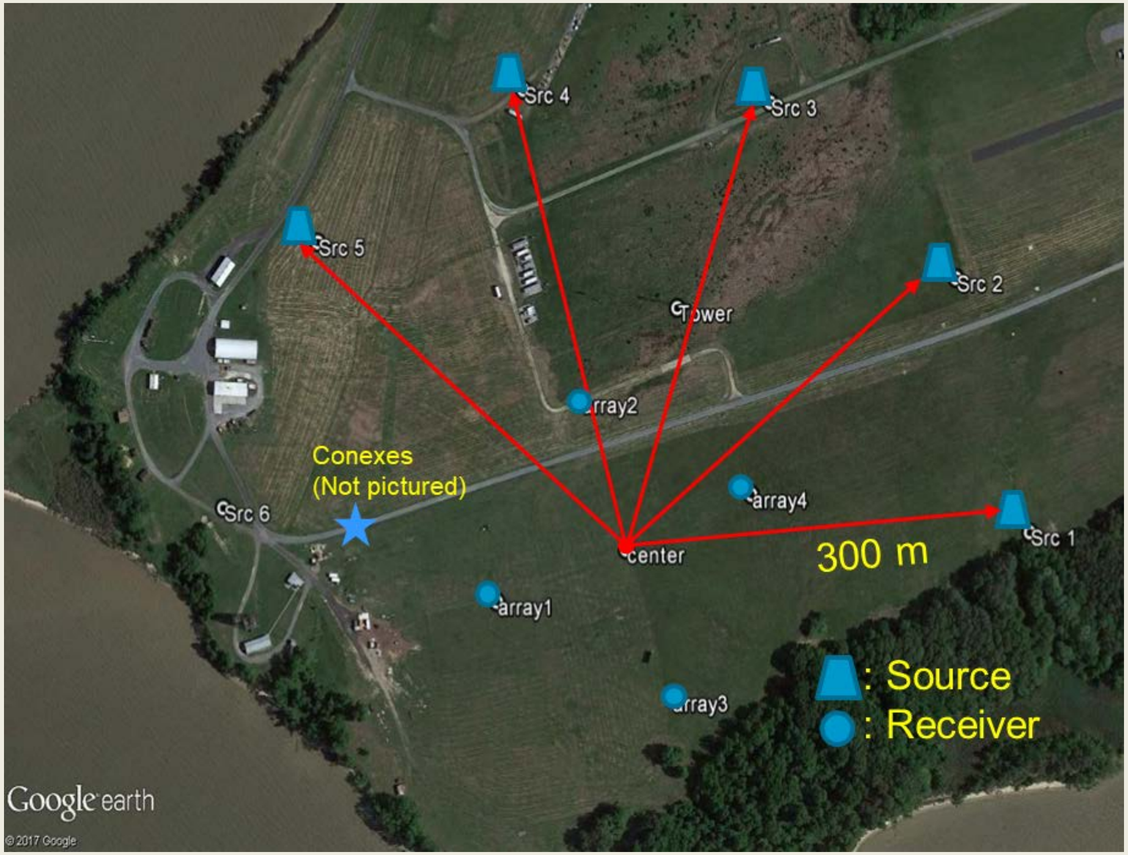

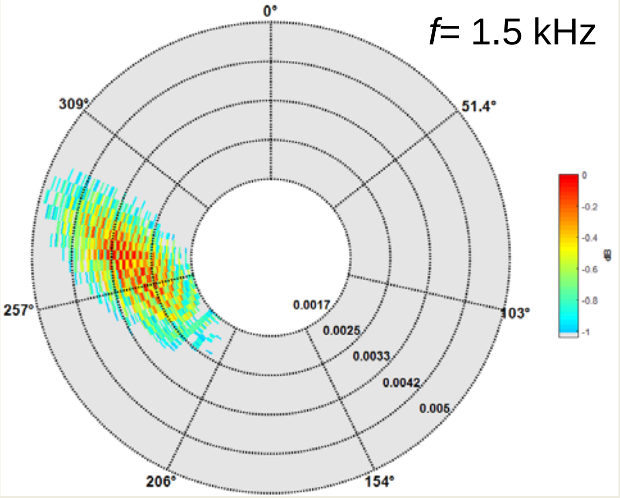

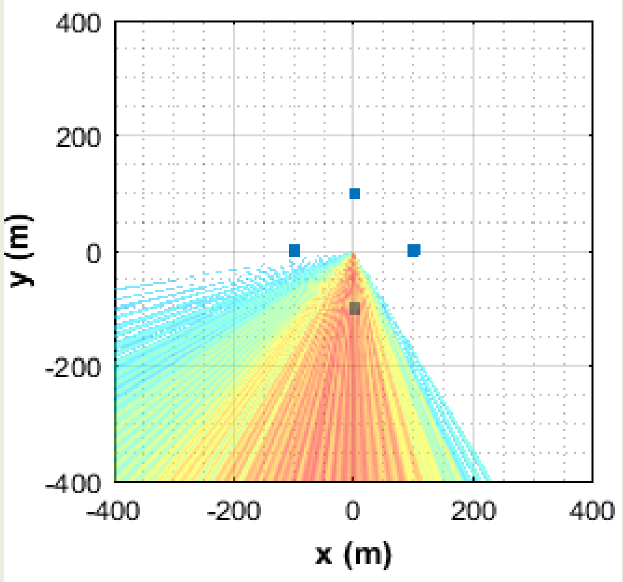

Acoustic Tomography

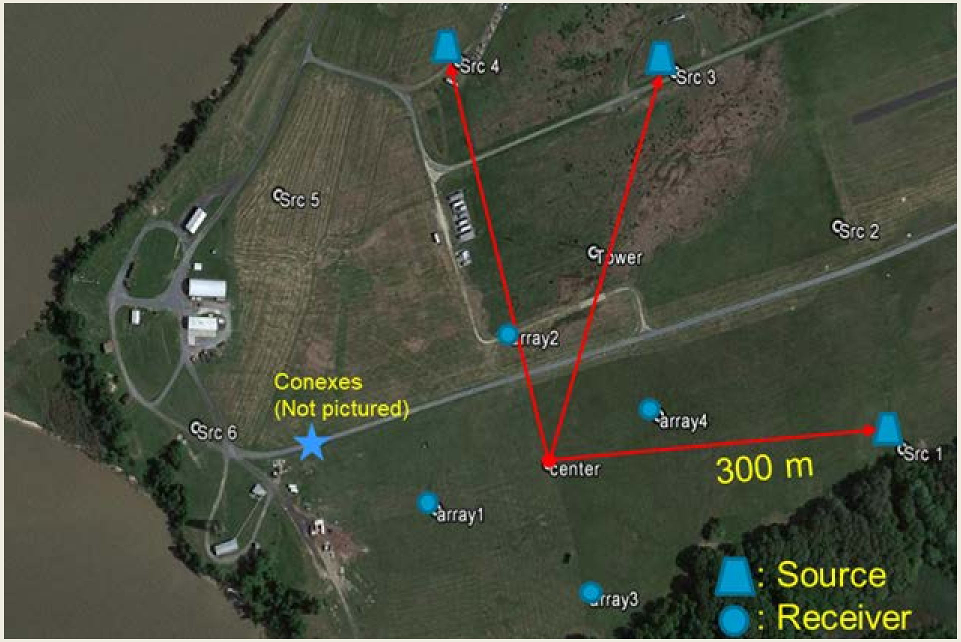

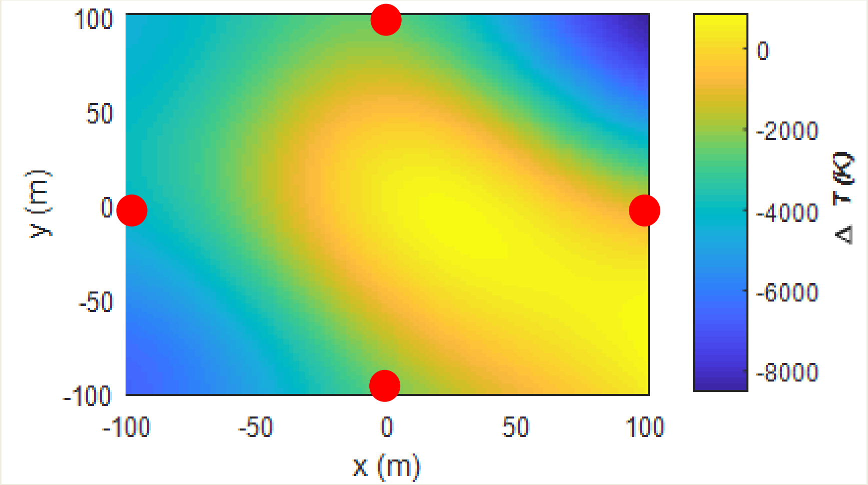

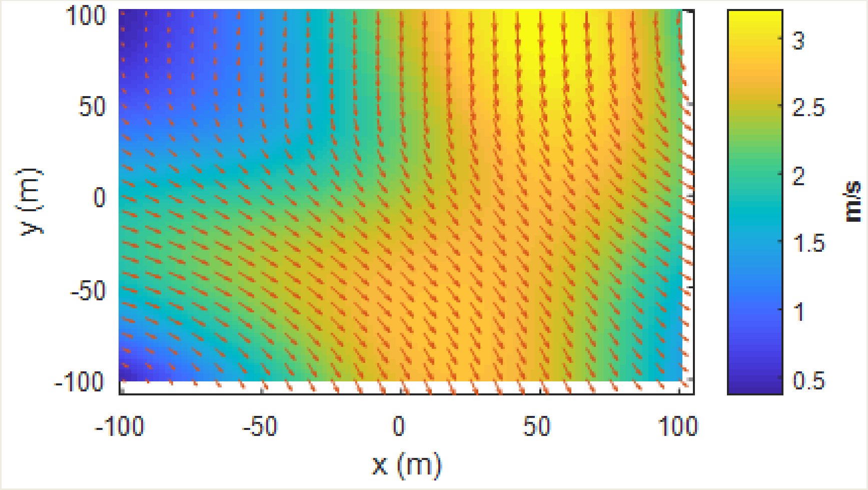

Summary

- Acoustic imaging techniques utilizing retrieved GFs were presented
  - Beamforming can localize acoustic sources and scatterers
  - Beamforming allowed for dispersion characterization
- Acoustic tomography using radial basis functions was presented
  - Coarse temperature and wind velocity maps were reconstructed
  - Additional microphone array stations are needed to increase the resolution
- Future Work
  - Incorporate MDD results for recorded signals into beamforming analysis
  - Increase the resolution for acoustic tomography maps.

An experimental study of the atmospheric-driven variability of impulse sounds

ISL, France	S. Cheinet, M. Cosnefroy, A. Dagallier
ARL, USA	S. Collier
CRREL, USA	V. Ostashev, K. Wilson
WTD91, Germany	W. Rickert, T. Wessling

Motivation

- **Context**

  Shot sounds change with the near-surface atmosphere,

  Major fluctuations in the shot sensing performance

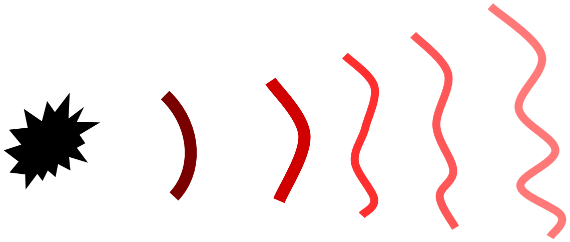

- **Topic of this study**

Experiment on the

sensitivity of model shots (impulse sounds) to environmental parameters

Emphasis on metrics relevant to sensing:

Pulse shape, pulse TOA, coherence between sensors

- **Overview**
    - Results
    - Summary

Overview

Meppen, NW Germany, 17-21 October 2016

500m x 600m flat field, Agricultural surroundings

Cloudy, 10-15°C, low-to-moderate winds

Experimental components

Gas cannon, 156 dB peak

Omni-directional loudspeaker

14 mics, bars of 3 mics

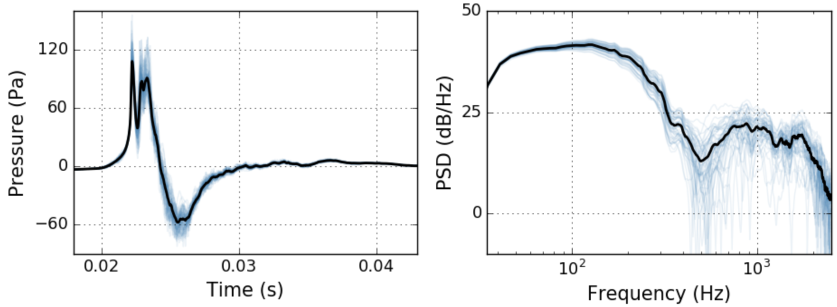

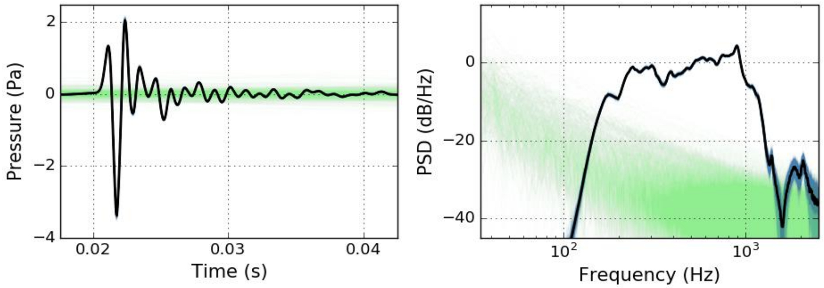

Experimental components

Gas cannon, 156 dB peak

Omni-directional loudspeaker

14 mics, bars of 3 mics

Atmospheric characterization
Including turbulence

Ground characterization

Environmental characterization

- ✓ Ground

  Grass surface,

  data fit with expectations

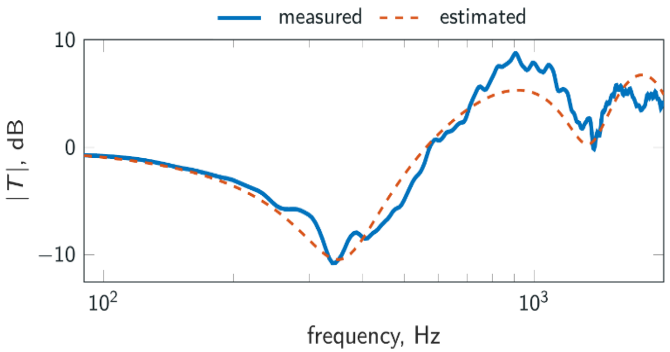

- ✓ Atmosphere

  Moderate wind, wind modulus fits with expectations (MOS)

  Turbulence is intemittent, and anisotropic, <u>even for short eddies</u>

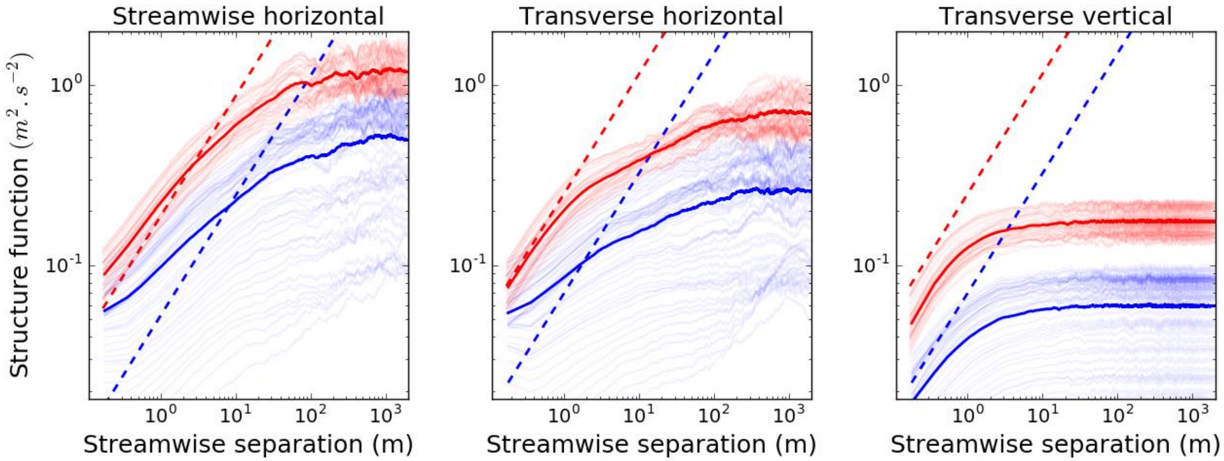

Overview

Results

Summary

Pulse modulations by the environment

Illustrate the 56 consecutive shots in a circle configuration, 30 mn

- More experimental tests
- Literature
- Modeling (FDTD, Rays)
- Cf. next presentation

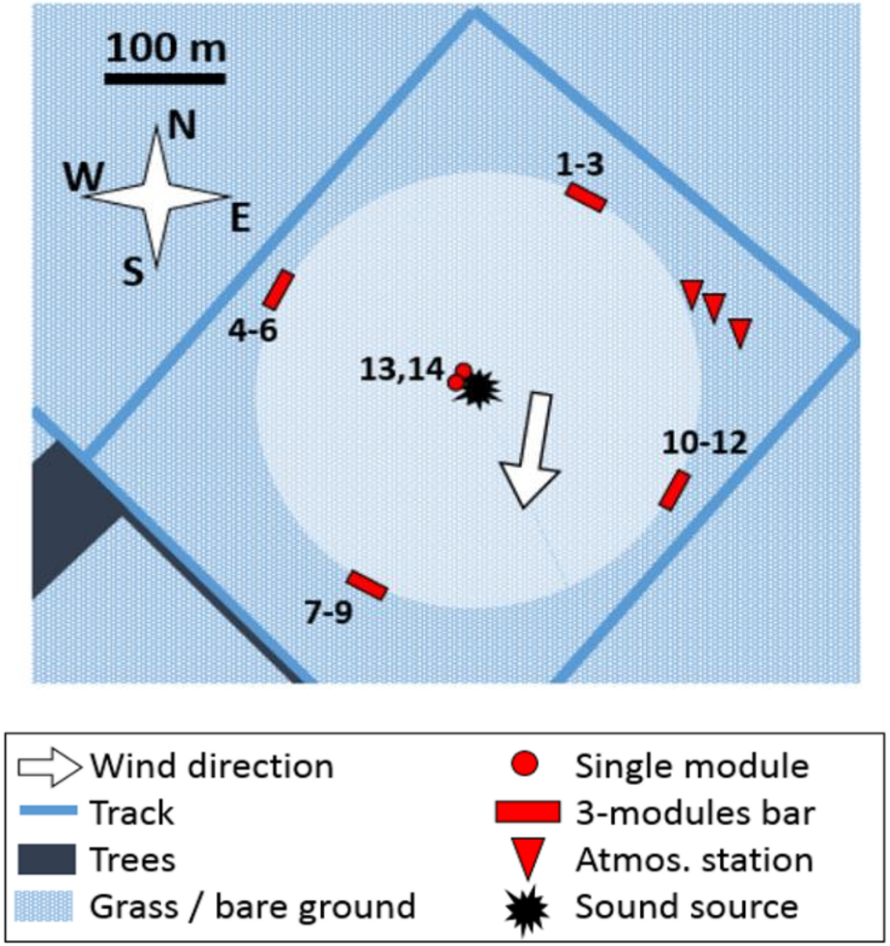

Pulse modulations / wind convection, range

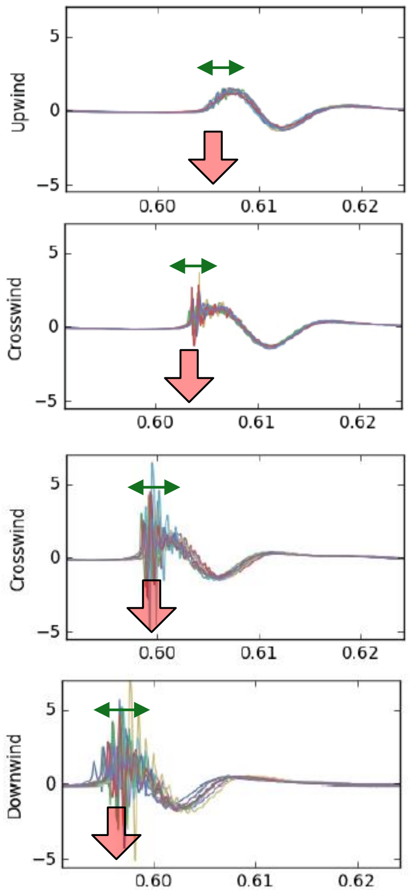

$$TOA \sim \frac{r}{(c_0 + \bar{u}\cos\theta)} + \Delta TOA + \cdots$$

Simple propagation

Wind convection

Pulse wander (turbulence)

Sensor positioning uncertainty

Refraction of ray, diffraction

Hereafter, resynchronize signatures to the TOA

Pulse modulations / synched signals

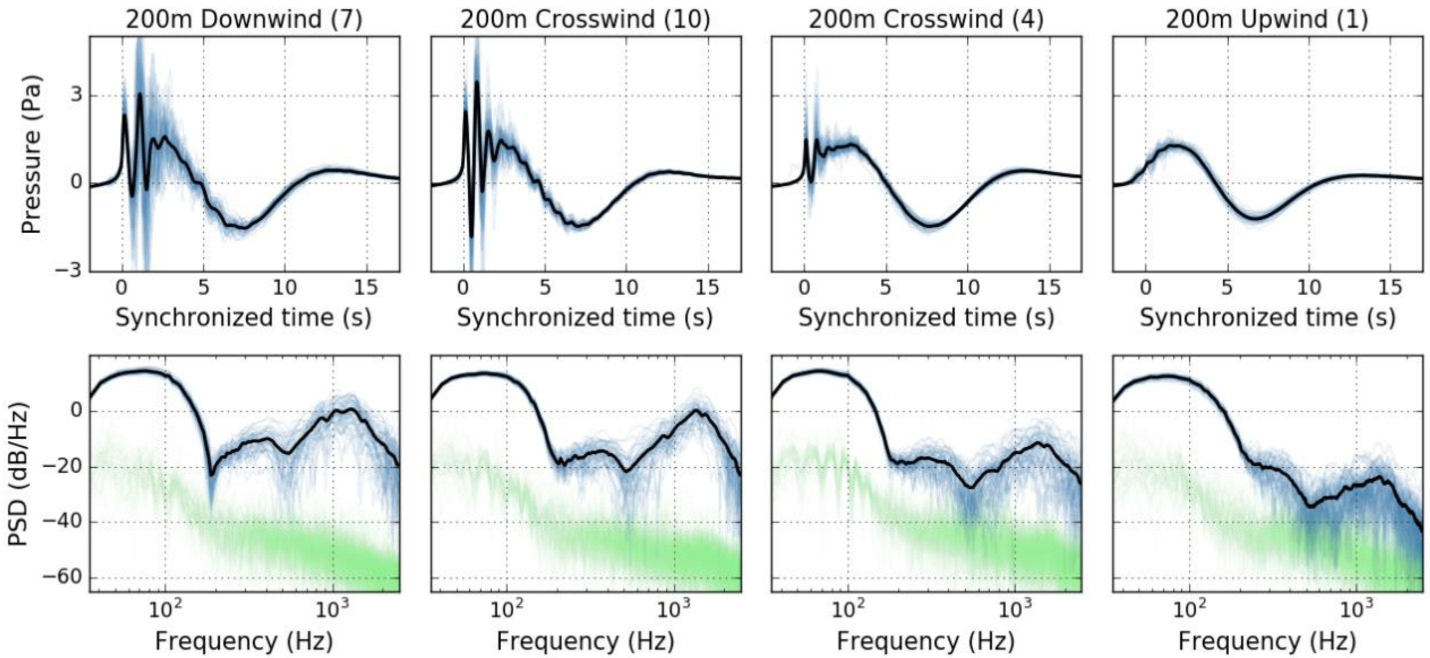

- Signal always above noise
- Strong recombinations of the signature
- Continuous transition vs. wind direction

Pulse modulations / refraction

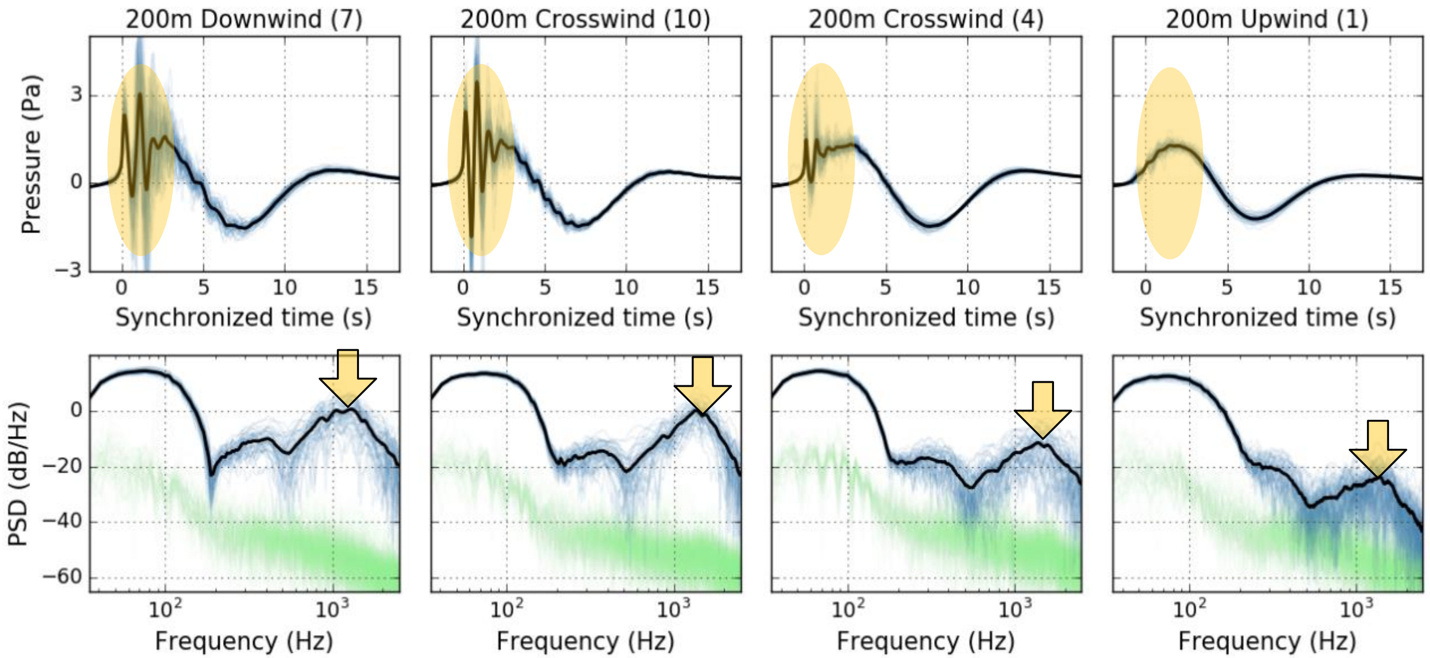

- **Refraction due to wind gradients**
- Induces duct, reflexions, shadows
- Early arrivals caused by direct rays
- Dispersive (HF)

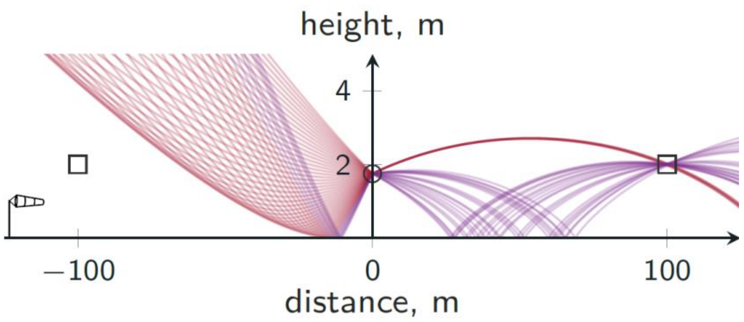

Pulse modulations / ground

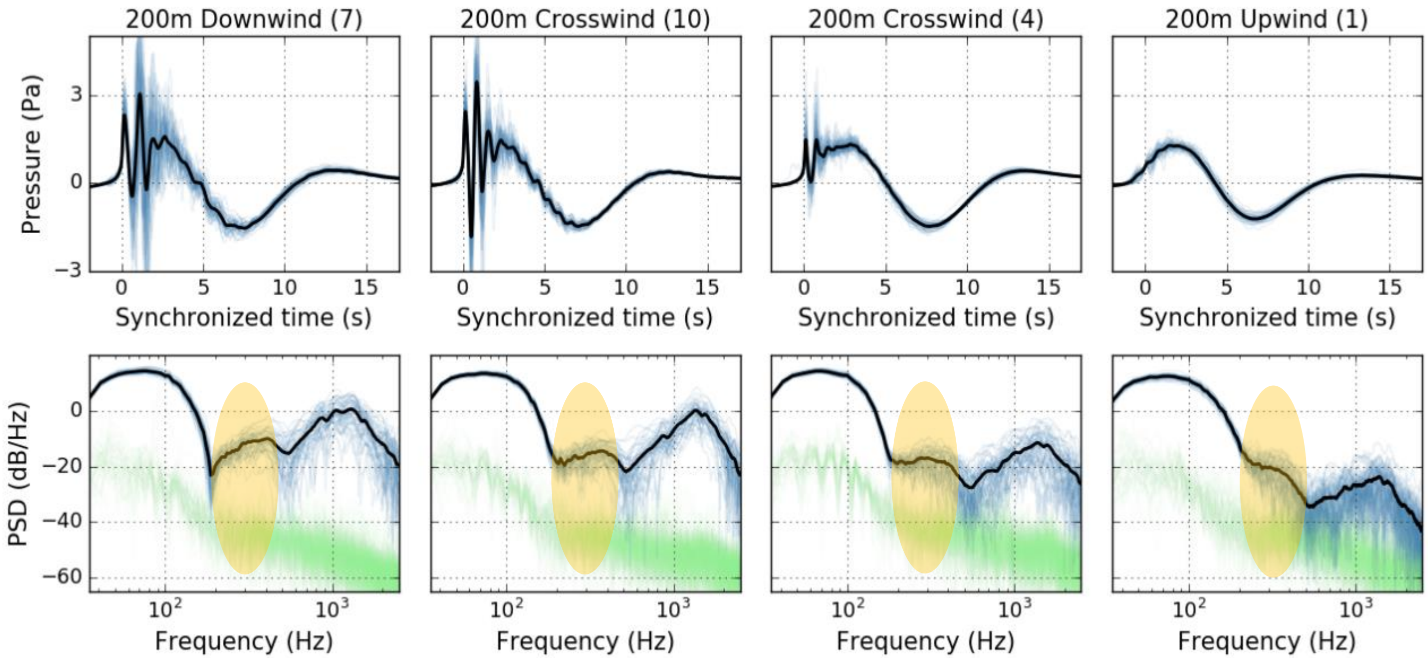

- Source-caused dip at 600 Hz
- Additional dip 200 Hz due to **ground absorption**
- Enhanced downwind (more reflexions)
- The dip reinforces with range

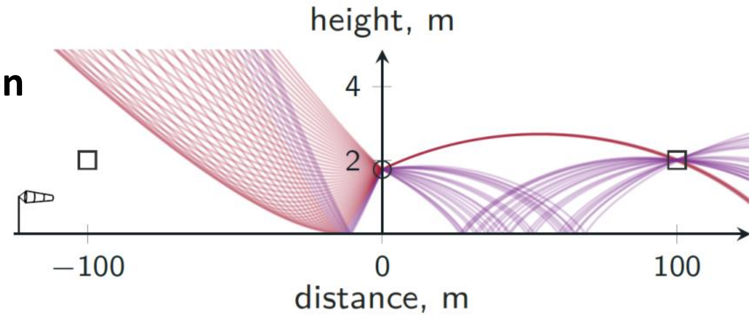

Pulse modulations / surface wave

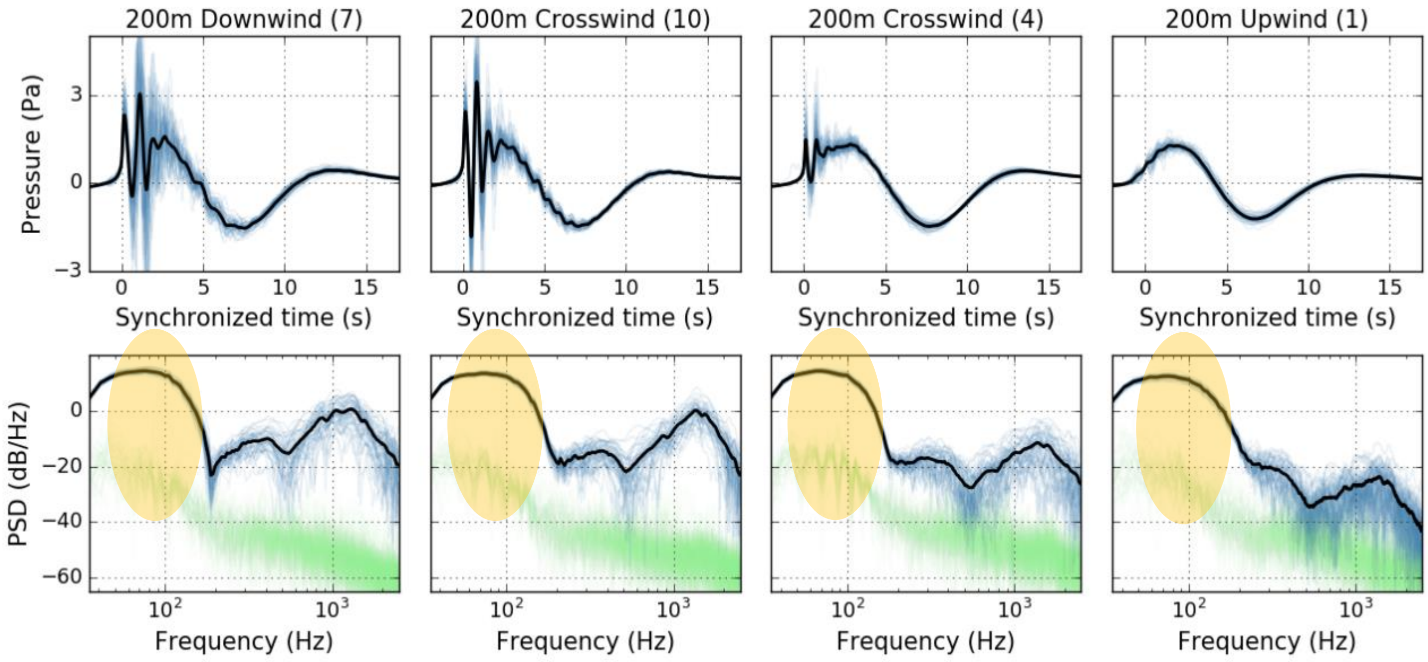

- **Low-frequencies are unaffected** (in this experiment)
- Sensitive to ground absorption, surface wave
- Dominates the signal upwind

Pulse modulations / pulse spread

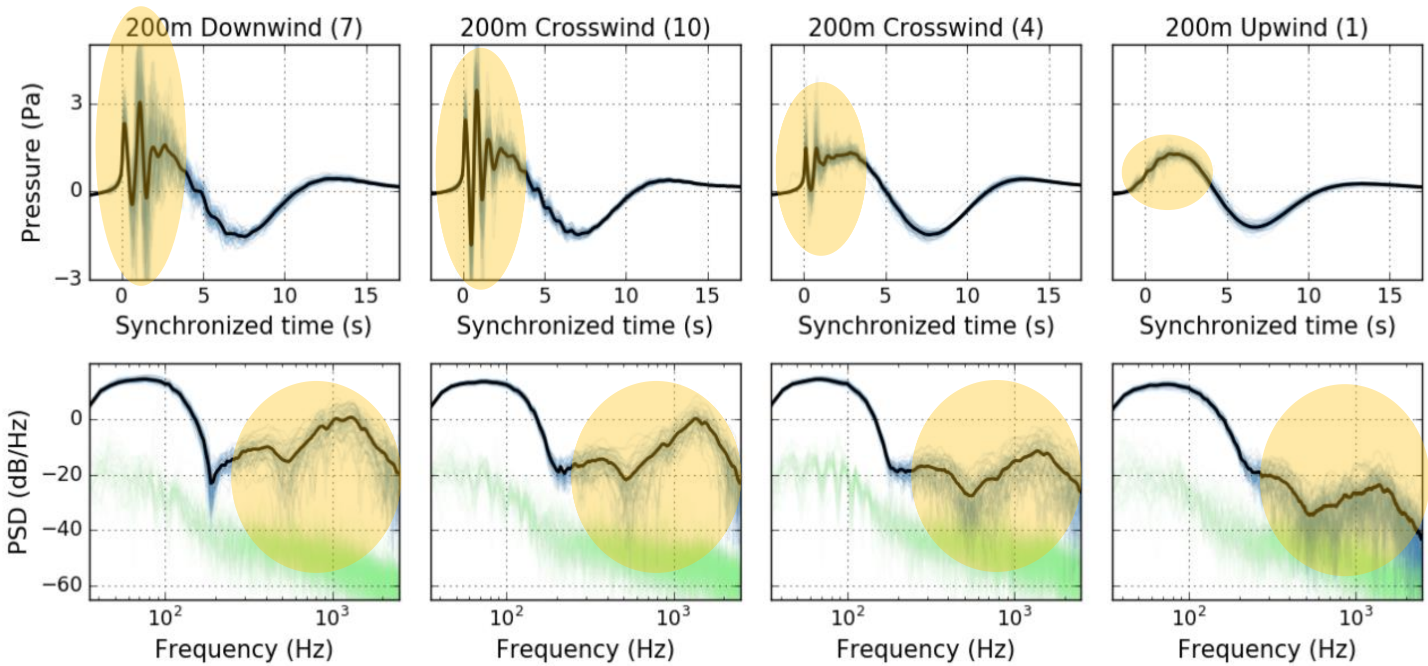

- All signals undergo major shot-to-shot fluctuations in shape, so-called **‘spread’**
- Stronger at HF, thus more visible downwind
- Low turbulence conditions show much less of these fluctuations
- Dominantly caused by **atmospheric turbulence** (ground heterog., source)

Pulse modulations / wander

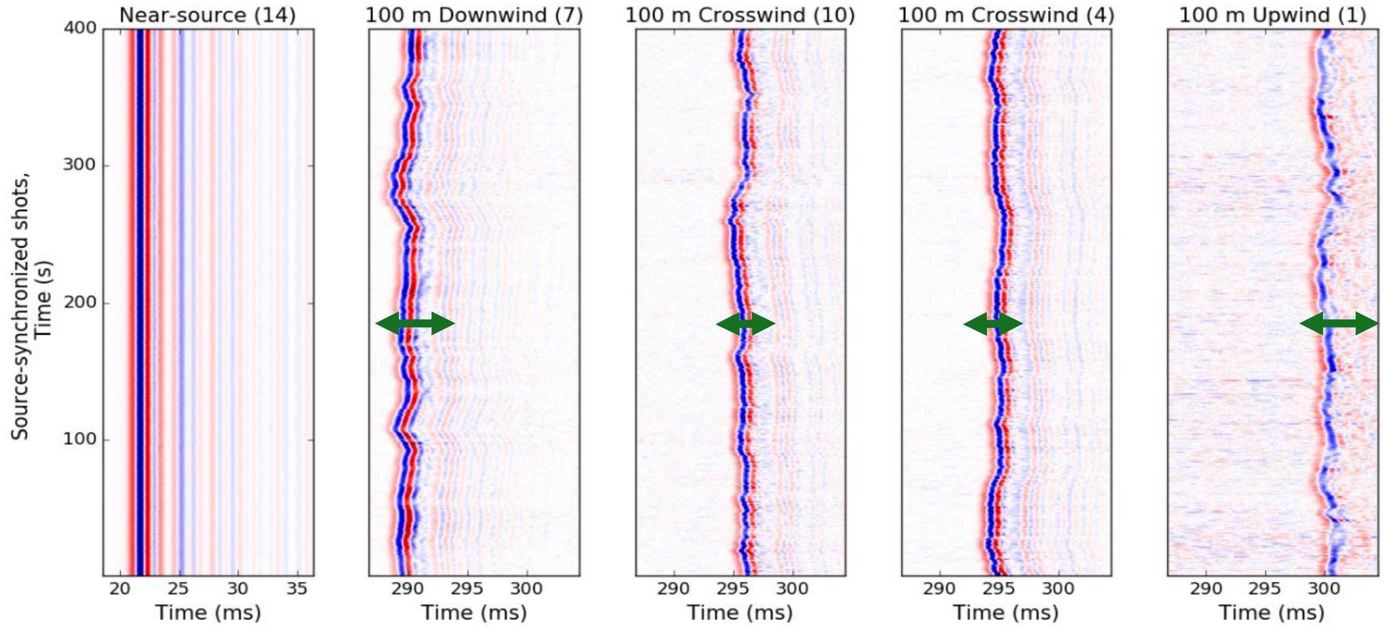

The pulse wanders (TOA randomness)
- non negligible, caused by **turbulence**

$\Delta t = \dfrac{\sigma_u}{c_0^2}\sqrt{2L_u X}$	Pulse wander scaling, classical for single freq. X (range increases) . $1/\sqrt{X}$ (path-averaging)
$\Delta t_u > \Delta t_v$	Turbulence anisotropy, $\sigma_u > \sigma_v; L_u > L_v$ Suggests larger wander streamwise

Pulse modulations / two-… coherence(s)

Coherence type	Formulation
Spatial / longitudinal	$\langle p(x,y,t)p(x+\Delta x,y,t)\rangle$
Spatial / transverse	$\langle p(x,y,t)p(x,y+\Delta y,t)\rangle$
Temporal	$\langle p(x,y,t)p(x,y,t+\Delta t)\rangle$
Frequency (FT)	$\langle p(x,y,\omega)p(x,y,\omega+\Delta\omega)\rangle$

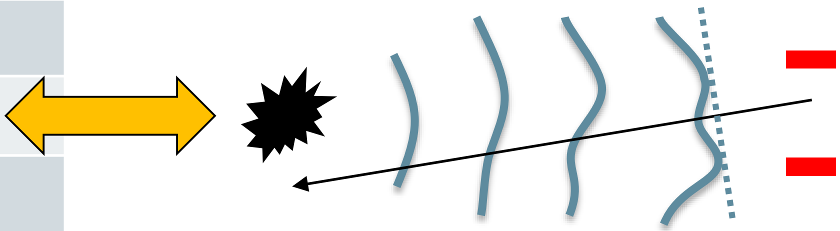

$\langle\ \ \rangle$ = average over shots
t = shot index
$\Delta. = 0$ gives normalization
$\Delta. = \infty$ gives 0

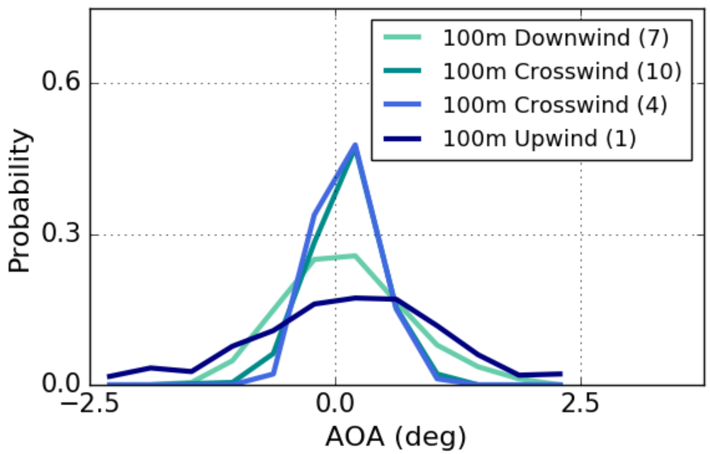

- Overview
- Results
- **Summary**

Summary

- Document the atmospheric-driven variability of impulse sounds

  Joint ISL – CRREL – ARL – WTD91 experiment, acoustics + atmospherics

  Key technical points: synchronization without wiring, turbulence assessment

- Salient results

  ✓ Even moderate wind / range induce large signature recombinations

  ✓ ToA depends on range, but not only - wander, refraction etc

  ✓ Shape undergoes major changes - deterministic & stochastic factors

  ✓ Coherence assessment, challenge of anisotropic turbulence

Impulse sound propagation in open environments: time-domain simulations versus measurements

M. Cosnefroy [1] S. Cheinet [1] A. Dagallier [1] D. Dragna [2] L. Ehrhardt [1] D. Juvé [2]

[1] French-German Research Institute of Saint-Louis, Saint-Louis, France

[2] Centre Acoustique, LMFA UMR CNRS 5509, École Centrale de Lyon, Écully, France

June 12, 2018

Introduction (1/4)

Applications:

military

transportation noise

...

Introduction (2/4)

The Atmospheric-Driven Variability of Impulse Sounds Experiment (ADVISE)

- Experiment in Meppen (Germany), October 2016

  Cheinet et al. (to be submitted to JASA)

  - quiet field (620 m × 500 m)
  - very flat, homogeneous ground with grass

  $\Longrightarrow$ complies with Monin–Obukhov Similarity!

- Acoustic measurements in different configurations
  - atmospheric monitoring
  - impulse sources
  - synchronized microphones
  - propagation over up to 450 m

in situ impedance measurements

variable porosity model

Attenborough (JASA, 2011)

eff. resistivity $\sigma = 25\,\mathrm{kPa\,s\,m^{-2}}$
rate of exponential decay $\alpha = 50\,\mathrm{m^{-1}}$

$\Longrightarrow$ no ground wave!

Introduction (3/4)

Circle of radius 200 m *(cannon)*

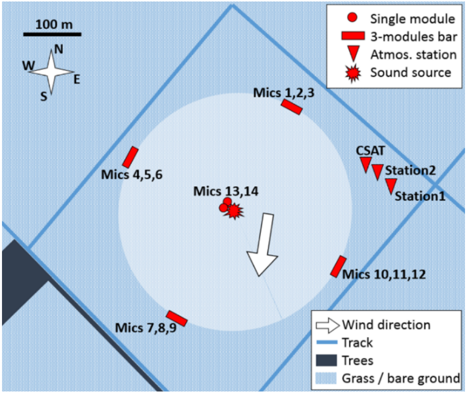

Introduction (4/4)

Circle of radius 200 m *(cannon), sample of results*

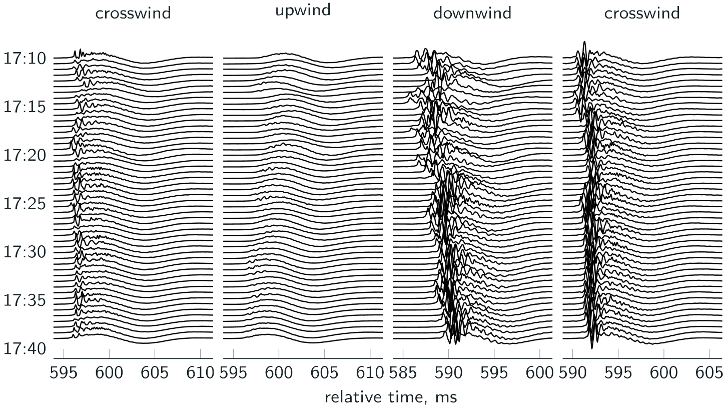

$\langle p_{\text{peak}} \rangle = 1.86\,\text{Pa}$, 1.40 Pa , 4.12 Pa , 3.79 Pa

major influence of wind direction!

Outline

1. Numerical Model
2. Time-Domain Simulations versus Measurements
3. Numerically-Aided Interpretation of Ground Effects

Numerical Model

Solving the Linearized Euler Equations

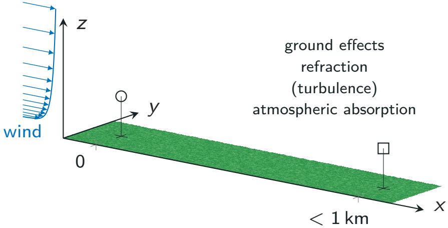

ITM: in-house Finite-Difference Time-Domain (FDTD) modeling tool

$$\frac{\partial p}{\partial t} + \mathbf{V} \,.\, \nabla p + \rho_0 c^2 \,\nabla \,.\, \mathbf{v} = \rho_0 c^2 \, Q$$

$$\frac{\partial \mathbf{v}}{\partial t} + (\mathbf{V} \,.\, \nabla)\,\mathbf{v} + (\mathbf{v} \,.\, \nabla)\,\mathbf{V} + \nabla p/\rho_0 = \mathbf{F}/\rho_0$$

Advantages:

- full 3D modeling / few assumptions
- broadband signals

Drawback: computationally intensive in 3D

$\Longrightarrow$ high-order Dispersion-Relation-Preserving schemes + parallel computations (MPI)

- 11-point optimized spatial stencils

  Bogey & Bailly (Journal of Computational Physics, 2004)

- 6-stage optimized Runge–Kutta

  Berland et al. (Computers & Fluids, 2006)

Numerical Model

Solving the Linearized Euler Equations, with a moving frame

The moving frame approach:

- pulse tracked over the propagation
- ground at the bottom
- absorbing boundaries elsewhere (PMLs)

$\Longrightarrow$ smaller computational domain

$\Longrightarrow$ computational cost $\propto$ distance

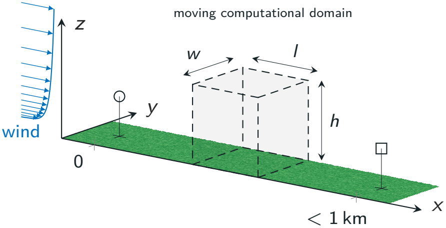

Constraints on the dimensions of the computational frame

In practice, computational cost not exactly $\propto$ distance...

- **height** h: high enough to account for downward refraction

  a priori knowledge from vertical profiles with ray theory

- **length** l: long enough to contain the source + broadening over time

  fixed size initial pressure distribution + deconvolution procedure

- **width** w & **height** h: large enough to limit the edge effects

  need for efficient absorbing boundaries $\Longrightarrow$ ⚠ (unphysical) limiting factor

Numerical Model

Efficient Perfectly Matched Layers

long propagation distances $\longrightarrow$ grazing waves $\Longrightarrow$ PMLs very inefficient

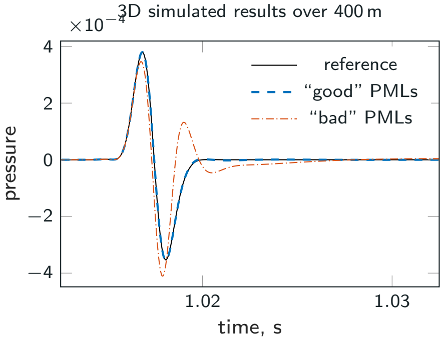

$\Longrightarrow$ "good" PMLs built using a stability analysis of the time integration scheme to maximize absorption coefficient, *Cosnefroy et al. (to be submitted)*

In 3D: accurate with propagation range/cross distance $\leqslant 50$

The Multipole Method

- desired plane wave reflection coefficient $R(\omega)$ approximated as a pole-residue model:

$$R(\omega) \simeq R_0 + \sum \frac{C_k}{\mathrm{i}\omega - \lambda_k} \quad \overset{\mathrm{FT}^{-1}}{\Longrightarrow} \quad r(t) \simeq R_0\,\delta(t) + \sum C_k\, \mathrm{e}^{\lambda_k t}\,\mathrm{H}(t)$$

- convolution integral $g(t) = (r * f)(t)$ solved with the ADE method

Some advantages of R over Z/Y:

- more accurate pole-residue models
- better rates of convergence (?)
- **simpler "causality" condition**: $\mathrm{Re}\,\{\lambda_k\} < 0$
  $\Longrightarrow$ **no condition on the zeros**
- *prediction* of numerical stability

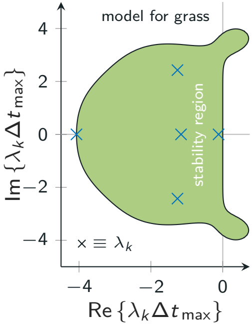

Outline

1. Numerical Model
2. Time-Domain Simulations versus Measurements
   - Short range data (100 m)
   - Propagation over 450 m, downwind
   - Propagation over 450 m, upwind
3. Numerically-Aided Interpretation of Ground Effects

Time-Domain Simulations versus Measurements

Propagation over 100 m

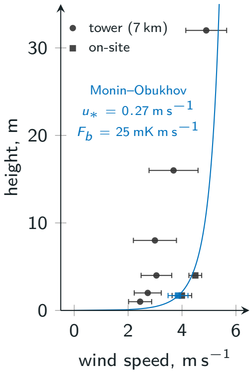

Here:

- loudspeaker
- upwind and downwind propagation over 100 m

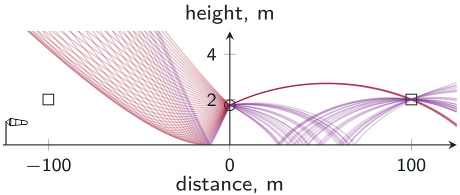

Mean wind vertical profile

- estimation with Monin–Obukhov Similarity from one instrument (in blue)
- good agreement with other on-site measurements
- not so much with tower: too far away?

Propagation over 100 m — *FDTD simulations*

./movies/19config1_output_upwind.mp4

upwind propagation

We know the...

- ground impedance
- wind profile
- atmospheric absorption

$\Longrightarrow$ FDTD computations in 3D
for up– & downwind cases
(on a personal laptop)

with an initial Gaussian pressure distribution

Time-Domain Simulations versus Measurements

Propagation over 100 m — FDTD simulations

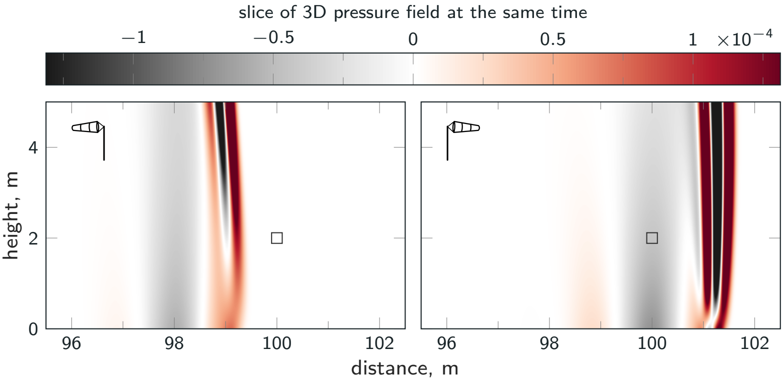

Differences in terms of...

- time of arrival
- amplitude
- shape

Now...

- extraction of pressure time series
- deconvolution procedure $\Longrightarrow$ Green function
- convolution with experimental source signal(s)

Time-Domain Simulations versus Measurements

Propagation over 100 m — *source signal(s)*

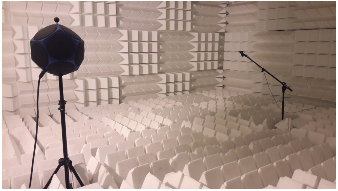

Measurements in anechoic chamber to assess:

- reproducibility
- directivity
- FDTD source signal

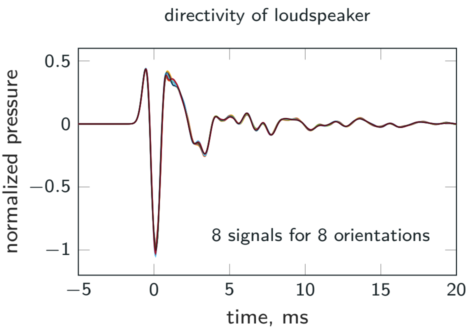

$\Longrightarrow$ very reproducible

$\Longrightarrow$ omnidirectional below 1.5 kHz

actual amplitude + emission time recovered from microphone close to the source

Time-Domain Simulations versus Measurements

Propagation over 100 m — validation in the time domain

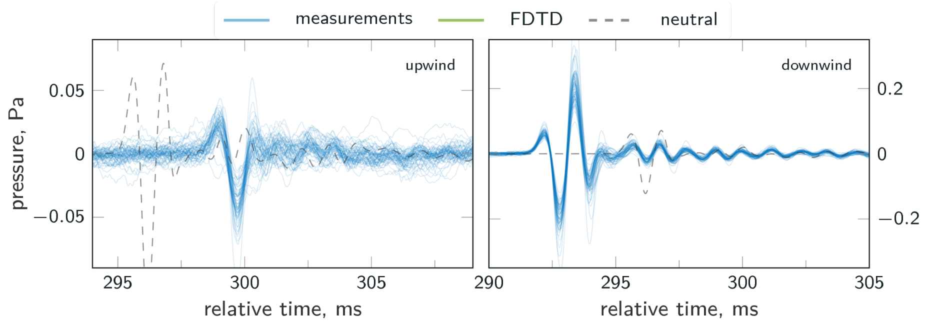

- measured shots synchronized to the TOA
- simulation without wind

Time-Domain Simulations versus Measurements

Propagation over 100 m — validation in the time domain

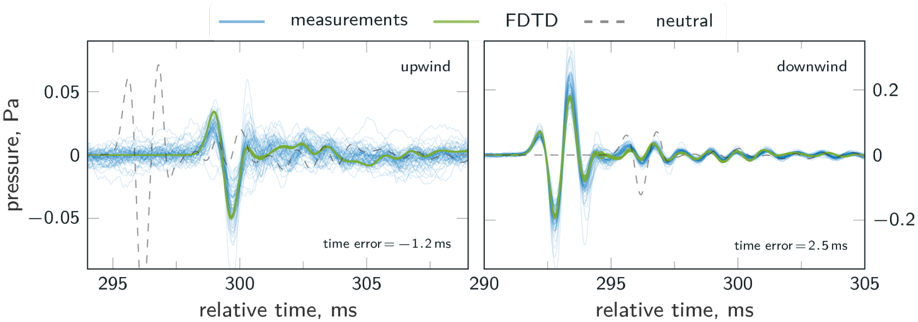

- measured shots synchronized to the TOA
- simulation without wind
- simulations with wind

$\Longrightarrow$ very good agreement in both cases

Time-Domain Simulations versus Measurements

Propagation over 100 m — *validation in the frequency domain*

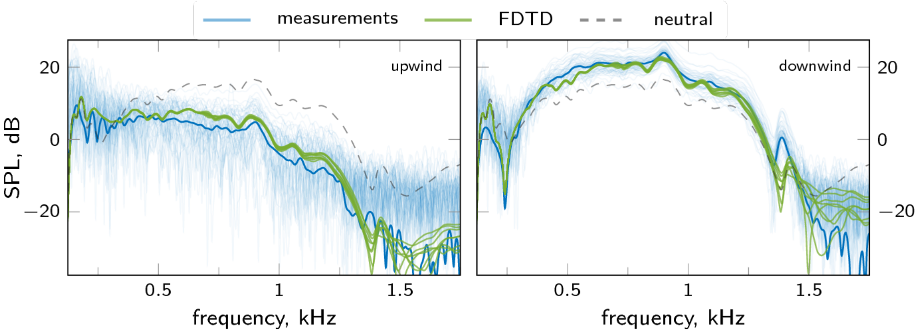

Time-Domain Simulations versus Measurements

Propagation over 100 m — *validation in the frequency domain*

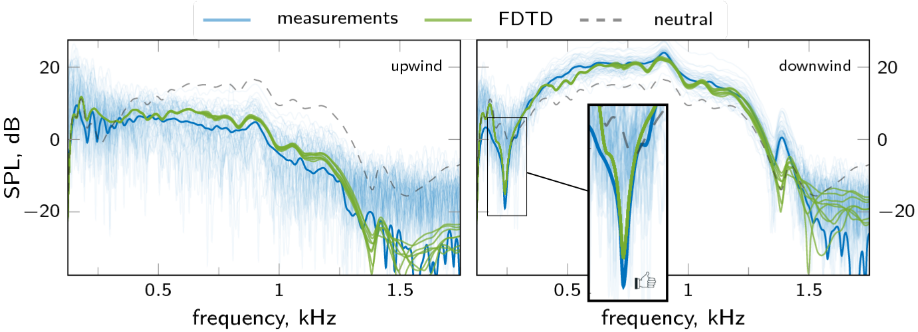

very good agreement with the SPL of measured mean pressure!

Time-Domain Simulations versus Measurements

Propagation over 450 m

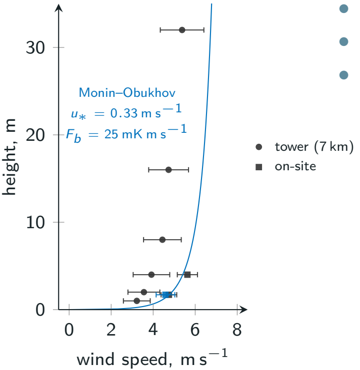

Configuration:

- gas cannon
- upwind and downwind propagation over 450 m
- microphones at 50, 150, 300 and 450 m

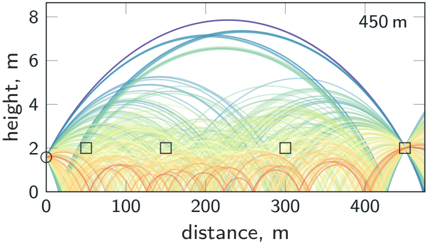

- again, wind profile in good agreement with on-site instruments
- downwind: height of computational domain chosen from ray theory

Time-Domain Simulations versus Measurements

Propagation over 450 m — numerical results, downwind

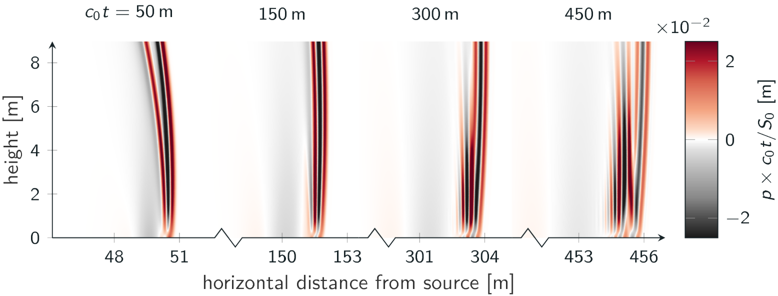

- high amplitudes
- complex interference pattern at long distance
- enhancement of high frequencies
- (small) ground wave

Time-Domain Simulations versus Measurements

Propagation over 450 m — *source signal(s)*

Assumptions:

- no horizontal directivity
- no influence of vertical directivity at long range

$\Longrightarrow$ large shot-to-shot variability

Advantage of deconvolution procedure

only 1 simulation for different source signals!

Indoor measurements of source signal not suitable...

$\Longrightarrow$ dedicated outdoor measurements

$\Longrightarrow$ cannon high enough to delay ground reflection

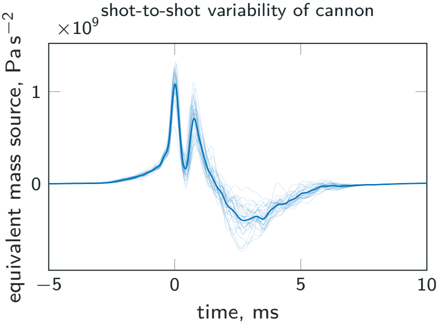

Time-Domain Simulations versus Measurements

Propagation over 450 m — validation, downwind

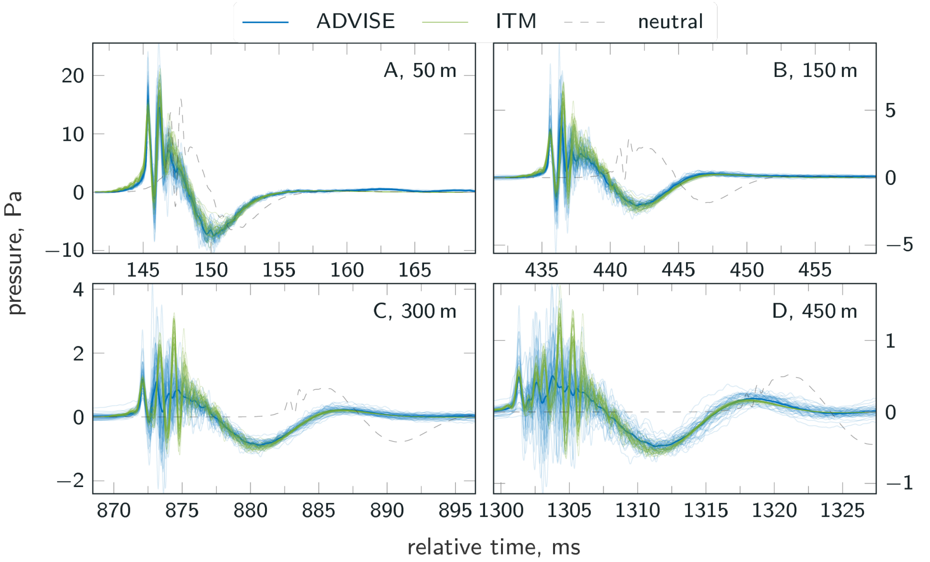

Time-Domain Simulations versus Measurements

Propagation over 450 m — numerical results, upwind

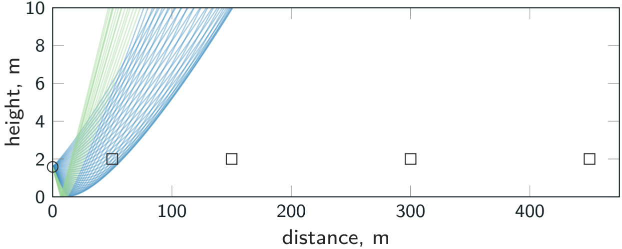

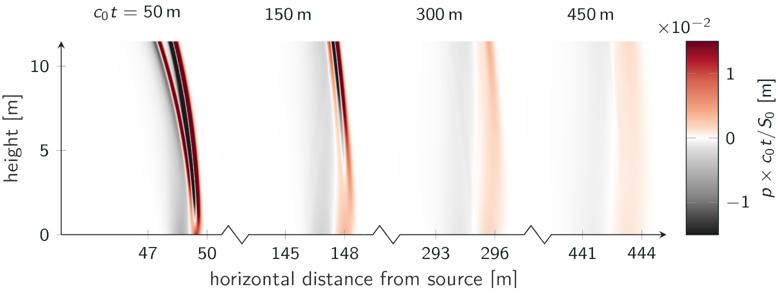

Time-Domain Simulations versus Measurements

Propagation over 450 m — validation, upwind

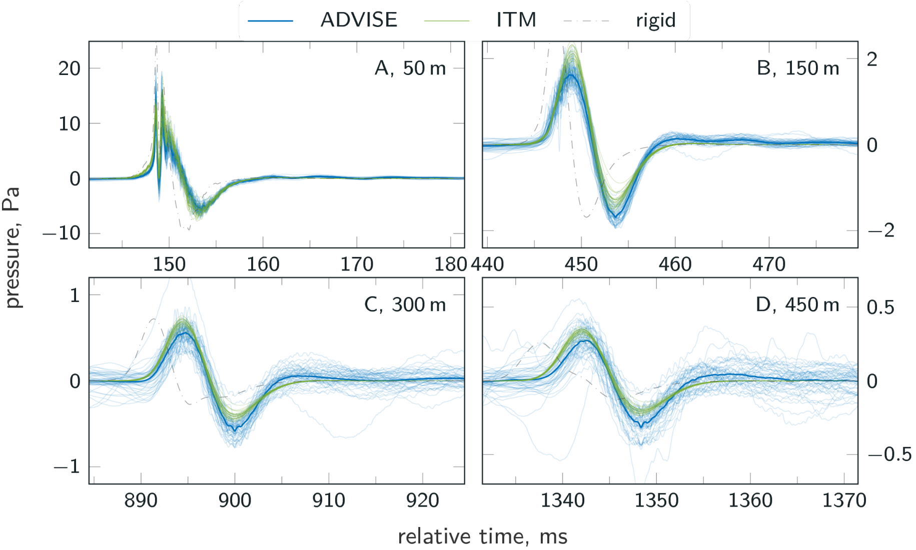

Time-Domain Simulations versus Measurements

Propagation over 450 m — validation, upwind

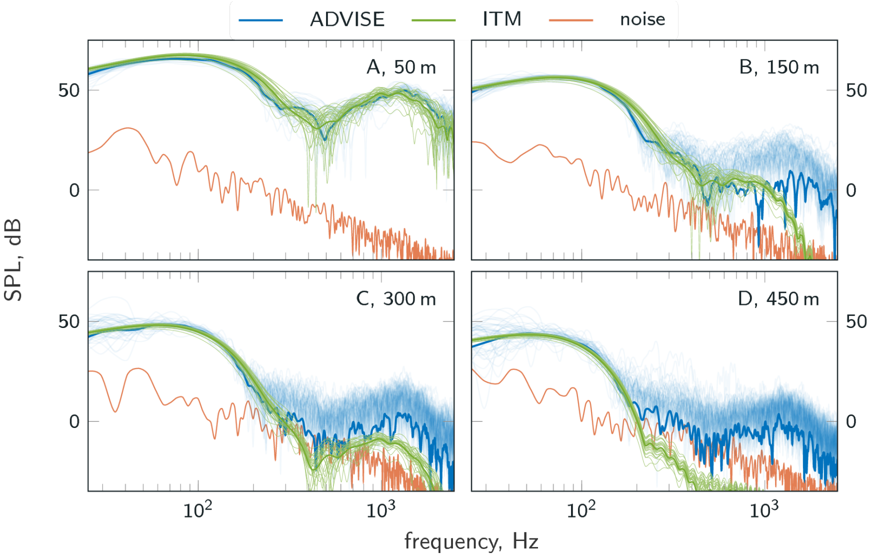

Outline

Numerically-Aided Interpretation of Ground Effects

Downwind case: porous vs rigid grounds

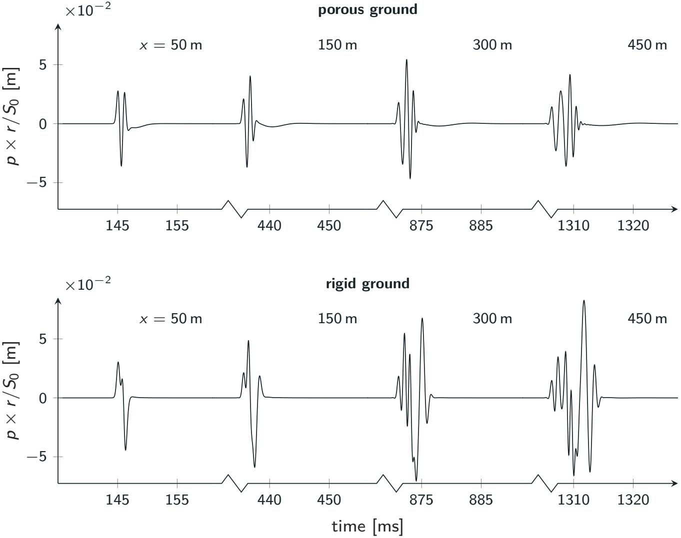

Numerically-Aided Interpretation of Ground Effects

Downwind case: porous vs rigid grounds

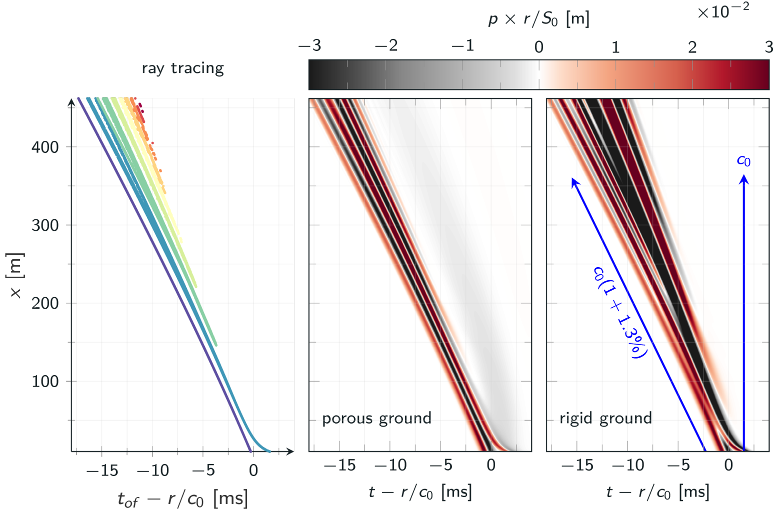

Numerically-Aided Interpretation of Ground Effects

Downwind case: porous vs rigid grounds

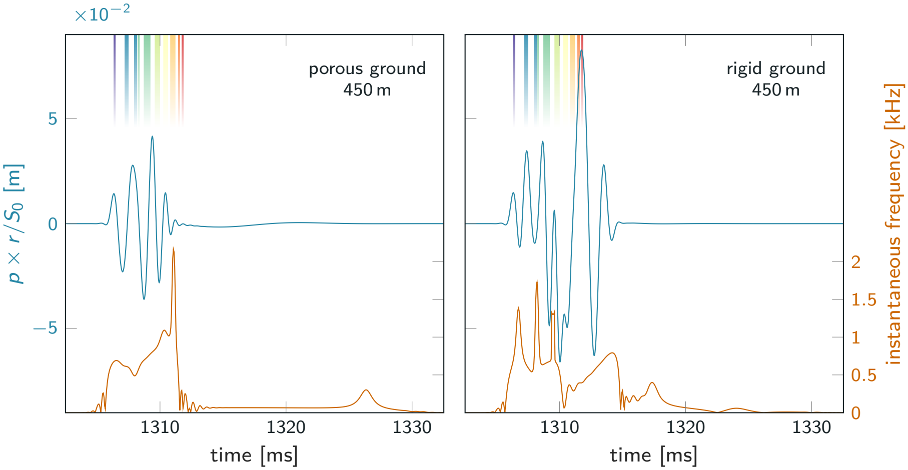

Numerically-Aided Interpretation of Ground Effects

Downwind case: porous vs rigid grounds

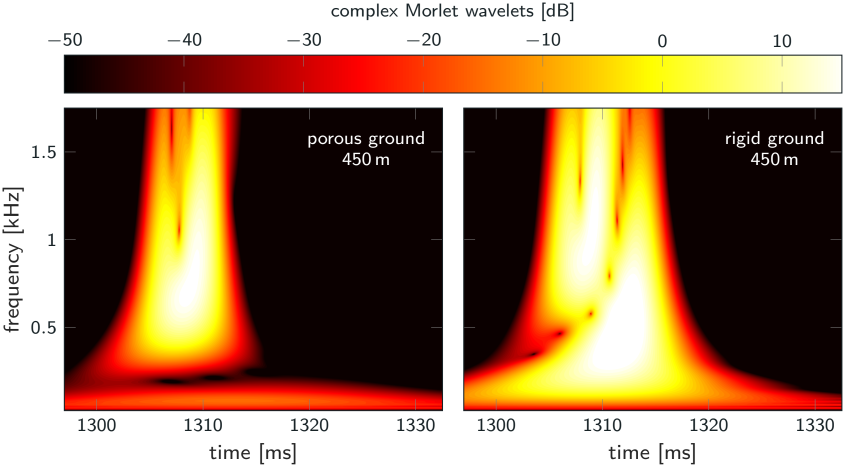

$\Longrightarrow$ progressive influence of the ground for downward refraction

Numerically-Aided Interpretation of Ground Effects

Upwind case: porous vs rigid grounds

- similar results between porous & rigid grounds for the amplitude / shape
- the time of arrival depends on the ground type:

	TOA at 450 m (in ms)
rigid ground	1335
porous ground	1340

the pulse arrives 5 ms later with absorbing ground! ($\simeq$ 2 m)

Conclusion

- efficient 3D numerical model
- validation with ground & refractive effects up to 450 m
- excellent agreement with measurements upwind & downwind (and crosswind)
- need for accurate input parameters (ground + vertical profiles)

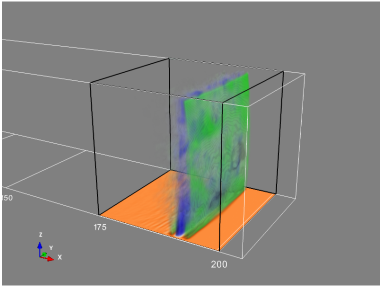

propagation with turbulence

Outlook

- propagation with turbulence: numerical sensitivity tests (GENCI-IDRIS)
- ground topography / longer ranges
- pending submissions

Measured sound level difference in relation to the effective sound speed gradient

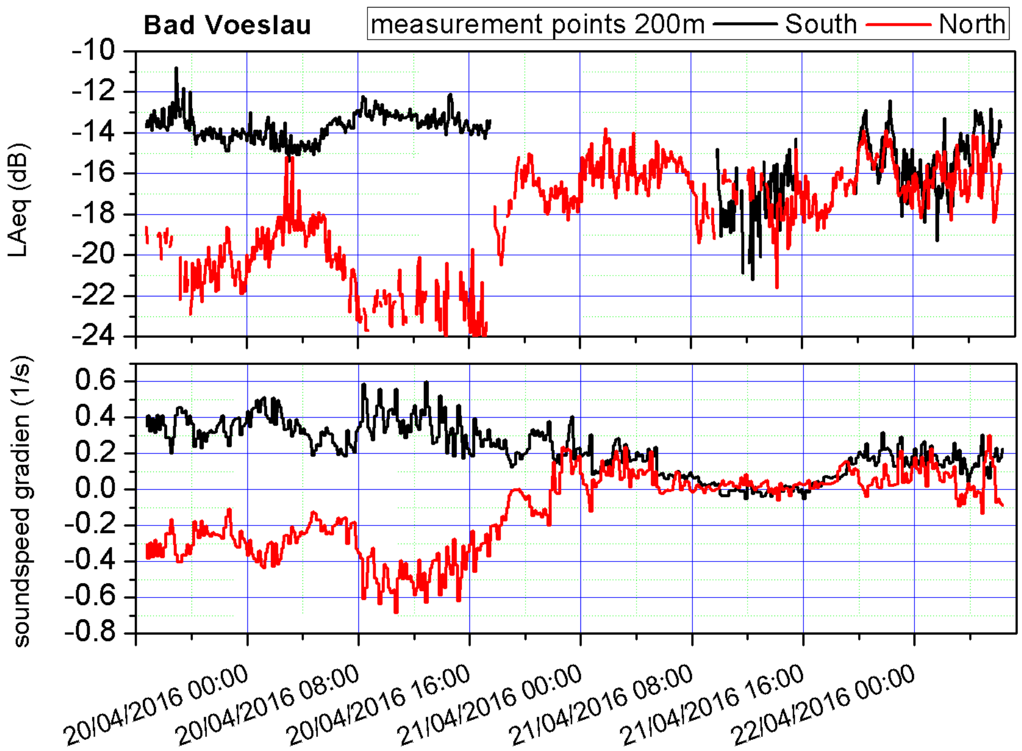

Mursch-Radlgruber Erich[1], Hohenwarter Dieter[2], Kirisits Christian[3]

[1] Institute of Meteorology, University of Natural Resources and Applied Life Sciences, Vienna, Austria
erich.mursch-radlgruber@boku.ac.at | www.boku.ac.at
[2] TGM – Institute of Technology, Department for Research and Testing,
[3] Kirisits- Chartered Engineering Consultants

presentation

- **Sound level differences** do to **train** and **highway emission**
- Mesurements of **meteorological profiles** – heights?
- and effective sound speed from **10m met mast** measurements
- Time Series and Correlations
- Conclusions

Adaklaa – train site – 1.-2.9.2015

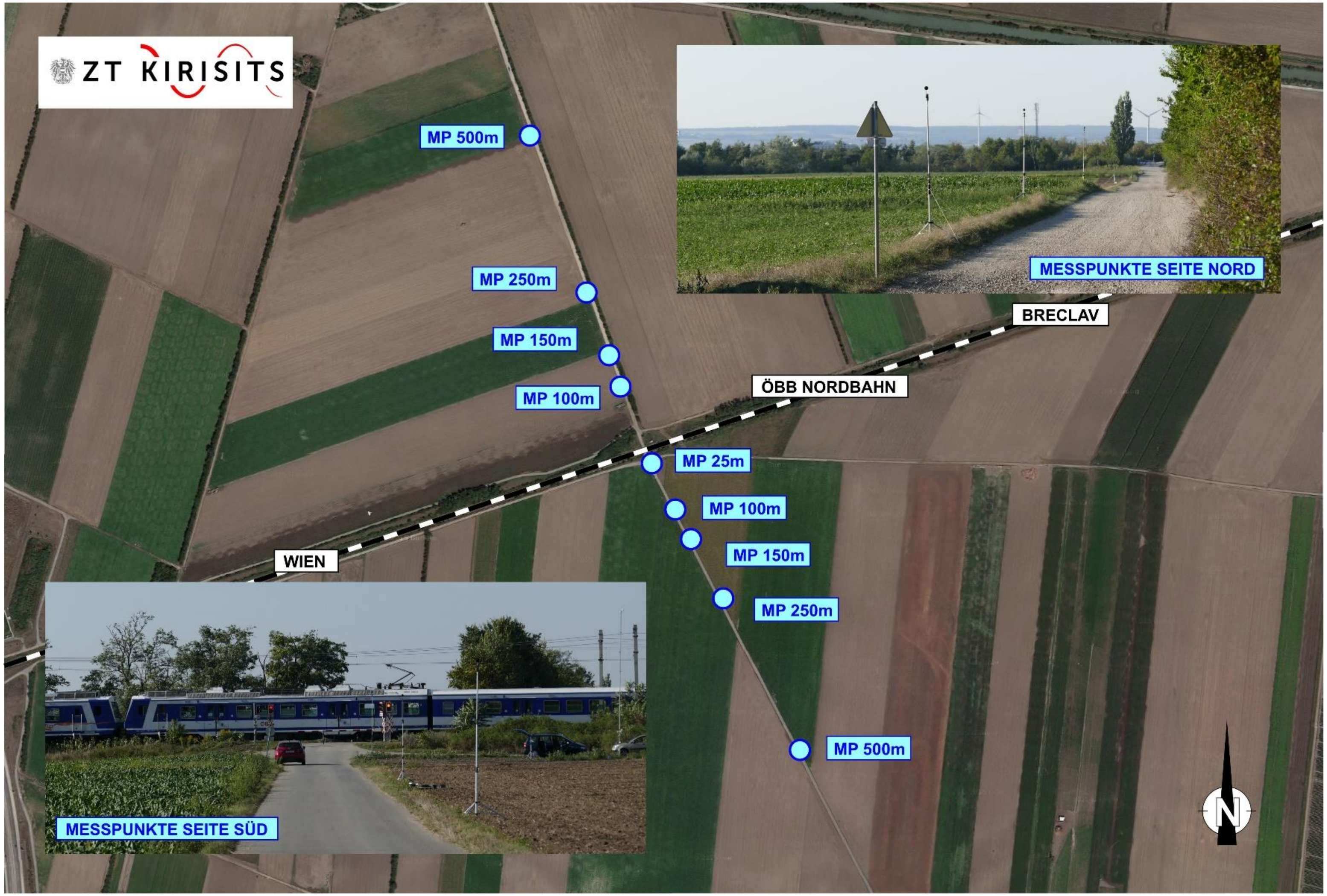

Measurement Train Noise Adaklaa – 1. - 2.9.2015

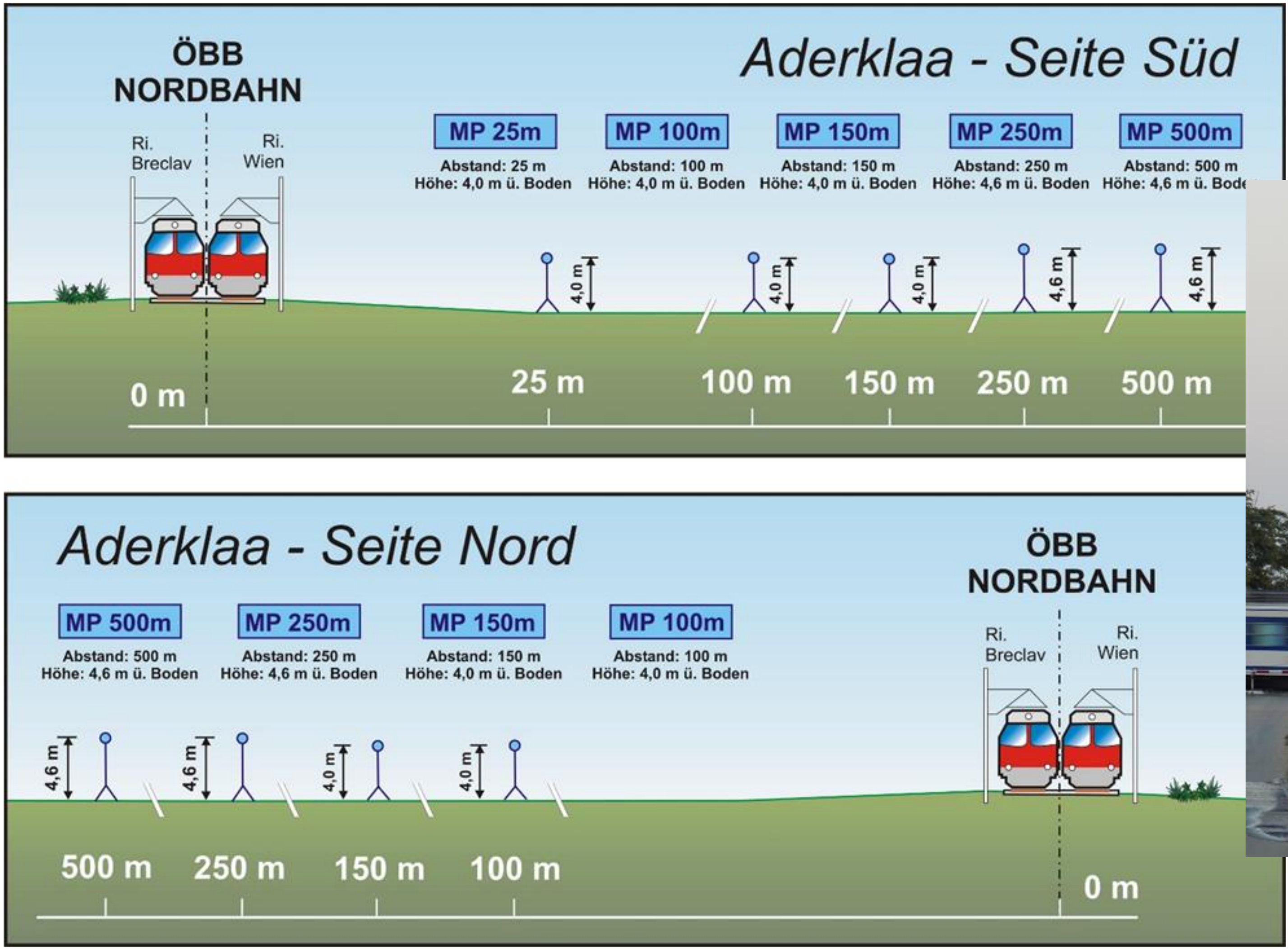

Bad Vöslau – highway 20.4. – 21.4.2016

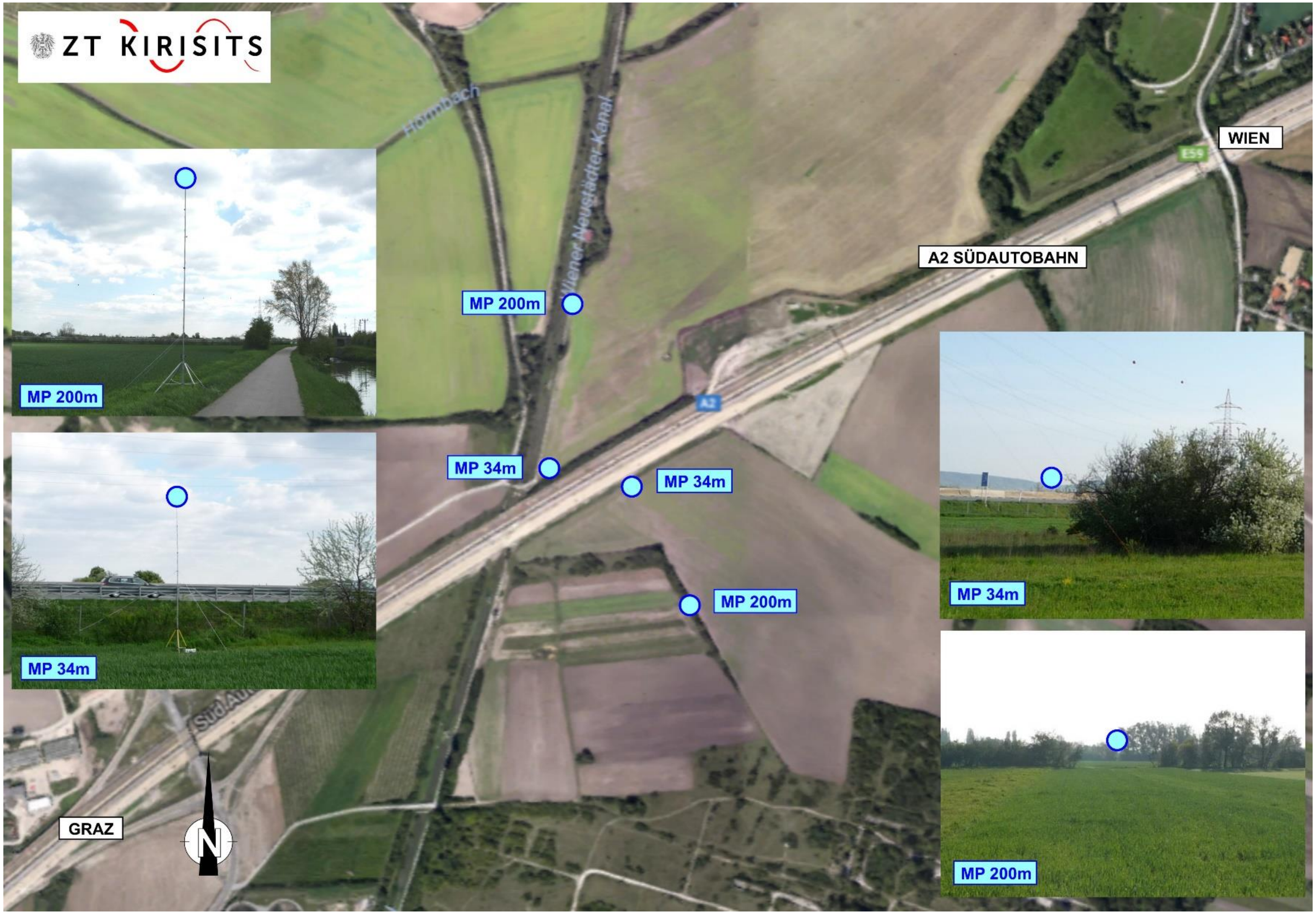

Bad Vöslau - measurement **north** and **south** of the highway A2

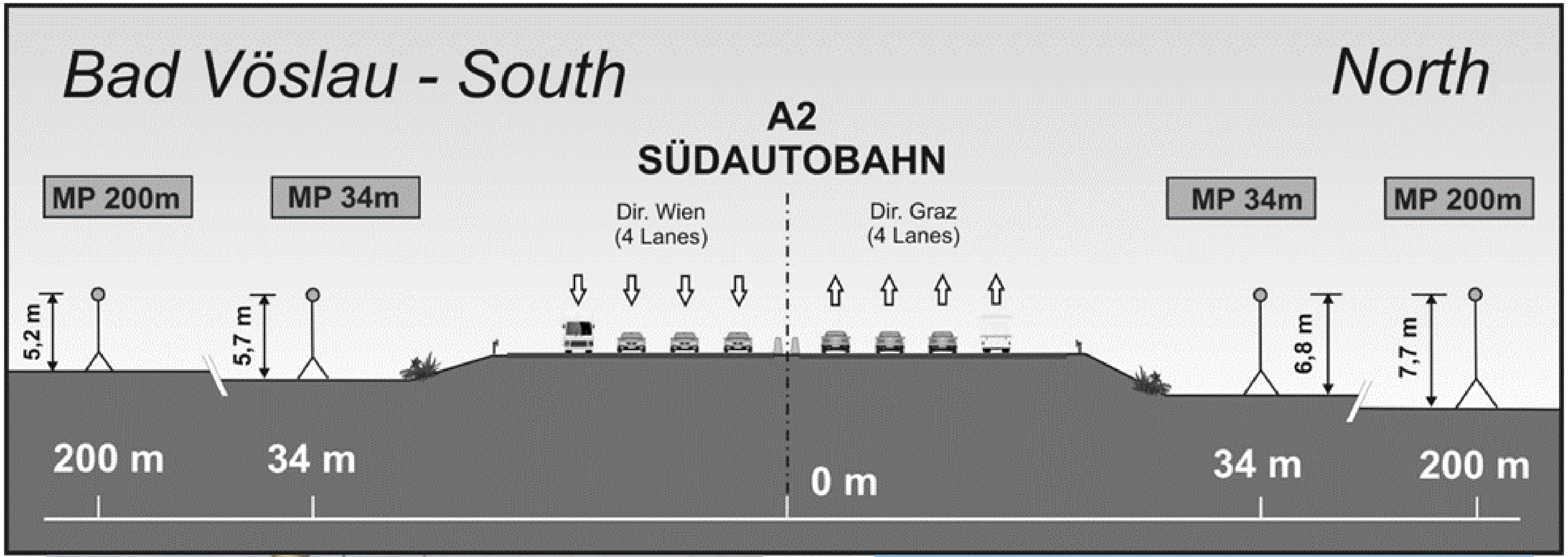

Bad Vöslau windprofile

20.4.-21.4.2016

Wind speed (ln (z))

z: 2 m, 5 m, 7 m, 10 m

Diabatic effects should deviate
From Linear
Stabil - increase with height (night)
Labil - decrease with height (day)

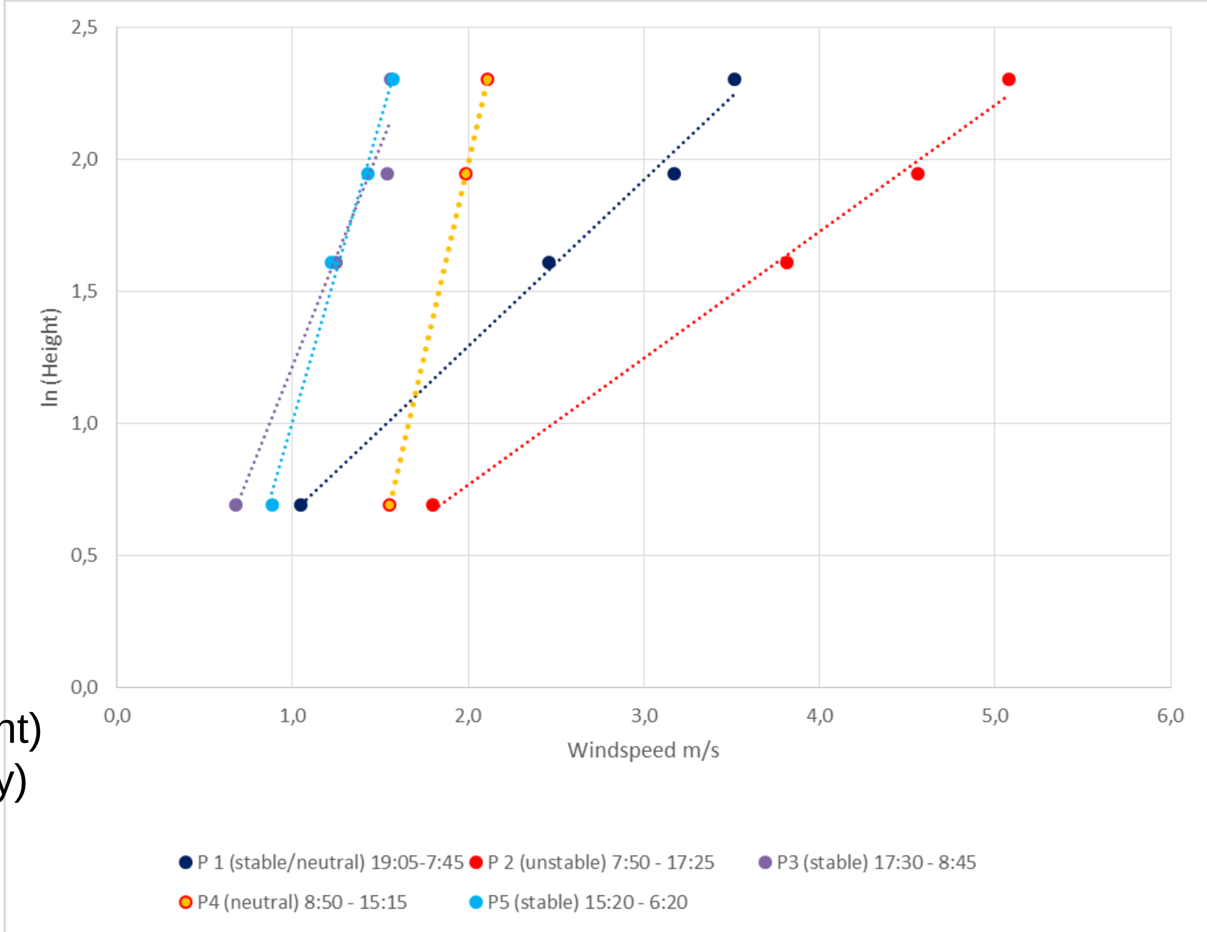

Bad Vöslau
Temperature profile

20.4.-21.4.2016

Temperature (ln (z))
z: 0,3m, 2 m, 5 m, 7 m, 10 m

Diabatic effects should deviate from Linear
Stabil - increase with height (night)
Labil - decrease with height (day)

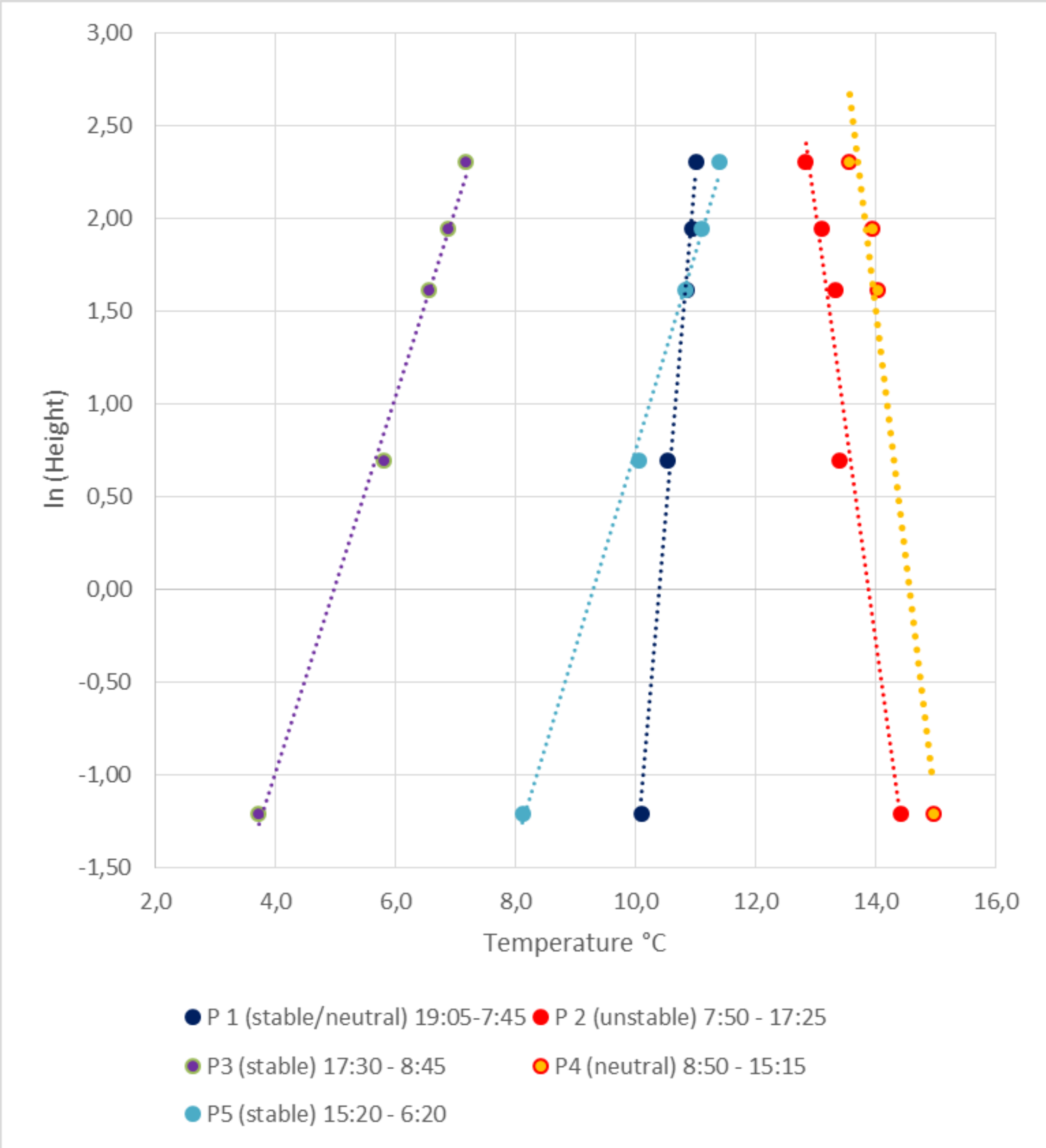

Monin-Obukov similaity theory MOST

wind- and temperature profiles

(from K. Attenborogh, 2007)

$$u(z) = \frac{u_*}{k}\left[\ln\left\{\frac{z+z_M}{z_M}\right\} + \psi_M\left(\frac{z}{L}\right)\right]$$

$$T(z) = T_0 + \frac{T_*}{k}\left[\ln\left\{\frac{z+z_H}{z_H}\right\} + \psi_H\left(\frac{z}{L}\right)\right] + \Gamma z$$

$$L = \frac{u_*\bar{\theta}(\Delta u/\Delta z)}{kg(\Delta\theta/\Delta z)}$$

where

u_*	Friction velocity (m s^{-1})	(depends on surface roughness)
z_M	Momentum roughness length	(depends on surface roughness)
z_H	Heat roughness length	(depends on surface roughness)
T_*	Scaling temperature °K	The precise value of this is not important for sound propagation. A convenient value is 283°K
k	Von Karman constant	(=0.41)
T_0	Temperature °C at zero height	Again it is convenient to use 283°K
Γ	Adiabatic correction factor	=−0.01°C m^{-1} for dry air Moisture affects this value but the difference is small
L	Obukhov length (m) >0→stable, <0→unstable	$= \pm u_*^2/kgT_*(T_{av}+273.15)$, the thickness of the surface or boundary layer is given by $2L$ m
T_{av}	Average temperature °C	It is convenient to use T_{av}=10 so that $(T_{av}+273.15)=\theta_0$
ψ_M	Diabatic momentum profile correction (mixing) function	$= -2\ln((1+\chi_M)/2) - \ln((1+\chi_M^2)/2) + 2\arctan(\chi_M) - \pi/2$ if $L<0$ if $L>0$; $= 5(z/L)$ if $L>0$
ψ_H	Diabatic heat profile correction (mixing) function	$= -2\ln\left(\frac{(1+\chi_H)}{2}\right)$ if $L<0$; $= 5(z/L)$ if $L>0$ or for $z \leq 0.5L$ [2]

Effective sound speed gradient – practical use

Example form measurements of Bad Vöslau 2016

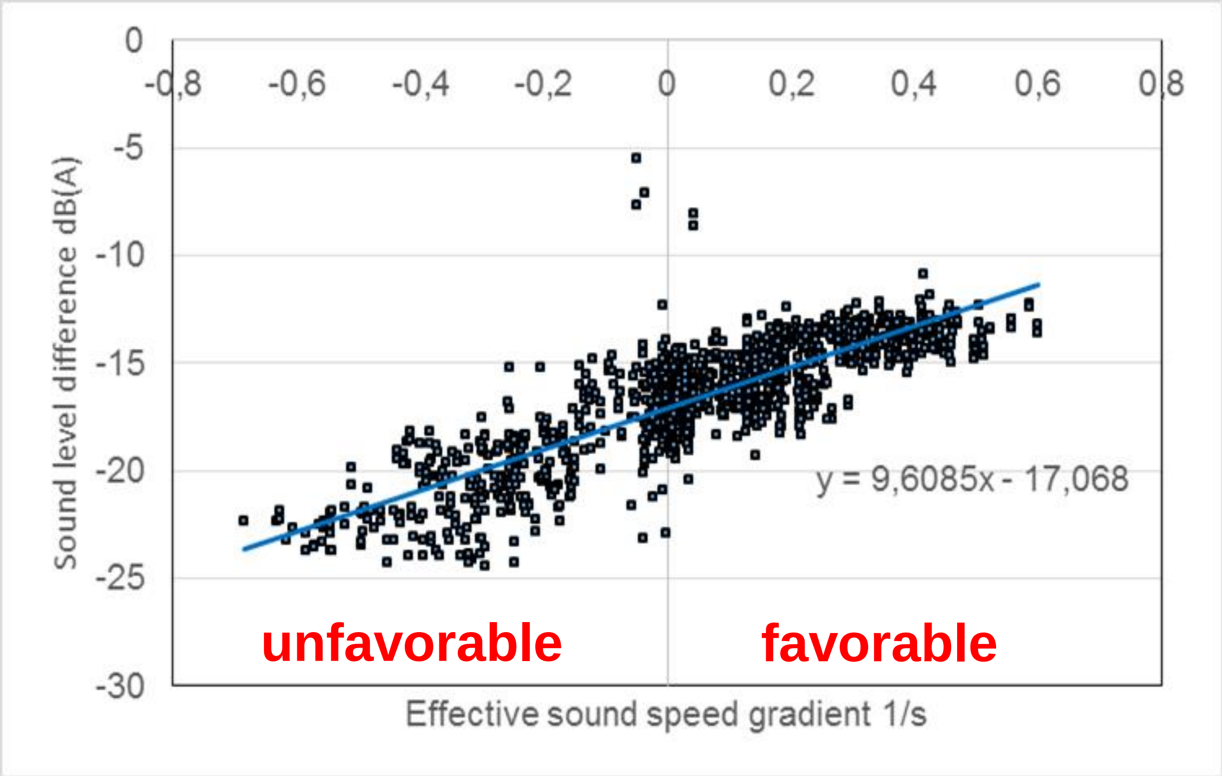

effective sound speed

$$c_{eff}(z) = c(z) + u(z)\cos\alpha$$

effective sound speed gradient (finite diffences)

$$\frac{\Delta c_{eff}}{\Delta z} = \frac{c_0}{2T_0}\frac{\Delta T}{\Delta z} + \cos\alpha\frac{\Delta u}{\Delta z}$$

diabatic and wind contribution

$\Delta c_{eff} / \Delta z < -0.1$ unfavourable sound propagation
$-0.1 \leq \Delta c_{eff} / \Delta z \leq 0.1$ neutral sound propagation
$\Delta c_{eff} / \Delta z > 0.1$ favourable sound propagation

Eff. Sound gradient and Laeq – Adaklaa - Train

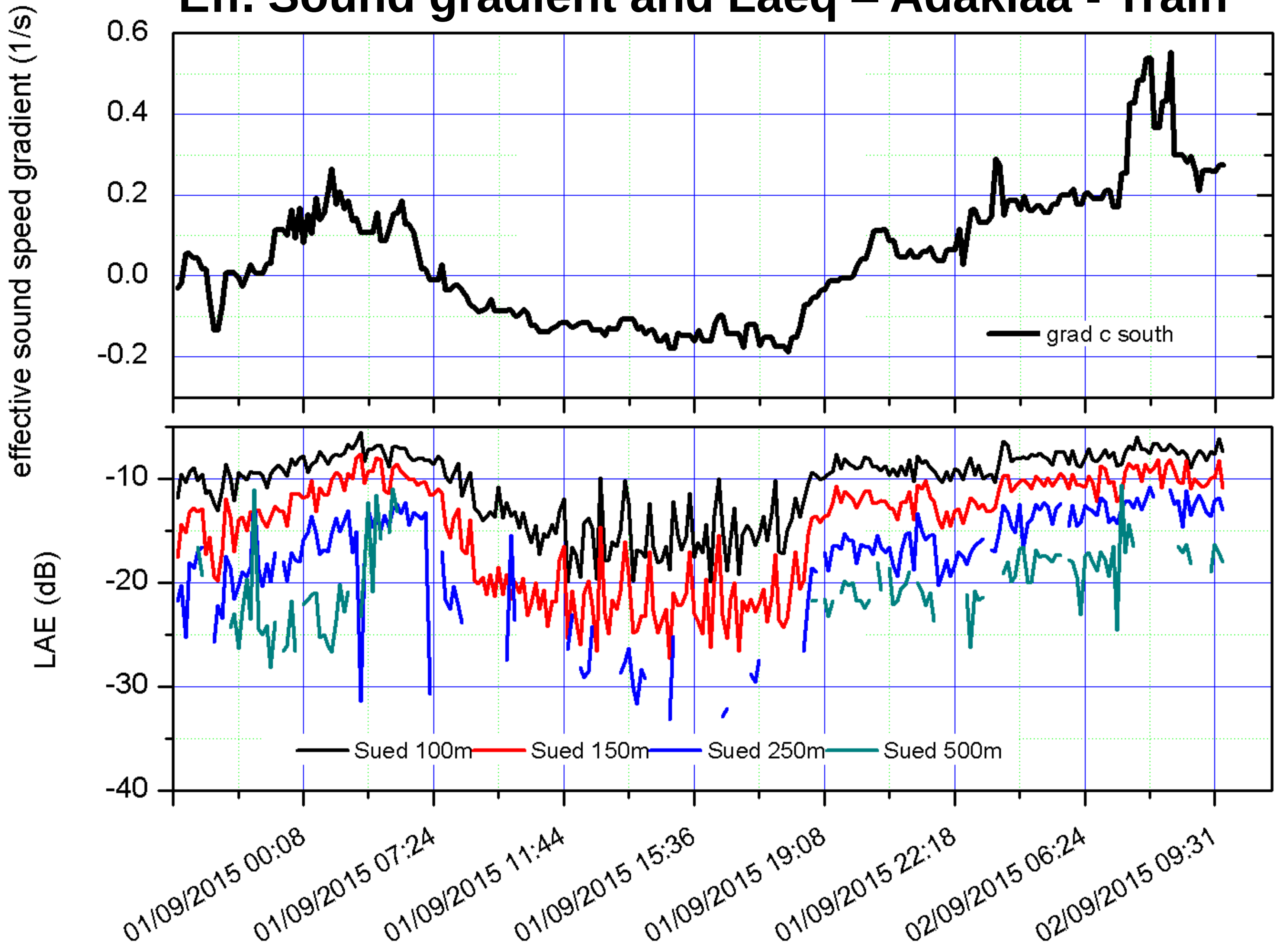

Adaklaa meteologie and LAeq – 1. -2-9.2015

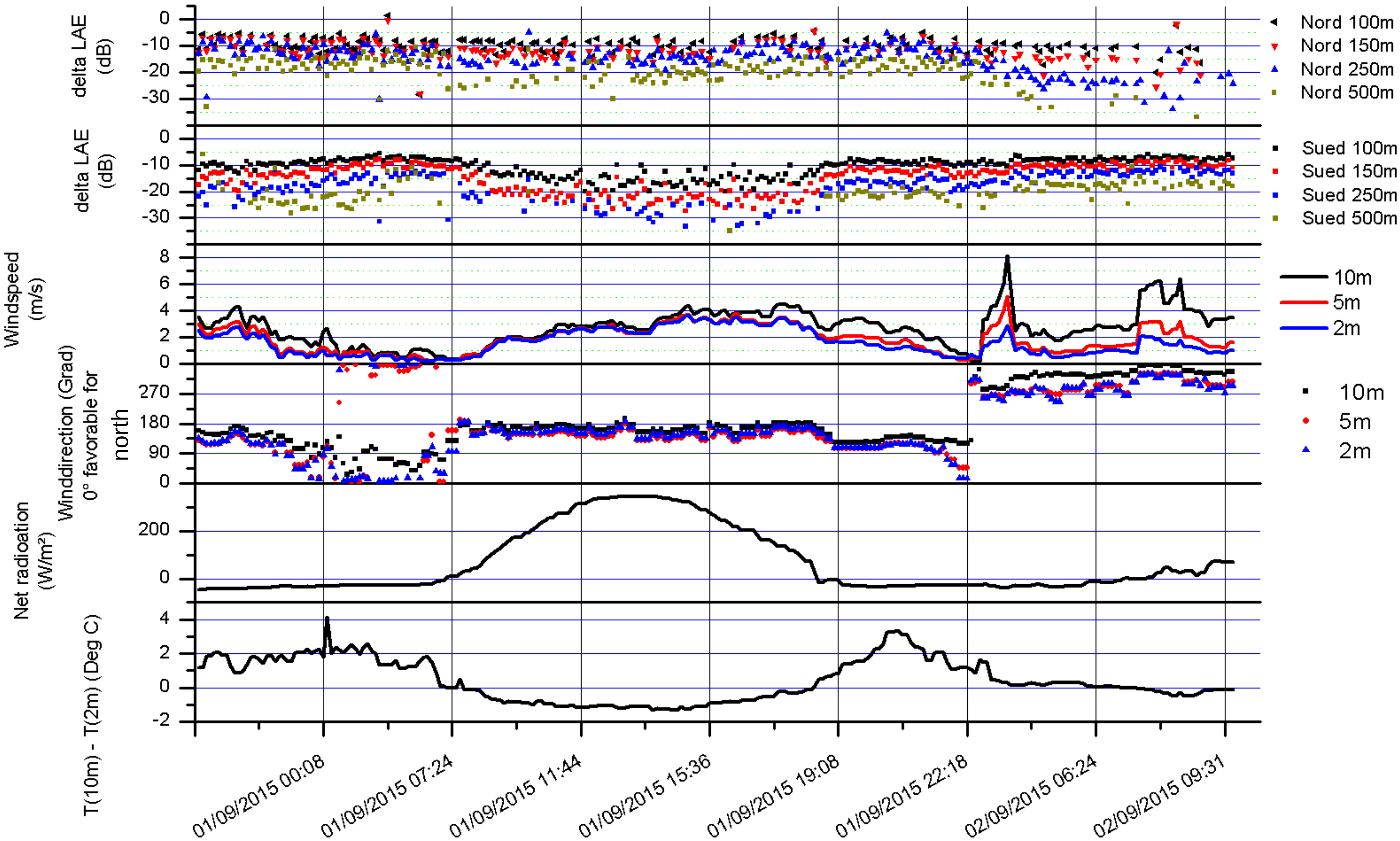

Adaklaa - LAeq – 1. -2-9.2015

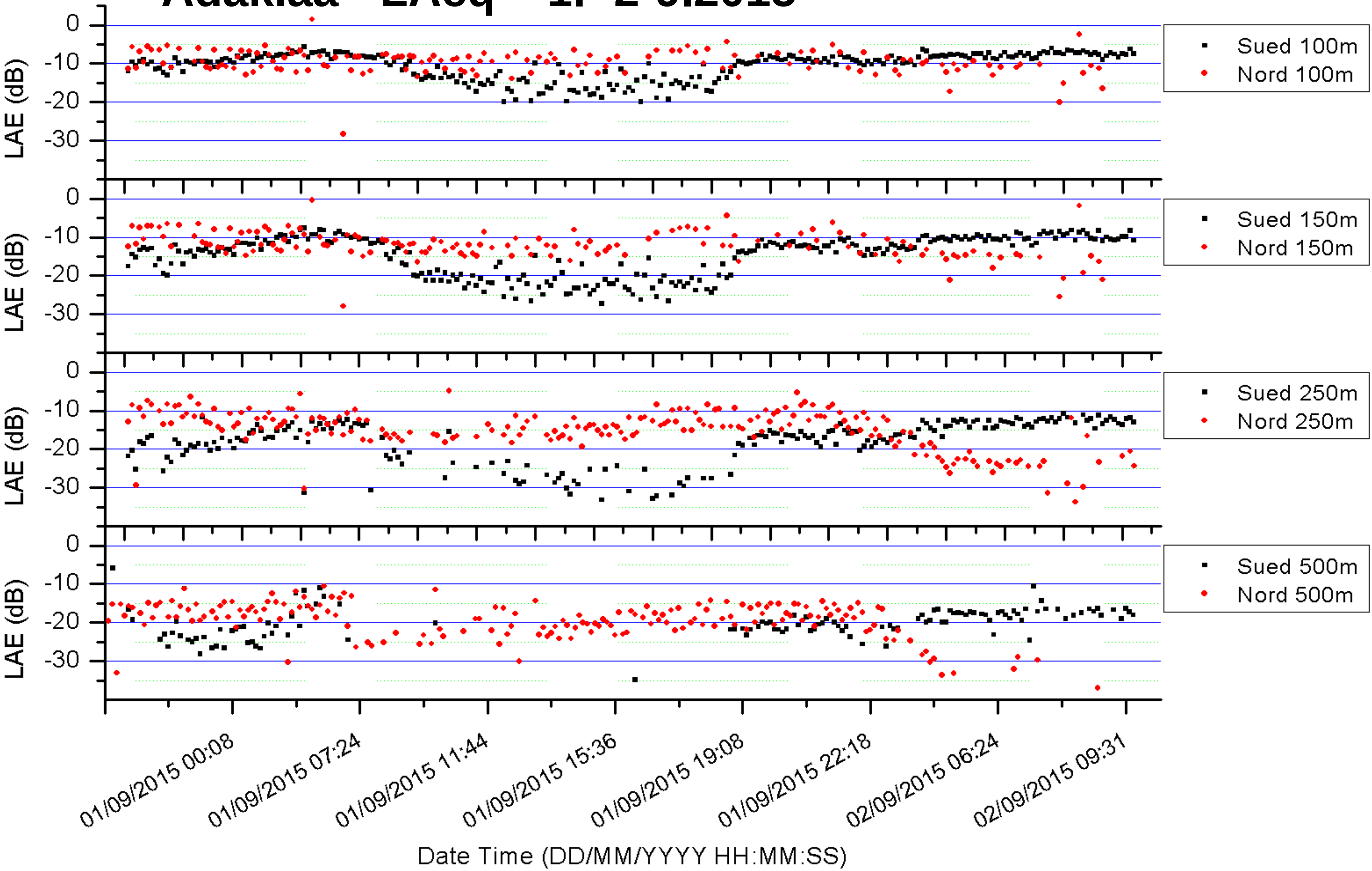

Adaklaa Train site – 100m and 150 m

Eff. Sound speed gradient – soundlevel difference

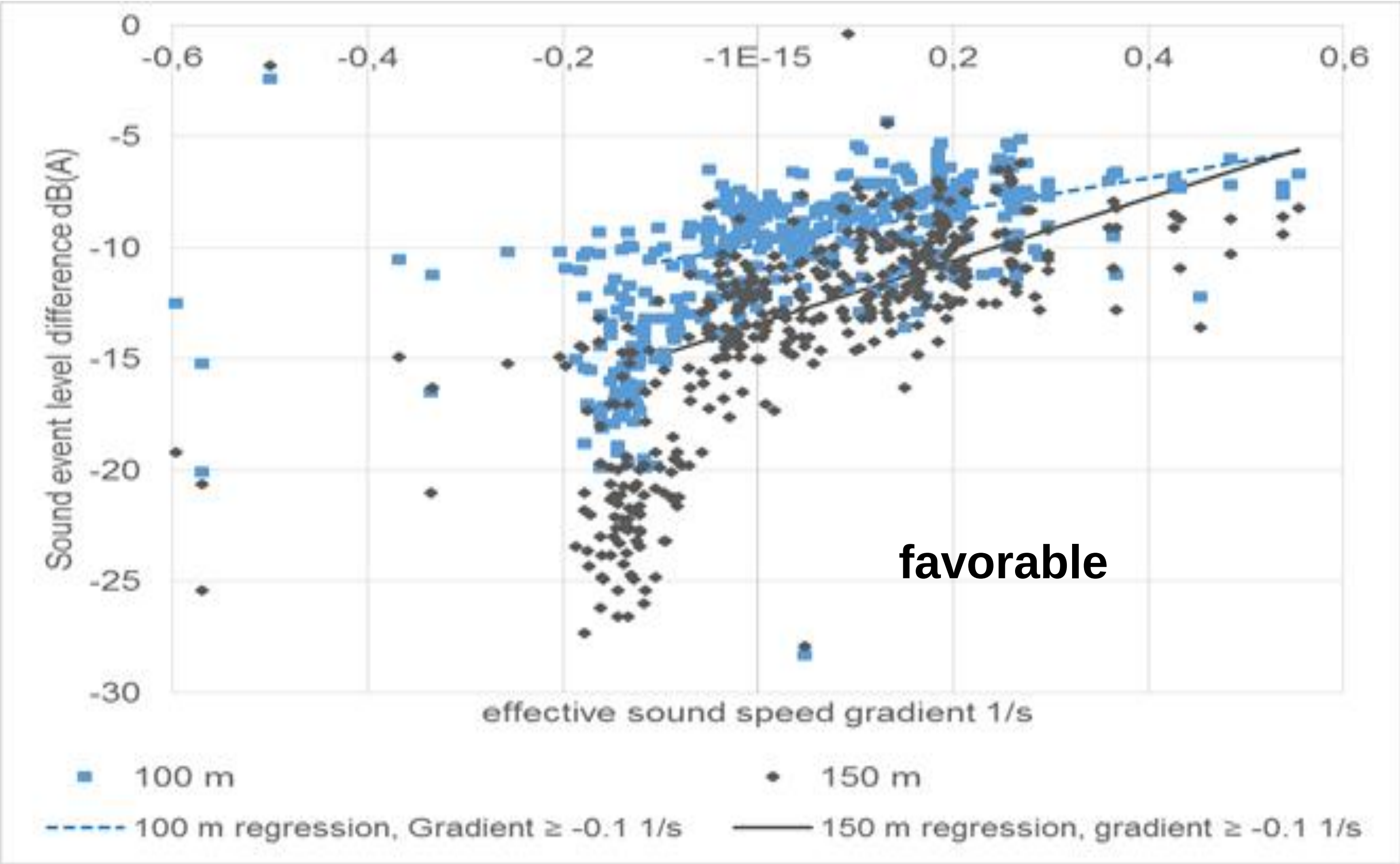

Adaklaa Train site – 250m and 500m

Eff. Sound speed gradient – soundlevel difference

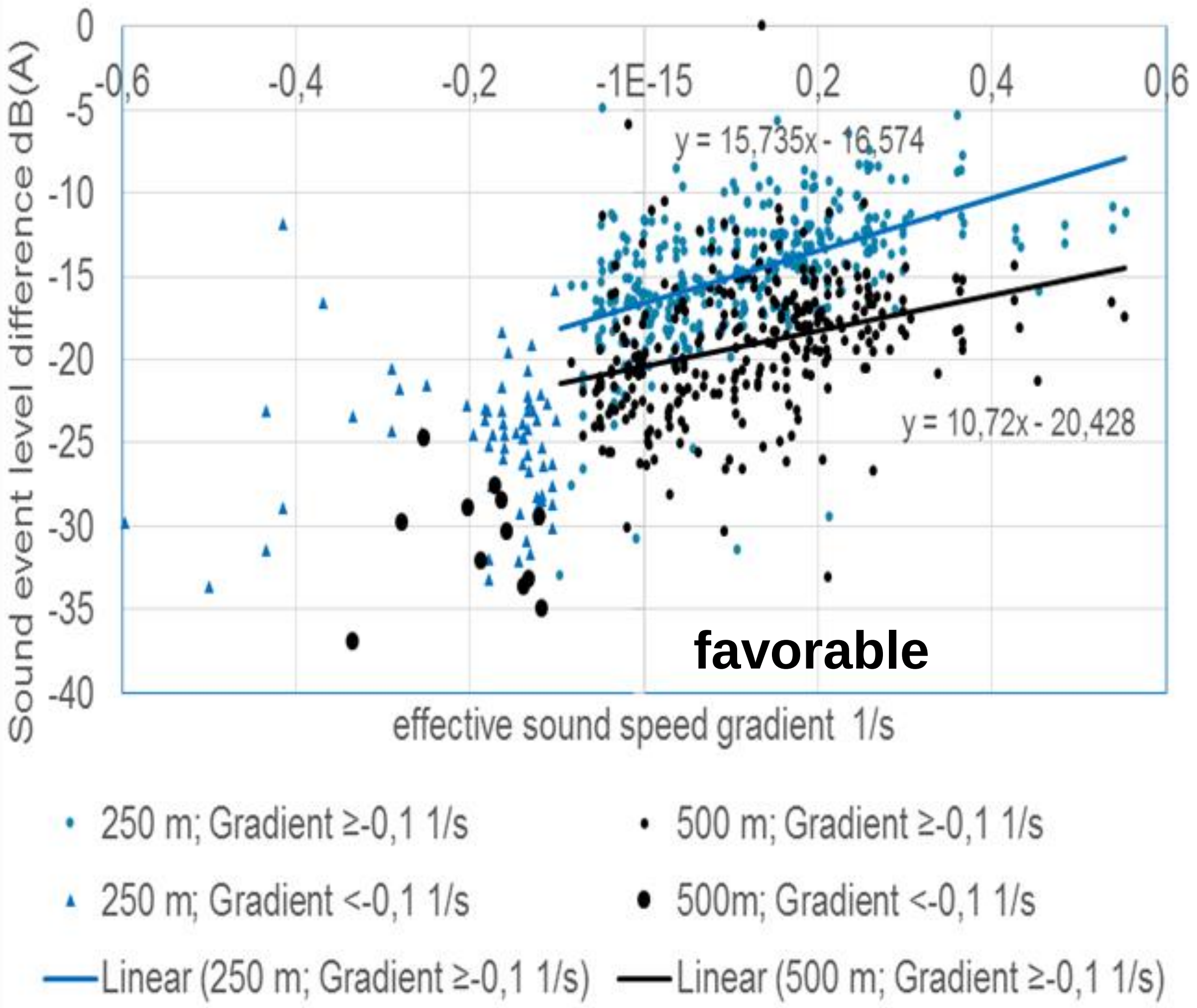

effective sound speed gradient and Laeq - highway

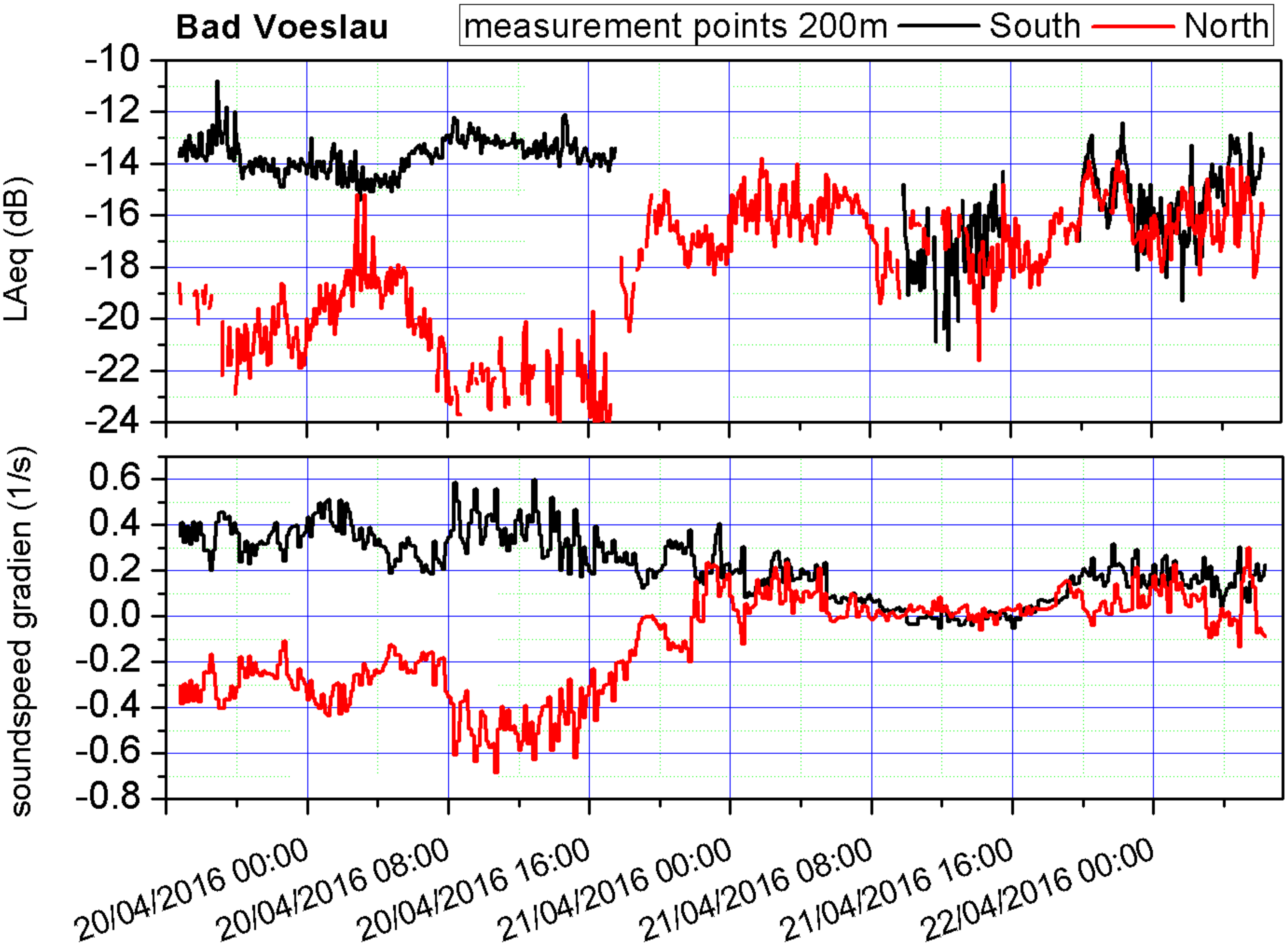

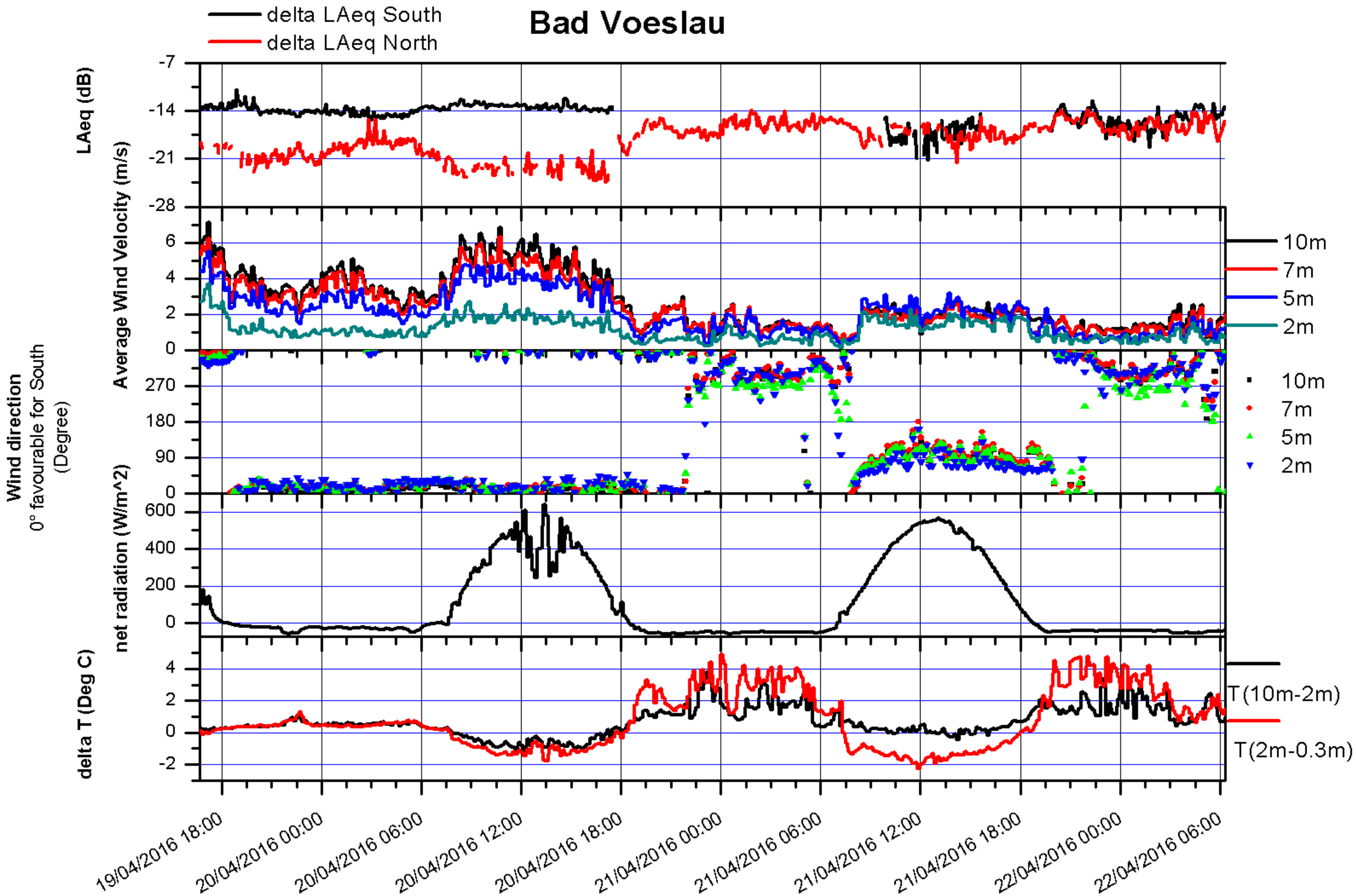

Bad Voeslau
delta LAeq South
delta LAeq North
LAeq (dB)
Average Wind Velocity (m/s)
10m
7m
5m
2m
Wind direction
0° favourable for South
(Degree)
net radiation (W/m^2)
delta T (Deg C)
T(10m-2m)
T(2m-0.3m)
19/04/2016 18:00
20/04/2016 00:00
20/04/2016 06:00
20/04/2016 12:00
20/04/2016 18:00
21/04/2016 00:00
21/04/2016 06:00
21/04/2016 12:00
21/04/2016 18:00
22/04/2016 00:00
22/04/2016 06:00

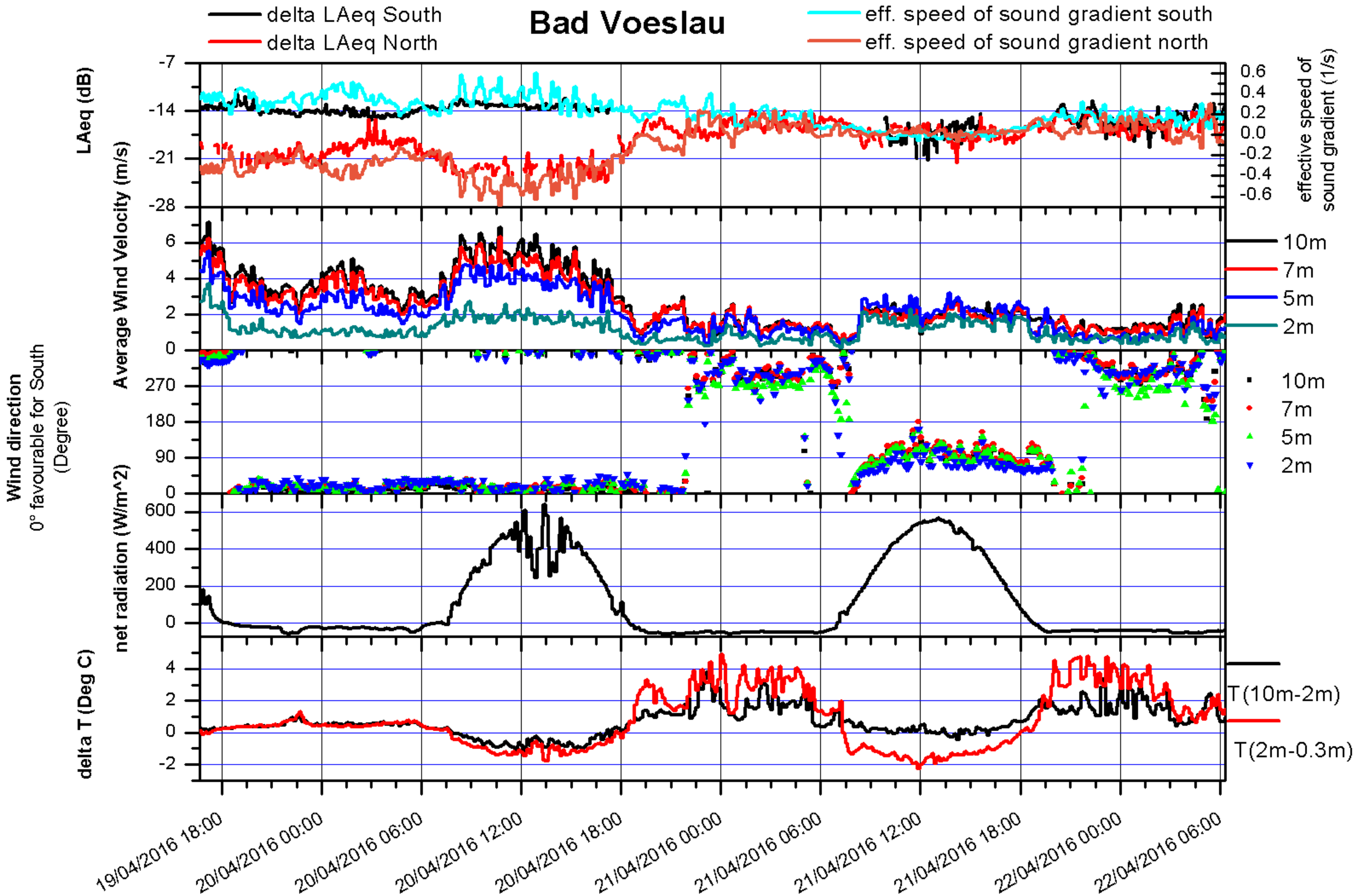

Bad Voeslau
delta LAeq South
delta LAeq North
eff. speed of sound gradient south
eff. speed of sound gradient north
LAeq (dB)
-7
-14
-21
-28
effective speed of sound gradient (1/s)
0.6
0.4
0.2
0.0
-0.2
-0.4
-0.6
Average Wind Velocity (m/s)
6
4
2
0
10m
7m
5m
2m
Wind direction 0° favourable for South (Degree)
270
180
90
0
10m
7m
5m
2m
net radiation (W/m^2)
600
400
200
0
delta T (Deg C)
4
2
0
-2
T(10m-2m)
T(2m-0.3m)
19/04/2016 18:00
20/04/2016 00:00
20/04/2016 06:00
20/04/2016 12:00
20/04/2016 18:00
21/04/2016 00:00
21/04/2016 06:00
21/04/2016 12:00
21/04/2016 18:00
22/04/2016 00:00
22/04/2016 06:00

Effective sound speed gradient – practical use

Example form measurements of Bad Vöslau 2016

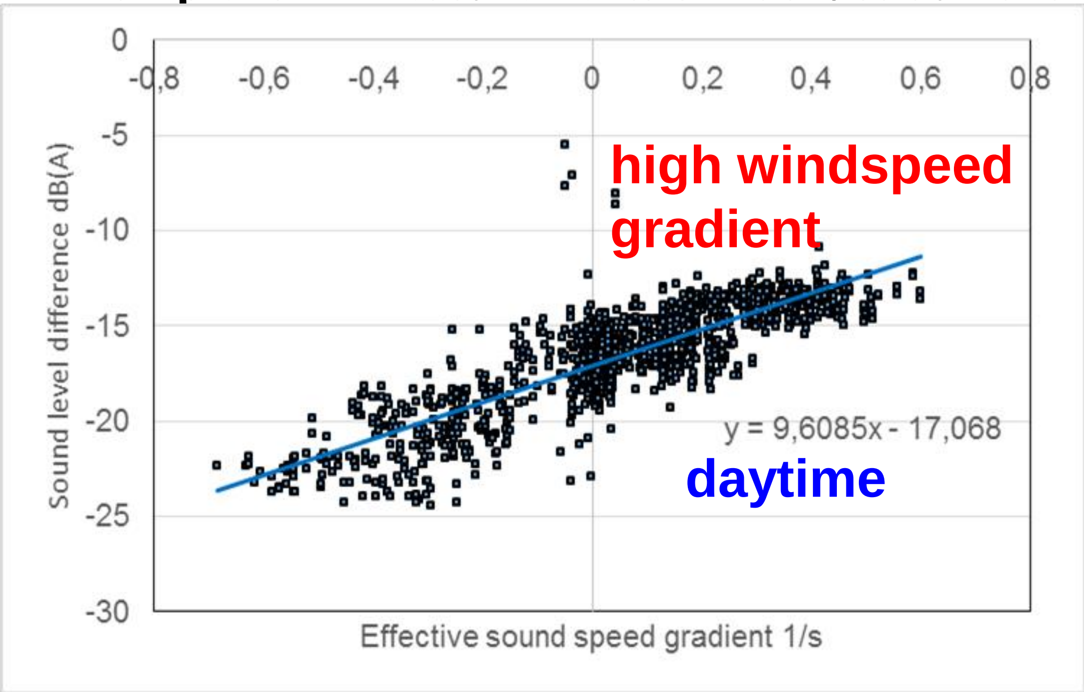

effective sound speed

$$c_{eff}(z) = c(z) + u(z)\cos\alpha$$

effective sound speed gradient

$$\frac{\Delta c_{eff}}{\Delta z} = \frac{c_0}{2T_0}\frac{\Delta T}{\Delta z} + \cos\alpha \frac{\Delta u}{\Delta z}$$

diabatic and wind contribution

$\Delta c_{eff} / \Delta z < -0.1$ unfavourable sound propagation

$-0.1 \leq \Delta c_{eff} / \Delta z \leq 0.1$ neutral sound propagation

$\Delta c_{eff} / \Delta z > 0.1$ favourable sound propagation

Conclusions

- Under normal terrain conditions **MOST is OK**
- Met Profiles are well represented
- Measurement heights are **uncritical for Met**
- Measurement heights are **critical for the eff. Sound level grad.**
- **Wind effect** are often very important (daytime)

Thank you for you attention

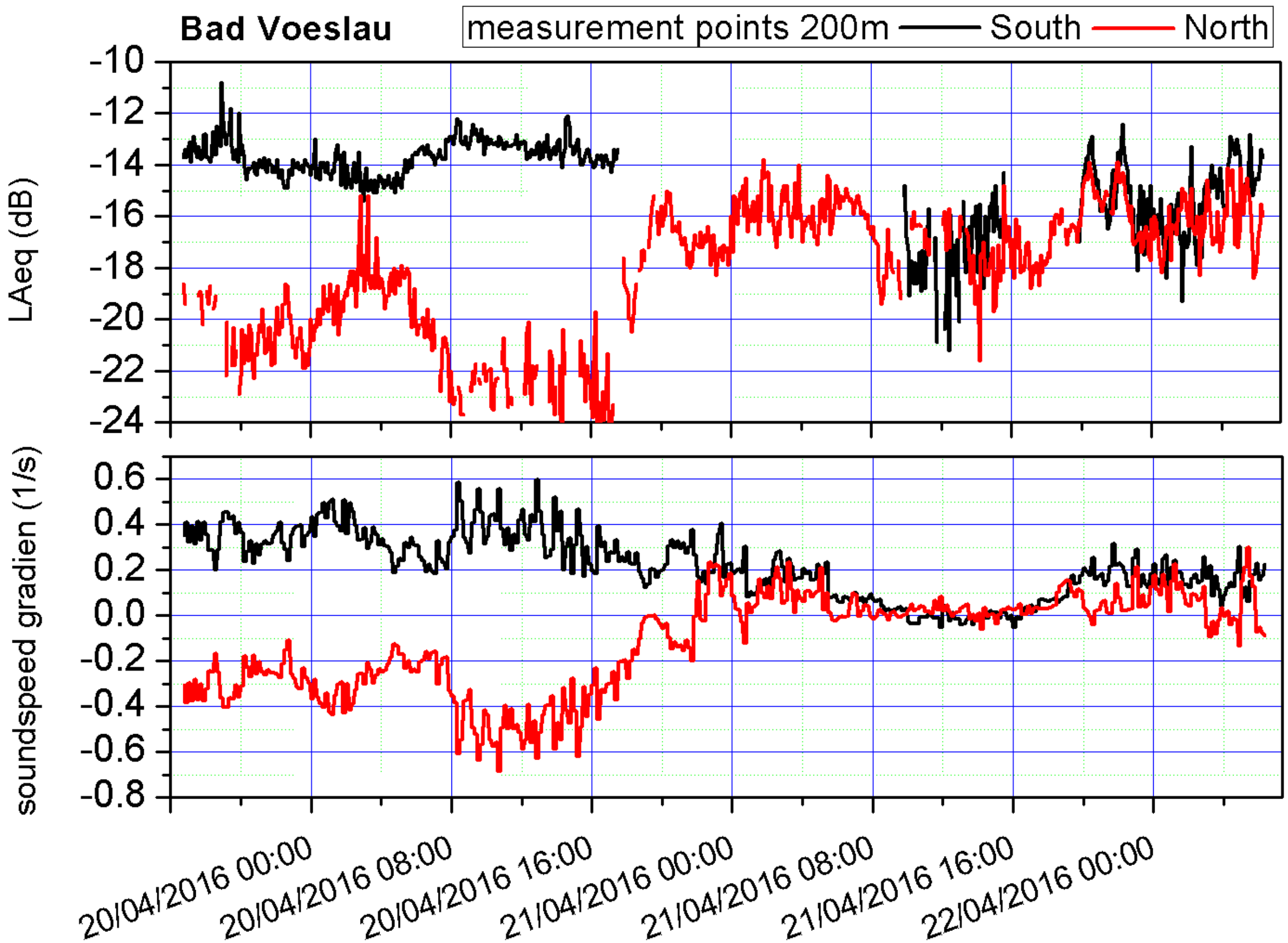

Spectral broadening of acoustic waves by a convected layer of synthetic turbulence

Vincent Clair [1] and Gwénaël Gabard [2]

[1] Université de Lyon, École Centrale de Lyon, LMFA UMR CNRS 5509, F-69134 Écully, France

[2] Le Mans Université, LAUM UMR CNRS 6613, F-72085 Le Mans, France

17th International Symposium on Long Range Sound Propagation

–

12-13th June 2018

Scattering of sound by turbulence

- Scattering occurs when acoustic waves propagate through a volume of turbulence.

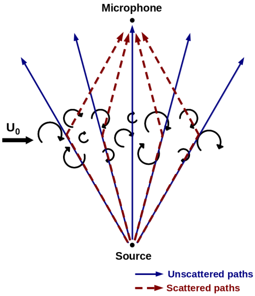

Figure 1: Scattering by a layer of turbulence.

Scattering of sound by turbulence

- Scattering occurs when acoustic waves propagate through a volume of turbulence.
- Spatial redistribution of the acoustic energy.
- Time-evolving turbulence: alteration of the spectral content (spectral broadening or "haystacking").

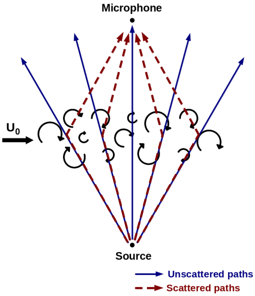

Figure 1: Scattering by a layer of turbulence.

Scattering of sound by turbulence

- Scattering occurs when acoustic waves propagate through a volume of turbulence.
- Spatial redistribution of the acoustic energy.
- Time-evolving turbulence: alteration of the spectral content (spectral broadening or "haystacking").

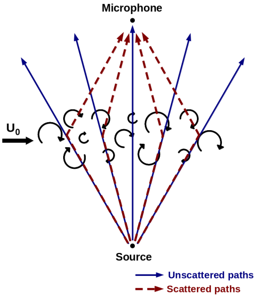

Figure 1: Scattering by a layer of turbulence.

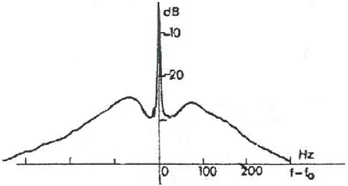

Figure 2: PSD of a harmonic source scattered by a turbulent shear layer, from Candel et al. (1975).

Examples

- Scattering of turbofan's turbine tones propagating through the downstream turbulent shear layers.

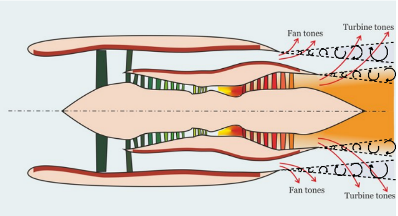

Figure 3: Scattering of turbine tones.

- Scattering of turbofan's turbine tones propagating through the downstream turbulent shear layers.
- Scattering of sound measurements outside of the jet core of open-jet wind tunnels.

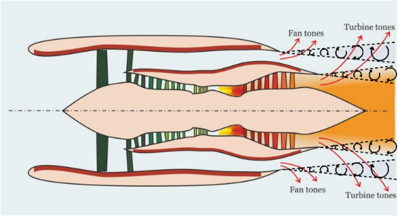

Figure 3: Scattering of turbine tones.

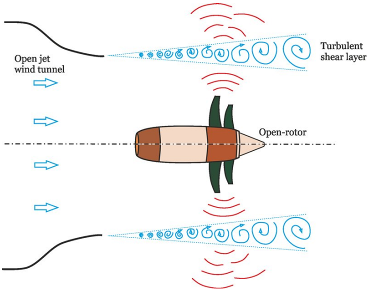

Figure 4: Scattering in open-jet wind tunnels

Examples

- Scattering of turbofan's turbine tones propagating through the downstream turbulent shear layers.
- Scattering of sound measurements outside of the jet core of open-jet wind tunnels.
- Propagation of sound through atmospheric turbulence (sounding techniques, scattering over barriers, ...).

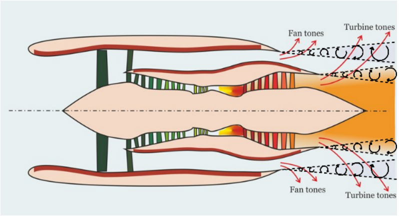

Figure 3: Scattering of turbine tones.

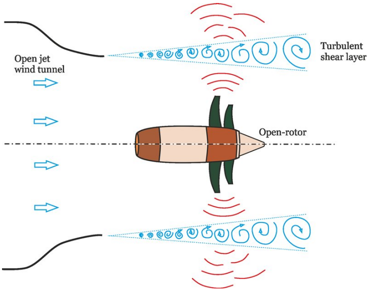

Figure 4: Scattering in open-jet wind tunnels

1. Introduction: scattering of sound by turbulence

2. Scattering by a single eddy
   - Plane waves scattered by a steady vortex
   - Scattering by a convected vortex

3. Scattering by a turbulent layer
   - Effects of the source frequency
   - Effects of the convection velocity

4. Conclusion

- Configuration: a plane wave $p_i'(r,\theta,t) = P\mathrm{e}^{\mathrm{i}\omega t - \mathrm{i}kx}$ is propagating through an inviscid vortex defined by:

$$\begin{cases} \boldsymbol{u}(r) = U_\mathrm{v}\dfrac{r}{L}\exp\left[\frac{1}{2}\left(1 - r^2/L^2\right)\right]\boldsymbol{e}_\theta \ , \\ p(r) = p_\infty\left[1 - \dfrac{\gamma-1}{2}M_\mathrm{v}^2\exp\left(1 - r^2/L^2\right)\right]^{\gamma/(\gamma-1)} \ , \\ \rho(r) = \rho_\infty\left[p(r)/p_\infty\right]^{1/\gamma} \ , \end{cases} \tag{1}$$

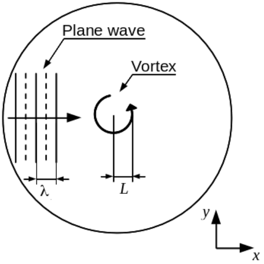

Figure 5: Sketch of the configuration considered.

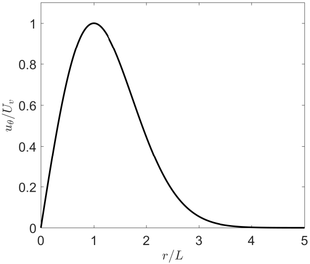

Figure 6: Radial evolution of the vortex azimuthal velocity.

Plane waves scattered by a steady vortex: semi-analytical method

- LEE in cylindrical coordinates:

$$\frac{\partial \boldsymbol{q}'}{\partial t} + A\boldsymbol{q}' + B\frac{\partial \boldsymbol{q}'}{\partial r} + C\frac{1}{r}\frac{\partial \boldsymbol{q}'}{\partial \theta} = \boldsymbol{0} \,, \tag{2}$$

- Fluctuations $\boldsymbol{q}' = (\rho', \boldsymbol{u}', p') = \boldsymbol{q}'_i + \boldsymbol{q}'_s$, with $\cdot_i$ incident and $\cdot_s$ scattered parts.
- The fluctuations are assumed to be time harmonic and decomposed into series of azimuthal modes.
- For each mode:

$$\mathrm{i}\omega\boldsymbol{q}'_{s,m} + A\boldsymbol{q}'_{s,m} + B\frac{\mathrm{d}\boldsymbol{q}'_{s,m}}{\mathrm{d}r} - \frac{\mathrm{i}m}{r}C\boldsymbol{q}'_{s,m} = -\mathrm{i}\omega\boldsymbol{q}'_{i,m} - A\boldsymbol{q}'_{i,m} - B\frac{\mathrm{d}\boldsymbol{q}'_{i,m}}{\mathrm{d}r} + \frac{\mathrm{i}m}{r}C\boldsymbol{q}'_{i,m} \,. \tag{3}$$

- This system is solved over a domain $0 \leq r \leq R$ using a high-order finite difference approximation for the radial derivatives.
- For each mode, a modal amplitude of the scattered field A_m is deduced. In the far-field:

$$p'_s(r,\theta,t) = \frac{D(\theta)}{\sqrt{r}}\mathrm{e}^{\mathrm{i}\omega(t-r/c_\infty)} \,, \quad \text{with} \quad D(\theta) = \sqrt{\frac{2\mathrm{i}}{k\pi}}\sum_{m=-M}^{M}\mathrm{i}^m A_m \mathrm{e}^{-\mathrm{i}m\theta} \,. \tag{4}$$

- Test case from Colonius et al. (1994).
- The vortex has a core size $L = 1$ and a maximum velocity $M_v = 0.125$.
- The plane wave has an amplitude $P = 1$ and a wavelength $\lambda = 4L$.

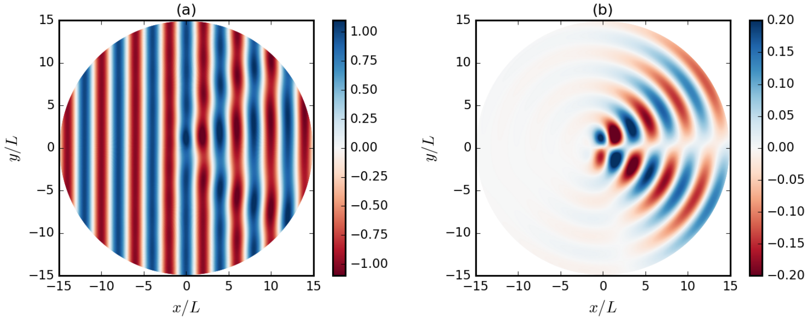

Figure 7: Snapshots of (a) the total field and (b) the scattered field calculated with the semi-analytical model for $M_\mathrm{v} = 0.125$ and $kL = \pi/2$.

Plane waves scattered by a steady vortex: parametric study

- Strong evolution of the directivity pattern, position of the maxima and amplitude of the scattered field with the frequency.

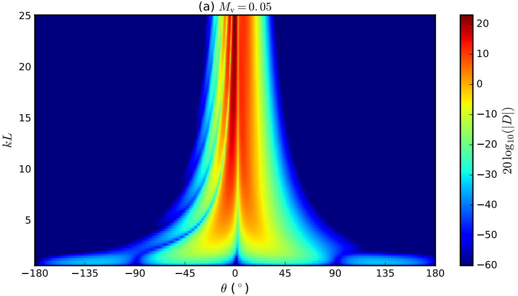

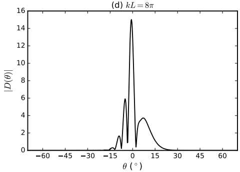

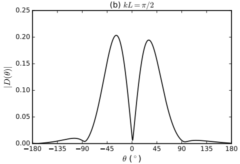

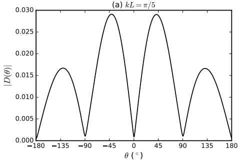

Figure 8: Directivity $D(\theta)$ of the scattered pressure in the far field (in dB) as a function of the direction θ and the Helmholtz number kL with a vortex magnitude $M_v = 0.05$. $\theta = 0°$ corresponds to the direction of the incident wave.

Scattering by a convected vortex

- The vortex is convected by a uniform mean flow in the x-direction with velocity U_c.

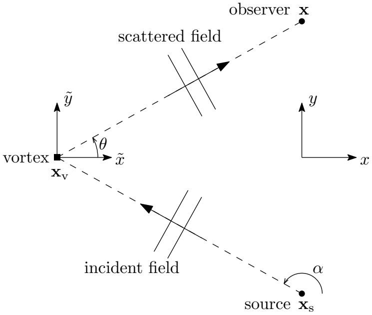

Figure 9: Scattering by a convected vortex.

- For a plane wave with an incidence angle α relative to the flow direction:
  - The semi-analytical model can be modified by working in a frame of reference moving with the vortex and considering an observer in motion.
  - The instantaneous frequency perceived by the observer is a combination of two Doppler factors: $\omega_{\mathrm{o}}(t) = \omega_{\mathrm{s}}(1 + M_{\mathrm{c}} \cos \tilde{\theta}(t))/(1 + M_{\mathrm{c}} \cos \alpha)$

- The *PIANO* solver, developed by the *DLR* is used to solve the LEE in cartesian coordinates and in the time domain.
  - High-order finite difference approximation for the spatial derivatives.
  - High-order explicit filter to damp spurious oscillations.
  - Standard 4th order Runge-Kutta time integration.
  - Buffer zones can be used to damp outgoing waves or to introduce the incident sound field.
- The LEE are linearised over an unteady base flow $(\rho, \boldsymbol{u}, p) = (\rho_0, \boldsymbol{u}_0, p_0) + (\rho_\mathrm{t}, \boldsymbol{u}_\mathrm{t}, p_\mathrm{t})$, where $\cdot_0$ is the steady component (convection) and $\cdot_t$ is the unsteady component (moving vortex).
- Accounting for $\nabla \cdot \boldsymbol{u}_t = 0$ and neglecting terms with ρ_t, p_t:

$$\begin{cases} \dfrac{\partial \rho'}{\partial t} + \boldsymbol{u}_0 \cdot \nabla \rho' + \boldsymbol{u}' \cdot \nabla \rho_0 + \rho_0 \nabla \cdot \boldsymbol{u}' + \rho' \nabla \cdot \boldsymbol{u}_0 = \boldsymbol{u}_\mathrm{t} \cdot \nabla \rho' \ , \\ \dfrac{\partial \boldsymbol{u}'}{\partial t} + (\boldsymbol{u}_0 \cdot \nabla)\boldsymbol{u}' + (\boldsymbol{u}' \cdot \nabla)\boldsymbol{u}_0 + \dfrac{\nabla p'}{\rho_0} - \rho' \dfrac{\nabla p_0}{\rho_0^2} = (\boldsymbol{u}_\mathrm{t} \cdot \nabla)\boldsymbol{u}' + (\boldsymbol{u}' \cdot \nabla)\boldsymbol{u}_\mathrm{t} \ , \\ \dfrac{\partial p'}{\partial t} + \boldsymbol{u}_0 \cdot \nabla p' + \boldsymbol{u}' \cdot \nabla p_0 + \gamma p_0 \nabla \cdot \boldsymbol{u}' + \gamma p' \nabla \cdot \boldsymbol{u}_0 = \boldsymbol{u}_\mathrm{t} \cdot \nabla p' \ , \end{cases} \tag{5}$$

- Increased scattered levels with frequencies.
- The beams are narrower at high frequencies.
- The direction of the scattered field is evolving in time because of the circular incident wavefronts.

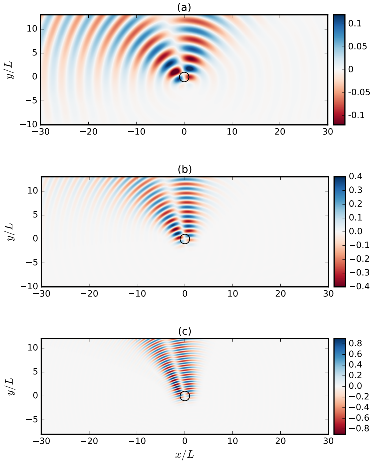

Figure 10: Scattered pressure at $t = 0$ for: (a) $\lambda = 4L$, (b) $\lambda = 2L$ and (c) $\lambda = L$. Other param.: $M_{\mathrm{c}} = 0.176$, $M_{\mathrm{v}} = 0.05$, $\boldsymbol{x}_{\mathrm{s}} = (0, -20L)$.

Scattering of a point mass source: simulations

- Increased scattered levels with frequencies.
- The beams are narrower at high frequencies.
- The direction of the scattered field is evolving in time because of the circular incident wavefronts.
- The wavepackets are narrower for high frequencies.

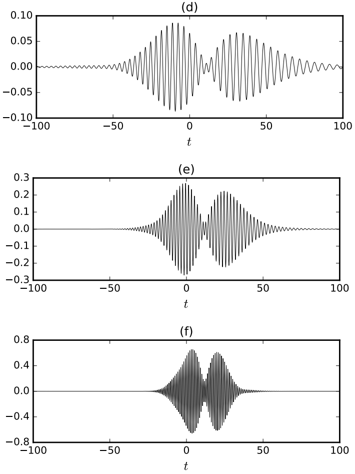

Figure 10: Scattered pressure recorded at $x = 0$, $y = 10L$ for: (d) $\lambda = 4L$, (e) $\lambda = 2L$ and (f) $\lambda = L$. Other param.: $M_c = 0.176$, $M_v = 0.05$, $\boldsymbol{x}_s = (0, -20L)$.

- Changes in the number of sidebands with frequency consistent with the number of lobes on the directivity (see steady vortex).
- The position of the sidebands is not evolving linearly with the source frequency.
- The scattered beams are narrower at higher frequency, reducing the extent of the Doppler shift between the vortex and the observer.

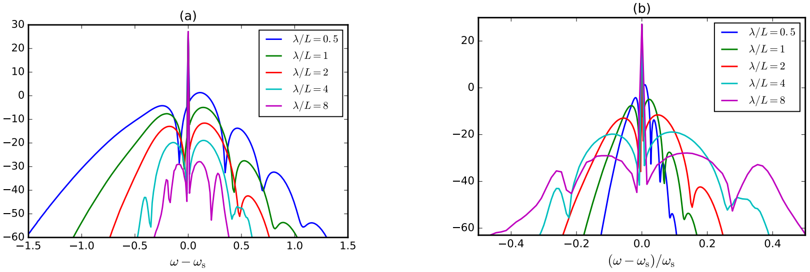

Figure 11: Sound Pressure Level (in dB/Hz re. 1) of the scattered field at $x = 0$, $y = 10L$ for different frequencies.

- Reduction of the sideband levels when U_c increases ($1/U_c$ factor for a plane wave).
- The convection velocity affects the frequency range received by the observer.
- For a plane wave with $\alpha = 90°$, the width of the sidebands evolves linearly with U_c.

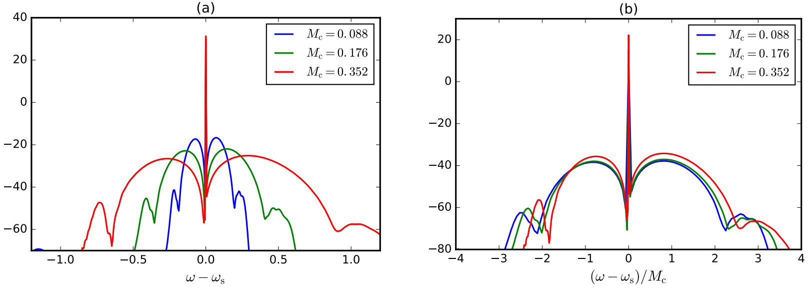

Figure 12: Sound Pressure Levels (in dB/Hz re. 1) of the scattered field at $x = 0$, $y = 10L$ for different values of the convection velocity M_c.

- The single vortex is replaced by a layer of homogeneous and isotropic turbulence.
- The turbulent layer has a constant width δ and is convected by a uniform mean flow.
- The turbulence is introduced as the unsteady part of the base flow in the numerical method presented earlier.

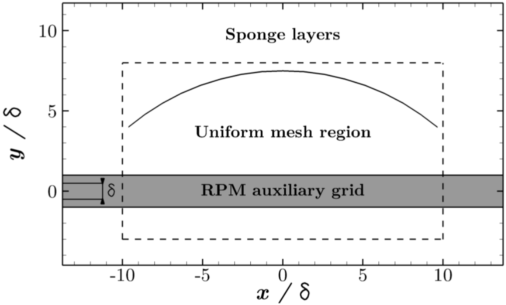

Figure 13: Schematic of the computational domain.

- The turbulent field is synthesized using the RPM stochastic method.
- It is based on the filtering of a white noise to prescribe chosen correlations.
- Random particles are distributed on an auxiliary grid and convected by the mean flow.
- The spatial correlations imposed are Gaussian
- The turbulence generated can be frozen or a time decorrelation can be imposed.

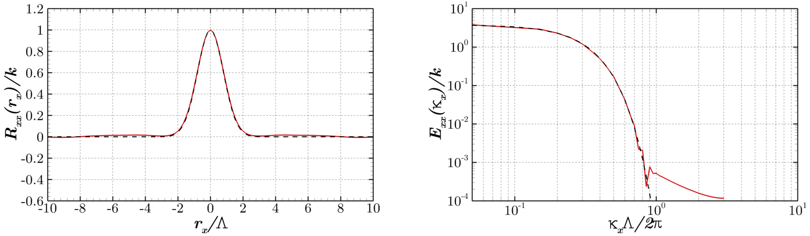

Figure 14: Examples of correlations and spectra of synthetic turbulence. (——) *RPM* and (– – –) analytical solution.

- The mean flow $(u_0, 0)$ is uniform and between $0.088 < M_c < 0.352$.
- The turbulence has an integral length scale $\Lambda = \delta/4$ and a turbulent intensity $T_I = 15\%$.
- The turbulent kinetic energy $k_t(y)$ evolves as a Gaussian in the y-direction with $k_t(\delta/2) \approx 0.3 k_{t,max}$.
- The turbulence is frozen (only convected by the mean flow).
- A point source is located at $(x_s, y_s) = (0, -30\Lambda)$ with wavelengths $8\Lambda > \lambda_0 = c_0/f_0 > \Lambda/2$.

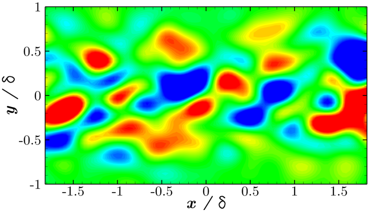

Figure 15: Example of a synthetic turbulent velocity field. u_x component.

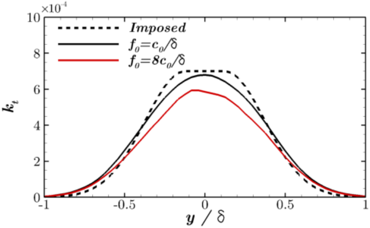

Figure 16: Turbulent kinetic energy through the turbulent layer.

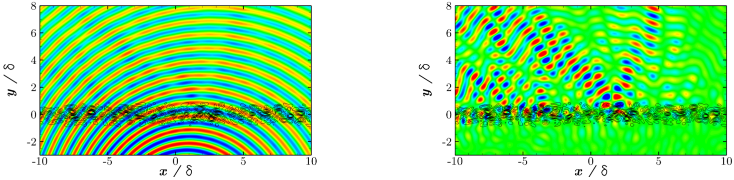

Figure 17: Total (left, ± 1.5) and scattered (right, ± 0.15) pressure fields for the case $f_0 = c_0/4\Lambda$, $M = 0.176$.

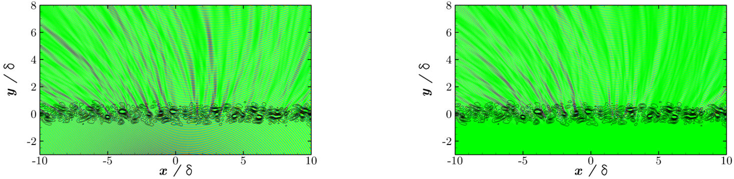

Figure 18: Total (left, ± 2) and scattered (right, ± 2) pressure fields for the case $f_0 = 2c_0/\Lambda$, $M = 0.176$.

- The scattered field is complex because of the interferences between the numerous turbulent structures scattering altogether.
- The amplitude of the scattered field is important at high frequency, about the same as the incident field.
- As a result, the total pressure is strongly affected at high frequency.

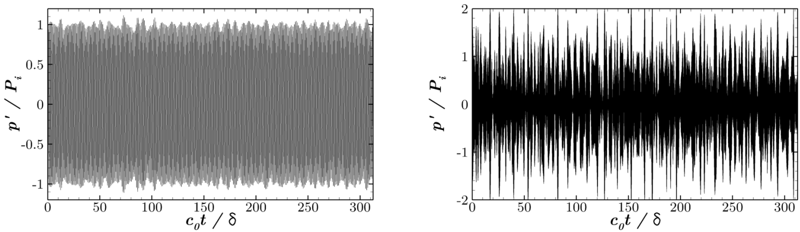

Figure 19: Pressure signals over a segment of the periodogram at $\theta = 90^\circ$ for $f_0 = c_0/4\Lambda$ (left) and $f_0 = 2c_0/\Lambda$ (right).

- For low frequency sources, the shape of the sidebands is similar to the simulations realized for a single vortex.
- The SPL for high frequency sources are quite similar to experimental observations, with wider sidebands decaying slowly.

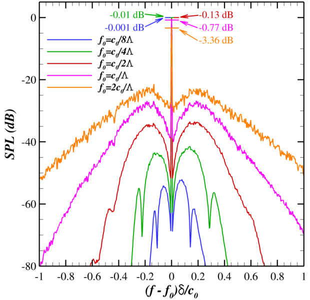

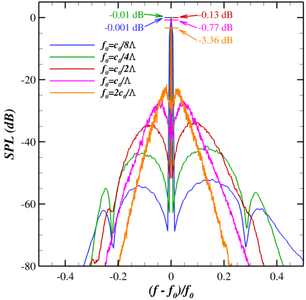

Figure 20: SPL at $\theta = 90^\circ$ for different source frequencies plotted as a function of the frequency (left) and reduced frequency (right).

Scattering by a turbulent layer: source frequency IV

- Plotted as a function of the reduced frequency, the sidebands are narrower for high frequency sources. This is consistent with the previous observations of smaller scattering angles at high frequency.
- Experimentally, the position of the sidebands does not evolve with the source frequency.
- Here, this is true only for the high frequency cases.
- The differences in the spectral content of the turbulence (size of the large eddies) may explain these differences.

- For a low frequency source, the convection velocity affects the width of the sidebands as for the study on the single vortex.
- The scattered levels are more important at higher convection velocity because the turbulent intensity is kept at 15%.

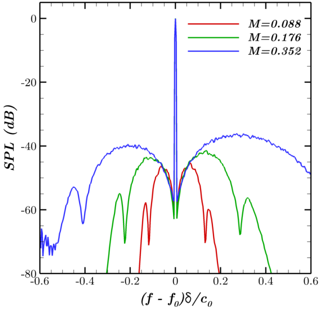

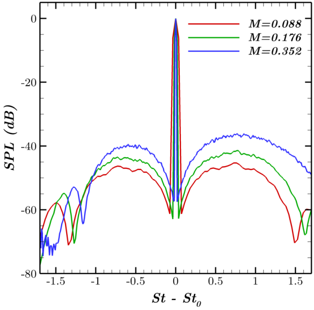

Figure 21: SPL for different convection velocities and $f_0 = c_0/4\Lambda$ plotted as a function of the frequency (left) and the Strouhal number (right).

- For a high frequency source, the sidebands are widening with the convection velocity for $M_c = 0.088$ and $M_c = 0.176$.
- The maximum level of the sidebands does not evolve much, but the sidebands are decaying more slowly when M_c increases.
- At $M_c = 0.352$, strong scattering is observed $\rightarrow$ single broadband hump and strong reduction of the peak.

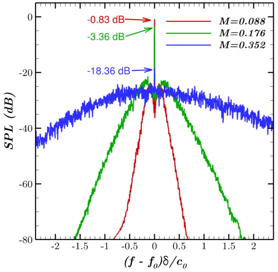

Figure 22: SPL for different convection velocities and $f_0 = 2c_0/\Lambda$ plotted as a function of the frequency (left) and the Strouhal number (right).

Conclusions I

- A semi-analytical method has been developed to consider the scattering of plane waves by a steady or convected vortex in two dimensions.
- A numerical method is also used to consider incident sound fields other than a plane wave. This method can also be coupled with a stochastic method to consider the scattering by a turbulent layer.
- Strong evolutions of the scattered field with the incident frequency and vortex strength are observed.
- For a convected vortex, the spectra observed display sidebands around the source frequency.
- The shape and position of these sidebands can be explained by the combination of the directivity of the scattered field with Doppler effects due to the relative motions between the source, the vortex and the observer.
- For a point source , the effects of the convection on the incident field also have to be considered.

Conclusions II

- When a turbulent layer is considered, the scattered field is more complex due to interferences caused by the multitude of turbulent eddies scattering simultaneously.
- For low frequency sources, the observed spectra are similar to the one observed for a single vortex.
- For high frequency sources, the sidebands are decaying slowly and are similar the experimental observations.
- For a strong turbulent field and a high frequency source, strong scattering can be observed.

CANDEL, S., GUEDEL, A. & JULIENNE, A. 1975 Refraction and scattering of sound in an open wind tunnel flow. *6th International Congress on Instrumentation in Aerospace Simulation Facilities* pp. 288–300.

COLONIUS, T., LELE, S. & MOIN, P. 1994 The scattering of sound waves by a vortex: numerical simulations and analytical solutions. *Journal of Fluid Mechanics* **260**, 271–298.

U.S.ARMY

A WIDE-ANGLE PARABOLIC EQUATION METHOD FOR HANDLING DISCONTINUITIES IN VERTICAL PROFILES

Michelle E. Swearingen, Michael J. White, and Mihan H. McKenna

US Army ERDC

17th Long-Range Sound Propagation Symposium

12 June 2018

Agenda

- Setting the Stage
- Mathematical Development
- Benchmark Examples
- Data Comparison
- Discussion of the Method

Setting the Stage

- Realistic, instantaneous profiles often contain abrupt changes
- Seeking a way to handle these types of profiles correctly
- Focused on low frequencies, < 200 Hz
- Topography inclusion would be nice too…

Mathematical Development

Based on the square root operator expansion used in the LSS method

$$\sqrt{1+X} \cong 1 + \frac{1}{2}X - \frac{1}{8}X^2$$

where $X = \left(n^2 - 1\right) + \frac{1}{k_0^2}\rho\frac{\partial}{\partial z}\frac{1}{\rho}\frac{\partial}{\partial z}$

and $\frac{\partial u}{\partial r} = ik_0\sqrt{1+X}$ is the one-way wave equation

where $p = u(r,z)H_0^{(1)}(k_0 r)$

Reference:
Lee, D., Schultz, M. H., & Saad, Y. (1990). A three-dimensional wide angle wave equation with vertical density variations. *Computational Acoustics*, *1*, 143-155.

Mathematical Development

Neglect the resulting $\left(\rho \frac{\partial}{\partial z}\frac{1}{\rho}\frac{\partial}{\partial z}\right)^2$ **term**

and let $a = \frac{ik_0}{2}\left(n^2 - 1\right)$ **and** $b = \frac{i}{2k_0}$

to obtain

$$(u)_r = \left[a(1 + ab) + b(1 + 2ab)\rho \frac{\partial}{\partial z}\frac{1}{\rho}\frac{\partial}{\partial z}\right]u$$

Now has z-dependence!

Mathematical Development

Applying the principle of virtual work (to get the finite element solution) and incorporating the horizontal boundary conditions*

$$p_j\Big|_{z=D_j} = p_{j+1}\Big|_{z=D_j} \quad \text{and} \quad \frac{1}{\rho_j}\frac{\partial p_j}{\partial z}\bigg|_{z=D_j} = \frac{1}{\rho_{j+1}}\frac{\partial p_{j+1}}{\partial z}\bigg|_{z=D_j}$$

and NOT neglecting the z-dependence of the index of refraction during the integration by parts, we get some additional complexity in the resulting equations.

*** Boundary conditions are applied during the integration by parts of the $\rho\frac{\partial}{\partial z}\frac{1}{\rho}\frac{\partial}{\partial z}$ term**

Example

Arbitrary effective sound speed profile with abrupt changes

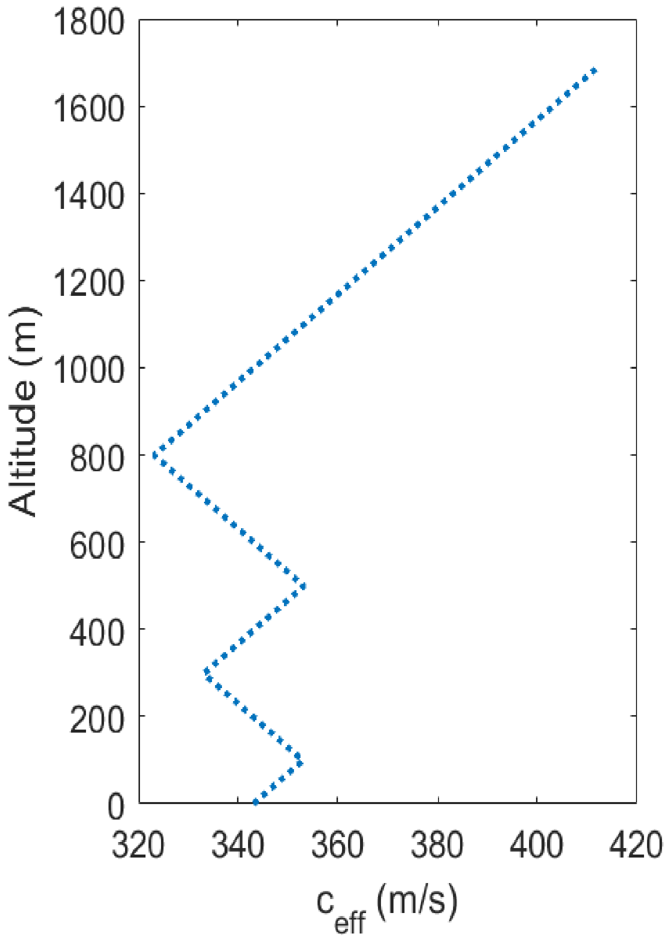

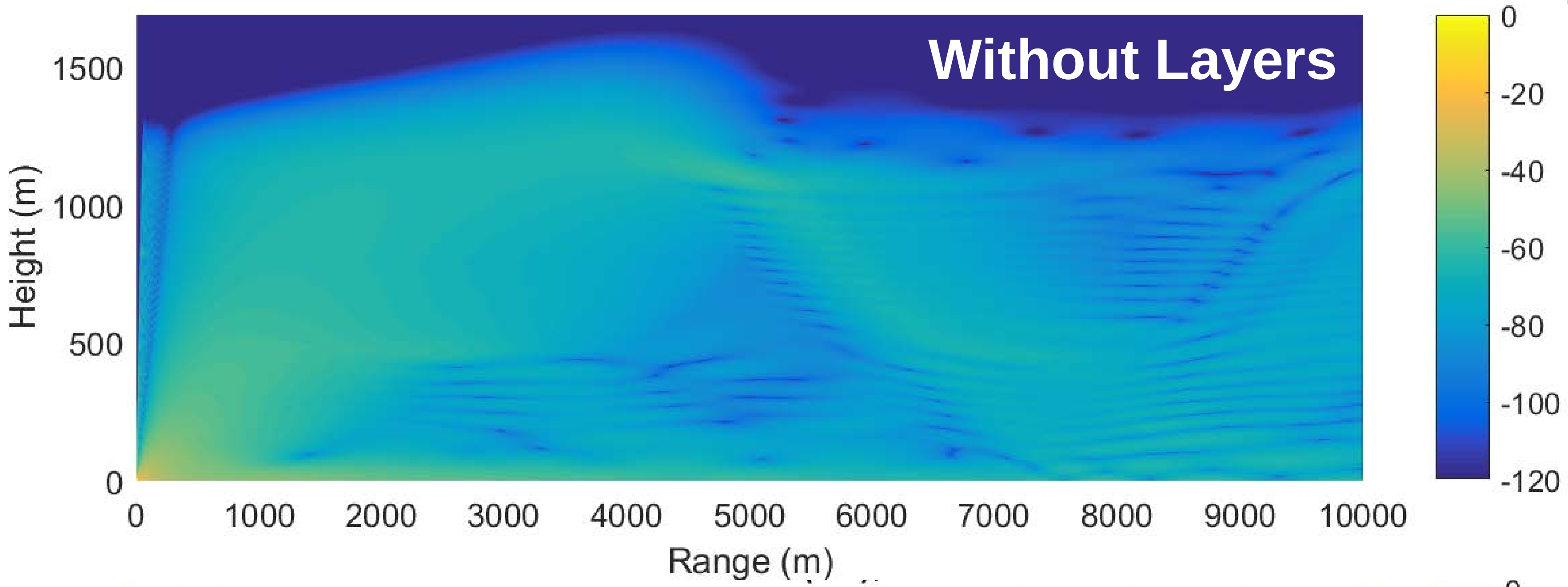

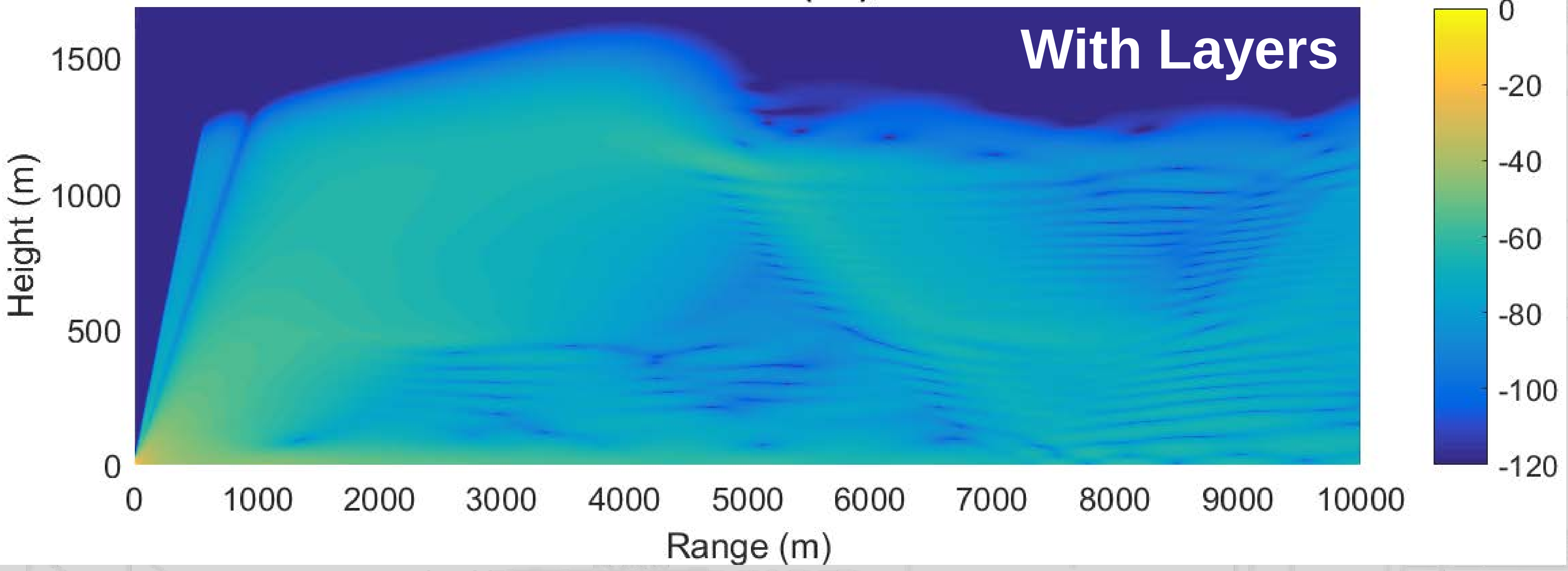

Example – dB difference (with layers – without layers)

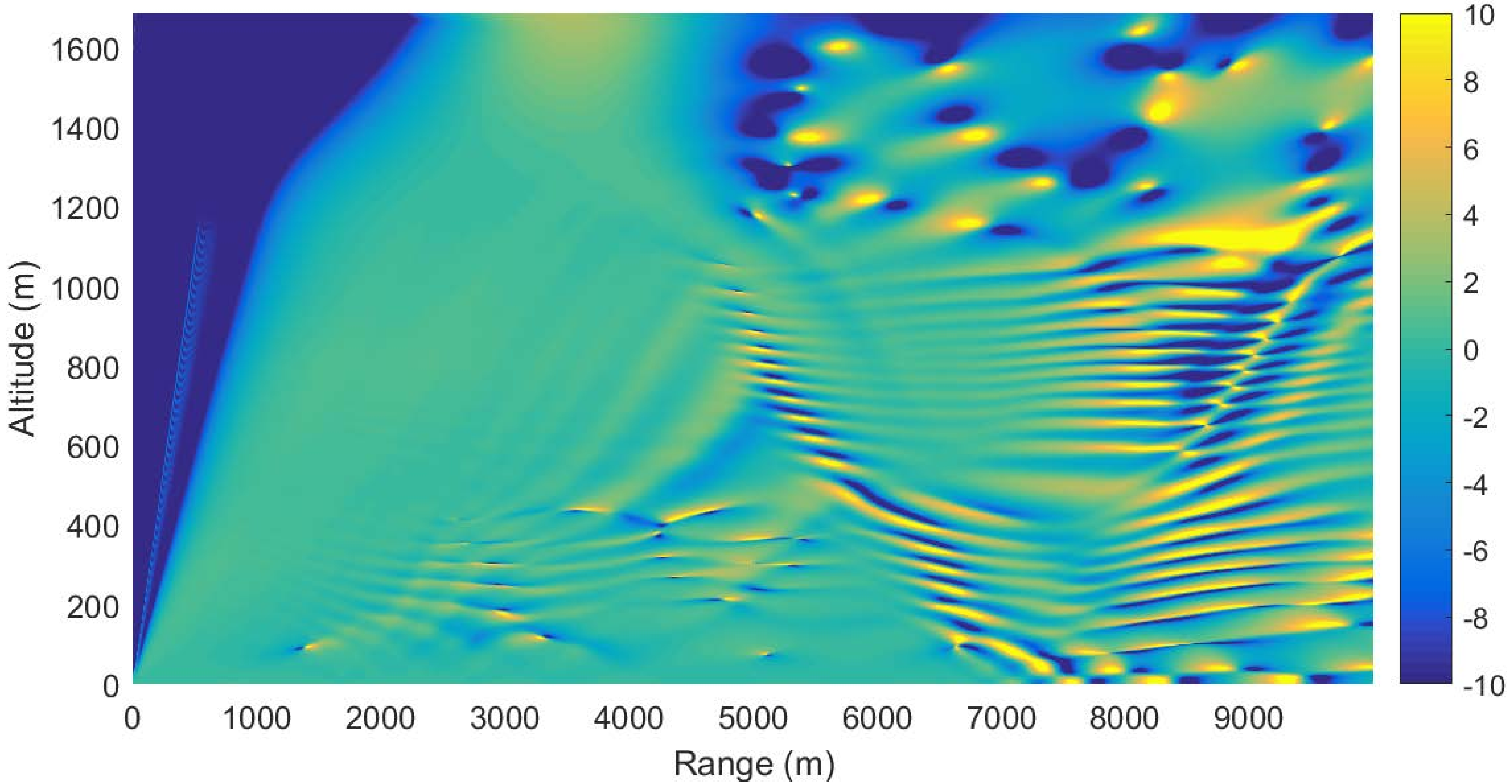

Benchmark Examples

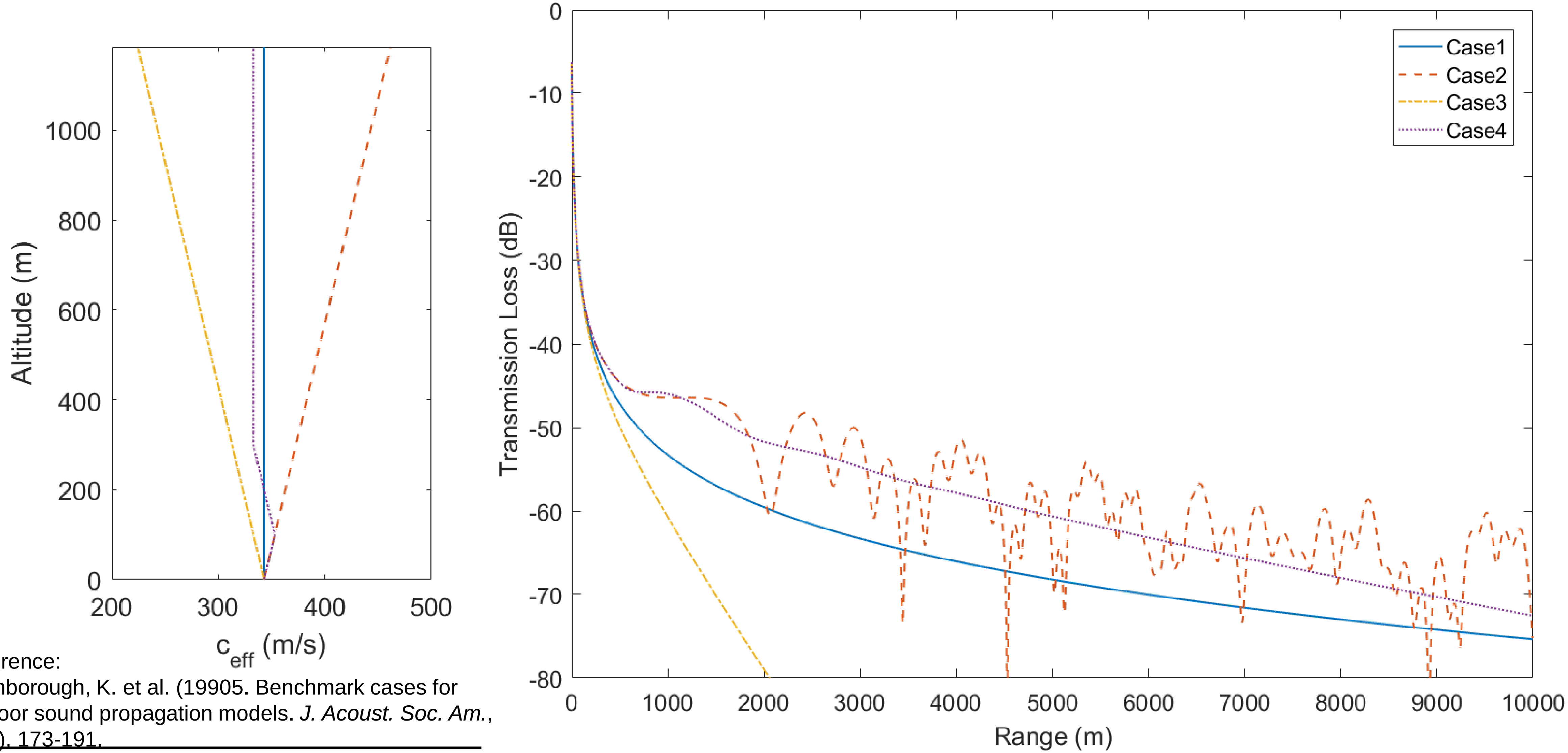

Reference:
Attenborough, K. et al. (19905. Benchmark cases for outdoor sound propagation models. *J. Acoust. Soc. Am.*, 97(1), 173-191.

Data Comparison – 24 lb C-4, 14.8 km

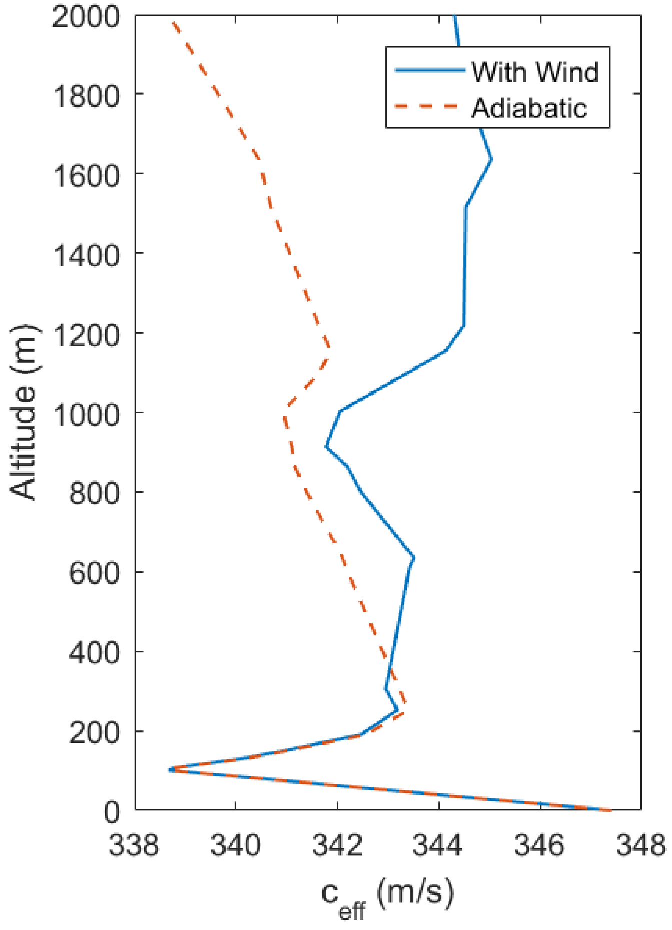

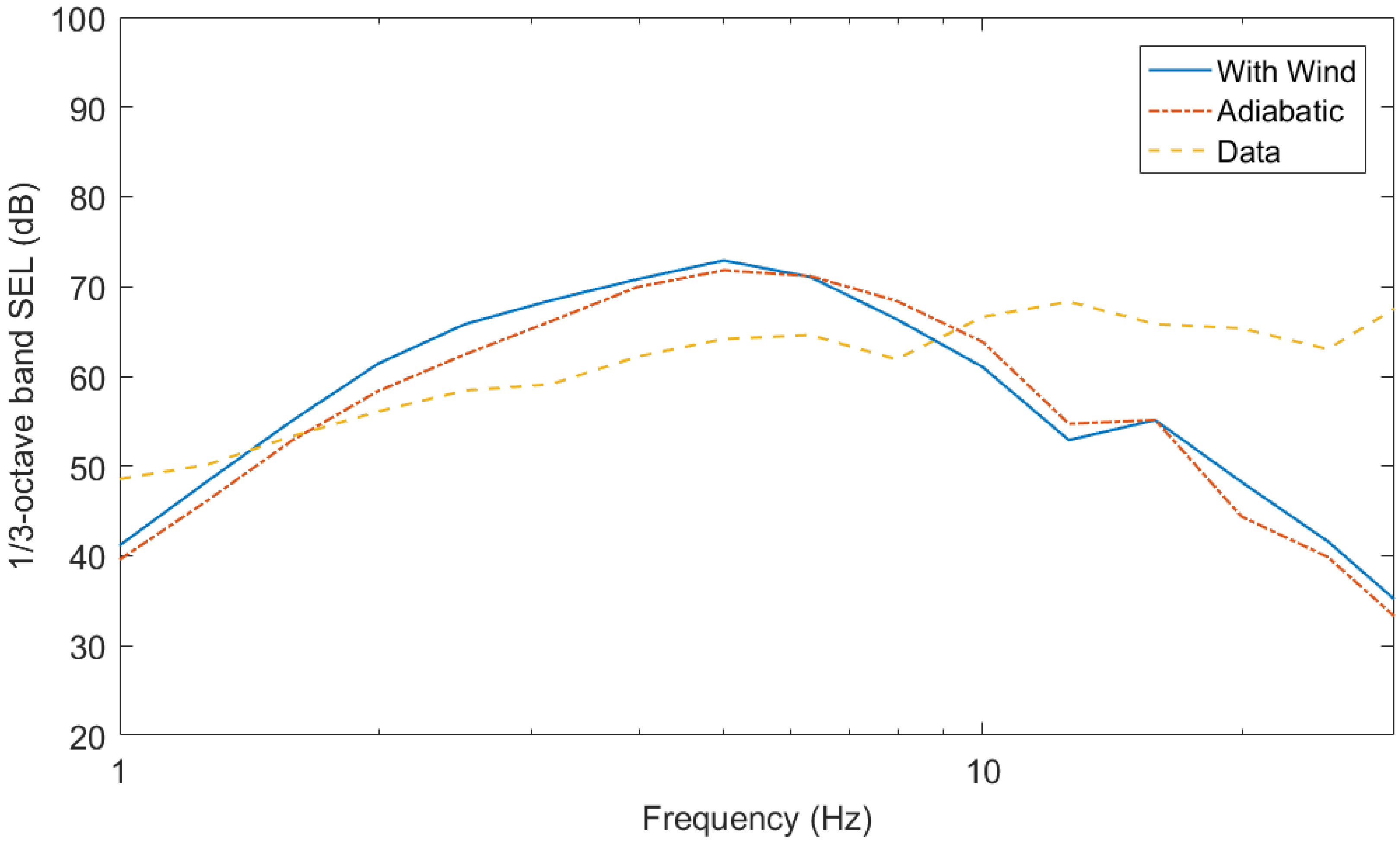

Match is not perfect, but not terrible either.

Discussion of the Method

- Handles discontinuities for horizontal layers by explicitly solving the boundary condition everywhere
- Efficient calculation without a lower layer – equivalent to a typical CNPE
- Wide-angle accuracy, ~40º, due to the more robust expansion
- Has potential to handle slopes as well…
  - But unfortunately this doesn’t work as desired

Wedge Example

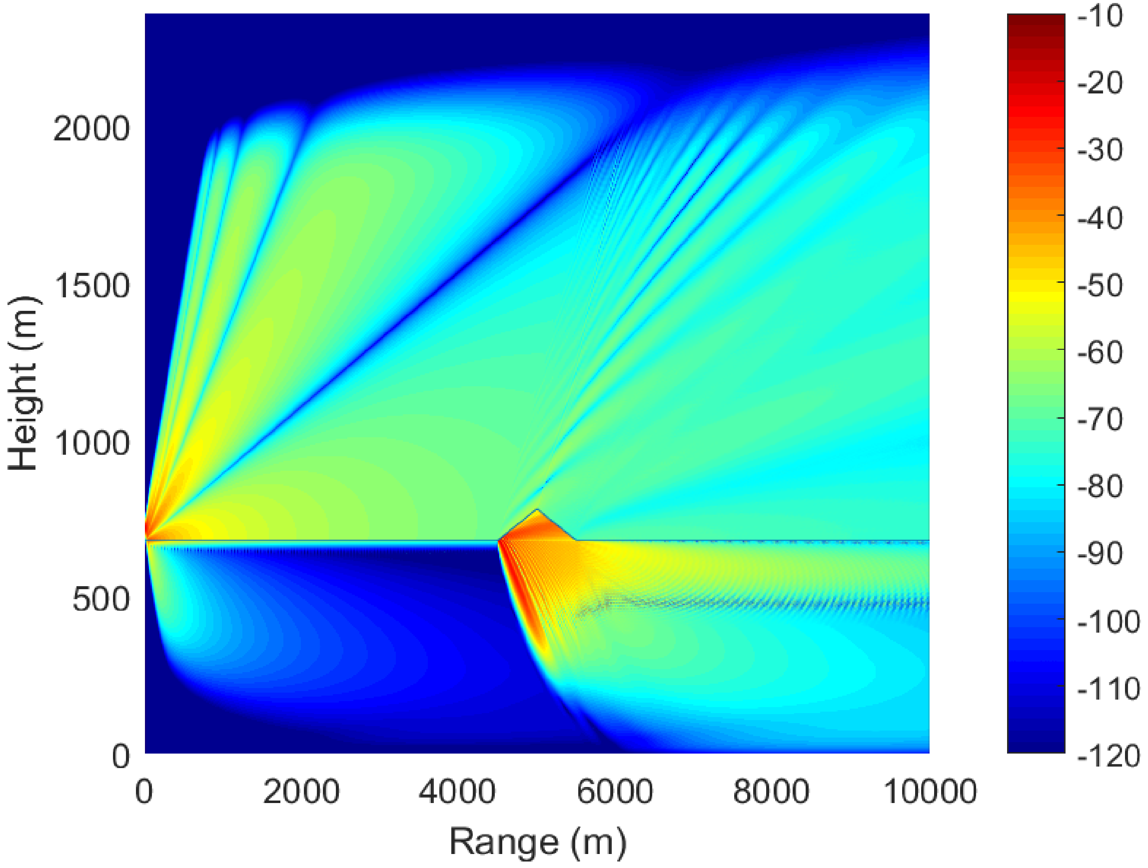

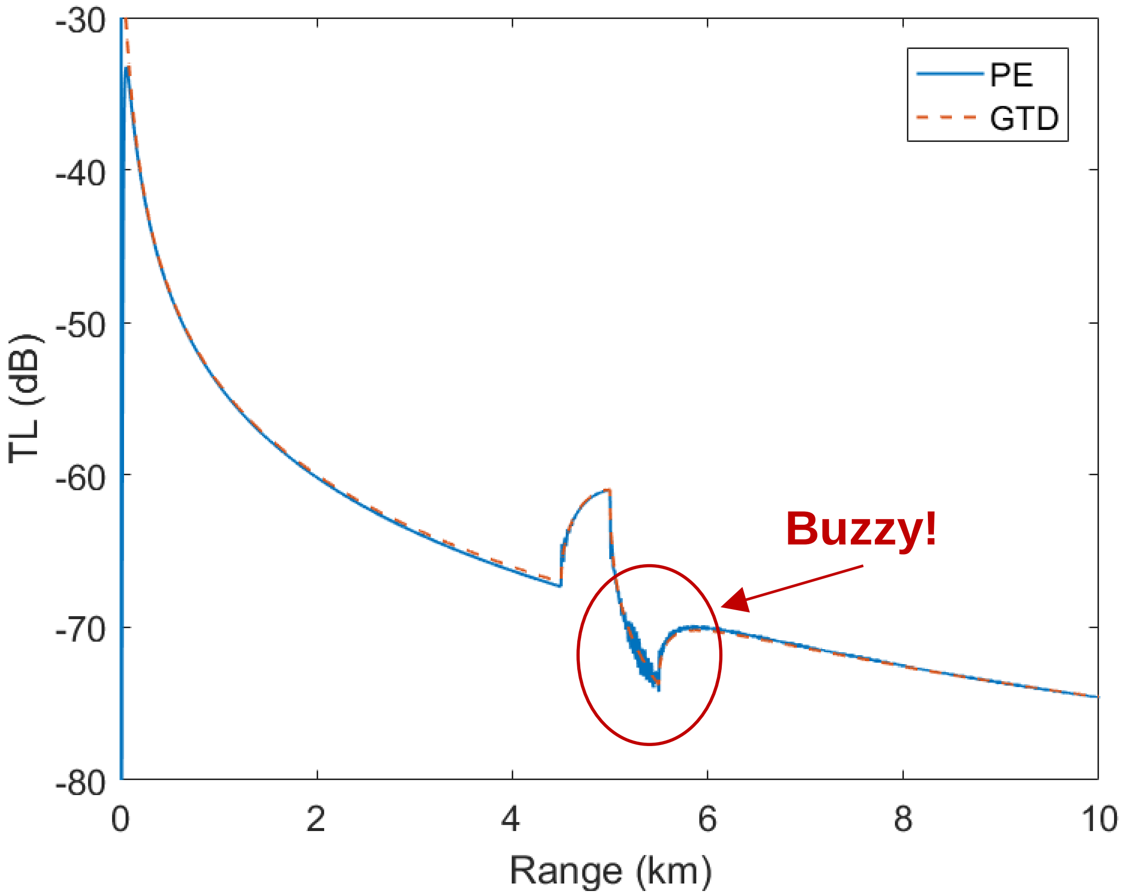

Reference:
Robertson, J. S. (1999). Sound propagation over a large wedge: A comparison between the geometrical theory of diffraction and the parabolic equation. *J. Acoust. Soc. Am.*, 106(1), 113-119.

17th International Symposium on Long Range Sound Propagation
École Centrale de Lyon, Écully, June 12-13, 2018

Sound propagation from a wind turbine in complex terrain

Arthur Schady

DLR Oberpfaffenhofen

German Aerospace Center

The work presented in this talk is part of the projects LIPS and DFWind which are funded by the Federal Ministry of Economy and Energy on the basis of a resolution of the German Bundestag under the contract numbers 0325518 and 0325936A.

DLR

Federal Ministry for Economic Affairs and Energy

Content

- Introduce the measurement campaign and site
- Show some general measurement results (database)
- The theoretical approach
- Proof the assumptions with data

- **Scientific question**:
- What could be the reason for complaints of citizens in the surrounding of a WT?
- Do we understand the interaction of sound propagation with the complex terrain and the meteorology?
- How should we characterize the WT as a source of sound?

NEWA field experiment in Portugal

Homepage

https://windsp.fe.up.pt/experiments/3/home

WindsP | Perdigão | Search experiments, equipment and people. | Arthur

Perdigão

- Home
- Maps
- Stations
- Datasets
- Documents
- Logbook
- Stations Timeline
- Personnel Timeline
- Useful info

Home

Objective

The purpose of this experiment is to study how an upstream hill with flow separation affects the mean wind speed and turbulence at a downstream hill. We shall also investigate how and if the presence of a turbine on the upstream hill will affect the flow separation behind the hill. Fortunately, there is a turbine on one hill already, but apart from that the experimental infrastructure is largely missing. Forwind will support the experiment with up to three scanning long range Lidars. In this experiment there is a strong interest in participation from American colleagues from NCAR, Notre Dame University and other universities. Within the NEWA project, several partners will lease some instruments from NCAR provided that they will come with even more instruments and expertise for the Perdigão experiment.

The particular interest of Perdigão is on:

- synoptically driven over multiple hills;
- flow over a vegetated hill in a roughness regime that has received little attention;
- extensive surface energy budget evaluation for different land cover types;
- interaction of thermal circulation and synoptically driven winds;
- vertical variation of surface layer properties under different stratification conditions; and
- data for a natural but somewhat less complicated flow configuration of interest in microscale modelling.

The experimental apparatus shall comprise three 100 m masts plus circa ten masts with height varying between 60 and 80 m able to receive equipment from partners and fitter with energy supply and data collection systems. Short term campaigns are also foreseen using meteorological balloons. Portugal is well covered in what concerns terrain orography and roughness, although this information needs to be adapted and refined to be used in the modelling procedures. Data from Task 2.7 will be adapted by LNEG for the national territory modelling input and suitably refined for the Perdigão experiment area (approx. 10 km × 10 km around the experiment location), based also on in-situ roughness classification.

Location

Region: Perdigão (Portugal)
UTM coordinates: 608431E, 4395370N, UTM29 ED50

Dates

Begin: 2016-12-26 (52nd week)

https://windsp.fe.up.pt/experiments/3/home

All Stations

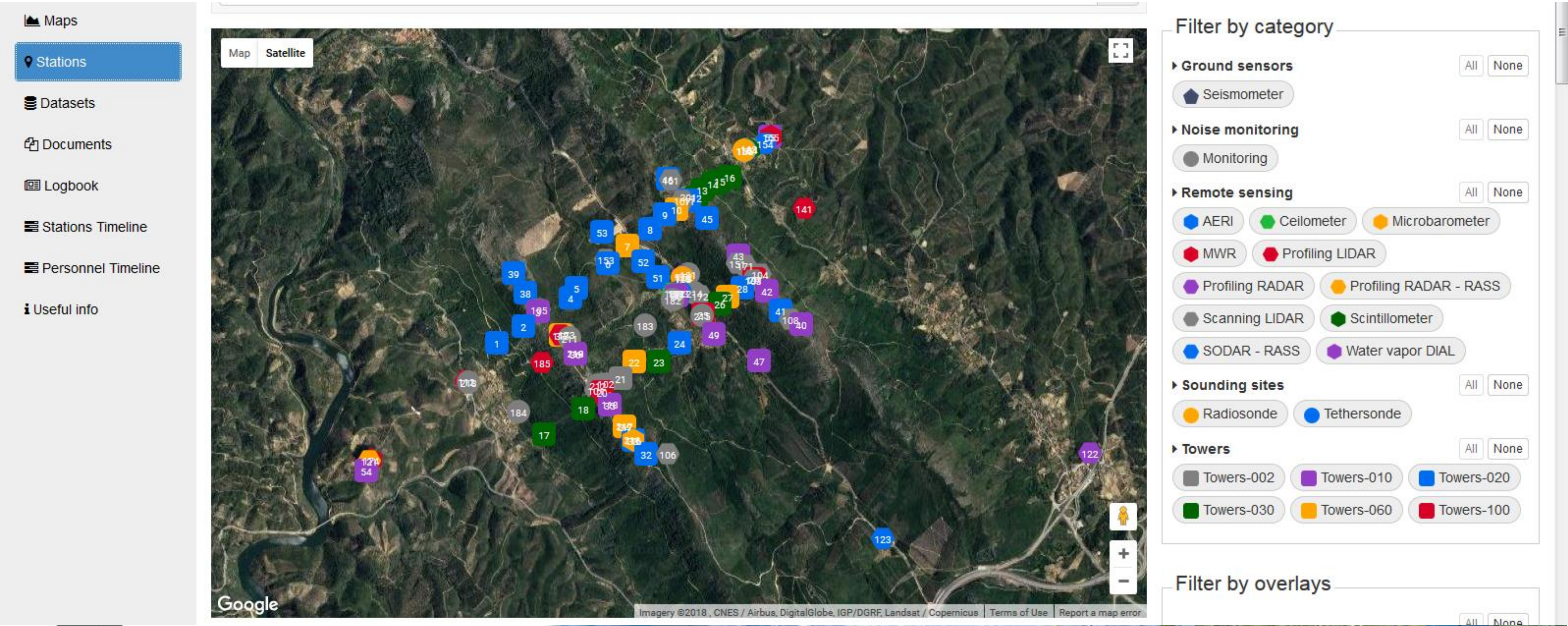

Perdigão

- Home
- Maps
- Stations
- Datasets
- Documents
- Logbook
- Stations Timeline
- Personnel Timeline
- Useful info

Stations

Filter stations

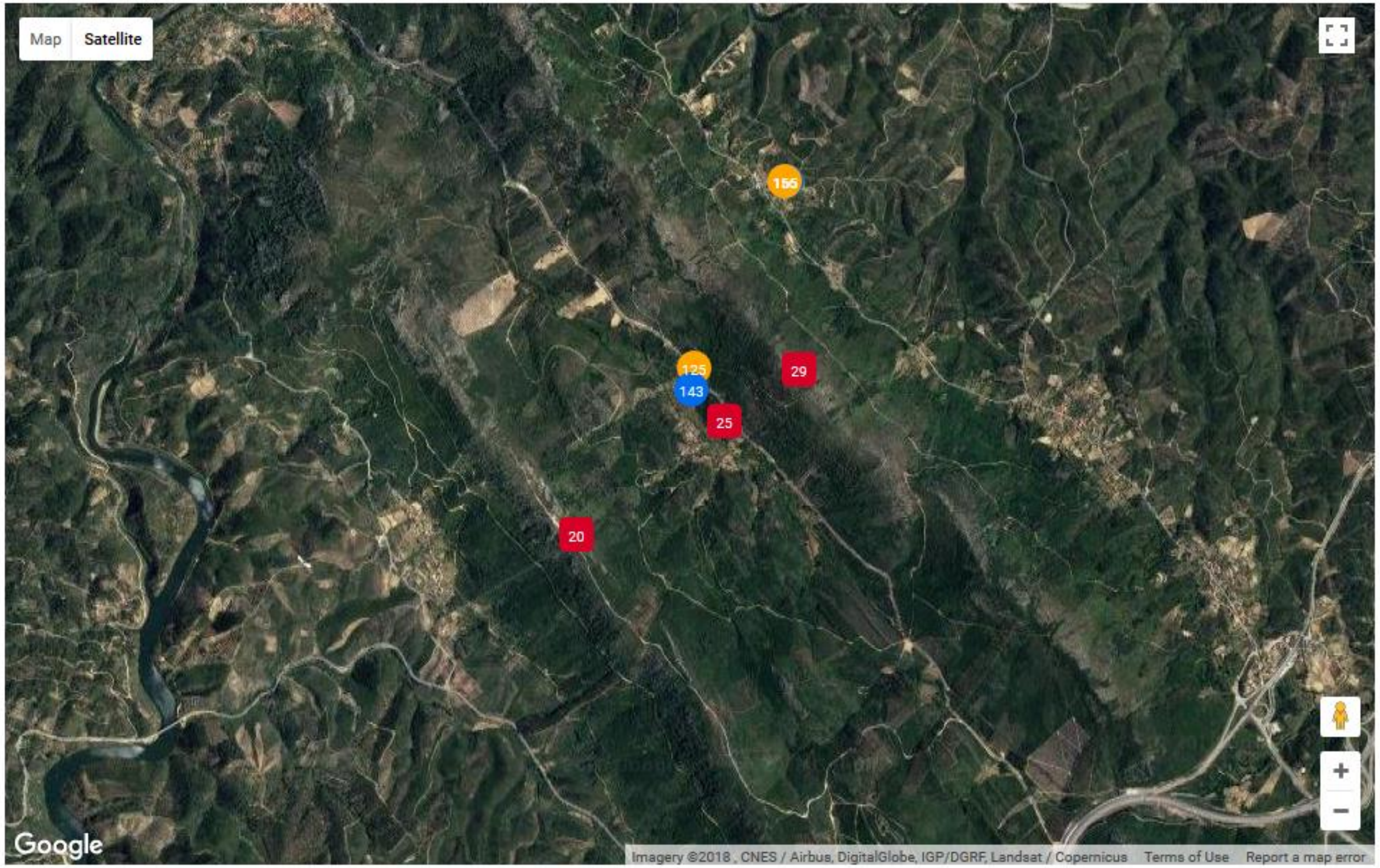

Filter by category

- Ground sensors — All None
- Noise monitoring — All None
- Remote sensing — All None
- Sounding sites — All None
  - Radiosonde
  - Tethersonde
- Towers — All None
  - Towers-002
  - Towers-010
  - Towers-020
  - Towers-030
  - Towers-060
  - Towers-100

Filter by overlays

All None

Buildings Lines Orthophotos (high res)

Perdigão

- Home
- Maps
- Stations
- Datasets
- Documents
- Logbook
- Stations Timeline
- Personnel Timeline
- Useful info

Stations

Filter stations

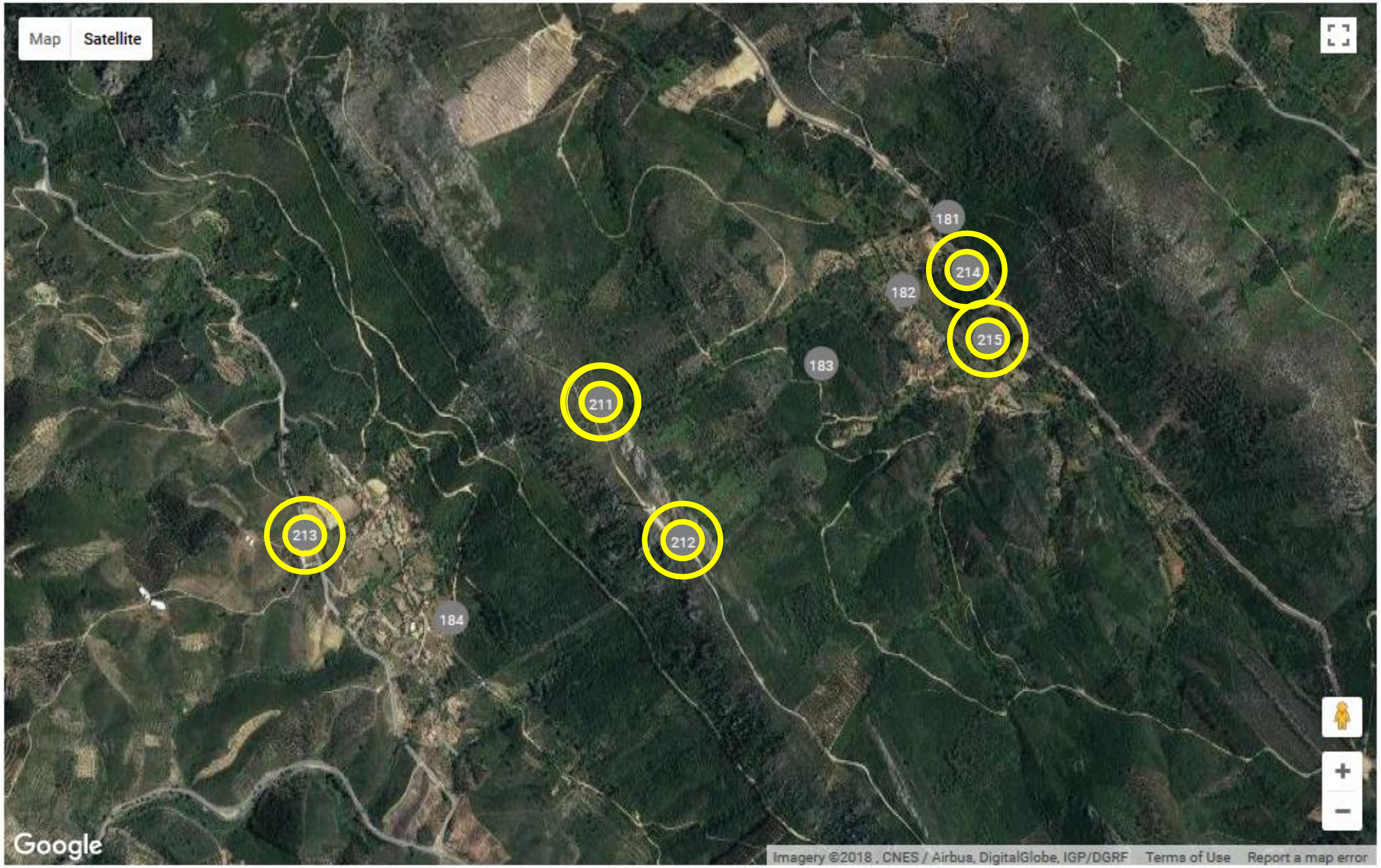

Filter by cat

- Ground senso
- Noise monitor

Monitoring

- Remote sensi
- Sounding site
- Towers

Filter by ove

Buildings Li

Measurement setup

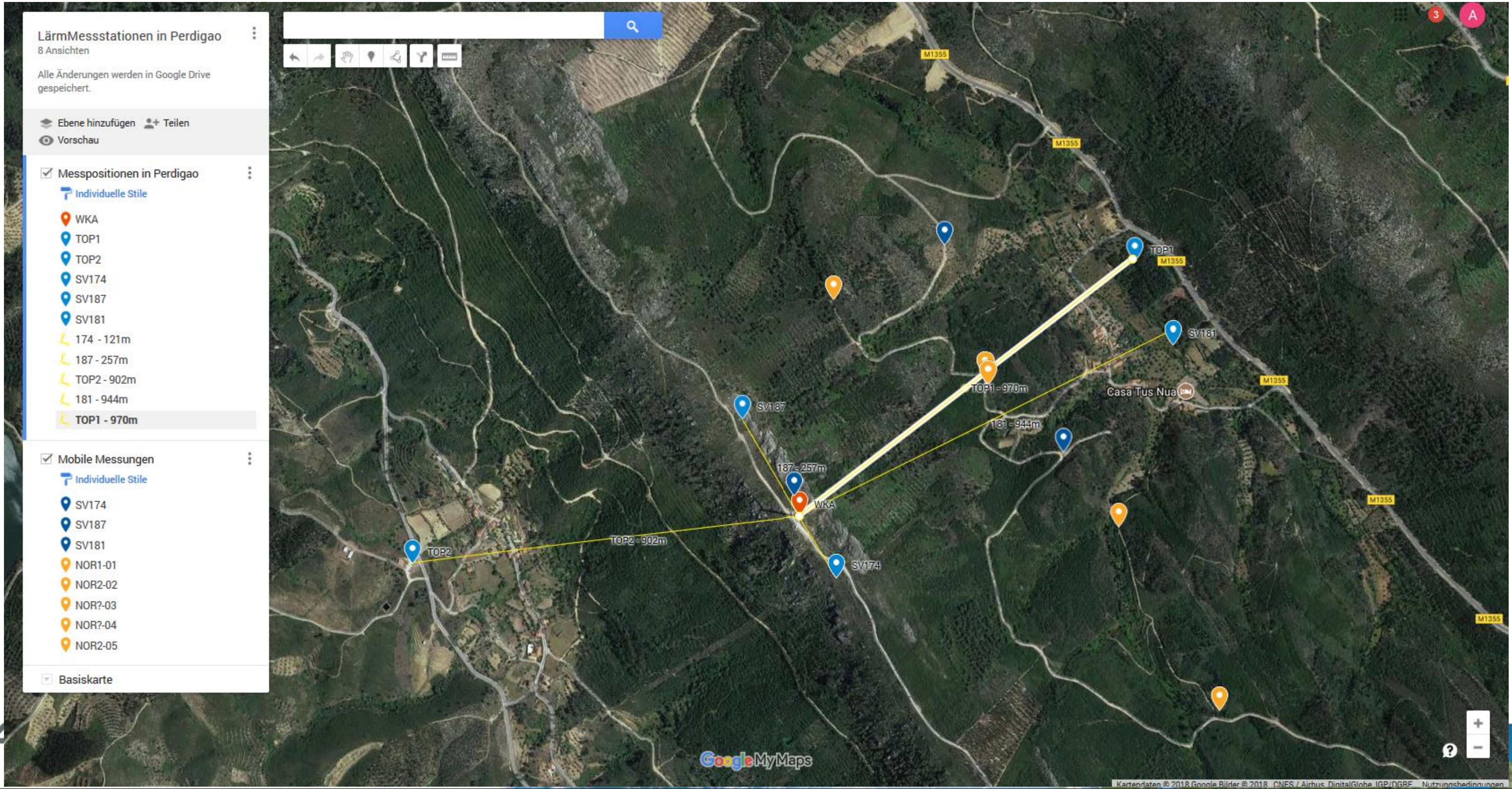

Characteristic numbers

wind velocity		
	12 m/s	4 m/s
rotations per minute		
	18 rpm	5 rpm
time for one rotation		
	3.3 s	15 s
signals per minute (blade passings)		
	54 spm	15 spm
blade passing frequency (signals per second)		
	0.9 Hz	0.25 Hz
groove passing frequency (tone)		
	130 Hz	40 Hz
	all values approximately	

THE WINDPOWER Wind Energy Market Intelligence

www.thewindpower.net
November 30, 2016

E82/2000 (Enercon)

Main data

Rated power: 2000 kW
Rotor diameter: 82 m
Available
Class: IEC IIa (WZ III)
Offshore model: no
Commissioning: 2005/12

Rotor

Number of blades: 3
Type: Pitch
Swept area: 5281 m²
Power density: 2.64 m²/kW
Maximum speed: 18 rd/min
Manufacturer: Enercon

Gearbox

Direct drive

Generator

Type: SYNC Wounded
Number: 1
Maximum speed: 18 rd/min
Voltage: 400 - 690 V
Manufacturer: Enercon

Tower

Minimum hub height: 78 m
Maximum hub height: 138 m
Manufacturer: SAM, WEC Turmbau

Weights

Rotor + hub: 55 t

Wind speeds

Cut-in wind speed: 2 m/s
Rated wind speed: 12,5 m/s
Cut-off wind speed: 25 m/s

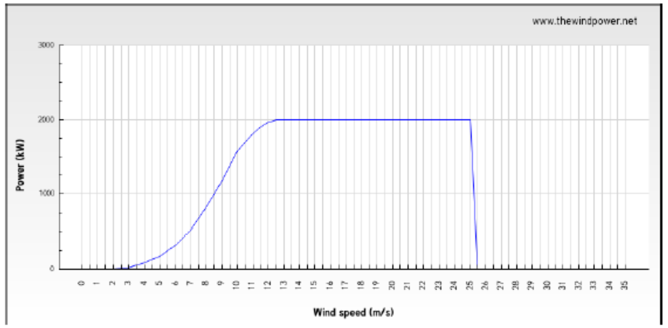

Identifying the signal of the WT

Shutdown hours

Windturbine 82127 Perdigao, Portugal

sunday	21.05.2017	03:00	04:00	N7
monday	22.05.2017	04:00	05:00	N8
tuesday	23.05.2017	21:00	22:00	N1

Birds ~ 7000 Hz

WT ~ 80 Hz shutdown

WT ~ 80 Hz restart

monday 22.05.2017 03:00 - 06:00 UTC

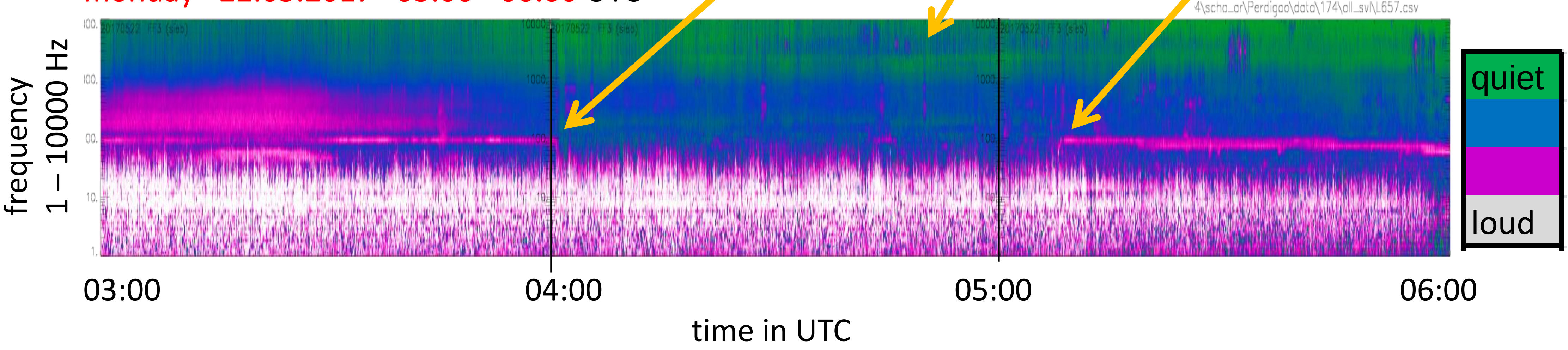

Theoretical approach

Simulate Wind field (Antonia Englberger and Johannes Wagner)

Simulate sound propagation with particle sound model (Dietrich Heimann)

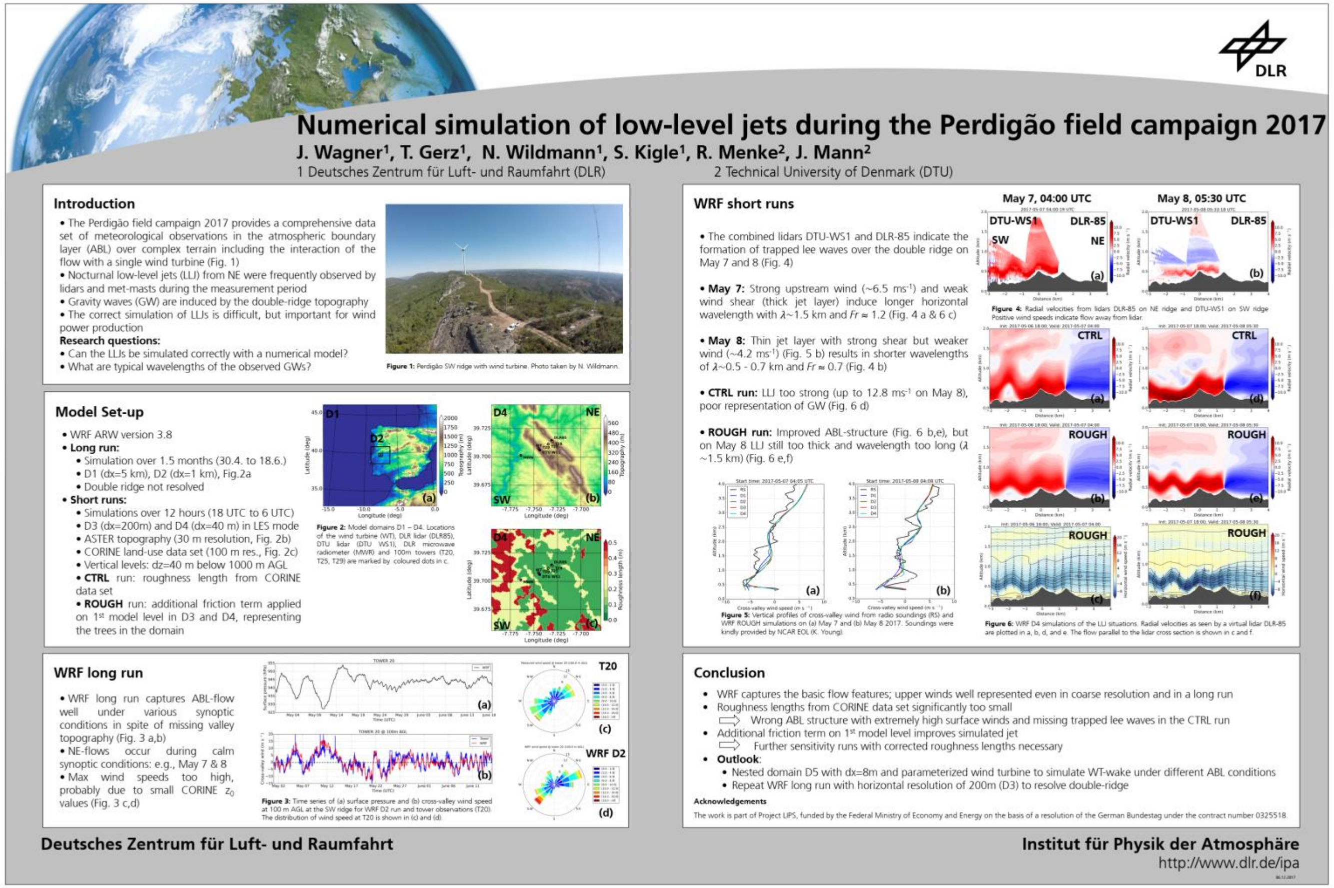

Numerical simulation of low-level jets during the Perdigão field campaign 2017

J. Wagner[1], T. Gerz[1], N. Wildmann[1], S. Kigle[1], R. Menke[2], J. Mann[2]
1 Deutsches Zentrum für Luft- und Raumfahrt (DLR) 2 Technical University of Denmark (DTU)

Introduction

- The Perdigão field campaign 2017 provides a comprehensive data set of meteorological observations in the atmospheric boundary layer (ABL) over complex terrain including the interaction of the flow with a single wind turbine (Fig. 1)
- Nocturnal low-level jets (LLJ) from NE were frequently observed by lidars and met-masts during the measurement period
- Gravity waves (GW) are induced by the double-ridge topography
- The correct simulation of LLJs is difficult, but important for wind power production

Research questions:

- Can the LLJs be simulated correctly with a numerical model?
- What are typical wavelengths of the observed GWs?

Figure 1: Perdigão SW ridge with wind turbine. Photo taken by N. Wildmann.

Model Set-up

- WRF ARW version 3.8
- **Long run:**
  - Simulation over 1.5 months (30.4. to 18.6.)
  - D1 (dx=5 km), D2 (dx=1 km), Fig.2a
  - Double ridge not resolved
- **Short runs:**
  - Simulations over 12 hours (18 UTC to 6 UTC)
  - D3 (dx=200m) and D4 (dx=40 m) in LES mode
  - ASTER topography (30 m resolution, Fig. 2b)
  - CORINE land-use data set (100 m res., Fig. 2c)
  - Vertical levels: dz=40 m below 1000 m AGL
  - **CTRL** run: roughness length from CORINE data set
  - **ROUGH** run: additional friction term applied on 1st model level in D3 and D4, representing the trees in the domain

Figure 2: Model domains D1 – D4. Locations of the wind turbine (WT), DLR lidar (DLR85), DTU lidar (DTU WS1), DLR microwave radiometer (MWR) and 100m towers (T20, T25, T29) are marked by coloured dots in c.

WRF long run

- WRF long run captures ABL-flow well under various synoptic conditions in spite of missing valley topography (Fig. 3 a,b)
- NE-flows occur during calm synoptic conditions: e.g., May 7 & 8
- Max wind speeds too high, probably due to small CORINE z_0 values (Fig. 3 c,d)

Figure 3: Time series of (a) surface pressure and (b) cross-valley wind speed at 100 m AGL at the SW ridge for WRF D2 run and tower observations (T20). The distribution of wind speed at T20 is shown in (c) and (d).

WRF short runs

- The combined lidars DTU-WS1 and DLR-85 indicate the formation of trapped lee waves over the double ridge on May 7 and 8 (Fig. 4)
- **May 7:** Strong upstream wind (~6.5 ms^{-1}) and weak wind shear (thick jet layer) induce longer horizontal wavelength with λ~1.5 km and $Fr \approx 1.2$ (Fig. 4 a & 6 c)
- **May 8:** Thin jet layer with strong shear but weaker wind (~4.2 ms^{-1}) (Fig. 5 b) results in shorter wavelengths of λ~0.5 - 0.7 km and $Fr \approx 0.7$ (Fig. 4 b)
- **CTRL run:** LLJ too strong (up to 12.8 ms^{-1} on May 8), poor representation of GW (Fig. 6 d)
- **ROUGH run:** Improved ABL-structure (Fig. 6 b,e), but on May 8 LLJ still too thick and wavelength too long (λ ~1.5 km) (Fig. 6 e,f)

Figure 4: Radial velocities from lidars DLR-85 on NE ridge and DTU-WS1 on SW ridge Positive wind speeds indicate flow away from lidar.

Figure 5: Vertical profiles of cross-valley wind from radio soundings (RS) and WRF ROUGH simulations on (a) May 7 and (b) May 8 2017. Soundings were kindly provided by NCAR EOL (K. Young).

Figure 6: WRF D4 simulations of the LLJ situations. Radial velocities as seen by a virtual lidar DLR-85 are plotted in a, b, d, and e. The flow parallel to the lidar cross section is shown in c and f.

Conclusion

- WRF captures the basic flow features; upper winds well represented even in coarse resolution and in a long run
- Roughness lengths from CORINE data set significantly too small
  ⇨ Wrong ABL structure with extremely high surface winds and missing trapped lee waves in the CTRL run
- Additional friction term on 1st model level improves simulated jet
  ⇨ Further sensitivity runs with corrected roughness lengths necessary
- **Outlook**:
  - Nested domain D5 with dx=8m and parameterized wind turbine to simulate WT-wake under different ABL conditions
  - Repeat WRF long run with horizontal resolution of 200m (D3) to resolve double-ridge

Acknowledgements

The work is part of Project LIPS, funded by the Federal Ministry of Economy and Energy on the basis of a resolution of the German Bundestag under the contract number 0325518.

Deutsches Zentrum für Luft- und Raumfahrt

Institut für Physik der Atmosphäre
http://www.dlr.de/ipa

N. Wildmann, N. Vasiljevic, and T. Gerz. Wind turbine wake measurements with automatically adjusting scanning trajectories in a multi-doppler lidar setup. Atmospheric Measurement Techniques Discussions, 2018:1--20, 2018.

Orography

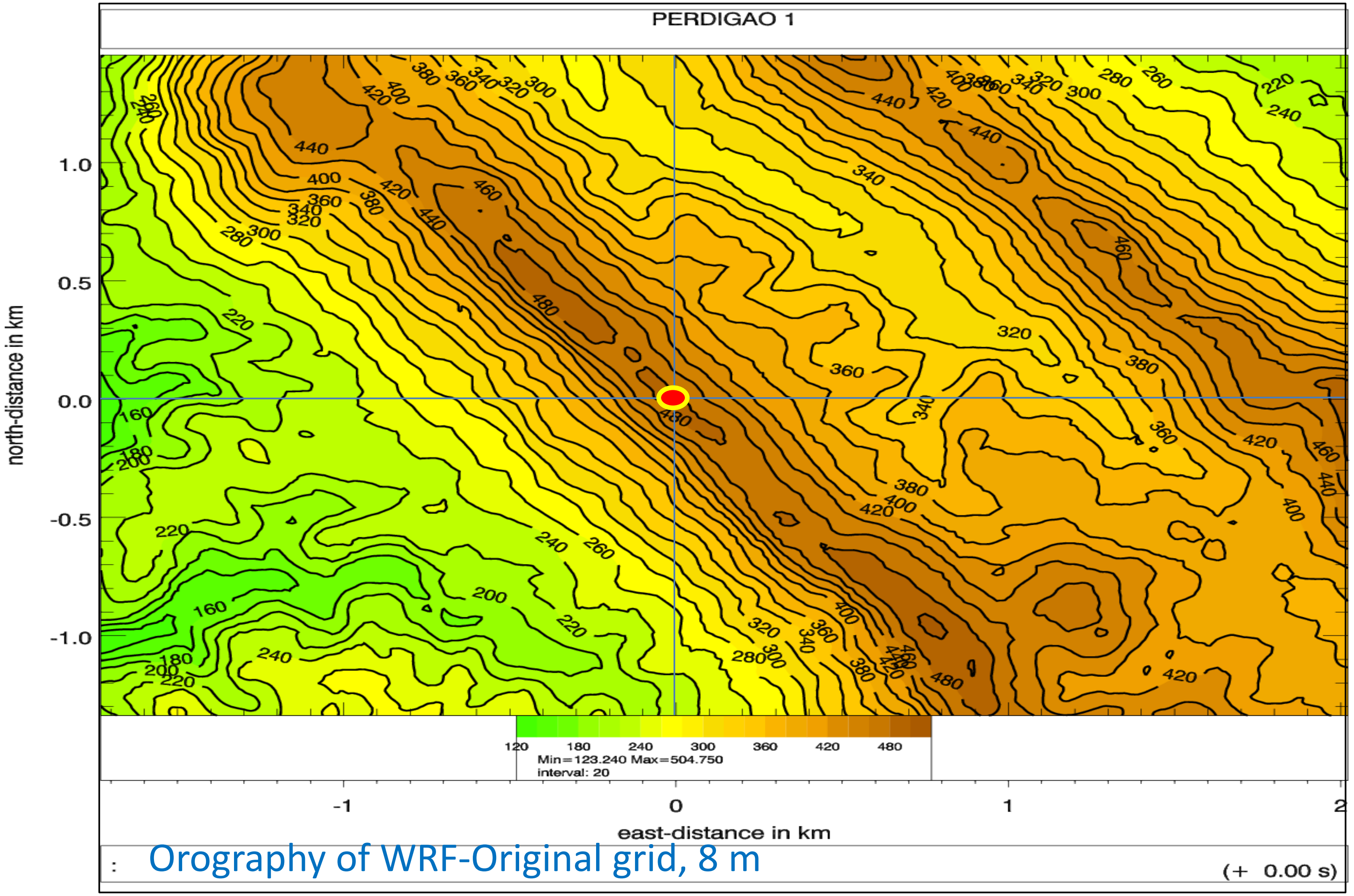

Orography of WRF-Original grid, 8 m

Orography turned according to wind direction

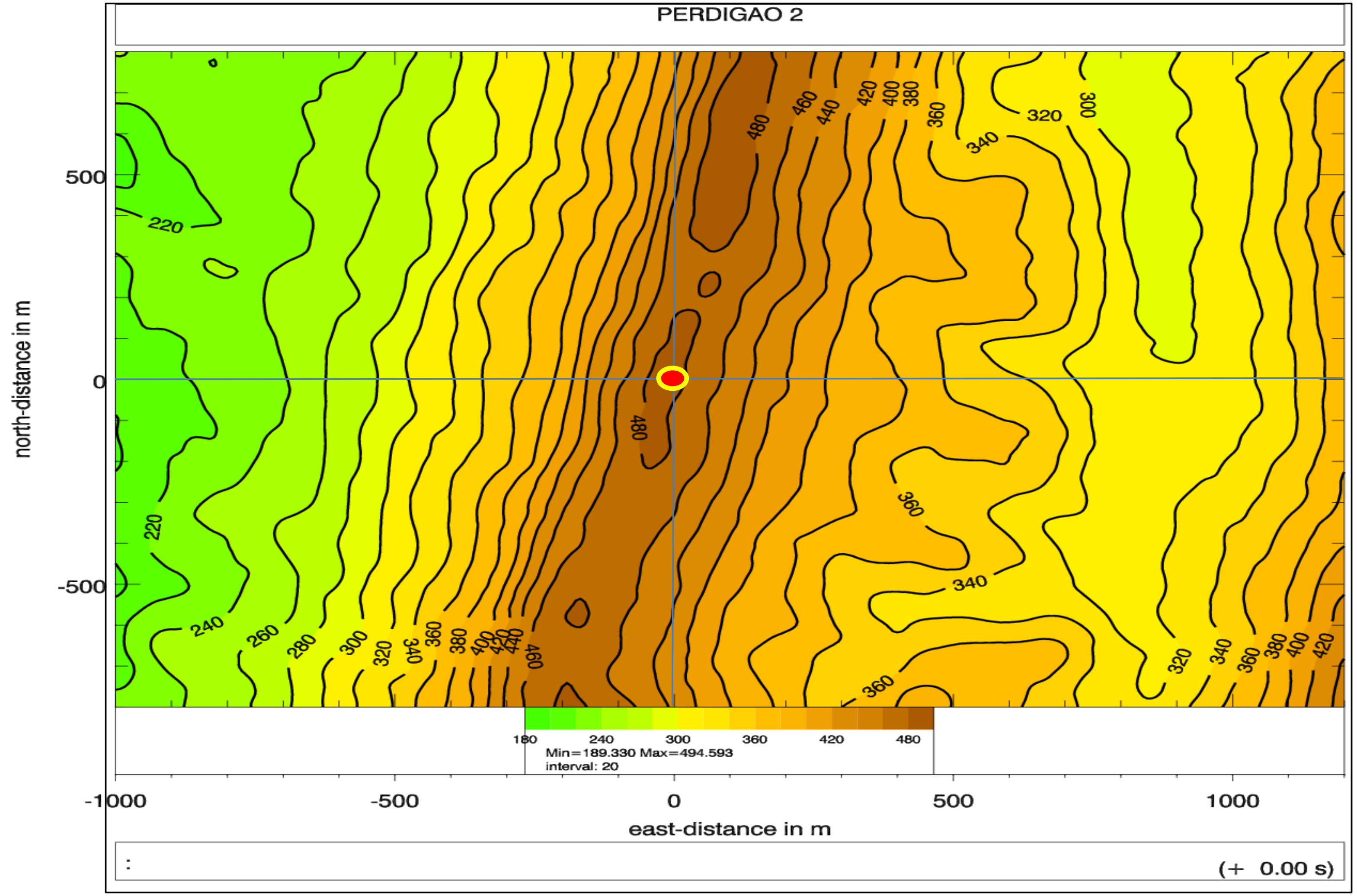

Wind 10 m above ground

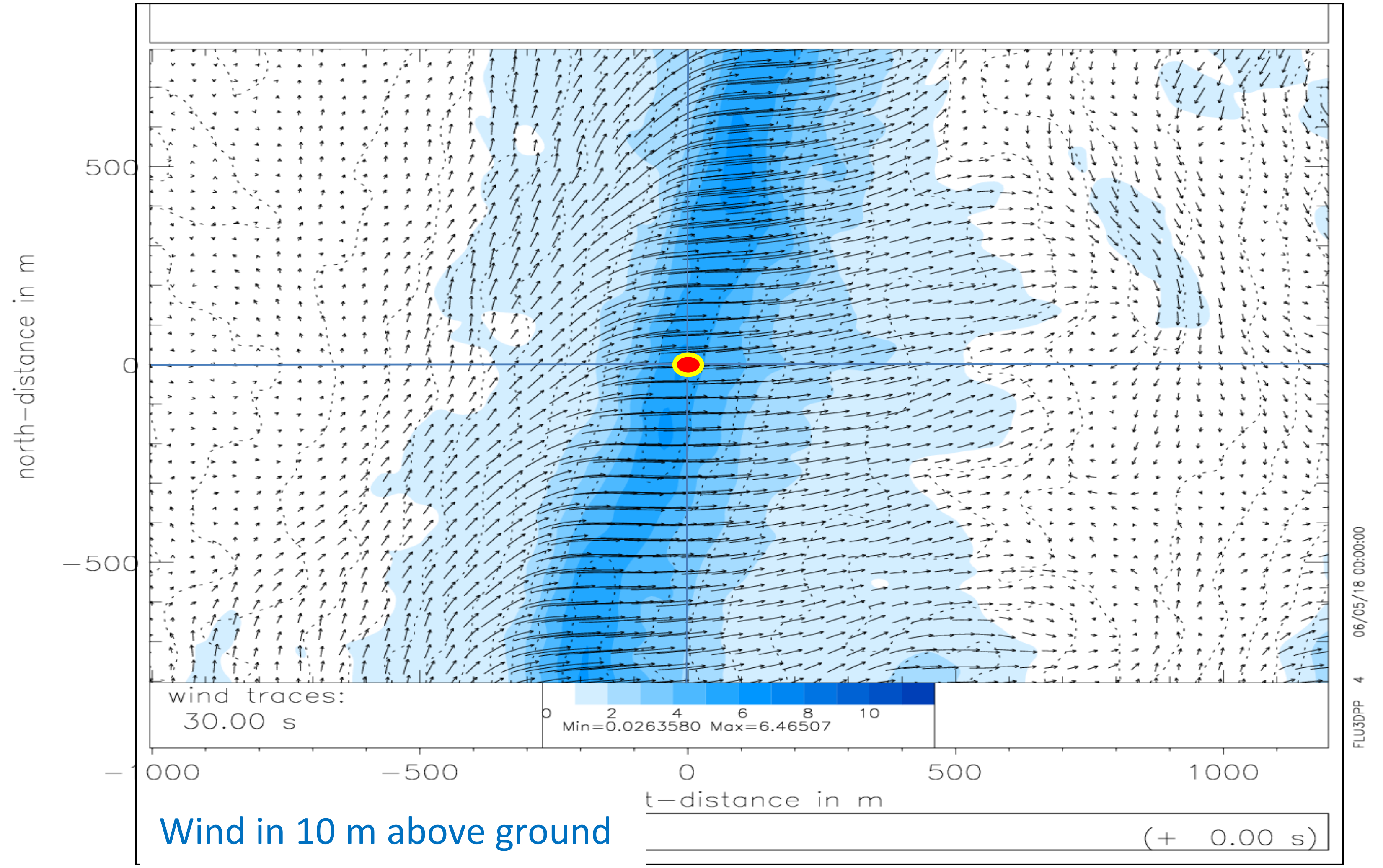

Wind in 10 m above ground

Wind 78 m above ground

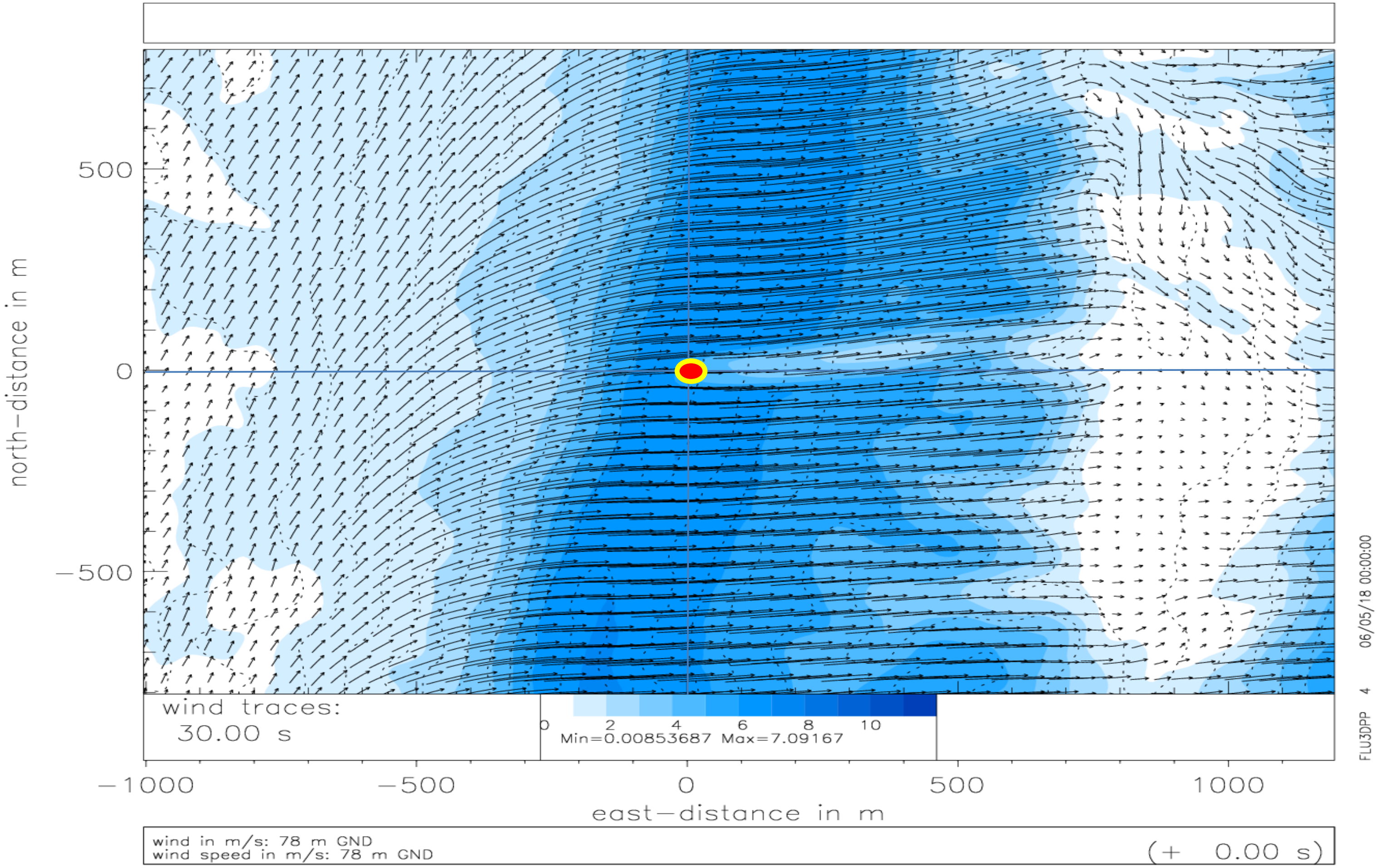

Wind 564 m above NN

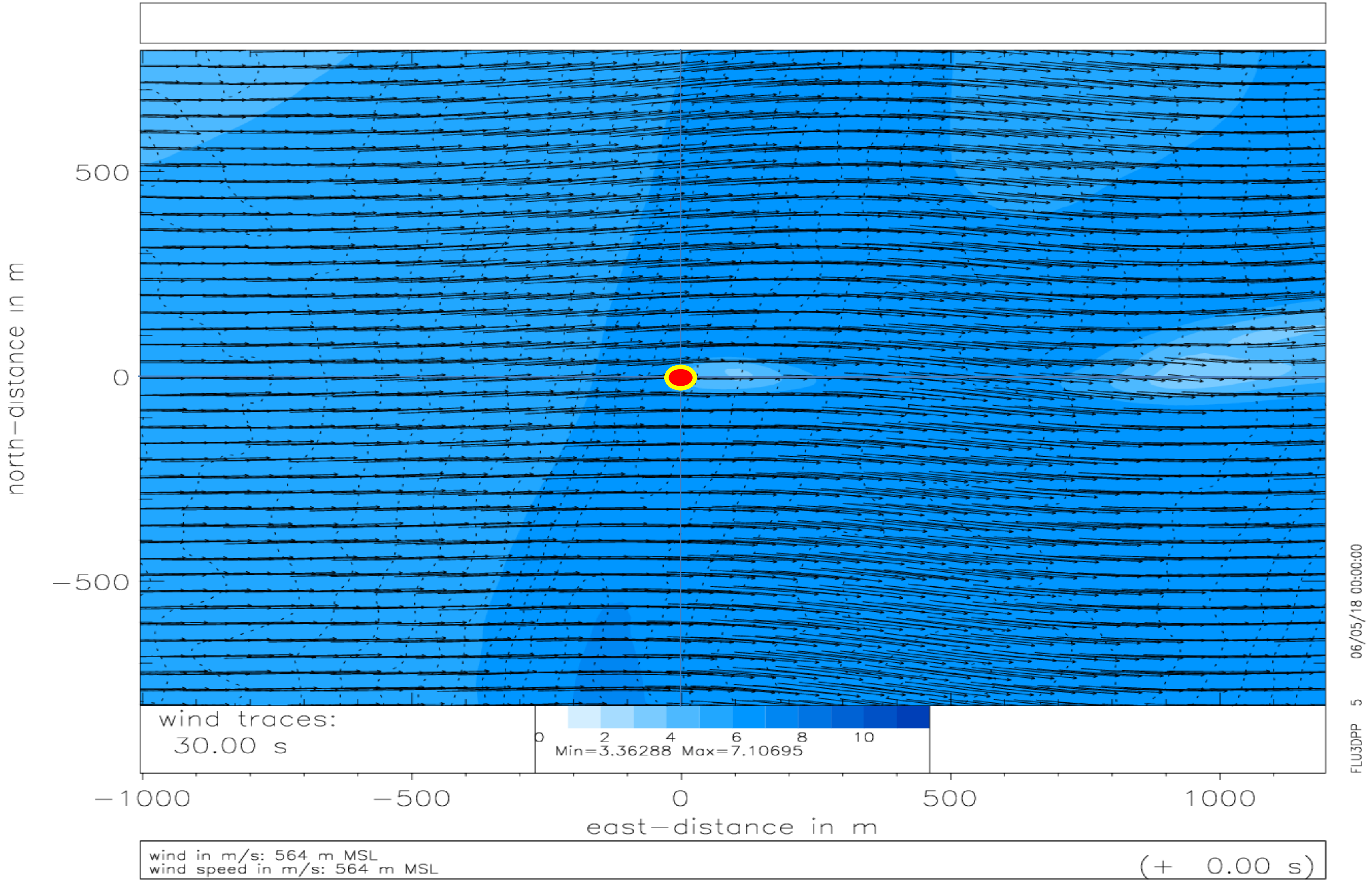

Windcomponent x-z slice (no WT)

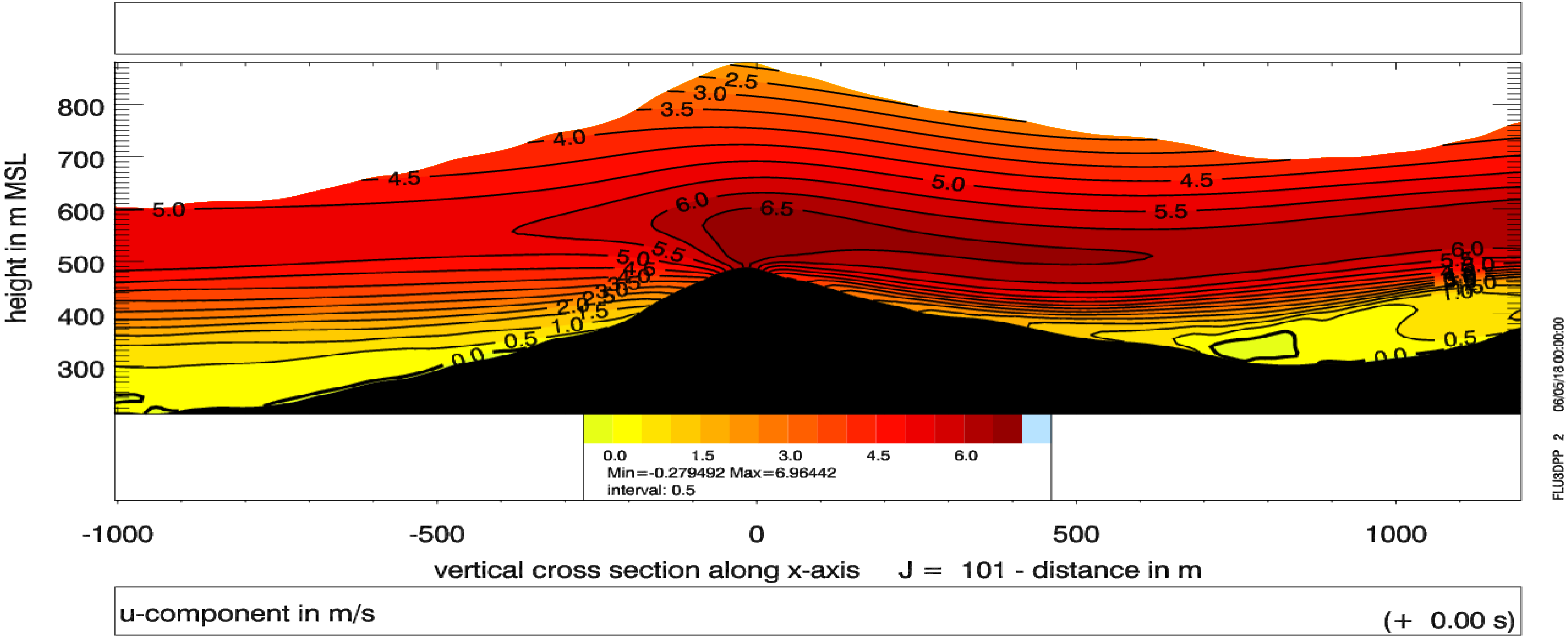

Windcomponent x-z slice (with WT)

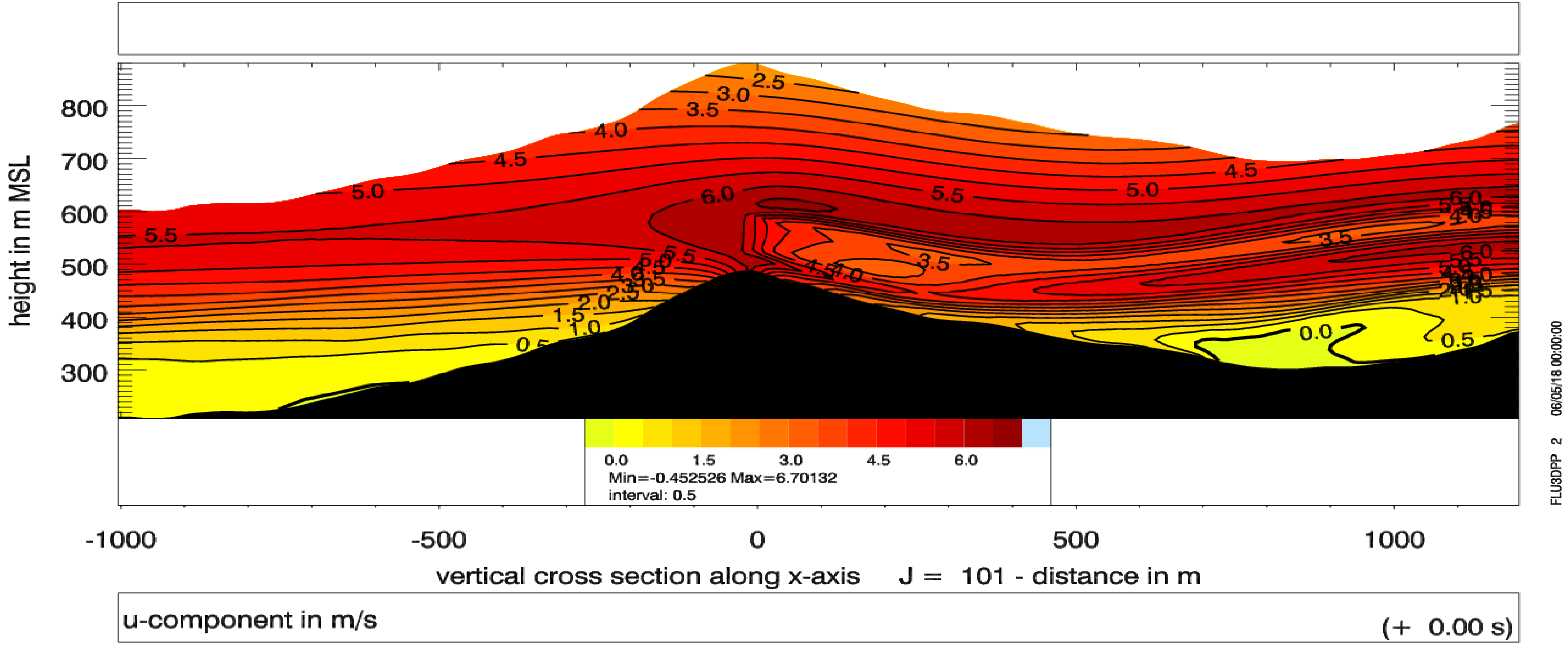

Difference of Wind field (no WT – WT)

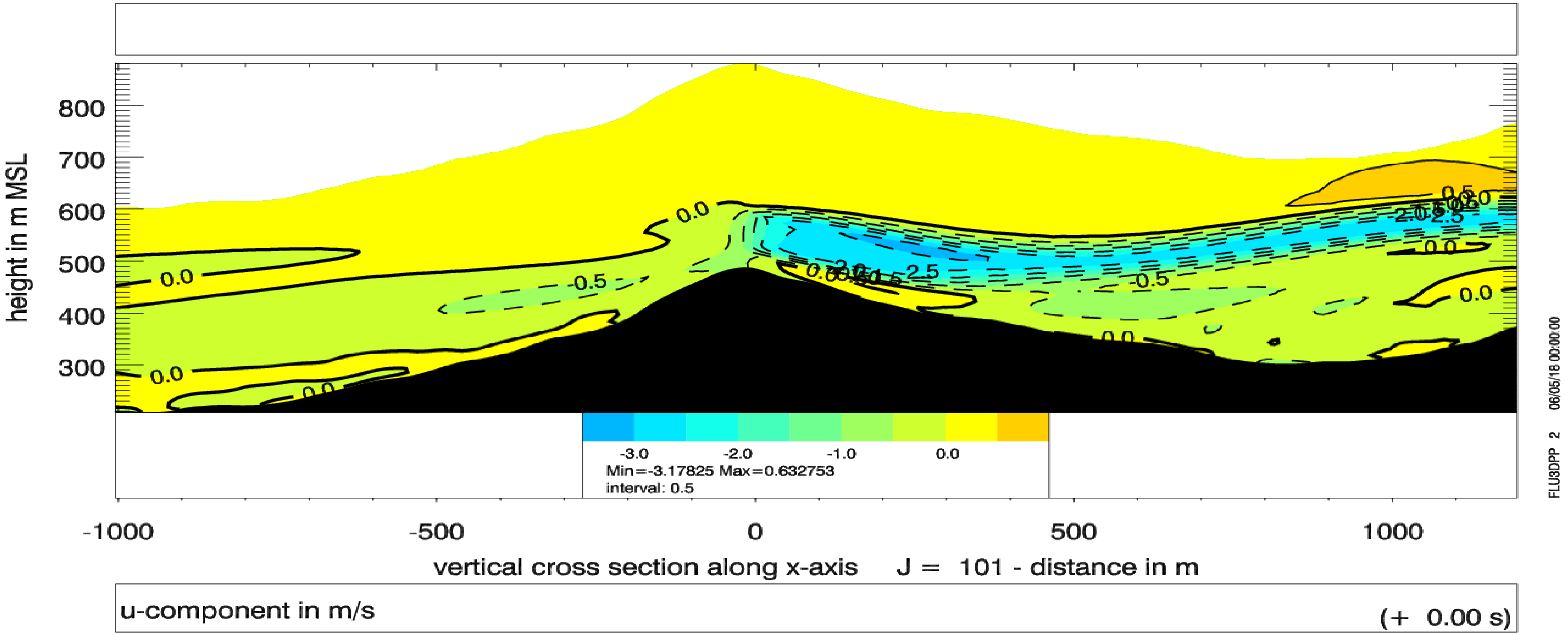

DLR

Temperature field (incl. WT)

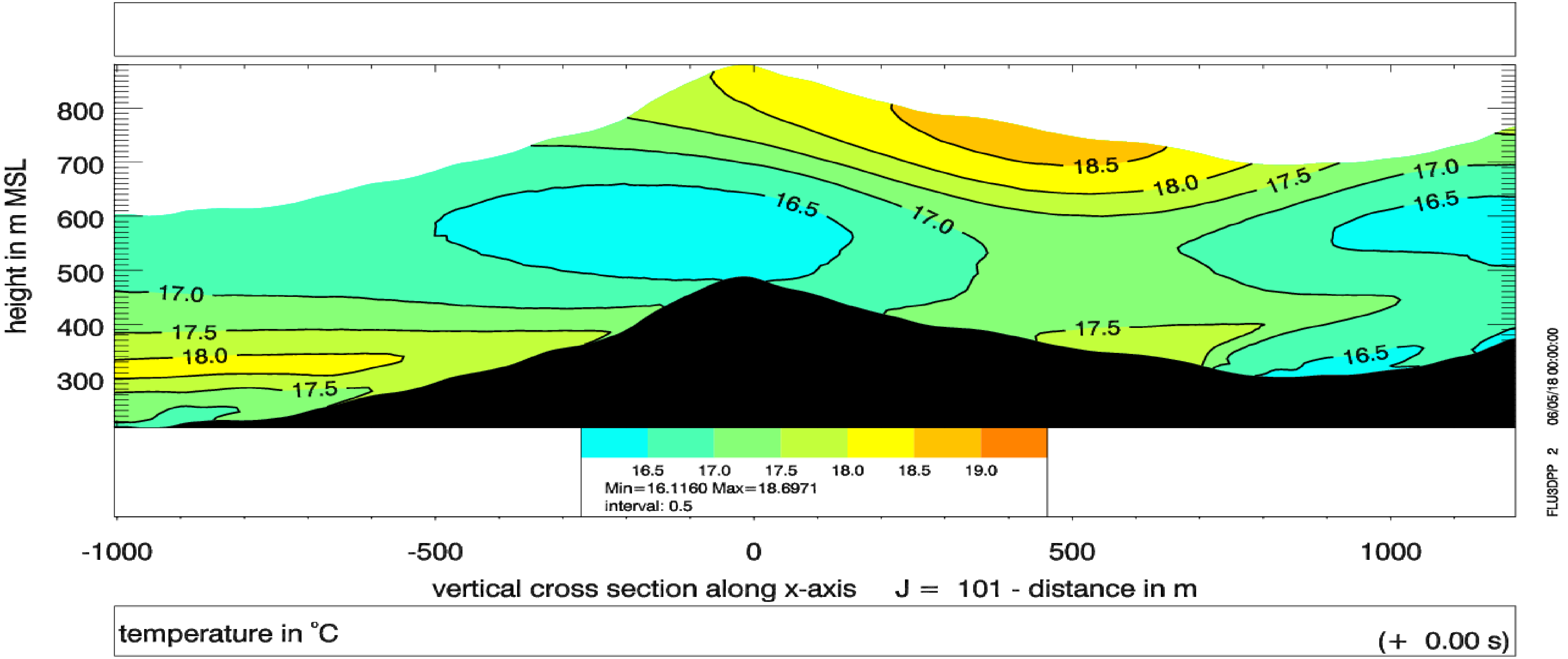

SPL (A-wighted) 4 m GND no orography, no meteorology (only aeroacoustic sound)

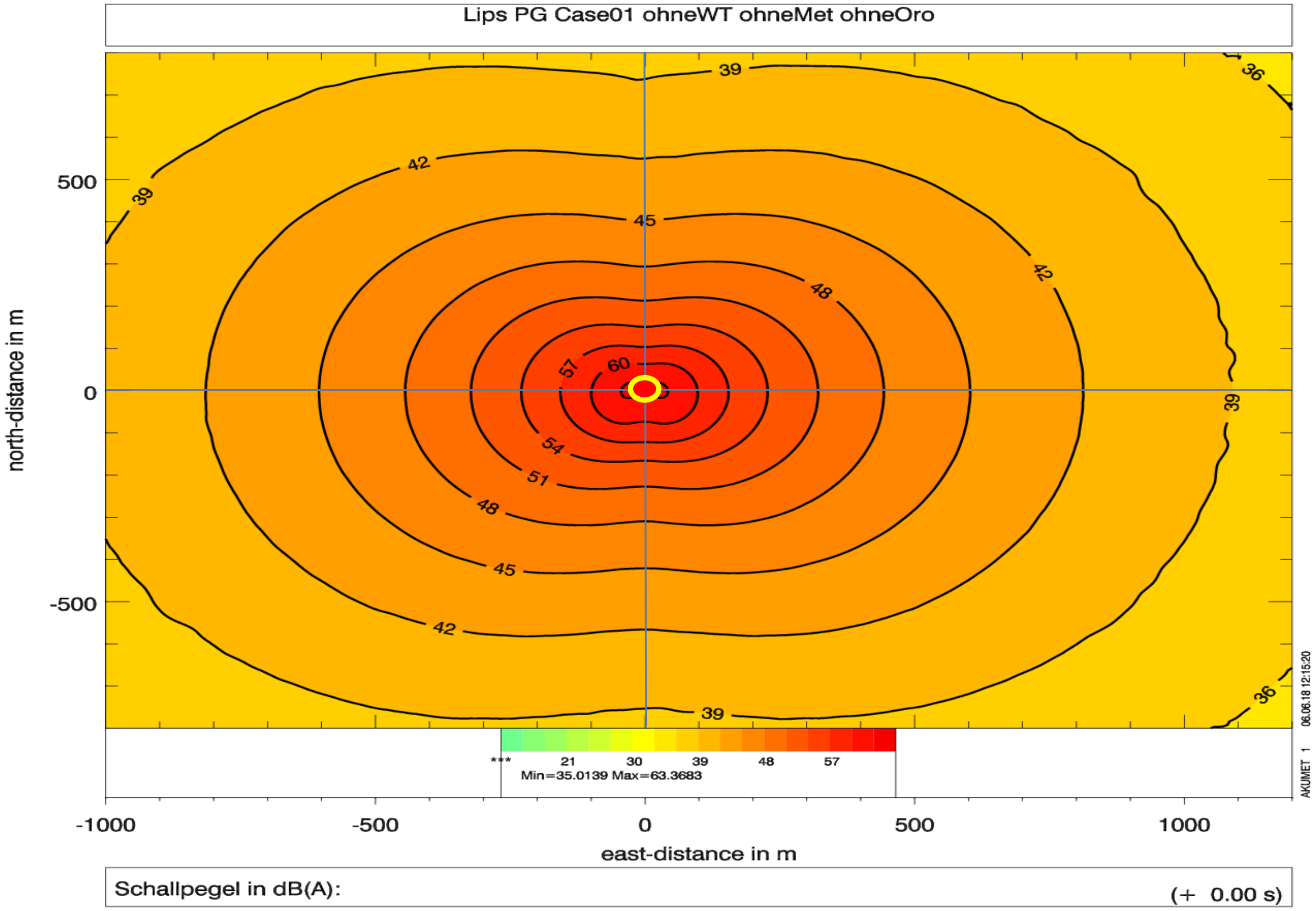

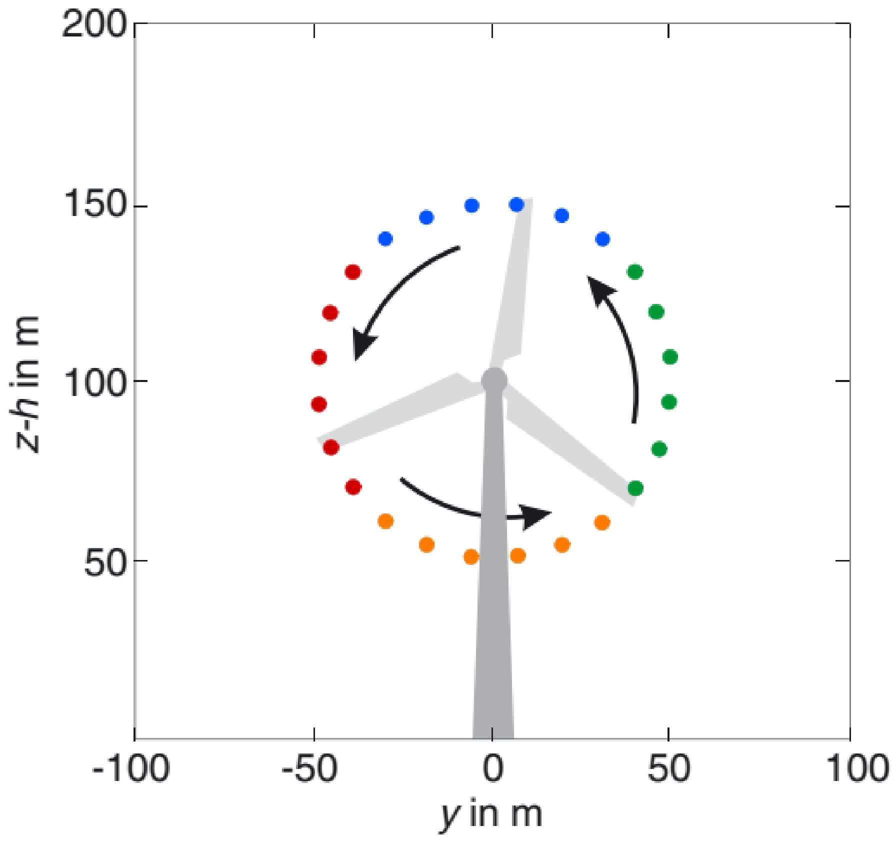

SPL (A-wighted) 4 m GND incl orography , meteorology and wake (only aeroacoustic sound)

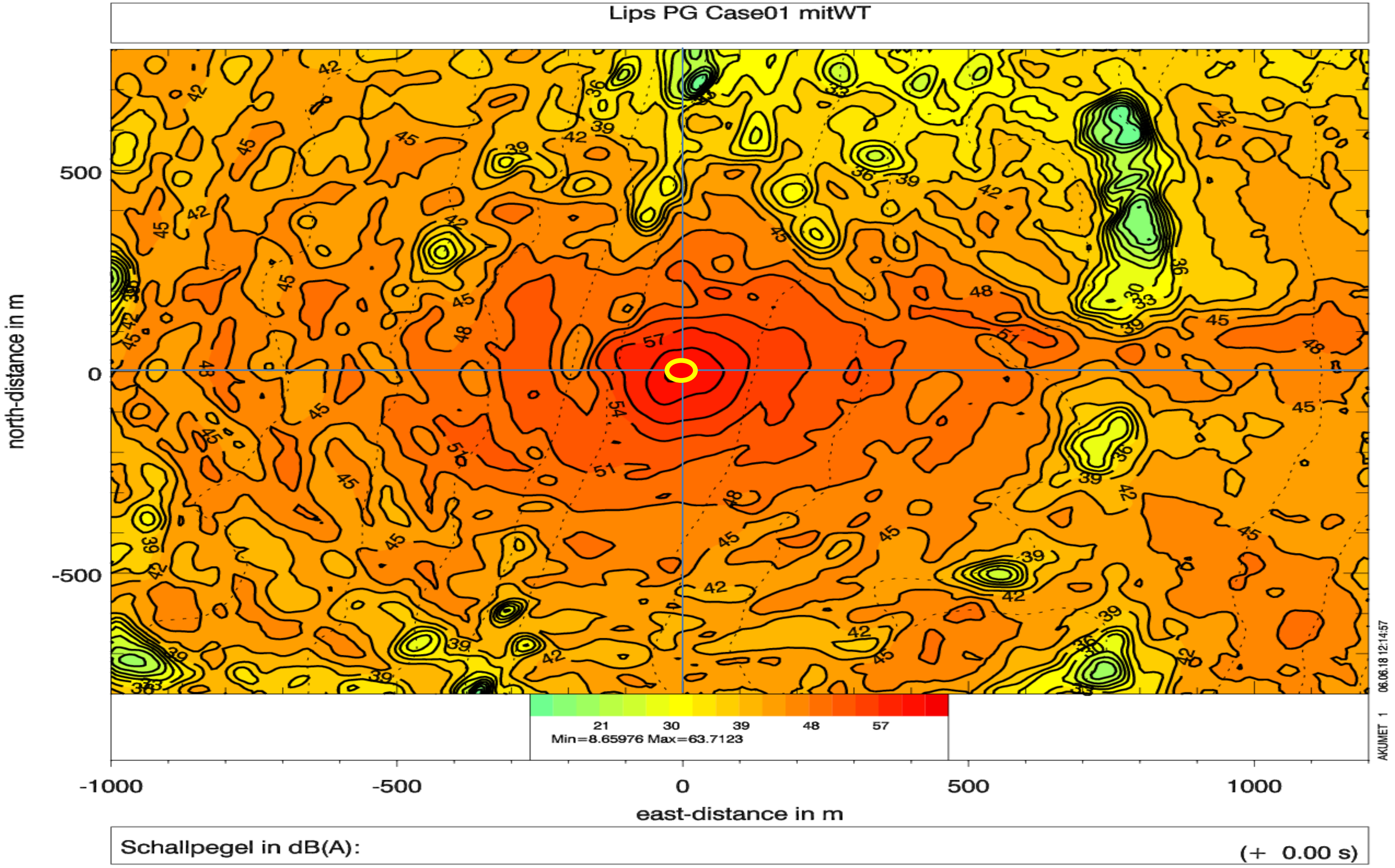

SPL (difference) 4 m GND Influence of orography (only aeroacoustic sound)

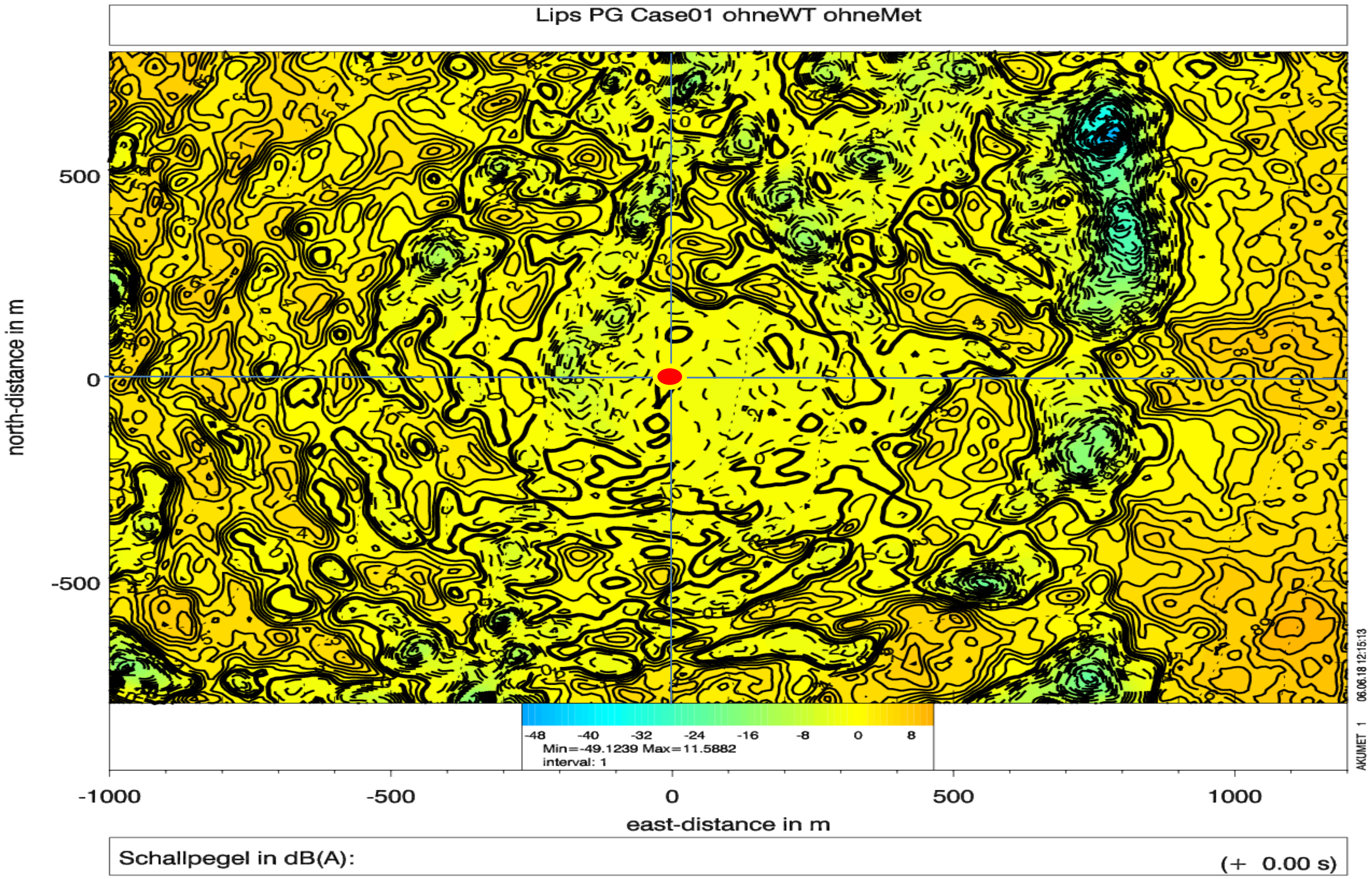

SPL (difference) 4 m GND Influence of meteorology (only aeroacoustic sound)

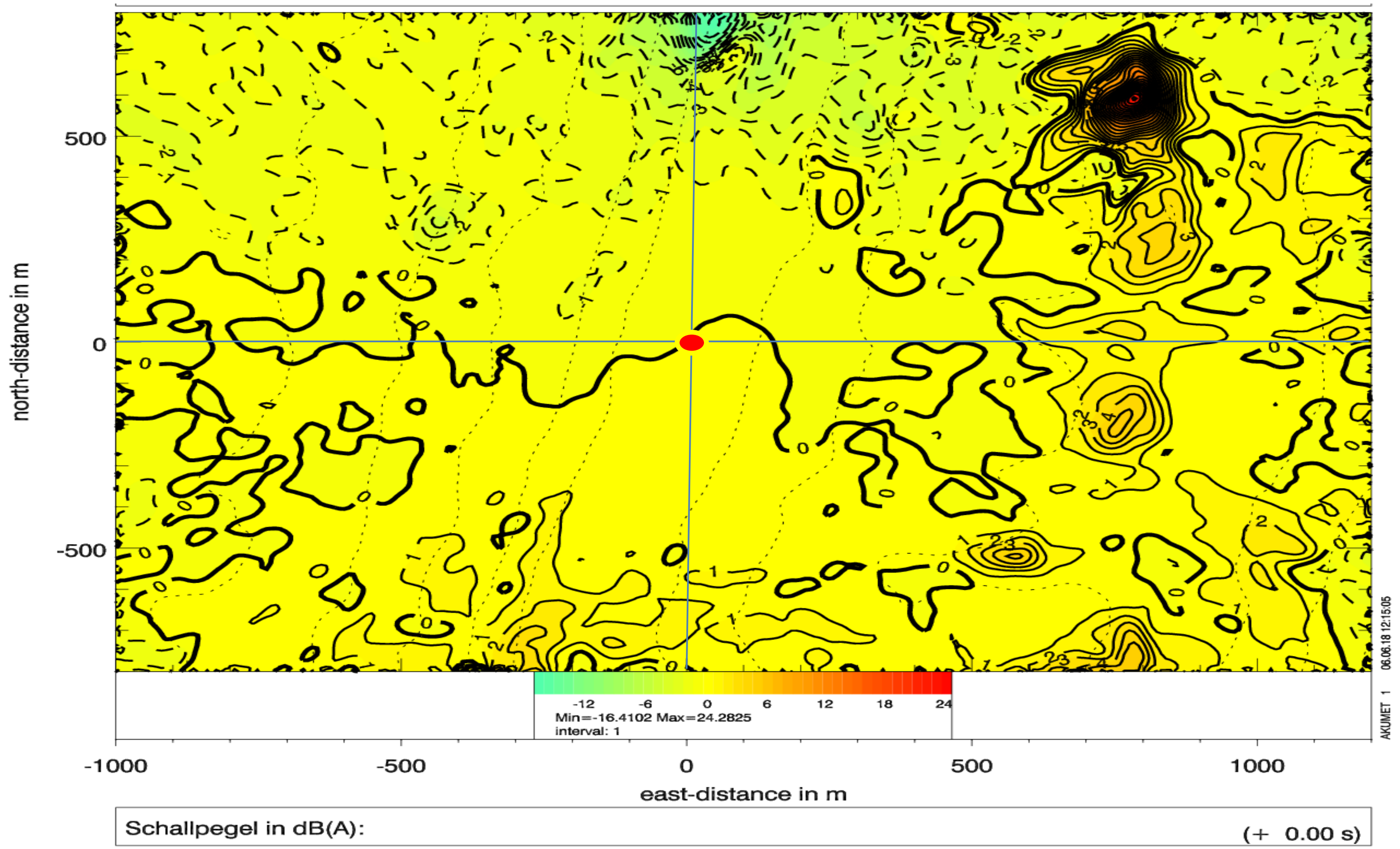

SPL (difference) 4 m GND Influence of the wake vortex (only aeroacoustic sound)

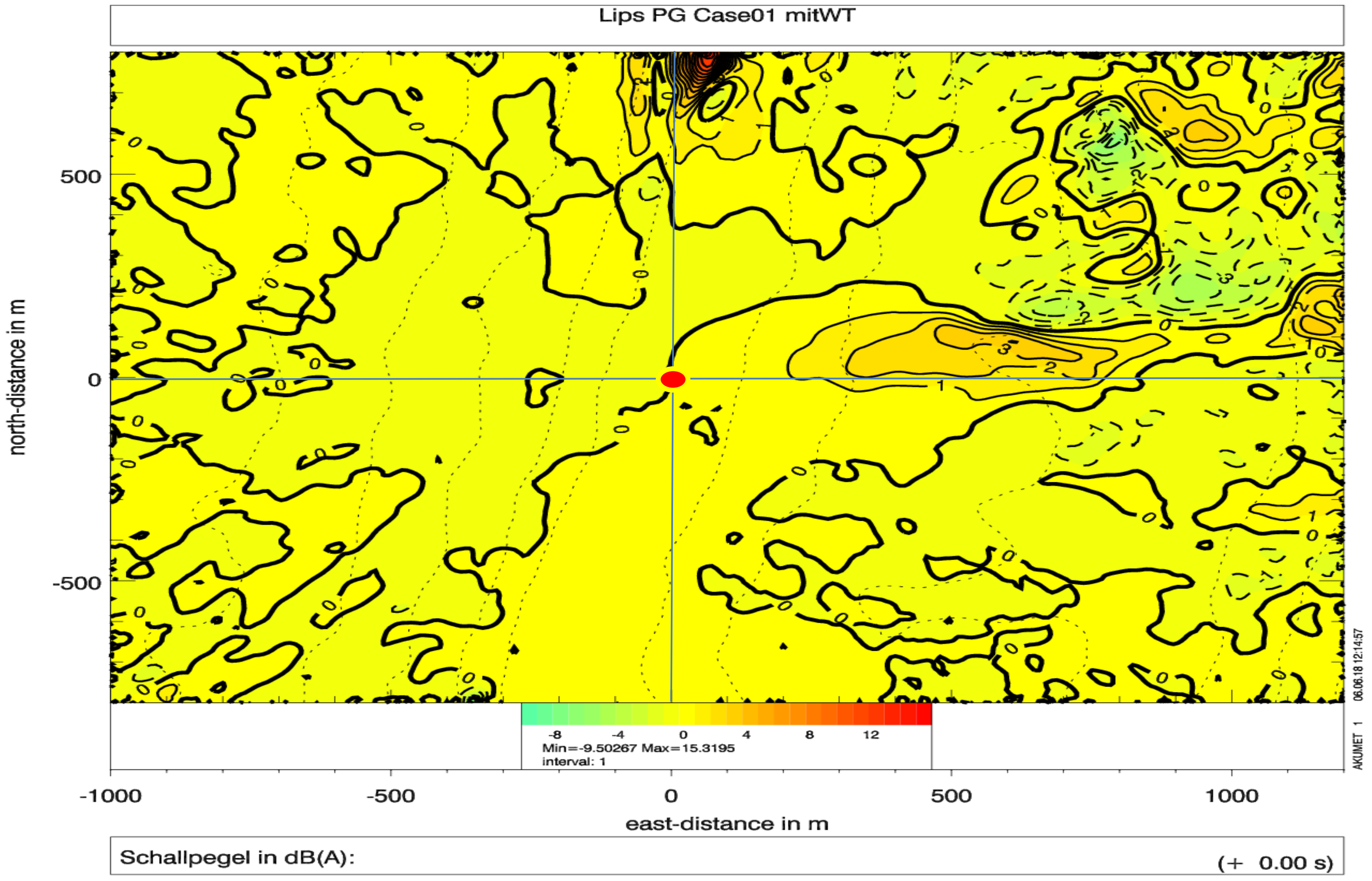

SPL (80 and 100 Hz) 4 m GND incl. orography, incl. meteorology and wake vortex (Generator – sound)

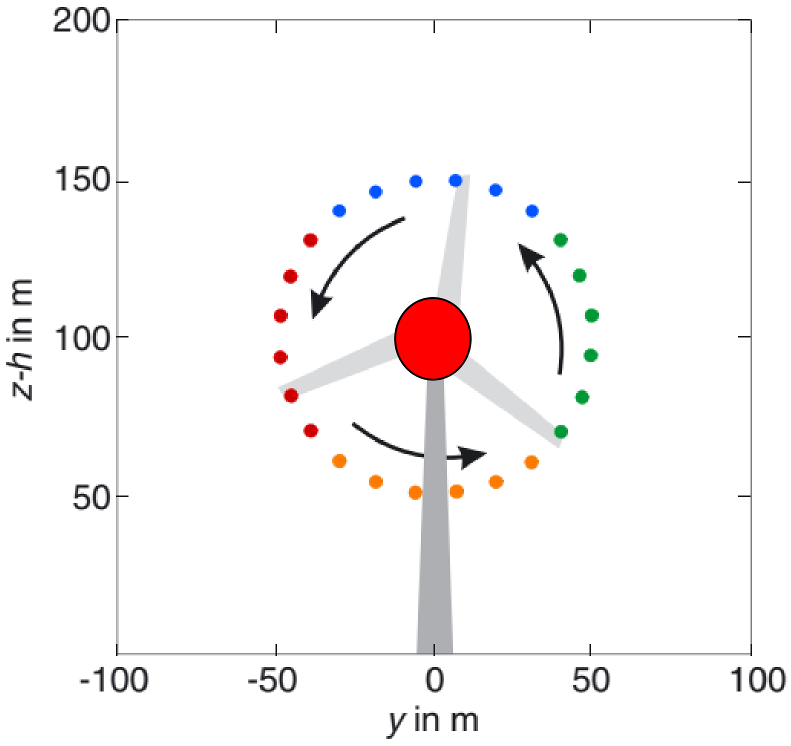

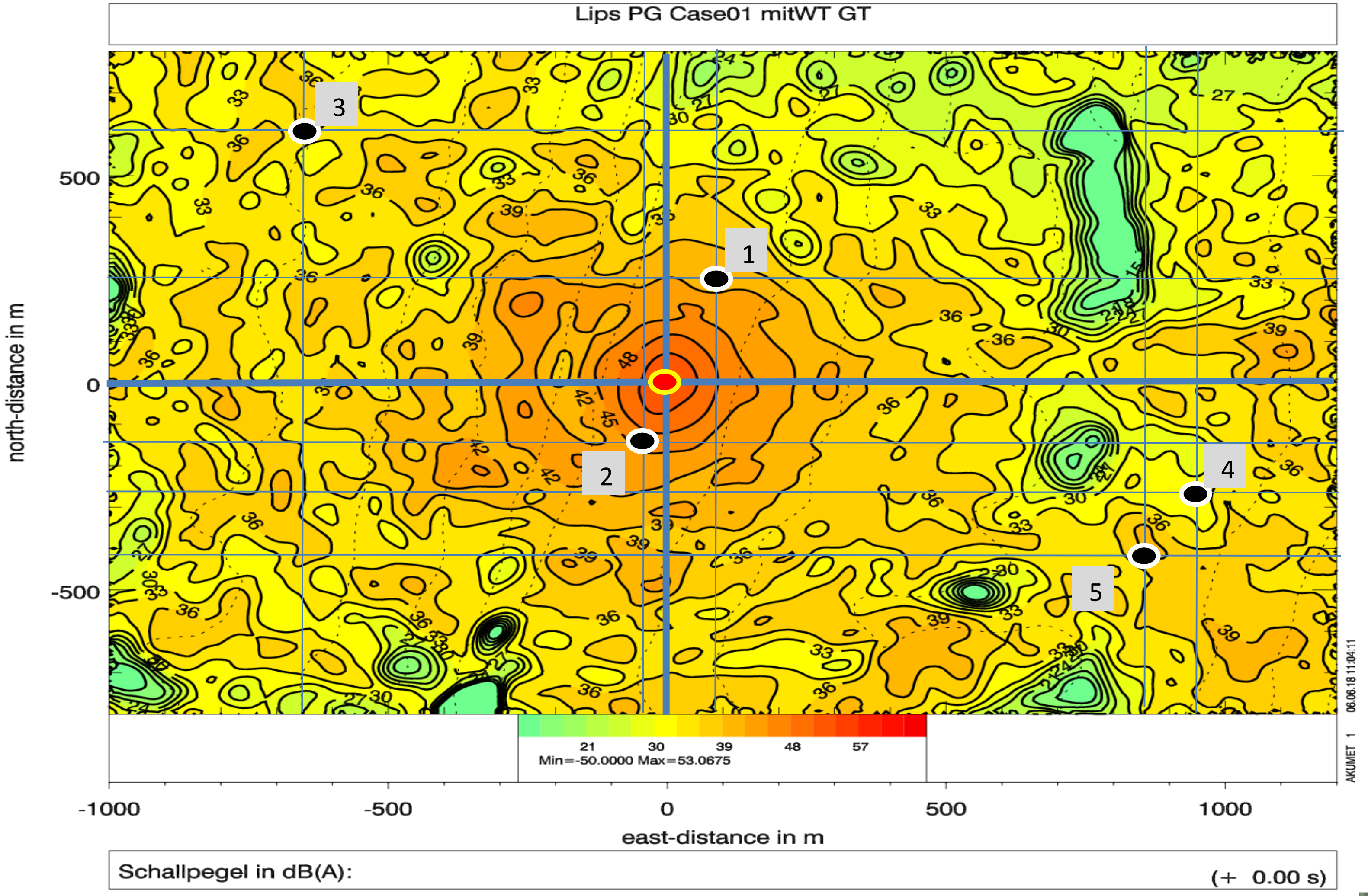

SPL (A-wighted) 4 m GND incl. orography, incl. meteorology and wake vortex (only aeroacoustic sound)

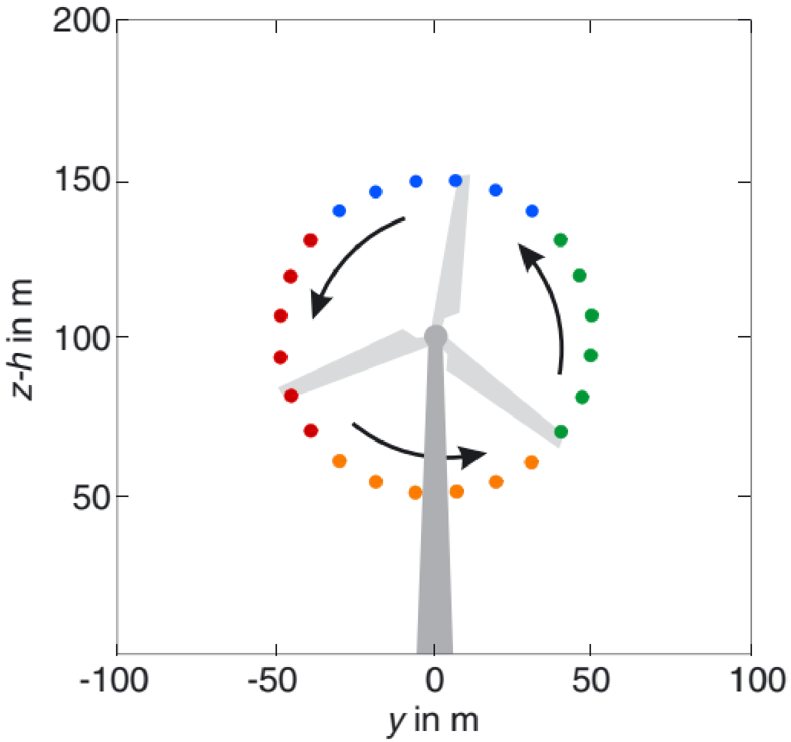

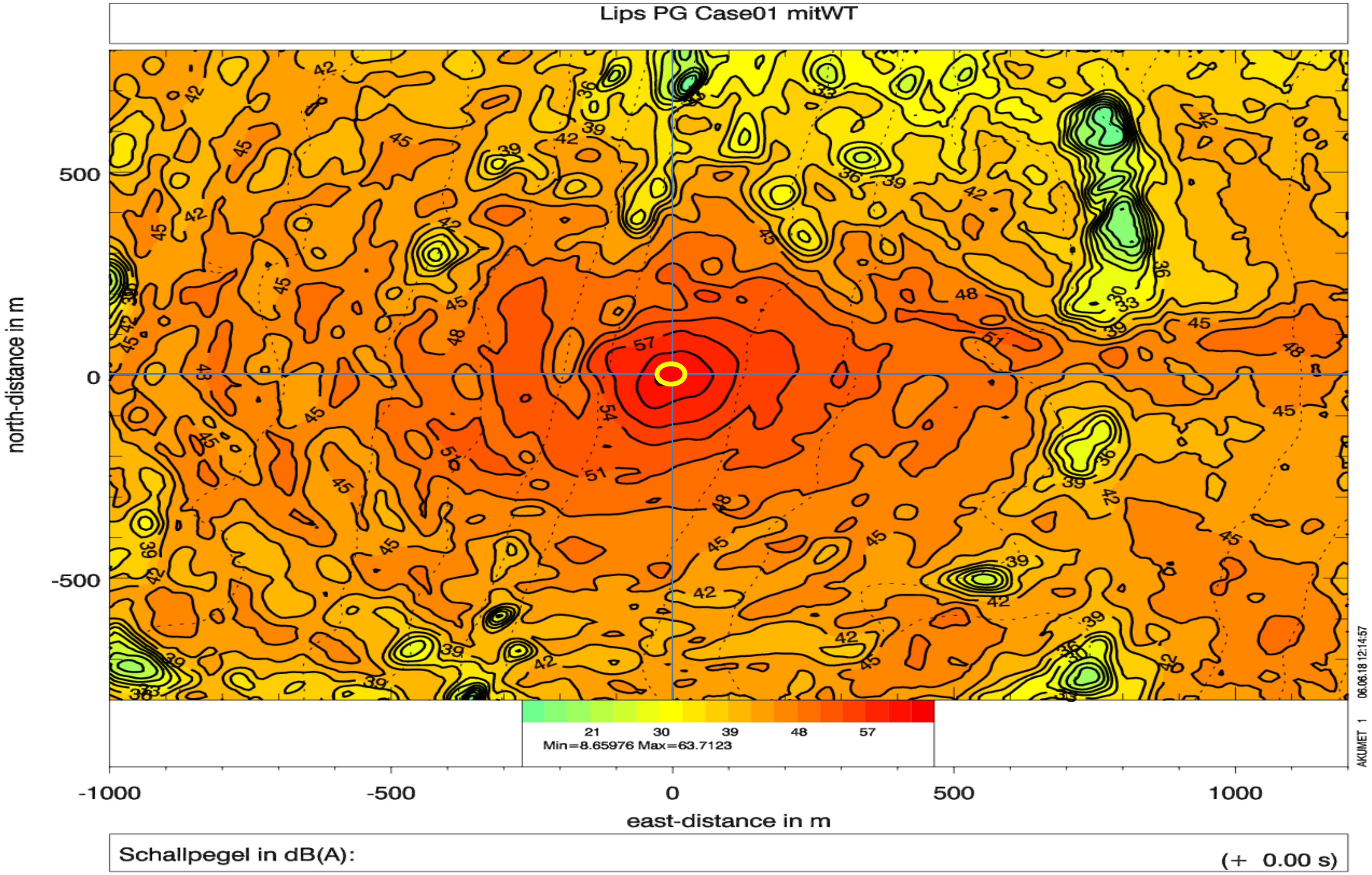

Detecting the signal of the WT

$$L_{all,MP} = 10*\lg[\,10**(L_{WT,MP}/10) + 10**(L_{back,MP}/10)\,]$$

WT-Generator-sound Background - sound

Calculated level-difference to measurement position one Generator-sound (80 and 100 Hz):

Mesasurem.position:	1	2	3	4	5
Background -30.0 dB:	0.0	5.1	-4.9	-9.7	-2.8 dB

measured: $L_{all,MP}$ and $L_{back,MP}$ → $L_{WT,MP} = 10*\lg[10**(L_{MP}/10)-10**(L_{back,MP}/10)]$

calculated: $L_{WT,MP} = L_E + dL_{dir,WT\text{-}MP} + dL_{prop,WT\text{-}MP}$

assumption 0 incl. Model error

Proof the assumptions with data

Bring the Data together

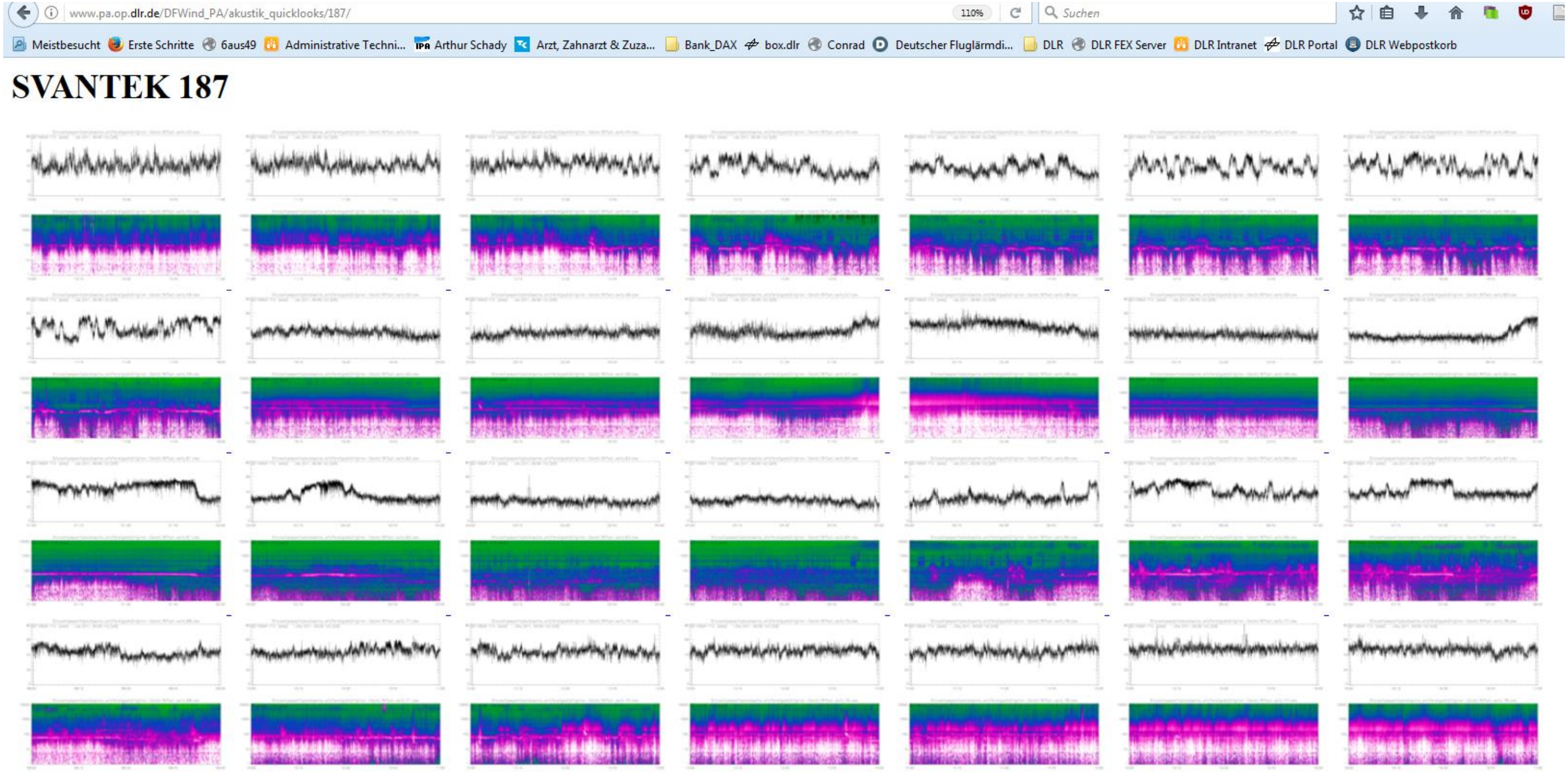
www.pa.op.dlr.de/DFWind_PA/akustik_quicklooks/187/
110%
Suchen
Meistbesucht
Erste Schritte
6aus49
Administrative Techni...
Arthur Schady
Arzt, Zahnarzt & Zuza...
Bank_DAX
box.dlr
Conrad
Deutscher Fluglärmdi...
DLR
DLR FEX Server
DLR Intranet
DLR Portal
DLR Webpostkorb
SVANTEK 187

187 – 05.05.2017 21:00-22:00 UTC

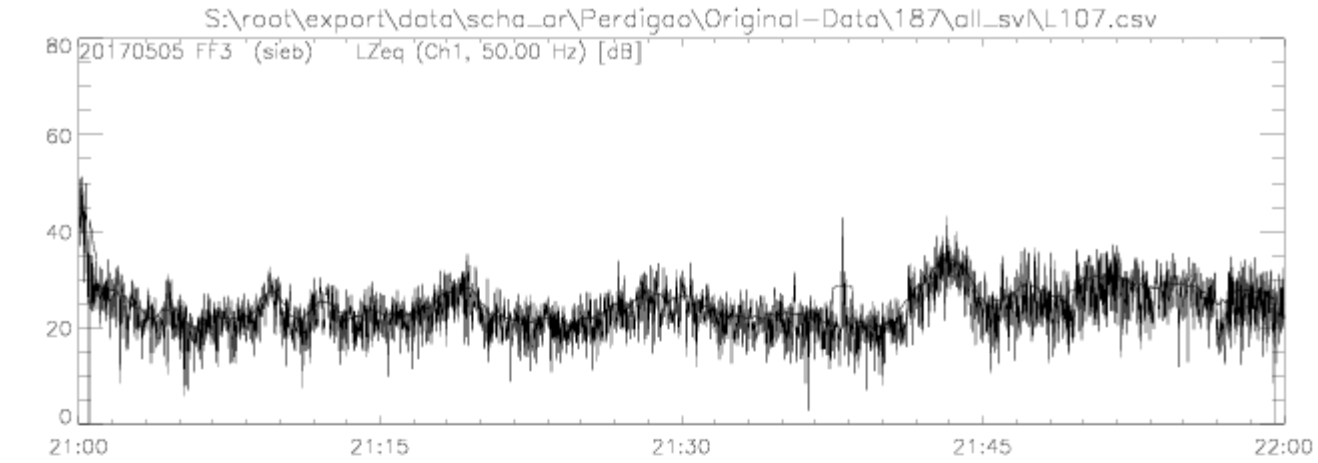

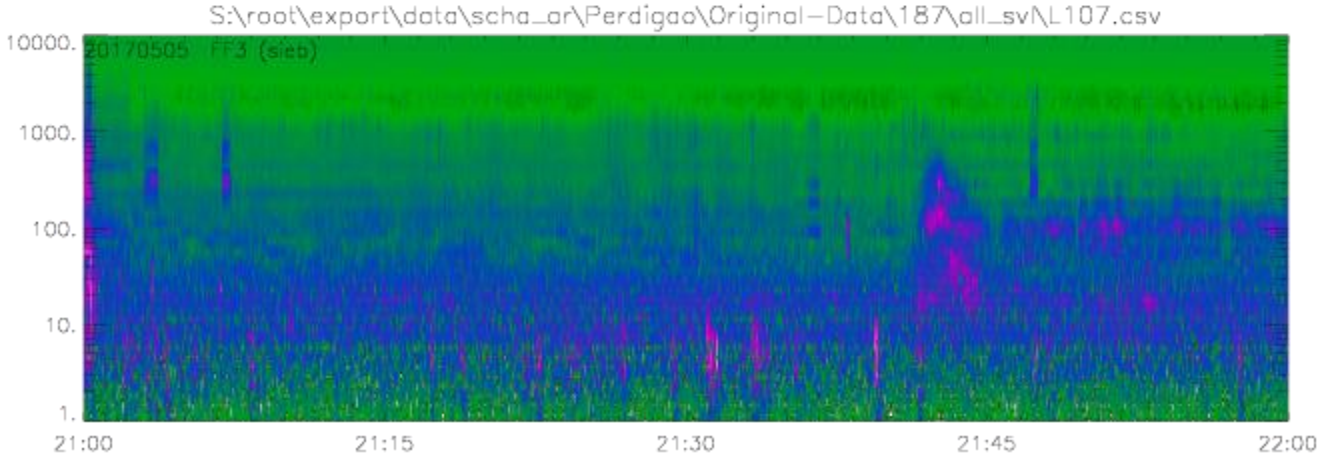

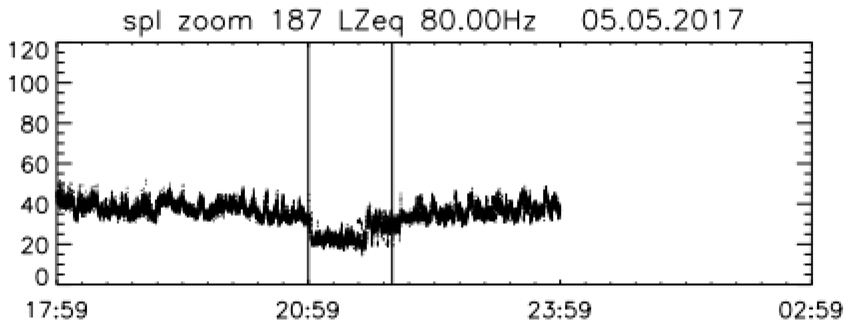

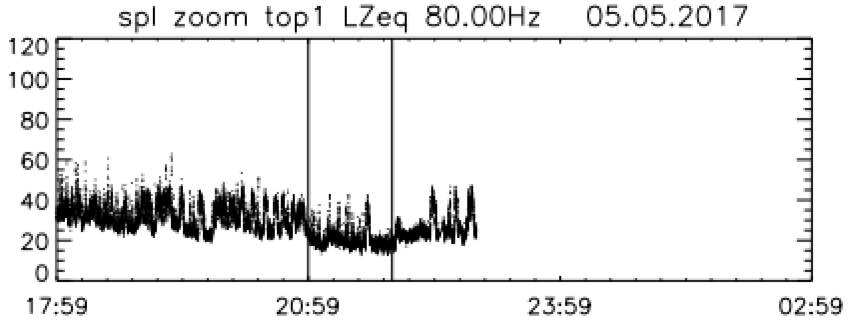

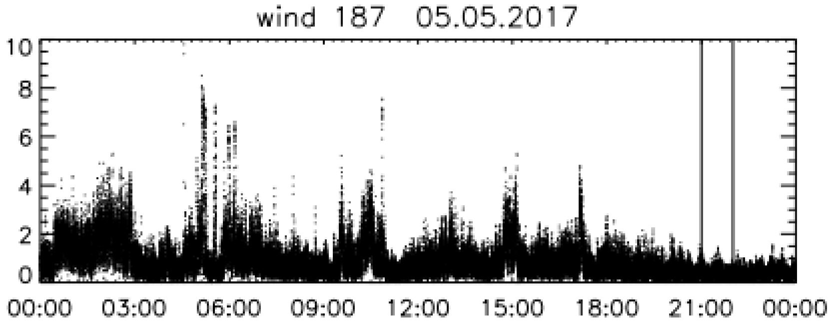

187 – 22.05.2017 04:00-05:00 UTC

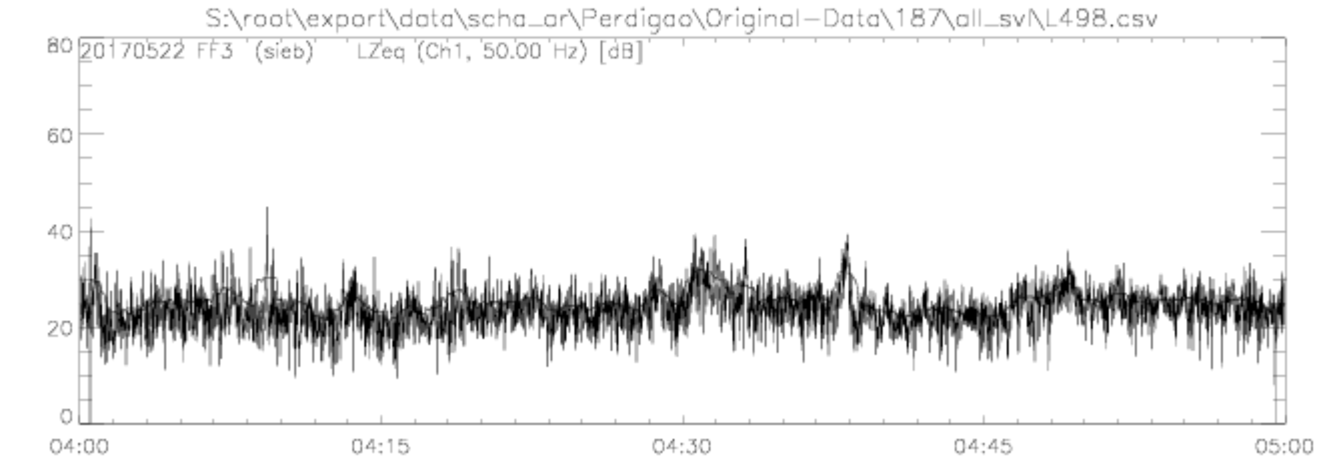

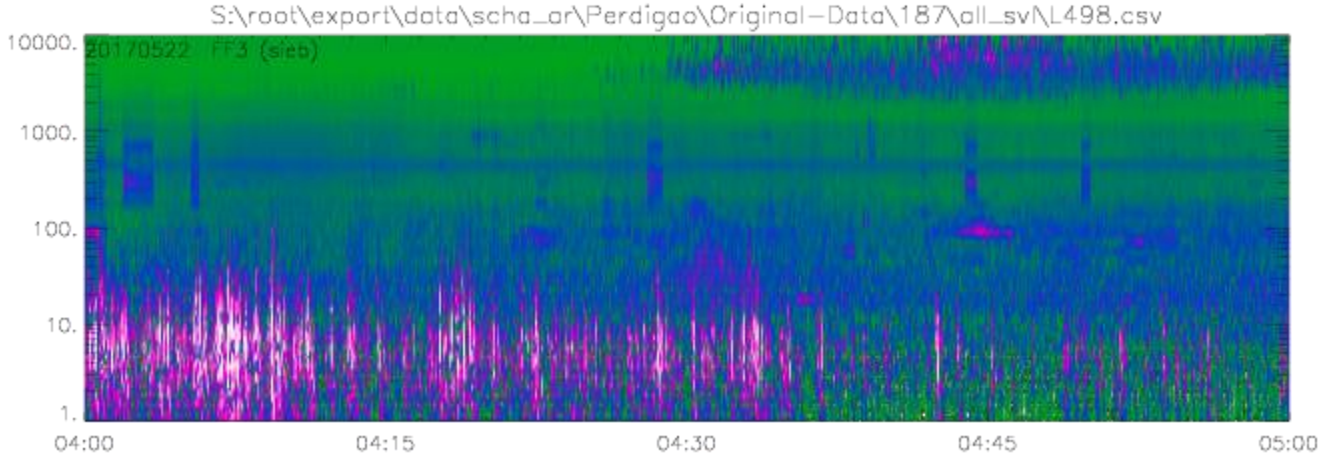

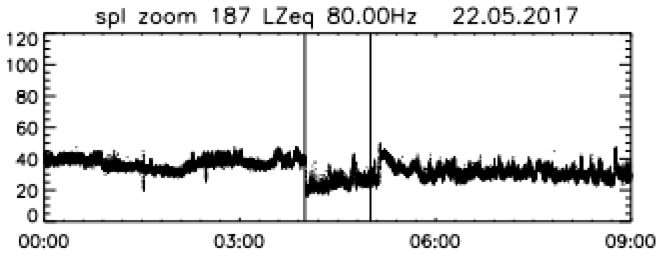

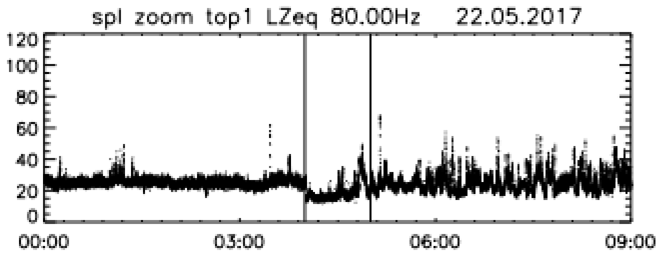

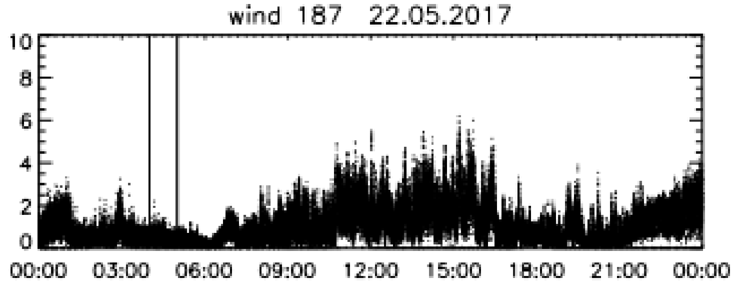

Assessing sound from wind turbines

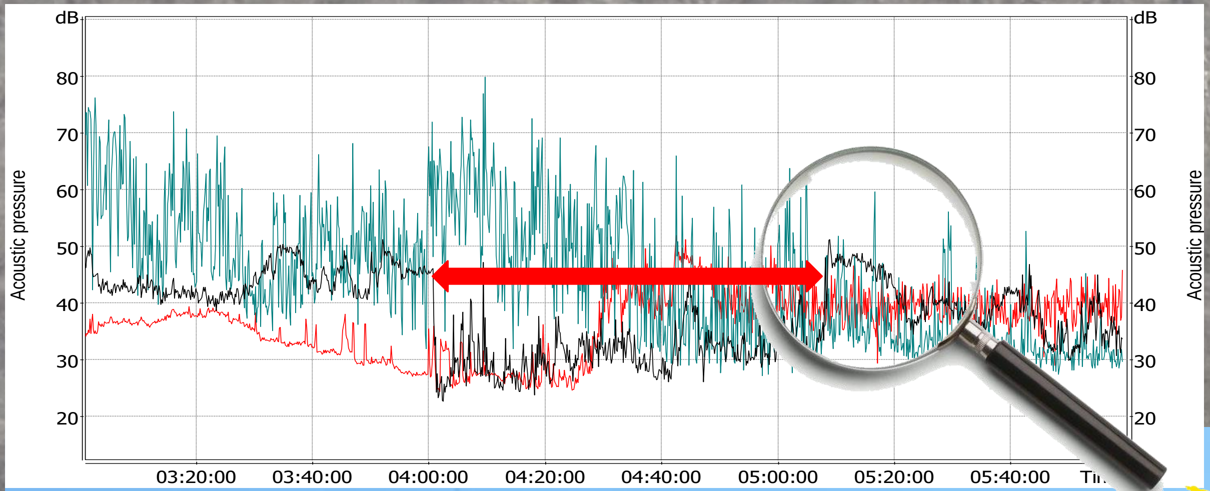

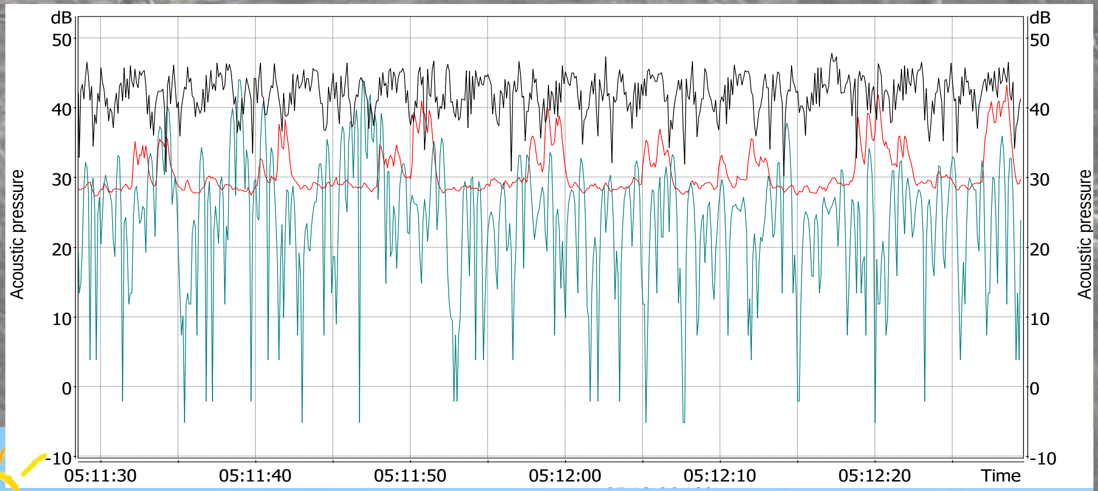

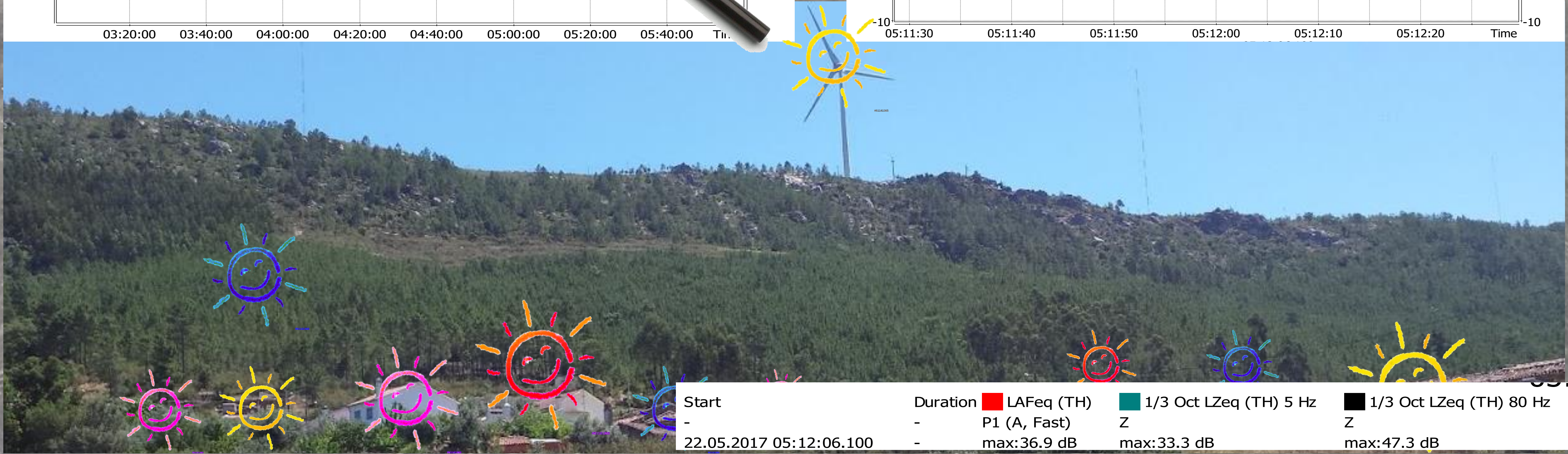

Start	Duration	LAFeq (TH)	1/3 Oct LZeq (TH) 5 Hz	1/3 Oct LZeq (TH) 80 Hz
-	-	P1 (A, Fast)	Z	Z
22.05.2017 05:12:06.100	-	max:36.9 dB	max:33.3 dB	max:47.3 dB

Periodic Signal, 1/3 Octave Band (80 Hz)

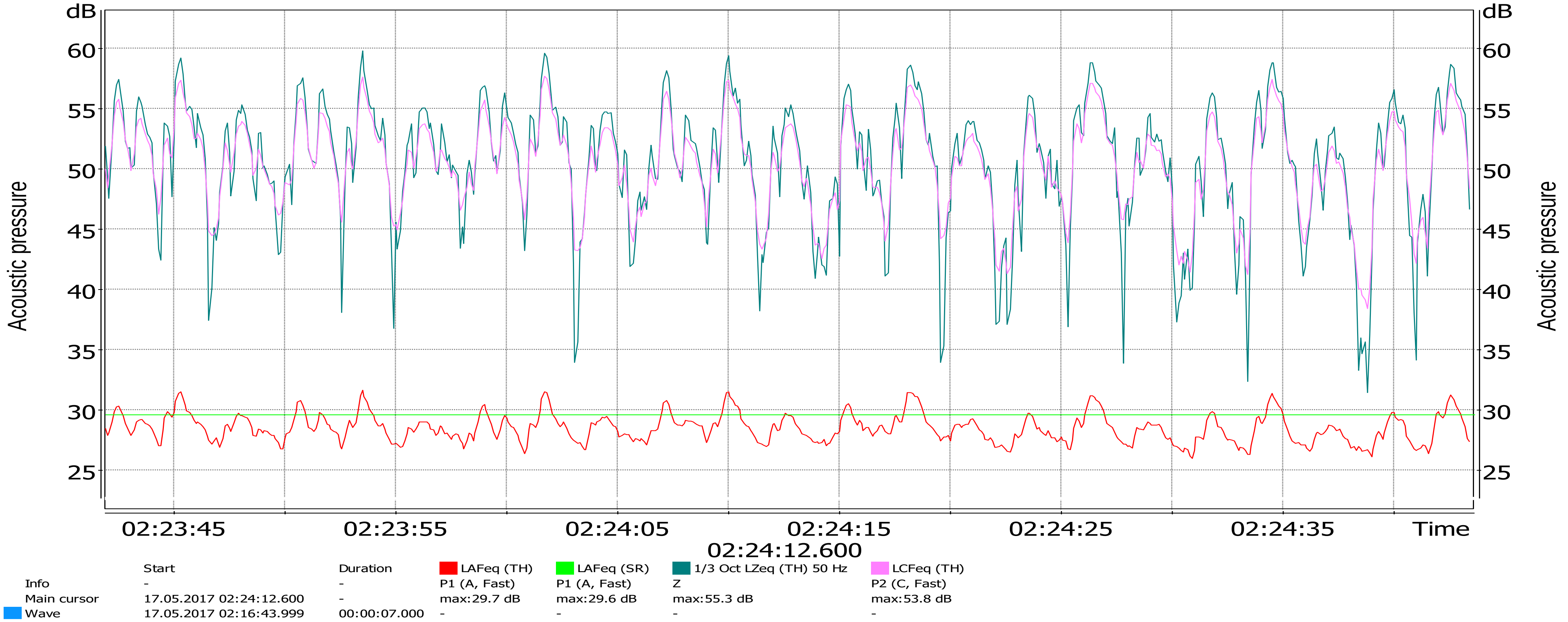

Content

- Introduce the measurement campaign and site
- Show some general measurement results (database)
- The theoretical approach
- Proof the assumptions with data

- **Scientific question**:
- What could be the reason for complaints of citizens in the surrounding of a WT?
- Do we understand the interaction of sound propagation with the complex terrain and the meteorology?
- How should we characterize the WT as a source of sound?

Contact:

Dr. Arthur Schady

Deutsches Zentrum für Luft- und Raumfahrt (DLR)
German Aerospace Center
Institute of Atmospheric Physics (IPA)
Oberpfaffenhofen
82234 Wessling | Germany

Telephone +49 8153 28-3001
arthur.schady@dlr.de
www.dlr.de/ipa

A new experimental database for wind turbine noise propagation in an outdoor inhomogeneous medium

B. Kayser (UMRAE), B. Gauvreau (UMRAE), D. Ecotière (UMRAE), C. Le Bourdat (Engie Green)

Introduction

○ Objectives

- Provide a reference database on wind turbine noise
  - -> acoustical measurements
  - -> meteorological measurements
  - -> ground characteristics measurements

- Fuel several works in progress
  - -> validation of forecasting models (Cibelius project, ANSES 2017-18)
  - -> validation of measurement methods
  - -> estimation of uncertainties in noise forecasting
  (PhD thesis Ifsttar/Cerema, 2017-20)

- Make available the database for the scientific community

Contents

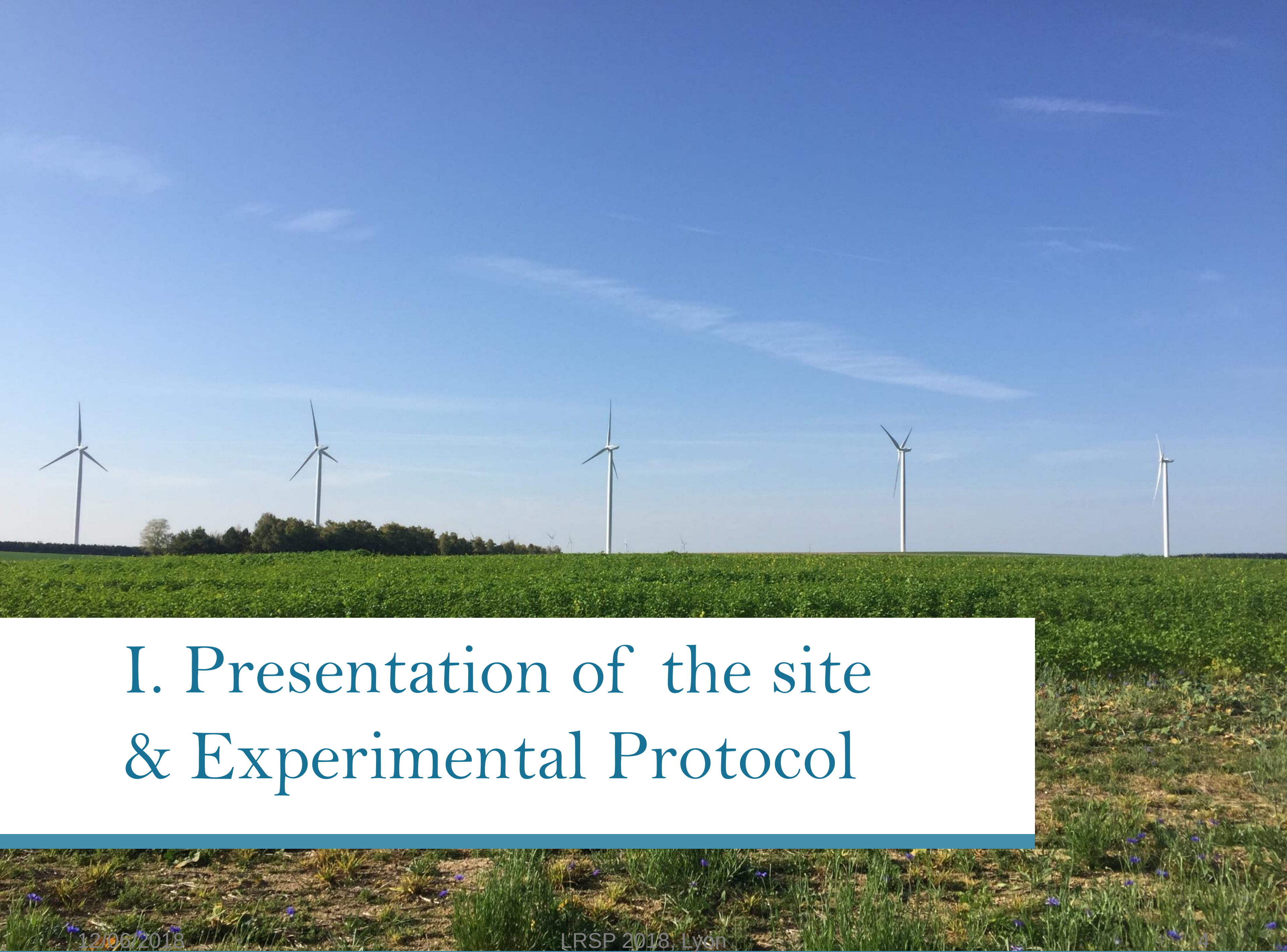

I. Presentation of the site & Experimental Protocol

I. Experimental site

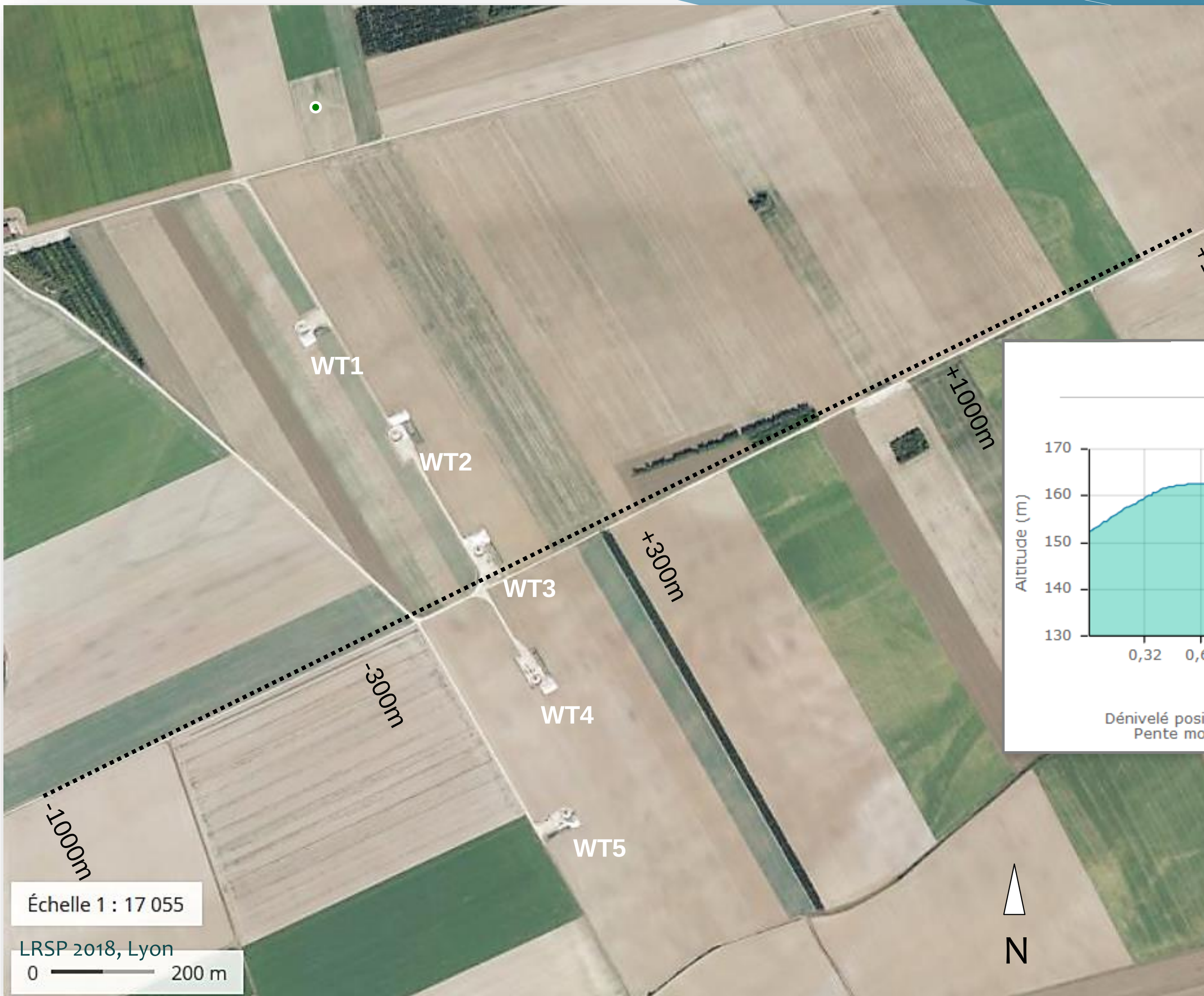

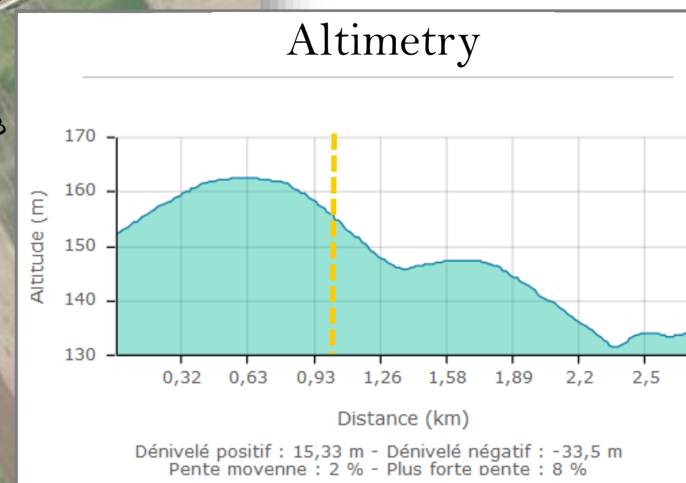

I. Experimental site

Sound Measurements
from -1km to +1.5km
[12.5Hz ; 20kHz]

I. Experimental site

Sound Measurements
from -1km to +1.5km
[12.5Hz ; 20kHz]

Acoustic Power Measurements
of wind turbines 1, 3 & 5 at 150m (IEC 61400-11:2012)

I. Experimental site

Sound Measurements
from -1km to +1.5km
[12.5Hz ; 20kHz]

Acoustic Power Measurements
of wind turbines 1, 3 & 5 at 150m (IEC 61400-11:2012)

Meteorological Measurements

- Temperature
- Wind
- > mean sound speed profiles
- > turbulence characteristics

I. Experimental site

Sound Measurements
from -1km to +1.5km
[12.5Hz ; 20kHz]

Acoustic Power Measurements
of wind turbines 1, 3 & 5 at 150m (IEC 61400-11:2012)

Meteorological Measurements

- Temperature
- Wind
- > mean sound speed profiles
- > turbulence characteristics

Ground Characteristics Measurements

- Impedance
- Roughness
- Density of vegetation

II. First results

II. The wind turbines

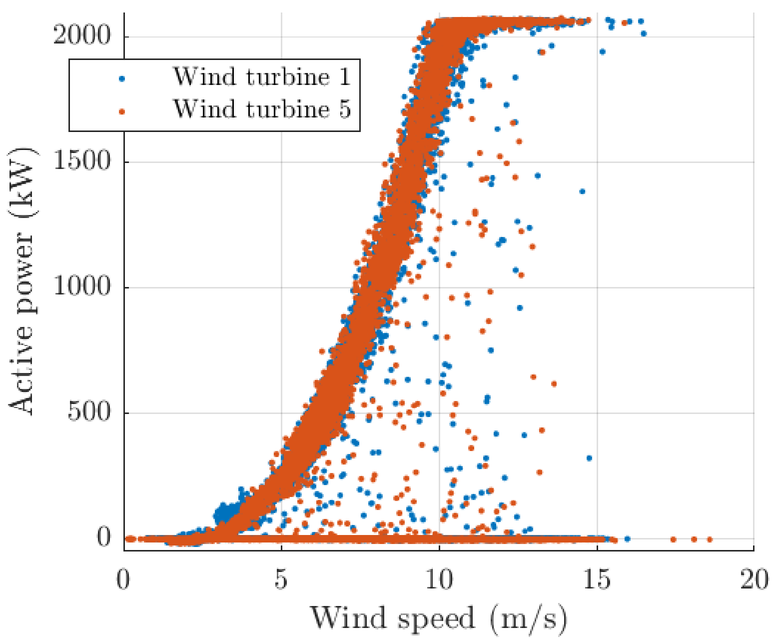

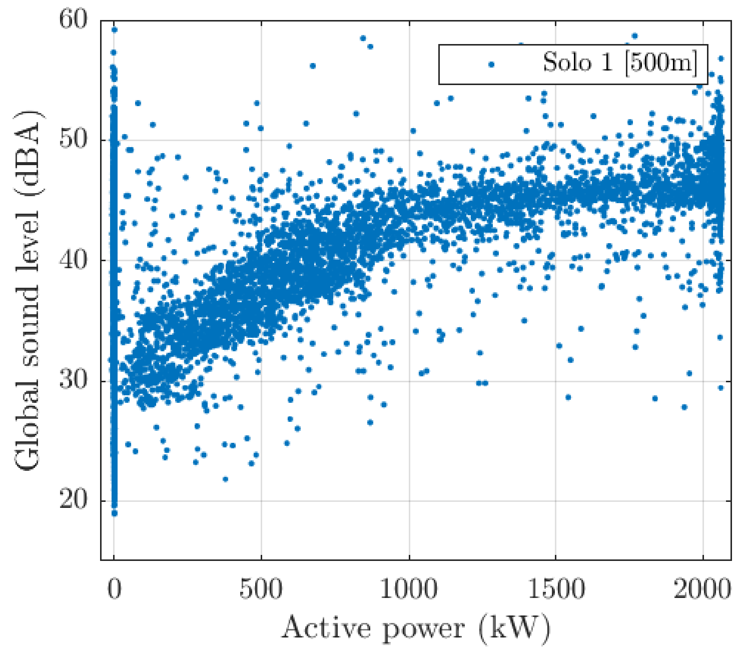

Non-stationary sound source

Global SPL = f("emission,propagation")

II. The wind turbines

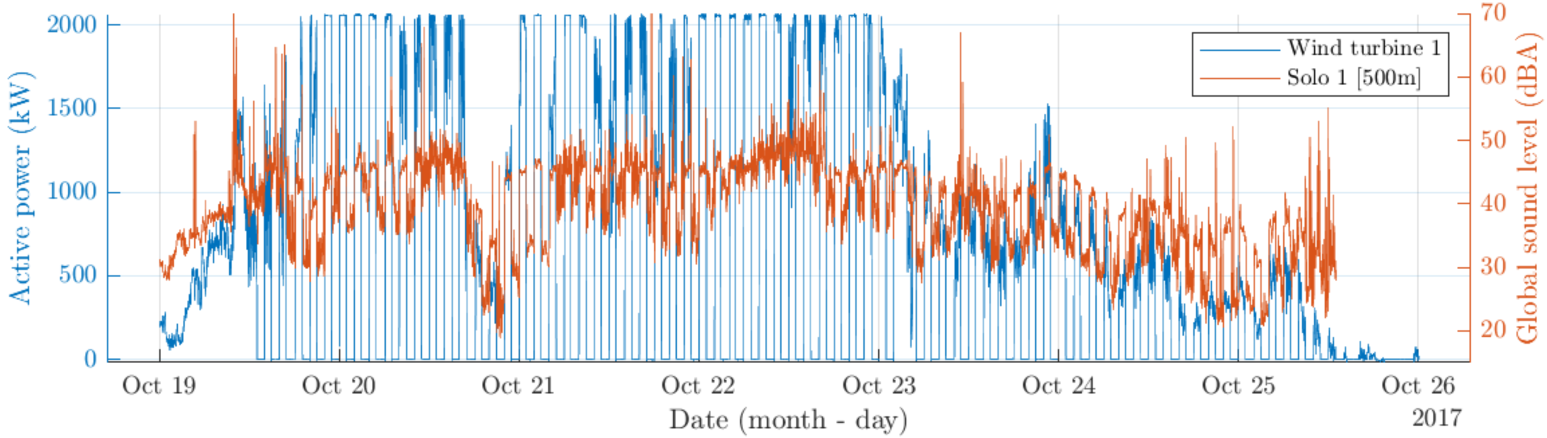

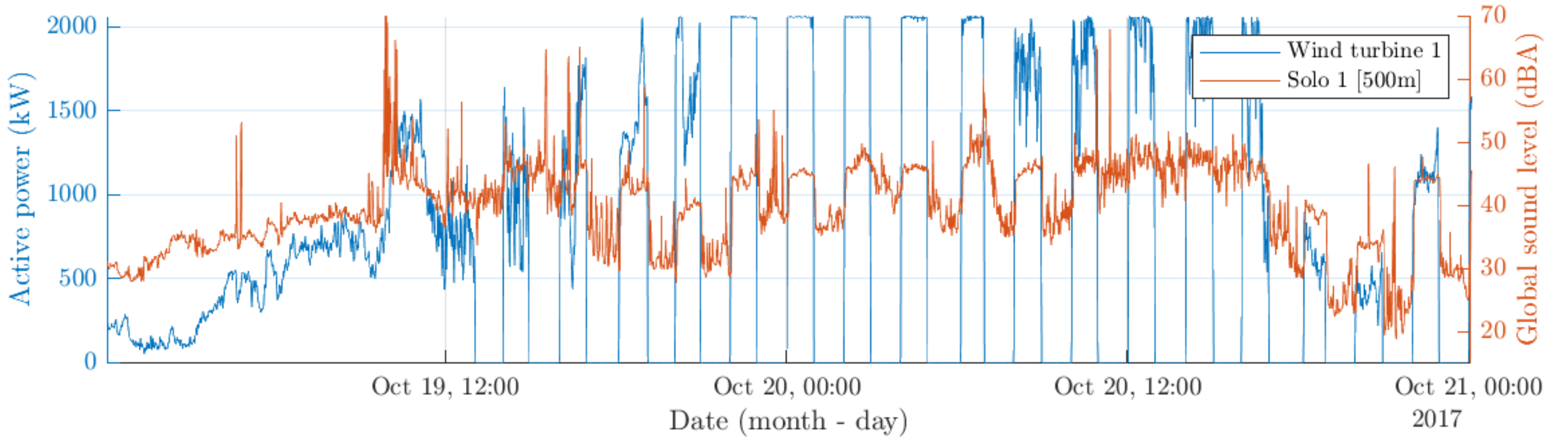

II. Acoustical Measurements

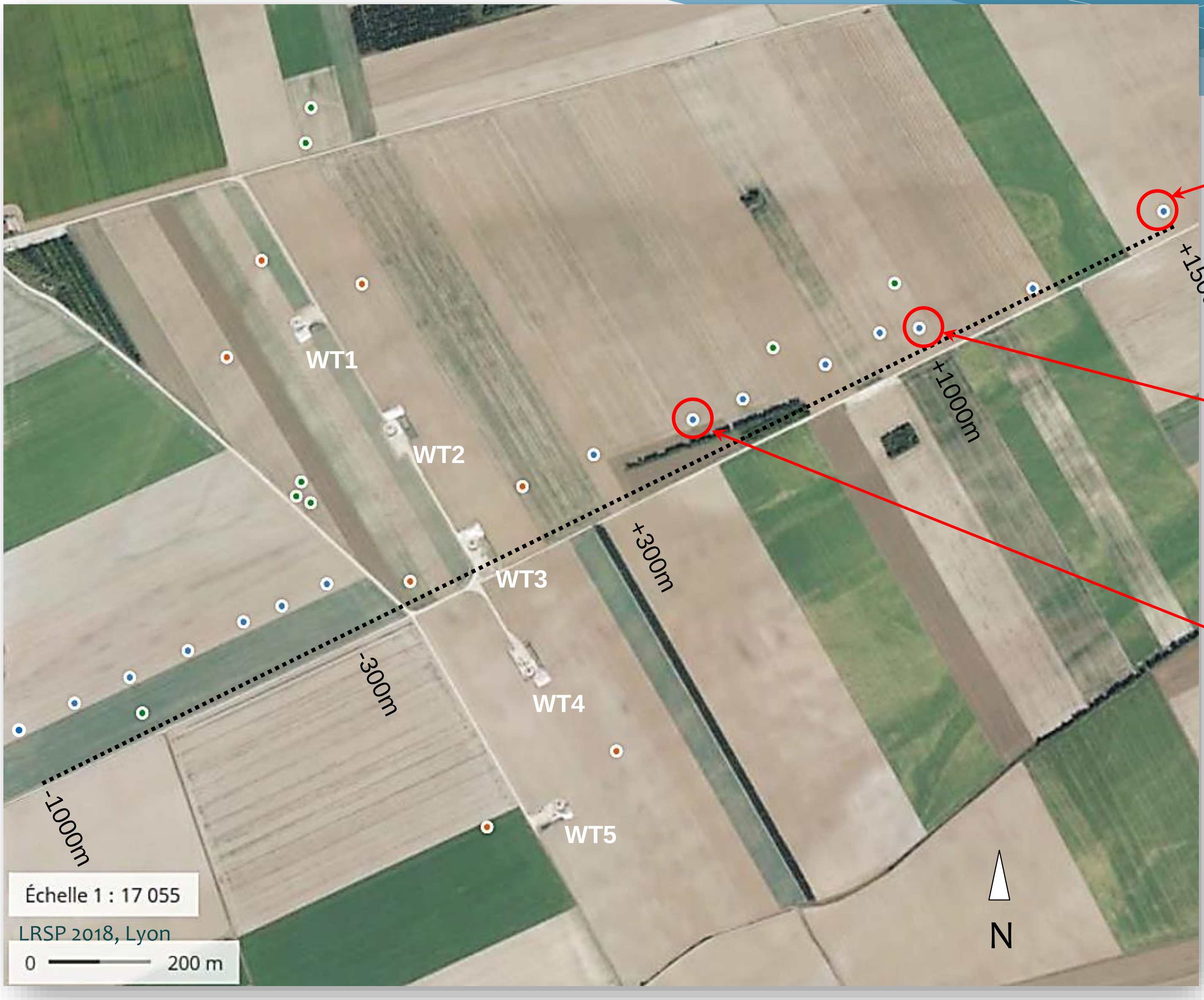

Sono **Rion** [1500m]

Sono **Solo 2** [1000m]

Sono **Solo 1** [500m]

II. Acoustical Measurements

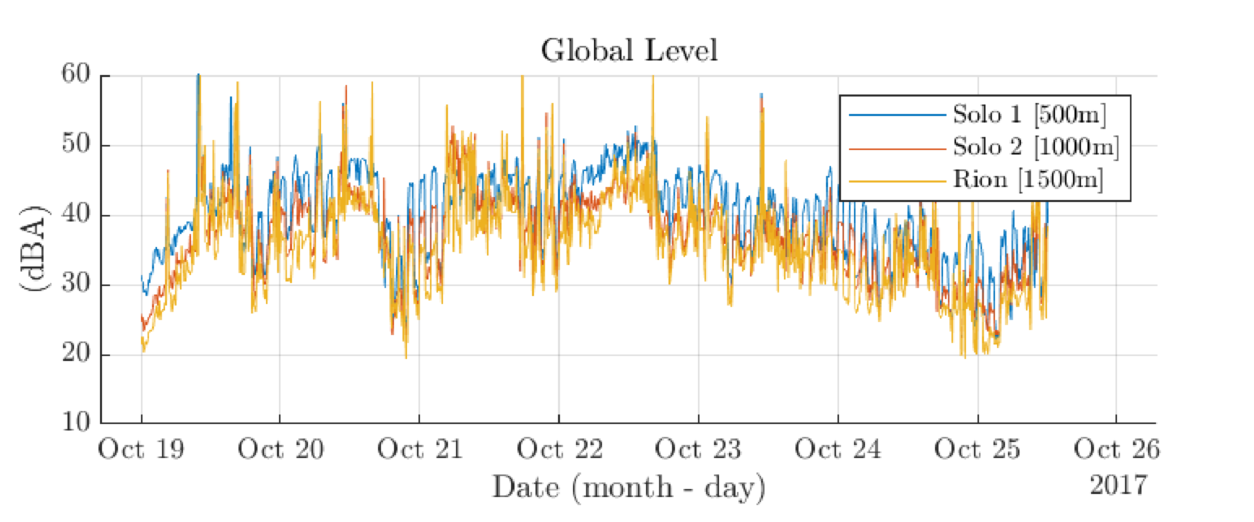

II. Acoustical Measurements

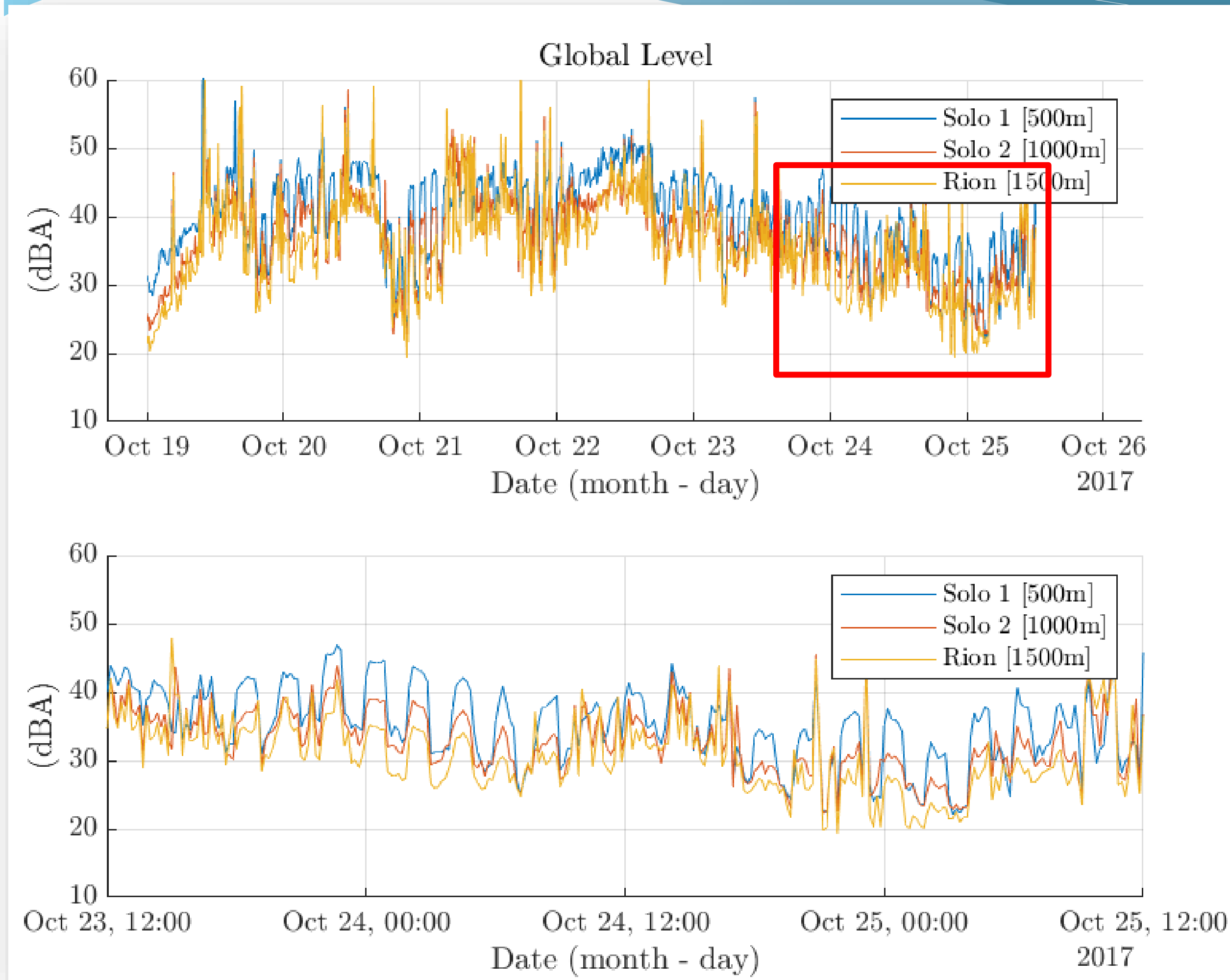

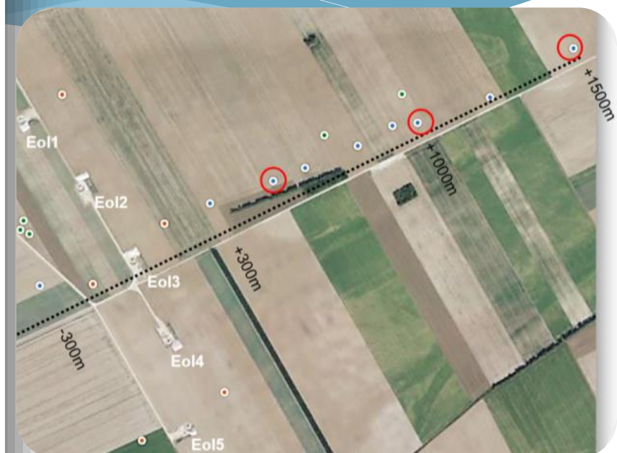

Still have contribution of wind turbine noise at 1.5km with a good S/N ratio

II. Acoustical Measurements

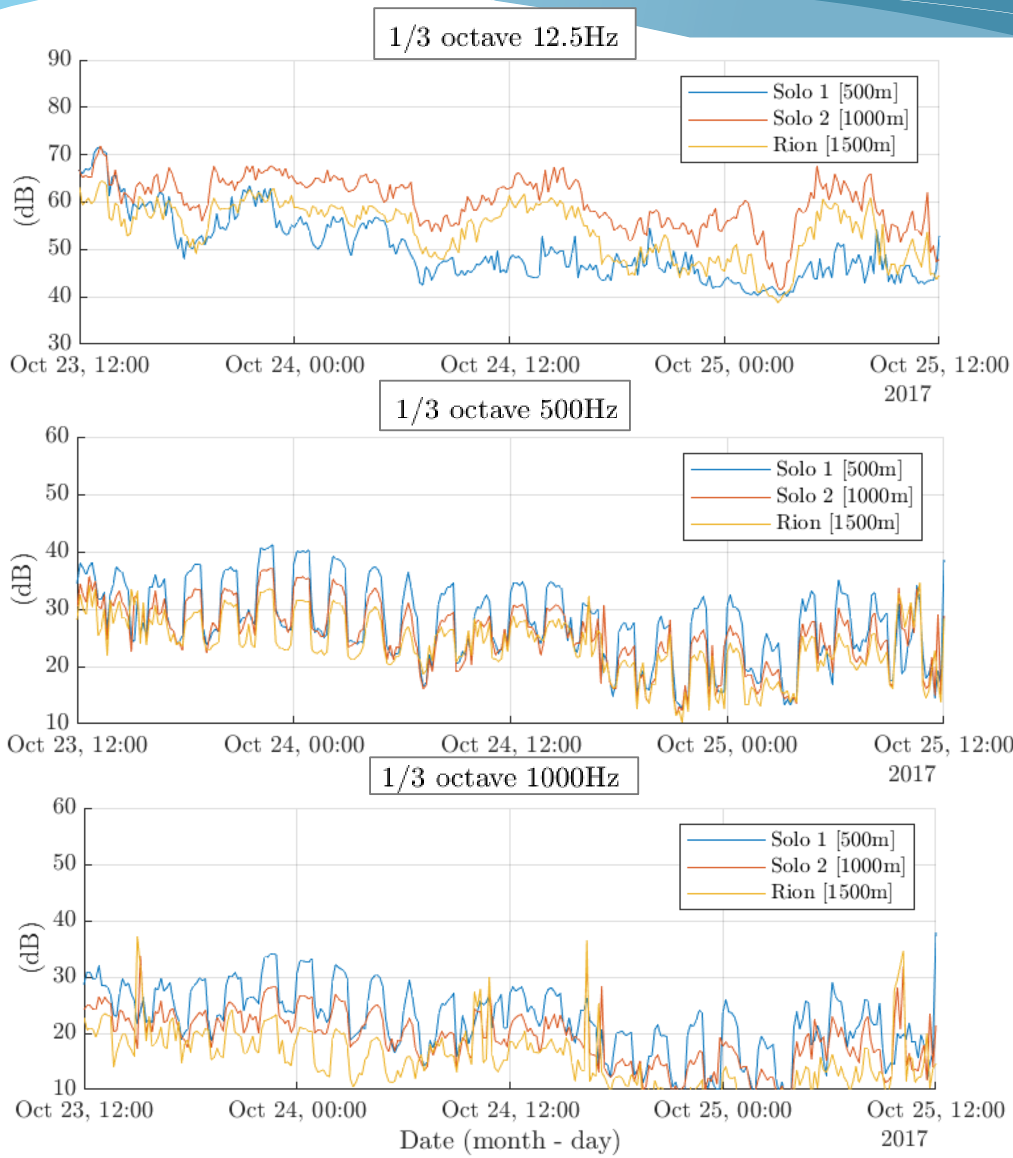

Levels are higher at low frequencies which is a characteristics of wind turbine noise

II. Meteorological Measurements

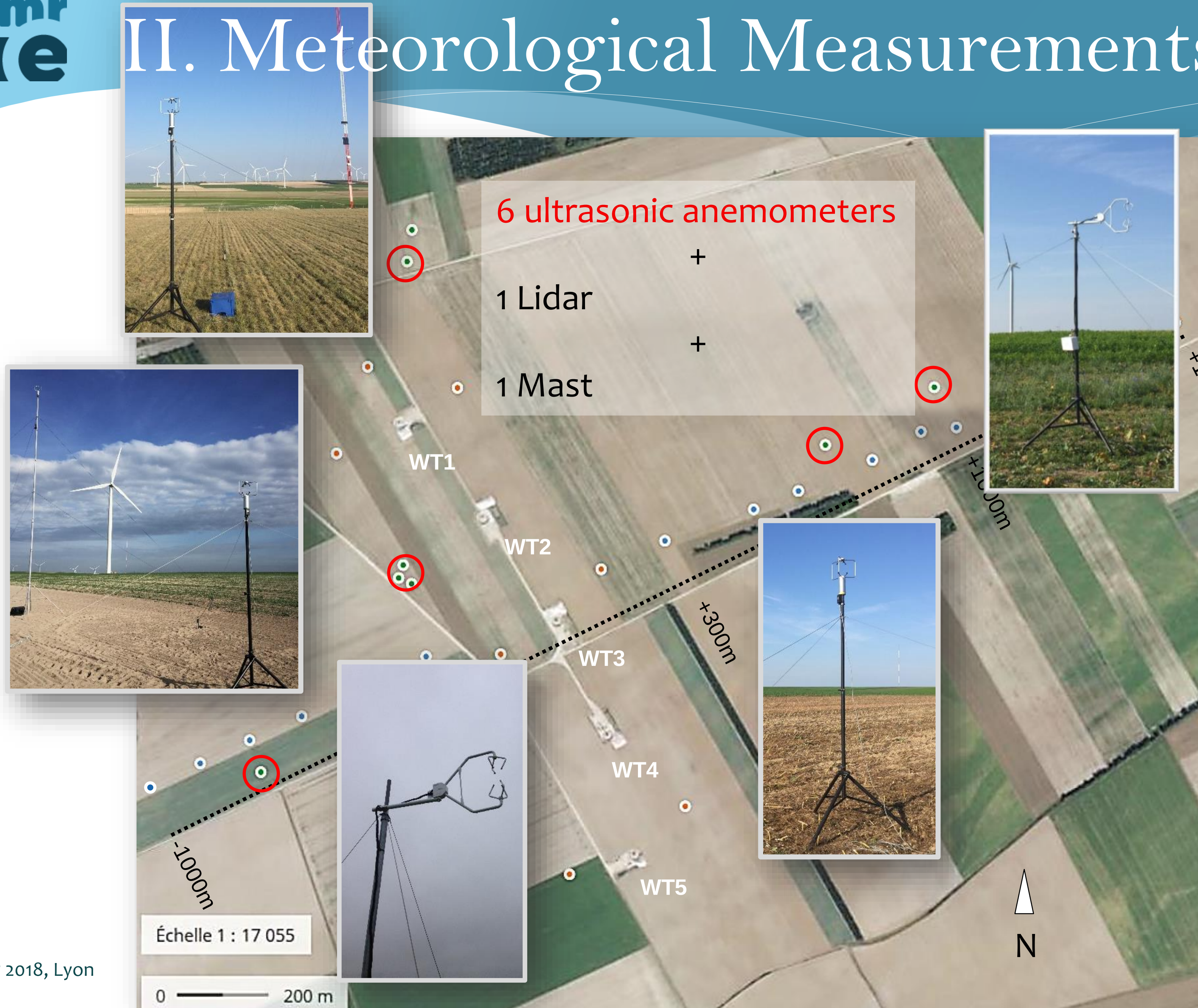

II. Meteorological Measurements

Raw data

Ultrasonic anemometer

↓

3D wind variations & temperature variations

<u,v,w> & <T>

↓

II. Meteorological Measurements

Raw data

Ultrasonic anemometer

3D wind variations & temperature variations

<u,v,w> & <T>

Post processing

Shear velocity, sensible heat flux & MO length

U*, T* & L_{MO}

Stability parameter $\xi = z/L_{MO}$

-2< ξ <1

Vertical Wind & Temperature gradients

$\partial_z u_z$ & $\partial_z T_z$

Vertical sound speed gradient

$\partial_z c_z$

II. Meteorological Measurements

Raw data

Ultrasonic anemometer

3D wind variations & temperature variations

<u,v,w> & <T>

Post processing

Shear velocity, sensible heat flux & MO length

U*, T* & L_{MO}

Stability parameter $\xi = z/L_{MO}$

-2< ξ <1

Vertical Wind & Temperature gradients

$\partial_z u_z$ & $\partial_z T_z$

Vertical sound speed gradient

$\partial_z c_z$

… Analysis under progress

II. Meteorological Measurements

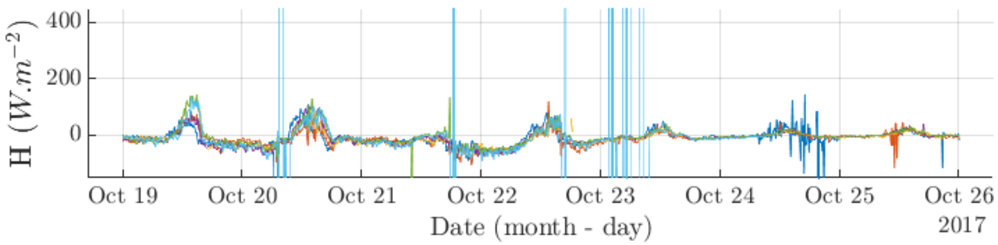

Vertical **heat flux** from the ground

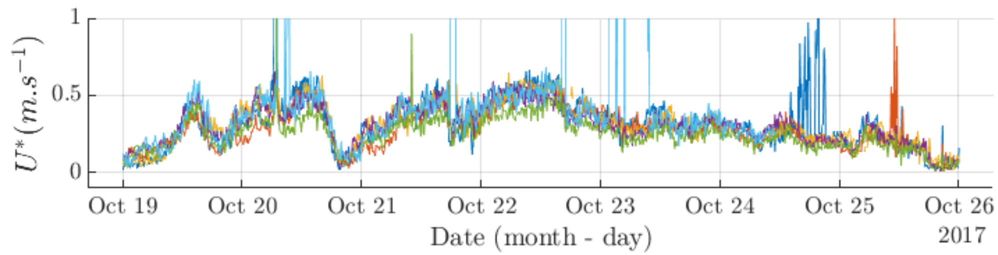

Shear velocity

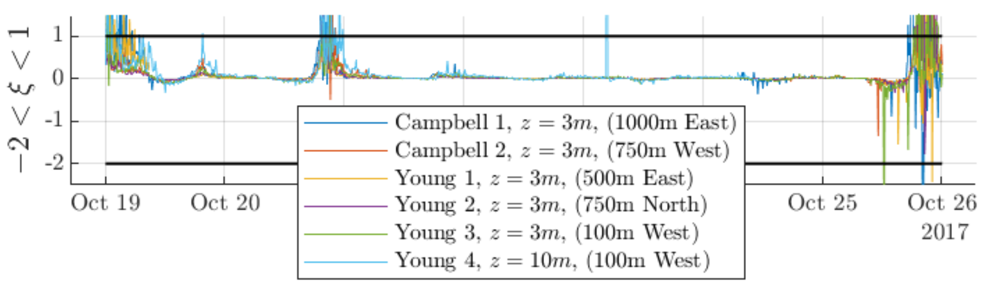

Stability parameter : z/L_{MO}

II. Meteorological Measurements

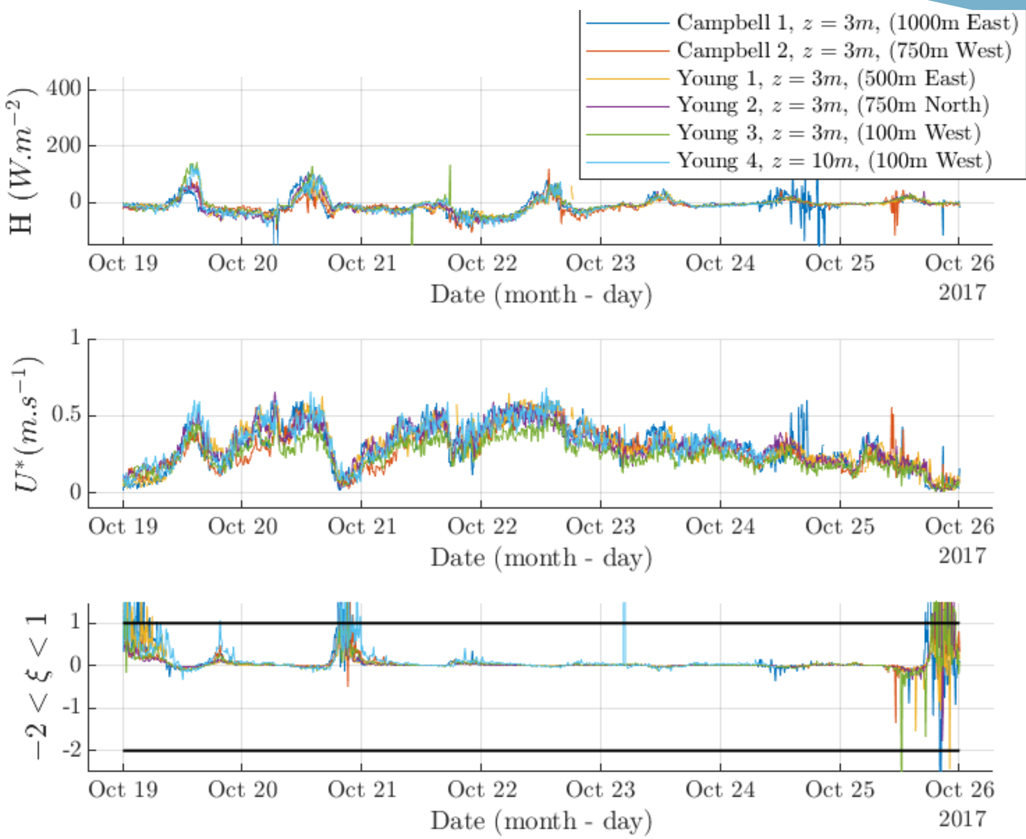

Vertical **heat flux** from the ground

- ➢ effect of day/night alternation

Shear velocity

Stability parameter : z/L_{MO}

II. Meteorological Measurements

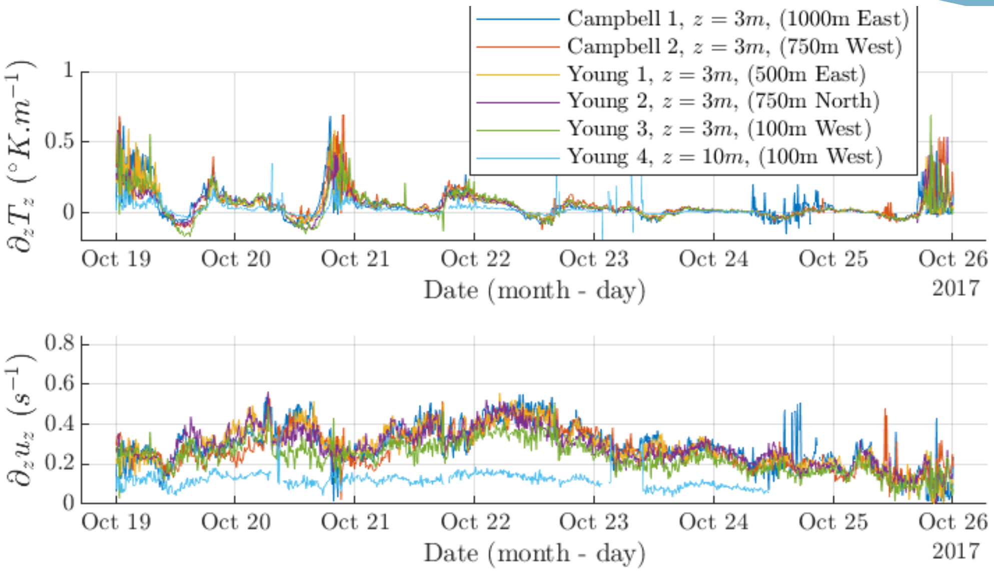

Temperature gradient

Wind gradient

II. Meteorological Measurements

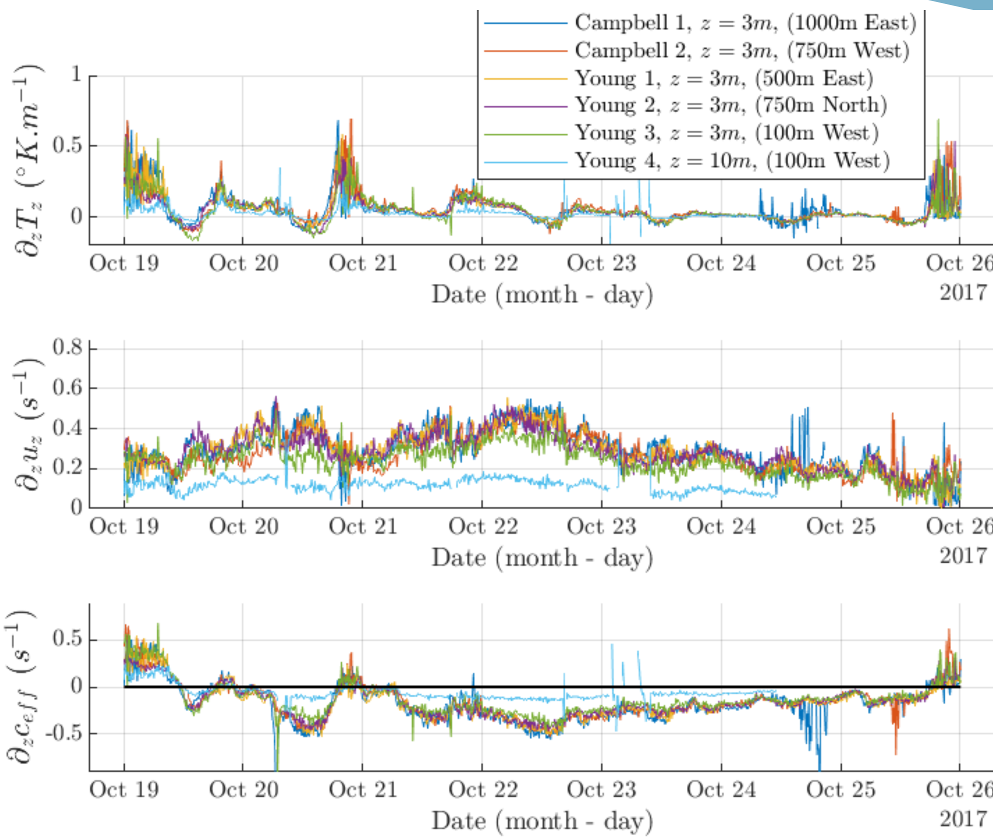

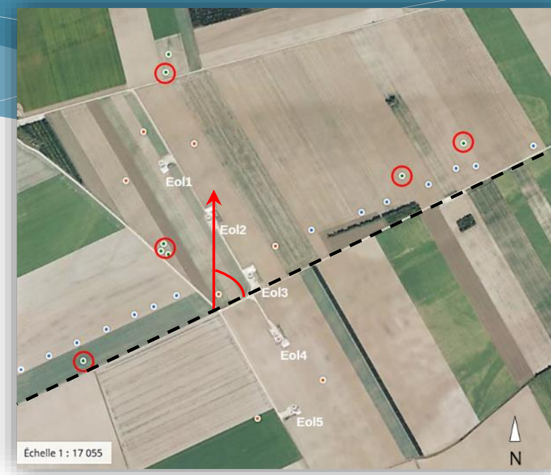

$$\frac{\partial c}{\partial z} = \frac{1}{2}\frac{gR}{C_0}\frac{\partial T(z)}{\partial z} + \frac{\partial V(z)}{\partial z} \cdot \cos\alpha$$

$\frac{dc}{dz} > 0$, downward conditions

$\frac{dc}{dz} = 0$, homogeneous conditions

$\frac{dc}{dz} < 0$, upward conditions

II. Meteorological Measurements

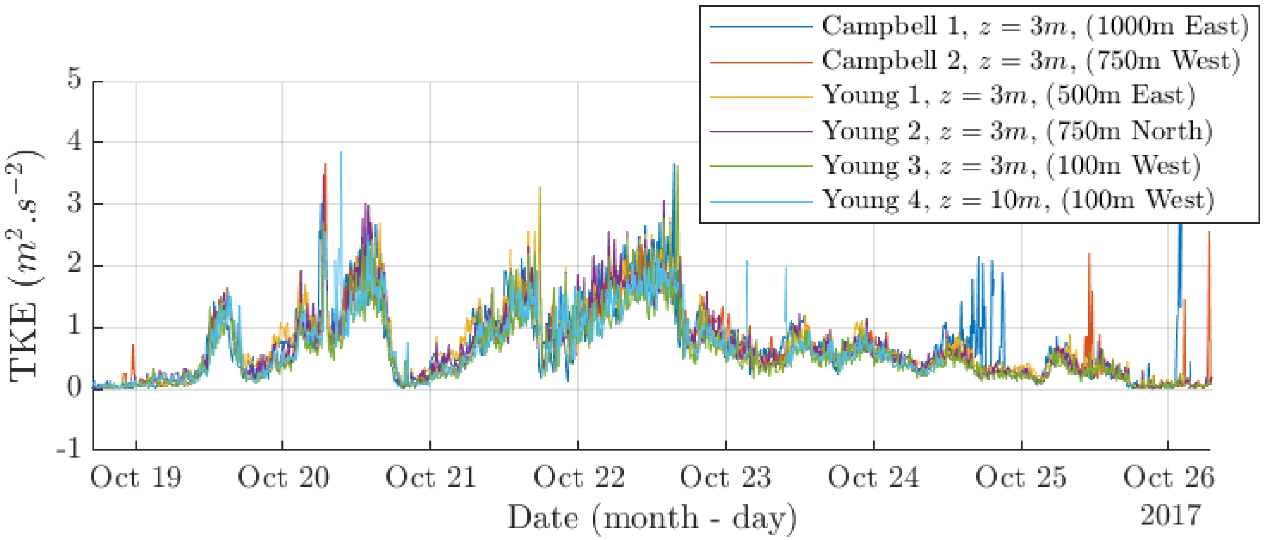

II. Meteorological Measurements

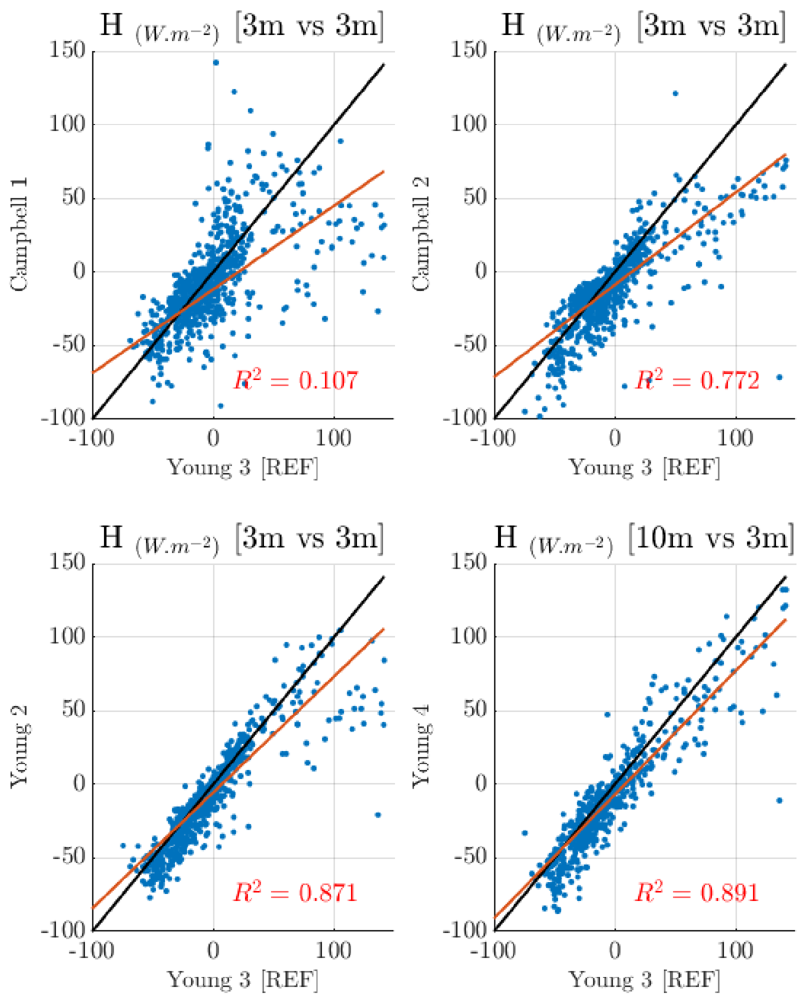

Sensible heat flux H

II. Meteorological Measurements

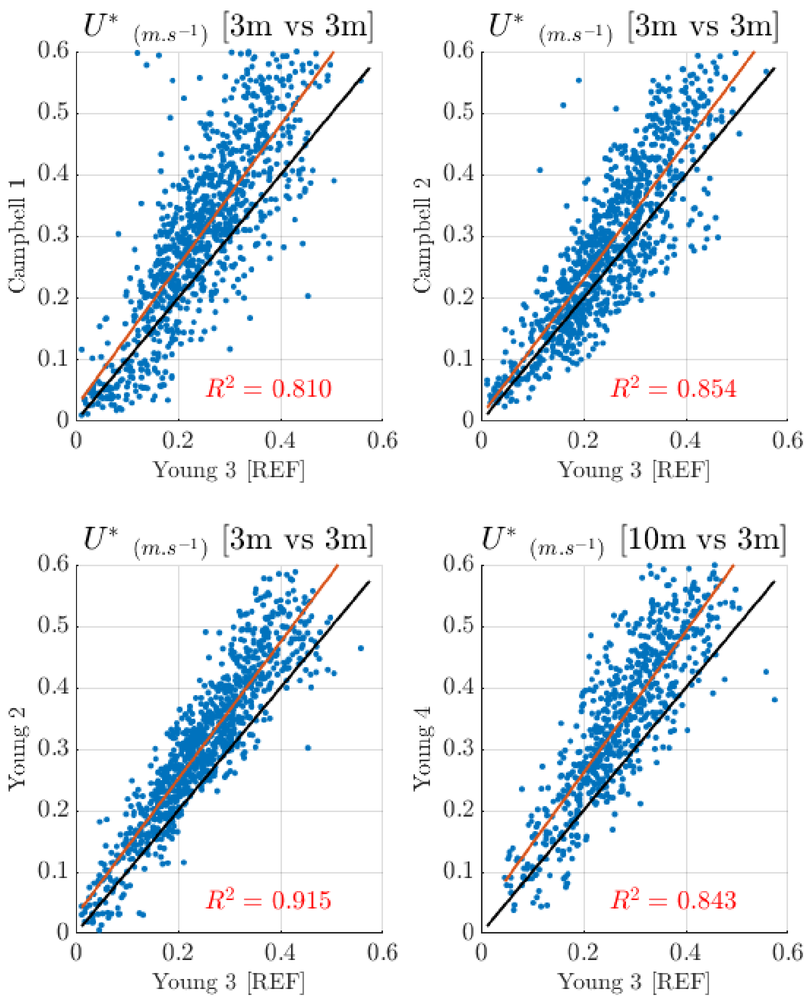

Shear velocity U*

II. Meteorological Measurements

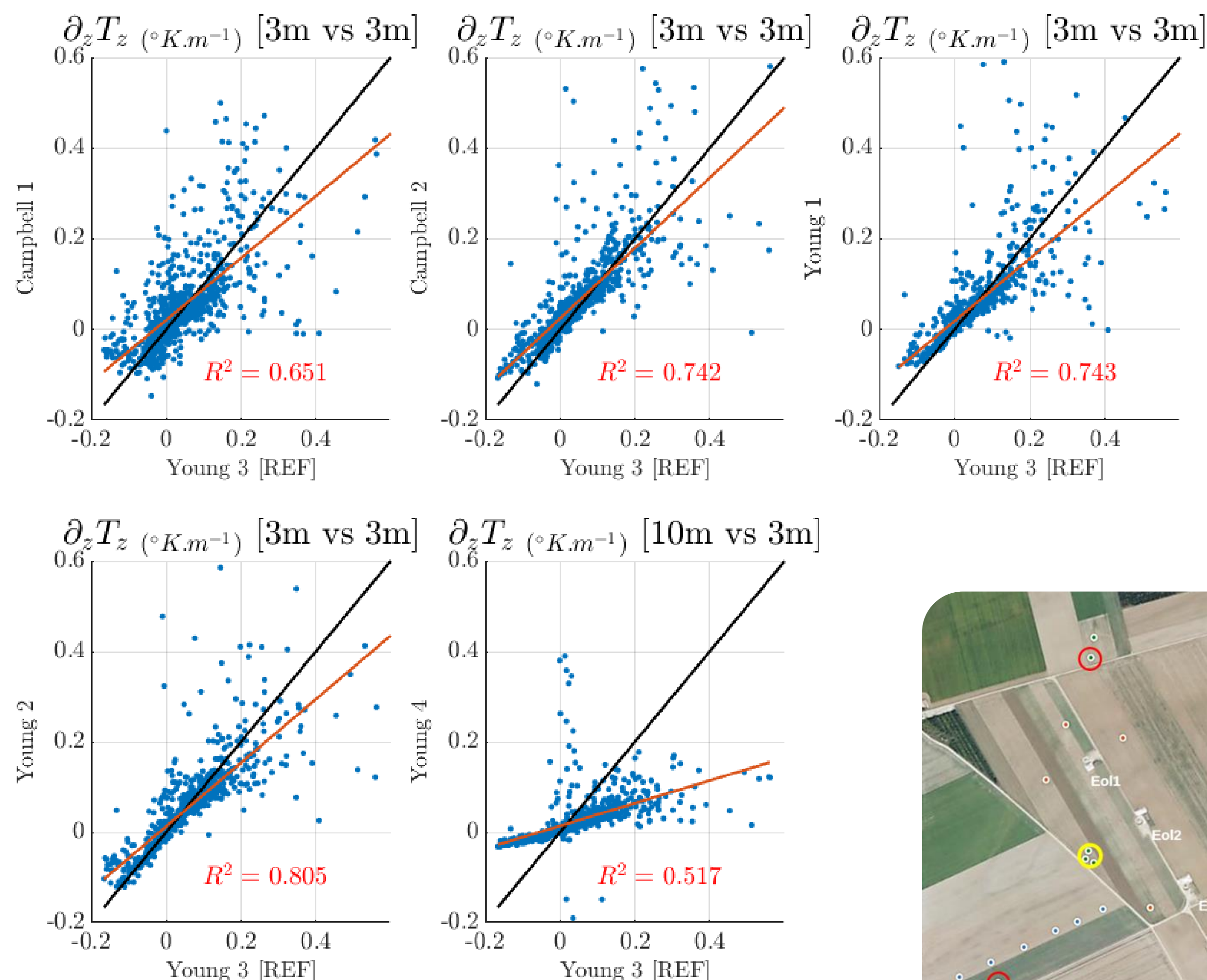

Vertical Temperature gradient

(h = 3 or 10m)

II. Meteorological Measurements

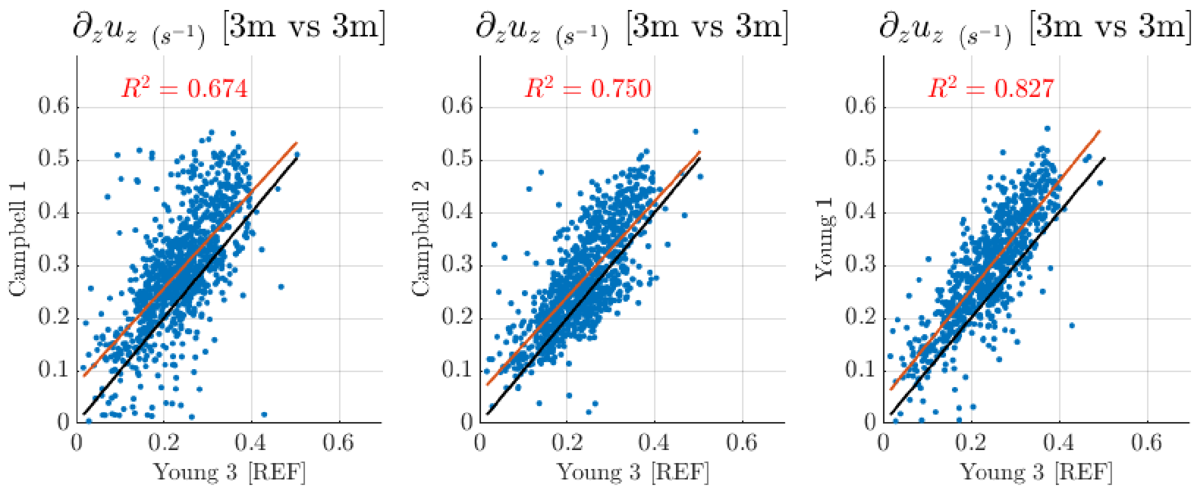

Vertical wind gradient
(h = 3 or 10m)

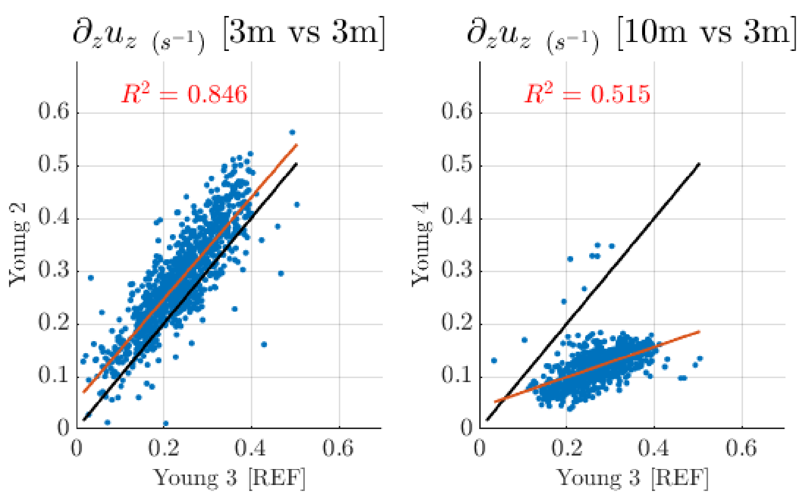

II. Meteorological Measurements

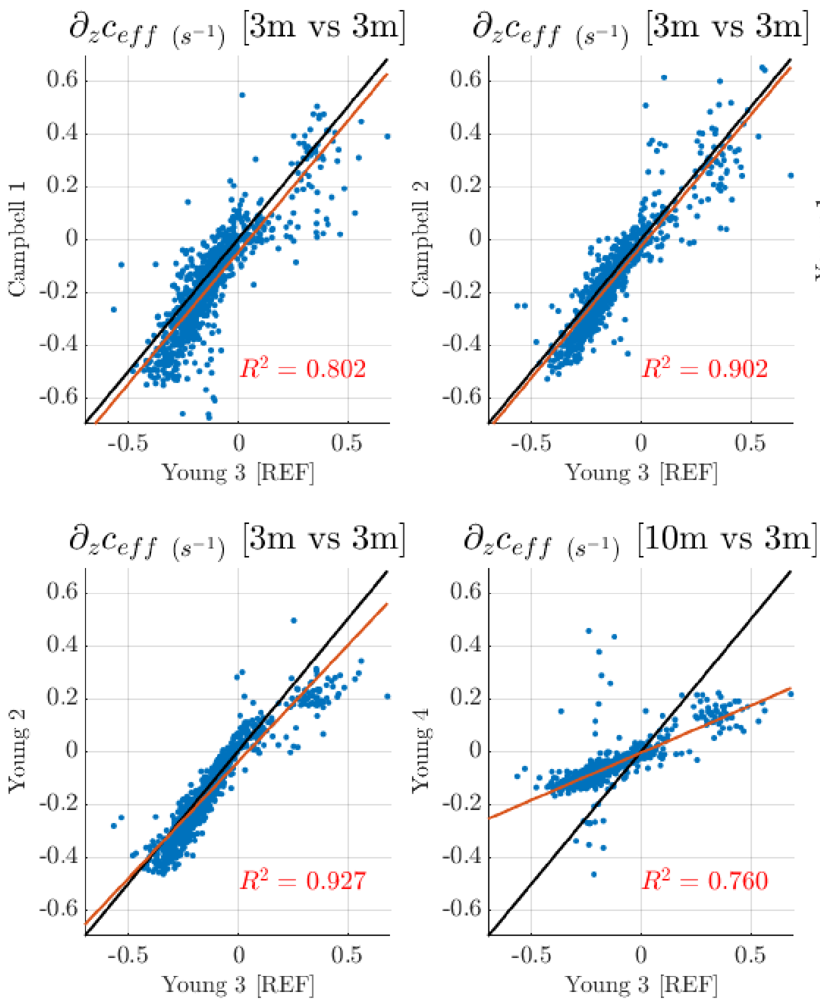

Vertical sound celerity gradient
(h = 3 or 10m)

II. Impedance Measurements

II. Impedance Measurements

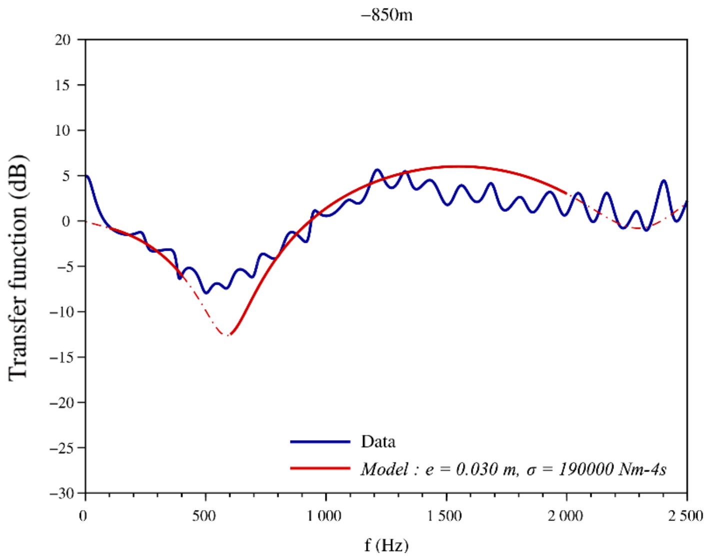

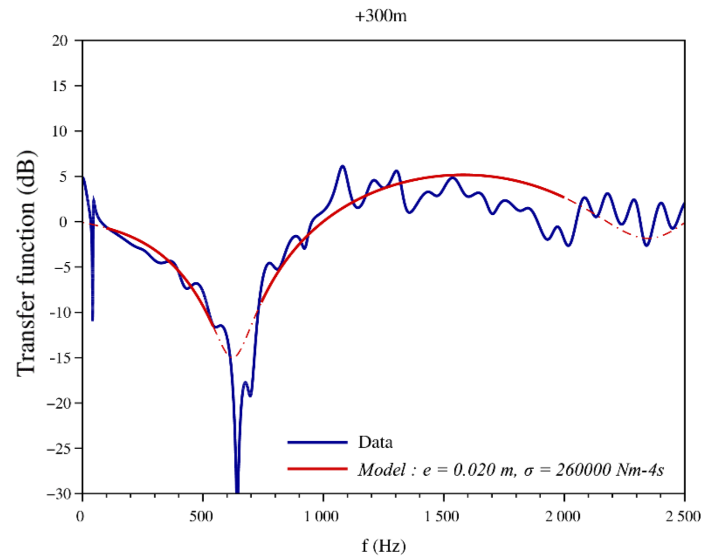

Miki impedance model:

$$Z(f) = \rho c \left[1 + 5.5 \left(\frac{f}{\sigma} \right)^{-0.632} + i8.43 \left(\frac{f}{\sigma} \right)^{-0.632} \right]$$

II. Impedance Measurements

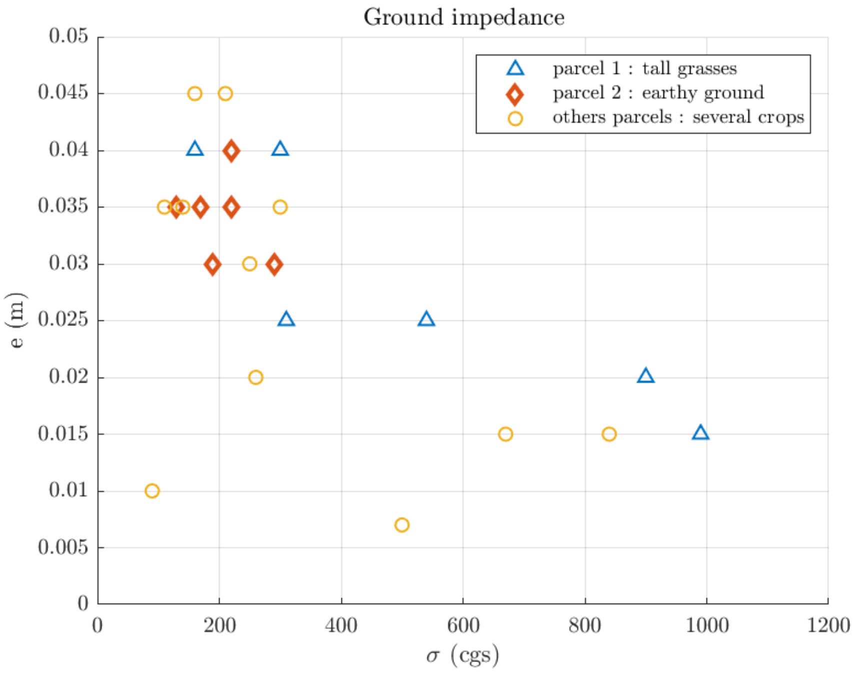

- Characteristic values of absorbing grounds
- Variability of ground properties encountered:

$\sigma \in$ [90 $kNsm^{-4}$; 990 $kNsm^{-4}$]
$e \in$ [0.007m ; 0.045m]

III. Conclusion & Perspectives

- Data processing phase
  - Filtering
  - Validation

III. Conclusion & Perspectives

- Data processing phase
  - Filtering
  - Validation

- Cross-statistical analysis
  - Sound indicators/ environment characteristics (meteo & ground)

- Validation of emission/propagation models
- Estimating uncertainties

- Putting the database online

Thank you for your attention

- Contact :
  - bill.kayser@ifsttar.fr
- Liens :
  - http://www.umrae.fr/

Scan me

L'**Unité Mixte de Recherche en Acoustique Environnementale** (UMRAE) est un laboratoire de recherche commun entre l'Ifsttar et le Cerema, U.S.ARMY

OVERVIEW OF SCATTERED SIGNAL DISTRIBUTIONS AND EXTENSIONS TO INCLUDE PARAMETRIC UNCERTAINTIES

D. Keith Wilson, Carl R. Hart, Daniel J. Breton, Vladimir E. Ostashev
U.S. Army Engineer Research and Development Center CRREL

Chris L. Pettit
U.S. Naval Academy

Edward T. Nykaza
U.S. Army Engineer Research and Development Center CERL

17th International Symposium on Long-Range Sound Propagation
Lyon, France, 12-13 June 2018

Distribution A: Approved for public release; distribution unlimited.

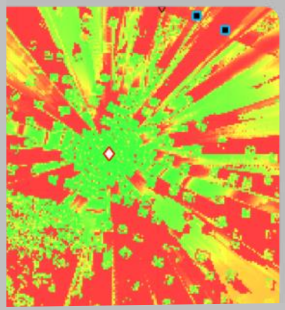

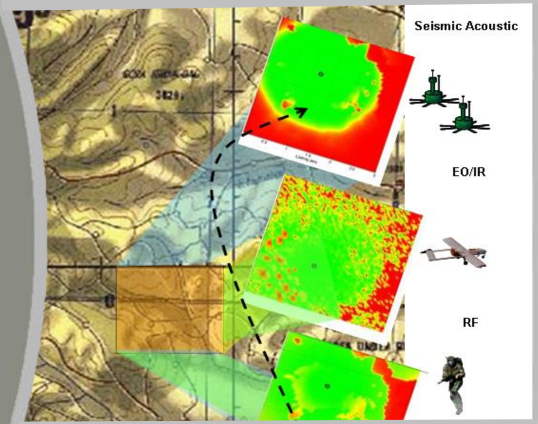

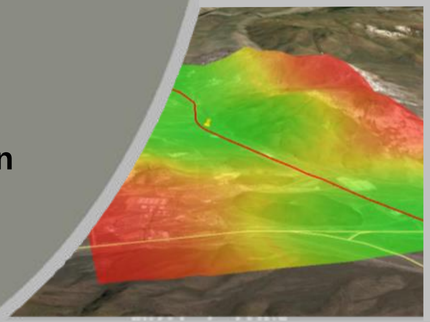

US Army Corps of Engineers®

ERDC
Engineer Research and Development Center

Innovative solutions for a safer, better world

File Name

Motivation

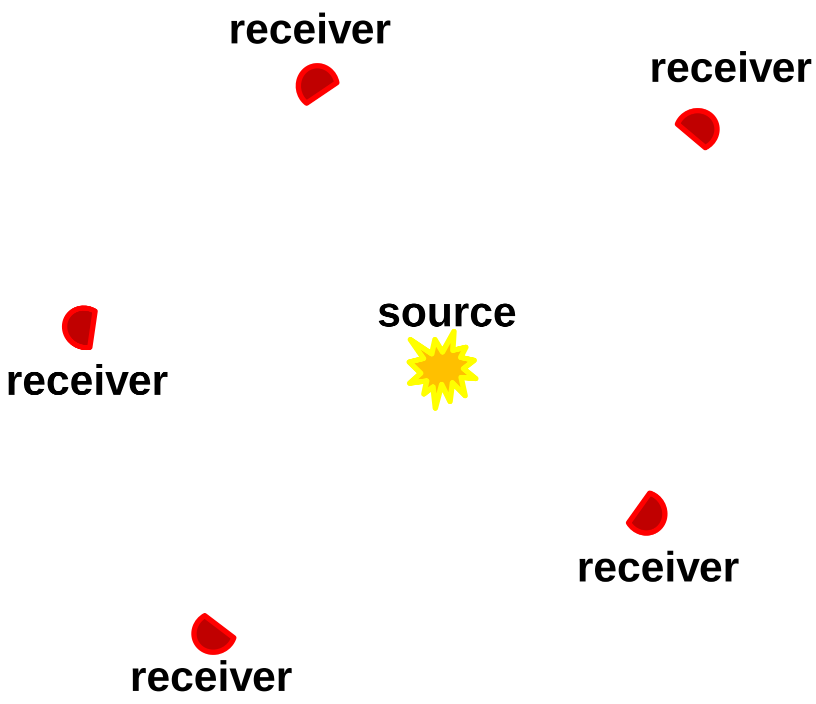

1. We wish to estimate the power emitted by a source.
2. The sound power is observed at multiple remote receiver locations.
3. The sound power at the receivers is assumed to depend on the source power, a known transmission loss, and uncertain, randomly varying contributions.
4. Can we formulate appropriate statistical models for the random signal and use them to predict the source power and its uncertainty?

Sounds Levels Random and Difficult to Predict…

Shown below are comparisons between recorded sound levels and predictions from the CASES-99 experiment, which was conducted at night in the Great Plains (Kansas). This experiment provided the best possible scenario for trying to predict sound propagation. (Ref: Wilson et al, *J. Atmos. Sci.* 60, 2473-2486, 2003)

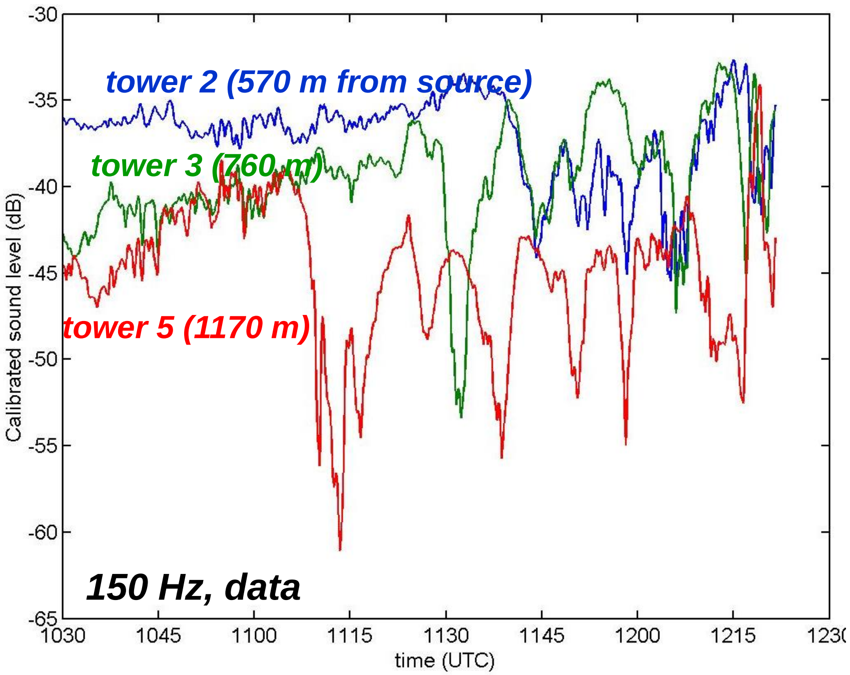

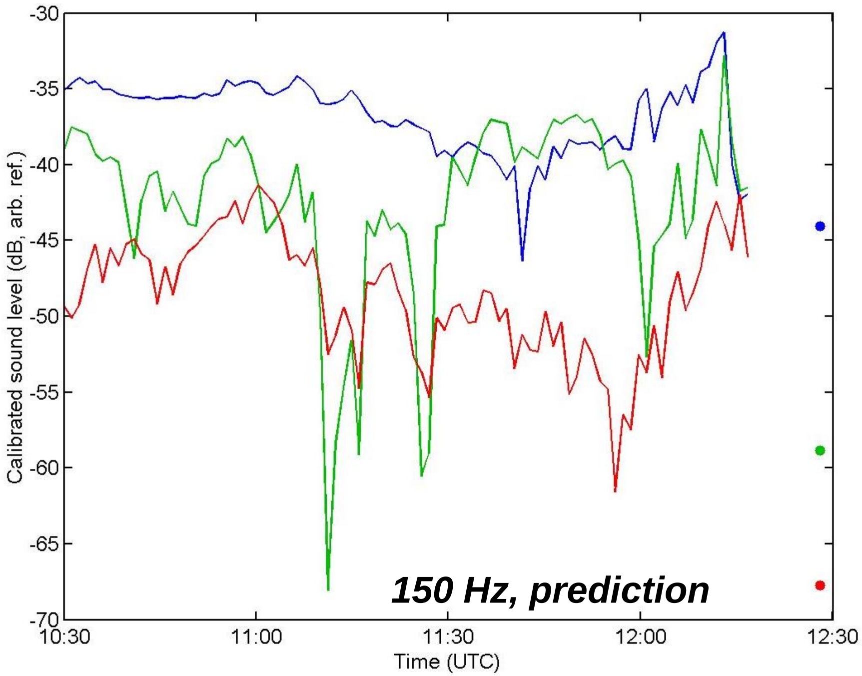

- **Predictions were based on data from a 55-m tower, with wind and temperature sensors every 5 m.**
- **A parabolic equation method was used to predict the sound propagation.**
- **Even with excellent atmospheric data (better than we would normally hope to have), predictive skill for signal variations is very limited.**

- **What causes the mismatches between predictions and observations?**
  - **Model imperfections (due to limited terrain data, finite resolution of atmospheric inputs, limitations of the acoustic propagation model, etc.).**
  - **Inherent randomness of sound propagation (scattering by atmospheric turbulence, variable ground properties, objects such as vegetation and buildings that can't be resolved, etc.).**
- **At best, we can predict the *statistical distribution* of the sound power at a receiver. The parameters of the distribution are imperfectly known – they depend on the type of signal, frequency, propagation geometry, intervening terrain, weather conditions, etc.**

"More decisive? How can I be more decisive? - I live by the uncertainty principle!"

Overview

- Many statistical models, physics-based and empirical, have been formulated for the random signal variations caused by wave scattering.
- This presentation considers extension of such models to include uncertainties in the wave scattering parameters, which may be due to:
  - Uncertainties in the properties of the propagation medium (from measurement errors, finite resolution, imperfect weather forecasts, or unmodeled complexities)
  - Random spatial and temporal variations in the propagation medium (intermittency)
- We show how the problem of modeling parametric uncertainties naturally relates to Bayesian inference of the wave scattering parameters. This relationship can be exploited to:
  - Identify statistical models for the parametric uncertainties that lead to convenient analytical solutions.
  - Develop sequential updating algorithms, which refine an initial prediction of the wave scattering parameters as new signal observations become available.

Outline

- **Basic single-variate distributions for scattered signals** (exponential, log-normal, Rician, gamma, generalized gamma)
- **Parametric uncertainties**
  - Compound pdf formulation
  - Turbulent intermittency (exponential/log-normal)
  - K-distribution and its generalization
- **Bayesian methods for incorporating signal observations**
  - Bayes' theorem and relationship to the compound pdf
  - Log-normal/normal (weak scattering)
  - Exponential/inverse gamma (strong scattering)
  - Gamma/inverse gamma (weak or strong scattering)
- **Multi-variate distributions**
  - Log-normal/normal (weak scattering)
  - Wishart (strong scattering)
  - Matrix gamma (weak or strong scattering)
- **Implications for signal detection**
- **Automated target recognition (ATR) with random signals**
- **Conclusions**

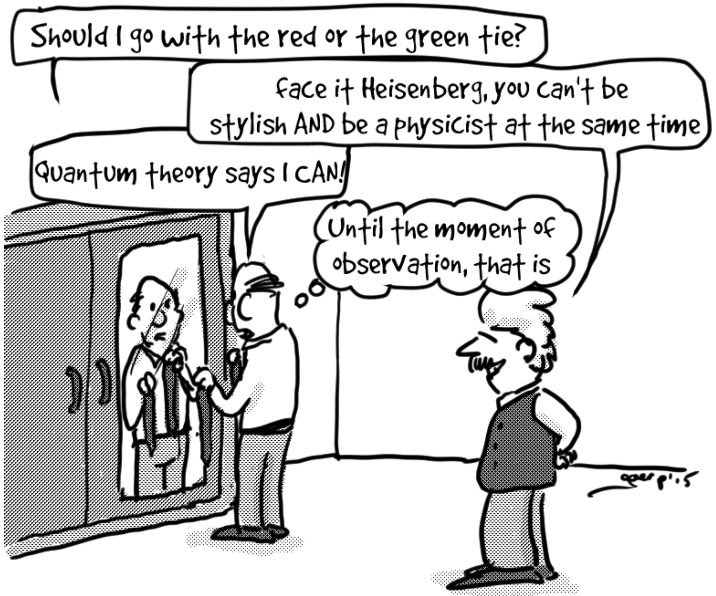

HEISENBERG'S UNCERTAINTY

Simple Conceptual Model (Single Receiver)

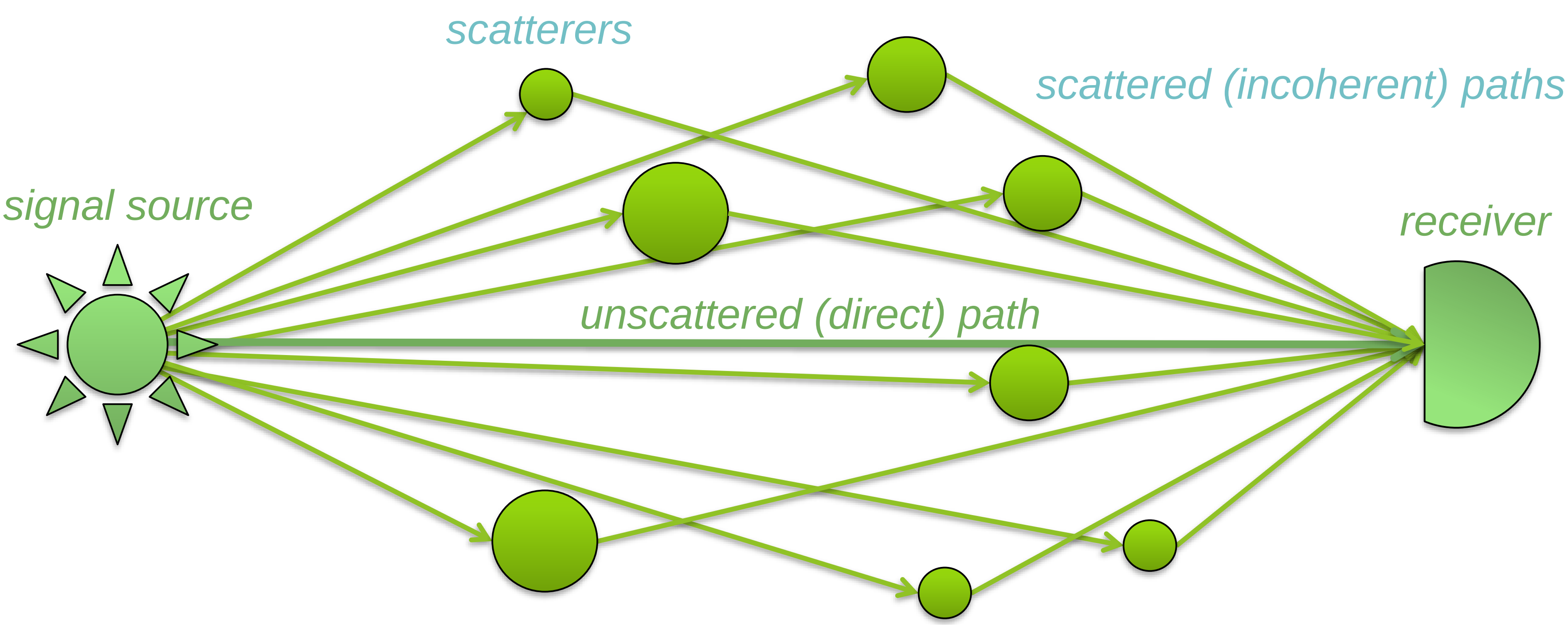

- The total received signal consists of contributions from an unscattered (direct) path and from multiple randomly scattered (incoherent) paths.
- *Weak scattering* means that the direct path dominates (small log-amplitude variance); *strong scattering* (*Rayleigh* or *deep fading*) means that the incoherent scattered paths dominate.
- *Parametric uncertainty* means that we don't exactly know the statistics of the coherent and/or incoherently scattered waves.

Distributions for Scattered Signal Power (Notation)

In general, we write the probability density function (pdf) for the scattered signal power as:

$$p(s|\boldsymbol{\theta})$$

signal power

parameters of the distribution (e.g., mean and variance)

Example: For strong scattering, the signal power has an exponential distribution:

$$p(s|m) = \frac{1}{m}\exp\left(-\frac{s}{m}\right) \quad \text{or} \quad p(s|\lambda) = \lambda \exp(-\lambda s)$$

where (first version) $\boldsymbol{\theta} \rightarrow m$ and (second version) $\boldsymbol{\theta} \rightarrow \lambda$. Here $\lambda = 1/m$, and m can be shown to equal the mean power.

(Note: for strong scattering, the signal *amplitude* has a Rayleigh distribution. Throughout this presentation, we will focus on distributions for *power*.)

Other Distributions for Scattered Signal Power

Following are some notable pdfs used for scattered signal power from the literature. (Many more can be found.)

Log-normal (applies to weak scattering, based on the Rytov approximation):

$$p(s|\mu,\phi) = \frac{1}{s\phi\sqrt{2\pi}}\exp\left[-\frac{(\ln s - \mu)^2}{2\phi^2}\right]$$

Rice (weak scattering based on the Born approximation, exact for strong scattering):

$$p(s|\nu,\varsigma) = \frac{1}{2\varsigma^2}\exp\left(-\frac{s+\nu^2}{2\varsigma^2}\right)I_0\left(\frac{\sqrt{s}\nu}{\varsigma^2}\right)$$

Gamma (weak scattering based on empirical evidence, exact for strong scattering):

$$p(s|k,\lambda) = \frac{\lambda^k s^{k-1}}{\Gamma(k)}e^{-\lambda s}$$

Generalized gamma (Ewart and Percival 1986) (reduces to gamma when $b = 1$):

$$p(s|k,\lambda,b) = \frac{b\lambda^{bk} s^{bk-1}}{\Gamma(k)}e^{-(\lambda s)^b}$$

Comparison of Log-normal, Rice, and Gamma pdfs
(with matching means and variances)

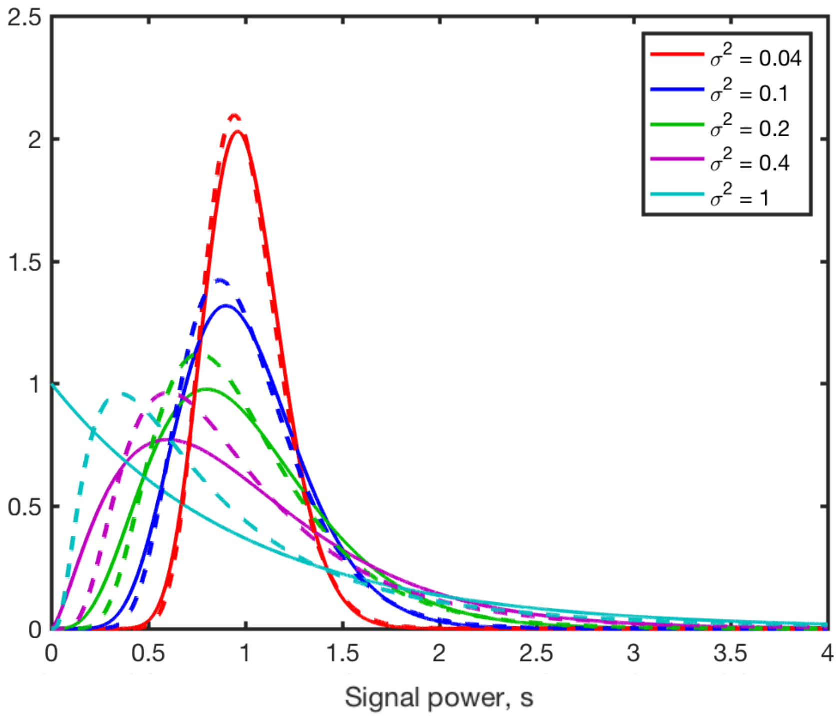

Gamma (solid lines) and log-normal (dashed lines) pdfs for various values of the variance normalized by the squared mean.

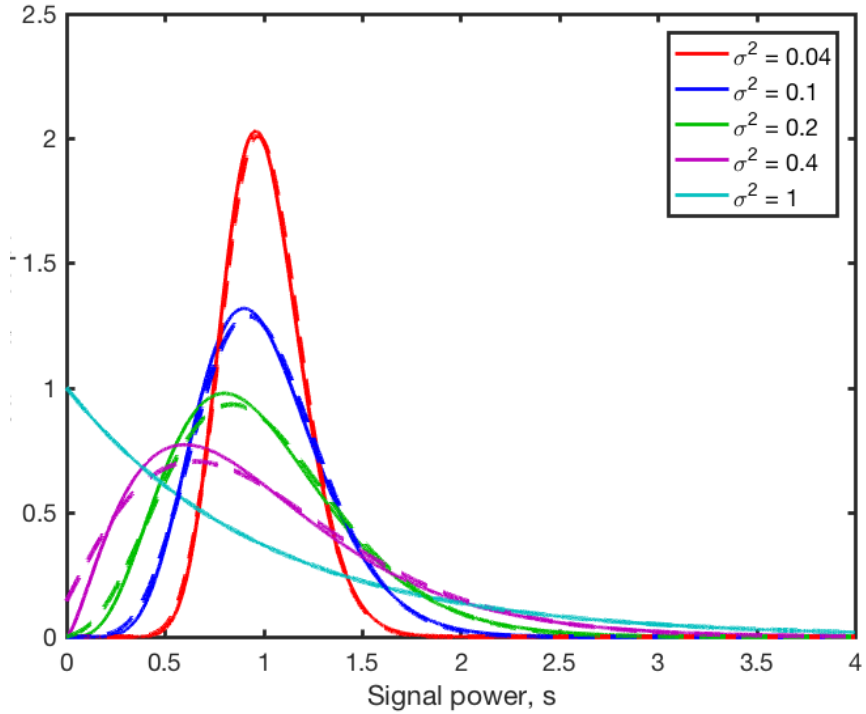

Gamma (solid lines) and Rice (dashed lines) pdfs for various values of the variance normalized by the squared mean.

Main point: Log-normal is useful only for weak scattering. Rice and gamma are useful (and very similar) for either weak or strong scattering.

Generalized Gamma Distribution

k = *1* (strong scattering)

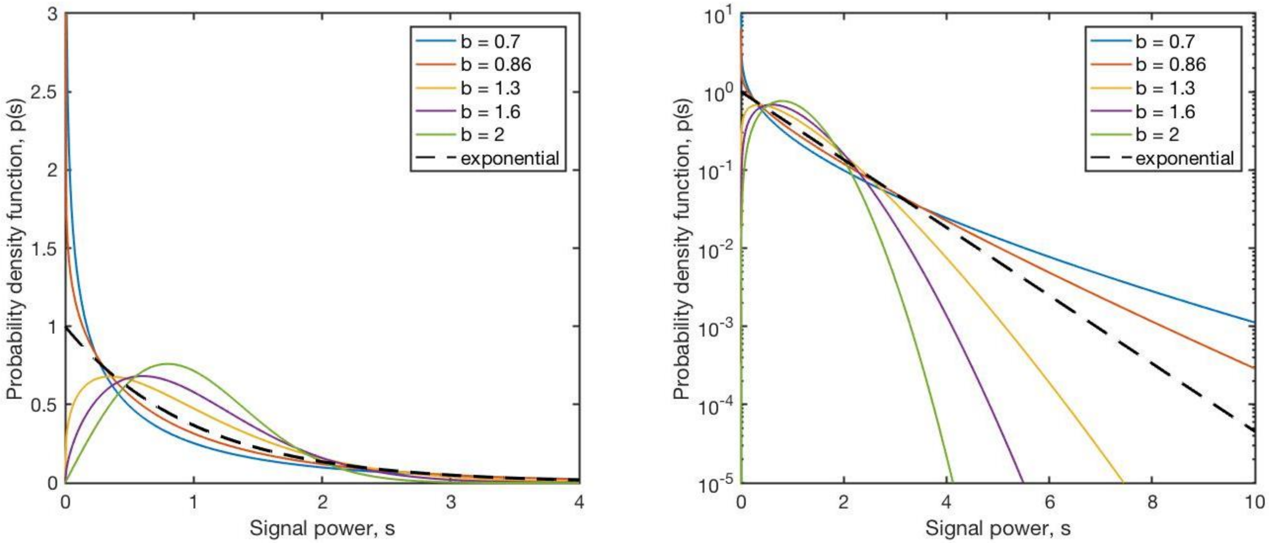

k = *8* (weak scattering)

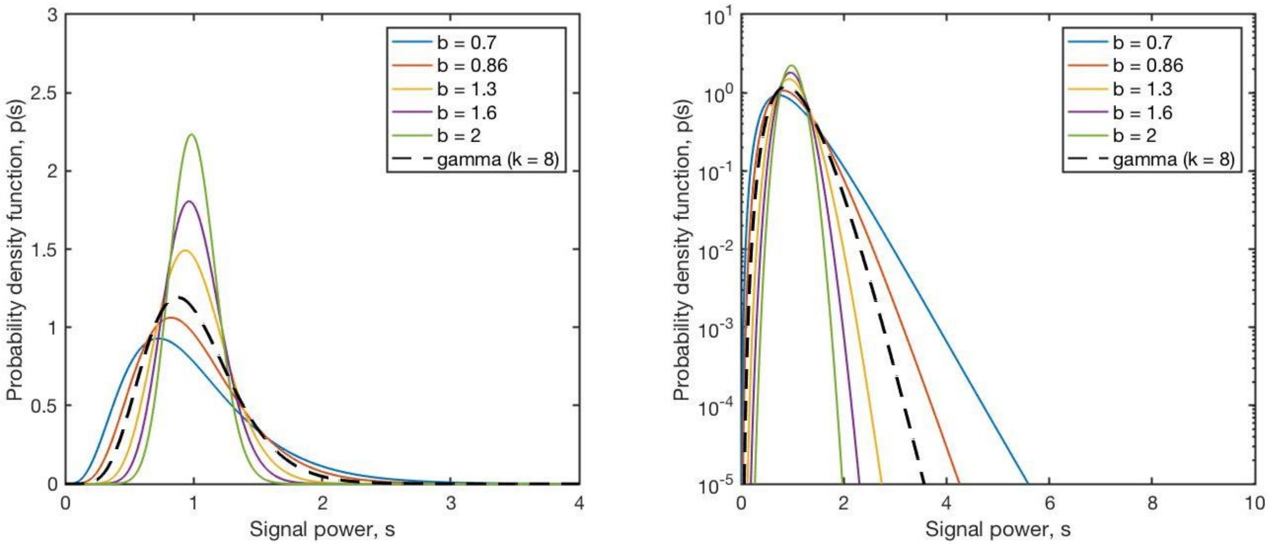

Here, we have set λ such that the signal mean is always 1.

The parameter *b* is seen to control the "tails" of the distribution. As *b decreases*, the pdfs change from a normal-like appearance to having tails exceeding the gamma distribution for the corresponding value of *k*.

Based on empirical fits to ocean acoustic data, Ewing and Percival (1986) find that *b* is *usually* less than 1 (elevated tails are present).

Parametric Uncertainties and the Compound pdf

We use a compound pdf to account for uncertainties:

$$p(s|\boldsymbol{\chi}) = \int \underbrace{p\,(s|\boldsymbol{\theta})}_{\text{pdf describing scattering (depends on parameters } \boldsymbol{\theta})} \underbrace{p(\boldsymbol{\theta}|\boldsymbol{\chi})}_{\text{pdf for scattering parameters } \boldsymbol{\theta} \text{ (depends on hyperparameters } \boldsymbol{\chi})} d\boldsymbol{\theta}$$

pdf describing scattering (depends on parameters θ)

pdf for scattering parameters θ (depends on hyperparameters χ)

Example: Turbulent intermittency with strong scattering
(Gurvich and Kukharets 1986; Wilson et al. 1996)

For strong scattering, the signal power has an exponential pdf:

$$p(s|\boldsymbol{\theta}) = p(s|m) = \frac{1}{m}\exp\left(-\frac{s}{m}\right)$$

By Kolmogorov's refined hypothesis (1962), the structure-function parameters of turbulence (and hence the scattering cross section in the inertial subrange) have a log-normal distribution. Thus

$$p(\boldsymbol{\theta}|\boldsymbol{\chi}) = p(m|\mu,\phi) = \frac{1}{m\phi\sqrt{2\pi}}\exp\left[-\frac{(\ln m - \mu)^2}{2\phi^2}\right]$$

The integral for $p(s|\boldsymbol{\chi}) = p(s|\mu,\phi)$ unfortunately does not have an analytical solution in this case and thus must be determined numerically.

UNCLASSIFIED

Connection to Bayesian Inference

Bayes' theorem:

$$\overbrace{p(\theta|s,\chi)}^{\textit{posterior}} = \frac{\overbrace{p(s|\theta,\chi)}^{\textit{likelihood}}\,\overbrace{p(\theta|\chi)}^{\textit{prior}}}{\underbrace{\int p\,(s|\theta',\chi)\,p(\theta'|\chi)\,d\theta'}_{\textit{“model evidence” (compound pdf from earlier)}}}.$$

The compound pdf formulation includes all the information we need to implement Bayes' theorem. The posterior updates the distribution for the uncertain signal parameters as new observations of the signal become available.

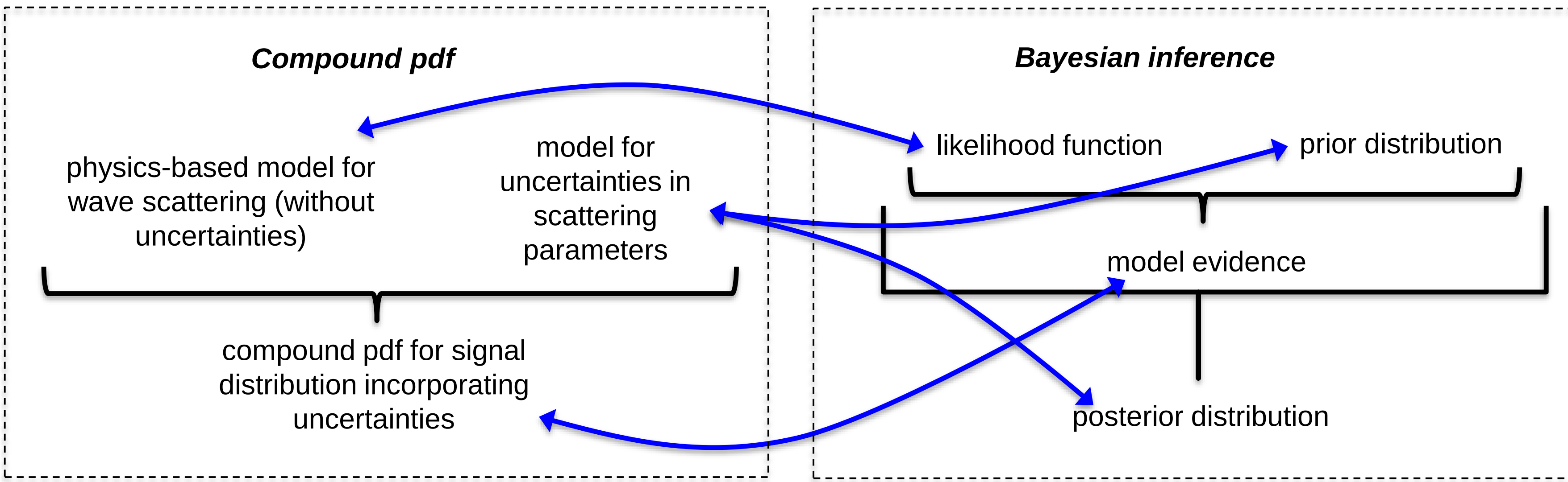

Utilization of Bayesian Conjugate Priors

We are especially interested in cases where the prior and posterior have the same functional form; the prior is then said to be the *conjugate prior* of the likelihood function. This leads to a convenient iterative process where we can sequentially update the hyperparameters as observations of the signal become available.

Strong scattering example: As discussed previously, the signal power has an exponential pdf for strong scattering. In the Bayesian context, this is the likelihood function. The conjugate prior for an exponential likelihood function is known to be the gamma distribution with parameters $\theta \rightarrow \{\alpha, \beta\}$. Hence we set

$$p(s|\lambda) = \lambda \exp(-\lambda s) \qquad p(\lambda|\alpha,\beta) = \mathrm{Gamma}(\lambda|\alpha,\beta) = \frac{\beta^\alpha \lambda^{\alpha-1}}{\Gamma(\alpha)} e^{-\lambda\beta}$$

Integrating, we find for the compound pdf/model evidence:

$$p(s|\alpha,\beta) = \frac{\alpha\beta^\alpha}{(s+\beta)^{\alpha+1}}$$

This is called a *Lomax* or *Pareto Type II* distribution. For the posterior, we then find

$$p(\lambda|s,\alpha,\beta) = \frac{(\beta+s)^{\alpha+1}\lambda^\alpha}{\Gamma(\alpha+1)} e^{-\lambda(\beta+s)}$$

This leads to the following simple formula for updating the distribution of the uncertain parameter λ each time a new signal observation *s* becomes available:

$$p(\lambda|s,\alpha,\beta) = \mathrm{Gamma}(\lambda|\alpha+1,\beta+s) \qquad \alpha \rightarrow \alpha+1, \qquad \beta \rightarrow \beta+s$$

Bayesian Adaptation for Strong Scattering: Simulation

Suppose we wish to know the mean received signal power. The signal varies randomly due to strong scattering (exponential pdf). We start with a prior (proposed) distribution for the mean scattered energy, specifically a gamma pdf, which describes our initially limited knowledge of the mean. We then begin to collect samples of the random signal. After each sample is collected, we can refine the distribution for the mean using Bayes' theorem.

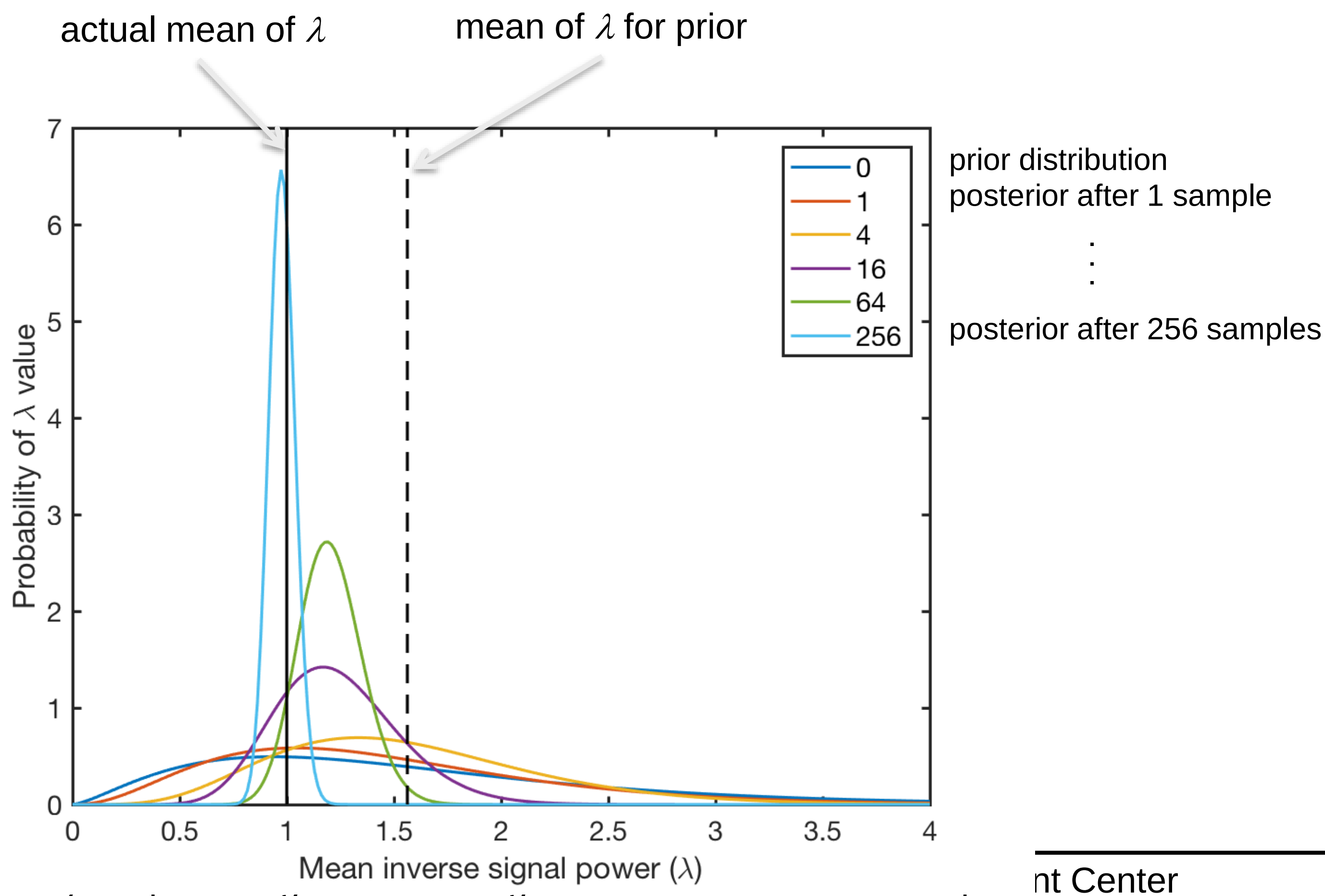

nt Center

K-Distribution and Generalized K-Distribution

Andrews and Phillips (2005): "…it has been observed that the lognormal PDF … can underestimate the peak of the PDF and also underestimate the behavior of the tails as compared with measured data. Underestimating the tails of a PDF has important consequences on radar and communication systems where detection and fade probabilities are calculated over the tails of the PDF".

Andrews and Phillips proposed using compound pdfs to provide models with more realistic tails. They refer to the compound pdf as a "modulation process."

Ewing and Percival (1986) found consistently elevated tails in ocean acoustic data. Wilson et al. (1996), Schomer (2003), and Schomer and White (2006) report elevated tails in atmospheric acoustic data.

The generalized K-distribution results from compounding a gamma pdf for *s* (with shape parameter *k*; valid for weak or strong scattering) with a gamma pdf (parameters α, β) for the mean power *b*:

$$p(s|\alpha,\beta,k) = \frac{2\beta}{\Gamma(k)\Gamma(\alpha)}(\beta s)^{(k+\alpha-2)/2} K_{\alpha-k}\left(2\sqrt{\beta s}\right)$$

For $k = 1$, the generalized K-distribution reduces to the ordinary K-distribution.

Comparison of K- and Lomax Distributions (Strong Scattering)

K-distributions

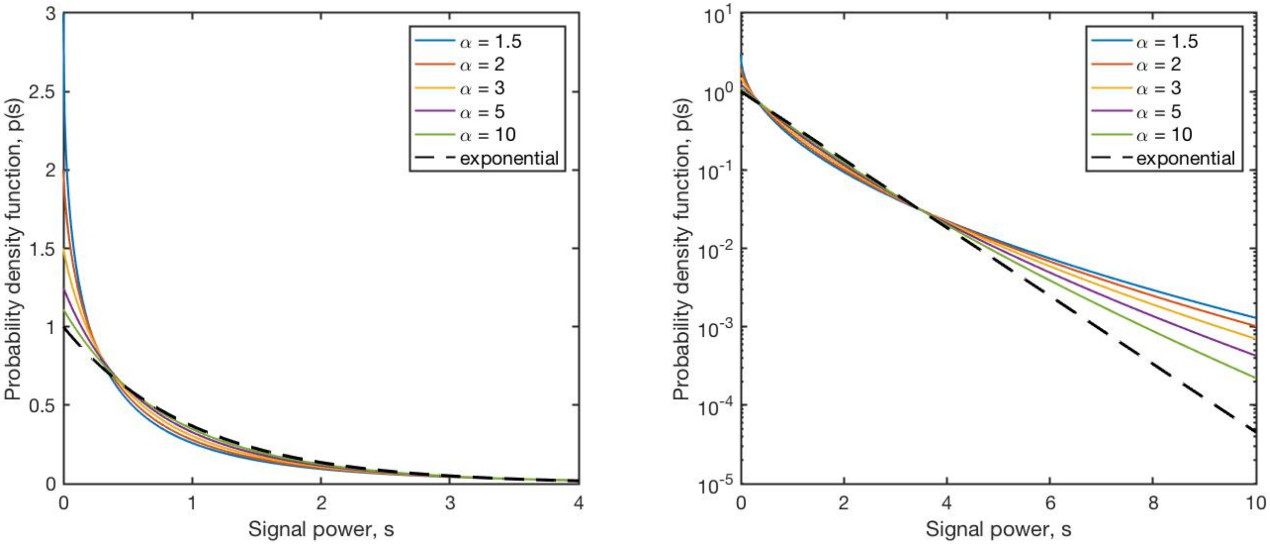

Lomax distributions

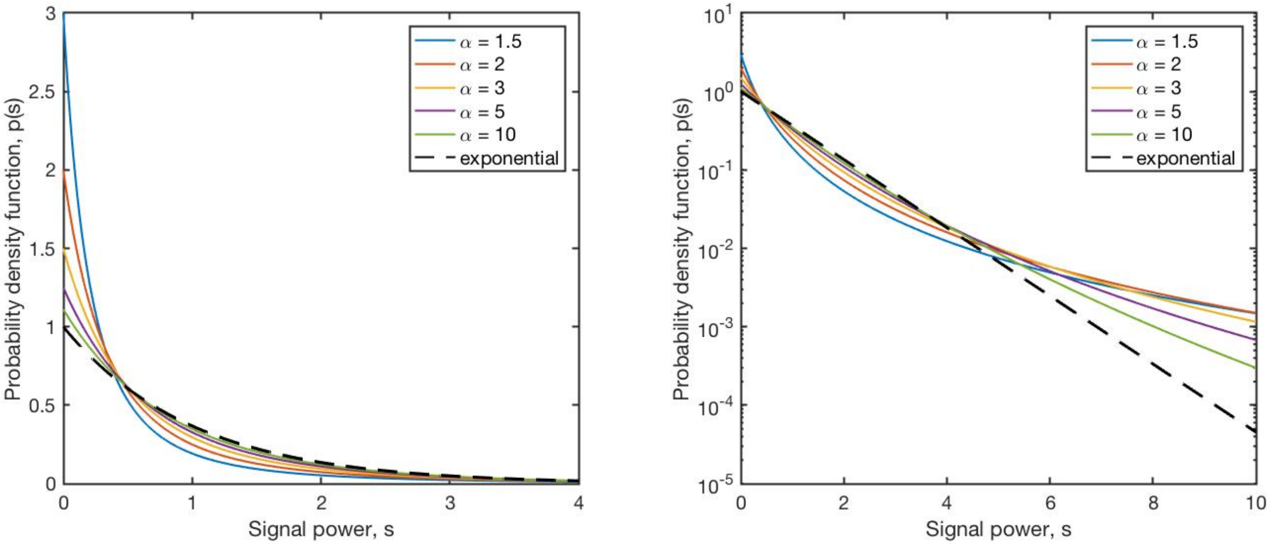

Here, we have set β such that the signal mean equals 1.

As α increases, the pdfs converge to the exponential pdf (that is, to the strong scattering case when no parametric uncertainties are present).

Note that decreasing α (increasing uncertainty) leads to much higher tails in the distribution.

Log-Normal Signal Model with Parametric Uncertainty

(Rytov Approximation for Weak Scattering)

A log-normal pdf can be used to describe a signal with weak scattering. Here we formulate the parametric model for the logarithm of the signal, $\eta = \ln s$:

$$p(\eta|m_\mu, \sigma_\mu^2) = \int p(\eta|\mu) p(\mu|m_\mu, \sigma_\mu^2) d\mu,$$

$$p(\eta|\mu) = \frac{1}{\phi\sqrt{2\pi}} \exp\left[-\frac{(\eta-\mu)^2}{2\phi^2}\right]$$

$$p(\mu|m_\mu, \sigma_\mu^2) = \frac{1}{\sigma_\mu\sqrt{2\pi}} \exp\left[-\frac{(\mu-m_\mu)^2}{2\sigma_\mu^2}\right]$$

We assume that μ (log-mean of the scattered signal strength) is normally distributed and that the variance of μ is known. Performing the integration, we find

$$p(\eta|m_\mu, \sigma_\mu^2) = \frac{1}{\sqrt{2\pi(\sigma_\mu^2+\phi^2)}} \exp\left[-\frac{(\eta-m_\mu)^2}{2(\sigma_\mu^2+\phi^2)}\right].$$

Hence the distribution for the log-signal is still normal, although the variance increases.

The Bayesian update for the posterior distribution is:

$$p(\mu|\eta, m_\mu, \sigma_\mu^2) = f_N(\mu|m'_\mu, \sigma'^2_\mu) = \frac{1}{\sigma'_\mu\sqrt{2\pi}} \exp\left[\frac{(\mu-m'_\mu)^2}{2\sigma'^2_\mu}\right]$$

$$m'_\mu = \left(\sigma_\mu^{-2}+\phi^{-2}\right)^{-1}\left(\sigma_\mu^{-2} m_\mu + \phi^{-2}\eta\right) \quad \sigma'^2_\mu = \left(\sigma_\mu^{-2}+\phi^{-2}\right)^{-1}$$

Multiple Receivers

- Suppose there are *N* receivers, and we sample the signals *K* times.
- Let $R_{nk} = X_{nk} + iY_{nk}$ where R_{nk} is the *k*th sample of the complex amplitude of the signal along path *n*, X_{nk} is the random real part, and Y_{nk} is the random imaginary part.
- Define the vectors

$$\mathbf{R}_k = [X_{1k}, X_{2k}, \dots, X_{Nk}] = \mathbf{X}_k + i\mathbf{Y}_k \qquad \mathbf{X}_k = [X_{1k}, X_{2k}, \dots, X_{Nk}] \qquad \mathbf{Y}_k = [Y_{1k}, Y_{2k}, \dots, Y_{Nk}]$$

- When there are multiple receivers, we can model the distributions using either random *vectors* or random *matrices.* The latter is advantageous in that it describes the covariances between the paths.

$$\mathbf{R} = \sum_{k=1}^{K} \mathbf{Z}_k \odot \mathbf{Z}_k^*$$

Vector approach
*(**R** is N x 1)*

$$\mathbf{R} = \sum_{k=1}^{K} \mathbf{Z}_k \tilde{\mathbf{Z}}_k$$

Matrix approach
*(**R** is N x N)*

Multivariate Log-Normal Distribution

(for Weak Scattering on Multiple Paths)

Extension of the log-normal signal model for the single variate case is straight forward, assuming that the logarithms of the signals follow a multivariate normal distribution:

$$p(\boldsymbol{\eta}|\mathbf{m}_\mu, \boldsymbol{\Sigma}_\mu) = \int p(\boldsymbol{\eta}|\boldsymbol{\mu}) p(\boldsymbol{\mu}|\mathbf{m}_\mu, \boldsymbol{\Sigma}_\mu)\, d\boldsymbol{\mu},$$

$$p(\boldsymbol{\eta}|\boldsymbol{\mu}) = \frac{1}{\sqrt{(2\pi)^K |\boldsymbol{\Phi}|}} \exp\left[-\frac{1}{2}(\boldsymbol{\eta}-\boldsymbol{\mu})^{\mathrm{T}} \boldsymbol{\Phi}^{-1} (\boldsymbol{\eta}-\boldsymbol{\mu})\right]$$

$$p(\boldsymbol{\mu}|\mathbf{m}_\mu, \boldsymbol{\Sigma}_\mu) = \frac{1}{\sqrt{(2\pi)^K |\boldsymbol{\Sigma}_\mu|}} \exp\left[-\frac{1}{2}(\boldsymbol{\mu}-\mathbf{m}_\mu)^{\mathrm{T}} \boldsymbol{\Sigma}_\mu^{-1} (\boldsymbol{\mu}-\mathbf{m}_\mu)\right]$$

We assume that μ (log-mean of the scattered signal strengths) is normally distributed. The variance of μ is assumed to be known. Performing the integration, we then find

$$p(\boldsymbol{\mu}|\mathbf{m}_\mu, \boldsymbol{\Sigma}_\mu) = \frac{1}{\sqrt{(2\pi)^K |\boldsymbol{\Phi}+\boldsymbol{\Sigma}_\mu|}} \exp\left[-\frac{1}{2}(\boldsymbol{\eta}-\mathbf{m}_\mu)^{\mathrm{T}} (\boldsymbol{\Phi}+\boldsymbol{\Sigma}_\mu)^{-1} (\boldsymbol{\eta}-\mathbf{m}_\mu)\right].$$

The Bayesian update for the posterior distribution is:

$$p(\boldsymbol{\mu}|\boldsymbol{\eta}, \mathbf{m}_\mu, \boldsymbol{\Sigma}_\mu) = \frac{1}{\sqrt{(2\pi)^K |\boldsymbol{\Sigma}'_\mu|}} \exp\left[-\frac{1}{2}(\boldsymbol{\mu}-\mathbf{m}'_\mu)^{\mathrm{T}} (\boldsymbol{\Sigma}'_\mu)^{-1} (\boldsymbol{\mu}-\mathbf{m}'_\mu)\right]$$

$$\mathbf{m}'_\mu = \left(\boldsymbol{\Sigma}_\mu^{-1} + \boldsymbol{\Phi}^{-1}\right)^{-1} \left(\boldsymbol{\Sigma}_\mu^{-1}\mathbf{m}_\mu + \boldsymbol{\Phi}^{-1}\boldsymbol{\eta}\right)$$

$$\boldsymbol{\Sigma}'_\mu = \left(\boldsymbol{\Sigma}_\mu^{-1} + \boldsymbol{\Phi}^{-1}\right)^{-1}$$

Complex Wishart Distribution
(for Strong Scattering on Multiple Paths)

- We assume that the real and imaginary parts of the signals are independent, zero mean, and have define variance τ_{n}^2 at microphone n.
- The $N \times N$ correlation matrix for the the complex signal as:

$$\mathbf{V} = \langle \mathbf{Z}\tilde{\mathbf{Z}} \rangle = 2 \begin{bmatrix} \tau_1^2 & \rho_{12}\tau_1\tau_2 & \cdots & \rho_{1N}\tau_1\tau_N \\ \rho_{12}\tau_1\tau_2 & \tau_2^2 & \cdots & \rho_{2N}\tau_2\tau_N \\ \vdots & \vdots & \ddots & \vdots \\ \rho_{1N}\tau_1\tau_N & \rho_{2N}\tau_2\tau_N & \cdots & \tau_N^2 \end{bmatrix}.$$

- Defining the correlation coefficients as

$$\rho_{mn} = \frac{\langle X_m X_n \rangle}{\tau_m \tau_n} = \frac{\langle Y_m Y_n \rangle}{\tau_m \tau_n}$$

- This model corresponds to a *complex Wishart distribution* with $K = d/2$. The Wishart distribution is a generalization of the chi-squared distribution to *matrices*.
- The complex Wishart distribution has the following form:

$$p(\mathbf{R}|K, \mathbf{V}) = \frac{|\mathbf{R}|^{K-N}}{|\mathbf{V}|^K \Gamma_N(K)} \exp[-\mathrm{tr}(\mathbf{V}^{-1}\mathbf{R})], \qquad \Gamma_N(K) = \pi^{N(N-1)/2} \prod_{n=1}^{N} \Gamma[K - n + 1] \ ,$$

Complex Wishart Distribution (*N* = 2, *K* = 1)

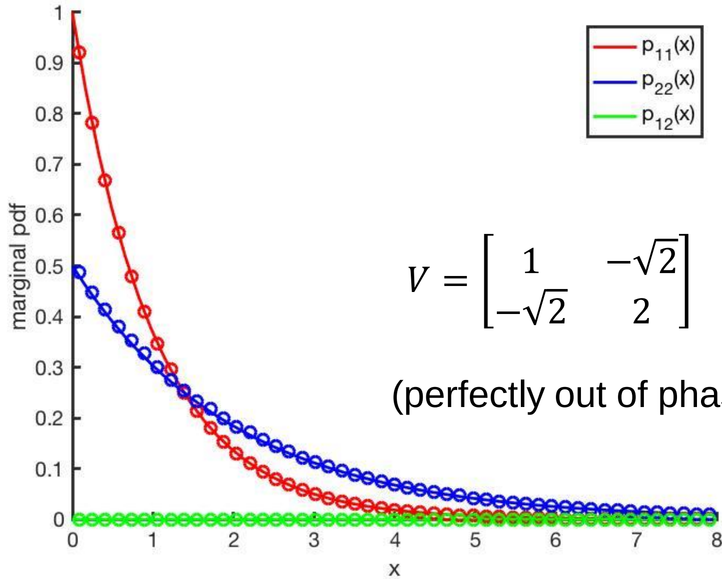

$$V = \begin{bmatrix} 1 & -\sqrt{2} \\ -\sqrt{2} & 2 \end{bmatrix}$$

(perfectly out of phase)

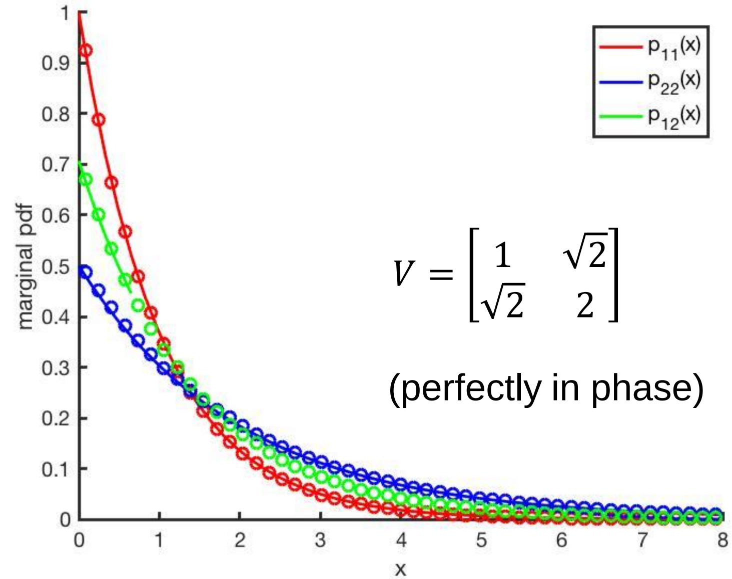

$$V = \begin{bmatrix} 1 & \sqrt{2} \\ \sqrt{2} & 2 \end{bmatrix}$$

(perfectly in phase)

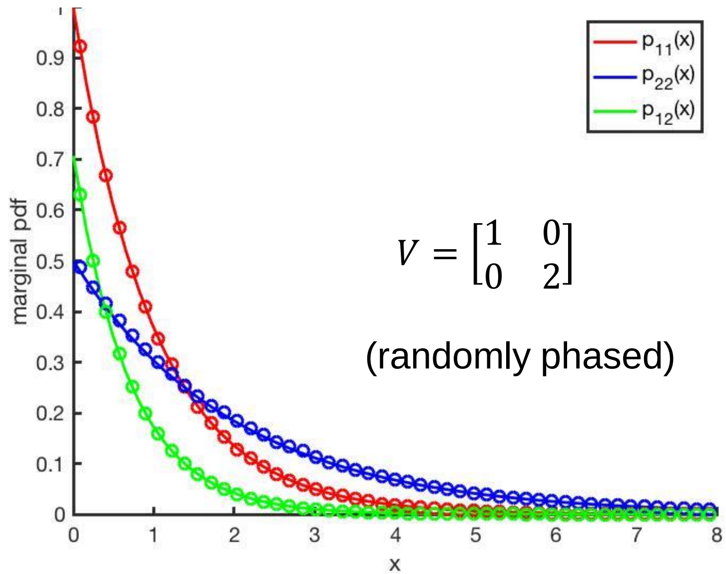

$$V = \begin{bmatrix} 1 & 0 \\ 0 & 2 \end{bmatrix}$$

(randomly phased)

Shown here are the marginal pdfs for two signals with differing phase relationships.

Complex Wishart Distribution

Compound pdf and Bayesian updating

- If one assumes the source power is unknown and given by an inverse gamma pdf, but the transmission loss along each path is unknown, we find the following compound pdf (where $\bar{\mathbf{V}} = \mathbf{V}/s$):

$$p(\mathbf{R}|\alpha,\beta,K,\bar{\mathbf{V}}) = \frac{\beta^{\alpha}\Gamma(NK+\alpha)|\mathbf{R}|^{K-N}}{\Gamma_N(K)\Gamma(\alpha)|\bar{\mathbf{V}}|^{K}[\beta+\mathrm{tr}(\bar{\mathbf{V}}^{-1}\mathbf{R})]^{Nk+\alpha}}.$$

- The posterior can then be calculated, and the update equations are found to be:

$$\alpha \to \alpha + NK \qquad \beta \to \beta + \mathrm{tr}(\bar{\mathbf{V}}^{-1}\mathbf{R})$$

Signal Distributions and Physical Associations

Likelihood function (random signal model)	Prior (for mean signal power)	Physical interpretation	Posterior (for mean signal power)	Model evidence (signal model with uncertainty)
Exponential	Gamma (mean)	Strong scattering, single receiver	(non-analytic)	K-distribution
Exponential	Gamma (rate)	Strong scattering, single receiver	Gamma (rate)	Lomax
Exponential	Log-normal	Strong scattering w/turbulent intermittency, single receiver	(non-analytic)	(non-analytic)
Rice	(?)	Weak (Born) or strong scattering, single receiver	(?)	(?)
Gamma	Gamma (mean)	Weak (empirical) or strong, single receiver	(non-analytic)	Generalized K-distribution
Gamma	Gamma (rate)	Weak (empirical) or strong, single receiver	Gamma (rate)	Compound gamma distribution
Log-normal	Normal	Weak (Rytov) scattering, single receiver	Normal	T distribution
Log-normal, multivariate	Multivariate normal	Weak (Rytov) scattering, multiple receivers	Multivariate normal	T distribution, multivariate
Complex Wishart	Inverse complex Wishart	Strong scattering, multiple receivers	Inverse complex Wishart	(?)
Matrix gamma	(matrix inverse gamma?)	Weak (empirical) or strong, multiple receivers	(matrix inverse gamma?)	(?)

Bayesian conjugate priors are available for the cases shown in red.

Conclusion

- Connections were examined between physics-based statistical modeling of signals, uncertainties in the wave scattering parameters, and Bayesian inference.
- Uncertainties can be addressed with a compound pdf, which incorporates separate pdfs for the wave scattering process, and for the uncertain parameters in the wave scattering. A number of formulations based on this approach (turbulent intermittency, K-distribution, Lomax distribution) were described and compared.
- Uncertainty tends to raise the tails of the signal pdfs, which can have important implications for detection and communication system performance.
- In the Bayesian context, the scattering models correspond to likelihood functions, which are conveniently paired with their conjugate priors to efficiently update the uncertain signal parameters.

"Is this needed for a Bayesian analysis?"

Application of a 3D multiple scattering theory to forest acoustics

V. E. Ostashev, D. K. Wilson, M. B. Muhlestein,
U.S. Army Engineer Research and Development Center

K. Attenborough
Open University, UK

17th Long Range Sound Propagation Symposium, 12-13 June 2018, Lyon, France

Outline

1. Introduction
2. 3D multiple scattering theory
3. Mean sound field
4. Radiative transfer equation
5. Correspondence between sound propagation in a forest and a turbulent atmosphere
6. Conclusions

Introduction

Sound propagation in a forest is a complicated phenomenon due to multiple scattering by trunks and branches, micrometeorology in a forest, and other factors. This problem is important in several applications such as noise reduction by a stand of trees and localization of sound sources. Despite significant efforts (FDTD, Nord2000 model, etc.) there are no satisfactory prediction methods based on first principles.

Recently, we have applied a 3D multiple scattering theory to forest acoustics. The results are published in four JASA papers (2017-2018):

1. Ostashev, Wilson, Muhlestein, Attenborough, "Correspondence between sound propagation in discrete and continuous random media with application to forest acoustics," JASA **143**, 1194-1205 (2018).
2. Muhlestein, Ostashev, Wilson, "Pulse propagation in a forest," JASA **143**, 968-979 (2018).
3. Ostashev, Muhlestein, Wilson, "Radiative transfer formulation for forest acoustics," JASA **142**, 3767-3780 (2017).
4. Ostashev, Wilson, Muhlestein, "Effective wavenumbers for sound scattering by trunks, branches, and the canopy in a forest," JASA **142**, EL177-183 (2017).

The main goal of the presentation is to overview results obtained in these papers.

Introduction

In a 3D multiple scattering theory, we assume that trunks, branches, and other scatterers have random locations and that their scattering amplitudes are known. This stochastic approach is often used in wave propagation in complex media. Using this approach, closed form equations for the mean sound field and mean intensity are derived.

In the literature, a 2D multiple scattering theory has been used to calculate the mean sound field:
Embleton. JASA, **40**, 667-670 (1966).
Price, Attenborough, Heap. JASA, 84, 1836-1844 (1988).
Defrance, Barrière, Premat. Proc. Forum Acusticum (2002).
Swearingen, White. JASA, **122**, 113-119 (2007).

Thus, our approach generalizes previous theories to 3D propagation and enables calculation of both the mean sound field and the mean intensity. These generalizations are not trivial and yield new important results.

Scattering properties of a random medium

Scattering properties of a forest (and a turbulent atmosphere) are completely described by the differential scattering cross section (DSCS) and total cross section (TCS). The DSCS is defined as

$$\sigma_d(\boldsymbol{n}',\boldsymbol{n}) = \frac{I_s(\boldsymbol{n}',\boldsymbol{n})R^2}{VI_0}.$$

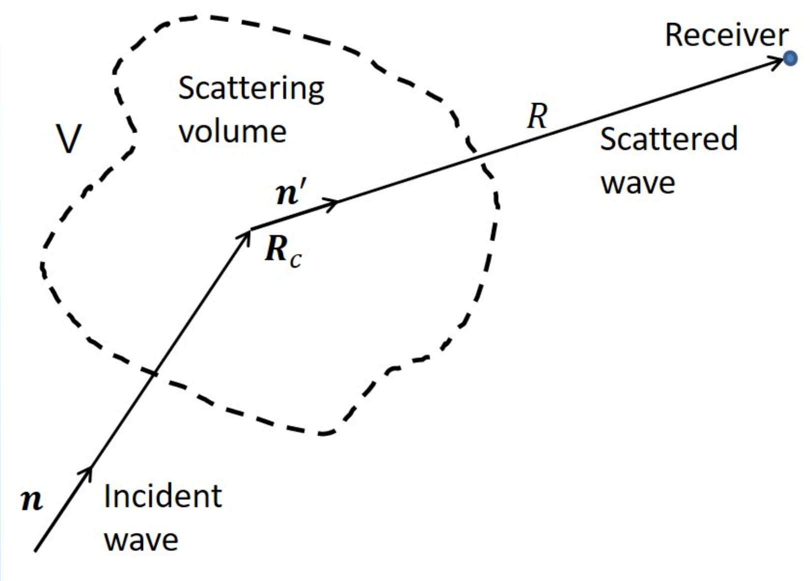

The geometry of sound scattering is shown in the figure. A sound wave propagating in the direction of the unit vector $\boldsymbol{n}$ is incident on the scattering volume V. This wave is scattered in all directions.

The DSCS is proportional to the intensity $I_s(\boldsymbol{n}',\boldsymbol{n})$ scattered in the direction of the unit vector $\boldsymbol{n}'$, normalized by the intensity of the incident wave, I_0, scattering volume, V, and the distance to the receiver, R. In a turbulent atmosphere, the DSCS is given by

$$\sigma_d(\boldsymbol{n}',\boldsymbol{n}) = 2\pi k^4\left[\frac{(\boldsymbol{n}'\cdot\boldsymbol{n})\Phi_T(k\boldsymbol{n}'-k\boldsymbol{n})}{4T_0^2} + \frac{(\boldsymbol{n}'\cdot\boldsymbol{n})^2 n_i n_j \Phi_{ij}(k\boldsymbol{n}'-k\boldsymbol{n})}{c_0^2}\right].$$

Here, $\Phi_T(k\boldsymbol{n})$ and $\Phi_{ij}(k\boldsymbol{n})$ are the spectra of the temperature and wind velocity fluctuations.

Scattering amplitude

In a forest, the differential scattering cross section can be specified further:

$$\sigma_{\mathrm{d}}(\boldsymbol{n}', \boldsymbol{n}) = \nu |f(\boldsymbol{n}', \boldsymbol{n})|^2.$$

Here, ν is the number of scatterers per unit volume and the scattering amplitude$f(\boldsymbol{n}', \boldsymbol{n})$ is defined simlary to the DSCS, but for one scatterer and the sound pressure rather than the sound intensity:

$$p_s(\boldsymbol{n}', \boldsymbol{n}) = p_0 f(\boldsymbol{n}', \boldsymbol{n}) \frac{\exp(ik|\boldsymbol{r} - \boldsymbol{r}'|)}{|\boldsymbol{r} - \boldsymbol{r}'|}.$$

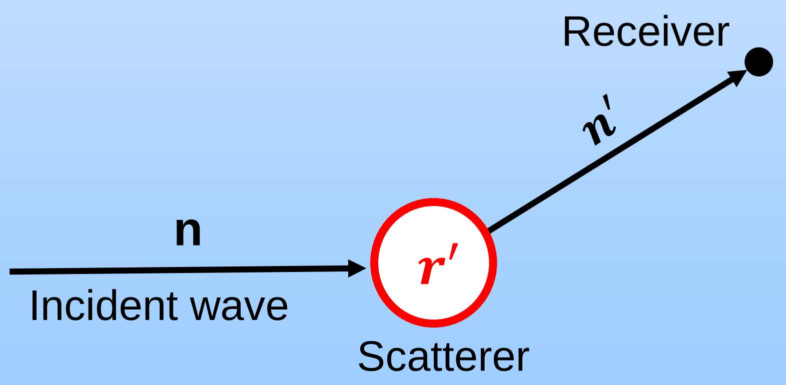

Determining the differential scattering cross section

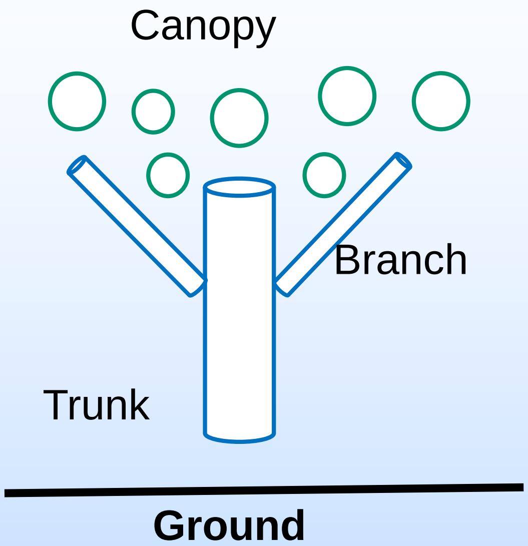

Two approaches for determining the differential scattering cross section:

1.The DSCS can be measured experimentally for different types of forests.

2. Trunks can be modeled as vertical finite cylinders, branches as slanted finite cylinders, and the canopy layer as diffuse scatterers. Using these scatterers, we can build different realistic forests.

Canopy layer: $\sigma_{\mathrm{d}}(\boldsymbol{n}', \boldsymbol{n})$ = const.

DSCS for finite cylinders

The differential scattering cross section is obtained by using the scattering amplitude of a finite vertical cylinder (Ye, JASA, 1997):

$$\sigma_d(\boldsymbol{n}', \boldsymbol{n}) = \nu |khb \operatorname{sinc}[\mu(\cos\theta - \cos\theta_0] \sum_{n=0}^{\infty} B_n \cos(n\varphi)|^2.$$

$$B_n = \frac{\varepsilon_n}{2} J_n'(kb\sin\theta_0) \left[\sin\theta_0 J_n(kb\sin\theta) - \sin\theta J_n'(kb\sin\theta) \frac{H_n^{(1)}(kb\sin\theta_0)}{H_n^{(1)'}(kb\sin\theta_0)} \right]$$

Although these formulas appear to be involved, they are relatively easy to implement numerically.

Branches can be modeled as slanted finite cylinders. The DSCS is still given by equations above with some transformation of the angles.

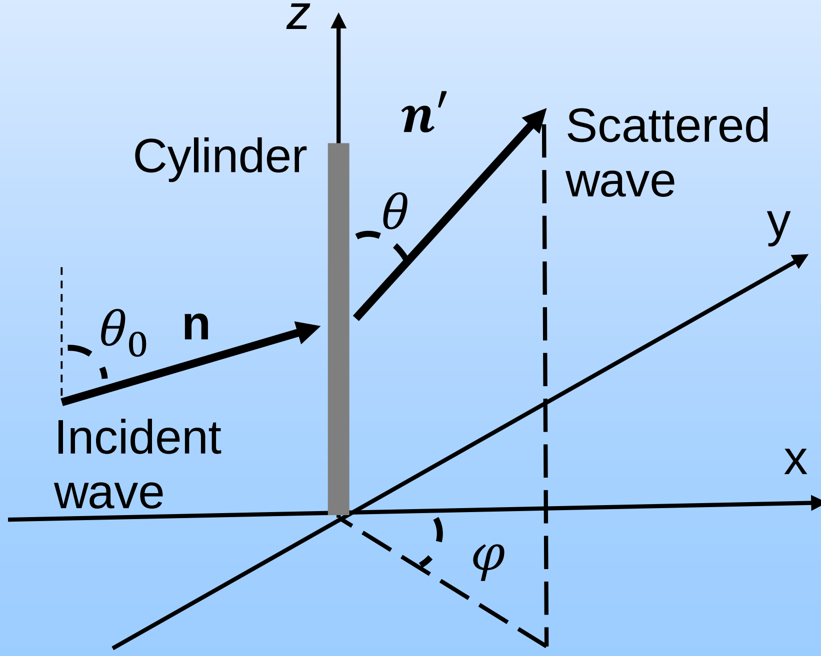

Other quantities pertinent to 3D multiple scattering theory

The scattering cross section (SCS) characterizes the loss of energy of a sound wave propagating in the direction of unit vector $\boldsymbol{n}$ due to sound scattering in all directions. It is obtained by integrating the DSCS over the unit vector $\boldsymbol{n}'$:

$$\sigma_s(\boldsymbol{n}) = \int_{4\pi} \sigma_d(\boldsymbol{n}', \boldsymbol{n})\, d\Omega(\boldsymbol{n}').$$

The absorbing cross section (ACS), $\sigma_a(\boldsymbol{n})$, has a similar meaning but is pertinent to sound absorption rather than scattering. The ACS accounts for sound absorption in a forest such as visco-thermal dissipation in foliage. The total cross section (TCS) is a sum of the SCS and ACS:

$$\sigma(\boldsymbol{n}) = \sigma_s(\boldsymbol{n}) + \sigma_a(\boldsymbol{n}) = \frac{4\pi\nu}{k} \operatorname{Im} f(\boldsymbol{n}, \boldsymbol{n}).$$

The effective wave number (propagation constant) is given by

$$k_{\mathrm{eff}}(\boldsymbol{n}) = k + i\sigma(\boldsymbol{n})/2.$$

All these equations are also valid for sound propagation in a turbulent atmosphere, for which $\sigma_a = 0$.

Mean sound field and mean intensity

In a random medium, the sound pressure is a random function:

sound field $\longrightarrow$ $p(\boldsymbol{r}) = \langle p(\boldsymbol{r})\rangle + \tilde{p}(\boldsymbol{r}).$

coherent field   sound field fluctuations

The coherent sound field (the first statistical moment) ignores sound field fluctuations $\tilde{p}(\boldsymbol{r})$, attenuates exponentially with range, and is applicable for relatively short ranges. To calculate $\langle p\rangle$ in a forest with temperature and wind velocity stratification, we can use the parabolic equation (PE) method with the following substitution:

sound wavenumber $k \rightarrow k_{\mathrm{eff}}$.

The mean sound intensity (the second statistical moment) is usually used to compare with experimental data:

$$I(\boldsymbol{r}) \equiv \langle p(\boldsymbol{r}) p^*(\boldsymbol{r})\rangle = \langle p(\boldsymbol{r})\rangle\langle p^*(\boldsymbol{r})\rangle + \langle \tilde{p}(\boldsymbol{r})\tilde{p}^*(\boldsymbol{r})\rangle.$$

mean intensity   coherent intensity   diffuse intensity

Radiative transfer equation

The specific intensity $J(\boldsymbol{r},\boldsymbol{n})$ is defined as the average energy flux within a unit frequency band within a unit solid angle Ω in the direction of the unit vector $\boldsymbol{n}$. The mean intensity is obtained by integrating the specific intensity overall directions of the unit $\boldsymbol{n}$:

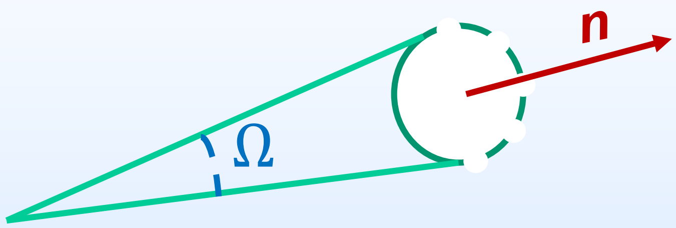

$$I(\boldsymbol{r}) = \int_{4\pi} J(\boldsymbol{r},\boldsymbol{n})d\Omega(\boldsymbol{n}).$$

The specific intensity can be found by solving the radiative transfer equation (RTE):

$$\left(\boldsymbol{n}\cdot\frac{\partial}{\partial\boldsymbol{r}}\right)J(\boldsymbol{r},\boldsymbol{n}) + \sigma(\boldsymbol{n})J(\boldsymbol{r},\boldsymbol{n}) = \int_{4\pi}\sigma_{\mathrm{d}}(\boldsymbol{n}',\boldsymbol{n})J(\boldsymbol{r},\boldsymbol{n}')\,d\Omega(\boldsymbol{n}').$$

In the RTE, the scattering properties of a medium are expressed in terms of the DSCS, $\sigma_{\mathrm{d}}(\boldsymbol{n}',\boldsymbol{n})$, and the TCS, $\sigma(\boldsymbol{n})$. Solutions of the RTE are well developed in many fields of physics and can be readily used in forest acoustics. The RTE accounts for diffraction. The RTE also describes sound propagation in a turbulent atmosphere with properly chosen DSCS and SCS. Given this similarity and similarities mentioned above, we arrive at an important conclusion:

The equations for the statistical moments of the sound field propagating in a forest have the same form as those for sound propagation in a turbulent atmosphere if the scattering properties of the two media are expressed in terms of the differential scattering and total cross sections.

High-frequency approximation

The theories of sound propagation in a turbulent atmosphere are relatively well developed and are summarized in the book:

Ostashev and Wilson, Acoustics in Moving Inhomogeneous Media, 2nd Edition (2015).

These theories can be used to advance forest acoustics. In particular:

1. In the high-frequency approximation, the RTE simplifies to the 2nd moment PE:

$$\left[\frac{\partial}{\partial x} - \frac{i}{k}\frac{\partial^2}{\partial \boldsymbol{\varrho}\,\partial \boldsymbol{\varrho}_d} + \sigma_\mathrm{a}(x, \boldsymbol{\varrho}) + \int \frac{\sigma_\mathrm{d}(x, \boldsymbol{\varrho}; \boldsymbol{\kappa}/k)}{k^2}\left(1 - \mathrm{e}^{i\boldsymbol{\kappa}\cdot\boldsymbol{\varrho}_d}\right) d^2\kappa\right] B(x; \boldsymbol{\varrho}, \boldsymbol{\varrho}_d) = 0.$$

Here, $B(x; \boldsymbol{\varrho}, \boldsymbol{\varrho}_d)$ is the correlation function of the sound field, sound propagates in the direction of the x axis, and $\boldsymbol{\varrho}$ are the transverse coordinates. The mean intensity is $\mathrm{I}(x, \boldsymbol{\varrho}) = B(x; \boldsymbol{\varrho}, 0)$. The 2nd moment PE can be generalized to account for atmospheric stratification and impedance boundary conditions at the ground. Numerical solutions of this generalized equation have been developed in atmospheric acoustics:

Wilson, Ostashev, Lewis. Waves in Random and Complex Media **19**(3), 369-391 (2009).
Cheinet. JASA **131**, 1946-1958 (2012).

Effect of a forest on the interference between the direct and ground reflected waves

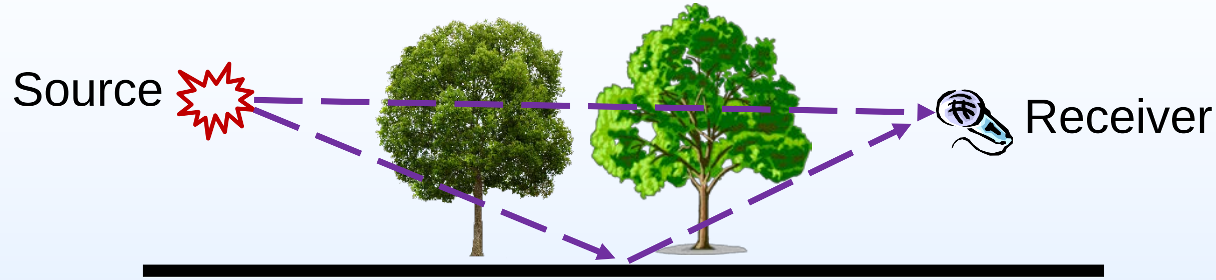

2. Using the similarity between sound propagation in a turbulent atmosphere and a forest, we rigorously account for the effect of trees on the interference between the direct and ground-reflected waves. The coherence factor, C_{coh}, describes the loss of coherence between these waves due scattering in a forest. It is expressed in terms of the DSCS.

$$\langle pp^* \rangle = \frac{1}{R_1^2} + \frac{1}{R_2^2} + \frac{2|\mathcal{R}|C_{\mathrm{coh}}}{R_1 R_2} \cos(k(R_2 - R_1) + \beta).$$

$$C_{\mathrm{coh}} = \exp\left[-\frac{x}{k^2}\int_0^1 d\eta \int_{-\infty}^{\infty} d\kappa_z\, \sigma_{\mathrm{d}}(\kappa_y, \kappa_z)\left(1 - e^{i\eta\kappa_z h_{sr}}\right)\right].$$

Slides below provide numerical results for sound propagation in a forest using formulations obtained with the 3D multiple scattering theory.

Mean sound pressure

The mean sound pressure for different geometries of sound propagation:

(a) A point source above an impedance ground in a homogeneous atmosphere.
(b) When a 10 m high trunk layer is added to a homogeneous atmosphere, the complex amplitude in this layer and above is significantly attenuated starting at the range of about 200 m.
(c) When a 20 m high canopy layer added to the previous geometry, this attenuation significantly increases with height.
(d) Accounting for the atmospheric stratification in the trunk and canopy layers results in downward refraction.

Dashed horizontal lines indicate the trunk and canopy layers. The sound frequency is 2 kHz, the source height is 2 m, the number of trees per unit area is 0.05 $1/\mathrm{m}^2$, and the tree radius is 0.1 m.

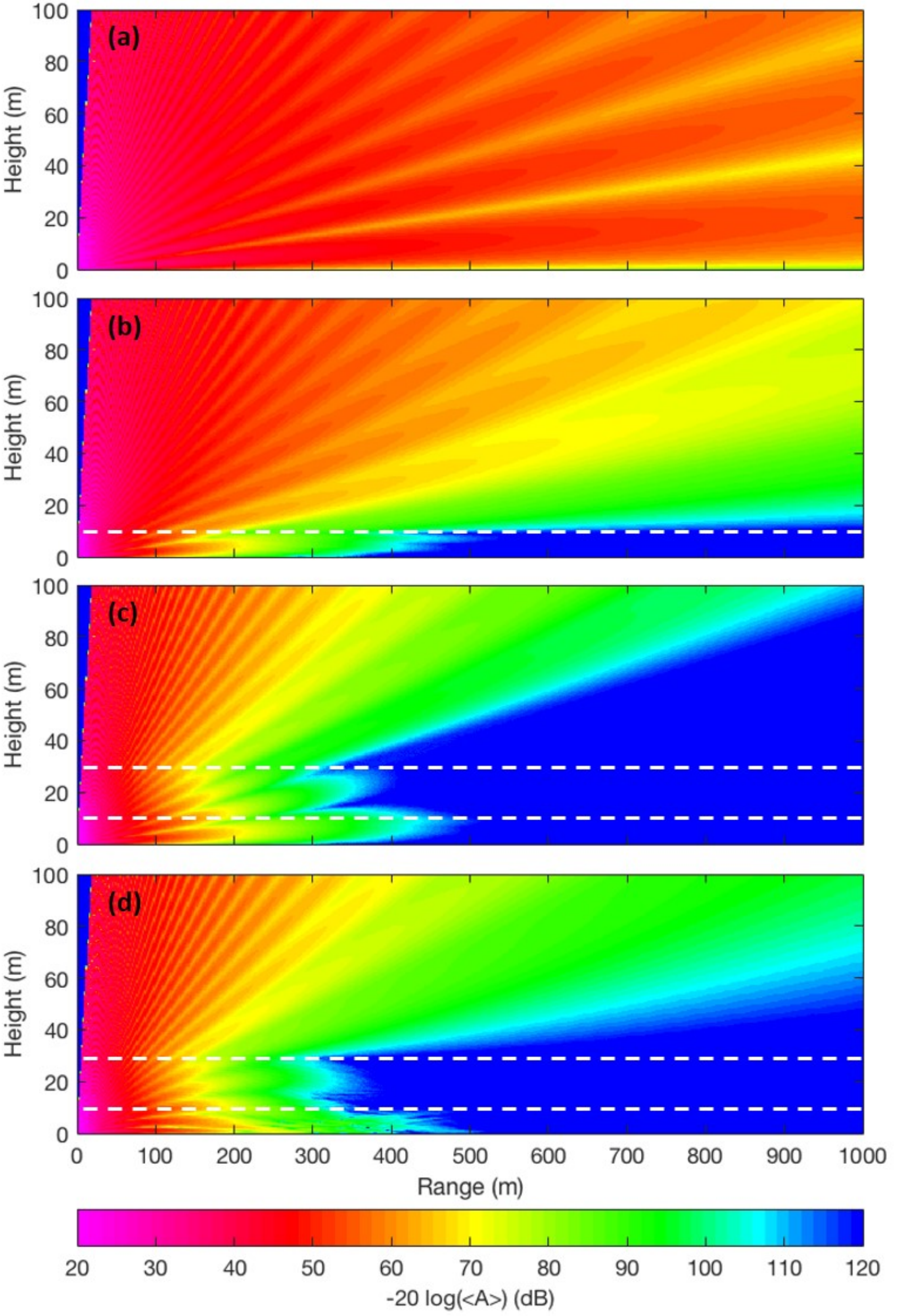

Schematic of sound propagation in the four-layer forest model

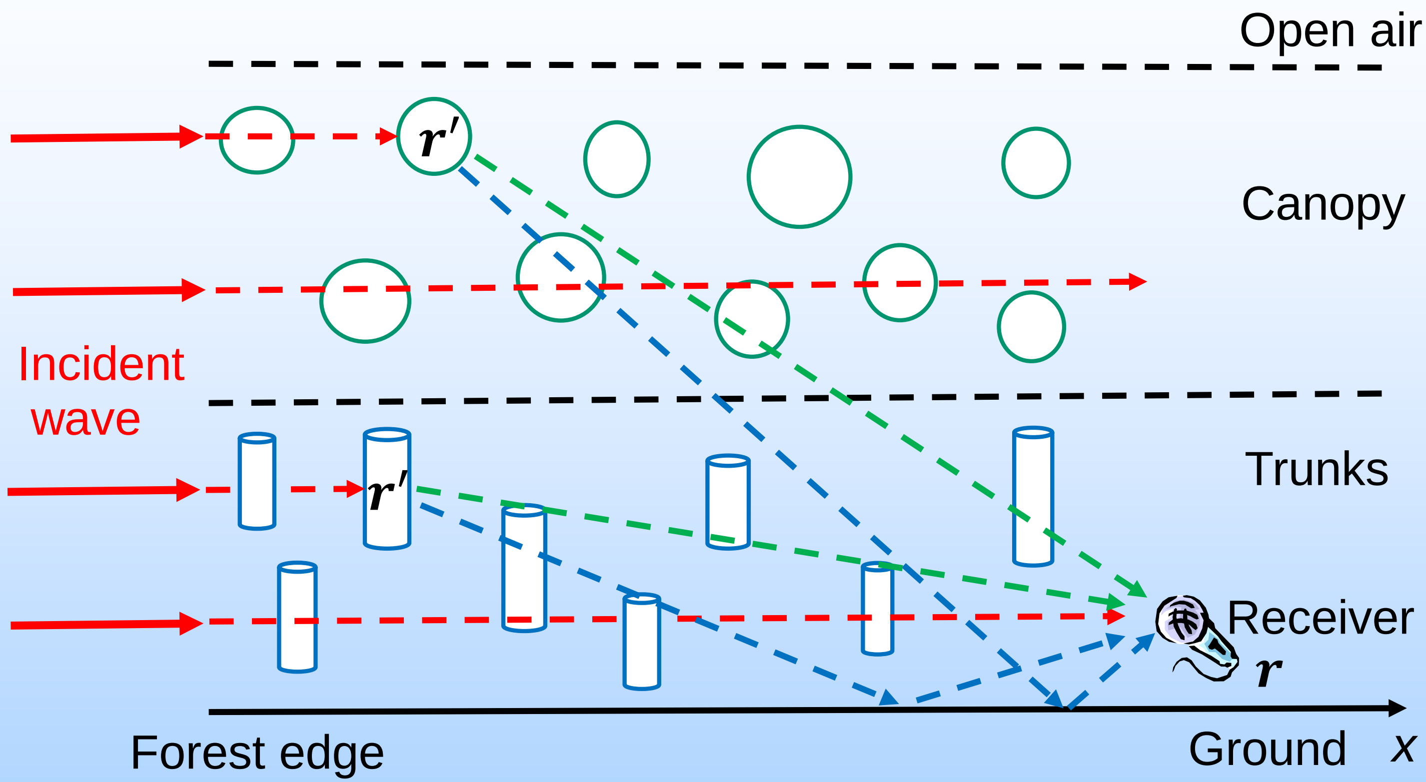

A plane wave is incident on a forest, while the receiver is located on the other edge of the forest. The forest is modeled with four layers: ground, trunks, canopy, and open air. This geometry is pertinent to sound attenuation by a stand of trees. In the numerical examples below, parameters typical for a temperate conifer forest are considered: the height of the canopy layer is 30 m, the height of the trunk layer is 10 m, the number of trees per unit area is 0.05 $1/\mathrm{m}^2$, and the tree radius is 0.1 m.

Mean, coherent, and diffuse intensities transmitted through a forest

Normalized mean (total), coherent, and diffuse intensities transmitted through the forest versus the forest length. The coherent intensity exponentially attenuates with increasing forest length. The diffuse intensity is zero at the forest edge, reaches a maximum at 59 m, and then decreases with the forest length.

The sound frequency is 1082 Hz, and the height of the receiver is 2m.

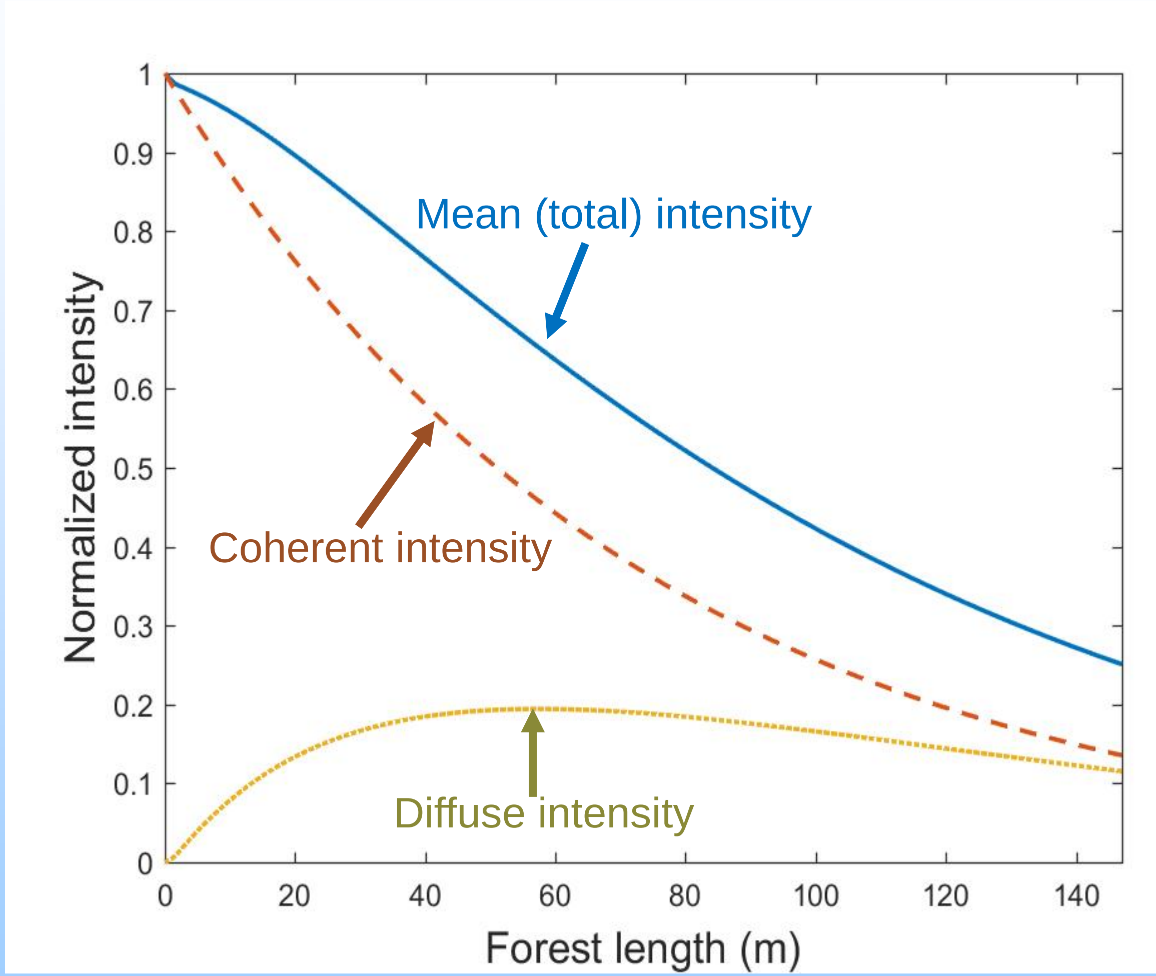

Backscattered intensity

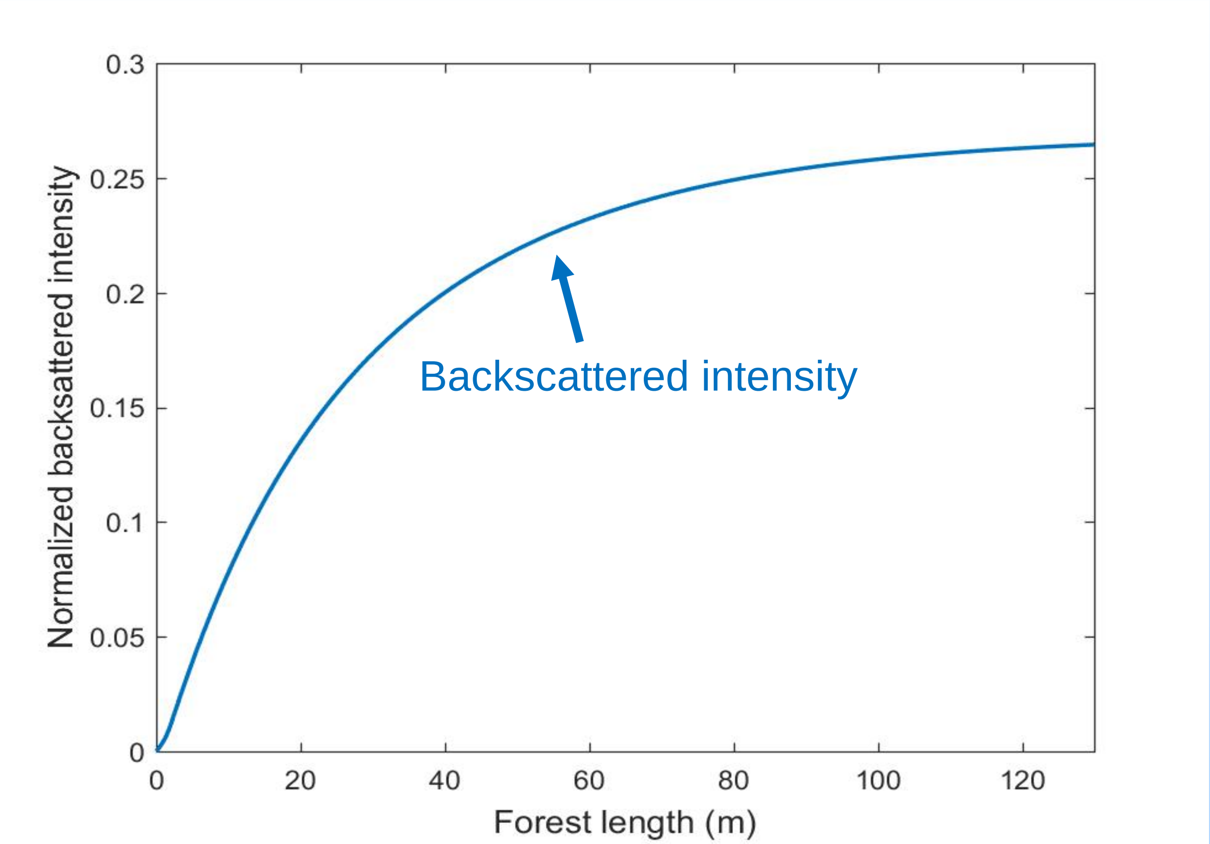

The diffuse intensity backscattered from the forest versus the forest length. The intensity monotonically increases with increasing forest length, as it should, and reaches a plateau at about 120 m.

Interference of direct and ground reflected waves in a forest

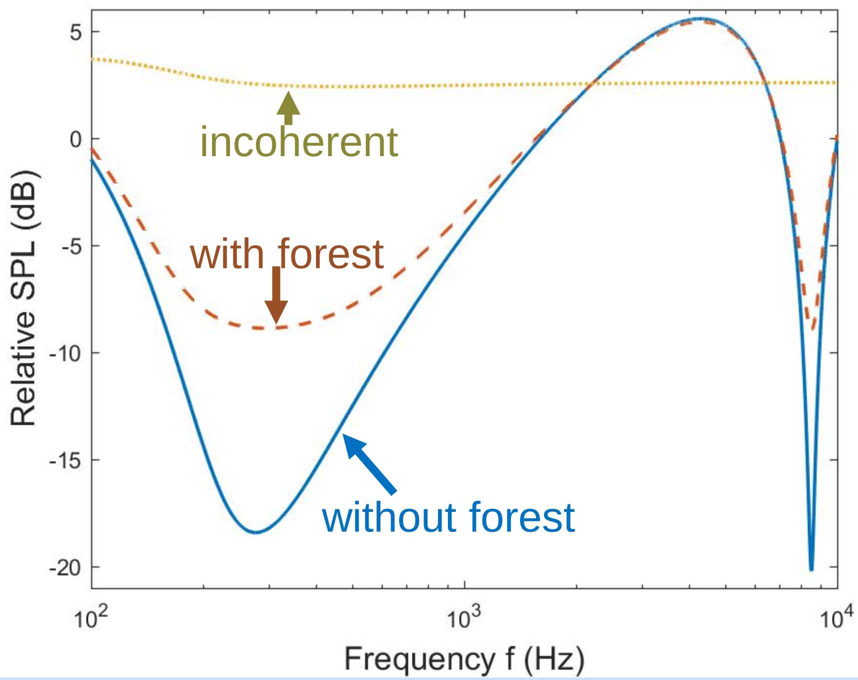

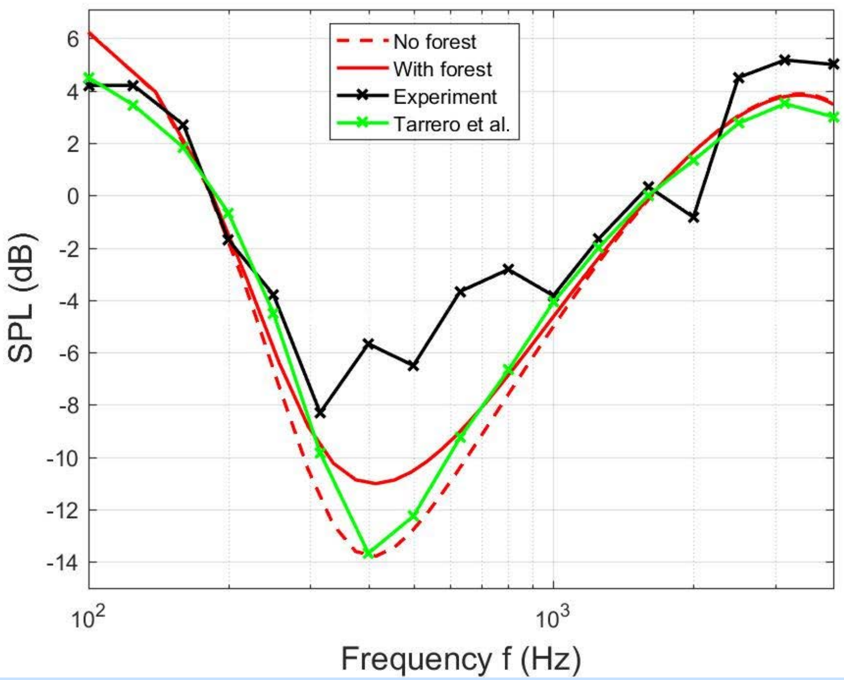

(Left) Interference of the direct and ground-reflected waves in a forest versus sound frequency. The propagation range is 75m, the source and receiver heights are 1 m and 1.5 m, the tree height is 20 m, the number of trees per unit area is 0.1 $1/\mathrm{m}^2$, and the tree's radius is 0.15 m. Without forest, the interference results in maxima and minima of the SPL as a function of the frequency. With forest, the interference minima are reduced due to the coherence loss between the direct and ground-reflected waves, resulting in an apparent increase in the SPL. When these waves are incoherent, the maxima and minima are completely suppressed and the SPL only slightly depends on the frequency. Thus, the SPL of the direct and ground-reflected waves significantly depends on the coherence between these waves.

(Right) Comparison with experimental data.

Pulse propagation in a forest

Normalized coherent and diffuse intensities in a forest in Pomfret, VT, based on an series of gunshots measured 60 m from the source. Both the instantaneous and short-time averaged (denoted by an over-line) intensities are shown. The reverberation time is T30=0.6 s.

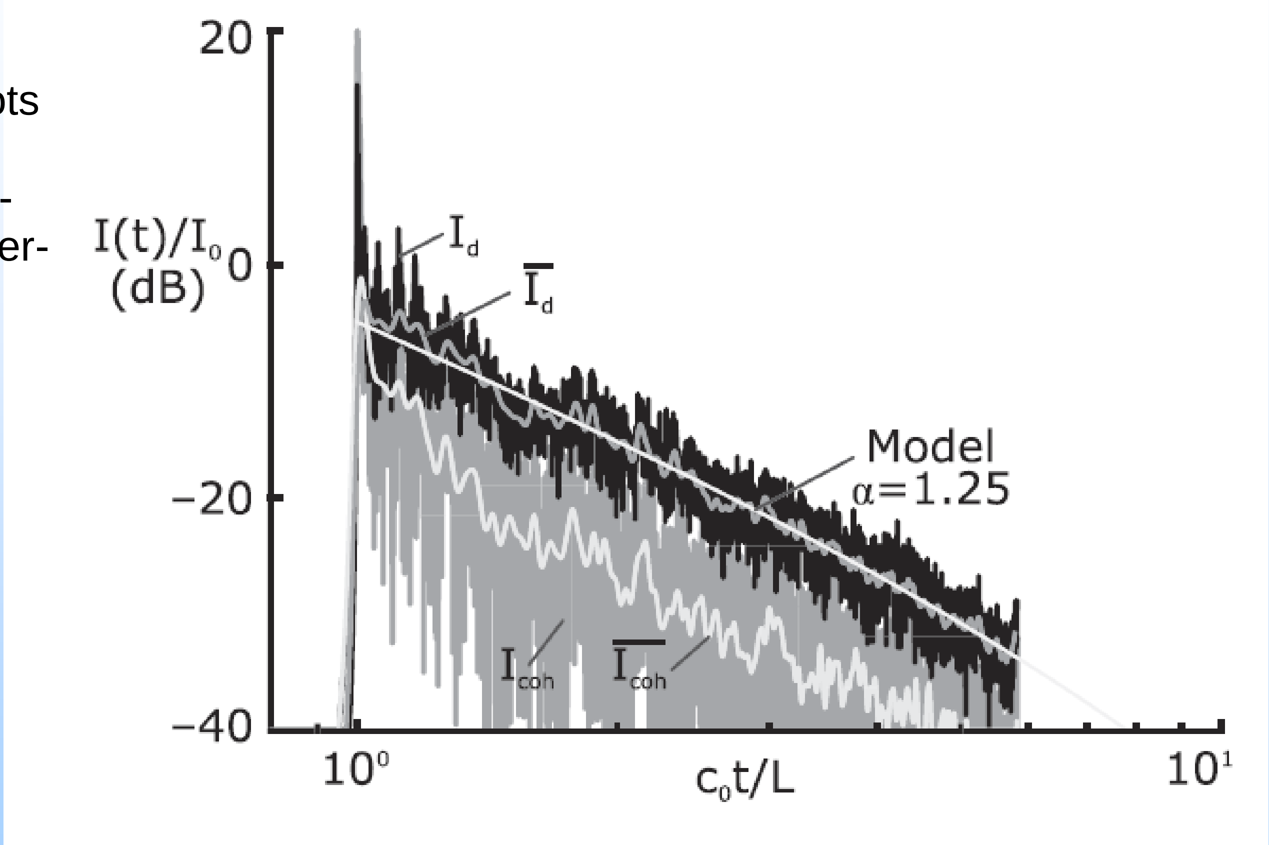

Theoretical predictions for the diffused intensity agree with experimental data.

$$I_d(\tau) \sim \frac{e^{-\alpha\tau}}{\tau^3},$$

where

$$\alpha = \sigma L, \qquad \tau = \frac{c_0 t}{L}.$$

Conclusions

1. A 3D multiple scattering theory has been recently applied to forest acoustics. The result were published in four papers in JASA (2017-2018).

2. This theory has been briefly outlined here. Approaches for calculating the mean sound field and the mean intensity in a forest were described.

3. Numerical results for sound propagation in a forest based on these approaches were presented. Some of the predictions were compared with experimental data.

4. The 3D multiple scattering theory appears to be a very suitable approach for forest acoustics.

*L*aboratoire de *M*écanique des *F*luides et d'*A*coustique
LMFA UMR CNRS 5509

Écully, 12th. of June 2018

Adjoint of an approximate wave operator applied to the acoustic propagation in an arbitrary mean flow

Étienne Spieser , Christophe Bailly

LABEX CELYA
UNIVERSITÉ DE LYON

17th. Symposium on Long Range Sound Propagation

- Adjoint method in propagation effects
- Wave equations for sheared flows
- Capability to account for refraction effects

- **How is the reciprocity principle established ?**

$$\mathfrak{L}_o = \partial^2/\partial t^2 - a_0^2 \Delta$$

$$\begin{cases} \mathfrak{L}_o \, p_1 = S_1 & (1) \\ \mathfrak{L}_o \, p_2 = S_2 & (2) \end{cases}$$

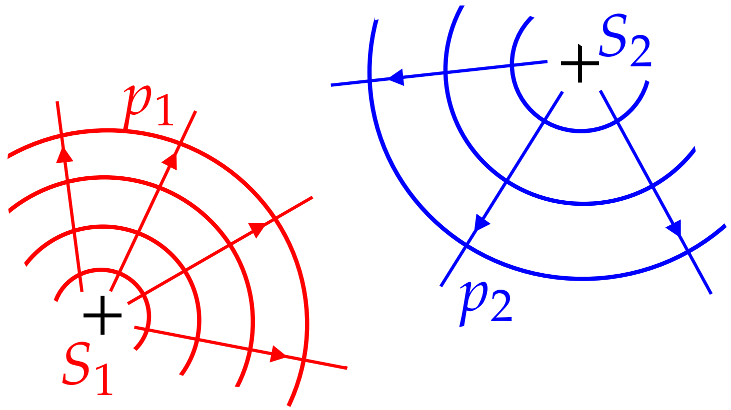

Consider $p_2 \cdot \{Eq(1)\} - p_1 \cdot \{Eq(2)\}$ and integrate over Ω and T

$$\int_T \int_\Omega p_2 \cdot \mathfrak{L}_o \, p_1 - p_1 \cdot \mathfrak{L}_o \, p_2 \, d\Omega dT = \int_T \int_\Omega p_2 \cdot S_1 - p_1 \cdot S_2 \, d\Omega dT$$

Using integration by parts, only B.T. remain for the $L.H.S$

$$L.H.S = \int_T \int_{\partial\Omega} a_0^2 \left[p_1(\nabla p_2) - p_2(\nabla p_1)\right] \cdot \mathbf{n} \, \partial\Omega dT + \int_\Omega \left[p_2 \frac{\partial p_1}{\partial t} - p_2 \frac{\partial p_1}{\partial t}\right]_{-\infty}^{t=\infty} d\Omega = 0$$ **Here**

Choosing $S_1 = \delta(\mathbf{x} - \mathbf{x}_1)$ and $S_2 = \delta(\mathbf{x} - \mathbf{x}_2)$, $\boxed{p_1(\mathbf{x}_2) = p_2(\mathbf{x}_1)}$

- **Let us do it again with some more adapted tools...**

$$\begin{cases} \mathfrak{L}_o\, p_1 = S_1 & (1) \\ \mathfrak{L}_o\, p_2 = S_2 & (2) \end{cases}$$

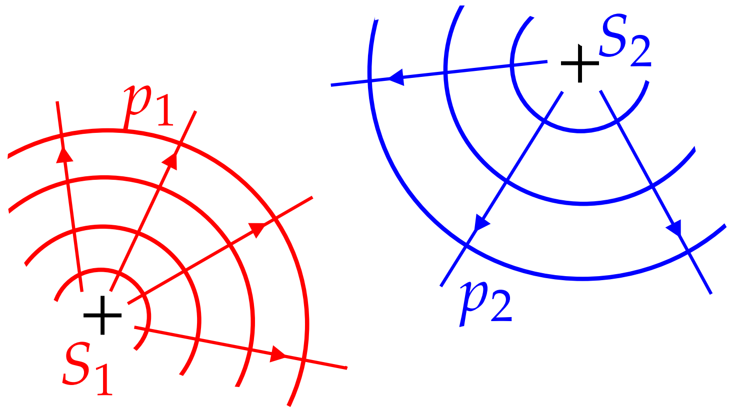

Scalar product $< f, g >= \int_T \int_\Omega f\, g \quad d\Omega dT$

$$< p_2 , \mathfrak{L}_o\, p_1 > - < p_1 , \mathfrak{L}_o\, p_2 >=< p_2 , S_1 > - < S_2 , p_1 >$$

Using integration by parts, $< p_2 , \mathfrak{L}_o\, p_1 > = < \mathfrak{L}_o\, p_2 , \ p_1 > + B.T.$

↳ $\mathfrak{L}_o$ is **symmetric** or **self-adjoint**

The reciprocity principle is recovered $\boxed{< p_2 , S_1 >=< S_2 , p_1 >}$

What if the problem is not self-adjoint?

$\mathfrak{L}_o$ is now associated with **LEE** or with **Lilley's Equation** in the presence of a flow, and is no more self-adjoint.

$$< p_2 \, , \, \mathfrak{L}_o \, p_1 > \neq < \mathfrak{L}_o \, p_2 \, , \, p_1 >$$

But, $\exists! \, \mathfrak{L}_o^\dagger \, , \, \forall \, p_2^\dagger$

$$< p_2^\dagger \, , \, \mathfrak{L}_o \, p_1 > = < \mathfrak{L}_o^\dagger \, p_2^\dagger \, , \, p_1 >$$

According to $\mathfrak{L}_o \, p_1 = S_1$, let $S_2^\dagger = \mathfrak{L}_o^\dagger \, p_2^\dagger$

$\mathfrak{L}_o^\dagger$ is the adjoint operator associated to $\mathfrak{L}_o$,
$S_2^\dagger$ is the adjoint source,
$p_2^\dagger$ is the adjoint field.

$$\boxed{< p_2^\dagger \, , \, S_1 > = < S_2^\dagger \, , \, p_1 >}$$

Some features of the adjoint method

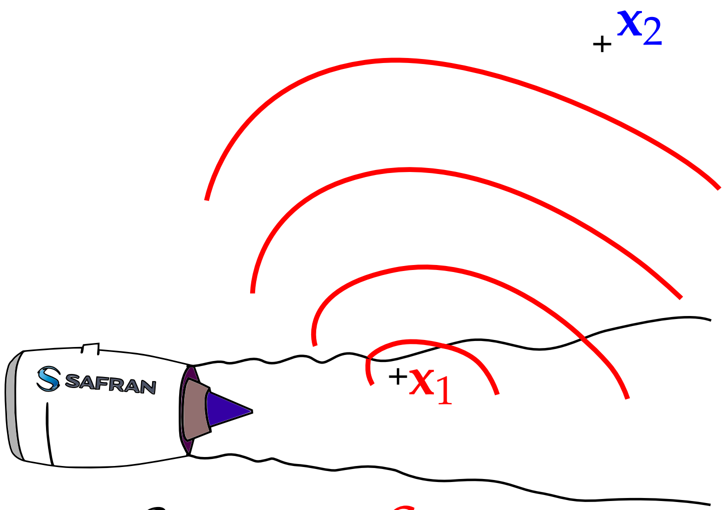

$\mathfrak{L}_o\, p_1 = S_1$

Physical space

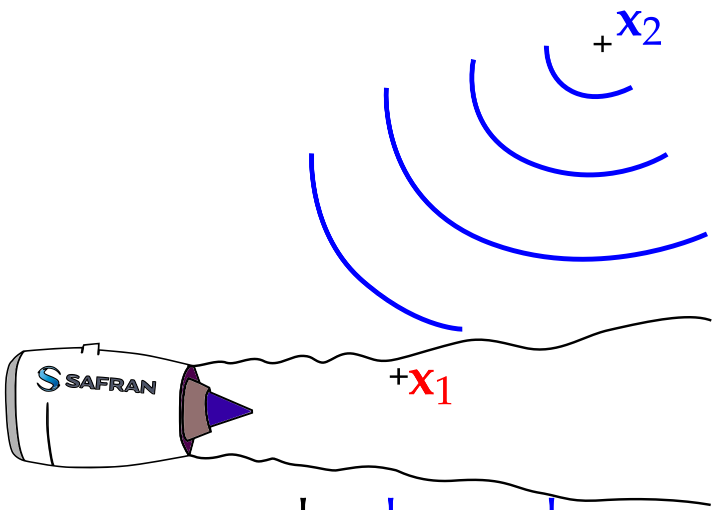

$\mathfrak{L}_o^\dagger\, p_2^\dagger = S_2^\dagger$

Adjoint space

The physical field is recovered by choosing a suitable $S_2^\dagger$.

$$S_2^\dagger = \delta(\mathbf{x} - \mathbf{x}_2) \quad \text{in} \quad < S_2^\dagger\, ,\, p_1 >=< p_2^\dagger\, ,\, S_1 > \Longrightarrow \boxed{p_1(\mathbf{x}_2) =< p_2^\dagger\, ,\, S_1 >}$$

Philosophy : solve the adjoint problem instead of the physical one.

For a given mean flow and a fixed microphone position, $p_2^\dagger$ can be **reused**.

Self-adjoint operators, i.e. $\mathfrak{L}_o^\dagger = \mathfrak{L}_o$, are valuable :

- In practice the **same solver** can be used for direct and adjoint analysis,
- Symmetry **guaranties energy conservation**, and thus stability (Möhring 1999).

In presence of a **sheared flow** acoustic can trigger instability wave (Yates 1978).

A heated $T_j/T_\infty = 2$ jet $M_j = 0,756$ is excited by acoustic waves $St \approx 0.085$.

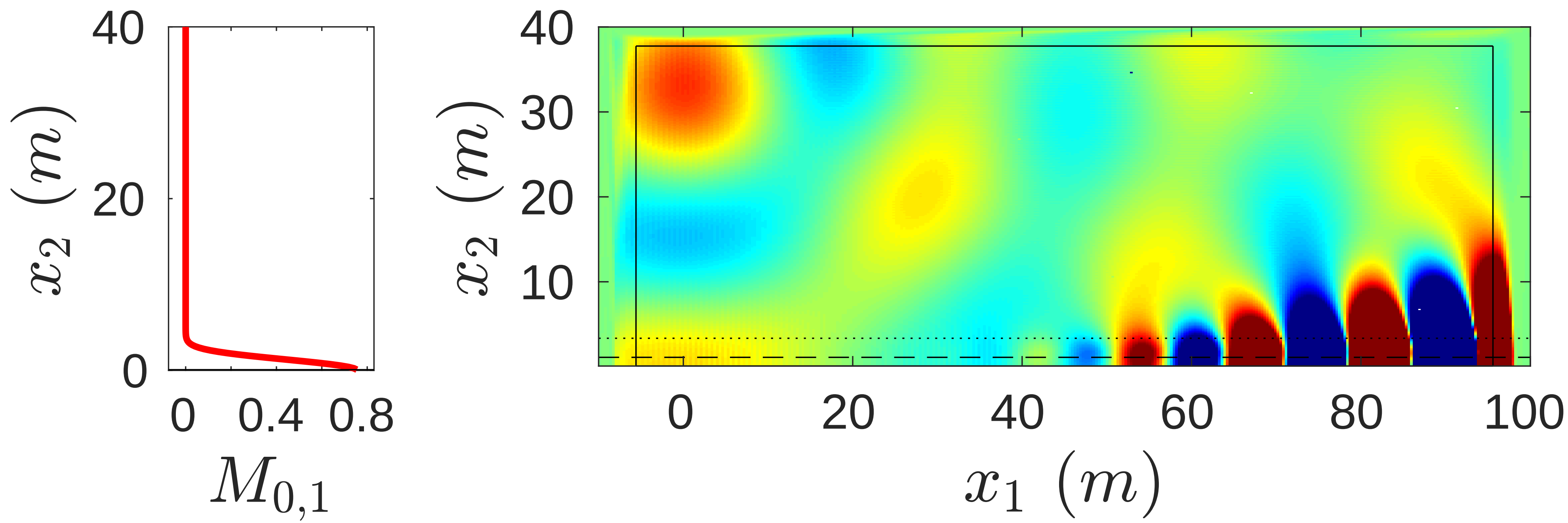

Whenever the **mean flow is sheared**, acoustical-vortical coupling may occur, and **acoustic energy is not conserved**.

One exception - geometrical acoustics : modes are **decoupled at high-frequency**.

In general, **no self-adjoint operator exist** to describe propagation effects.

- Purpose of the study :

Find the best self-adjoint approximated operator for propagation.

- Adjoint method in propagation effects
- Wave equations for sheared flows
- Capability to account for refraction effects

Some classical operators

Considering a stratified $\rho_0(x_2)$ and sheared mean flow $\mathbf{u}_0(x_1, x_2) = \begin{pmatrix} u_{0,1}(x_2) \\ 0 \end{pmatrix}$

$$D_{\mathbf{u}_0} = \frac{\partial}{\partial t} + \mathbf{u}_0 \cdot \nabla$$

Linearised Euler's equation

$$\begin{cases} D_{\mathbf{u}_0}(\rho') + \nabla \cdot (\rho_0 \mathbf{u}') = 0 \\ D_{\mathbf{u}_0}(\rho_0 \mathbf{u}') + \nabla p' + (\nabla \mathbf{u}_0)(\rho_0 \mathbf{u}') = \mathbf{0} \\ D_{\mathbf{u}_0}(p') + \gamma p_0 \nabla \cdot \mathbf{u}' = 0 \end{cases}$$

Lilley's equation (1972)

$$D_{\mathbf{u}_0}\left(\mathbf{D}^2_{\mathbf{u}_0}(p') - \nabla \cdot (\mathbf{a}_0^2 \nabla p')\right) + 2a_0^2 \nabla u_{0,1} \cdot \nabla \frac{\partial p'}{\partial x_1} = 0$$

exact hence unstable !

Helmholtz's equation

$\mathbf{D}^2_{\mathbf{u}_0}(p') - \nabla \cdot (\mathbf{a}_0^2 \nabla p') = 0$, not exact, **self-adjoint** part of Lilley's equation.

Some known stable operators

The community tackled the stability issue resulting in two main contributions :

1/ Ewert *et al.* (jcp 2003) derived the **Acoustic Perturbation Equations** (APE) as an **acoustical-mode preserving** reformulation of the LEE.

2/ Bogey *et al.* (aiaaj 2002) identified in the LEE the $\frac{\partial u_{0,1}}{\partial x_2}$ term to be responsible for the instability, removed it and proposed a **stable version of Lilley's equation** :

$$D_{\mathbf{u}_0}\left(D^2_{\mathbf{u}_0}\left(p'\right) - \nabla\cdot\left(a_0^2 \nabla p'\right)\right) + \mathbf{1}\; a_0^2 \nabla u_{0,1} \cdot \nabla \frac{\partial p'}{\partial x_1} = 0$$

However none of the suggested solution provide a **self-adjoint operator**.

Euler's Wave Equation (EWE)

Starting from the momentum and energy equations

$$\begin{cases} D_{\mathbf{u}_0}(\mathbf{u}') + (\nabla \mathbf{u}_0)\mathbf{u}' + \dfrac{\nabla p'}{\rho_0} = \mathbf{0} \\ D_{\mathbf{u}_0}(p') + \gamma p_0 \nabla \cdot \mathbf{u}' = 0 \end{cases}$$

A wave equation for $\mathbf{u}'$ can be derived

$$D^2_{\mathbf{u}_0}(\mathbf{u}') + \left[(\nabla \mathbf{u}_0) + (\nabla \mathbf{u}_0)^T\right] D_{\mathbf{u}_0}(\mathbf{u}') + (\nabla \mathbf{u}_0)^T (\nabla \mathbf{u}_0)\mathbf{u}' - a_0^2 \Delta \mathbf{u}' - a_0^2 \nabla \times \boxed{\nabla \times \mathbf{u}'} = \mathbf{0}$$

By removing the non-symmetric curl term, **Stabilised-EWE** (SEWE)

$$D^2_{\mathbf{u}_0}(\mathbf{u}') + \left[(\nabla \mathbf{u}_0) + (\nabla \mathbf{u}_0)^T\right] D_{\mathbf{u}_0}(\mathbf{u}') + (\nabla \mathbf{u}_0)^T (\nabla \mathbf{u}_0)\mathbf{u}' - a_0^2 \Delta \mathbf{u}' = \mathbf{0}$$

Overview of the propagation operators

	stable	self - adjoint	mean flow shearing
A) Linearised Euler Equation (LEE)	🙁	🙁	
B) Lilley's Equation	🙁	🙁	
C) Stabilised Lilley's Equation	🙂	🙁	
D) Helmholtz's Equation	🙂	🙂	
E) Euler's Wave Equation (EWE)	🙁	🙁	
F) Stabilised EWE (SEWE)	🙂	🙂	

- Adjoint method in propagation effects
- Wave equations for sheared flow
- Capability to account for refraction effects

Numerical method chosen to solve PDEs

The six previously mentioned **operators are tested** using an in-house high-order finite difference direct frequency solver (LU decomposition, *Matlab*).

Non-reflecting boundary conditions are achieved using PML (Hu 2001).

To allow comparisons, **p' and ρ' are rebuilt from $\mathbf{u}'$ computed by *EWE* and *SEWE*** solving continuity and energy equation

$$D_{\mathbf{u}_0}(\rho') = -\nabla \cdot (\rho_0 \mathbf{u}') \qquad D_{\mathbf{u}_0}(p') = -\gamma p_0 \nabla \cdot \mathbf{u}'$$

The 4th. NASA Workshop test case

A **2D isobar heated subsonic jet** $M_j = 0.756$, which mean density $\rho_0(x_2)$ obeys Crocco-Busemann's relation, is considered.

The **jet is not spreading**, its velocity profiles follows $u_{0,1}(x_2) = u_j\, e^{-\log(2)(x_2/b)^2}$

A Gaussian **acoustic source** on the axis $St \approx 0.085$ triggers **jet instability**.

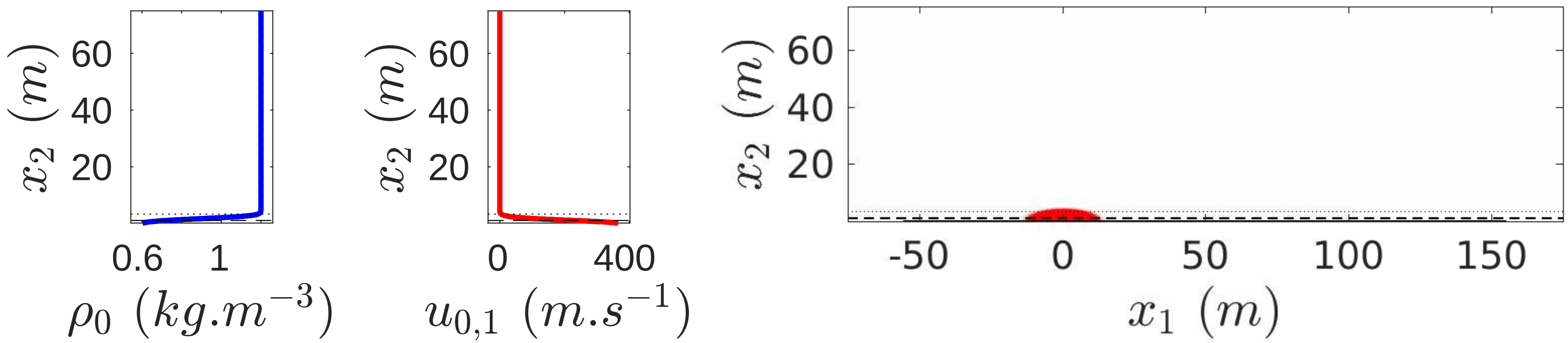

Capability to account for refraction effects

NASA Workshop test case

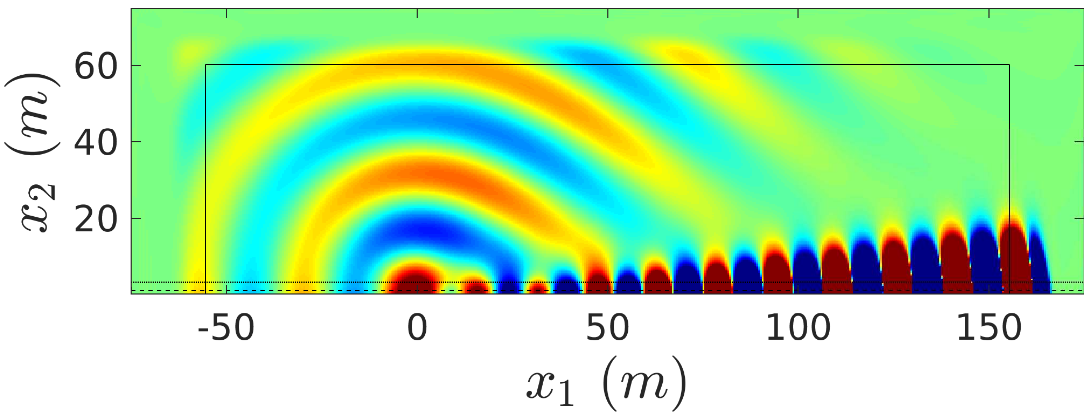

LEE, Lilley, EWE

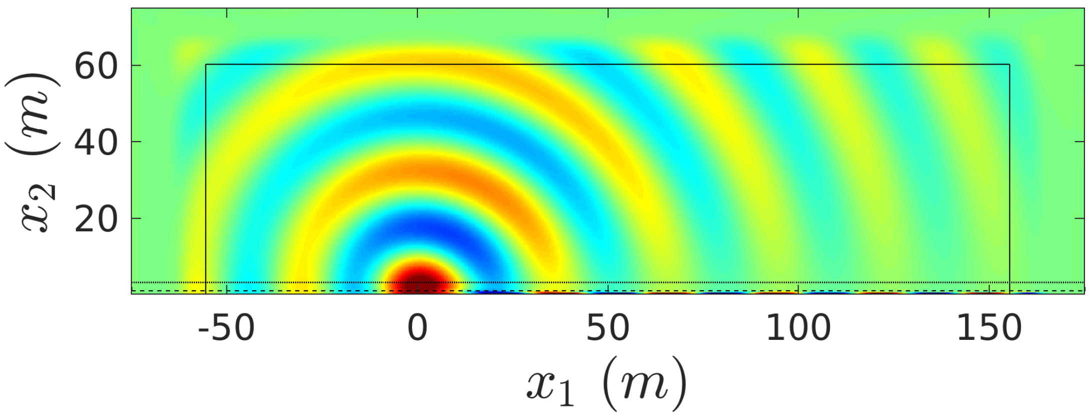

SEWE

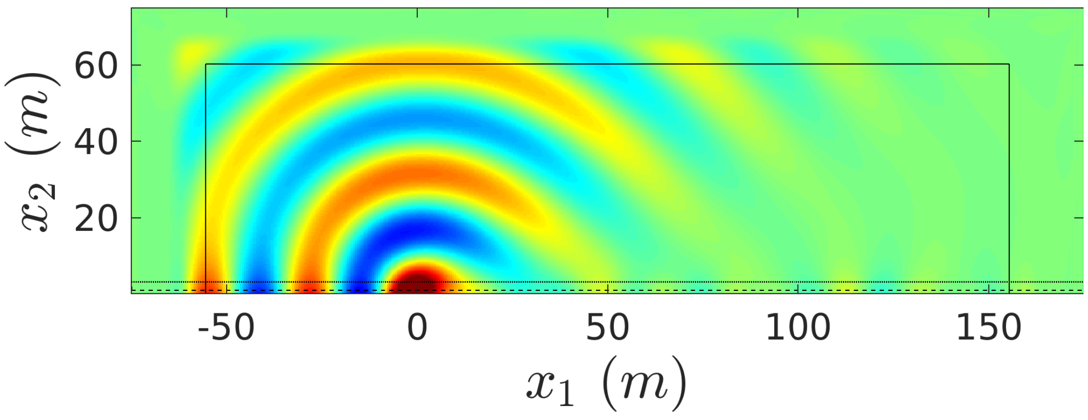

stable-Lilley

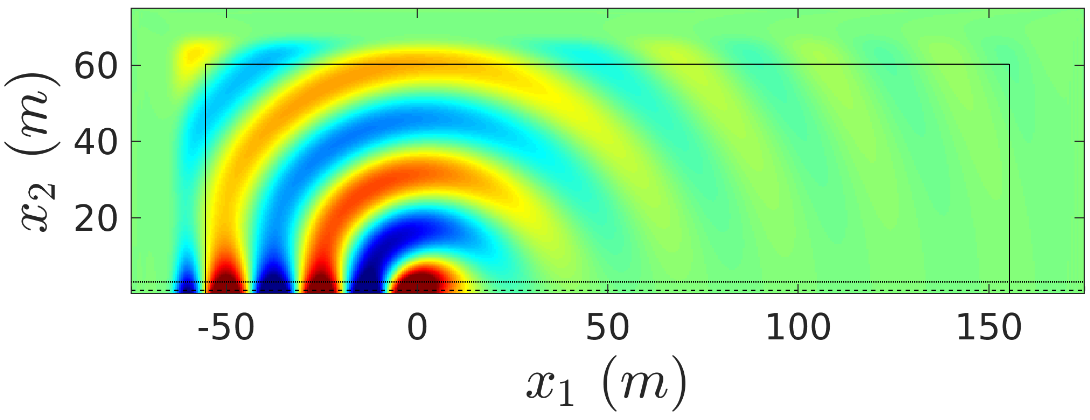

Helmholtz

- **NASA Workshop test case**

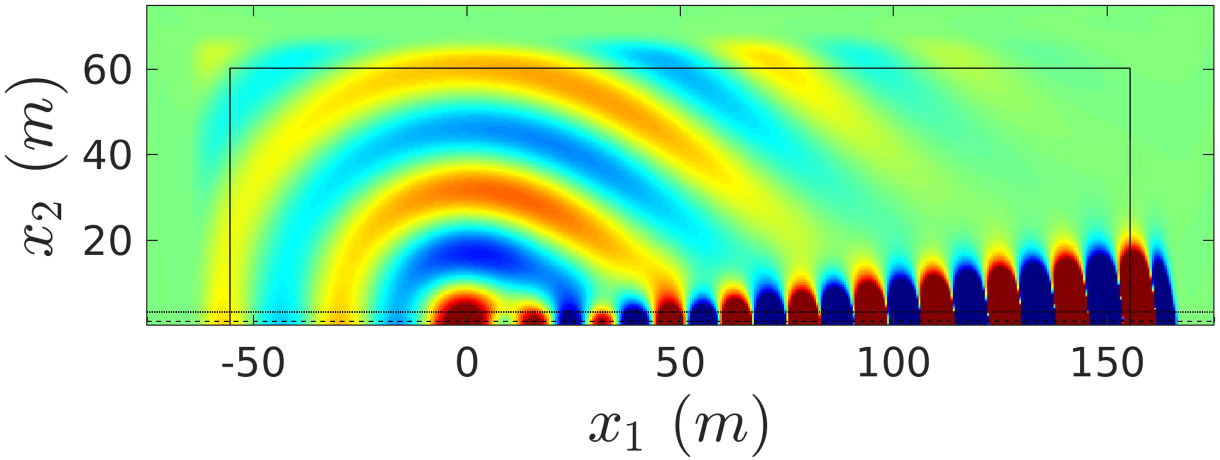

LEE

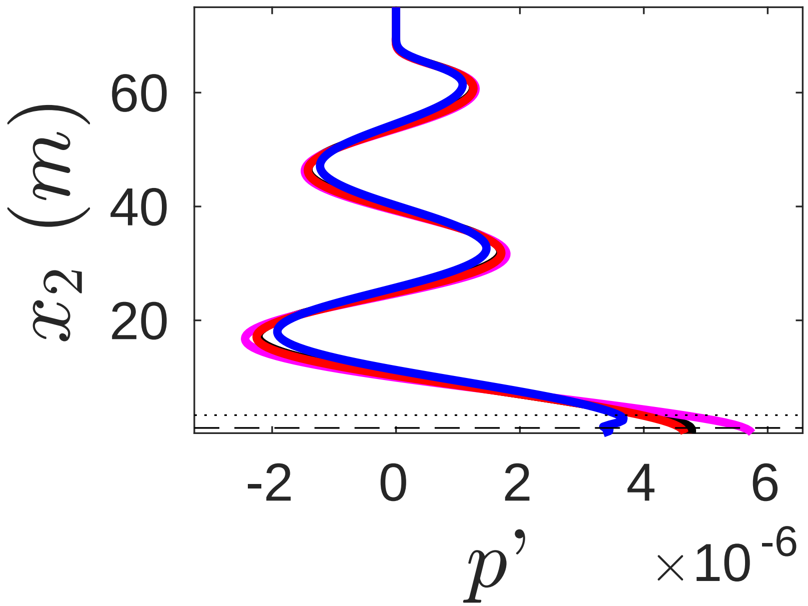

profile at $x_1 = 0m$

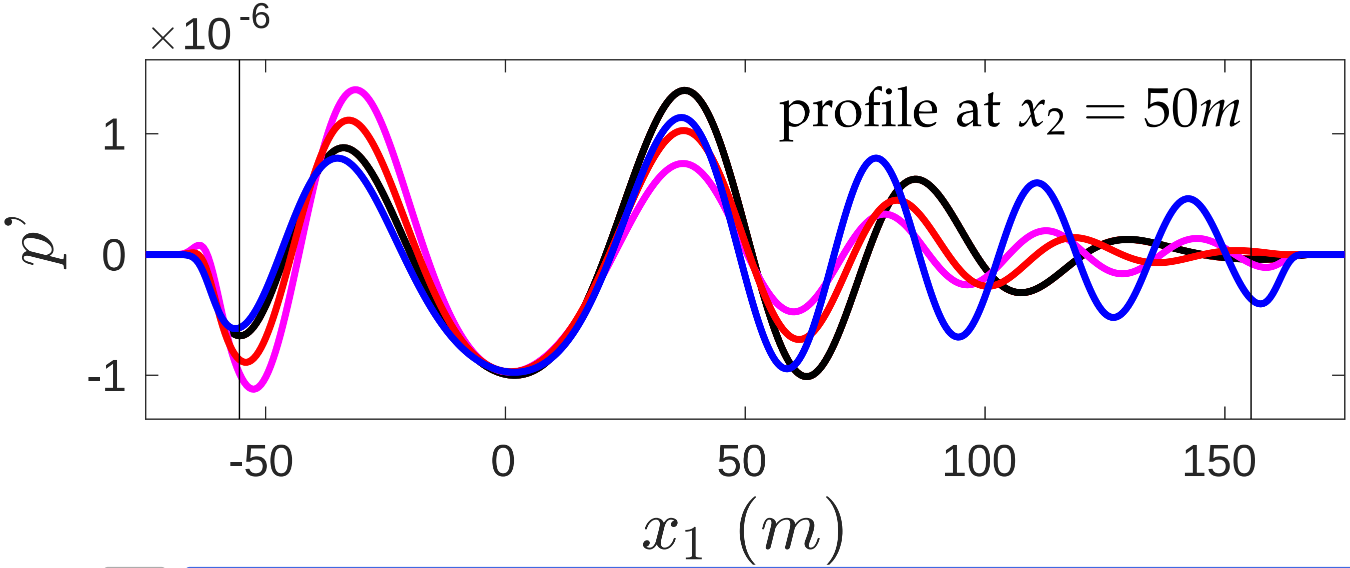

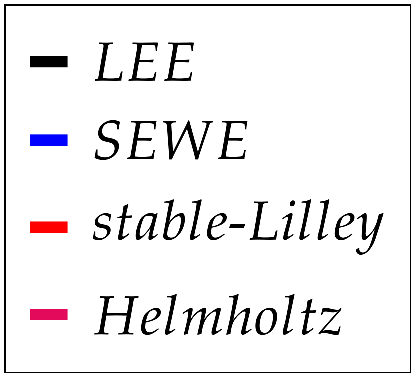

Overview of the propagation operators

	stable	self - adjoint	mean flow shearing
A) Linearised Euler Equation (LEE)			
B) Lilley's Equation			
C) Stabilised Lilley's Equation			
D) Helmholtz's Equation			
E) Euler's Wave Equation (EWE)			
F) Stabilised EWE (SEWE)			

Overview of the propagation operators

	stable	self - adjoint	mean flow shearing	density gradients
A) Linearised Euler Equation (LEE)				
B) Lilley's Equation				
C) Stabilised Lilley's Equation				
D) Helmholtz's Equation				
E) Euler's Wave Equation (EWE)				
F) Stabilised EWE (SEWE)				

Future perspectives

1. Examine deeper the **properties of SEWE**, links with potential acoustic theory
2. **Investigate on APE** and source filtering
3. **Parametric study** on a simplified but realistic jet configuration

Euler's Wave Equation (EWE)

Starting from the momentum and energy equations for sheared flows :

$$\begin{cases} D_{\mathbf{u}_0}(\mathbf{u}') + (\nabla \mathbf{u}_0)\mathbf{u}' + \dfrac{\nabla p'}{\rho_0} = \mathbf{S}_{\{\mathbf{u}'\}} \\ \\ D_{\mathbf{u}_0}(p') + \gamma p_0 \nabla \cdot \mathbf{u}' = S_{\{p'\}} \end{cases}$$

A wave equation for $\mathbf{u}'$ can be derived, namely **Euler's Wave Equation** :

$$D^2_{\mathbf{u}_0}(\mathbf{u}') + \left[(\nabla \mathbf{u}_0) + (\nabla \mathbf{u}_0)^T\right] D_{\mathbf{u}_0}(\mathbf{u}') + (\nabla \mathbf{u}_0)^T (\nabla \mathbf{u}_0)\mathbf{u}' - a_0^2 \Delta \mathbf{u}' - a_0^2 \nabla \times \nabla \times \mathbf{u}' = \mathbf{S}_{EWE}$$

Where : $\mathbf{S}_{EWE} = -\dfrac{\nabla S_{\{p'\}}}{\rho_0} + D_{\mathbf{u}_0}(\mathbf{S}_{\{\mathbf{u}'\}}) + (\nabla \mathbf{u}_0)^T \mathbf{S}_{\{\mathbf{u}'\}}$

By removing the curl term, the **Stabilised-EWE** (SEWE) can be obtained :

$$D^2_{\mathbf{u}_0}(\mathbf{u}') + \left[(\nabla \mathbf{u}_0) + (\nabla \mathbf{u}_0)^T\right] D_{\mathbf{u}_0}(\mathbf{u}') + (\nabla \mathbf{u}_0)^T (\nabla \mathbf{u}_0)\mathbf{u}' - a_0^2 \Delta \mathbf{u}' = \mathbf{S}_{EWE}$$

Sub-case A - stratified media at HF

Without flow

Same $\rho_0(x_2)$

$\omega_{HF} \approx 13\omega_{NASA}$

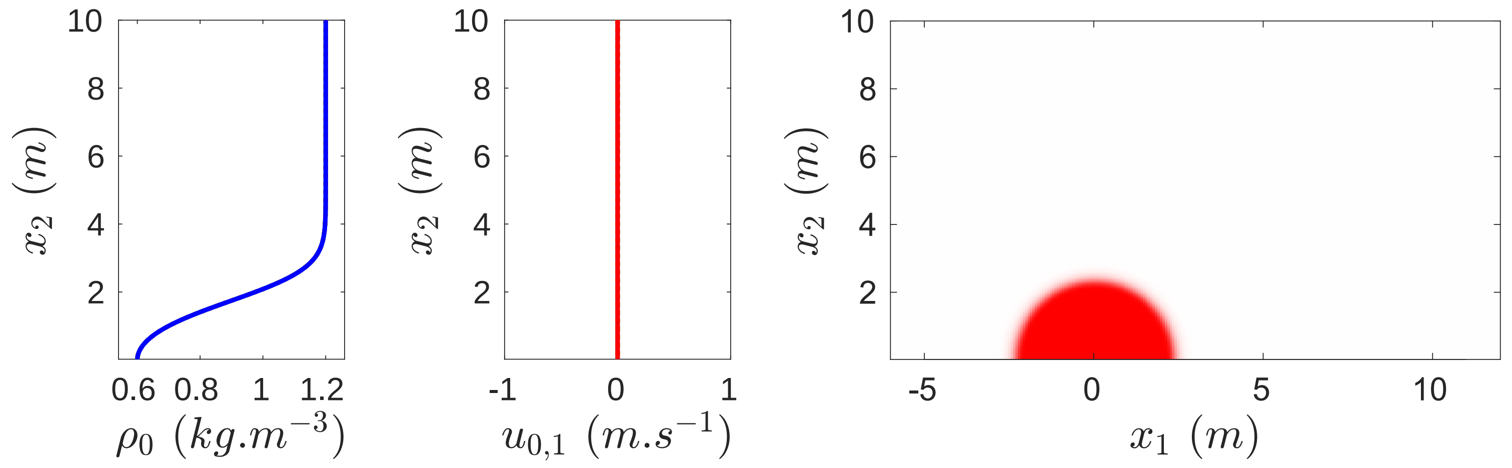

Sub-case B - stratified and sheared media at HF

Same $u_{0,1}(x_2)$

Same $\rho_0(x_2)$

$\omega_{HF} \approx 13\omega_{NASA}$

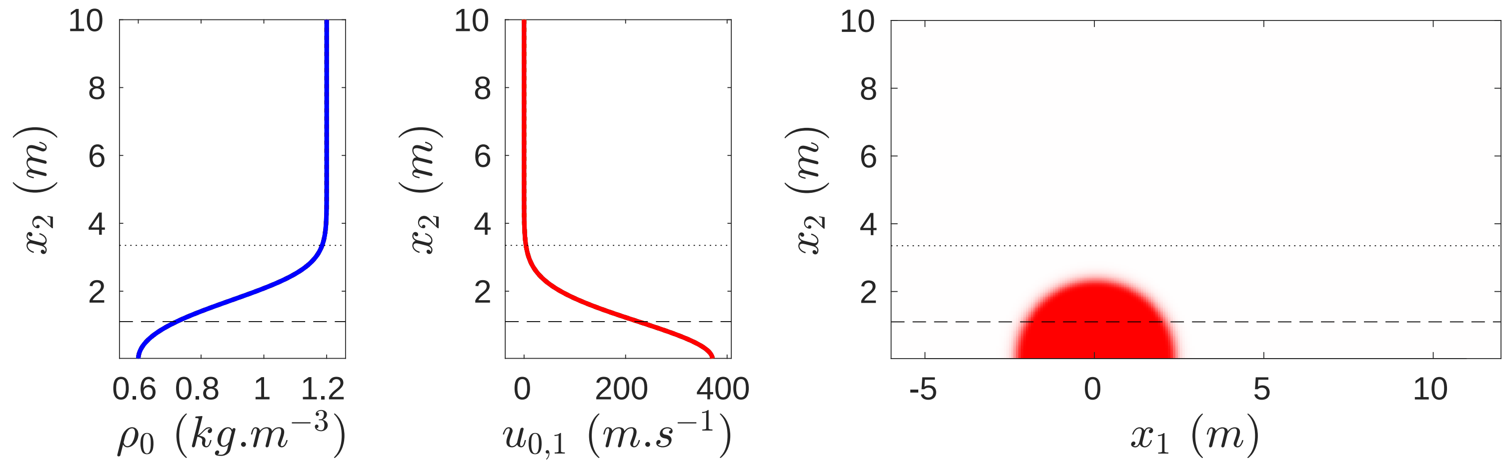

Sub-case A - stratified media at HF

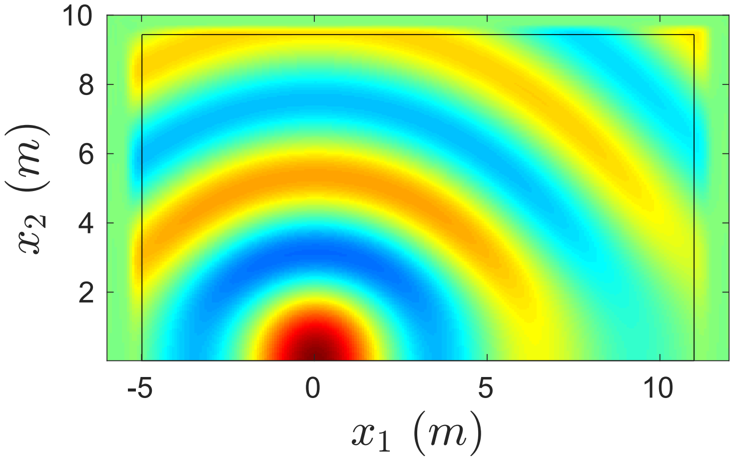

LEE, Lilley, stable-Lilley, Helmholtz, EWE

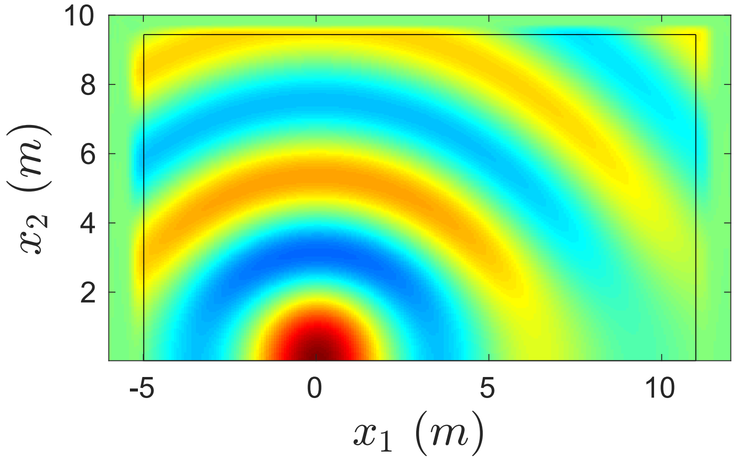

SEWE

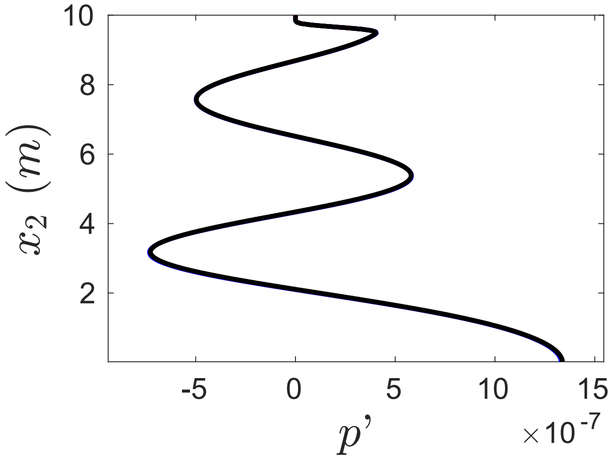

profile at $x_1 = 0m$

Field obtained with *SEWE* do not match perfectly with others!!

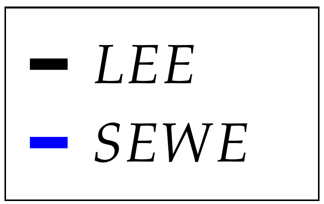

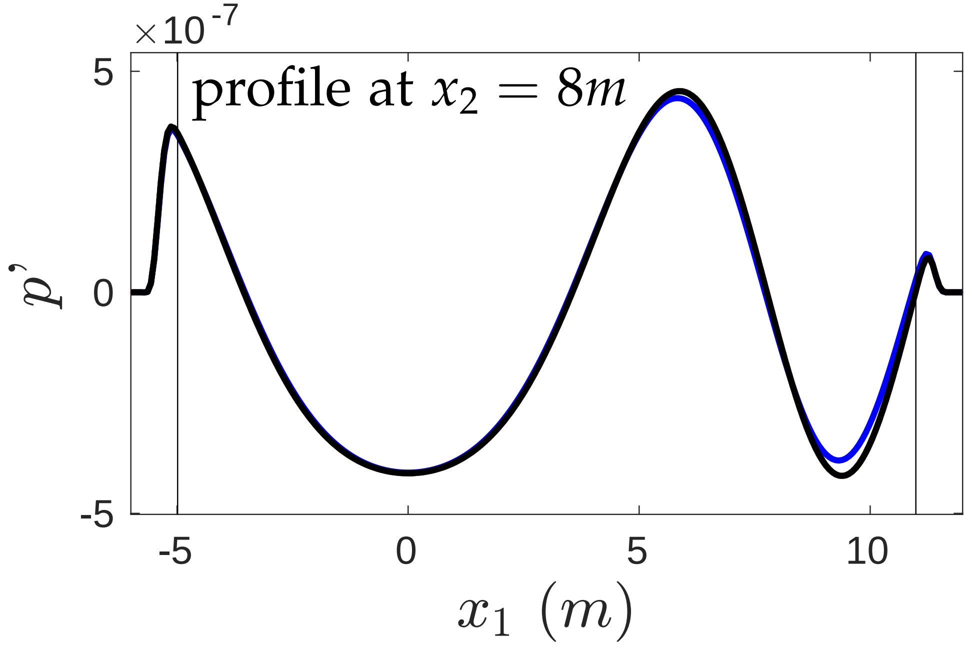

- **How to explain the differences ?**

Euler's Wave Equation **without flow**

$$\boxed{\frac{\partial^2 \mathbf{u}'}{\partial t^2} - a_0^2 \nabla \left(\nabla \cdot \mathbf{u}' \right) = \mathbf{0}}$$

With $\nabla \left(\nabla \cdot \mathbf{u}' \right) = \Delta \mathbf{u}' + \nabla \times \nabla \times \mathbf{u}'$

SEWE assumes $\nabla \times \nabla \times \mathbf{u}' = \mathbf{0} \implies \mathbf{w}' = \nabla \times \mathbf{u}' = \mathbf{0}$ **potential acoustic**

Considering $\nabla \times \{EWE\} \implies$ $\boxed{\frac{\partial^2 \mathbf{w}'}{\partial t^2} = \nabla a_0^2 \times \nabla \left(\nabla \cdot \mathbf{u}' \right) \neq \mathbf{0}}$

In presence of density gradients, acoustic is no more a potential field.

- ## Overview of the propagation operators

	stable	self - adjoint	density gradients	mean flow shearing
A) Linearised Euler Equation (LEE)				
B) Lilley's Equation				
C) Stabilised Lilley's Equation				
D) Helmholtz's Equation				
E) Euler's Wave Equation (EWE)				
F) Stabilised EWE (SEWE)				

- **Sub-case B - stratified and sheared media at HF**

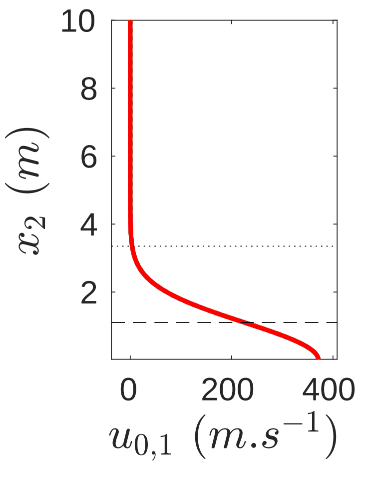

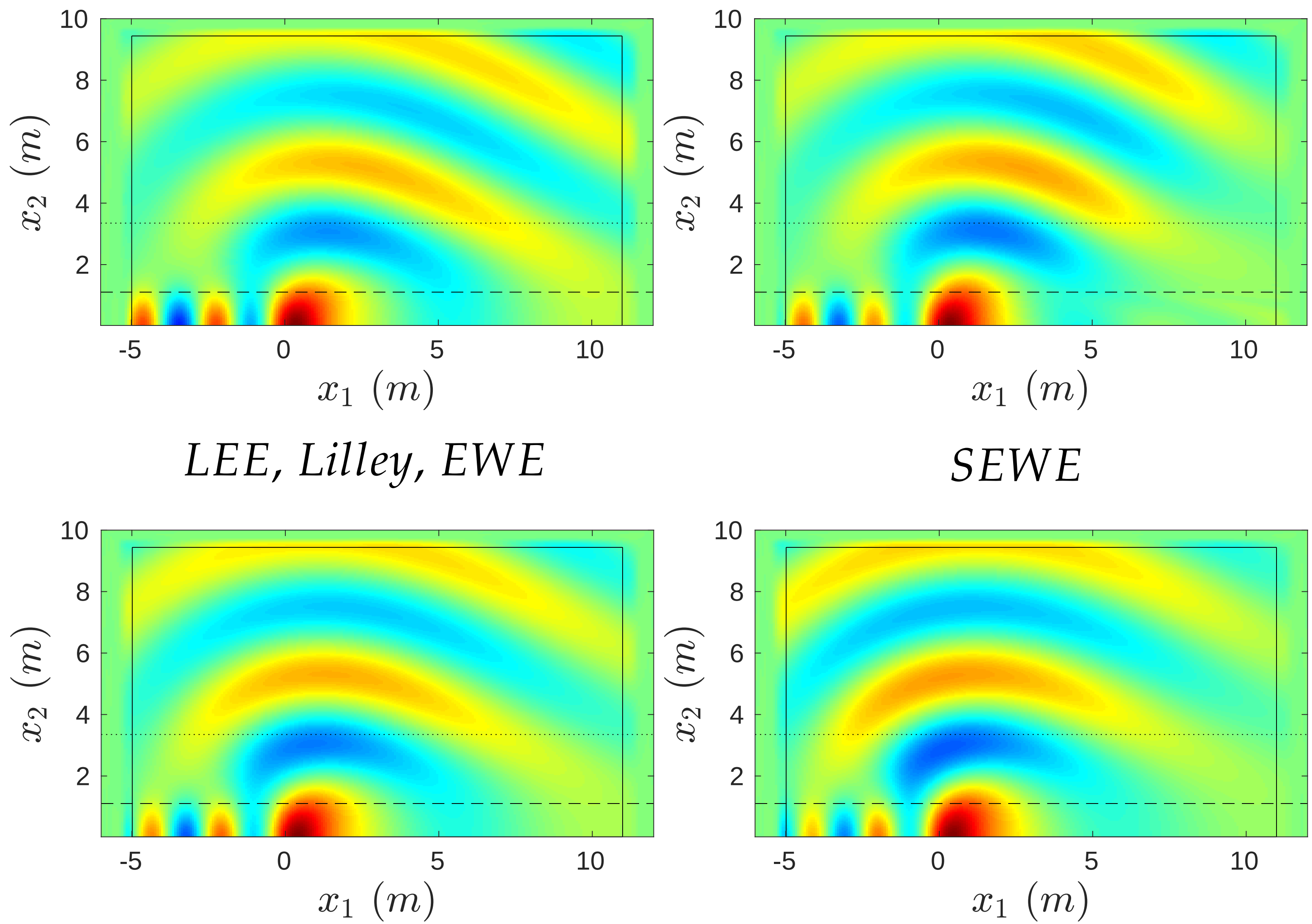

LEE, Lilley, EWE

SEWE

stable-Lilley

Helmholtz

- **Sub-case B - stratified and sheared media at HF**

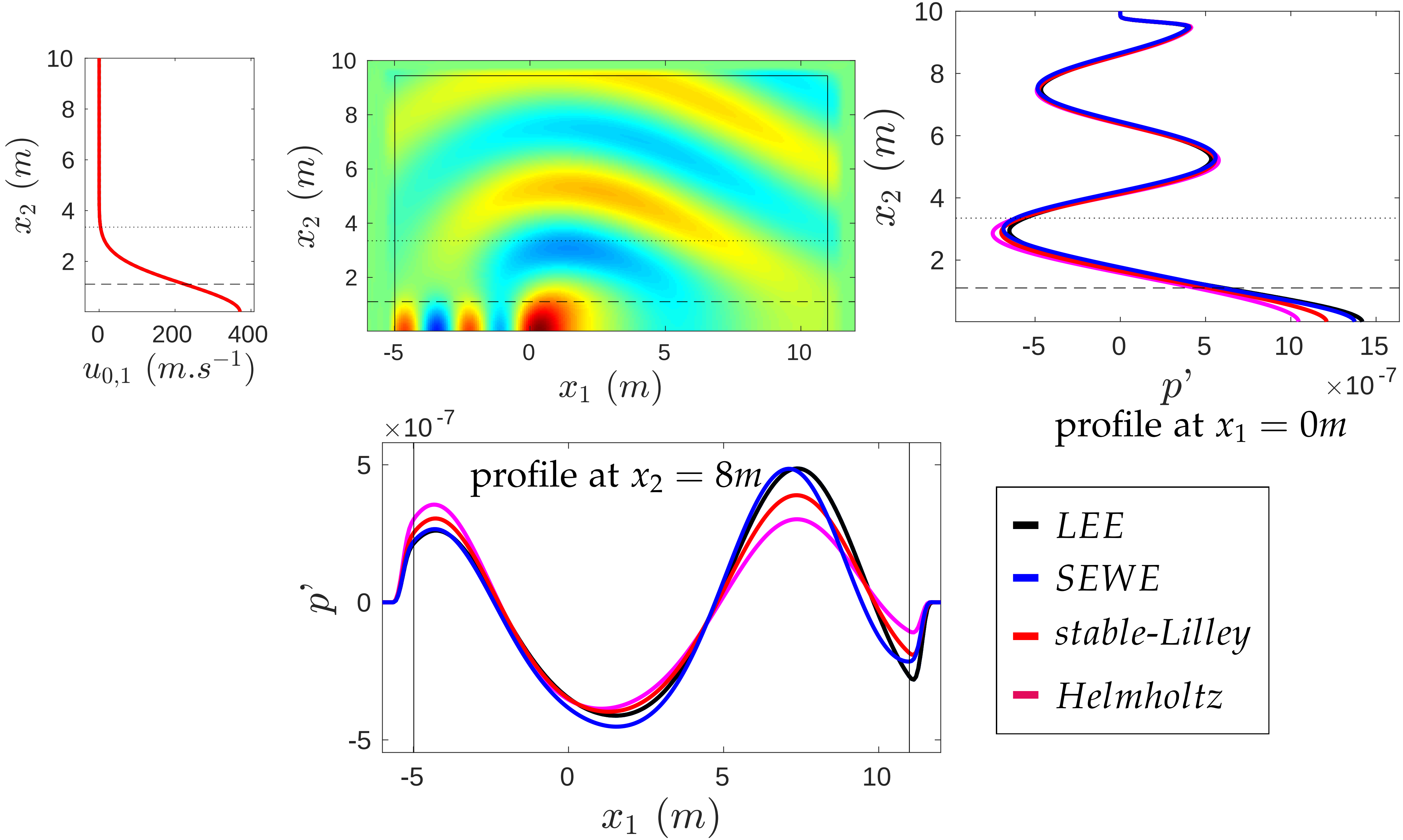

- NASA Workshop test case

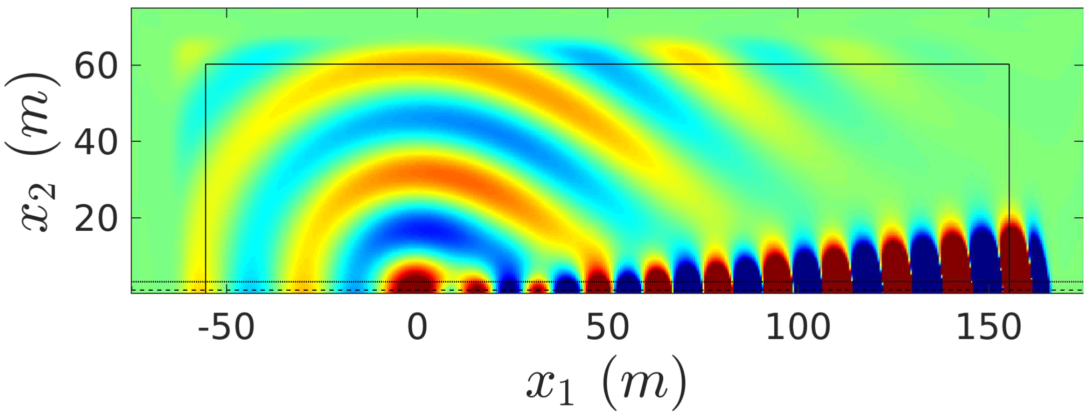

LEE

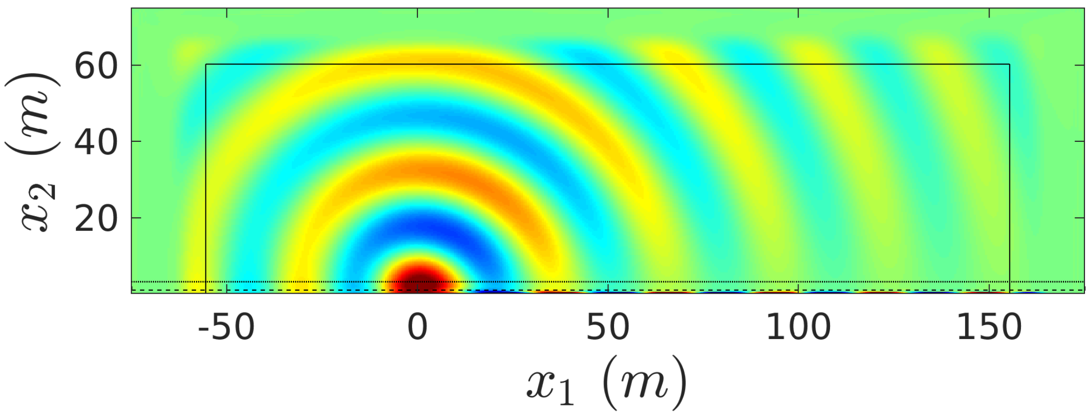

SEWE

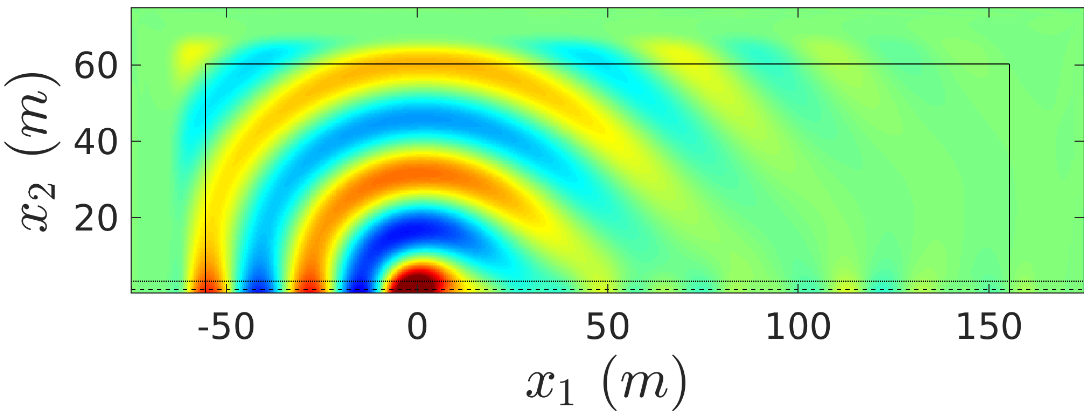

stable-Lilley

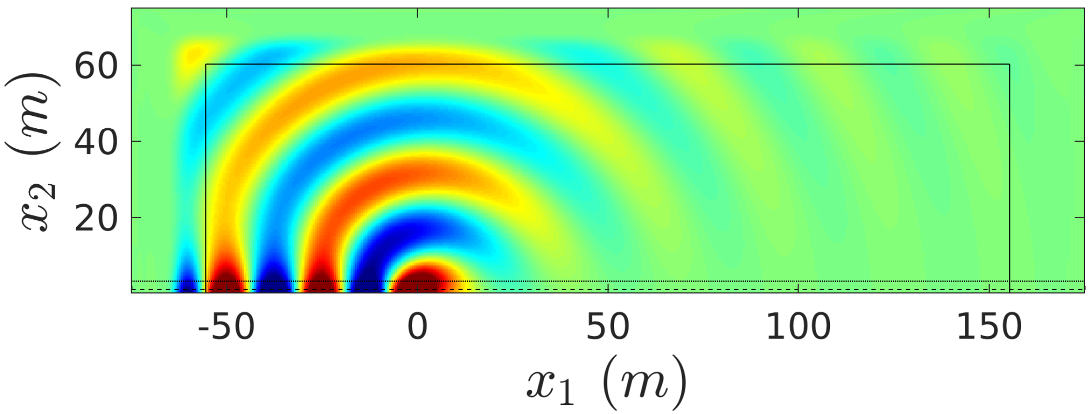

Helmholtz

NASA Workshop test case

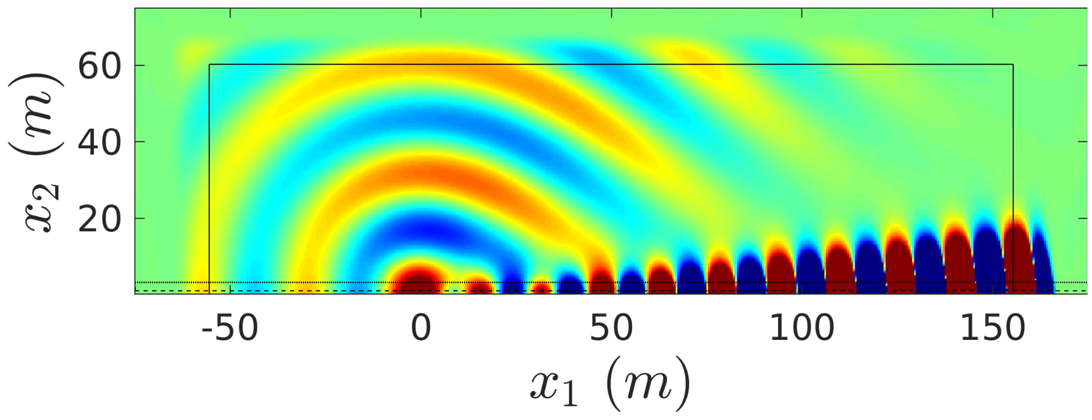

LEE

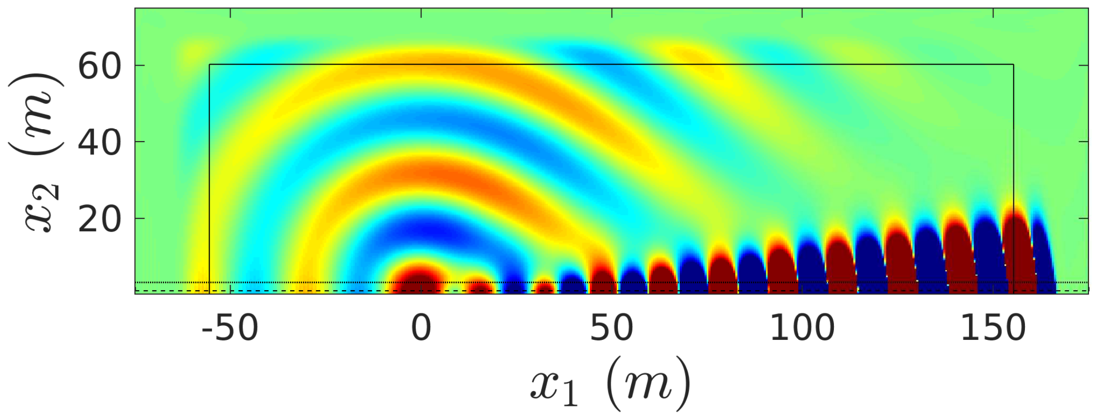

EWE

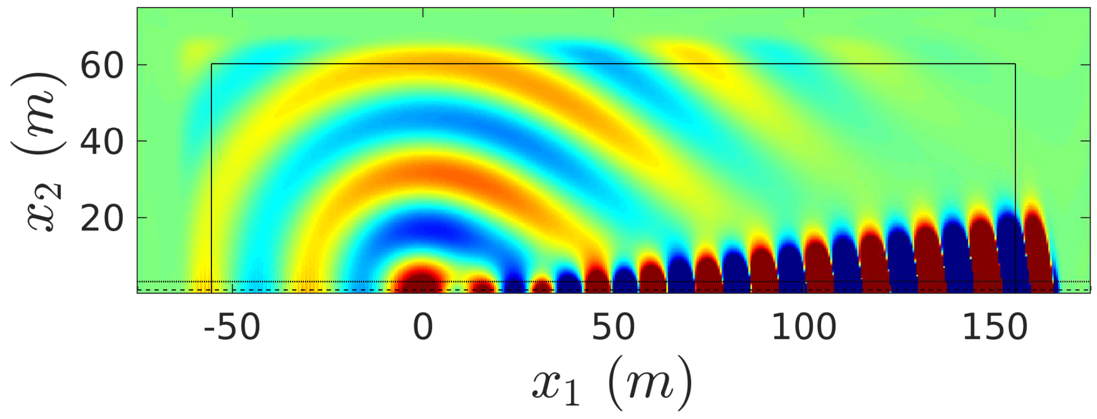

Lilley

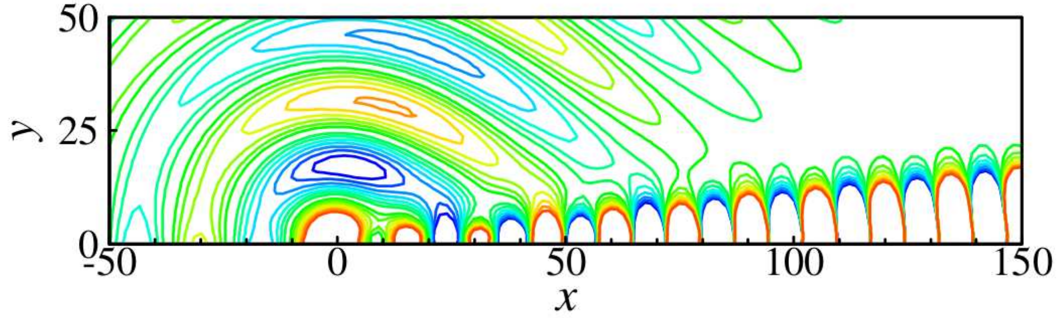

Zheng, Miller, Zhuang (LEE)

Propagation Effects on Acoustic Particle Velocity Sensing

Sandra L. Collier[1*], Max F. Denis[1], David A. Ligon[1], Latasha I. Solomon[1], John M. Noble[1], W.C. Kirkpatrick Alberts, II[1], Leng K. Sim[1], Christian G. Reiff[1], Deryck D. James[1], and Madeline M. Erikson[2],

[1]U.S. Army Research Laboratory
[2]U.S. Military Academy
*sandra.l.collier4.civ@mail.mil

International Symposium on Long Range Sound Propagation
12-14 May 2018, Lyon, France

Atmospheric Effects on Particle Velocity

Wave propagation in a random medium may be characterized by the scattering regime. From previous studies of the pressure field:

- Unsaturated regime
  - Weak scattering from inhomogeneities
  - Small turbulent fluctuations and/or the propagation range is short, both with respect to wavelength
  - Minimal variations in amplitude and phase
- Saturated regime
  - Strong scattering from inhomogeneities
  - Large turbulent fluctuations and/or the propagation range is large, with respect to wavelength.
  - Strong fluctuations in both amplitude and phase
- Partial Saturation
  - Transition between regimes

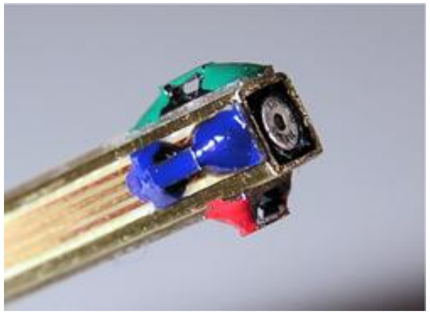

Microflown Vector Sensor

- Atmospheric turbulence in the fully saturated regime significantly degrades the signal which results in poor beamforming capabilities.
- The atmospheric conditions, together with other propagation factors, lead to different statistical distributions of the received signal.

Experimental and theoretical investigations have been conducted for the pressure field, we wish to do the same for the particle velocity field.

Experimentally, we use direct measurements of the particle velocity (Microflown vector sensors).

Scattering Regimes

$\psi = p/|p| = e^{\chi}$, $\phi = \Im(\chi)$, $u = \Re(\chi)$

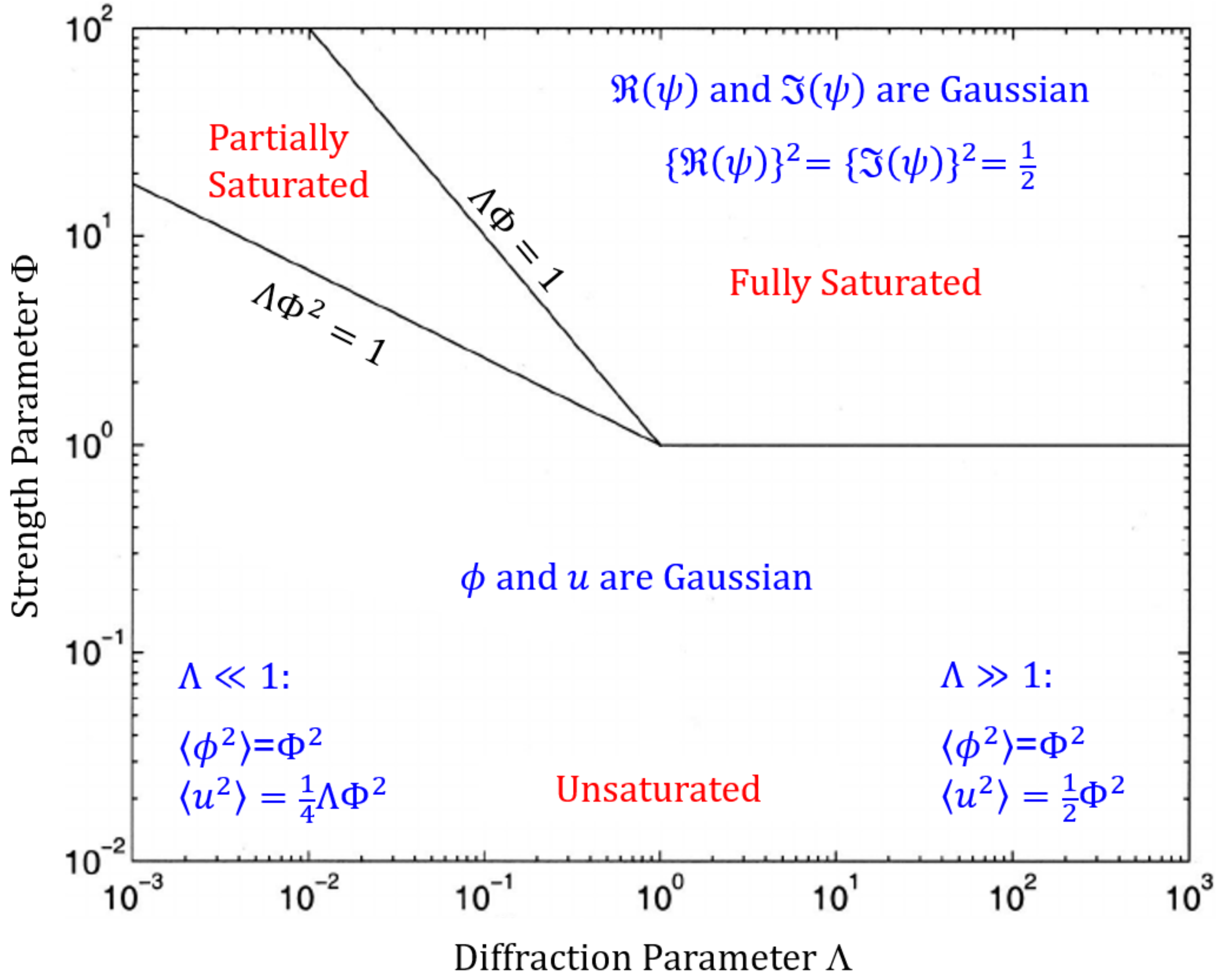

Southern Maryland

Experimental Day	Temperature (C)	Humidity (%)	Sound speed (m/s)	Wind speed (m/s)	Wind direction (deg)
13 Sep 2016	24.1±0.1	70.6±0.6	346.0±0.1	2.7±0.6	233.0±9.3
14 Sep 2016	23.0±0.1	77.5±0.7	345.9±0.1	2.6±0.4	273.0±19.3

Experimental Site

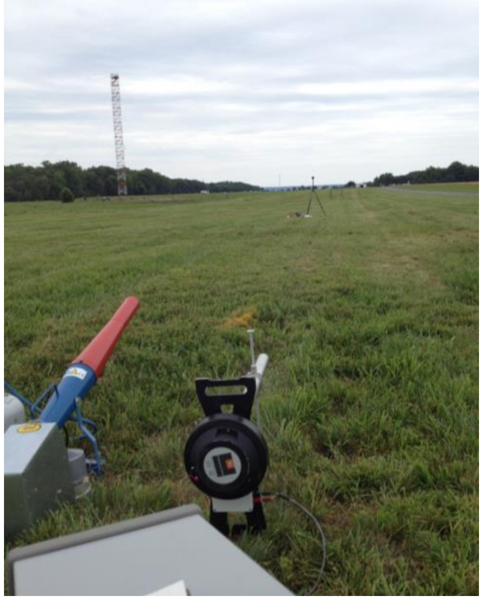

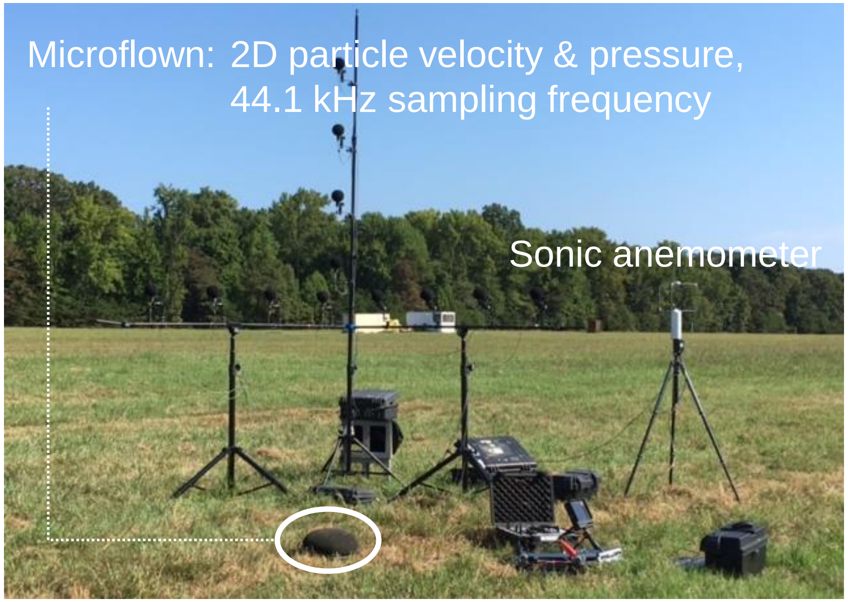

Typical Propane Cannon Measurements: Unfiltered, B & K Microphone Arrays

Pressure @ 10 m | Pressure @ 100 m | Pressure @ 400 m

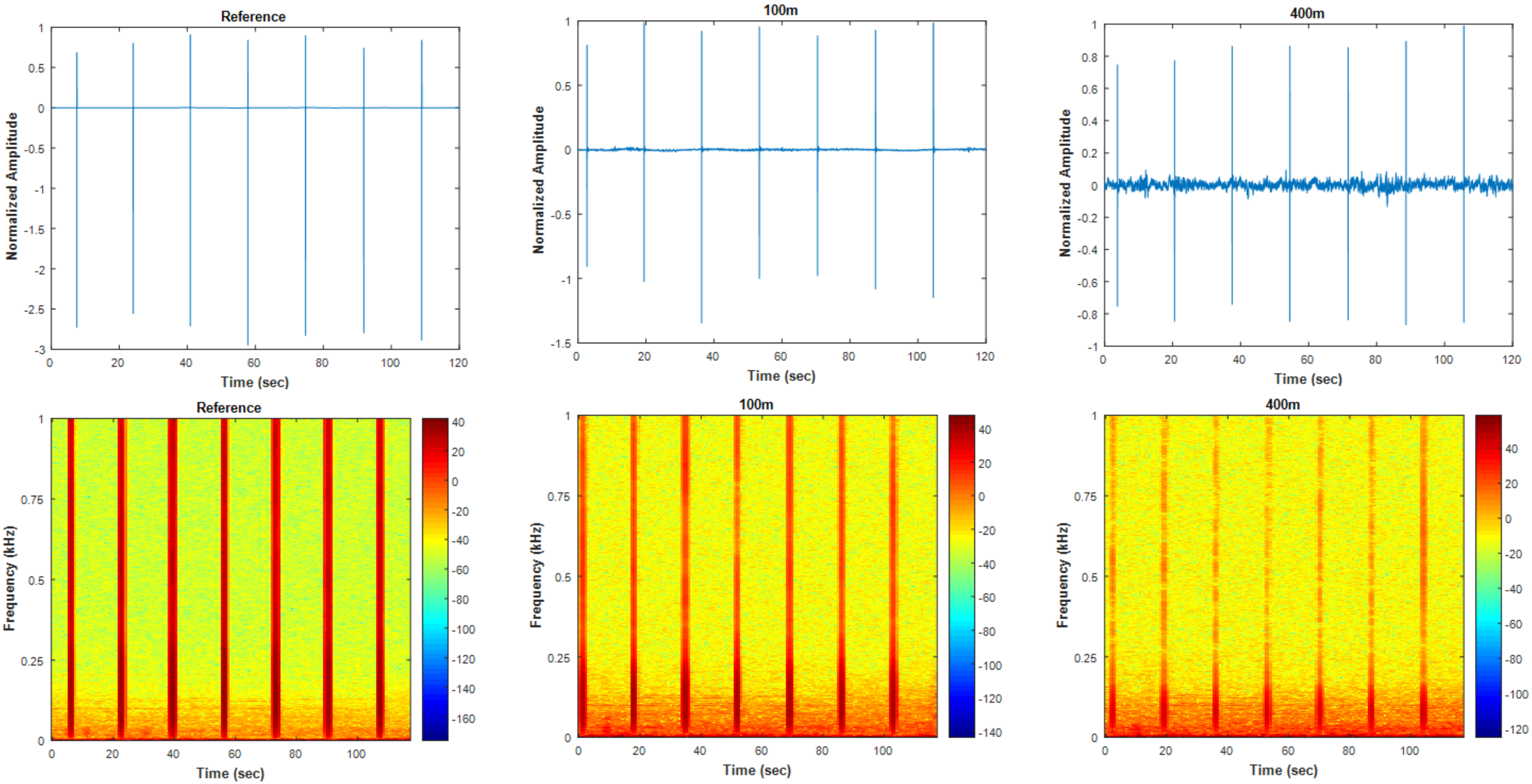

Unfiltered data.

Typical Propane Cannon Measurements: Filtered, B & K Microphone Arrays

Pressure @ 10 m | Pressure @ 100 m | Pressure @ 400 m

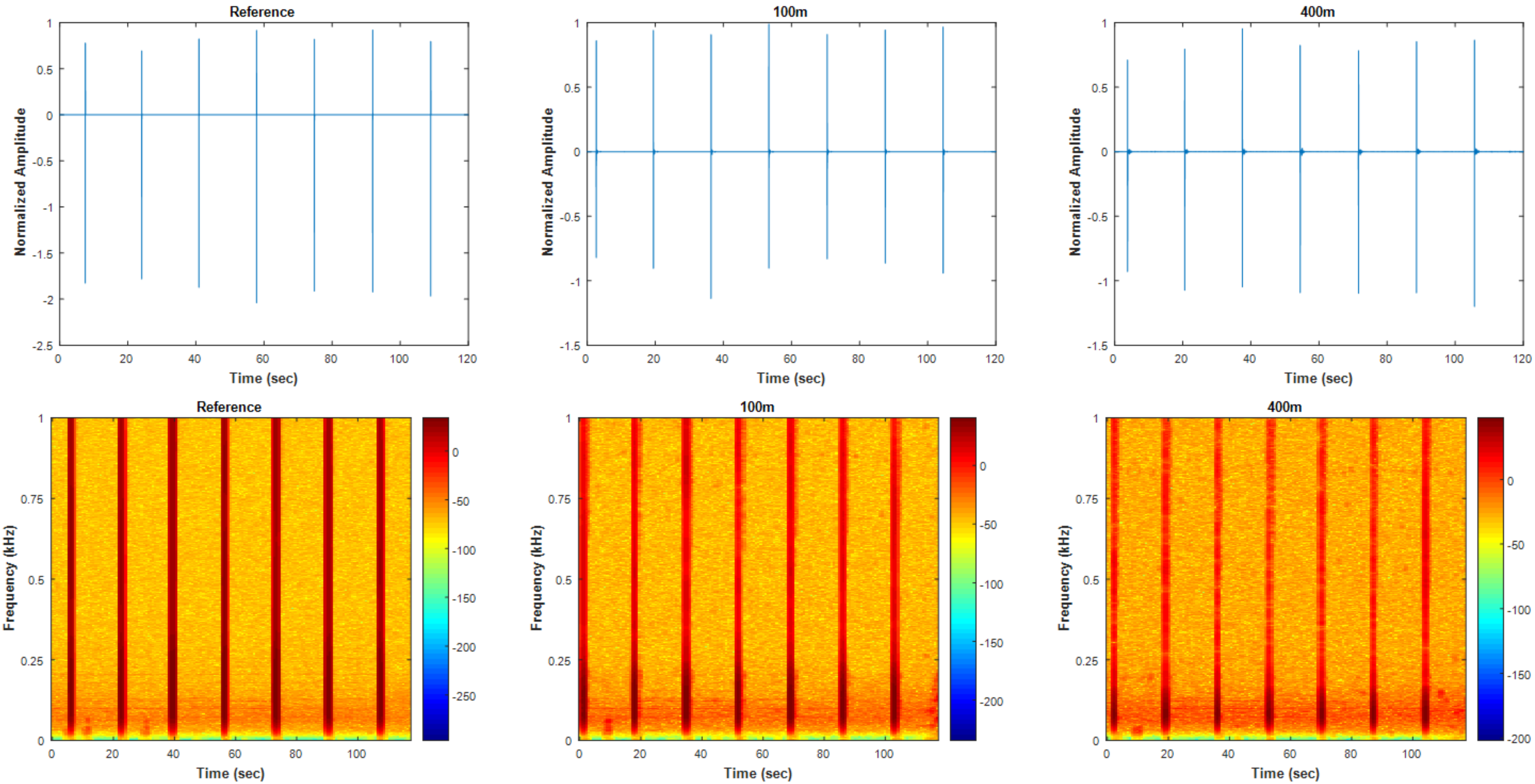

Filtered data: Weiner filter (~20 ms window) and band-pass filter (60 Hz – 3 kHz).

Typical Propane Cannon Measurements 2D Microflown @ 100 m (Unfiltered)

Pressure

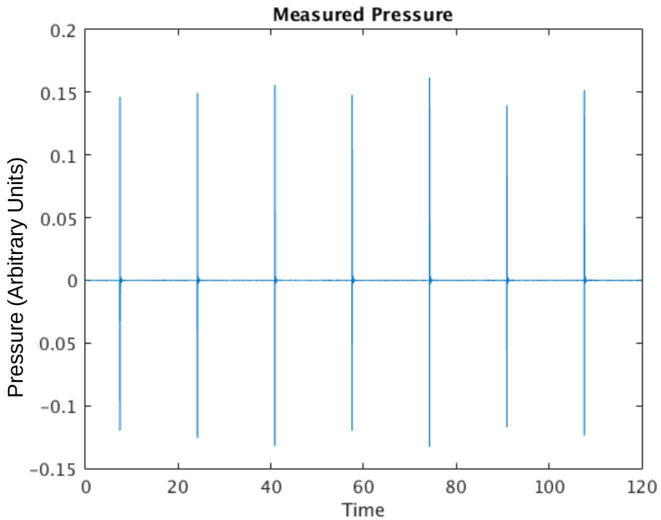

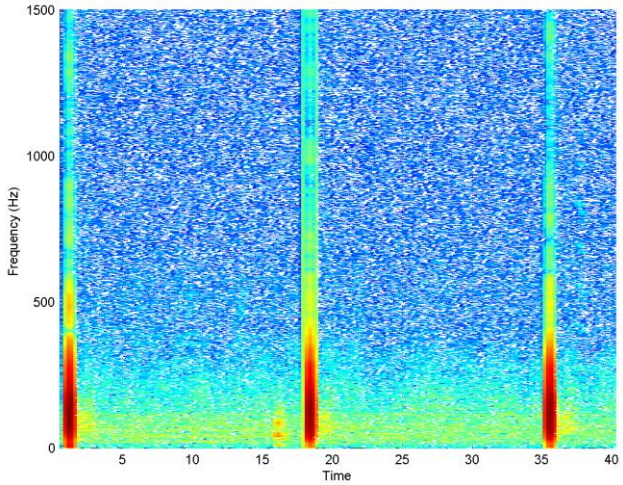

Particle Velocity

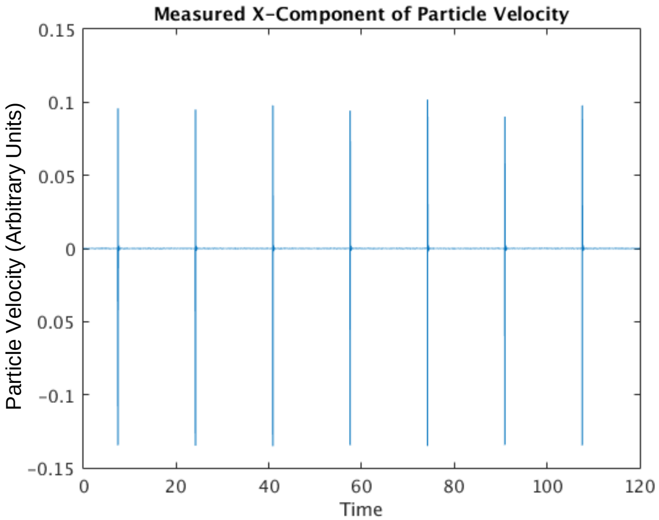

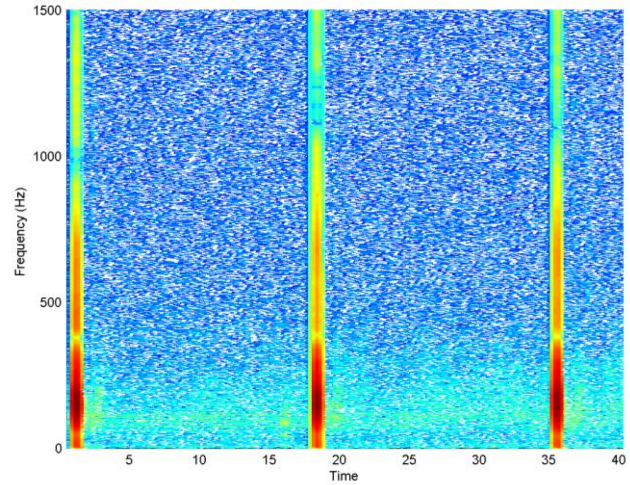

Scatter Plots for Normalized Signals @ 100 m: 80 Hz (upper) & 100 Hz (lower), 472 Shots

Pressure | Particle Velocity

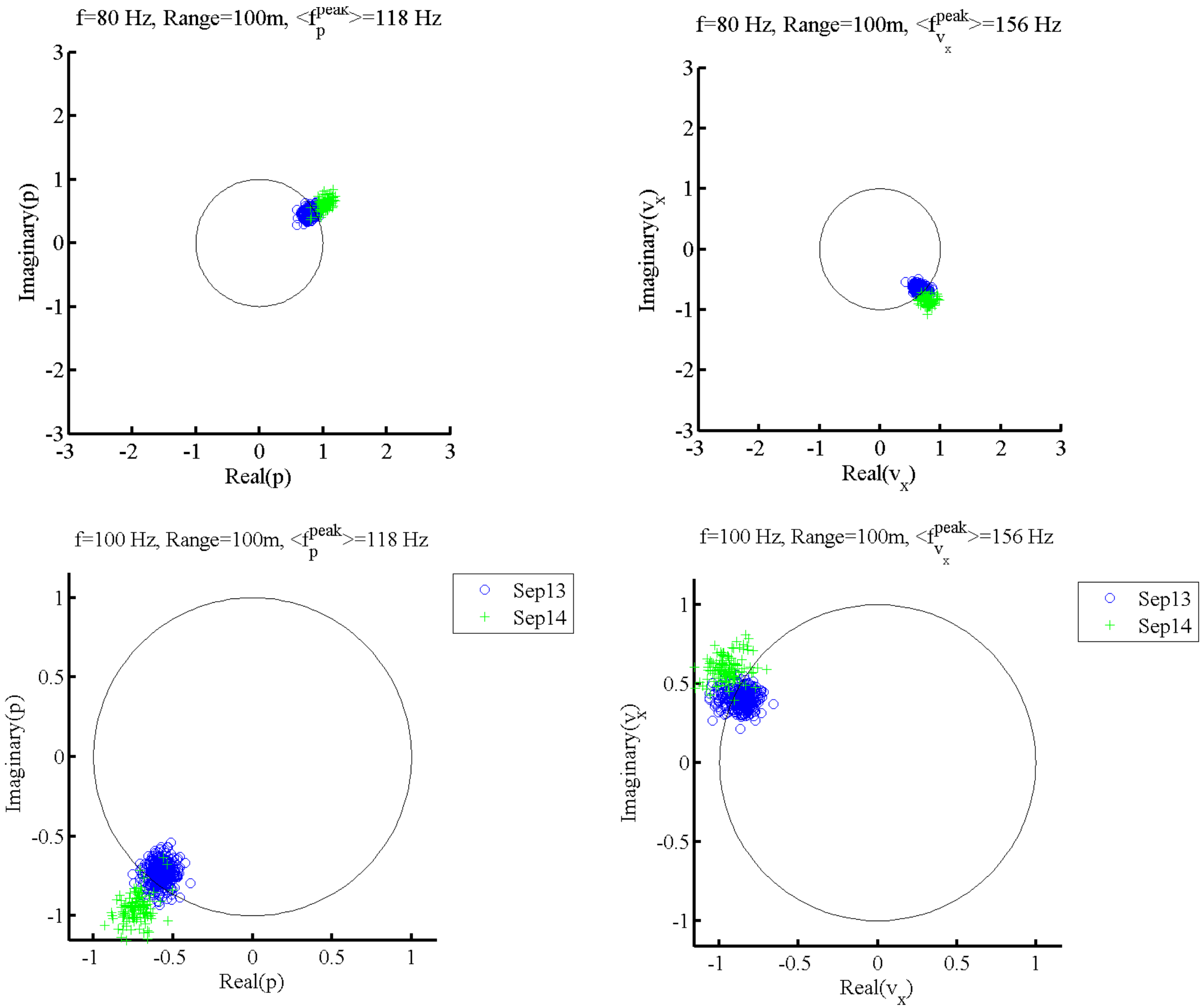

Scatter Plots for Normalized Signals @ 100 m: 150 Hz (upper) & 200 Hz (lower), 472 Shots

Pressure

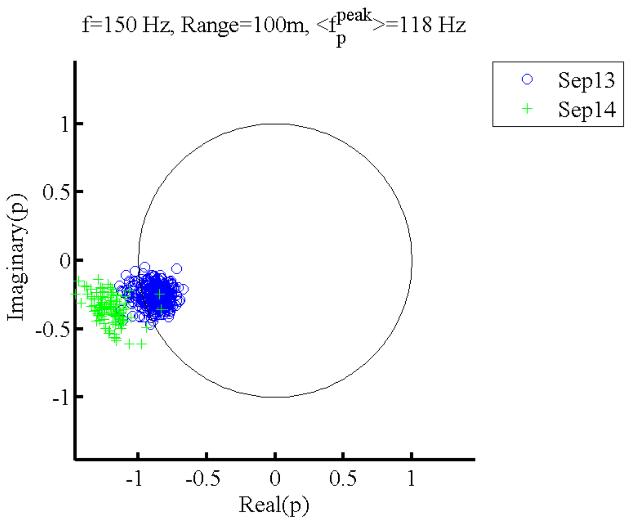

Particle Velocity

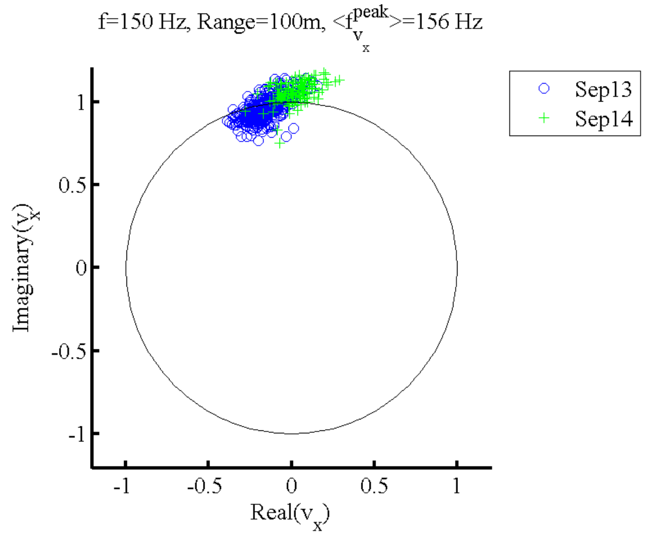

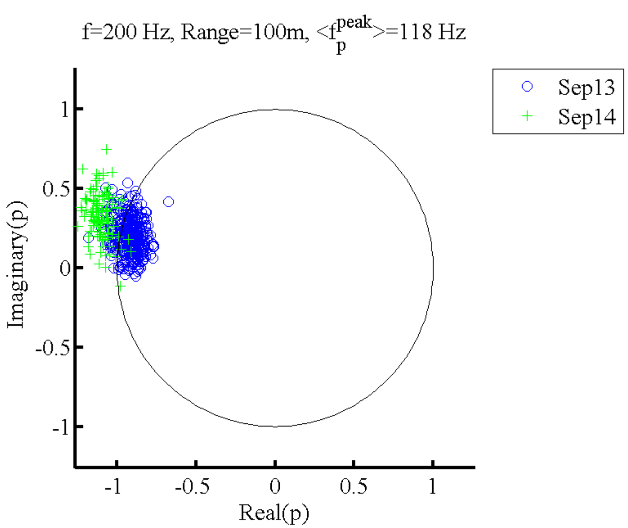

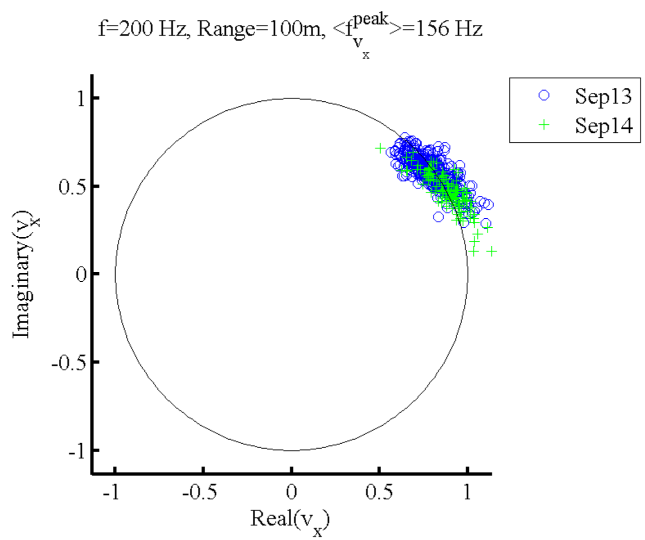

Scatter Plots for Normalized Signals @ 100 m: 250 Hz (upper) & 300 Hz (lower), 472 Shots

Pressure

Particle Velocity

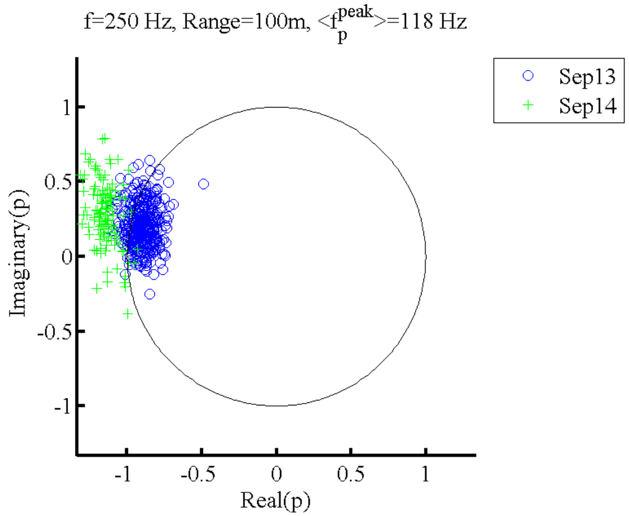

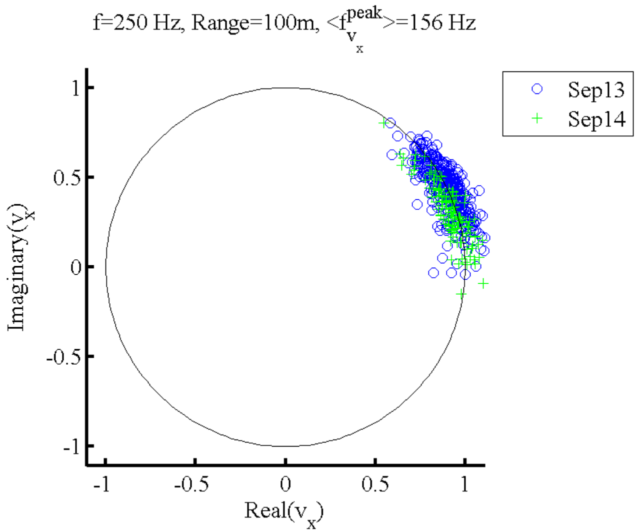

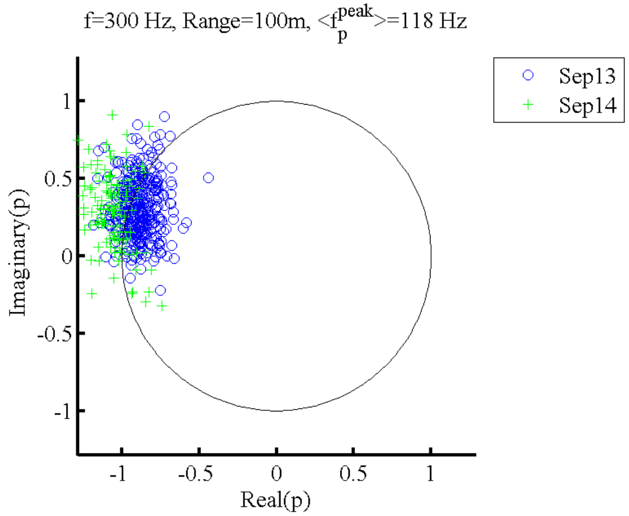

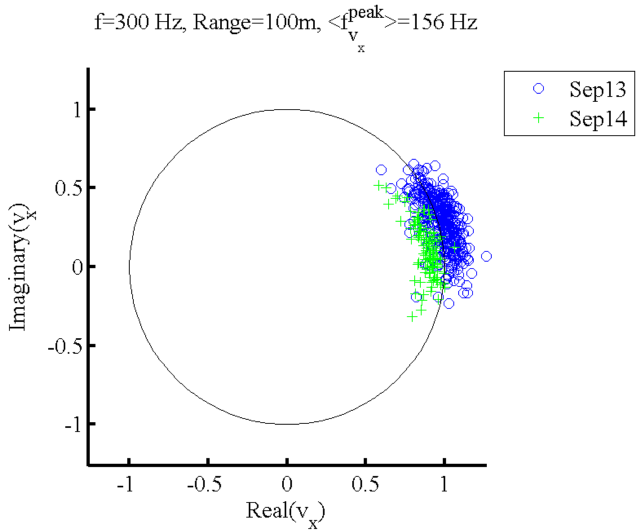

Scatter Plots for Normalized Signals @ 100 m: 400 Hz (upper) & 500 Hz (lower), 472 Shots

Pressure

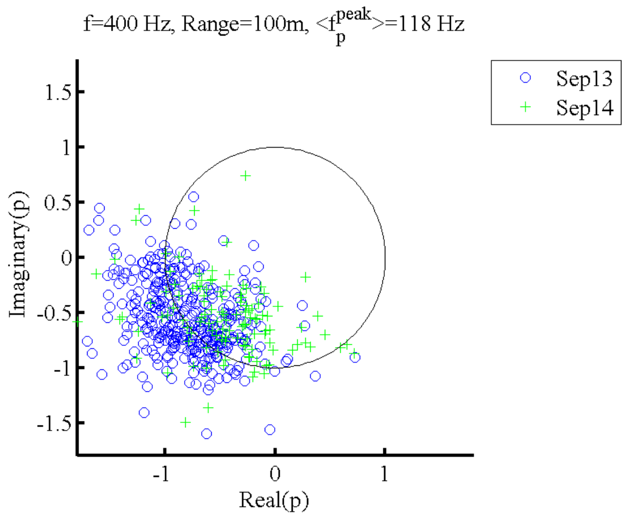

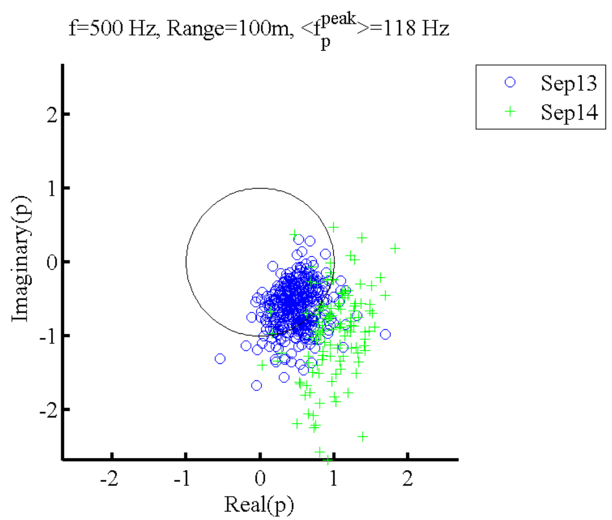

Particle Velocity

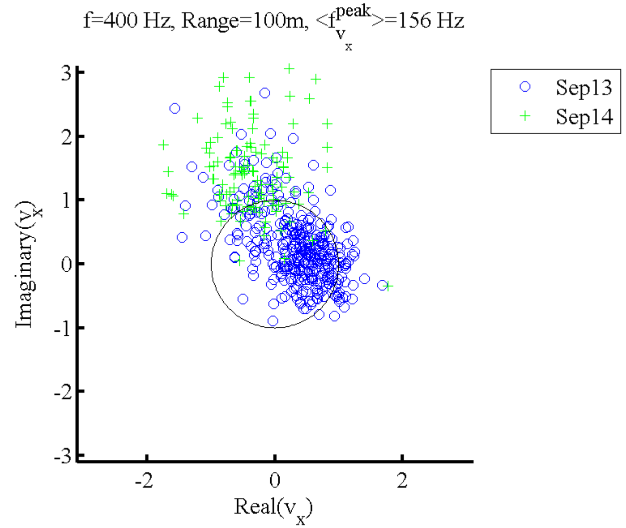

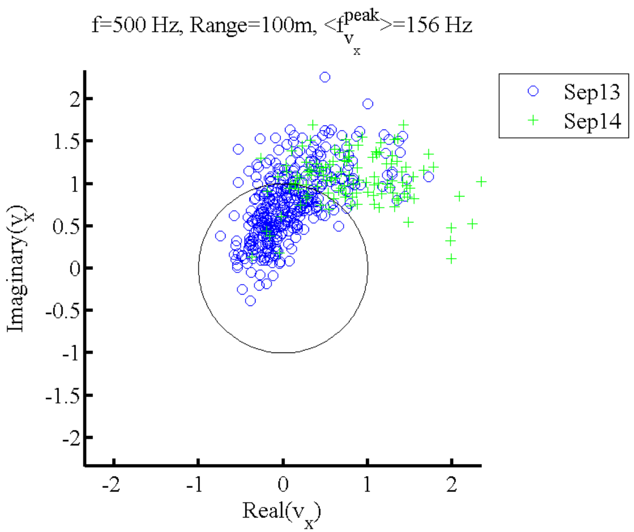

Typical Propane Cannon Measurements 2D Microflown @ 400 m (Unfiltered)

Pressure

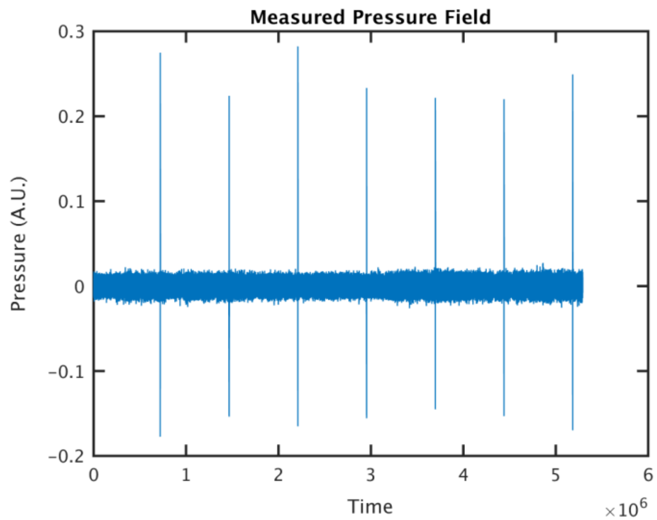

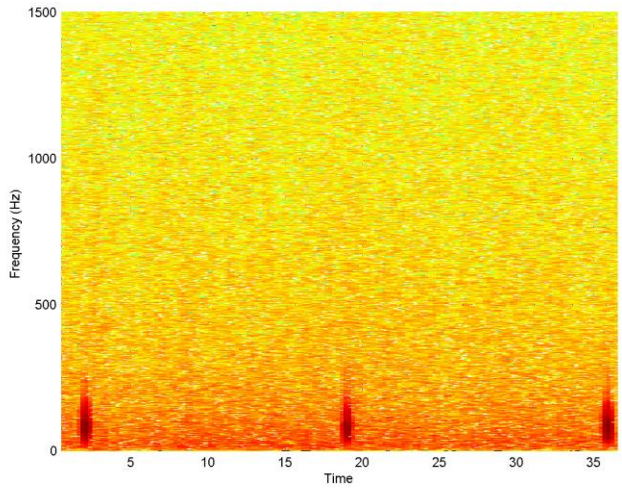

Particle Velocity

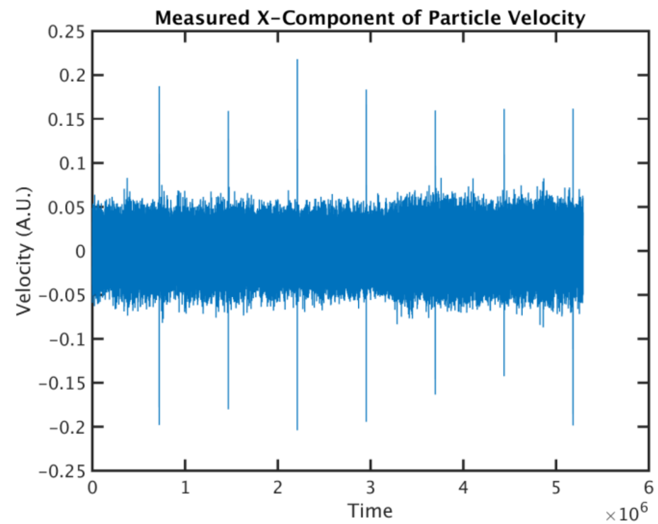

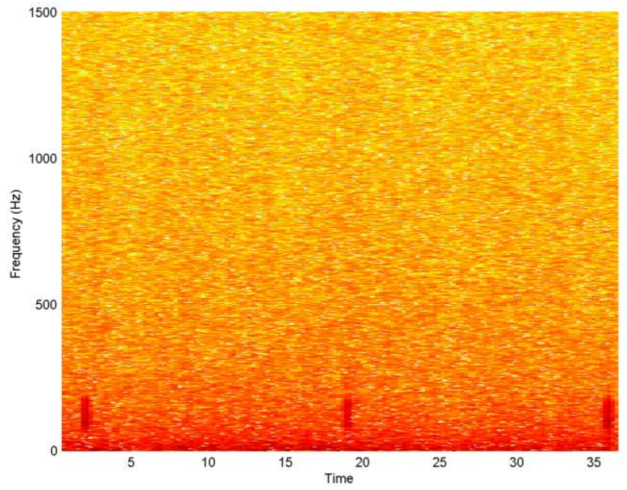

Scatter Plots for Normalized Signals @ 400 m: 80 Hz (upper) & 100 Hz (lower), 427 Shots

Pressure | Particle Velocity

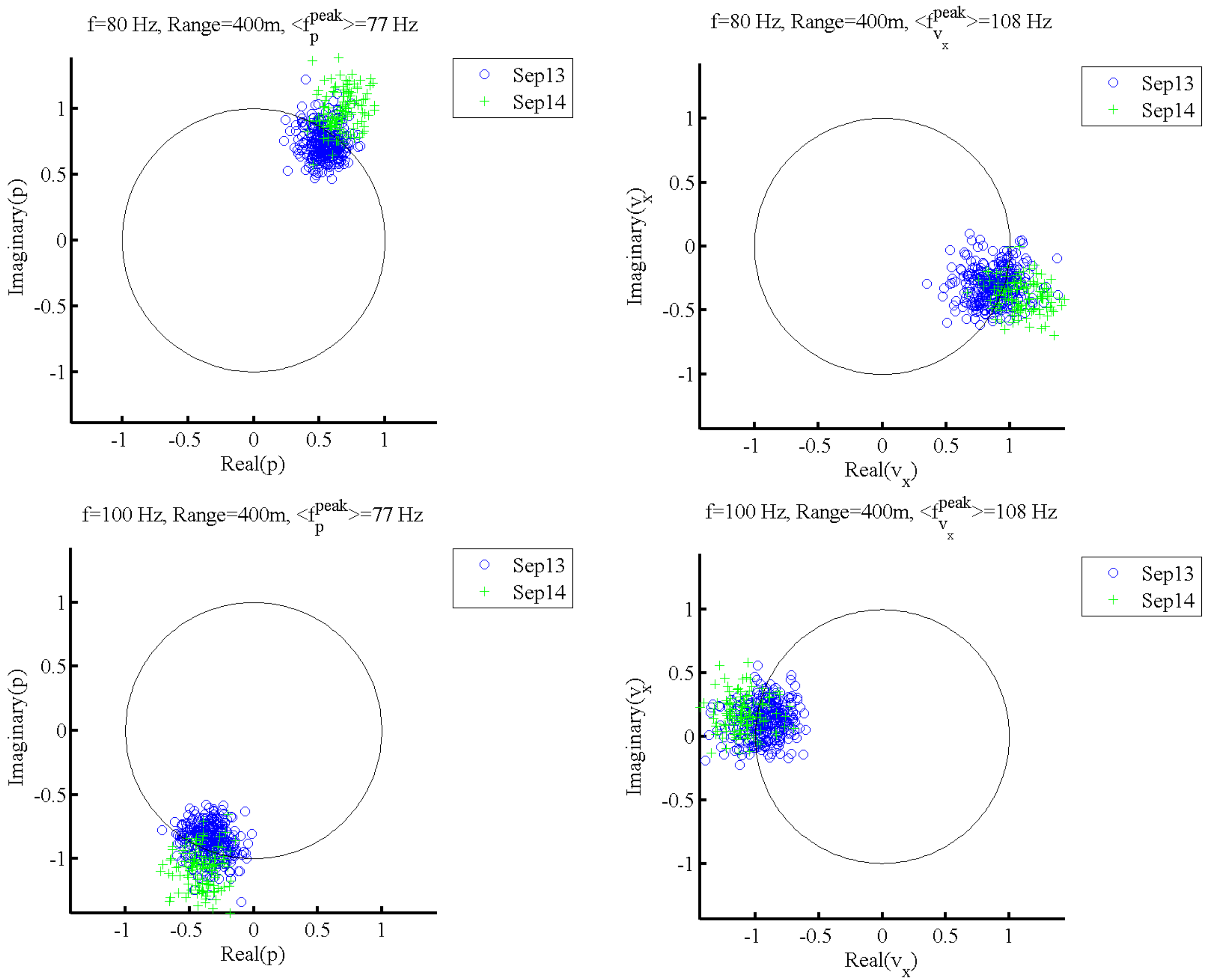

Scatter Plots for Normalized Signals @ 400 m: 150 Hz (upper) & 200 Hz (lower), 427 Shots

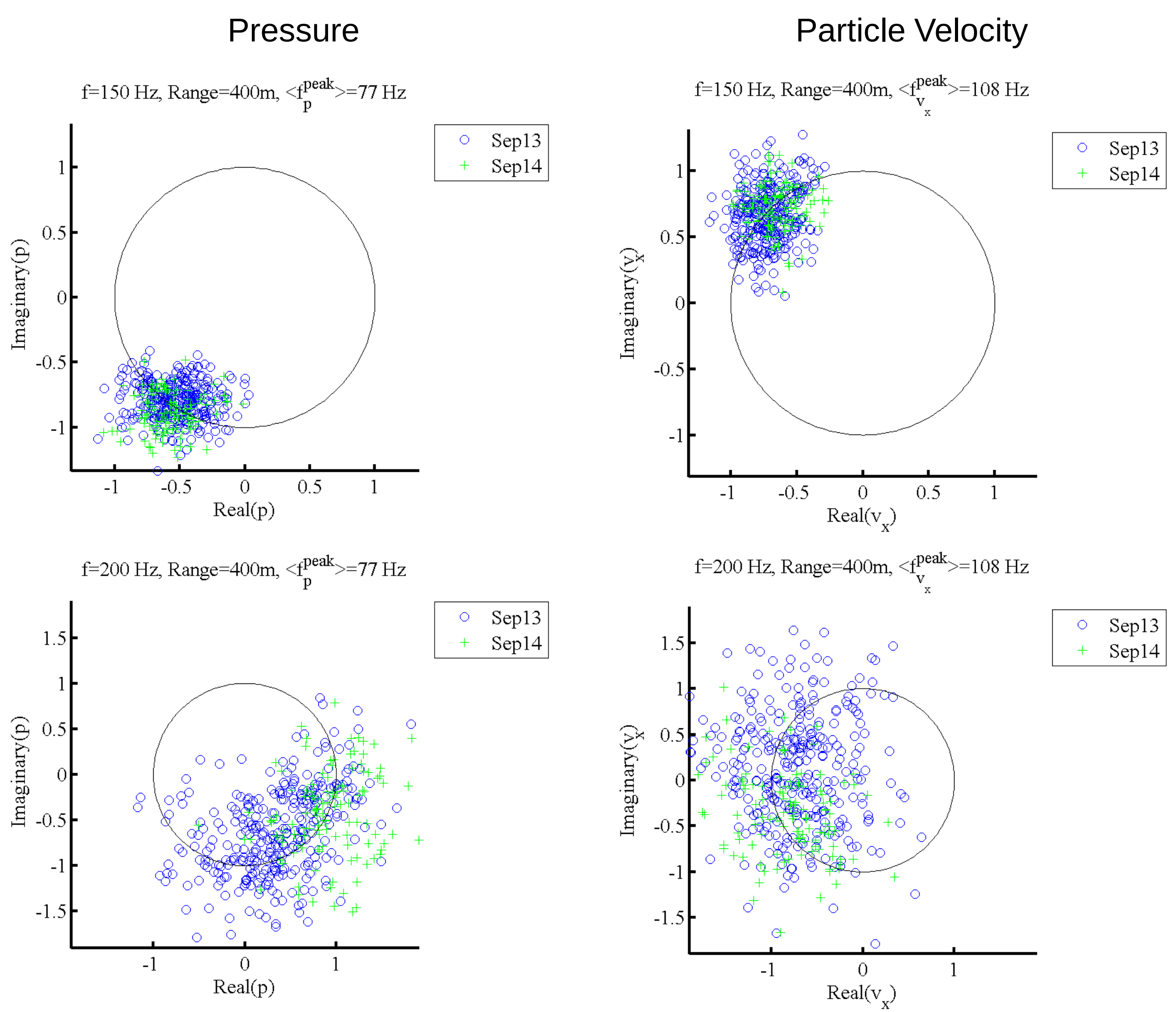

Scatter Plots for Normalized Signals @ 400 m: 250 Hz (upper) & 300 Hz (lower), 427 Shots

Pressure

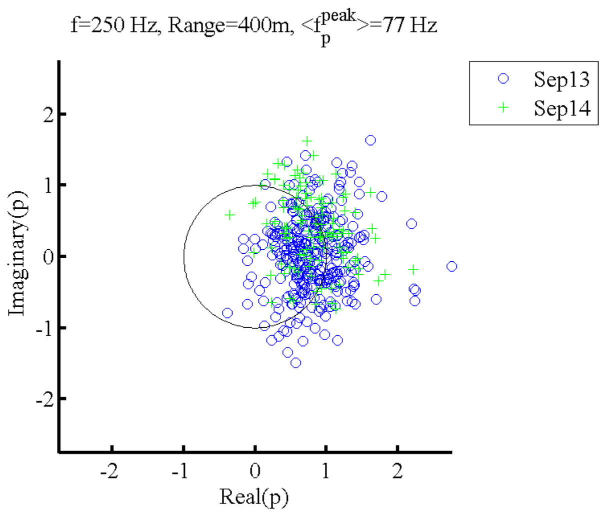

Particle Velocity

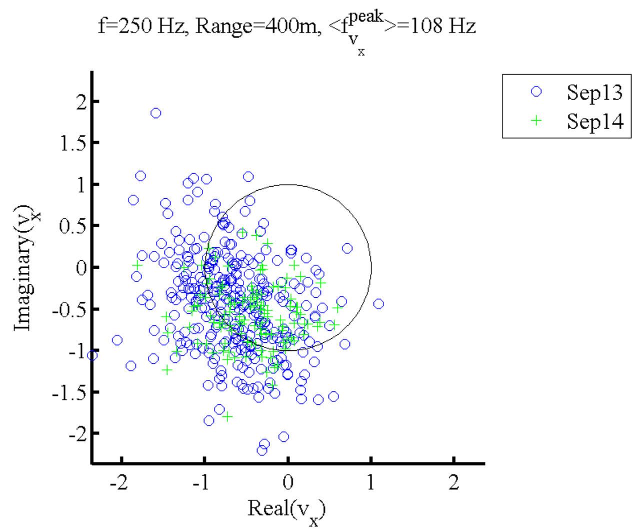

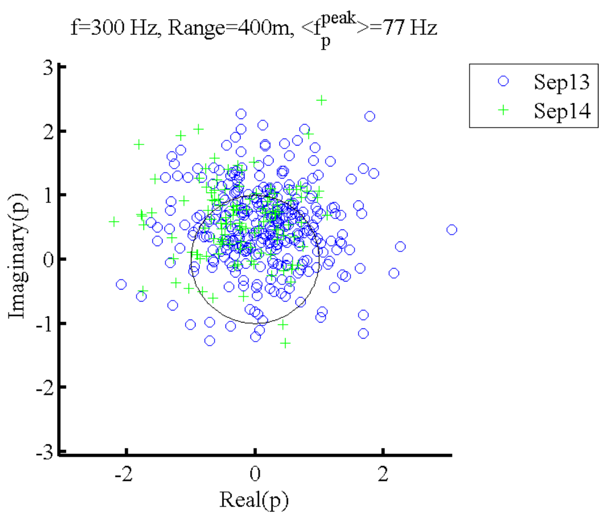

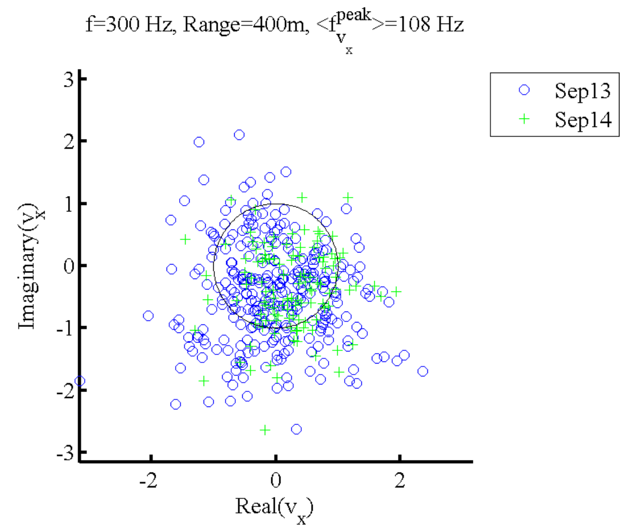

Scatter Plots for Normalized Signals @ 400 m: 350 Hz (upper) & 400 Hz (lower), 427 Shots

Pressure

Particle Velocity

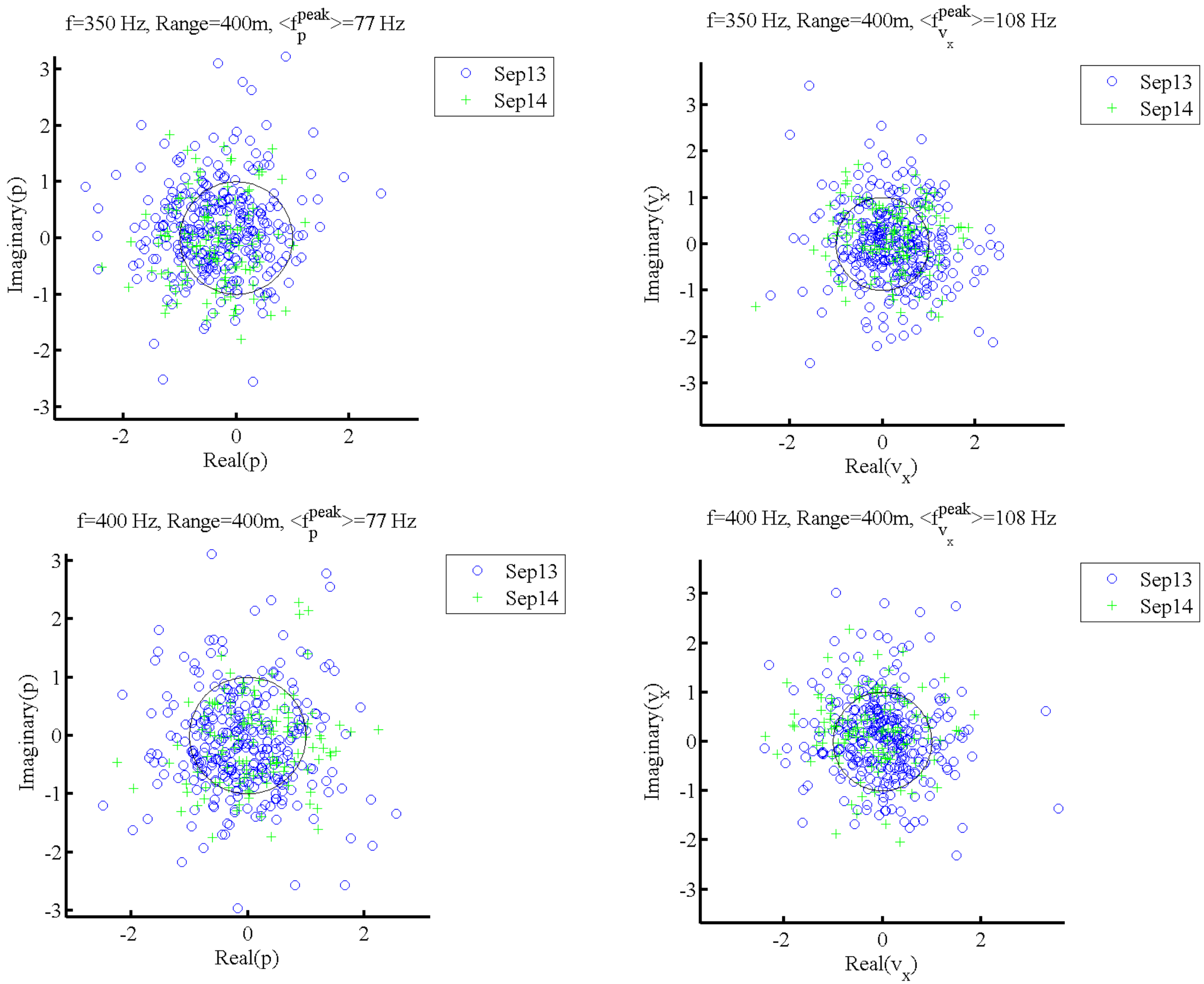

Spectral Effects on Broadband and Harmonic Sources

Recorded Sweep
2D Microflown @ 100 m, 31 Aug 2017

Pressure

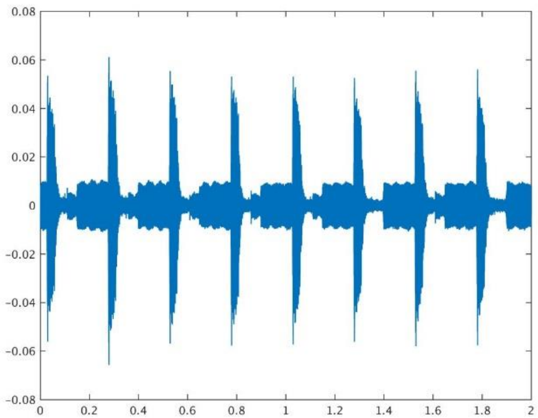

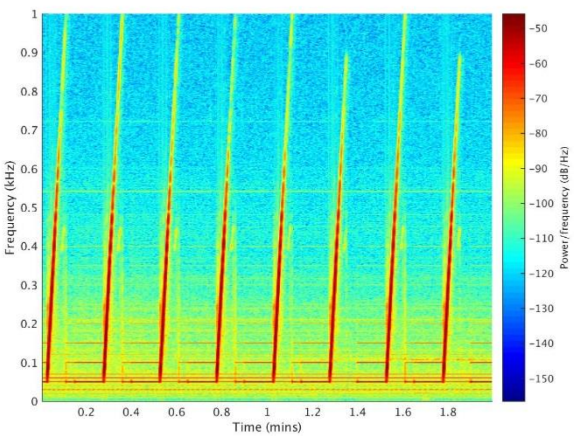

Particle Velocity - X

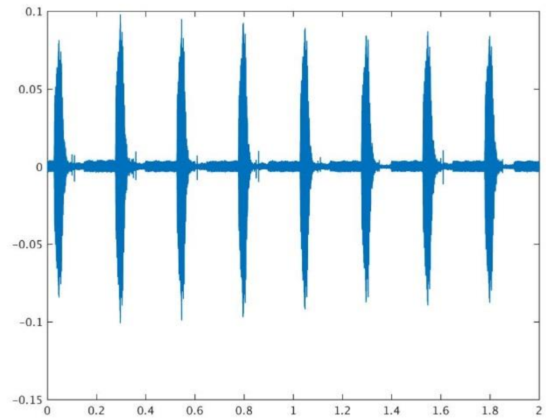

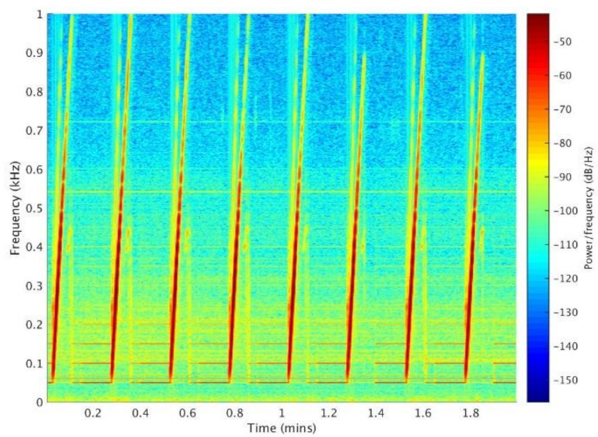

Particle Velocity - Y

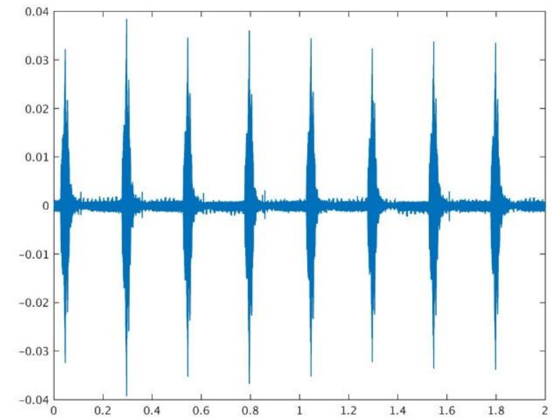

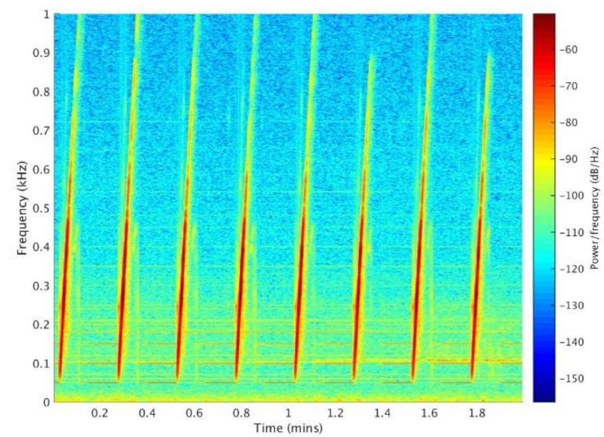

Recorded Sweep
2D Microflown @ 400 m, 31 Aug 2017

Pressure	Particle Velocity - X	Particle Velocity - Y
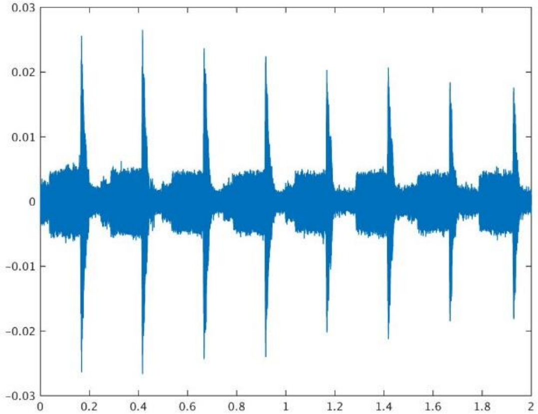	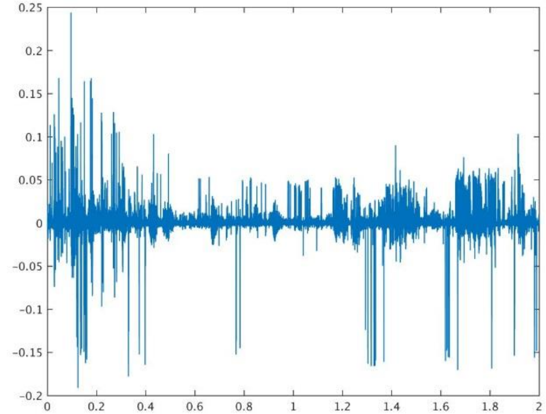	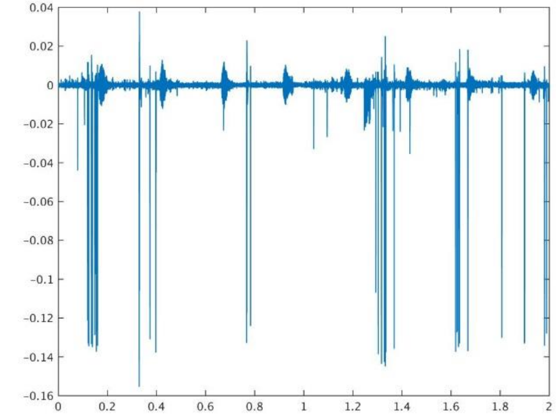
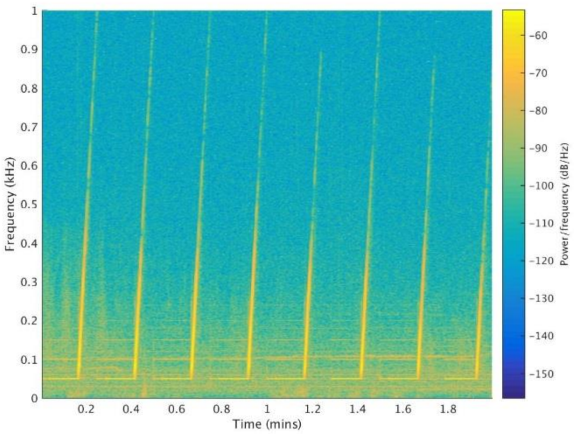	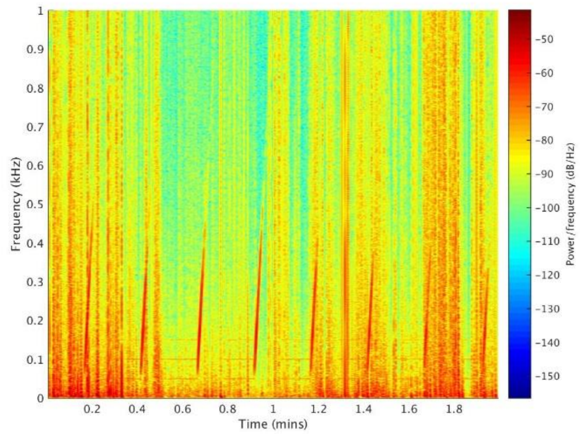	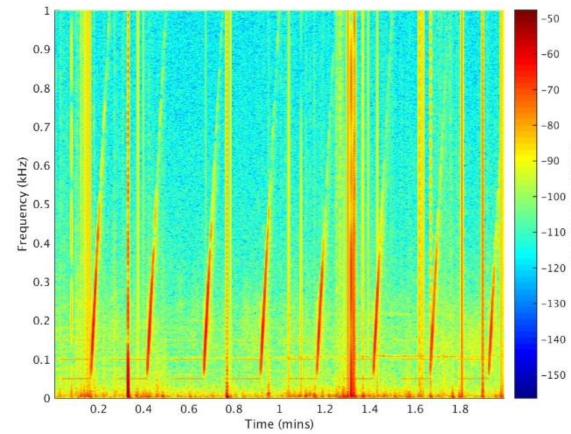

100 Hz Square Wave
2D Microflown @ 100 m, 31 Aug 2017

Pressure | Particle Velocity - X | Particle Velocity - Y

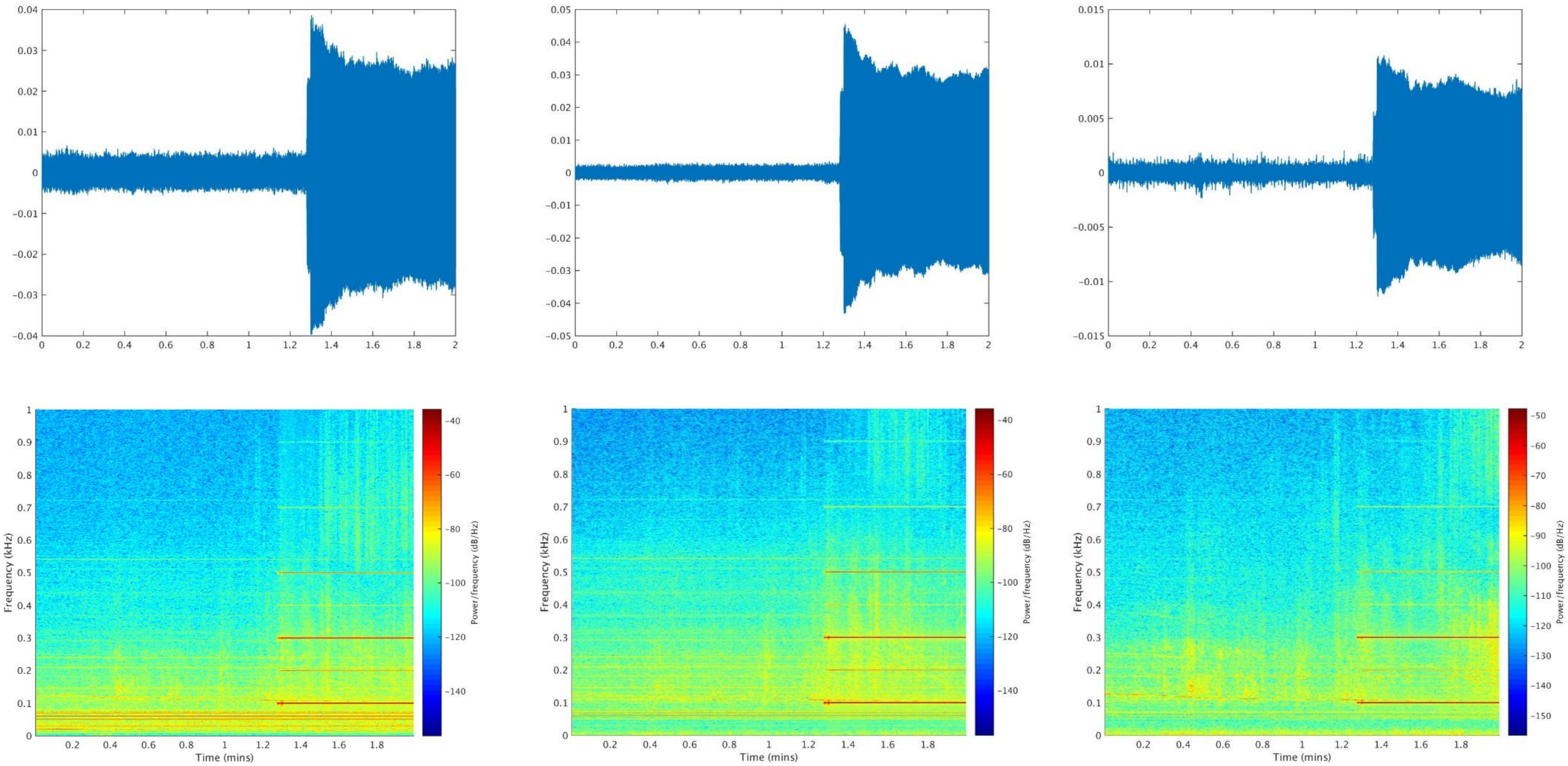

100 Hz Square Wave
2D Microflown @ 400 m, 31 Aug 2017

Pressure	Particle Velocity - X	Particle Velocity - Y

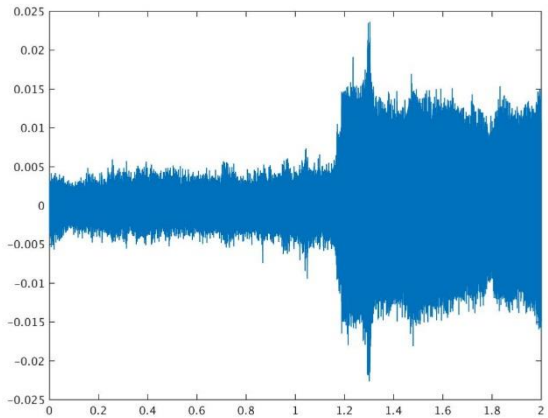
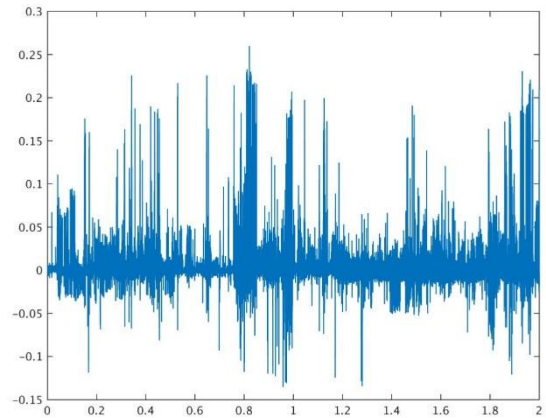
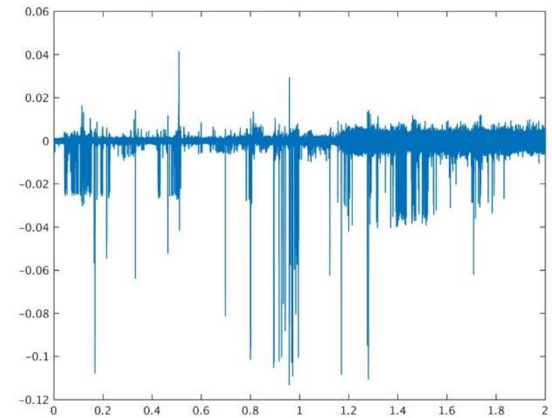
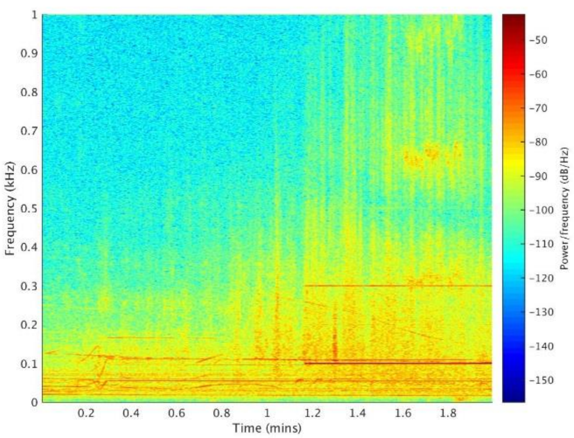

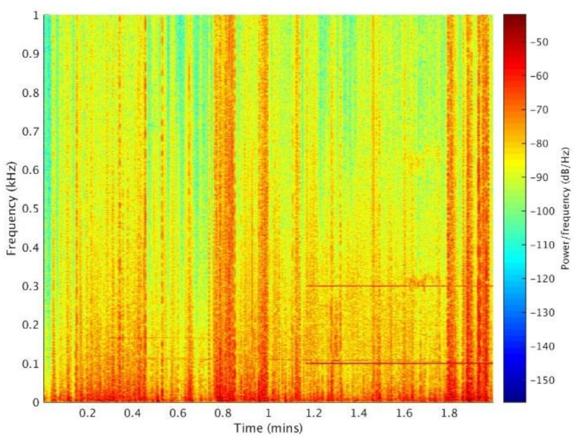

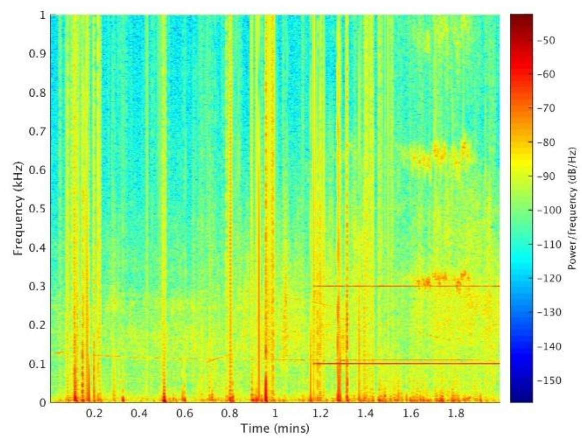

100 Hz Square Wave
2D Microflown @ 100 m, 31 Aug 2017

Pressure	Particle Velocity - X	Particle Velocity - Y

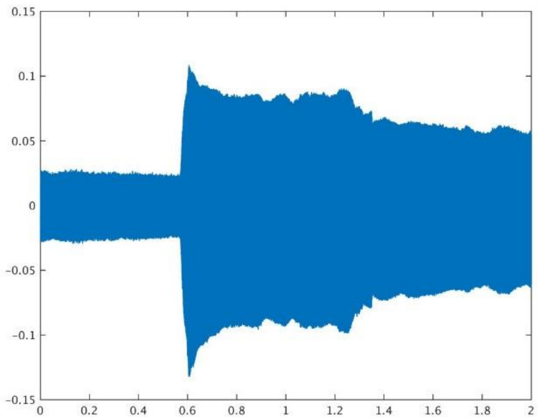

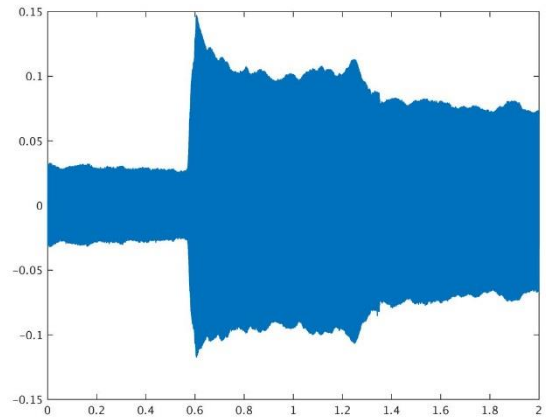

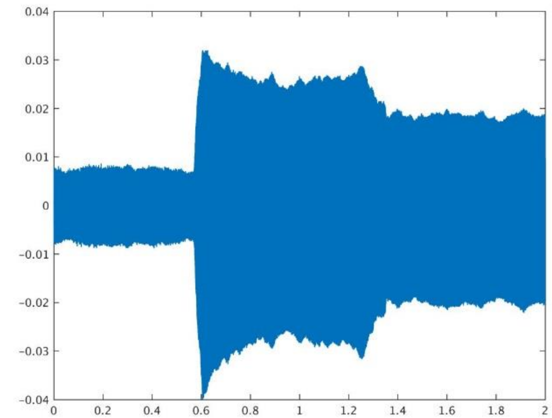

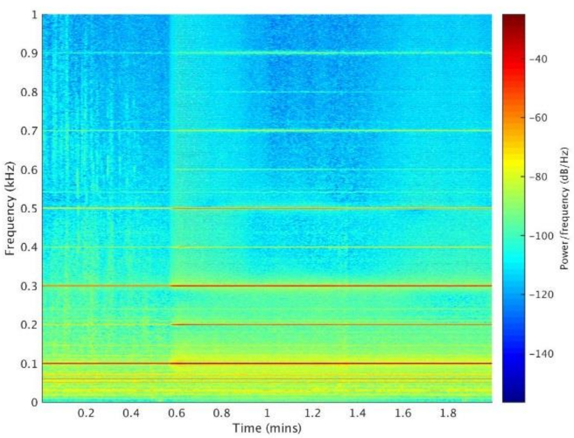

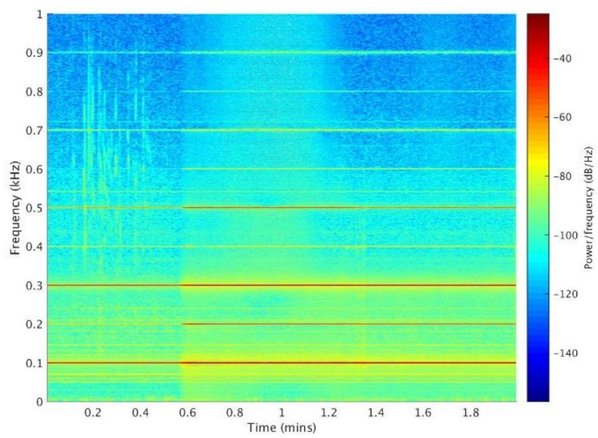

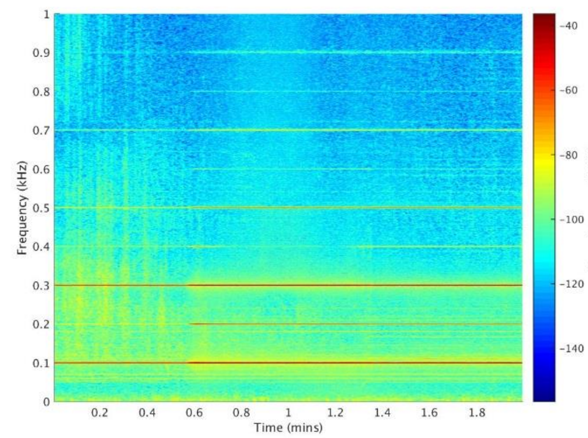

100 Hz Square Wave
2D Microflown @ 400 m, 31 Aug 2017

Pressure | Particle Velocity - X | Particle Velocity - Y

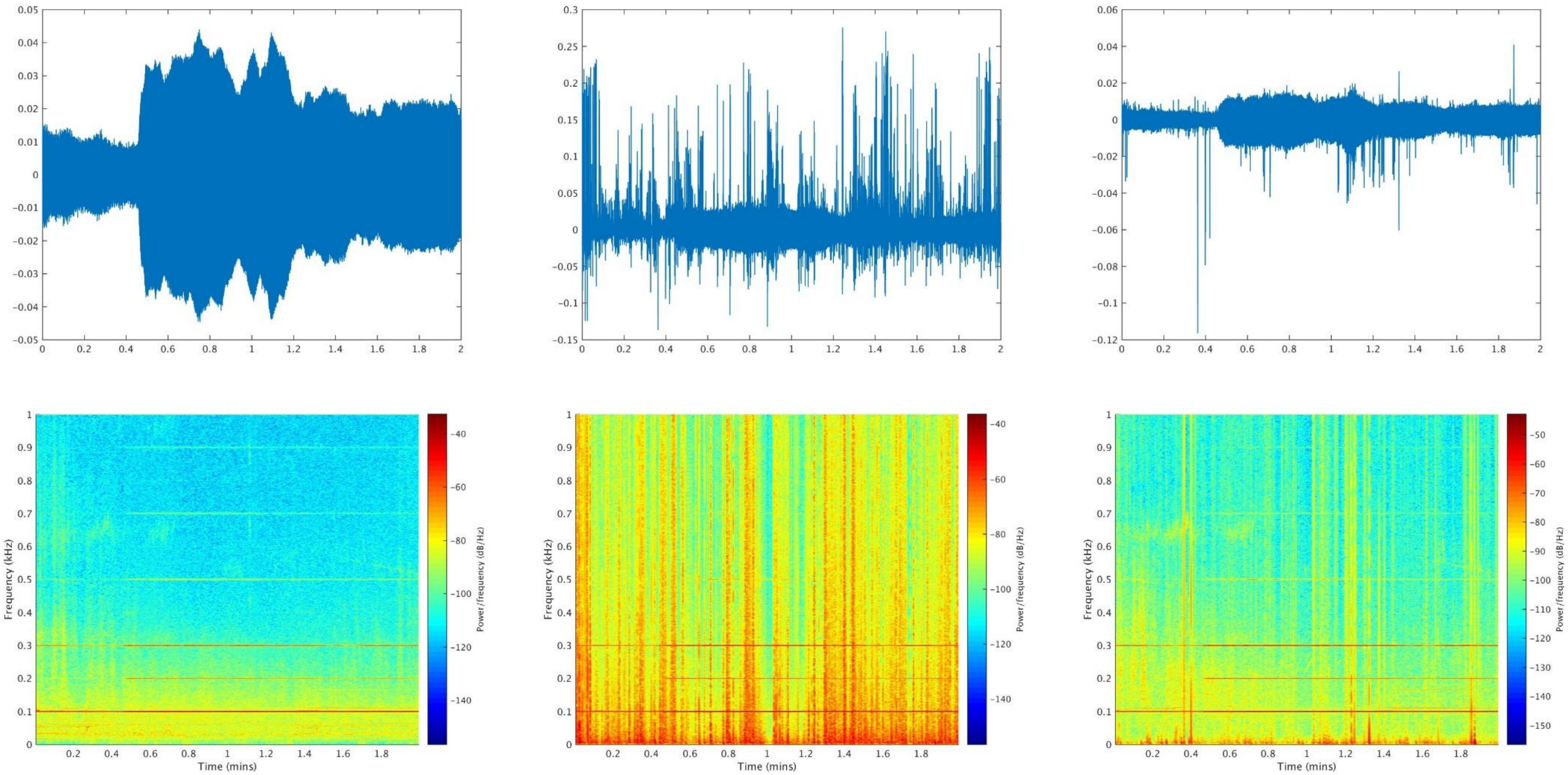

100 & 200 Hz Square Waves
2D Microflown @ 100 m, 31 Aug 2017

Pressure | Particle Velocity - X | Particle Velocity - Y

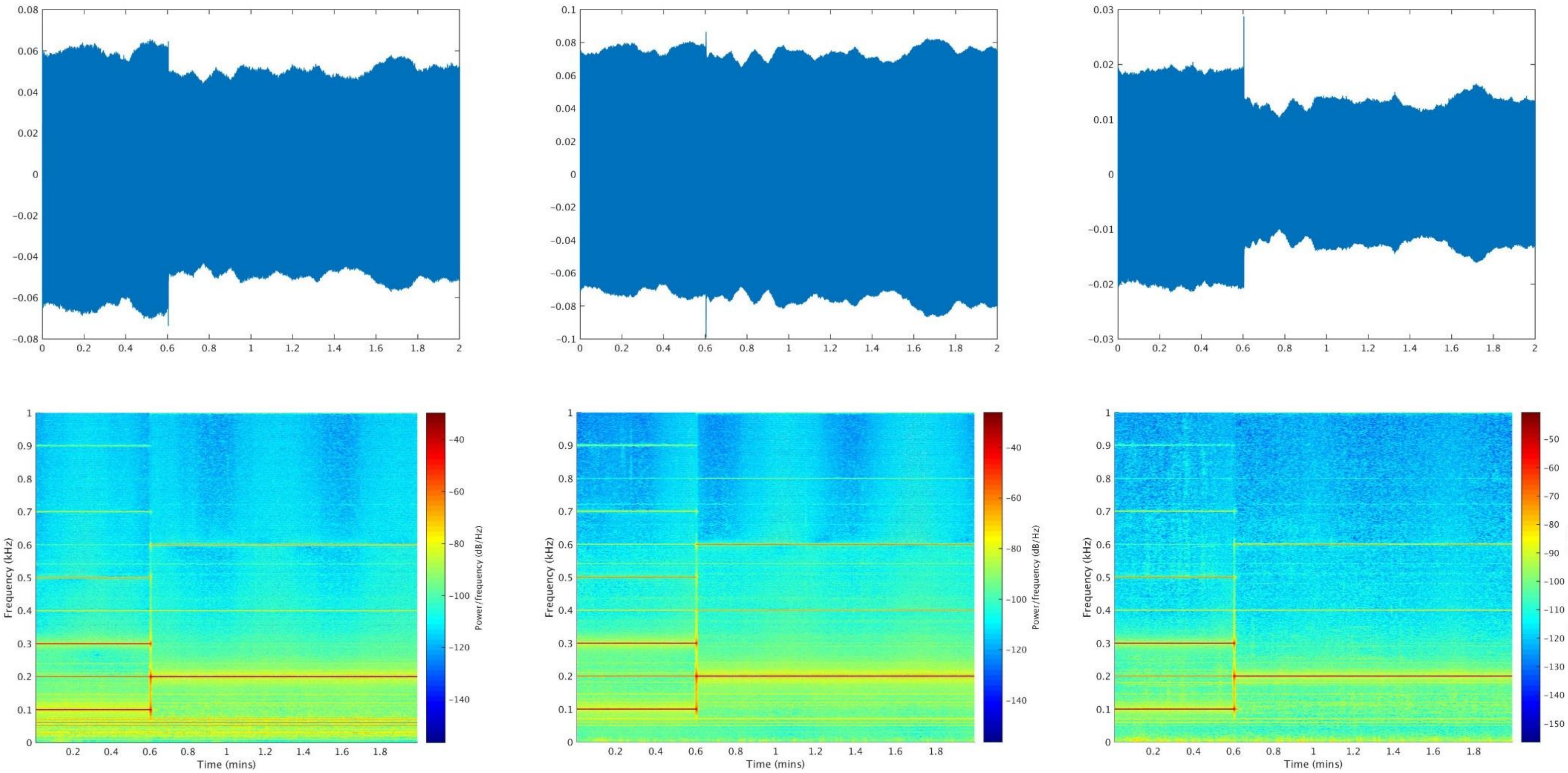

200 Hz Square Wave
2D Microflown @ 400 m, 31 Aug 2017

Pressure | Particle Velocity - X | Particle Velocity - Y

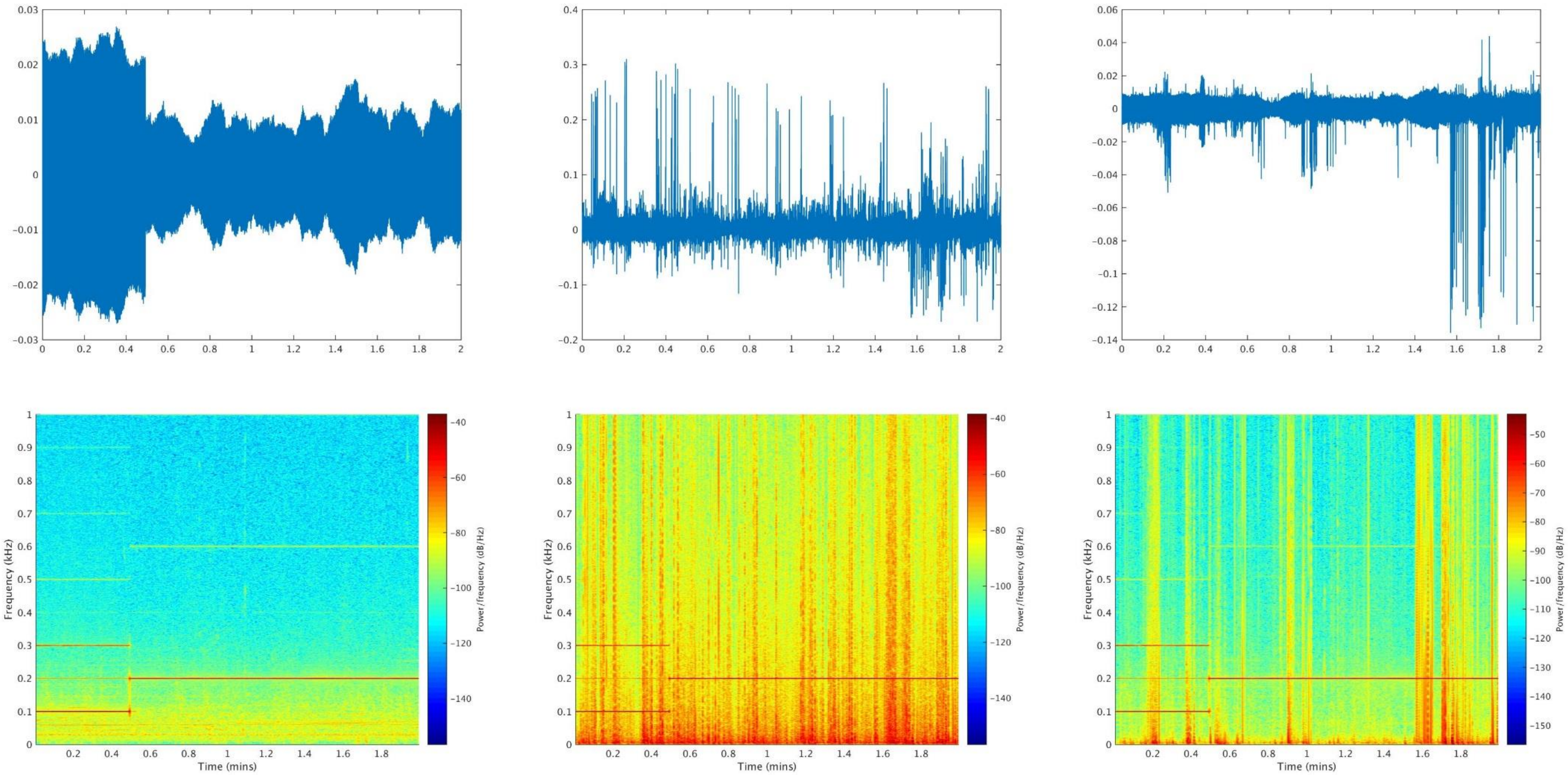

200 Hz Square Wave
2D Microflown @ 100 m, 31 Aug 2017

U.S. ARMY RDECOM ARL

Pressure	Particle Velocity - X	Particle Velocity - Y

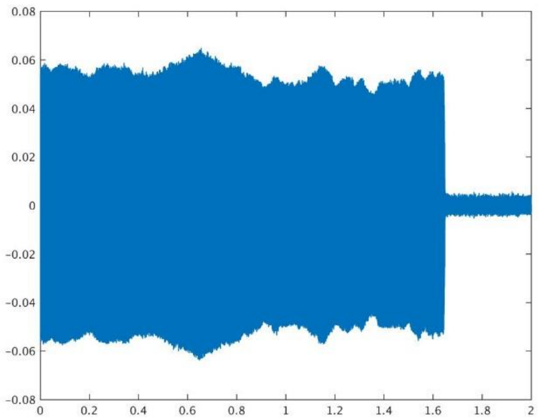

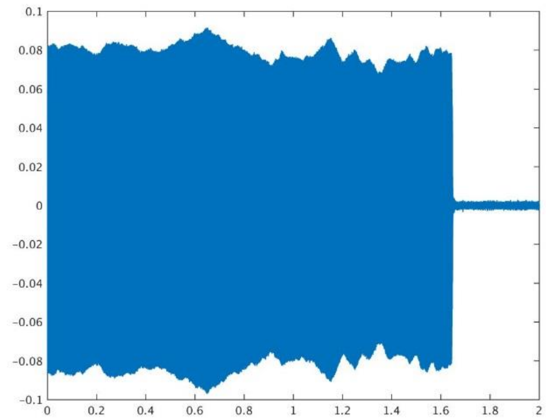

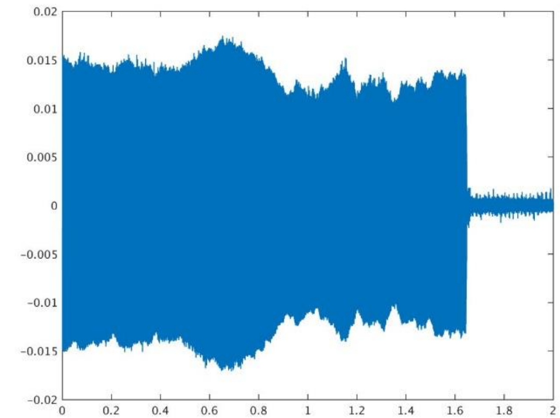

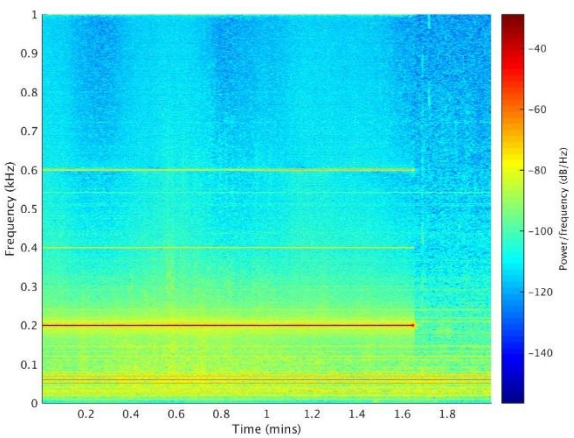

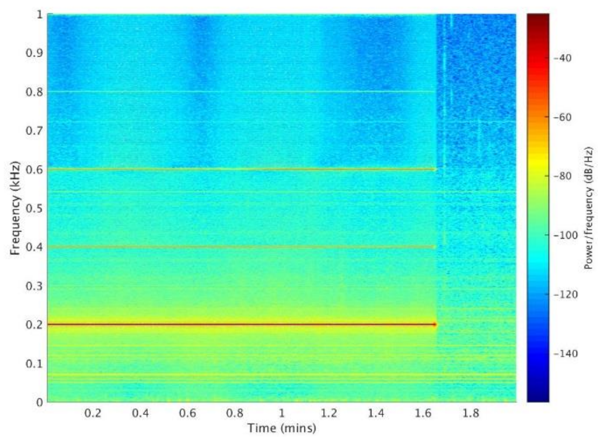

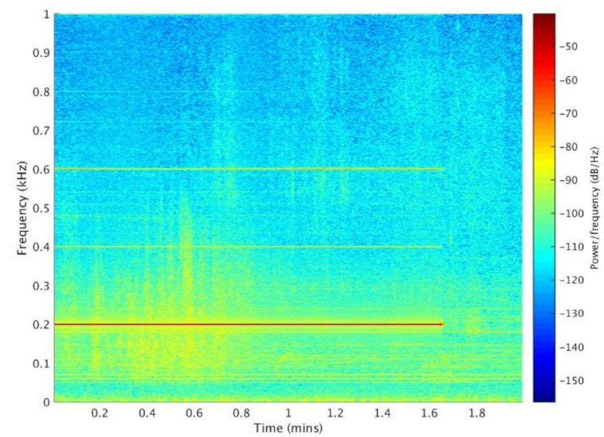

200 Hz Square Wave
2D Microflown @ 400 m, 31 Aug 2017

Pressure | Particle Velocity - X | Particle Velocity - Y

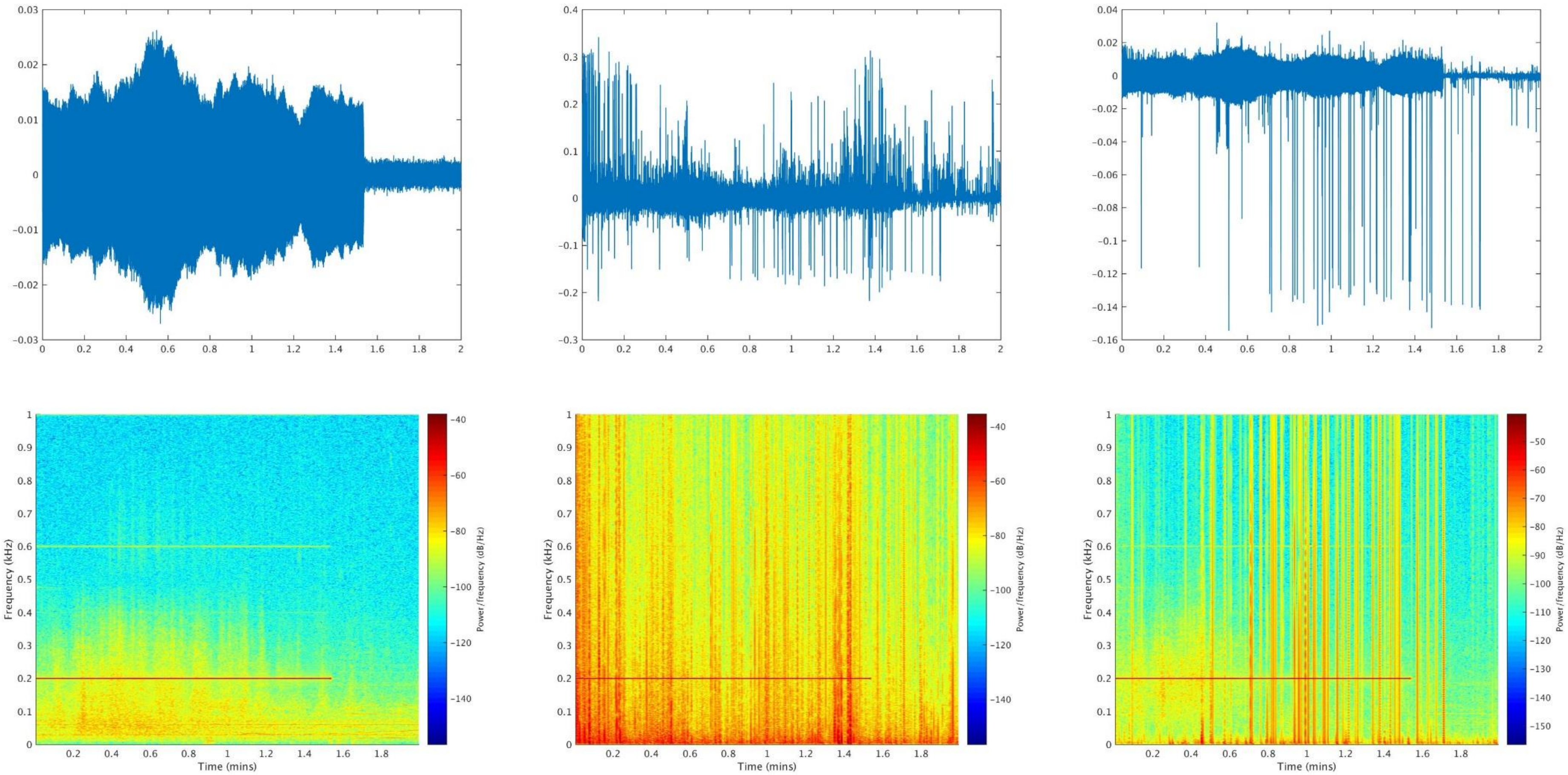

Conclusions

- Distribution for pressure fields similar to previous studies by Cheinet *et al* (2016), Ehrhardt *et al* (2013), and Norris *et al* (2001).
  - Unsaturated regime – lower frequencies, shorter ranges
  - Saturated regime – higher frequencies, longer ranges
- Additional studies
  - Continue analysis of data sets from several experiments
  - Need additional measurements in more turbulent conditions
  - Examine different filtering methods – Weiner filter did not make significant impact on noise reduction for spectrograms due to type of interfering sources (insect & bird chirps, wind noise, airplanes, and other unknown sources)
  - Source characterization (very short range < 10 m)
  - Proper calibration of Microflown sensors (higher SNR, absolute units, gain, etc.)
- Statistical effects on AOA estimations using particle velocity
  - Current theoretical models do not consider atmospheric effects
  - Scattering by atmospheric turbulence is known to be detrimental to AOA estimation using microphone arrays
  - Signal processing models that incorporate the effects of atmospheric turbulence exist for the pressure field - similar methods should be applied to particle velocity

References

- L. Ehrhardt, S. Cheinet, D. Juvé and Ph. Blanc-Benon, “Evaluating a linearized Euler equations model for strong turbulence effects on sound propagation,” *J. Acoust. Soc. Am.*, **133**, 1922-1933 (2013).
- D.E. Norris, D. K. Wilson and D. W. Thomson, “Correlations Between Acoustic Travel-Time Fluctuations and Turbulence in the Atmospheric Surface Layer,” *Acta Acust. Acust.*, **87**, 677-684 (2001).
- Sylvain Cheinet, Matthias Cosnefroy, D. Keith Wilson, Vladimir E. Ostashev, Sandra L. Collier, Jericho E. Cain, “Effets de la turbulence sur des impulsions acoustiques propageant près du sol (Effects of turbulence on acoustic impulses propagating near the ground),” *Congrès Français d'Acoustique (French Congress of Acoustics), 11-15 April 2016, Le Mans, France.*
- S. M. Flatte, *Sound Transmission Through the Fluctuating Ocean* (New York, Cambridge Univ. Press, 1979).
- Sandra L. Collier, “Fisher Information for a Complex Gaussian Random Variable: Beamforming Applications for Wave Propagation in a Random Medium," *IEEE Trans. Sig. Proc.* **53**, 4236-4248 (2005).
- S. L. Collier and D. K. Wilson, “Performance Bounds for Passive Sensor Arrays Operating in a Turbulent Medium II: Spherical-Wave Analysis," *J. Acoust. Soc. Am.* **116**, 987 1001 (2004).
- S. L. Collier and D. K. Wilson, “Performance Bounds for Passive Sensor Arrays Operating in a Turbulent Medium: Plane-Wave Analysis," *J. Acoust. Soc. Am.* **113,** 2704-2718 (2003).

Thank You.
Questions?

Modeling of nonlinear *N*-wave propagation in a turbulent layer: pressure field distortions and statistics

Petr V. Yuldashev[1], Maria M. Karzova[1,2], Sébastien Ollivier[2],

Vera A. Khokhlova[1,3] and Philippe Blanc-Benon[2]

[1]Physics Faculty
Moscow State University
Moscow, Russia

[2]Ecole Centrale de Lyon,
LMFA UMR CNRS 5509

[3]Center for Industrial and
Medical Ultrasound
Applied Physics Laboratory
University of Washington
Seattle, WA, USA

June 12 2018, LRSP, Lyon

Outline

- Introduction: sonic boom problem
- Physical effects controlling shock rise time in the process of propagation of high amplitude *N*-waves through atmospheric turbulence
- Laboratory scale experiments on *N*-wave propagation
- Theoretical model: 2D KZK-type nonlinear equation
- Results of numerical simulations
- Conclusions

Relevance of the research: sonic boom problem

High amplitude pulse propagation in the turbulent atmosphere

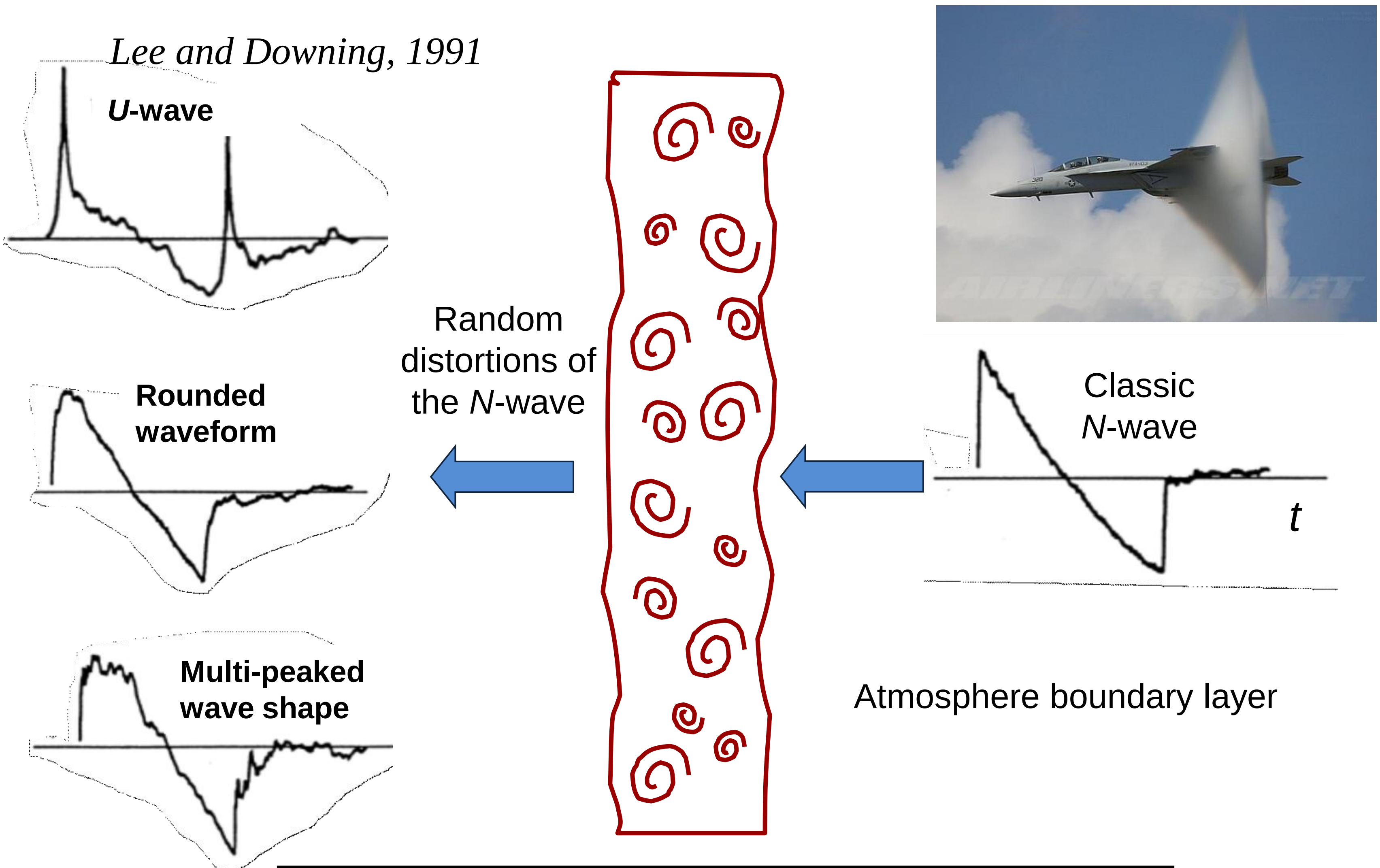

Acceptability of supersonic flights.

Variability of sonic boom waveforms

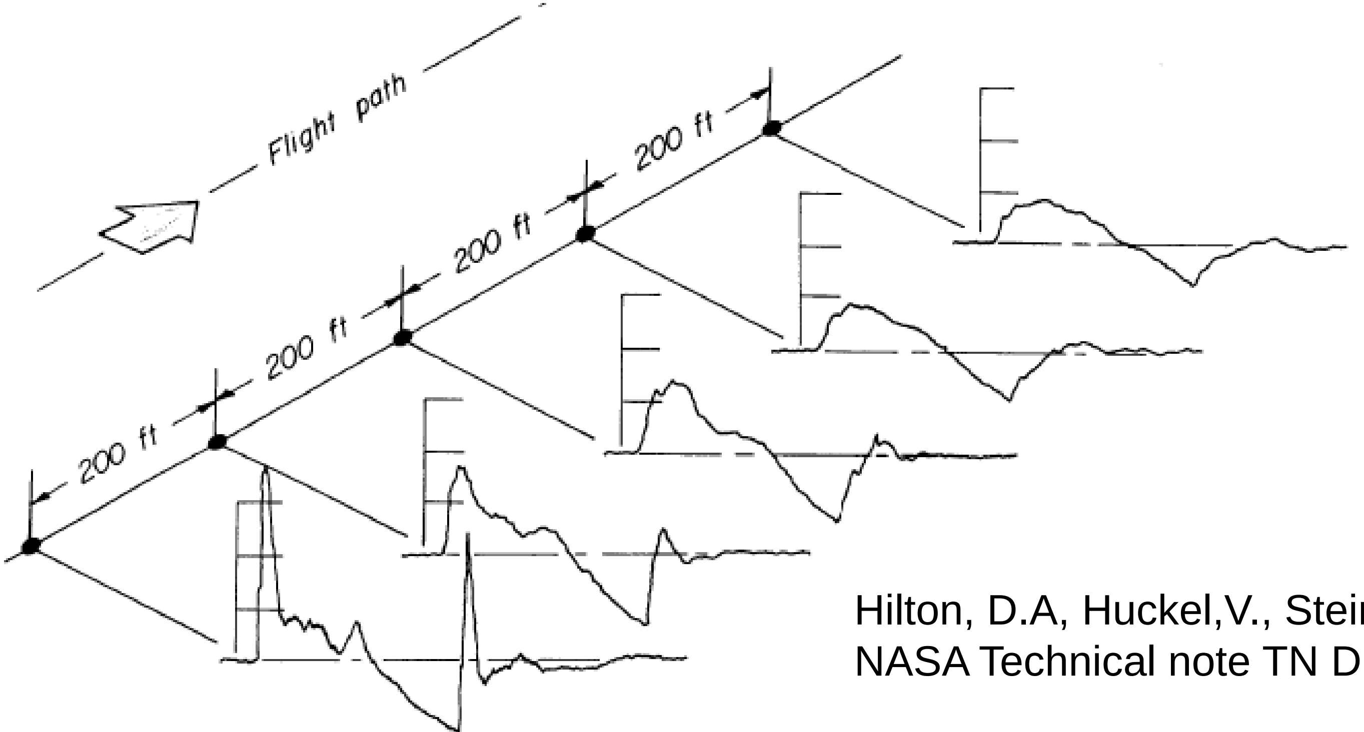

Hilton, D.A, Huckel,V., Steiner R., Maglieri, D.J.,
NASA Technical note TN D-2539,1964

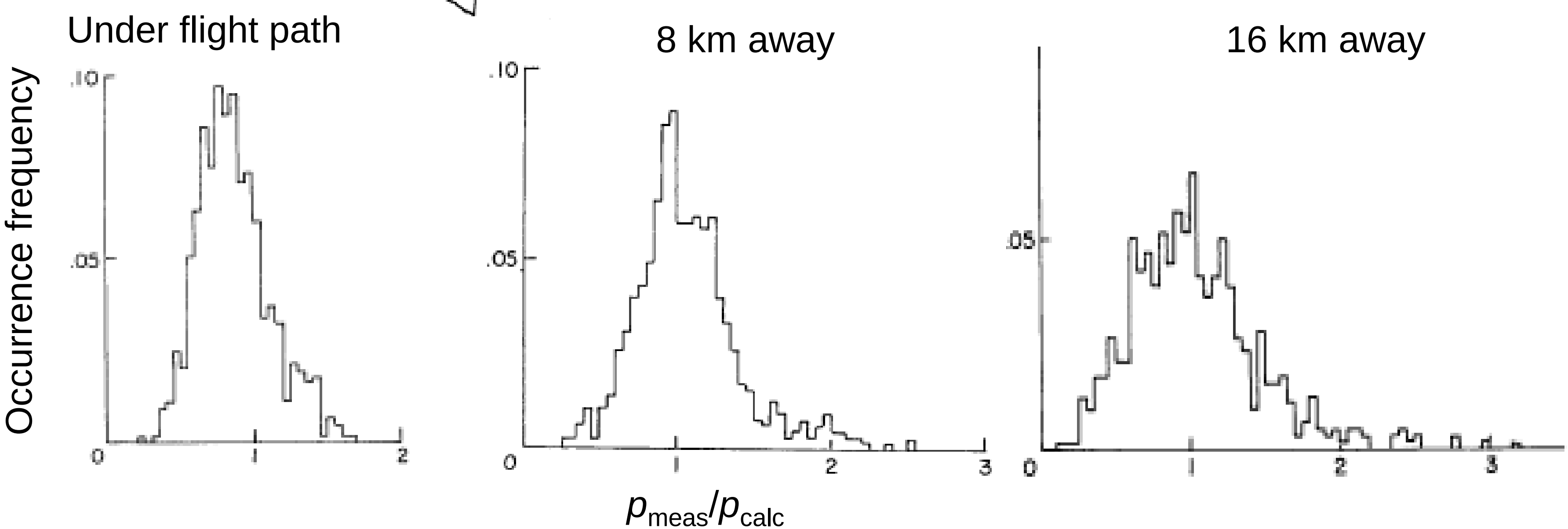

Sonic boom characteristic parameters

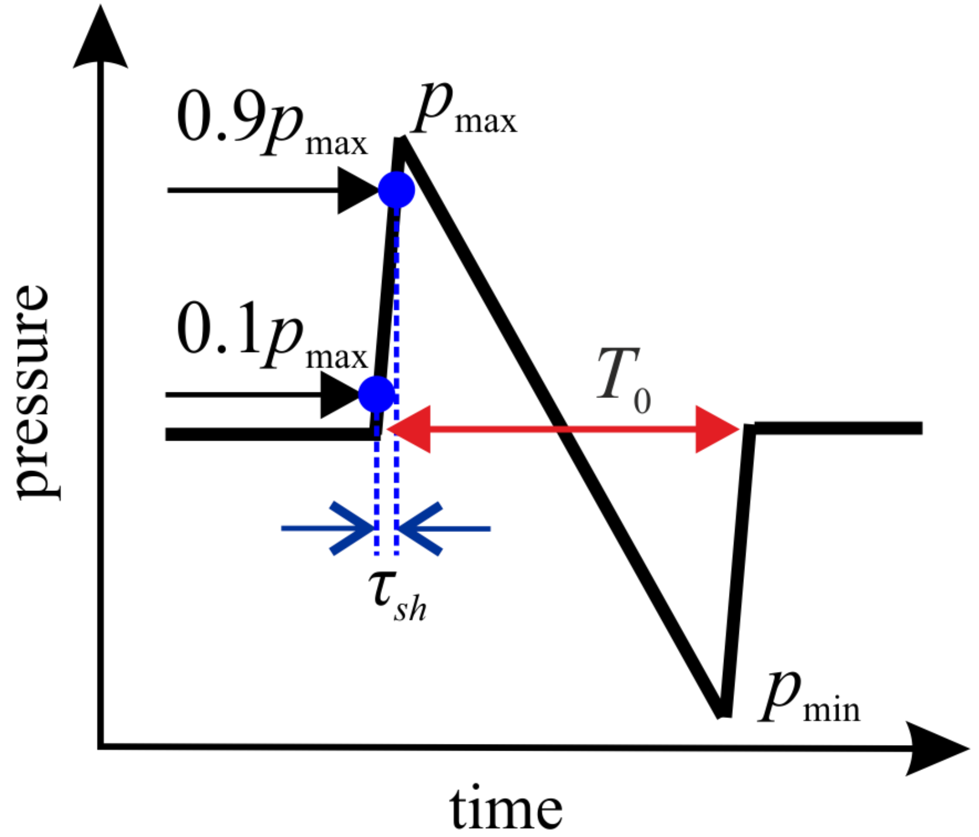

Peak overpressure p_{max}	Classical rise time τ_{sh} :	Duration T_0
10-100 Pa	0.5-10 ms	100-300 ms

Shock front steepness definition I

Examples of waveforms distorted by turbulence

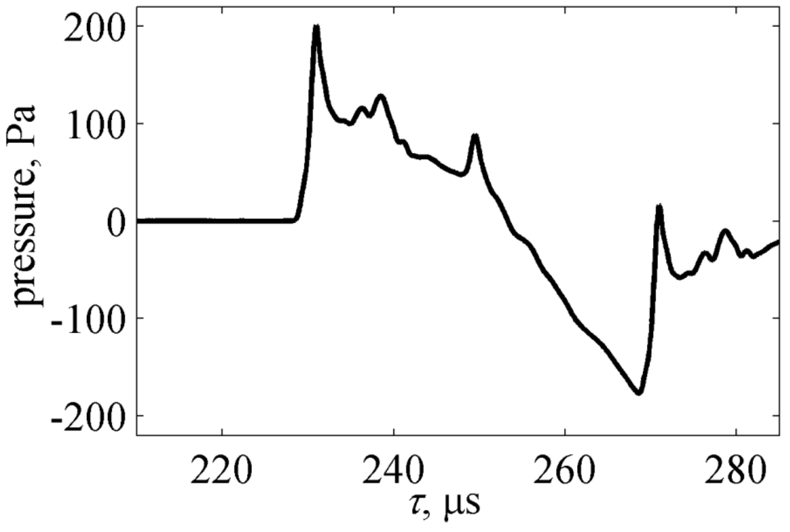

Moderate peak overpressure
and low rise time (1.5 μs)

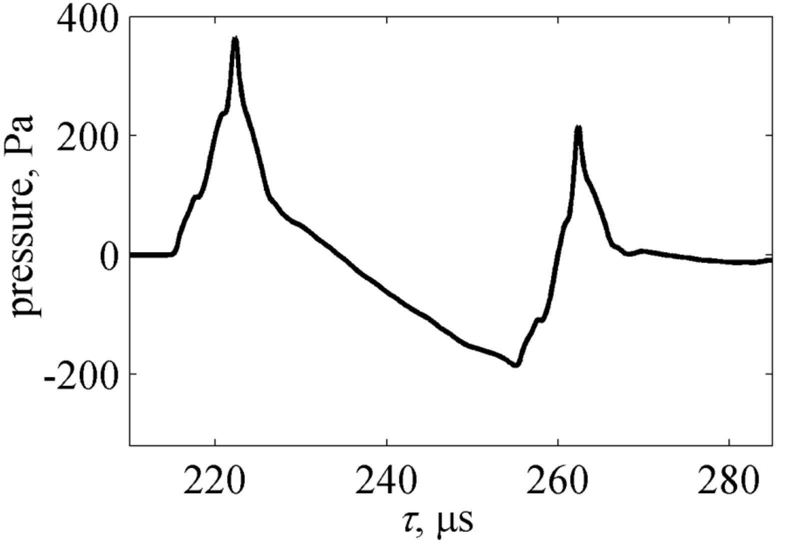

High peak overpressure
and large rise time (6 μs)

In turbulence different combinations of rise time and peak overpressure are possible.
Rise time is not sufficient itself to characterize shock front structure
Shock front steepness has to be defined

Shock front steepness definition II

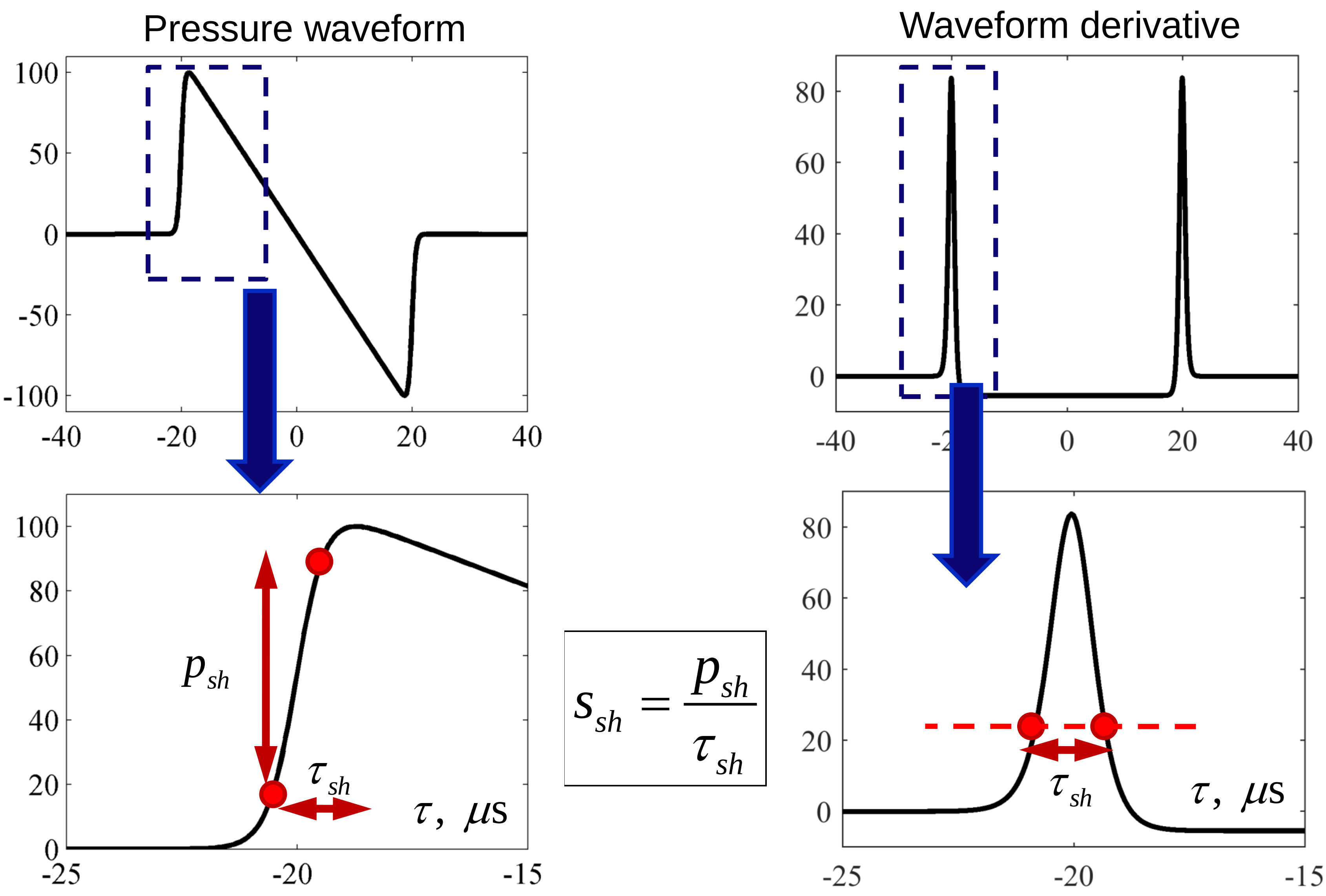

Steepness is defined as a ratio of shock front amplitude to the rise time.

Random focusing and multifolded shock front

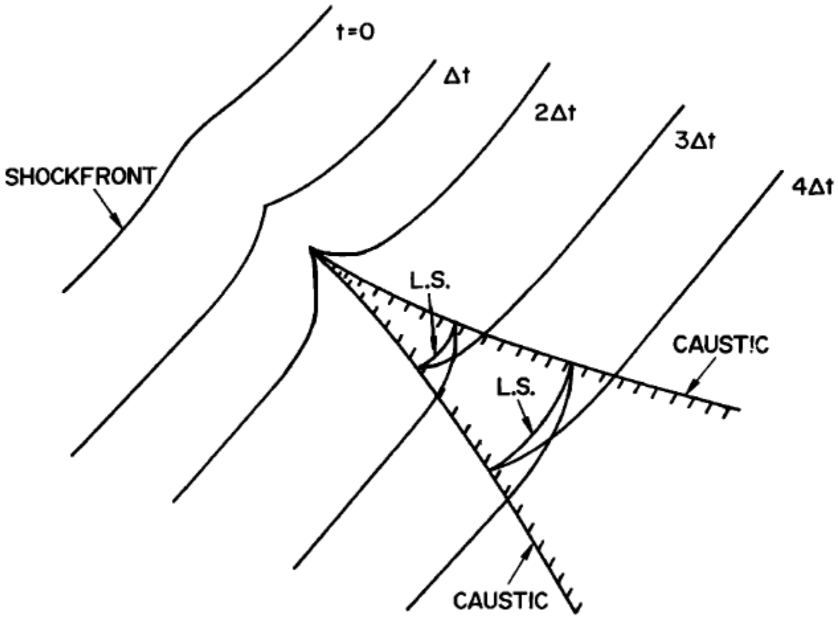

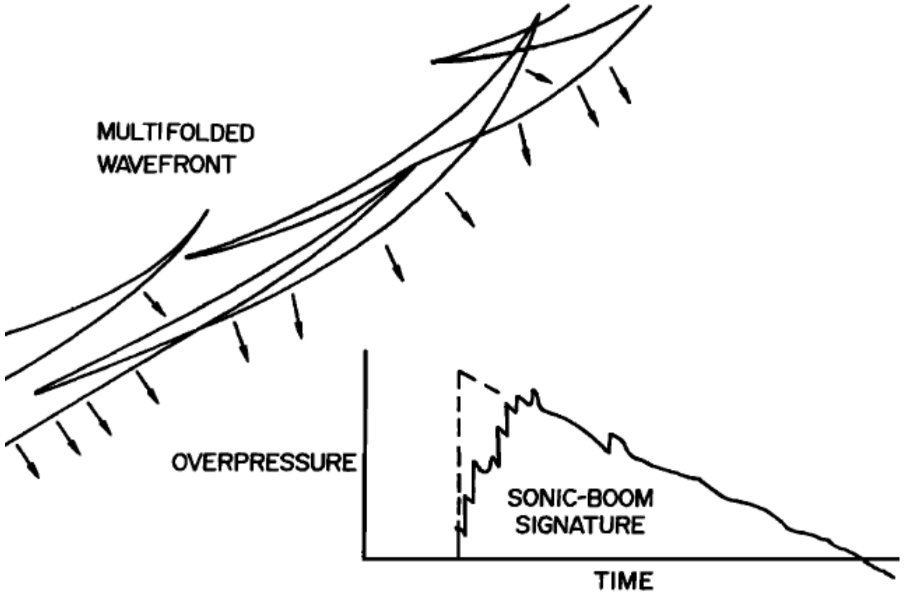

Pierce, A.D., Maglieri, D.J, J. Acoust. Soc. Am., 1972, V.51, 2(3), P. 702-721

Shock front focusing on random inhomogeneities results in wavefront folding

Shock front folding occurs many times along propagation path and leads to large rise times and variability of rise time and peak overpressure

Turbulence “smears” initial shock and results in increase of rise time

Finite amplitude waves: nonlinear steepening

Burgers' equation

$$\boxed{\frac{\partial p}{\partial z} = \frac{\beta}{\rho_0 c_0^3} p \frac{\partial p}{\partial \tau} + \frac{\delta}{2c_0^3} \frac{\partial^2 p}{\partial \tau^2}}$$

p – pressure,
z – propagation distance
$\tau = t - z/c_0$ retarded time

$$c(p) = c_0 + \frac{\beta p}{\rho_0 c_0}$$

Local sound speed depends on wave amplitude

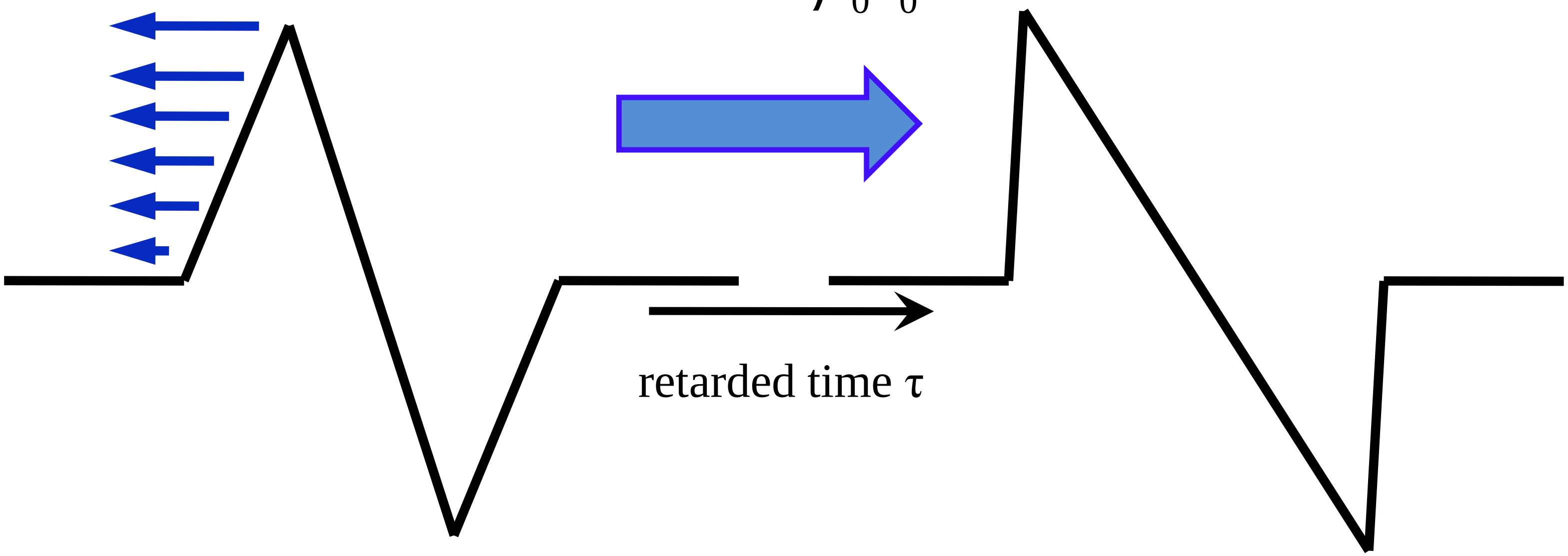

Rise time of a steady shock:
Inversely proportional to wave amplitude

$$\tau_{sh} = \frac{4.4\delta\rho_0}{\beta p_{\max}}$$

Rise time on the order of millisecond is explained by relaxation effects

Problem formulation: two opposite physical effects

Turbulence → Shock front smearing, increase rise time, decrease steepness

Acoustic nonlinearity → Shock front steepening, decrease rise time increase steepness

What is the result of two counteracting effects on the shock front?

Outdoor studies vs model laboratory-scale experiments

Outdoor studies

M. Kanamori et al. // AIAA Journal, 2018
Lee & Downing, 1991, *Maglieri et al., 1992, Elmer & Joshi, 1994,*
Hilton et al., 1964, Willshire & Devilbiss, 1992

Laboratory scale experiments

B. Lipkens and D. Blackstock // J. Acoust. Soc. Am. 1998.
S. Ollivier & Ph. Blanc-Benon, // 10th AIAA/CEAS, Manchester, UK, 2004
M.V. Averiyanov et al. // J. Acoust. Soc. Am. 2011.
E. Salze et al. // J. Acoust. Soc. Am. 2014

Scaling factor is between 1:1000 and 1:10000

Experiments on *N*-wave propagation in turbulence

Kinematic turbulence

Averiyanov M.V. et al. // J. Acoust. Soc. Am. 2011.

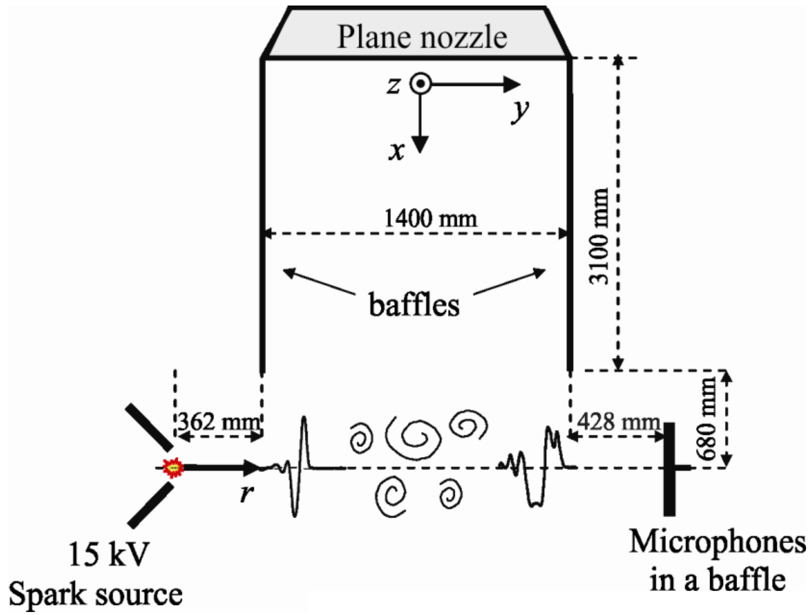

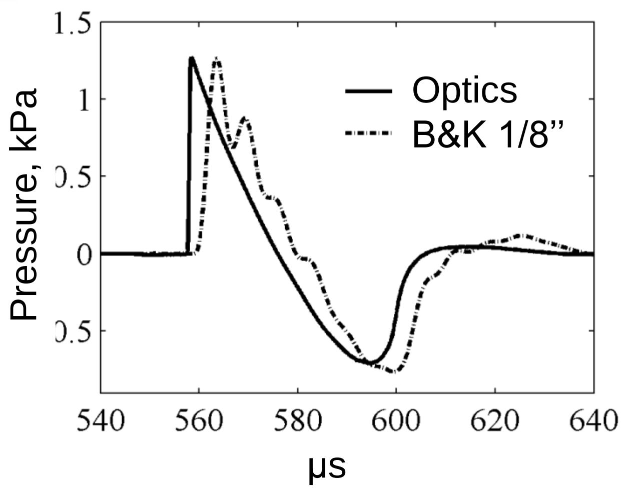

Thermal turbulence

E. Salze et al. // J. Acoust. Soc. Am. 2014

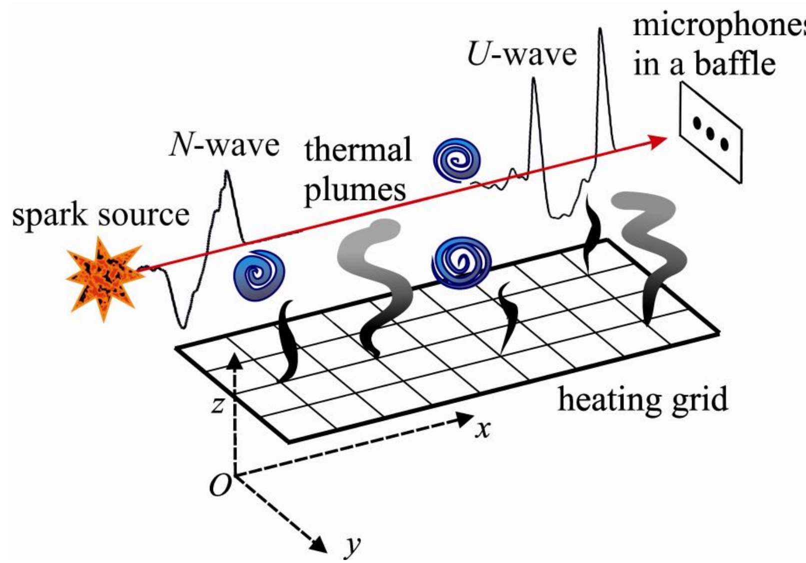

Peak pressure p_{max}, Pa	from 1100 to 60
Rise time τ_{sh}, μs	from 0.2 to 2.0
Duration T, μs	from 40 to 50

Effect of turbulence: random waveform distortions

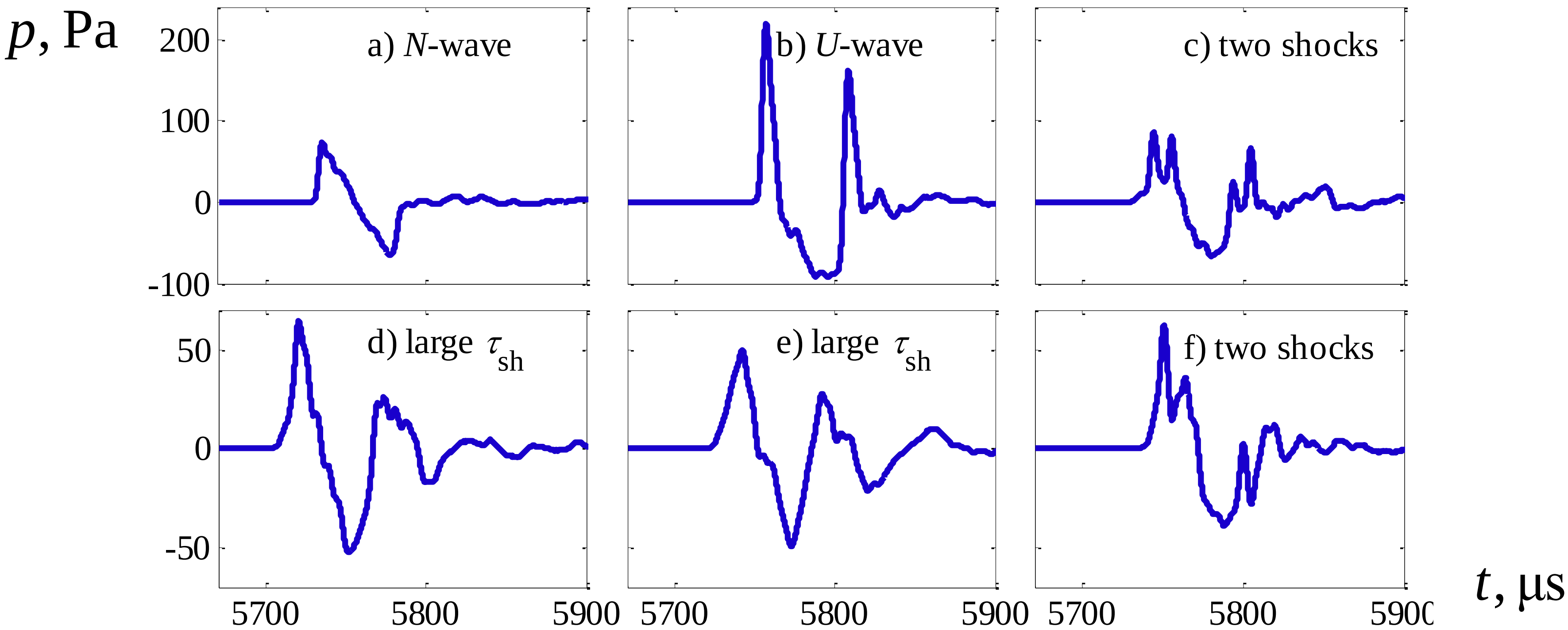

Probability distribution functions of normalized peak pressure p_{max}/p_{max0}

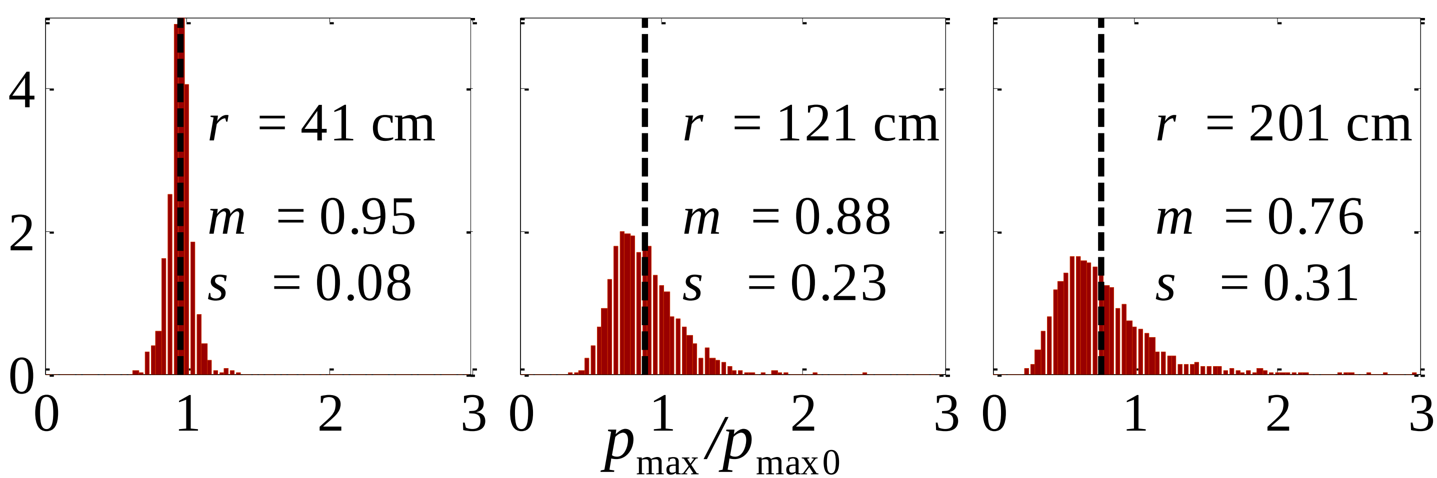

Effect of turbulence: rise time distributions

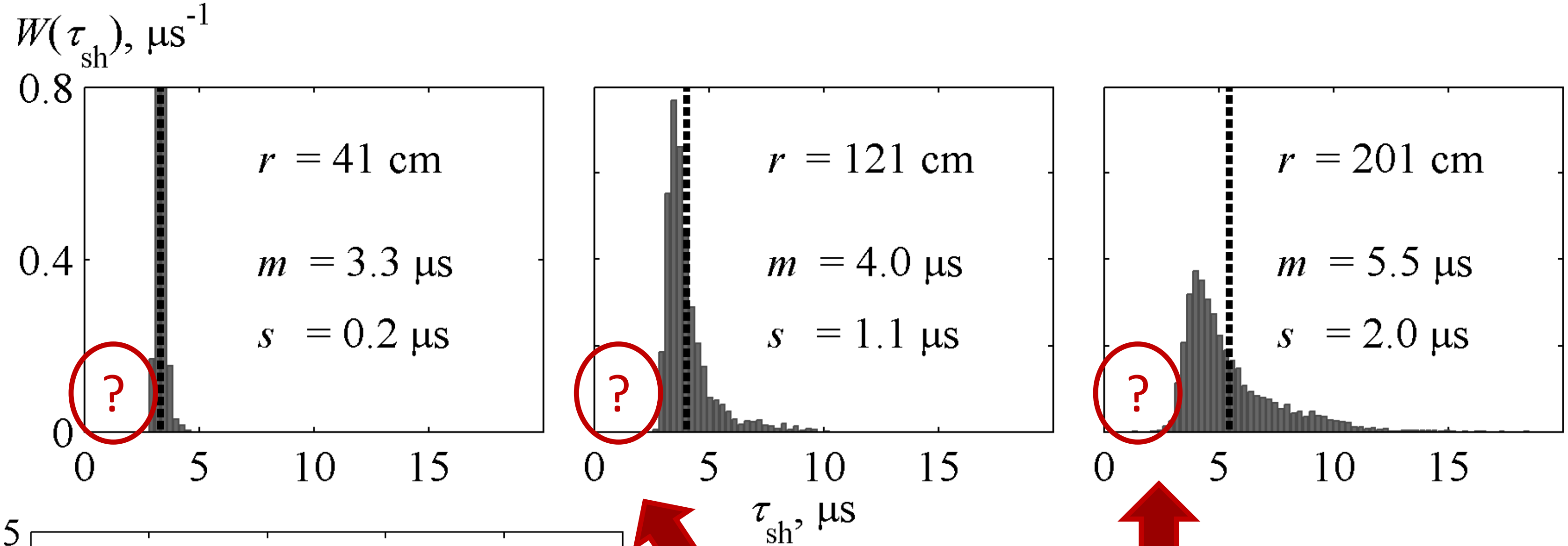

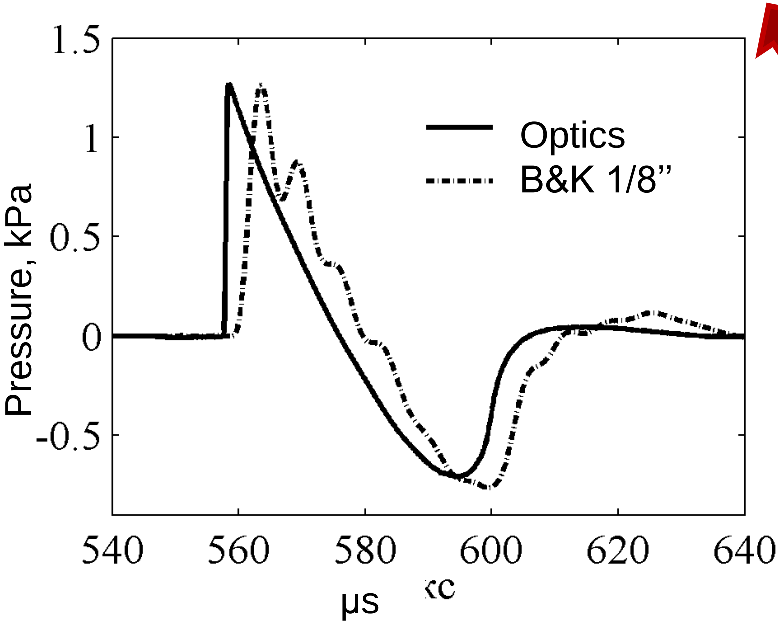

Microphone bandwidth imposes lower limit on rise time of measured waveform

With measured waveforms it is difficult to understand do waves with short rise times occur or not?

P. V. Yuldashev *et al.*, J. Acoust. Soc. Am. 137(6), pp. 3314-3324, 2015

Theoretical model of the *N*-wave propagation through turbulent medium: 2D KZK-type equation

$$\frac{\partial^2 p}{\partial z \partial \tau} = \frac{c_0}{2}\frac{\partial^2 p}{\partial x^2} + \frac{\mu}{c_0}\frac{\partial^2 p}{\partial \tau^2} + \frac{\beta}{2\rho_0 c_0^3}\frac{\partial^2 p^2}{\partial \tau^2} + \frac{\delta}{2c_0^3}\frac{\partial^3 p}{\partial \tau^3}$$

diffraction **inhomogeneities** **nonlinearity** **absorption**

The equation is a one-way propagation equation and includes four main effects

The equation was solved using a FDTD numerical scheme

Applicability conditions

Small diffraction angles,
low back scattering -
weak refraction index
inhomogeneities of large scale.
Weak shock waves:
acoustical Mach number << 1

Initial waveform: symmetrical *N*-wave

Duration 40 μs
(wavelength 14 mm)
Amplitude
50, 100, 200 and 400 Pa
Acoustical Mach number

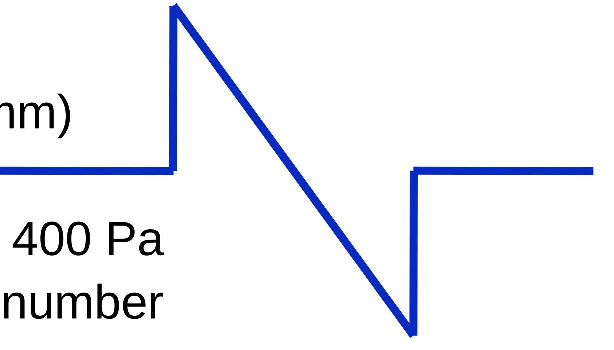

$$M_a = (0.33,\ \ 0.66,\ \ 1.32,\ \ 2.7)\cdot 10^{-3}$$

Advantage of the model: relatively simple, but includes all necessary effects

2D turbulent medium model

Kinematic turbulence $\mu = u_z / c_0$

$$\boxed{E(K) = \frac{55}{18} < \mu^2 > \frac{K^3}{L_0^{5/3}} \frac{\exp(-K^2 / K_m^2)}{\left(K^2 + K_0^2\right)^{17/6}}}$$

1D spectrum of refraction index

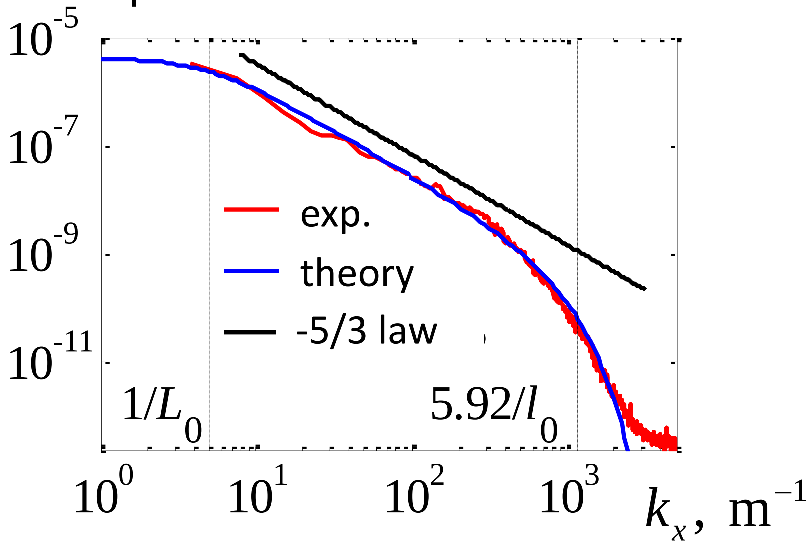

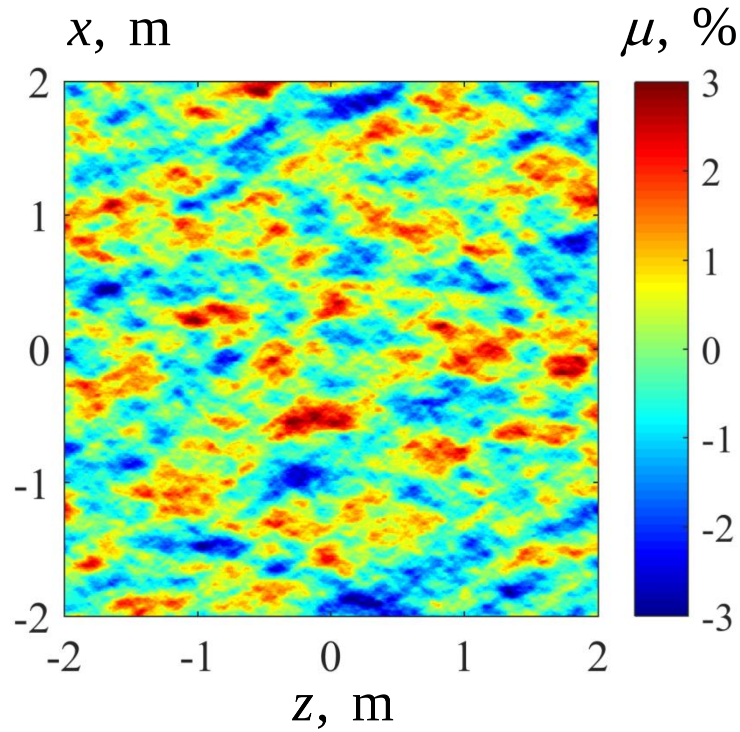

Propagation direction

Parameters of the spectra correspond to laboratory scaled experiments:
S. Ollivier & Ph. Blanc-Benon 2004. *Averiyanov M.V. et al*. 2011.

The outer scale L_0 = 16-20 cm

The inner scale l_0 = 5 mm

Refraction index root-mean-square μ_{rms} was set to 1%

Results of numerical simulations: acoustic field

Peak pressure realization

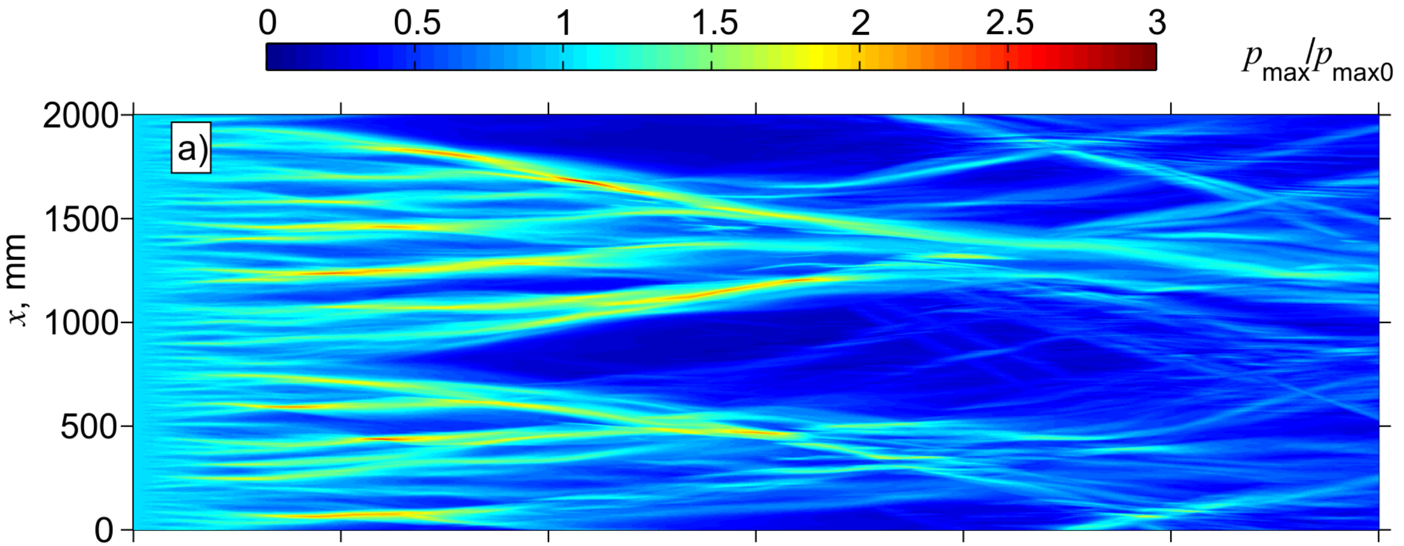

Refraction index realization

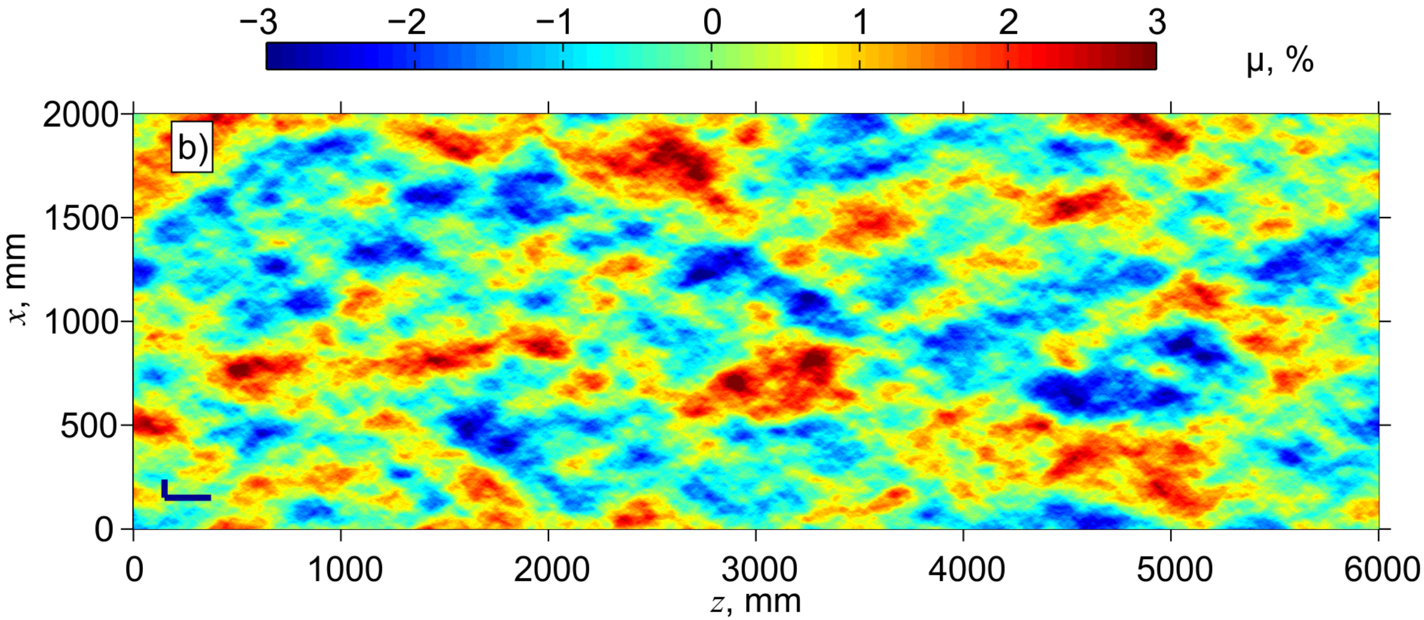

Root-mean-square μ_{rms} = 1%

Complex structure of random acoustic field with caustics and defocusing zones

Results of numerical simulations: waveforms

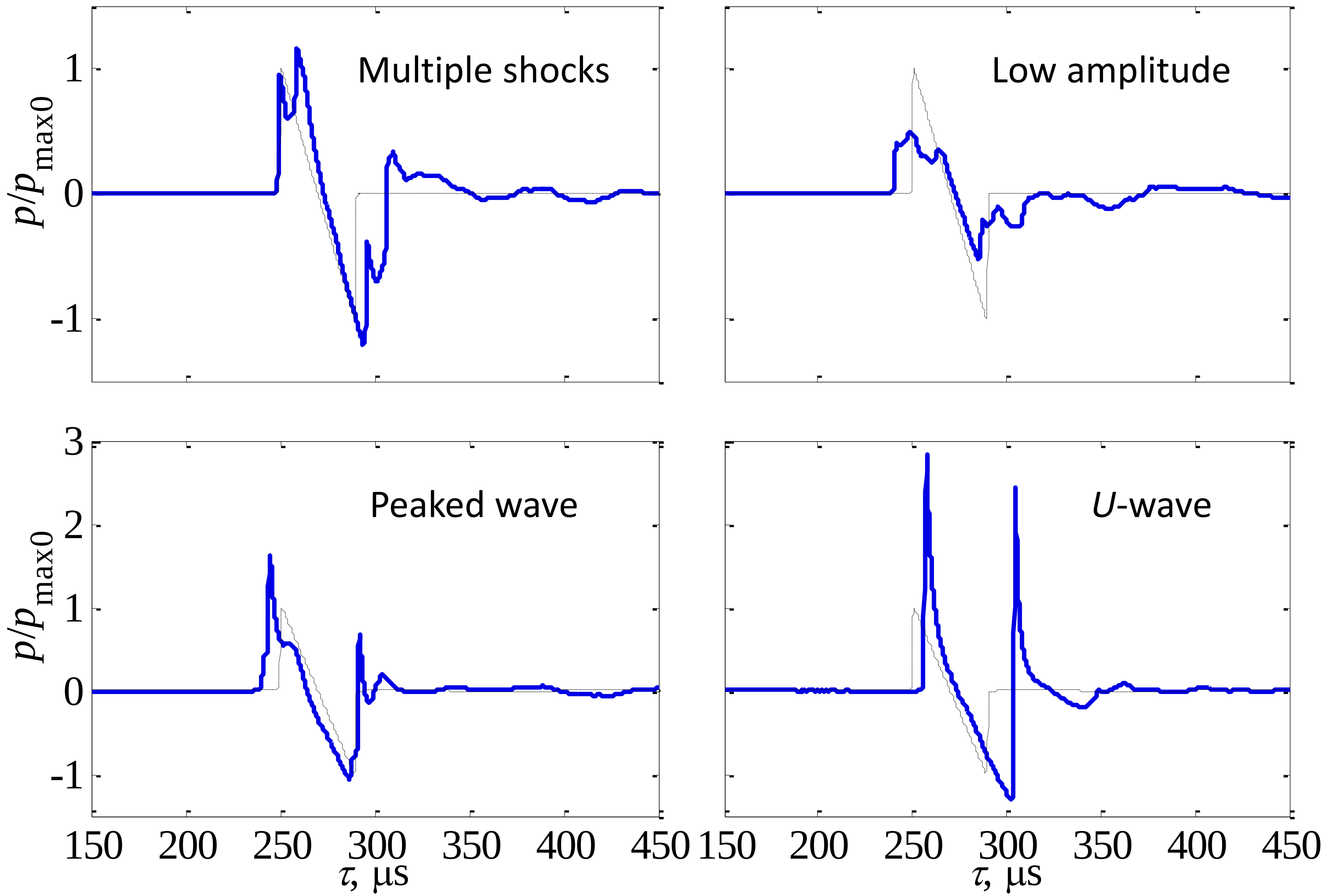

Classical distortions of random waveforms are observed

Probability distributions of peak positive pressure

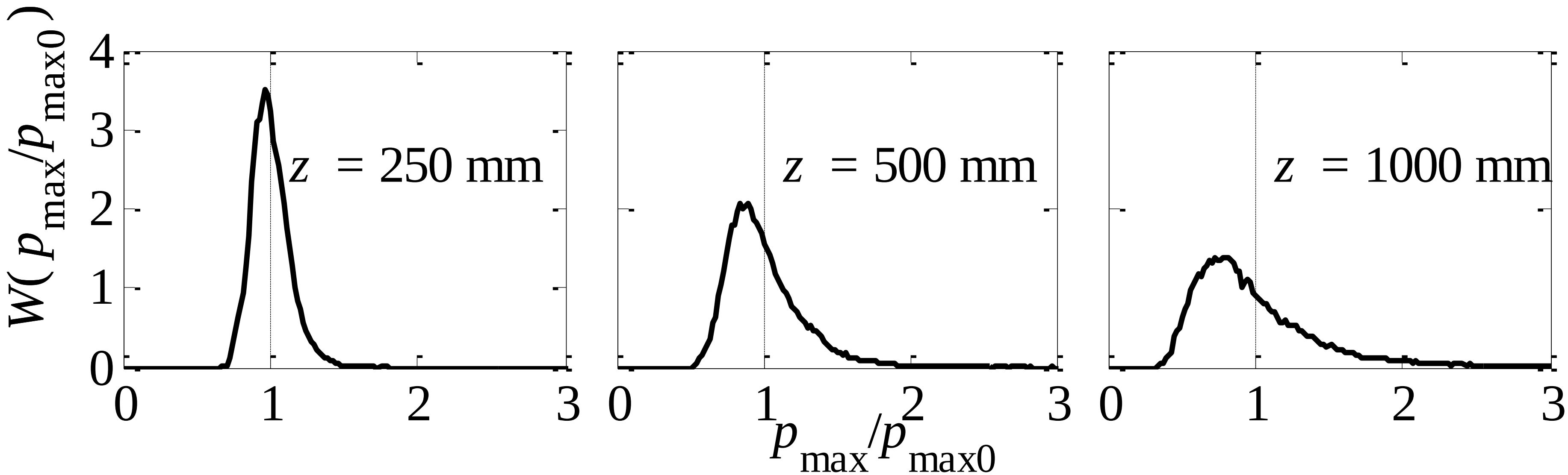

Statistical moments: mean value and standard deviation *vs*. propagation distance

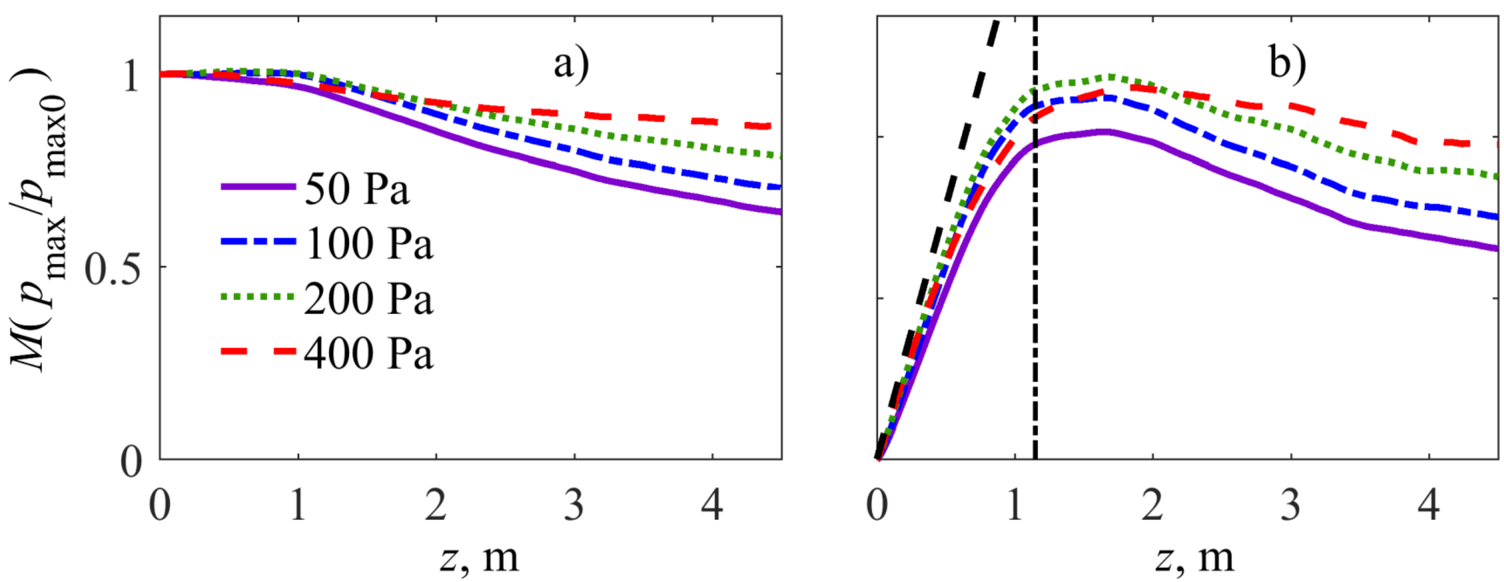

Cumulative probability for waves in random caustics

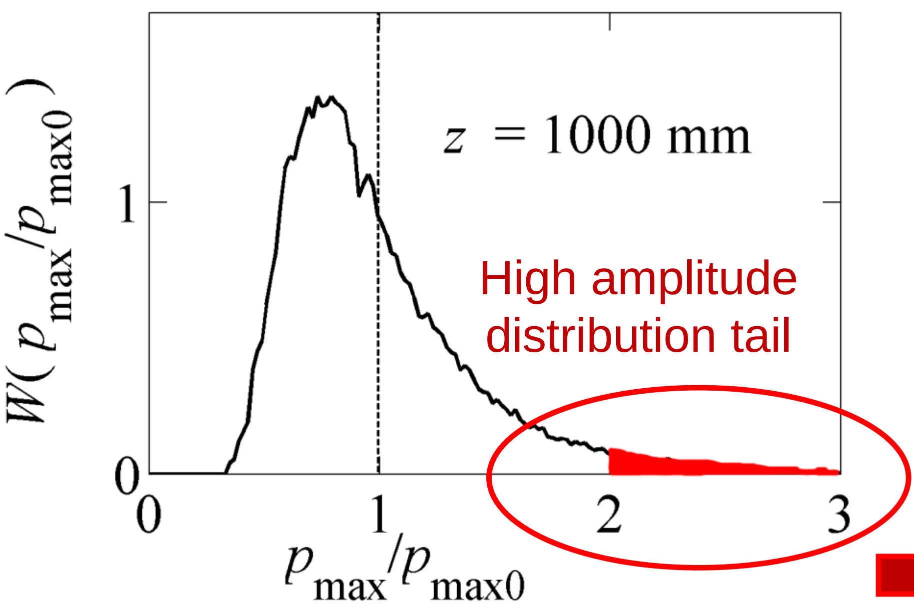

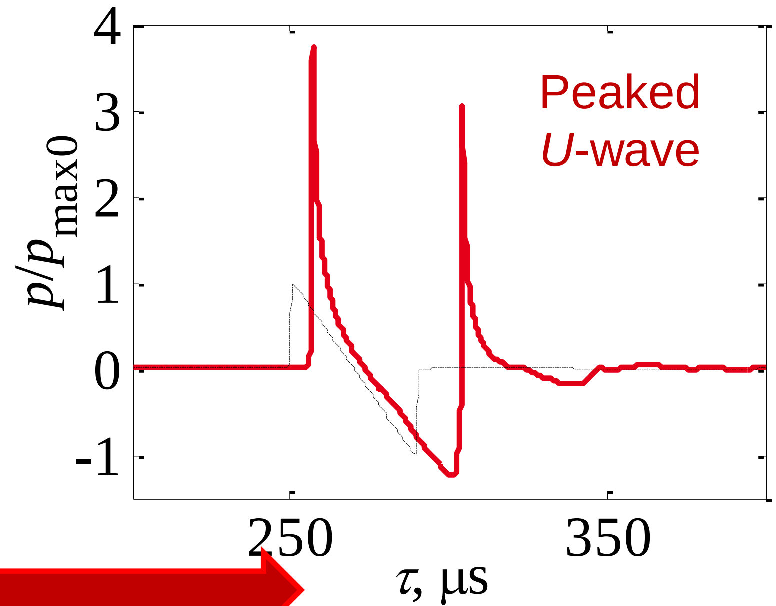

High amplitude distribution tail corresponds to amplified waveforms such as *U*-wave

Statistical measure of appearance of such “outliers” is a cumulative probability to observe the waveforms with peak overpressure exceeding a given threshold

Normalized peak overpressure: $P_{\max} = p_{\max} / p_{\max 0}$

$$\mathrm{Prob.}(P_{\max} > 2) = \int_2^{\infty} W(P_{\max}) dP_{\max}$$

Peak overpressure and steepness statistic: linear propagation

$$\frac{\partial^2 p}{\partial z \partial \tau} = \frac{c_0}{2}\frac{\partial^2 p}{\partial x^2} + \frac{\mu}{c_0}\frac{\partial^2 p}{\partial \tau^2} + \cancel{\frac{\beta}{2\rho_0 c_0^3}\frac{\partial^2 p^2}{\partial \tau^2}} + \cancel{\frac{\delta}{2c_0^3}\frac{\partial^3 p}{\partial \tau^3}}$$

Peak overpressure cumulative probability

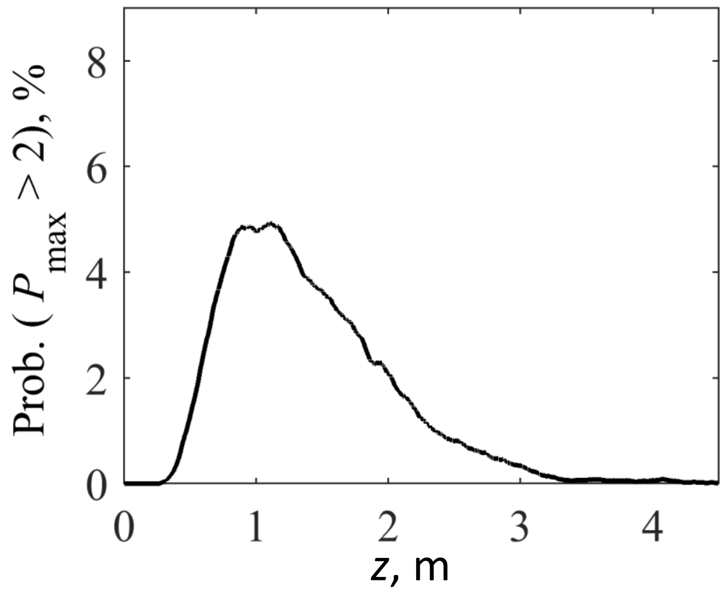

Shock front steepness cumulative probability

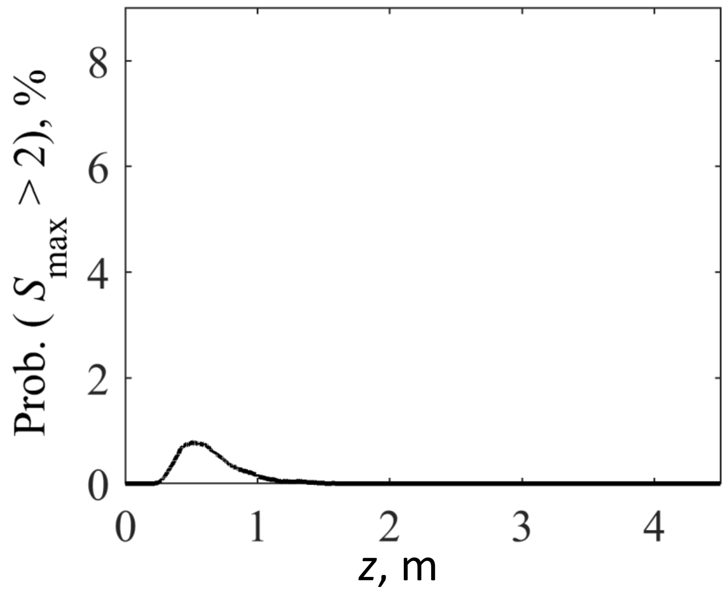

Steepness cumulative probability is low (1%) in comparison with peak overpressure cumulative probability (5 %). Indication of shock front smearing produced by turbulence

Peak overpressure and steepness statistic: nonlinear propagation

$$\frac{\partial^2 p}{\partial z \partial \tau} = \frac{c_0}{2}\frac{\partial^2 p}{\partial x^2} + \frac{\mu}{c_0}\frac{\partial^2 p}{\partial \tau^2} + \frac{\beta}{2\rho_0 c_0^3}\frac{\partial^2 p^2}{\partial \tau^2} + \frac{\delta}{2c_0^3}\frac{\partial^3 p}{\partial \tau^3}$$

Peak overpressure cumulative probability

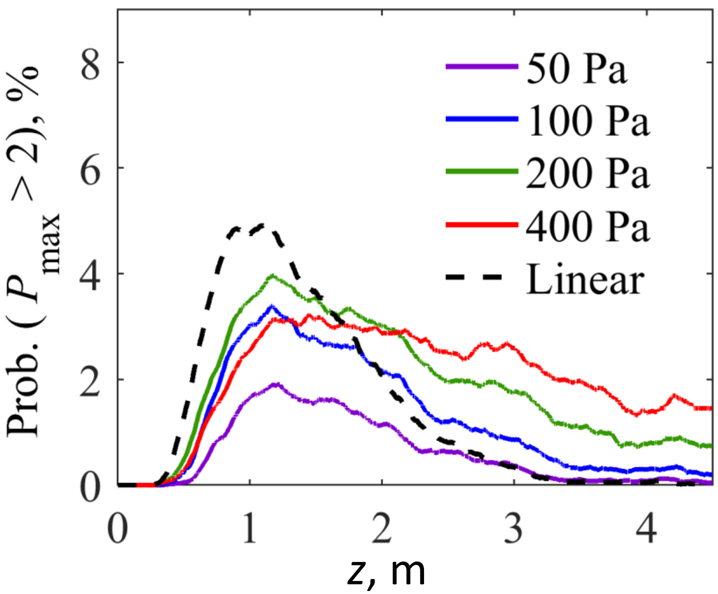

Shock front steepness cumulative probability

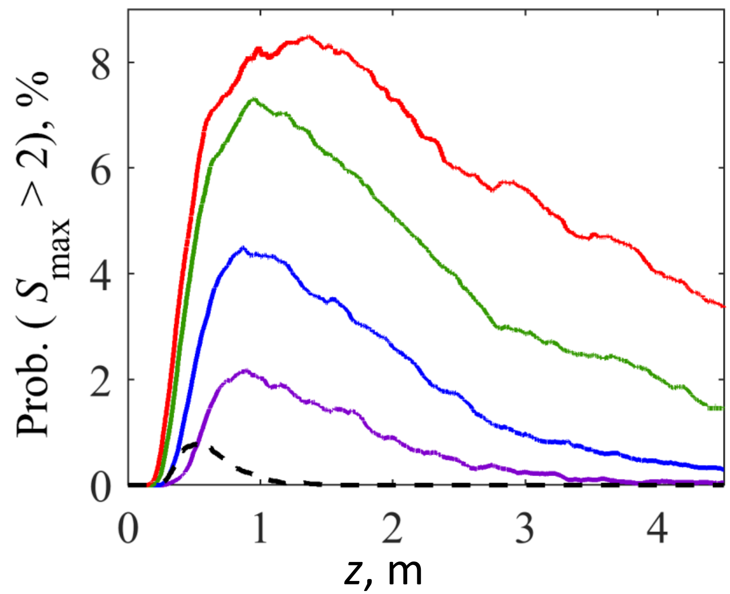

Steepness cumulative probability is high (2-8%) in comparison with peak overpressure cumulative probability (2-4 %) and depends on wave amplitude. Nonlinear effect seems to be important in *N*-wave interactions with turbulence.

Conclusions/Discussion

1. A numerical model based on 2D KZK-type nonlinear parabolic equation can be used to simulate propagation of acoustic pulses through turbulent media.
2. In the linear propagation regime, the presence of turbulence leads to smearing the shock front. In this case probability to observe waveforms with steep shock front is relatively small in comparison with probability to observe waves with high peak overpressure.
3. Nonlinear simulations showed that nonlinear shock front steepening could counteract shock front smearing resulting in higher values of cumulative probabilities of steepness. In this case the probability to observe outliers with high shock steepness significantly depends on the wave amplitude.

Shock front steepness definition II

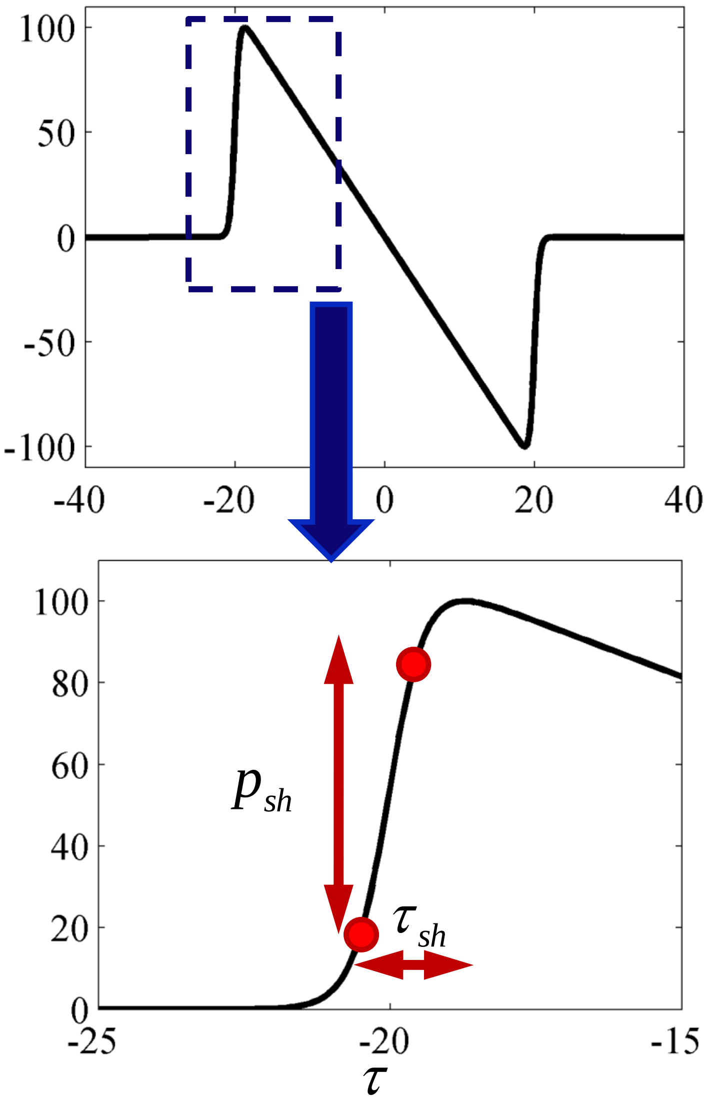

Steepness is defined as a ratio of shock front amplitude to the rise time.

The rise time is calculated using derivative based definition.

$$\tau_{sh} = \frac{4.4\delta\rho_0}{\beta p_{\max}} = \frac{C}{p_{\max}} \propto \frac{1}{p_{\max}}$$

$$s = \frac{p_{sh}}{\tau_{sh}} = \frac{0.8\, p_{\max}^2}{C} \propto p_{\max}^2$$

In the case of plane wave steepness is proportional to peak overpressure square

Alternative view on shock rise time

Distorted waveform example

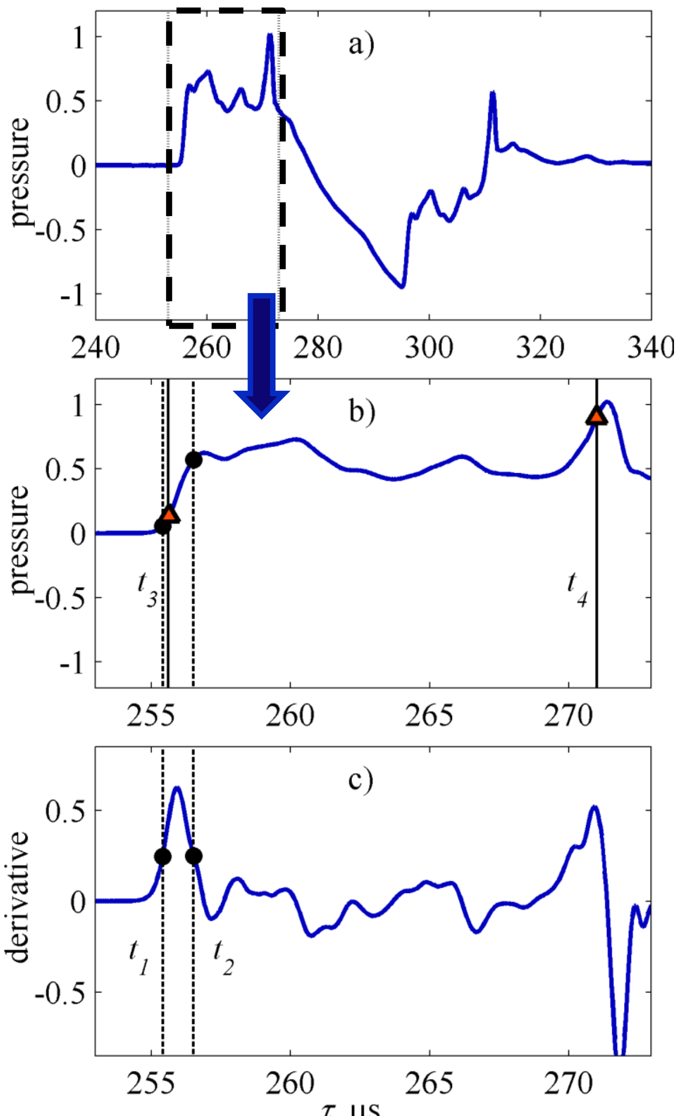

Distorted waveform has several shocks which is the result of interference of waves diffracted on different inhomogeneities

Classical rise time from 10% to 90% of p_{max} is about 15 µs

Very large rise time value, comparable to the total duration of waveform !

Alternatively rise time is defined as a width of highest peak of waveform derivative. Derivative based rise time is about 1 µs.

Derivative based definition of rise time is more suitable in the case of strongly distorted waveforms

Distance of formation of the first strong caustics II

Theoretical estimation of the distance of the most probable appearance of caustics is provided by

Kulkarny & White, 1982. Blanc-Benon, Ostashev and Wandelt, 1995

where the approximation of geometrical acoustics was used

$$z_{caust} \propto \frac{L_0}{\mu_{rms}^{2/3}}$$

Power = 2/3

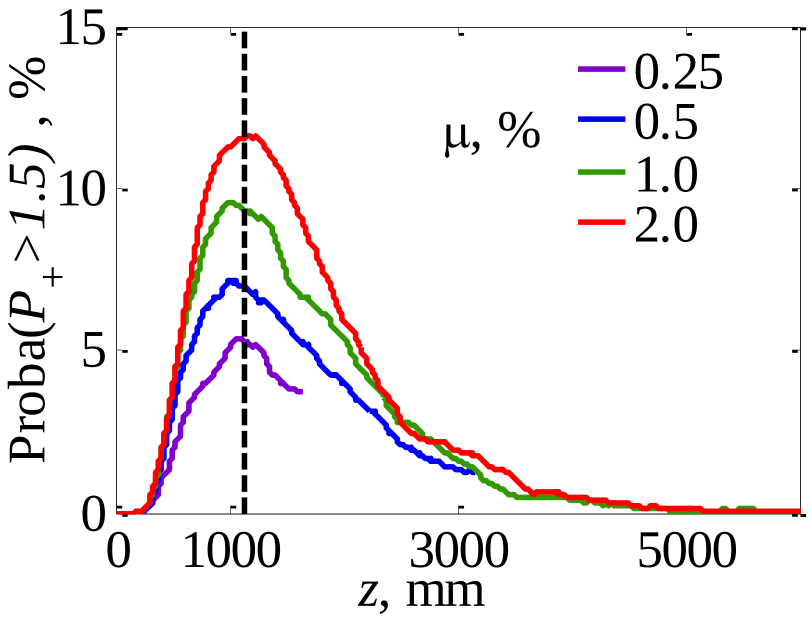

Plot the cumulative probability as function of scaled distance *z*

$$z_{scaled} \propto z\left(\frac{\mu}{\mu_0}\right)^{\alpha} \qquad z_{caust} \propto \frac{1}{\mu_{rms}^{0.93}}$$

The result is

Power = 0.93

Parabolic approximation gives quite different result than rays theory

Effect of nonlinearity on waveforms

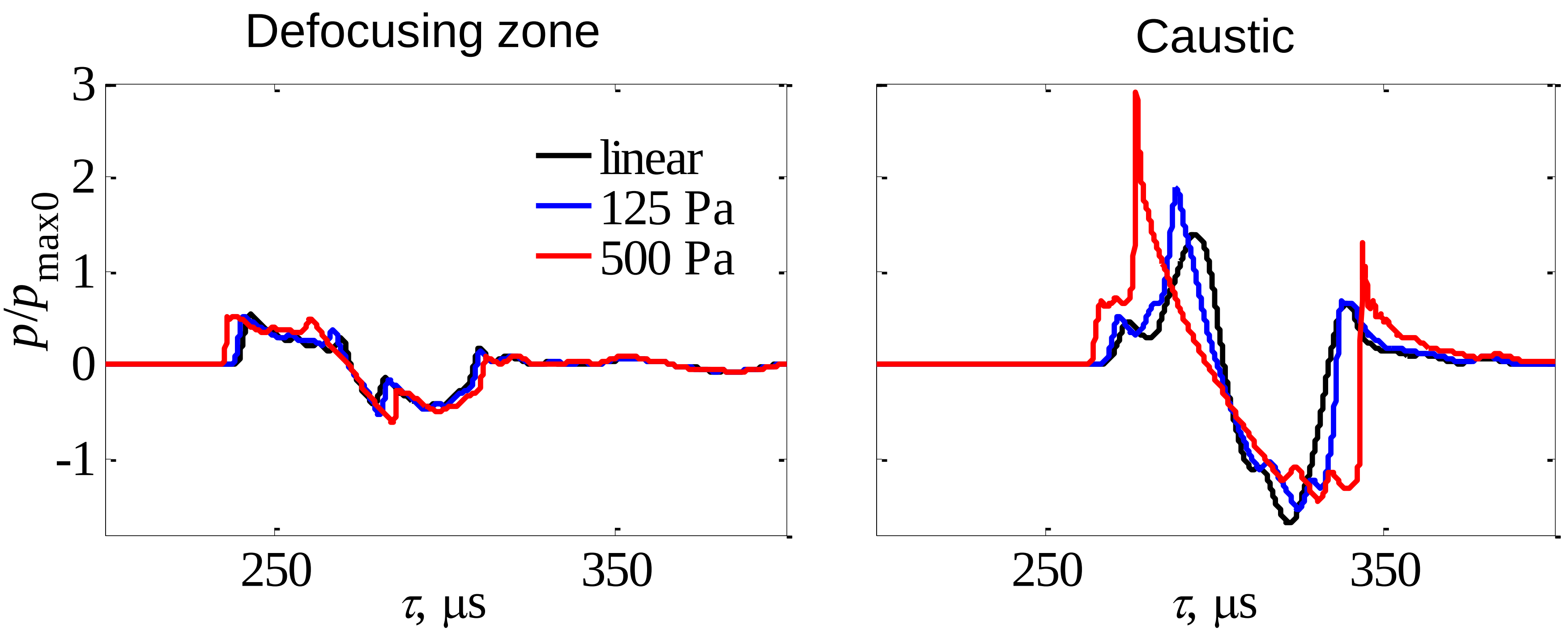

Nonlinear effects considerably increase peak pressure in caustics

Effect of nonlinearity on statistical distributions of peak positive pressure

Probability distributions at a fixed distance for different amplitudes of incident wave

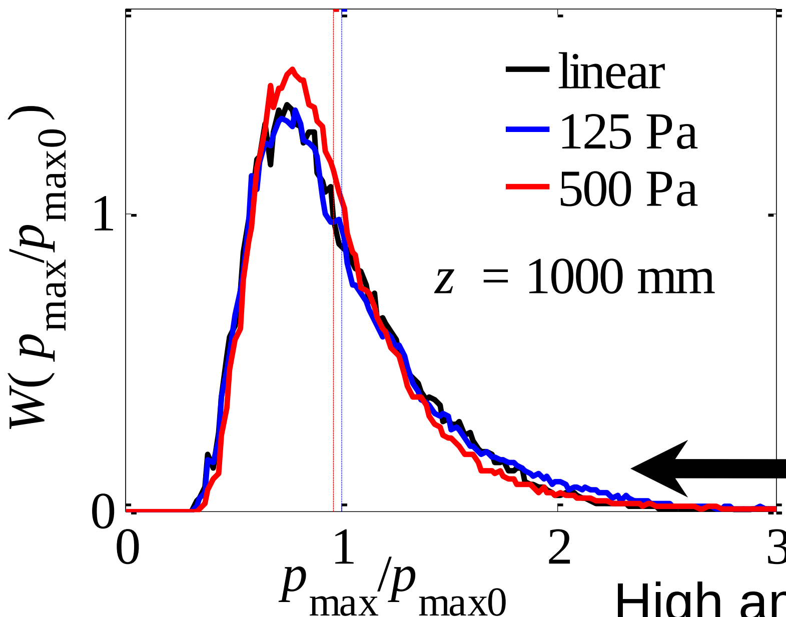

Probability to observe waveforms with peak pressure doubled or more

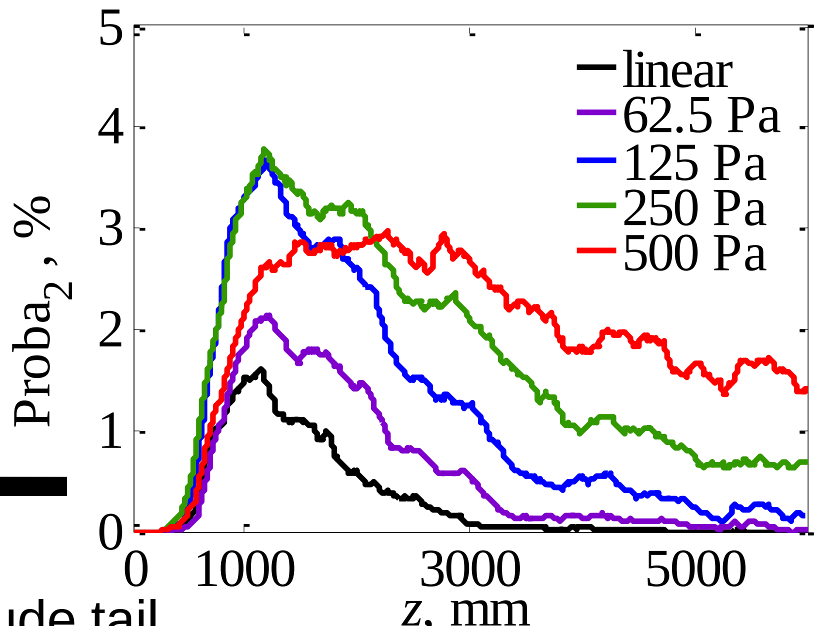

High amplitude tail

Nonlinear effects considerably increase probability to observe peaked waveforms and keep peaked waveforms longer

Conclusions/Discussion

1. The problem of propagation of nonlinear pulses through turbulent media is considered using 2D KZK-type nonlinear parabolic equation. Probability distributions of peak positive pressure of randomly distorted waveforms are calculated using numerical simulations of wave propagation through sufficiently long realizations.

2. Impact of turbulence intensity and initial amplitude of *N*-wave on statistical distributions of peak positive pressure is considered.

3. The distance of the most probable appearance of caustics establish scaling law $\mu^{-0.93}$ which is different from rays theory result $\mu^{-2/3}$.

4. Nonlinear effects considerably increase probability to observe peaked waveforms.

Perspectives

1. Consider statistics of other parameters of the waveforms:
    A. peak negative pressure
    B. rise time $\Delta\tau$
    C. steepest slope $\Delta p/\Delta\tau$
    D. duration
    E. arrival time

2. Crosscorrelation analysis of statistics of different parameters, for example peak pressure and risetime

3. Try to vary all set of parameters: turbulence outer scale L_0 , turbulence intensity μ, initial wave amplitude.

4. How to provide consistent view on the statistical results?

A laboratory-scale experiment for *N*-wave propagation through a layer of thermal turbulence

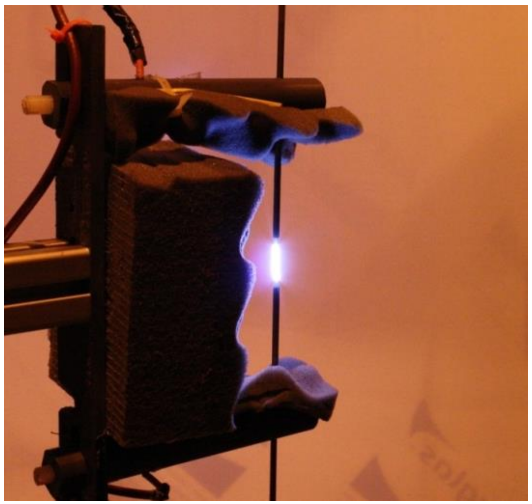

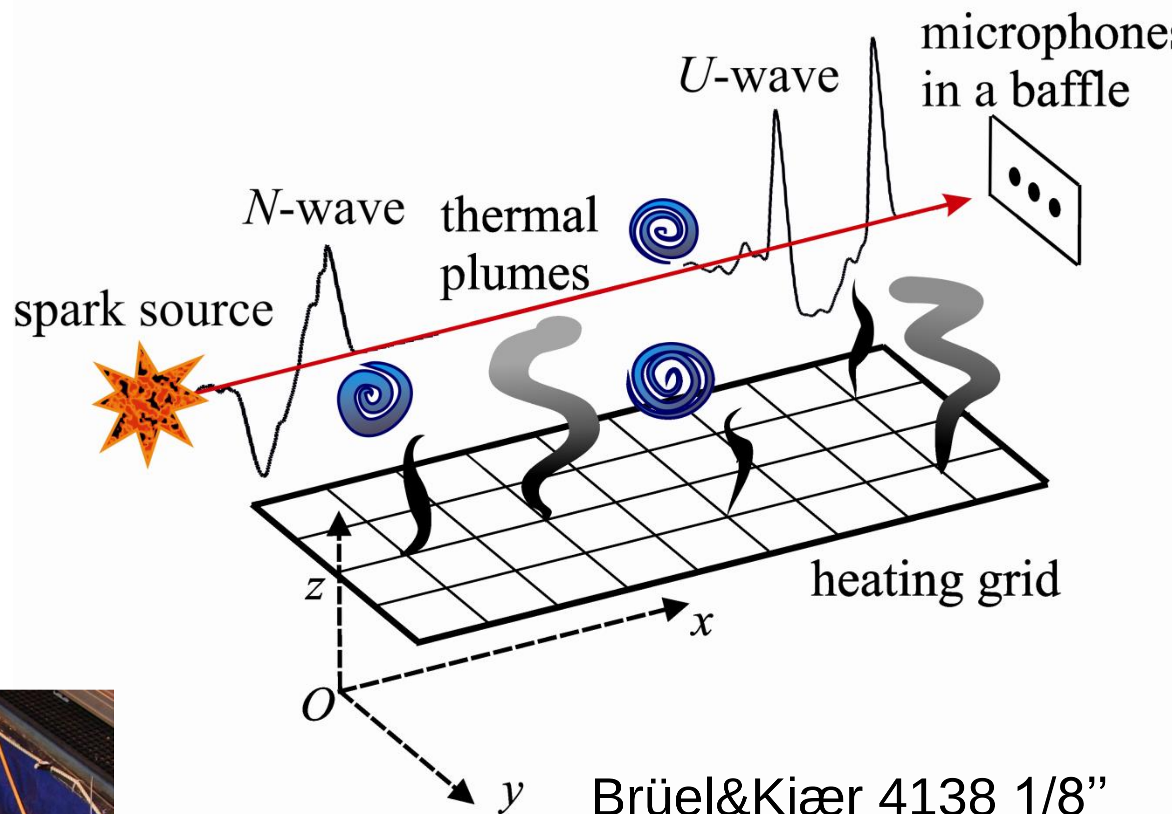

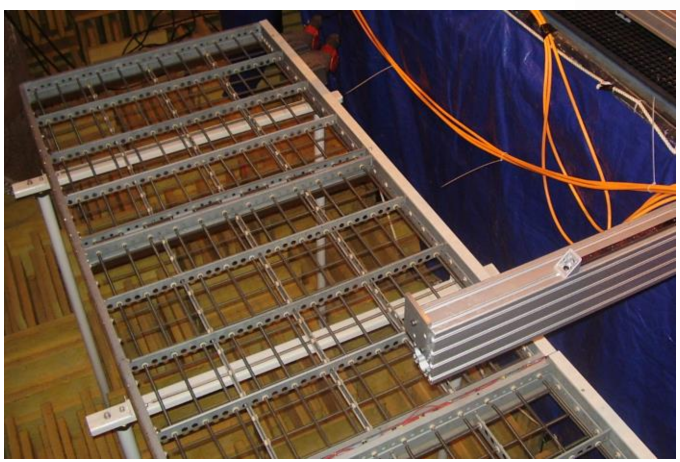

Brüel&Kjær 4138 1/8''

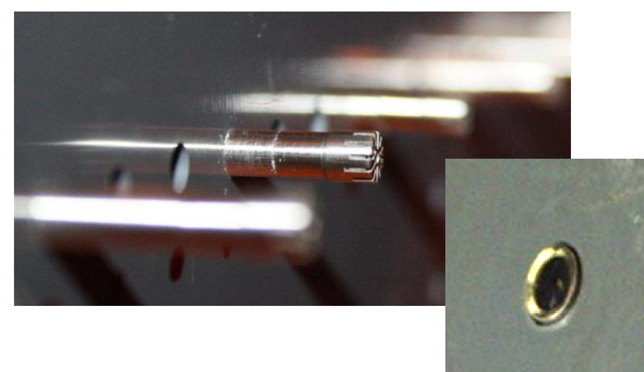

Yuldashev P.V. et al. // Acoustics 2012 (Nantes, France)

DE LA RECHERCHE À L'INDUSTRIE

Outdoor Blast Wave Simulation in Real Environment

LRSP Lyon, June 12-13, 2018

Olaf Gainville
Nicolas Lardjane
Maxime Nguyen-Dinh

CEA, DAM, DIF
F-91297 Arpajon

www.cea.fr

OUTLINE

Context

Euler model

One-way parabolic model

Coupling procedure

Sound annoyance

Waveguide / topography effects

Conclusions

CONTEXT

Context

- Explosion of ~300kg eq.TNT of ANFO for clad steel welding in a pyrotechnic site
- Sound annoyance quantification in both the **near** and **far** vicinity of the site
- Main physical effects:
  - Topography
  - Nonlinear/linear propagation
  - Nature and roughness
  - Near field: shape/position of the source
  - Far field: atmospheric conditions

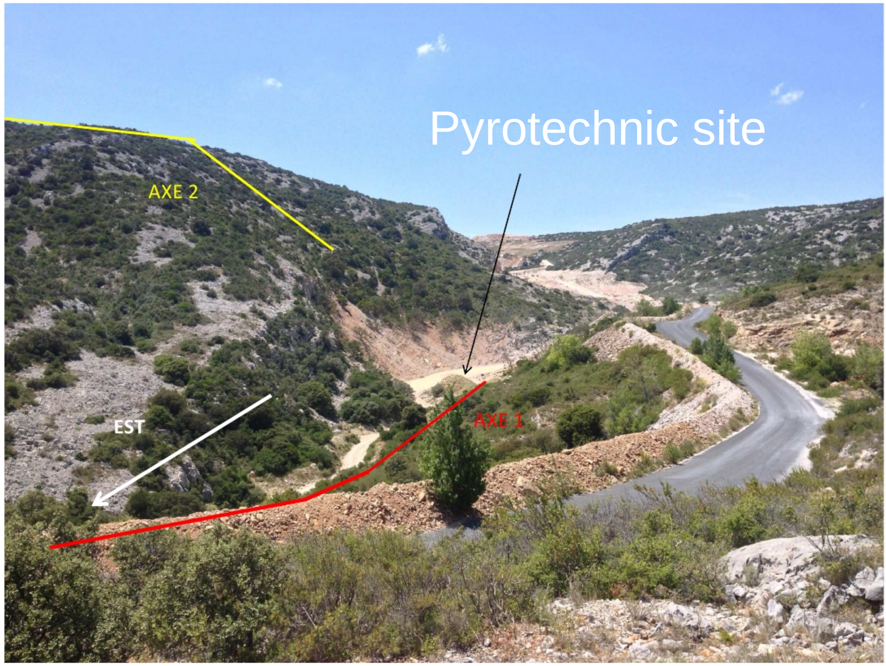

Objectives

- Numerical simulation of blast wave propagation in both near and far fields
  Quantify main physical effects contribution …
  … but at a limited computational cost

Blast wave simulation methods

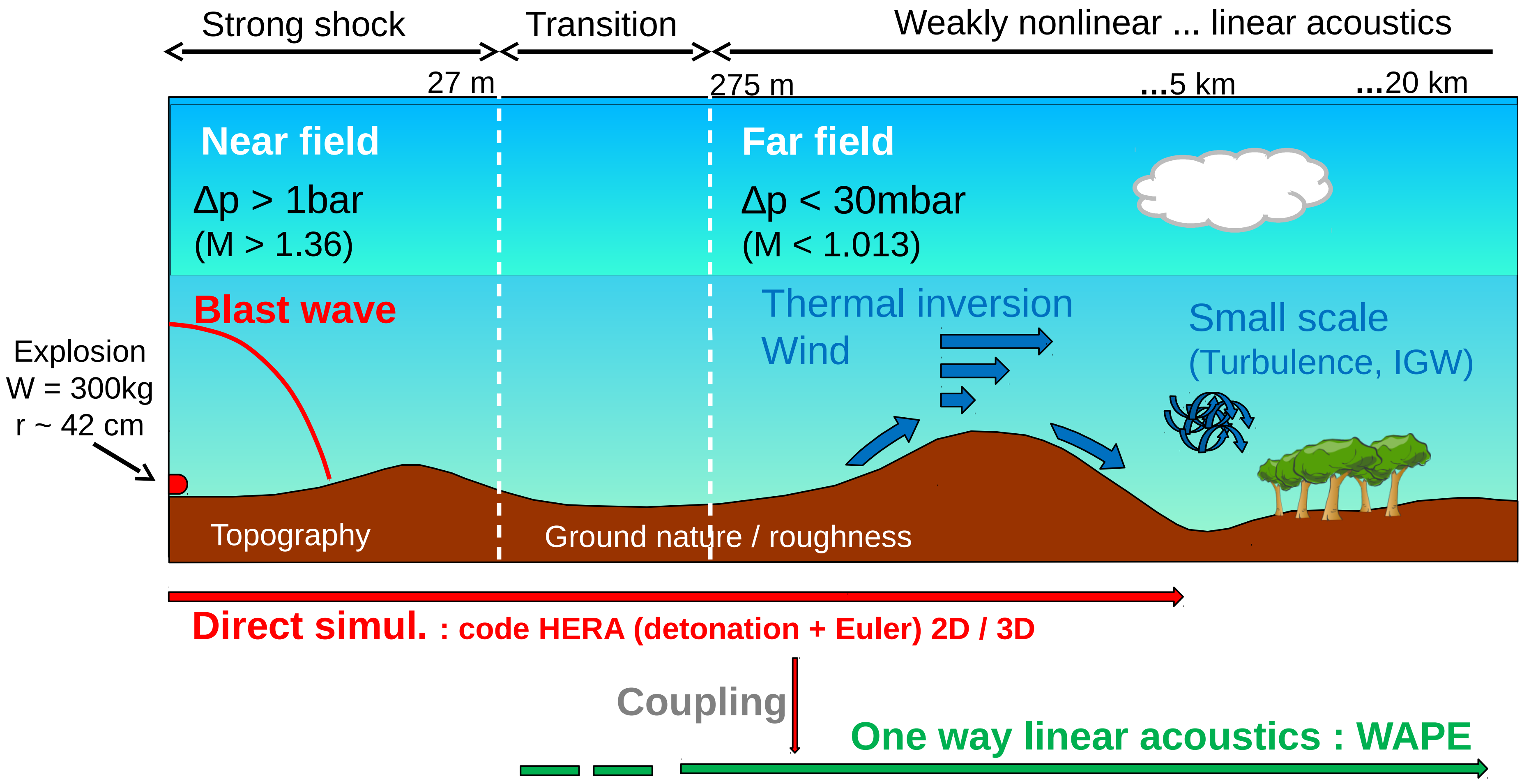

New developments:

AMR protocol, … ground roughness, wind

Topography, coupling with Euler model … wind, weakly nonlinear

HPC Euler code

- HERA : hydrodynamic CEA code
  - Eulerian, 1D-2D-3D, multi-materials, cartesian mesh, AMR (Adaptive mesh refinement) to follow the wavefront
  - Cf. Jourdren, H., HERA in Adaptive Mesh Refinement Theory 2005
  - Highly parallel code adapted to CEA supercomputer ($10\cdot10^9$ cells AMR@10KPEs)

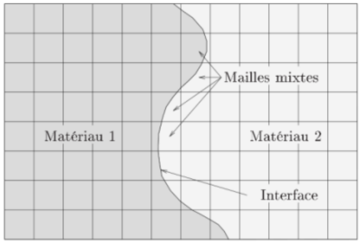

- Acoustic propagation specific developments
  - Detonation & Euler's equations (Δx=1 cm.kg$^{1/3}$ ⇨ ~10cm)
  - High order finites volumes scheme (GAIA)
  - AMR method based on wavefront arrival time
  - Roughness : drag force close to the ground
  - Meteorology : effective sound speed (2D)
  - W=300kgTNT, R_{max} = 5km ⇨ ~36h@256 PEs

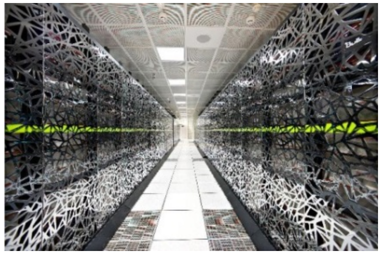

Tera100 : ~140Kprocs
1,2Pflops (2010)

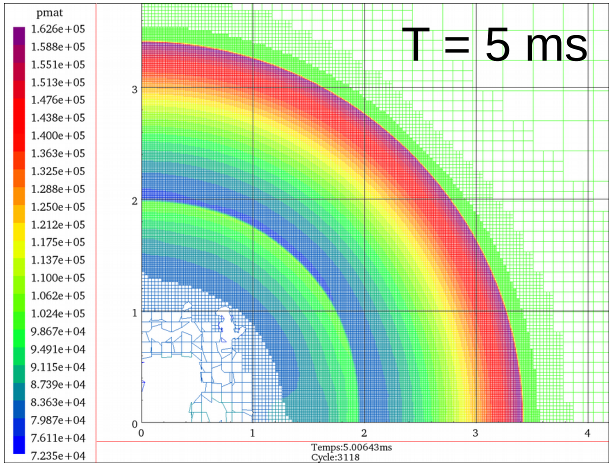

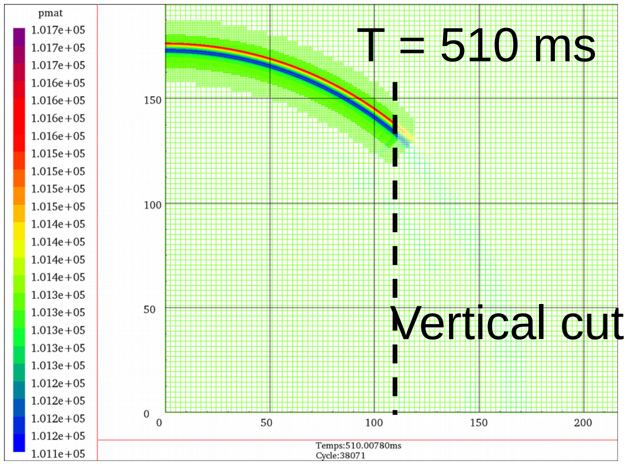

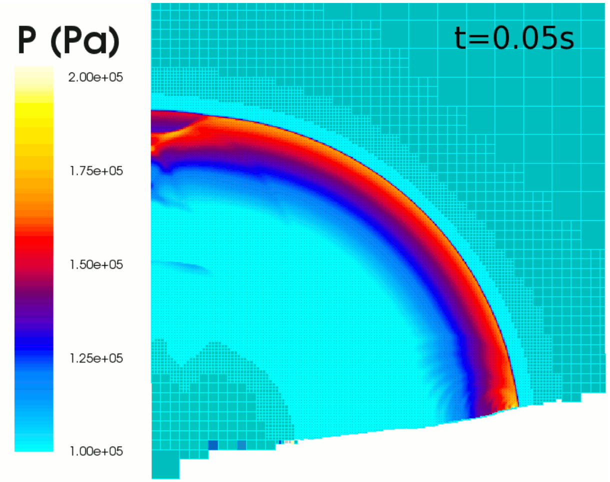

Parabolic approximation for the far field

- One way approximation of the wave equation (WAPE)

$$\frac{\partial \varphi}{\partial r}(\mathbf{r}) = ik_0(Q-1)\varphi(\mathbf{r})$$

- Include topography
  - Peacewise linear topography
  - Phase rotation strategy (Shift map PE)
- Meteorological conditions
  - Effective sound speed
- Coupling between Euler eq. & WAPE
  - Euler (Detonation, meteo, topo, nonlinear)
  - Initial condition at 500 m (unaliased interpolation)
  - Parabolic eq. (topo, meteo, linear)
- CPU time cost reduction (f=60 Hz, Rmax=5km)
  Starter : ~40min@1PE
  Coupling : ~40min@1PE + 10h@128PEs(Euler)

Stepper scheme toward the main direction

Source
- empirical
- coupling

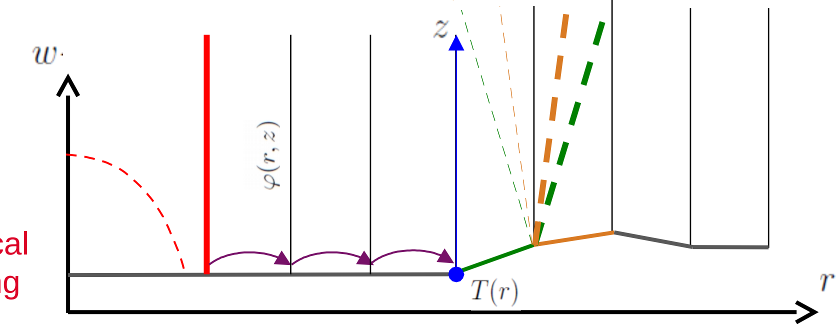

Reference topography: Parakkal 2010

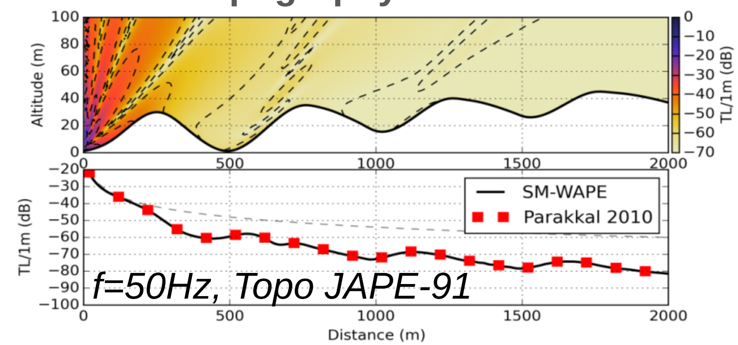

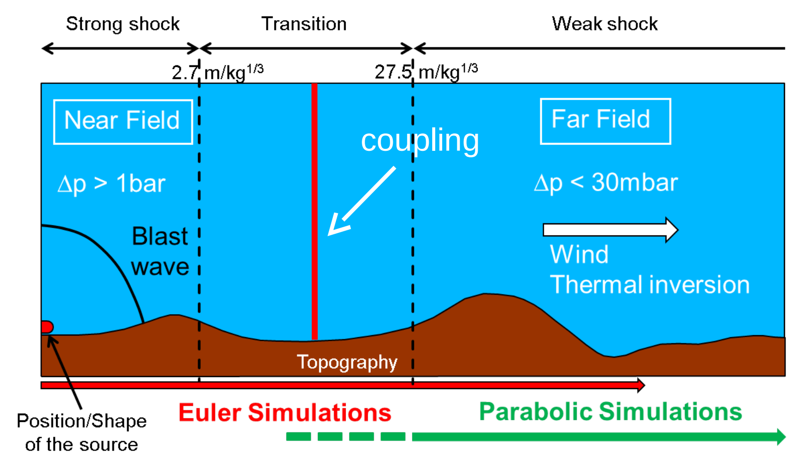

Main methods to include topography in one way approximation

- One way method with topography
  - Conformal mapping (Di & Gilbert 1993, Lu 2001)
  - Domain rotation and interpolation (Blairon 2000)
  - Generalized terrain PE (Sack & West 1995)
  - Generalized terrain WAPE (Donohue 2000, Holm 2007, Parrakal & al. 2010)
- *Wide-Angle Shift-Map PE*[1]

Helmholtz ⇒ $\boxed{z = w - T(r)}$ ⇒ $\varphi(r,z) = e^{-i\theta(r,z)}\tilde{p}(r,z)$ ⇒ WAPE (SSPadé)

$\tilde{p}(r,z)$

$$\theta(r,z) = k_0 T' z + \frac{1}{2} k_0 T'^2 r + k_0 r$$

$$\frac{\partial \varphi}{\partial r}(r,z) = i k_0 (Q-1)\varphi(r,z)$$

$$Q = \sqrt{1 + (n^2 - 1) + \frac{\partial^2}{\partial z^2}}$$

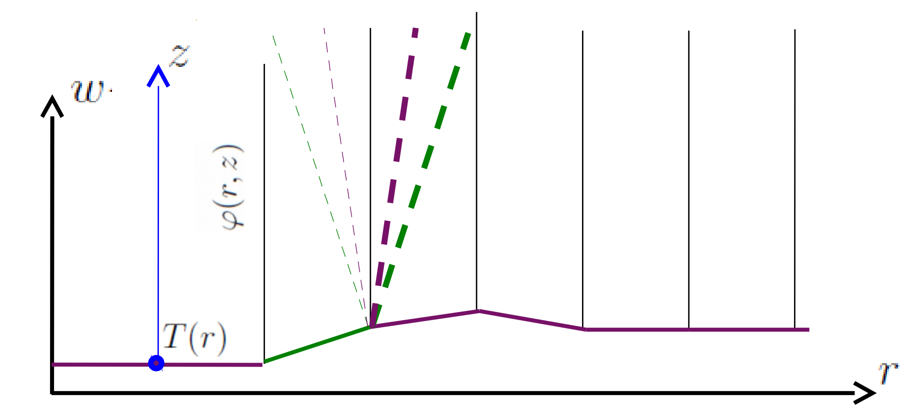

- Ground condition ⇒ modified impedance

$$\left[\frac{\partial}{\partial z} + i k_0 \left(\frac{T'^3}{2} + \beta\right)\right]\varphi(r,z) = 0$$

Angular limit when T'<0

[1]Holm IEEE Transactions on Antennas and propagation, 2007.

Euler HPC simulations
Application to a pyrotechnic quarry

- Computations up to 5km for 300kg TNT

	Azimuth	Distance
VPDE	~30º	~4000m
CARR	~40º	~1500m
MASR	~90º	~4300m
TAUT	~250º	~2500m

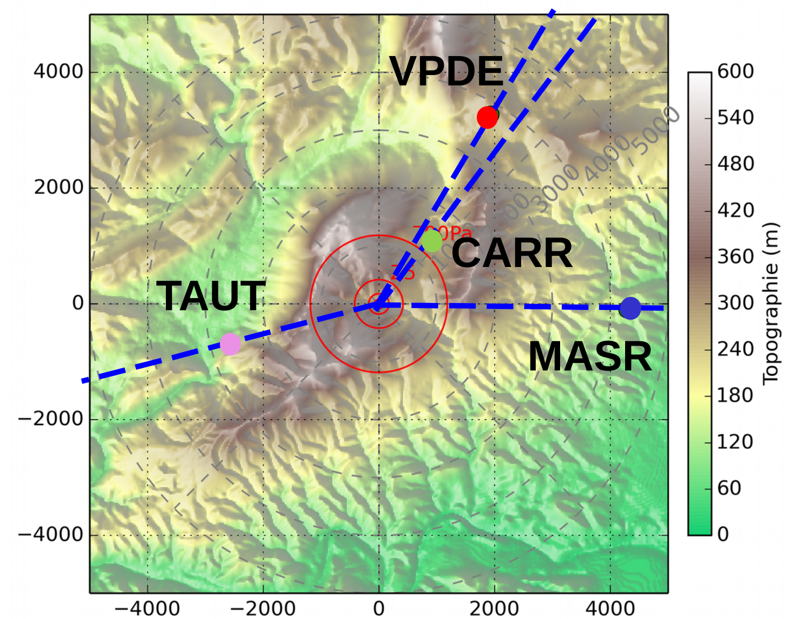

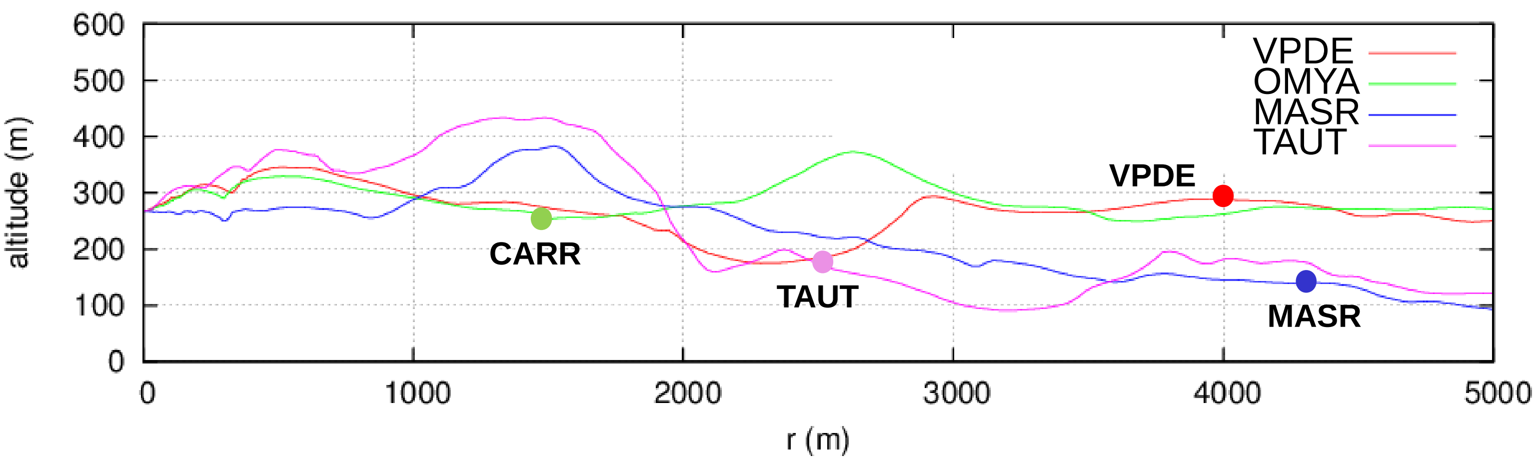

Euler HPC simulations in the far field
Topography effect on max overpressure

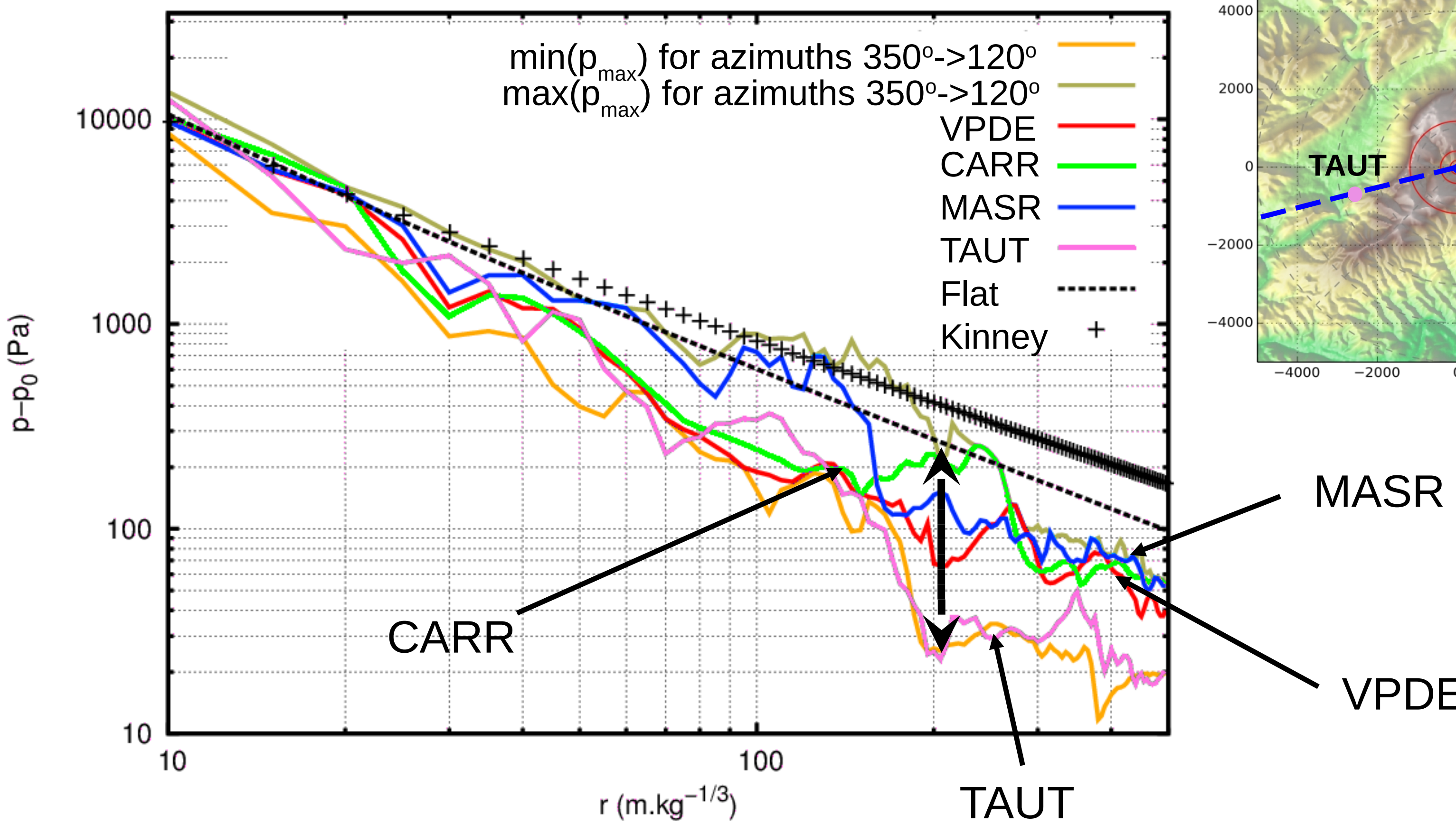

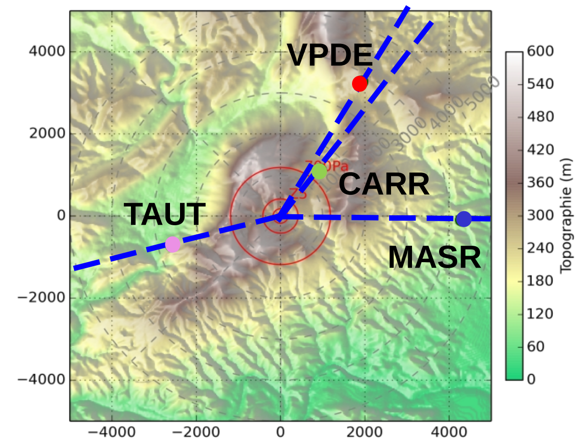

- Noticeable effect of topography in comparison with flat ground
- Up to 90% difference with respect to flat ground at 2000m

HPC Euler simulations in the far field
Comparison to measurements

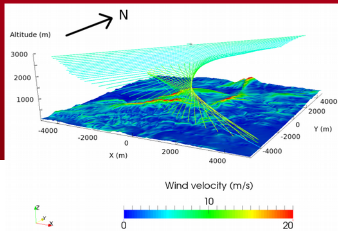

- HERA simulation in far field for W=300 kg TNT

  Three atmospheric conditions: homogeneous, waveguide, low wind (topo. compliant)

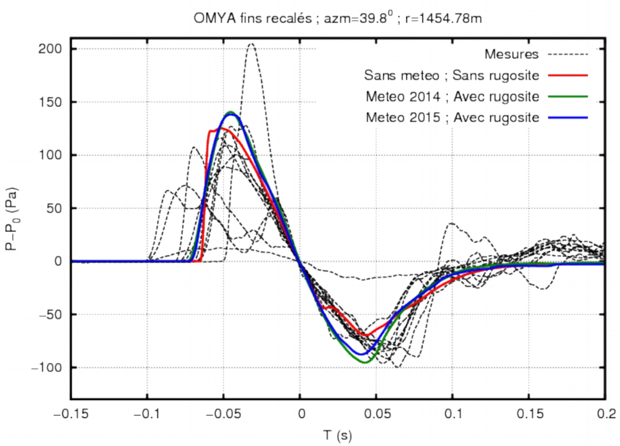

Simulations and measurements at CARR

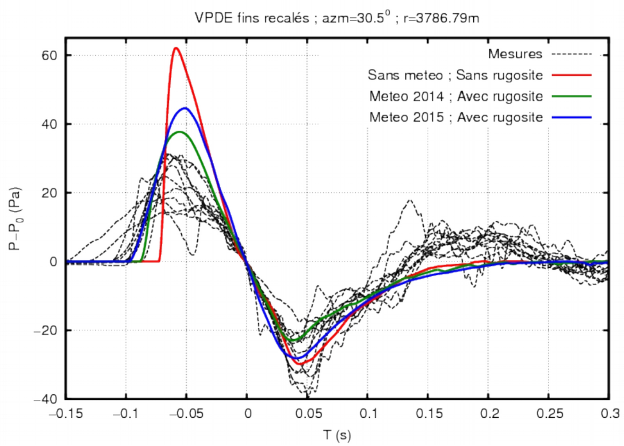

Simulations and measurements at VPDE

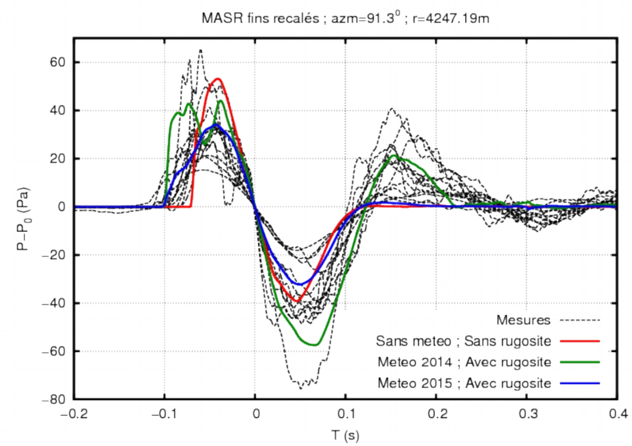

Simulations and measurements at MASR

  - CARR station : good comparison with records, signal are similar for the two meteorological conditions
  - VPDE station : bad comparison with records, overestimate maximum overpressure, 3D effects possible (strong transversal topography variations)
  - MASR station : good comparison with records, various waveforms (U wave for the waveguide condition)
- Main physical effects: Topography > Meteo > Roughness

Euler / Parabolic approximation coupling
Results at MASR (best case)

- Parabolic simulations in the direction of MASR for W=300 kg TNT
  - Good agreement with HPC Euler reference solution
  - Best results with the coupling than with the starter

Analytical starter | **Coupling at 500 m**

Homogeneous media | **Waveguide meteo**

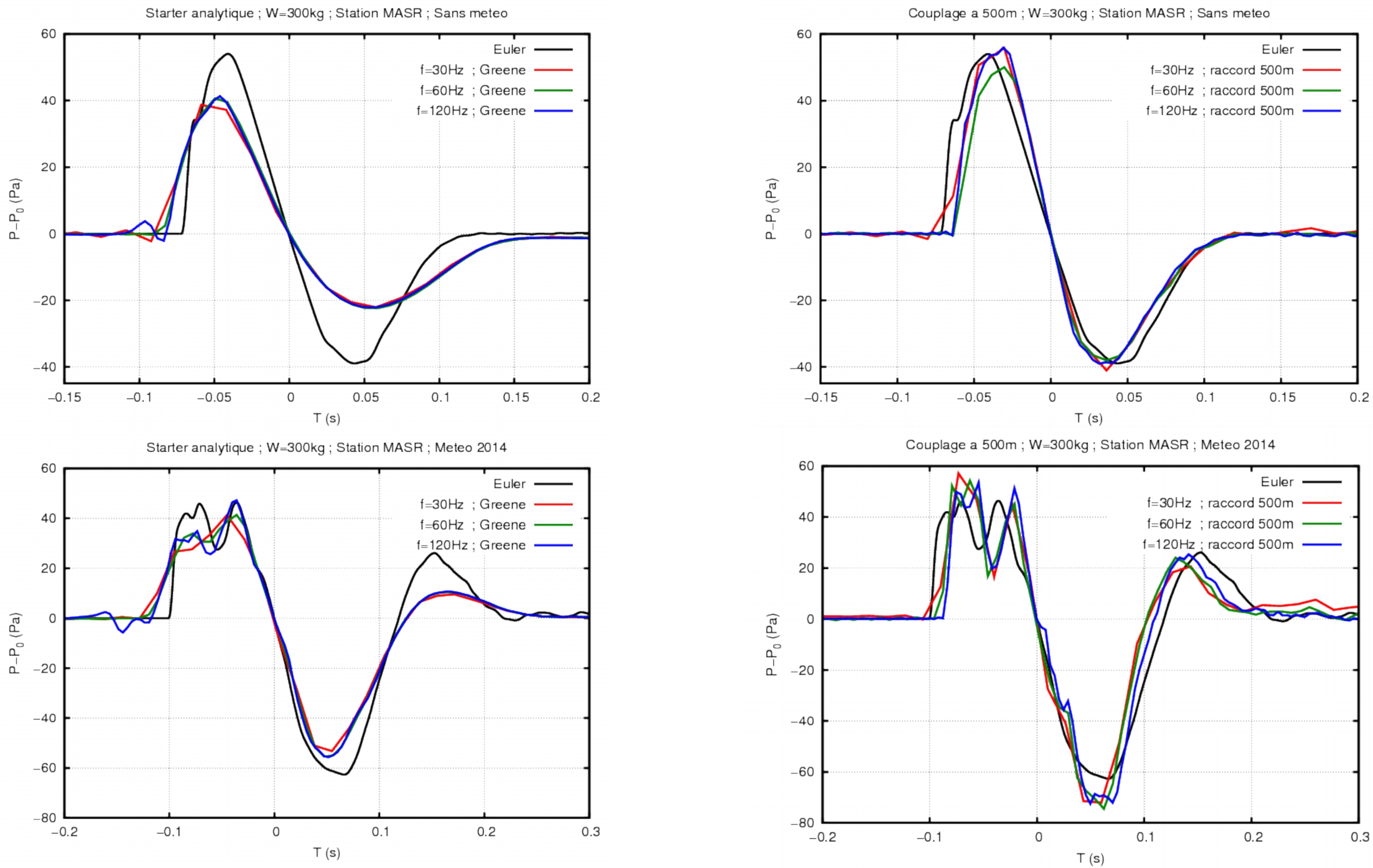

Annoyance
Maximum overpression observed at MASR (4 km)

- Maximum overpressure as the simplest indicator of sound annoyance
- Few days with high level (meteorological conditions)

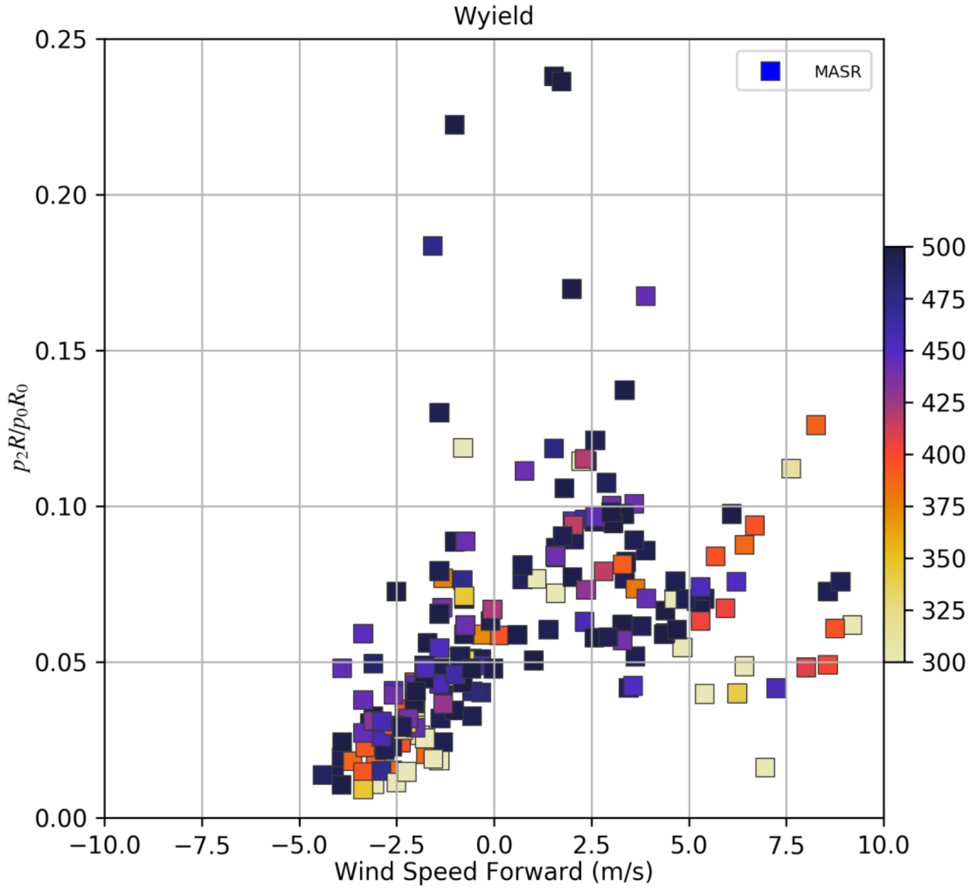

- Wind speed at ground level gives a first order
- Highest level cases are associated with small wind speed at ground level and strong vertical gradient

Annoyance
Anomalous propagation toward the Est at 4 and 9 km

- 4 identical explosions in 2015

2015-10-08T09

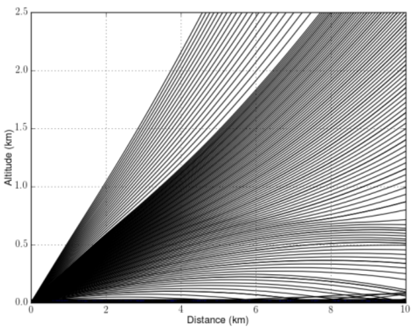

2015-10-05T09

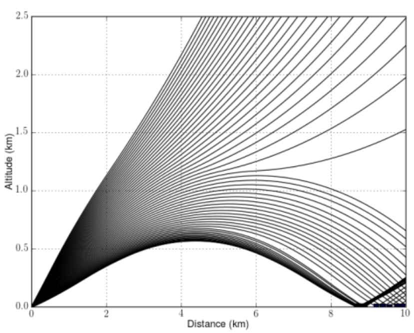

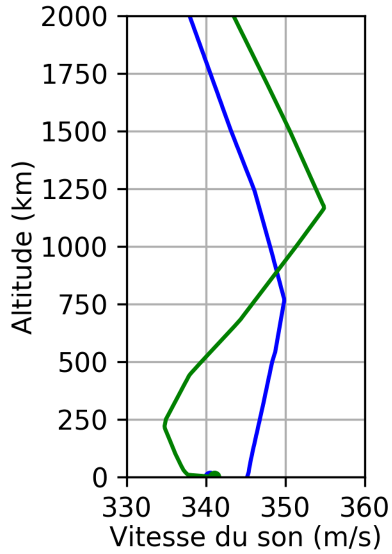

Arome meteorological effective sound speed profils toward the Est

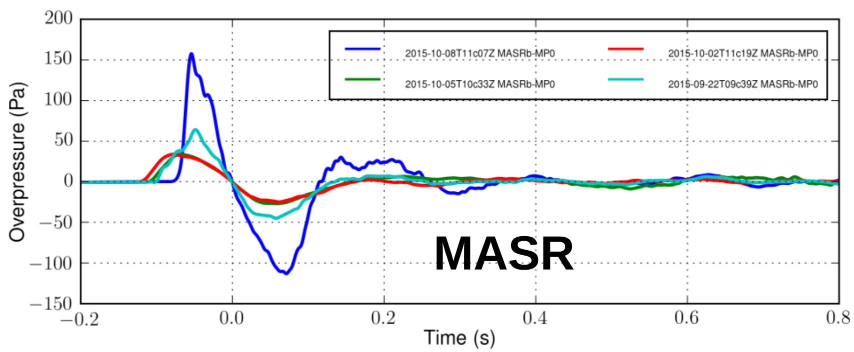

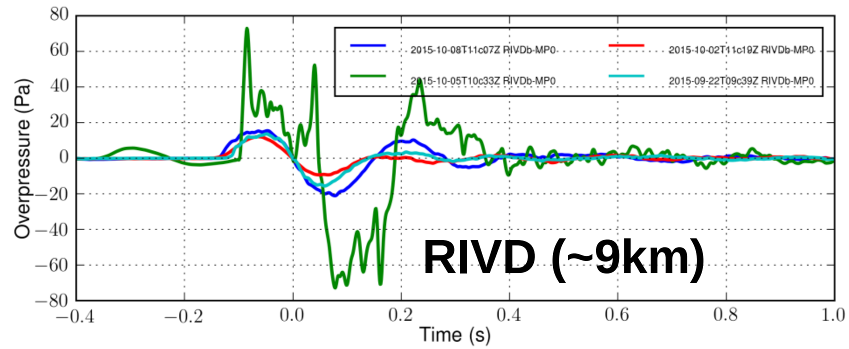

Competition between topography and waveguide effects

- Parabolic approximation (30 Hz) toward Est with W=300 kg TNT
- Simplified profiles of effective sound speed truncated by the topography

Waveguide height effects U = 10 m/s

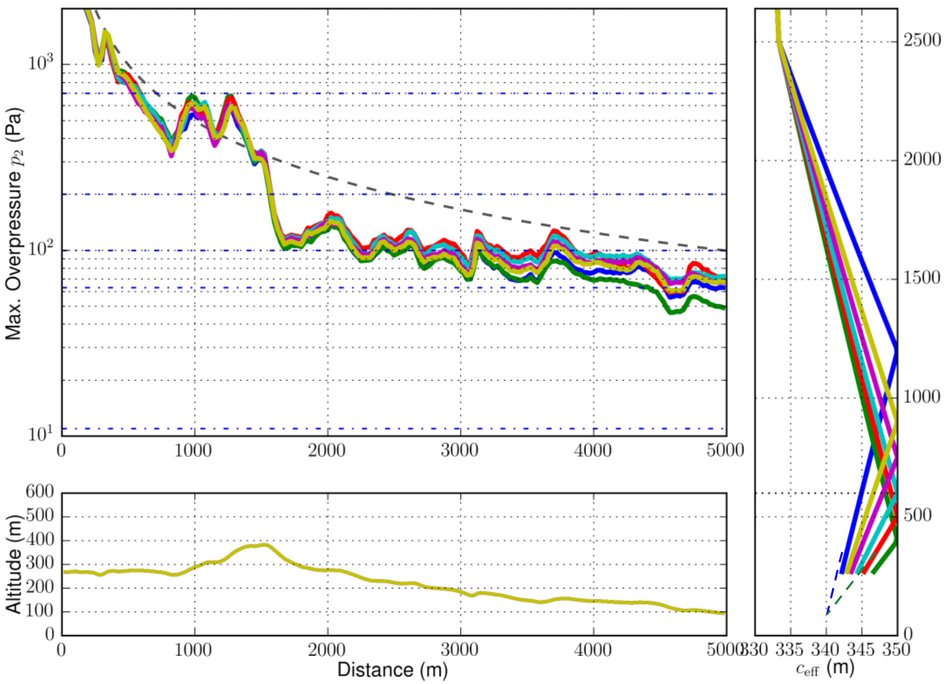

Waveguide/topography competition:
Worst case with H_{guide} = 600 m/sea level

Less annoyance conditions are neutral or downwind
⇨ Use Arome forecast for shoot decision ?

Wind speed effects

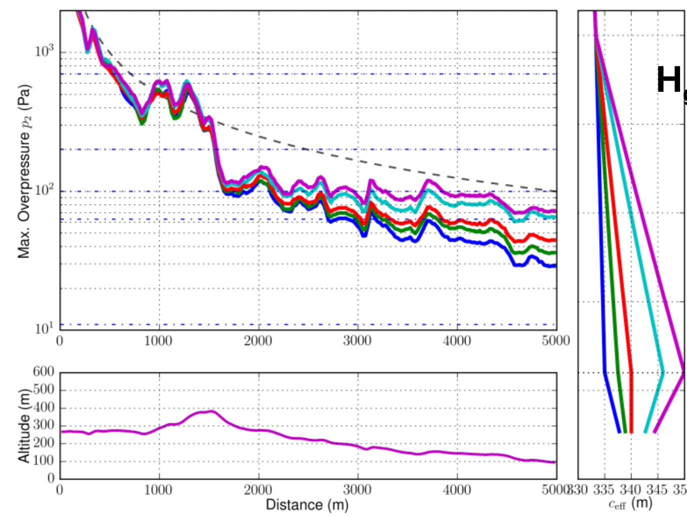

H_{guide} = 600 m

+10 m/s
+ 6 m/s
0 m/s
Thermique
- 5 m/s

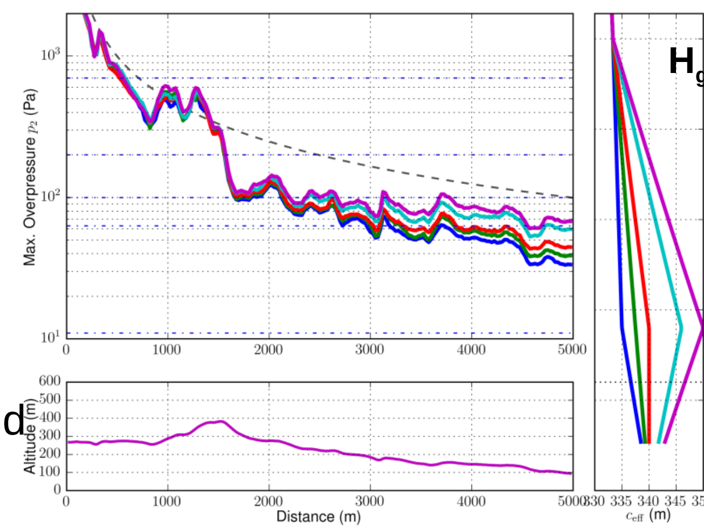

H_{guide} = 900 m

CONCLUSIONS

- HPC simulations with HERA
  - Reference solutions from near field (with detonation) up to far field
  - 2D, Euler + detonation, AMR (mesh size reduction ~100 for 2D), ~36h@256PEs
  - take into account « effective » meteo and roughness (preliminary tests)
- One way model for long range propagation with topography
  - Coupling HERA / WAPE allows parametric studies at low CPU cost (~10h@128PEs+40min@1PE)
- Application simulations for W = 300kg TNT up to 5 km:
  - Good agreement with measurements (except 3D effects at VPDE)
  - Main physical effects: Topography > Meteo > Roughness
  - Waveguide main effect at 4km for a maximum altitude at 600m

- To go forward
  - Realistic meteorological conditions (topography compliant)
  - Weakly nonlinear effects in the one-way model
  - 3D simulations for Euler and one-way
  - Statistical analysed of measurements/simulations

- Scientific contributions:

Y. Noumir *et al.* : A fast marching like algorithm for Geometrical Shock Dynamics, J. Comp. Physics 284, (2015)
M. Nguyen-Dinh *et al.* : Simulation of blast wave propagation from source to long distance with topography and atmospheric effects, 20th ISNA, (2015)
M. Nguyen-Dinh *et al.* : Direct simulations of outdoor blast wave propagation from source to receiver, Shock Waves (2017)
J. Ridoux et al. : Comparison of geometrical shock dynamics and kinematic models for shock-wave propagation, Shock Waves (2017)
M. Nguyen-Dinh *et al.* : A one-way coupled Euler and parabolic model for outdoor blast wave simulation in real environment, JCA (2018)

ANY QUESTION?

Commissariat à l’énergie atomique et aux énergies alternatives
CEA, DAM, DIF | F-91297 Arpajon
T. +33 (0)1 69 26 40 00

LRSPS 17, 12-13 June 2018, ECL Lyon

VARIATION OF IMPULSIVE SOUND EVENTS ON AND AROUND SHOOTING RANGE

Frits van der Eerden, Peter Wessels, Frank van den Berg

OVERVIEW

- Acoustic Environmental Management
  - Combining measurements and calculations
- Detection & localization
  - Using a large dataset with recordings
- Identifying & quantifying uncertainty of sound propagation
  - Using a sensitivity analysis
- Conclusions & Outlook

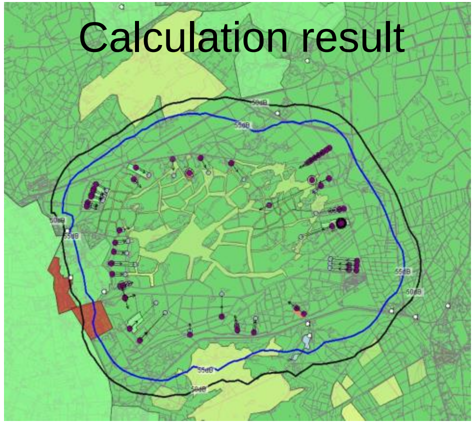

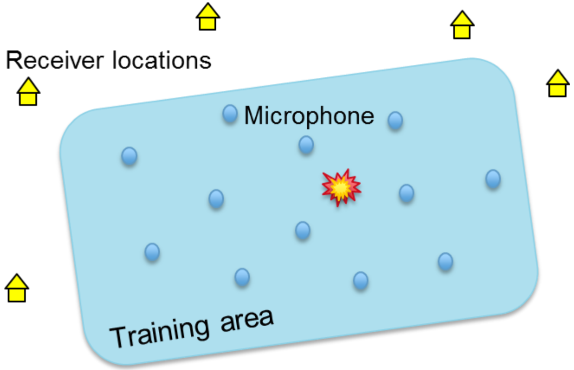

ACOUSTIC ENVIRONMENTAL MANAGEMENT

- Scope:
  - Heavy weapons / large distances (> 1km)

- Applications (check & plan):
  - Keep track of levels at receivers
  - Compare to rated sound level (cumulative one year / conservative)
  - Use insights for planning or possible mitigation measures
  - Respond to complaints

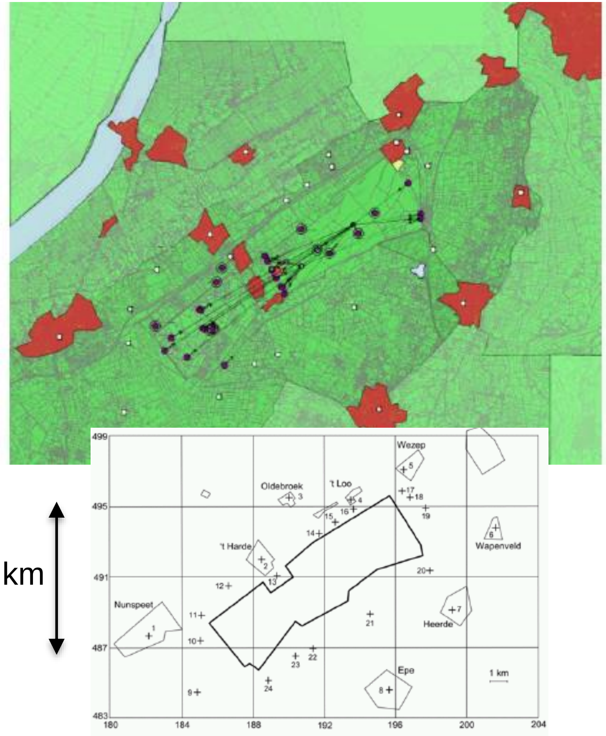

8 km

DIFFERENT CONFIGURATIONS

0) No use of sound measurements
1) Measurements at receiver locations
2) Measurements near source and at receiver
3) Measurements at perimeter + source
4) Distributed measurements within the training area

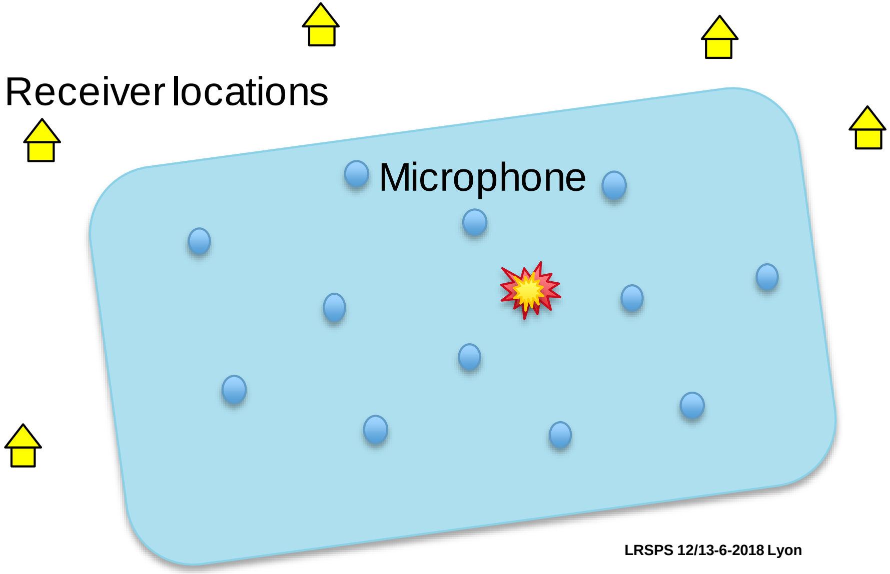

- Investigate the possible use of a management system.
- Anticipate on future developments that may involve (permanent) sound measurements, either by a governmental organization or otherwise

DETECTION AND LOCALISATION

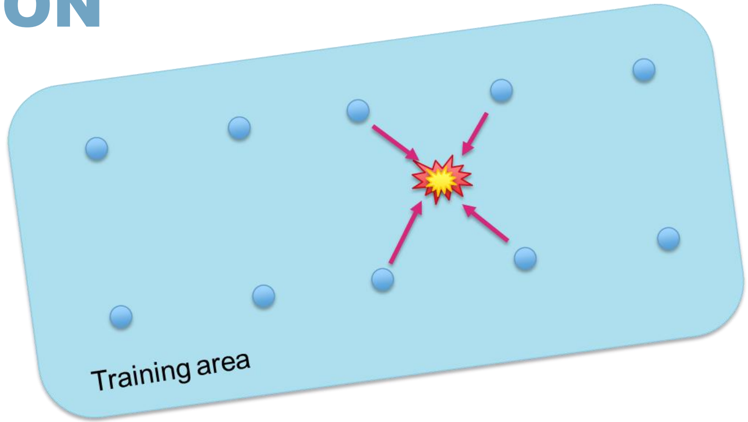

- Detect & localize: to what distances?
  - Large weapon systems
  - Difficult meteorology
  - Distances up to several km
  - Various background levels

- Performance tests using a dataset with simulated event recordings

TEST SETS

- Using actual recordings <200m distance

- Receiver distances 0.25 0.5 1 2 4 8 12 km
- Sound velocity profiles (15)
- Wind speed: 1, 4, 8 (12) m/s
- Ground type: grass/sand

- Audio mixing diagram
  - Include background & wind noise

- ~5000 recordings

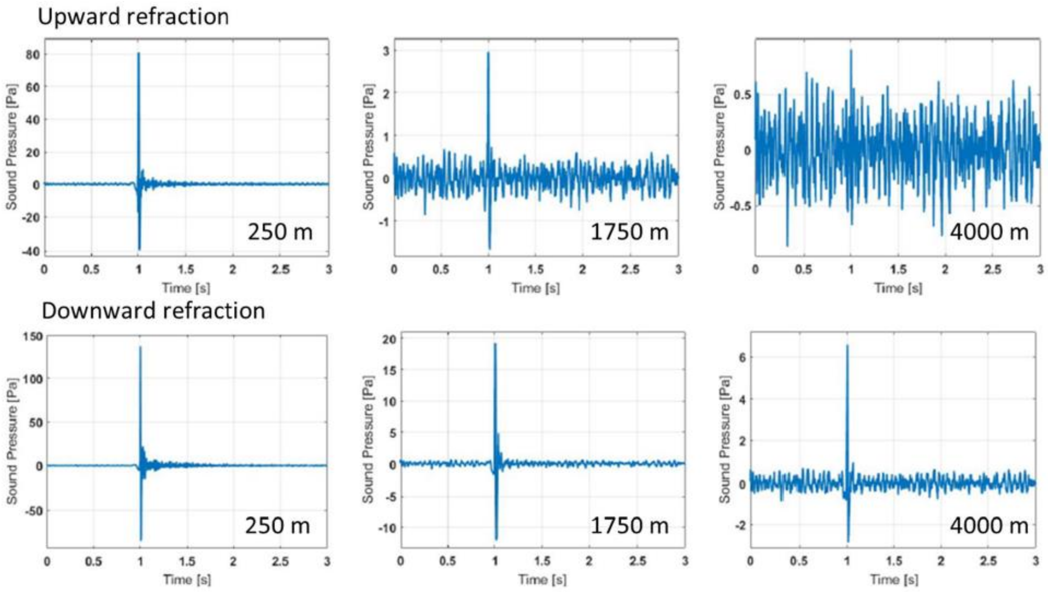

EVALUATING DETECTION & LOCALIZATION

- Testing detectors
  - rate of false detections per minute
  - 35 mm muzzle blast
  - upward refraction, 8 m/s

Detector \ Distance	250 m	500 m	1 km	2 km	3 km	4 km	8 km	12 km
1	0	0	0	15,9	600	600	600	600
2	0	0	0,1	0,6	600	600	600	600
3	0,2	0,2	0,2	0,6	1,6	600	600	600
4	0	0	0	0,1	0,7	224,2	600	224,2
5	0	0	0	0,6	9	600	600	600
6	0	0	0,2	26,4	600	600	600	600

- Testing localization (TDoA)
  - 1000 hours of simulation
  - including effect of wind
  - percentage of correctly found events
    - distance between microphones
    - introducing false detections

→ 2km distance

Estimated percentage of correctly localized events (including wind effect)							
nr false detections simulated per minute \ measurement distance [km]	0,25	0,5	1	2	3	4	6
0	100,0	100,0	100,0	100,0	100,0	100,0	100,0
1	100,0	100,0	100,0	99,9	99,8	99,6	99,3
2	100,0	100,0	99,9	99,6	99,2	98,6	97,0
3	100,0	99,9	99,8	99,2	98,3	97,0	93,3
4	99,9	99,9	99,6	98,7	96,9	94,5	87,8

UNCERTAINTY

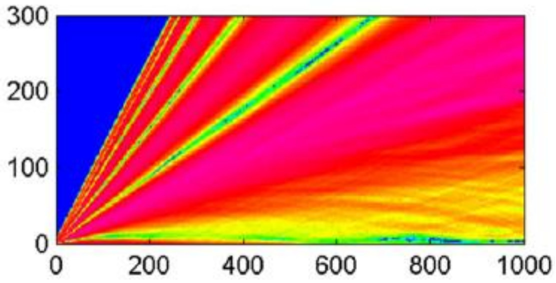

- Sound propagation simulations are used to get:
  - Sound source levels
  - Immission levels

- Impact of missing or limited environmental data on accuracy:
  - Identify main sources of environmental uncertainty
  - Quantify their impact

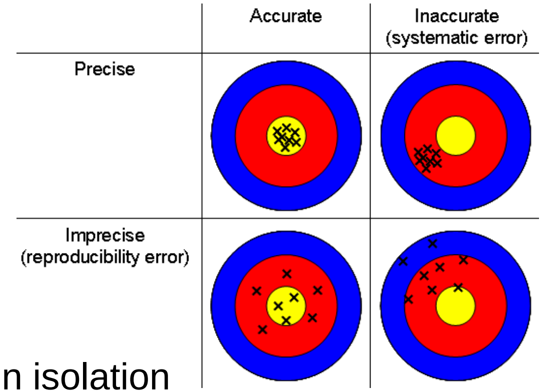

- Using a sensitivity analysis and GFPE simulations
  - Sensitivity to changes in one parameter is affected by the values of other parameters
  - The impact of uncertainty cannot be calculated for each parameter in isolation

PREVIEW RESULT

- Numerous different inputs for parameters in GFPE
  - E.g. ground impedance, wind speed & direction, …

- Selecting/visualizing results around the source location
  - SEL's at distance 1 or 3 km
  - For a single atmospheric stability class
  - For one representative ground type (here: heath)
  - Median and spread
  - Include main sensitive parameter
    (GI=ground impedance, WD = wind direction, Sz=source height)

Sound exposure levels for Pasquill class D (Neutral)

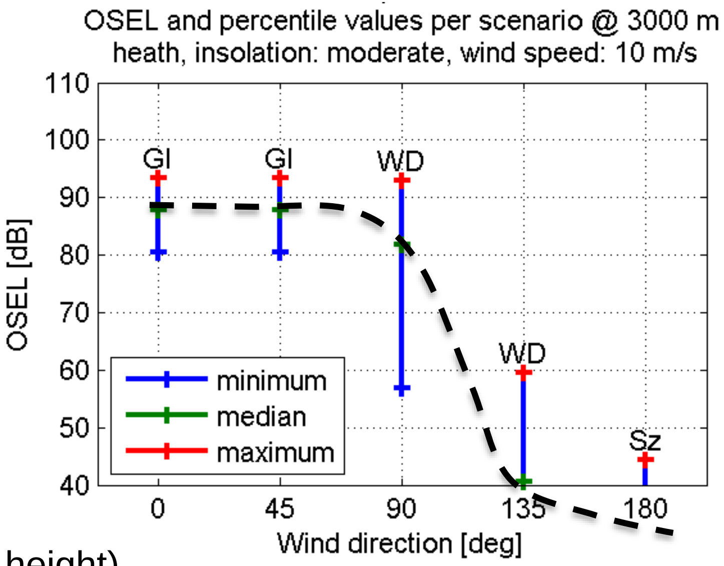

DIFFERENT PARAMETERS

- Choice for 80 “scenarios” with a mean input

Name parameter	**Values**	**Scenarios: 80**
1 Source-receiver distance	1000, 3000m	2
2 wind direction	0 (downwind), 45, 90 (crosswind), 135, 180 (upwind) in degrees	5
3 Wind speed	3, 10 m/s	2
4 Ground	***Sand*** or ***Heath***	2
5 Receiver height	5 m	1
6 Topography	flat surface	1
7 Insolation	***Moderate***: summer afternoon with mostly clear sky. Low (night, morning, evening, cloudy weather). Called ***Night***.	2

VARIATIONS OF PARAMETERS

- For each scenario, a range of parameters (>12.000 “cases”)

- Pasquill stability classes:
  A=extremely unstable … G=extremely stable
  Combining wind speed & insolation

	Scenario	Cases	
Source height	–	3x	0.1m 2.5m 5m
Receiver height	5m	5x	1, 3, 5, 7, 9m
Distance	1000 / 3000m	5x	max 25m offset
	B		σ=20 deg (-2σ…2σ)
Wind direction	D	5x	σ=10 deg
	E		σ=5 deg
Wind speed	3 / 10 m/s	5x	σ=0.5 m/s (-2σ…2σ)
Ground type	Sand	3x	f.r. = 200, 300, 400k
	Heather	5x	f.r. = 40, 70,100, 150, 200k

Pasquill class	Wind speed	Insolation	Description of Pasquill class
B	3 m/s	Moderate	Moderately unstable
D	10 m/s	Moderate	Neutral
D	10 m/s	Night	Neutral
E	3 m/s	Night	Slightly stable condition

SOUND SPEED PROFILES

- Wind & temperature: Buysinger-Dyer profiles for non-neutral surface layers (~Monin-Obukhov similarity)
- Input: roughness length, wind at 10m height, Pasquill klasse (Obukhov length L & temperature)

- Example: 3 m/s, wind direction 135 degrees w.r.t. source-receiver line, slightly stable (E)

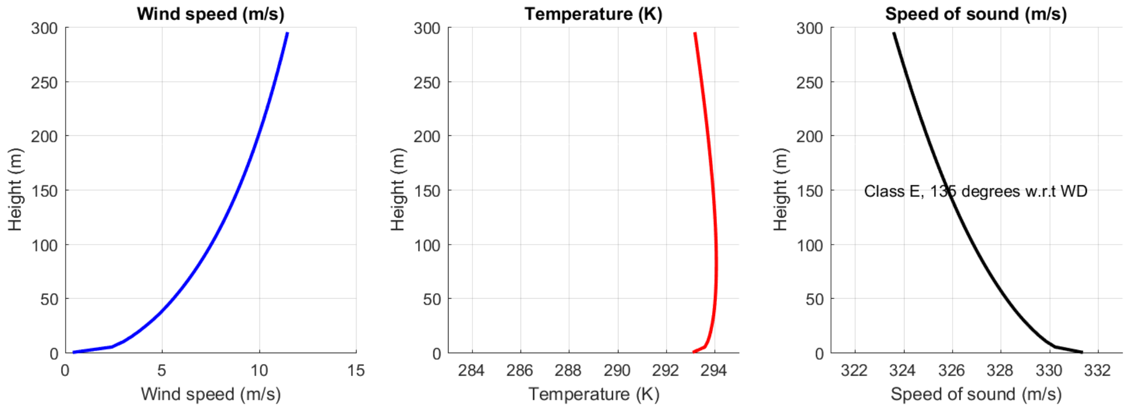

SCALED SENSIVITY

- Scaled sensitivity S_S is the mean spread in results when one studied parameter is changed $<\Delta c>$, divided by the mean spread when the parameter is held constant $<\Delta r>$

- Matrix:
  - Row: all the cases with the <u>studied parameter</u> held <u>constant</u>: standard deviation $\Delta r(i)$
  - Column: all <u>other parameters constant</u>: standard deviation $\Delta c(j)$
  - Using averaged standard deviations: Scaled sensitivity = $< \Delta c >/< \Delta r >$,

		Case ->								
		1	2	3	...	...	...	N	Spread	Avg
Study Param.	V1	SEL_{11}	SEL_{12}	...	...	...	...	SEL_{1N}	Δ_{r1}	
	V2	SEL_{21}	...	...	...	...	...	...	Δ_{r2}	
	V3	SEL_{31}	...	...	...	...	...	...	Δ_{r3}	$<\Delta_r>$
	V4	SEL_{41}	...	...	...	...	...	...	Δ_{r4}	
	Spread	Δ_{c1}	Δ_{c2}	...	...	...	...	Δ_{cN}		
	Avg	$<\Delta_c>$								

$S_S = <\Delta_c>/< \Delta_r>$

OVERALL SOUND EXPOSURE LEVEL (OSEL)

- Sensitivity to OSEL's; here C4 source (16…500 Hz)
- OSEL's are calculated for all cases (> 12.000)

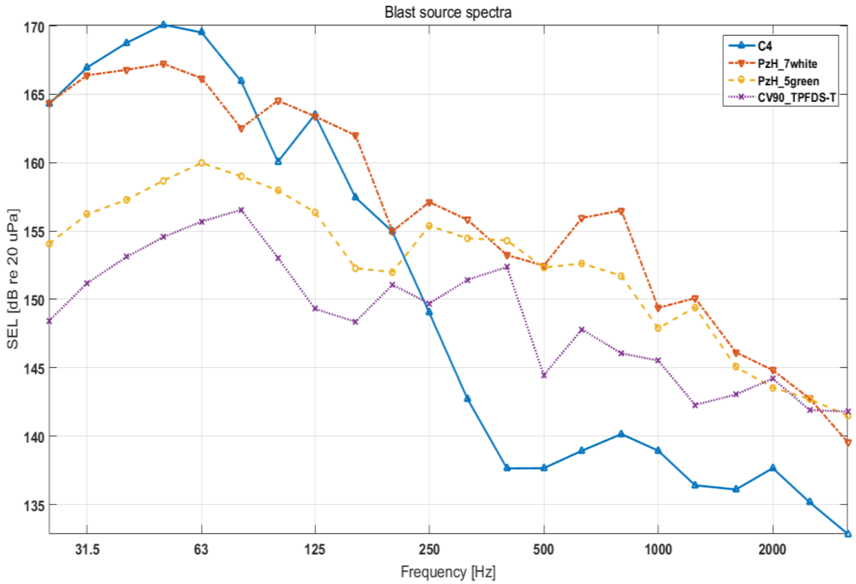

INTERMEDIATE RESULTS

- Scenario: Neutral (10m/s cloudy), WD 90º, Heath, @1000m

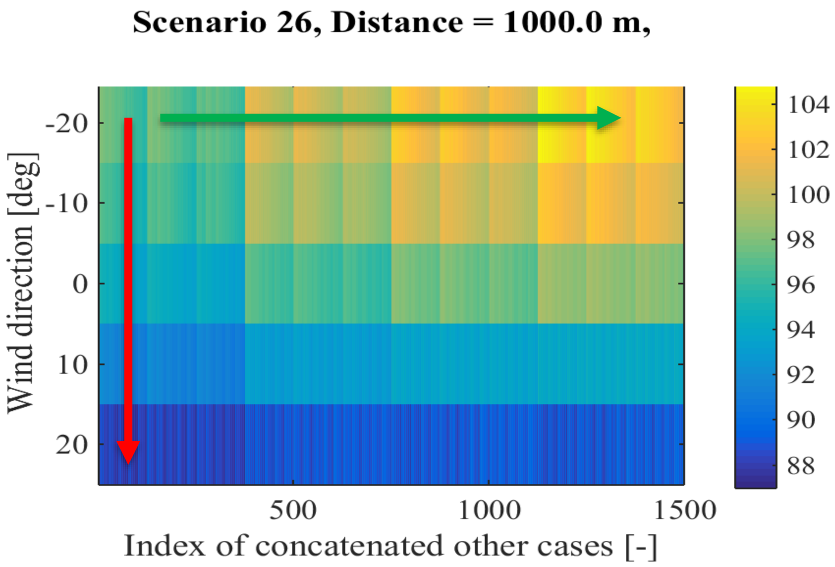

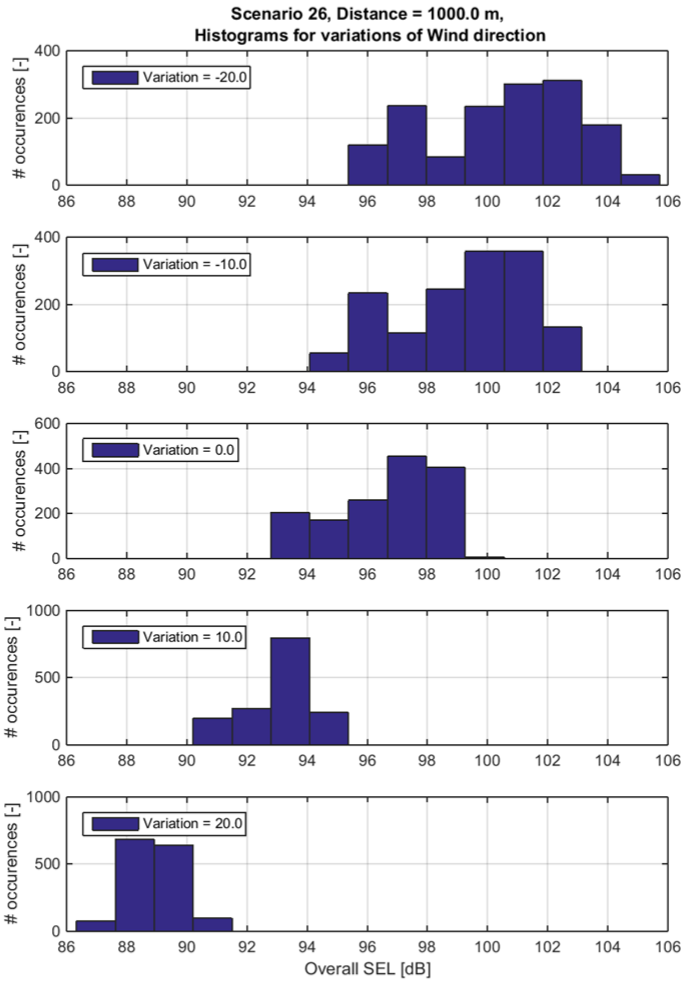

INTERMEDIATE RESULTS

- Scaled sensitivity for two scenario's
  - WD 90 deg.
  - WD 45 deg.

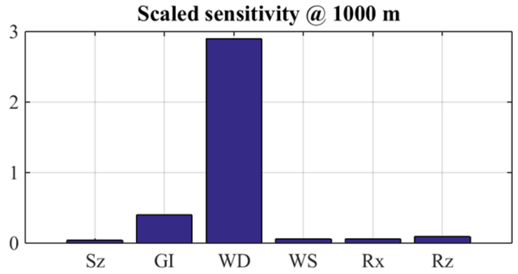

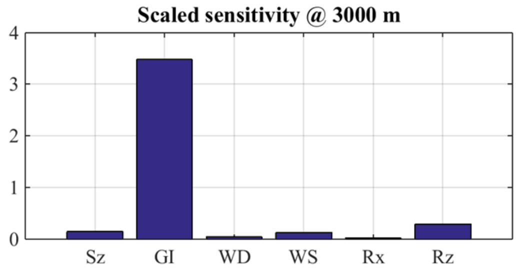

- 2.9 means that changes due to this parameter are 2.9 times as high as changes when parameter is held constant

Abbreviation	Full name
Sz	Source height
GI	Ground impedance
WD	Wind direction
WS	Wind speed
Rx	Receiver distance
Rz	Receiver height

- Next:

  Sets of 5 scenarios (via WD = 0, 45 ,90,135,180)

  For 4 atmospheric stability classes (B, D, D, E)

GROUPED

- Aiding acoustic environmental management (providing context)
- Other sets: at 1000m & for sand

- E.g. for a cloudy day
  - Downwind 5 dB uncertainty (low & high wind speed)
  - Upwind 20 dB uncertainty (high wind)
- Main uncertainty due to
  - Ground impedance
  - Wind direction

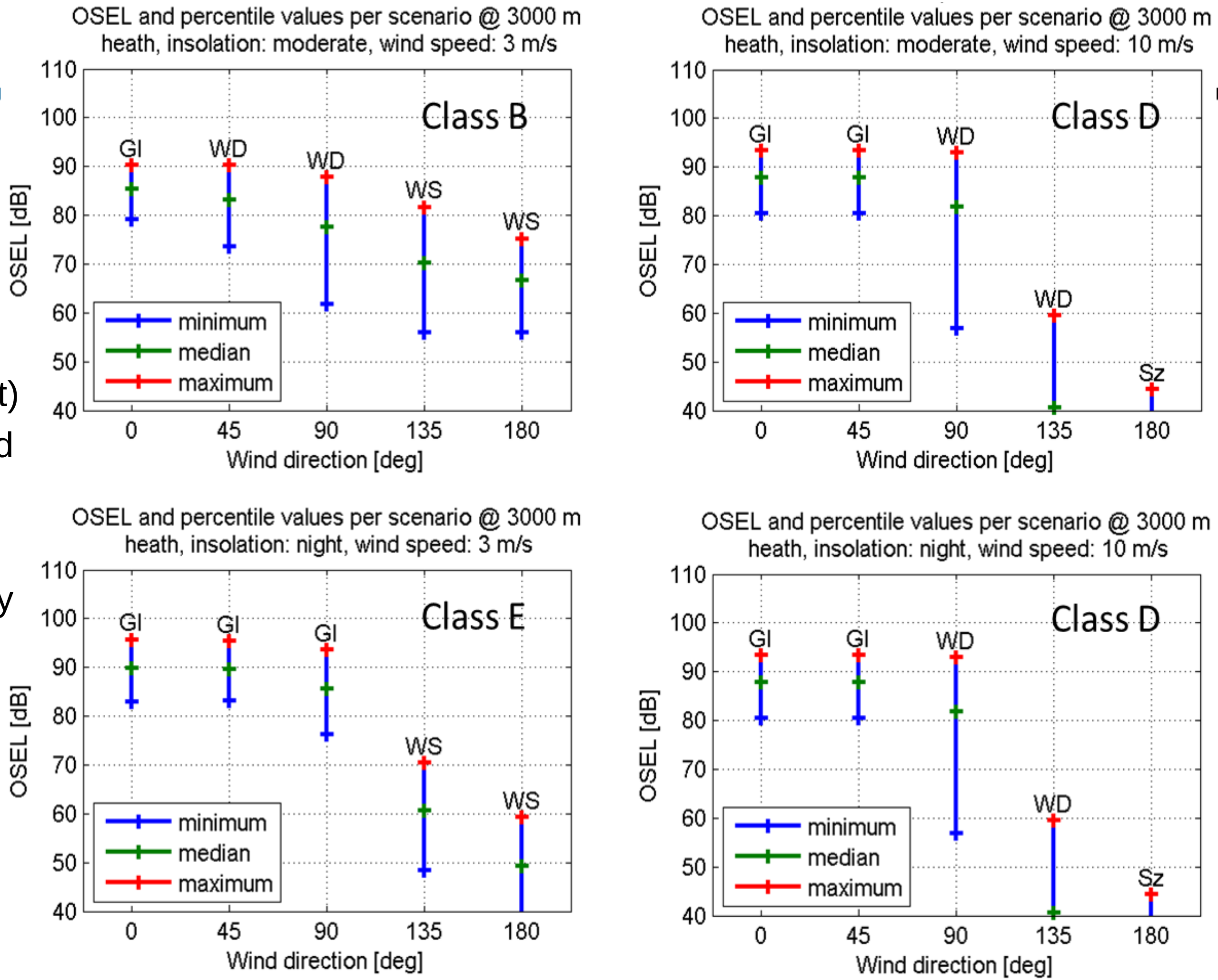

CONCLUSIONS

ACOUSTIC MODEL-BASED MEASUREMENT SYSTEM

- “Lookup-table” given meteo or weather-forecast
  - Using selection of scenario’s
  - Uncertainty can be quantified

- Model can learn from measurements
  e.g. seasonal changes of ground impedance
- Improve measurement results
  e.g. to exclude false detections

- Improved model input leads to smaller uncertainties
- Not all uncertainties can be reduced (e.g. turbulence)

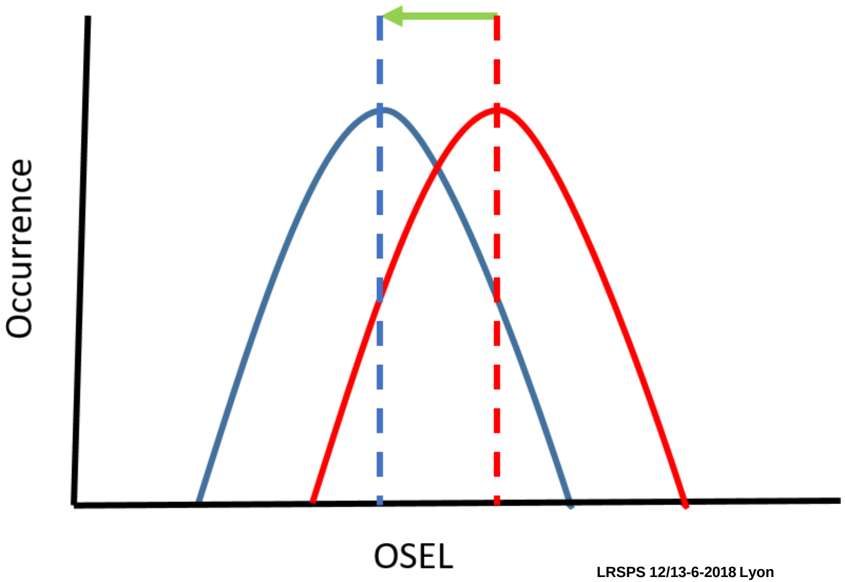

OUTLOOK

- Include turbulence in the calculations & reconsider parameter distributions
- Analyse results for other weapon-munition combinations
- For a specific shooting range:
  - Include spatially varying ground impedance
  - Include topography
- Acoustic environmental management of military shooting ranges involves:
  - Policy making and weighting pros and cons
  - Methods for robust acoustic environmental management*
  - Assessment of impulsive sounds

Acoustical analysis of artillery shots

A. Dagallier [1] S. Cheinet [1] M. Cosnefroy [1] P. Wey [1] D. Juvé [2]

[1] French-German Research Institute of Saint-Louis, Saint-Louis, France

[2] Centre Acoustique, LMFA UMR CNRS 5509, École Centrale de Lyon, Écully, France

2018, June 13th

Context

Motivation: Meppen WTD 91

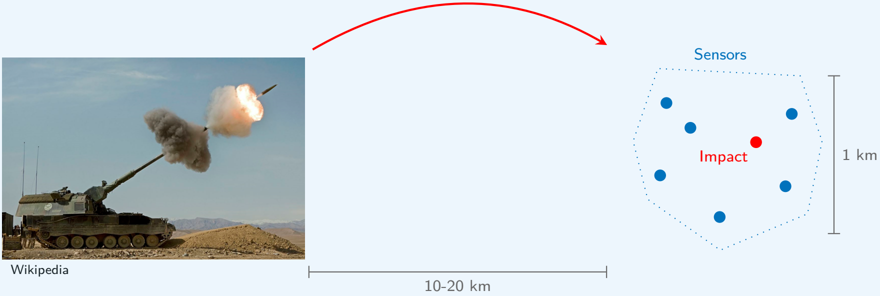

Context

Shot example

Sensors

- robust
- synchronous
- low frequencies (< 10 Hz)

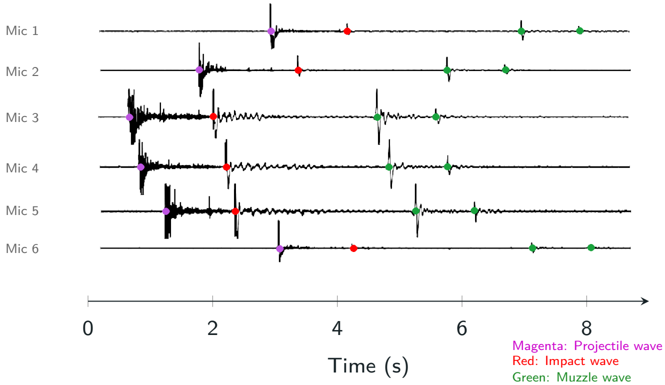

Context

Shot to shot variations

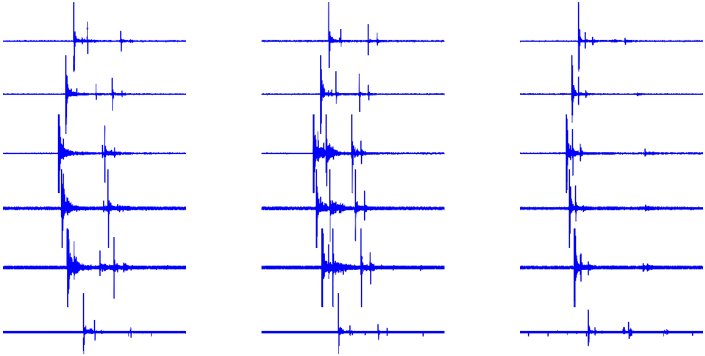

Context

Challenge : identification of the peaks

movie example shot

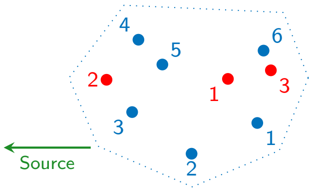

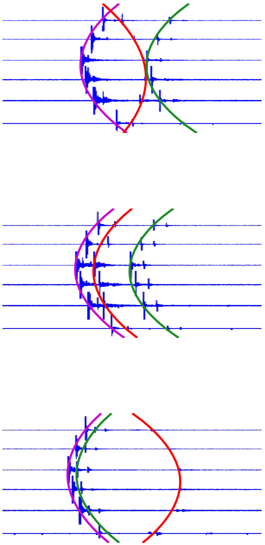

Color Legend

Magenta: Projectile wave

Red: Impact wave

Green: Muzzle wave

Context

Challenges

- Peak identification
- Muzzle wave: poor ranging
- Propagation in complex environment
- Automatization of the processing

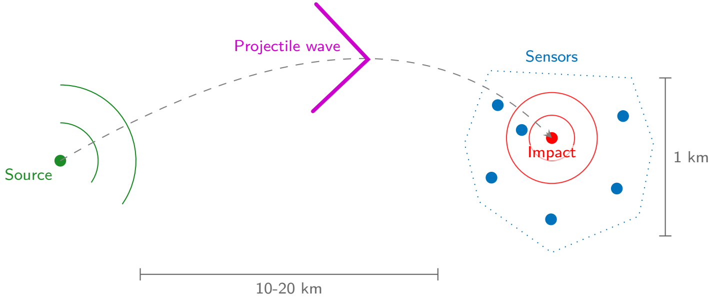

Outline

- Context
- Time-Matching
- Ballistic model
- Acoustic propagation model

Time-Matching

Principle

Time-Matching principle

- Working with TOAs: no calibration required, very robust
- Modeling of the environment (temperature, wind, obstacles...)
- Mapping of a shot configuration to TOAs at the sensors
- Building of a database of the TOAs at the sensors/everywhere for a set of fictitious sources
- Minimisation measured TOAs - simulated TOAs

→ Contributions of all waves, in complex environments

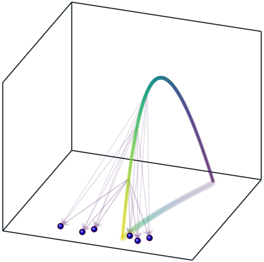

Outline

- Context
- Time-Matching
- Ballistic model
- Acoustic propagation model

Ballistic model

Effects to consider

- Weight
- Drag = f(M)

- $\begin{cases} \rho = \rho(z) \\ c = c(z) \\ M = M(z) \end{cases}$
- Wind
- Attitude
- Magnus Effect
- Coriolis
- Gravity model

BALCO, NATO ballistic code (from Pierre Wey, ISL, pierre.wey@isl.eu)

Wey *et al.*, BALCO 6/7-DoF trajectory model, 29th International Symposium on Ballistics, 2016, Edinburgh, Scotland, UK

Outline

- Context
- Time-Matching
- Ballistic model
- **Acoustic propagation model**

Acoustic propagation model

Review

Rays

- large distances $\Longrightarrow$ lots of rays
- shadow zones (complex celerity + wind profiles) $\Longrightarrow$ sometimes, no TOA!

2D, 3D time or frequency solvers

- (really) heavy calculations

Graph search

- fast and optimized algorithms
- TOAs even in shadow zones
- angular discretization: large geometrical errors

Acoustic propagation model

Solution: Fast-Marching

Fast-Marching

- interface tracking (level set methods, Sethian)
- local resolution of the ray equation $||\nabla\phi||^2 = \dfrac{1}{c^2}$
- fast calculations (analytic solution): potentially real-time
- TOAs even in shadow zones

Acoustic propagation model

Comparison FDTD - Fast-Marching

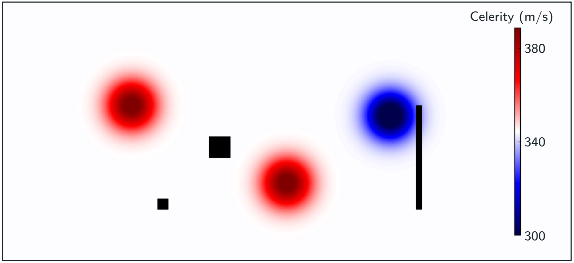

Acoustic propagation model

Comparison FDTD - Fast-Marching

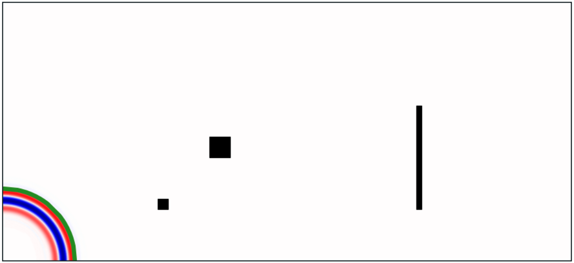

Blue and red: FDTD pressure field
Green: Fast-marching wavefront

Acoustic propagation model

Comparison FDTD - Fast-Marching

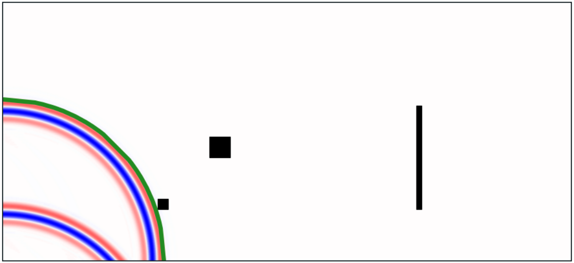

Blue and red: FDTD pressure field
Green: Fast-marching wavefront

Acoustic propagation model

Comparison FDTD - Fast-Marching

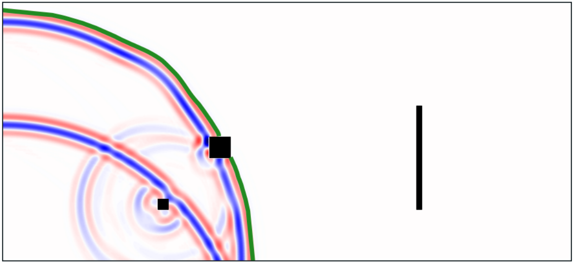

Blue and red: FDTD pressure field
Green: Fast-marching wavefront

Acoustic propagation model

Comparison FDTD - Fast-Marching

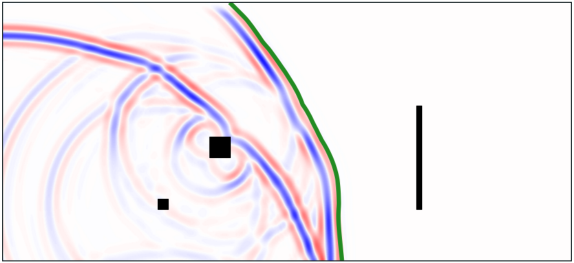

Blue and red: FDTD pressure field
Green: Fast-marching wavefront

Acoustic propagation model

Comparison FDTD - Fast-Marching

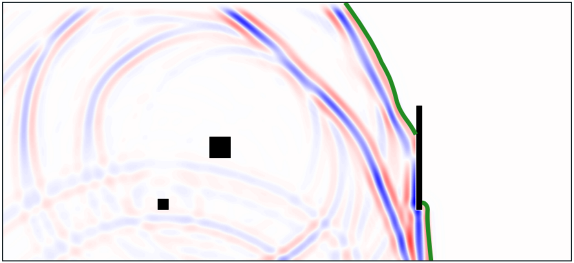

Blue and red: FDTD pressure field
Green: Fast-marching wavefront

Acoustic propagation model

Comparison FDTD - Fast-Marching

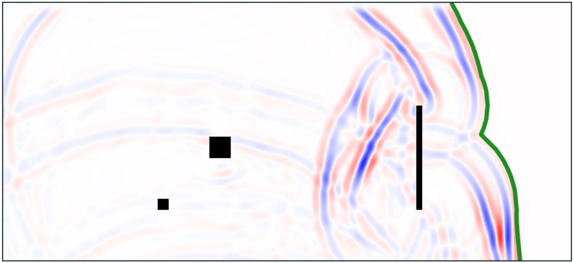

Blue and red: FDTD pressure field
Green: Fast-marching wavefront

- ✓ Refraction accounted for
- ✓ Diffraction accounted for

Localization

Use of projectile wave

Projectile wave

- first TOA
- largest amplitude

→ impossible to miss!

Source localization

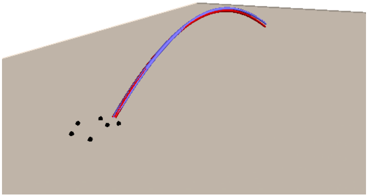

- Adds information on the supersonic part of the trajectory

→ Allows ranging from sensors in target area

→ Major potential improvement on artillery threat localization

Conclusion

Summary: Time-Matching

BALCO

- 3D trajectories with large projectile velocity variations

Fast-Marching

- Atmospheric gradients
- Urban environments, mountains
- Real-time

Outlooks

- number, positions of sensors can be changed (e.g. line configuration, or mobile sensors)
- extensible to non-flat ground (mountains), or complex urban environments (*movie urban 1*,*movie urban 2*)

17th International Symposium on Long Range Sound Propagation
Ecole Centrale de Lyon, Ecully, June 12-13, 2018

Irregular reflection of spark-generated *N*-waves from a rigid surface: optical measurements in air and numerical modeling

Maria Karzova,[1,2] Thomas Lechat,[2] Didier Dragna,[2]
Sébastien Ollivier,[2] Petr Yuldashev,[1] Vera Khokhlova,[1]
Philippe Blanc-Benon[2]

[1]*Physics Faculty*
M.V. Lomonosov Moscow State University, Russia

[2]*Laboratoire de Mécanique des Fluides et d'Acoustique*
Ecole Centrale de Lyon, France

Nonlinear acoustics

Sonic boom

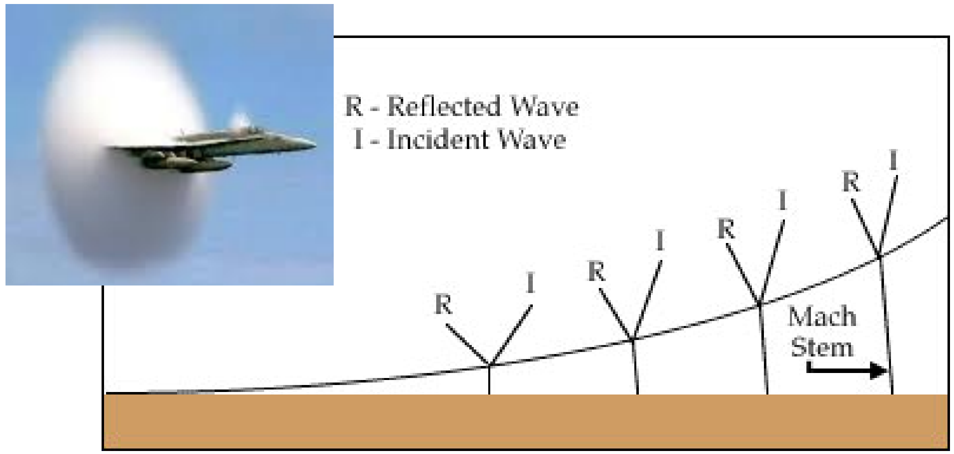

- ⇨ Laboratory-scale experiment, scale 500:5000 relative to sonic boom
- ⇨ Weak acoustic shock waves (pressure amplitude < 5 kPa)
- ⇨ Reflection on flat surface

Outline

- **Introduction**
  - ⇨ Mach stem formation and von Neumann paradox
  - ⇨ Types of an *N*-wave reflection from a rigid boundary
- **Optical methods for measuring an *N*-wave reflection**
  - ⇨ Schlieren visualization
  - ⇨ Mach-Zehnder interferometer
- **Numerical modeling**
  - ⇨ Euler equations (finite-difference time-domain algorithm)
- **Results**
  - ⇨ Dynamic irregular reflection of an *N*-wave
  - ⇨ Interaction of the front and rear shocks above the surface
  - ⇨ Evolution of the Mach stem
- **Conclusions**

Mach reflection effect

1875: Experiments by E. Mach

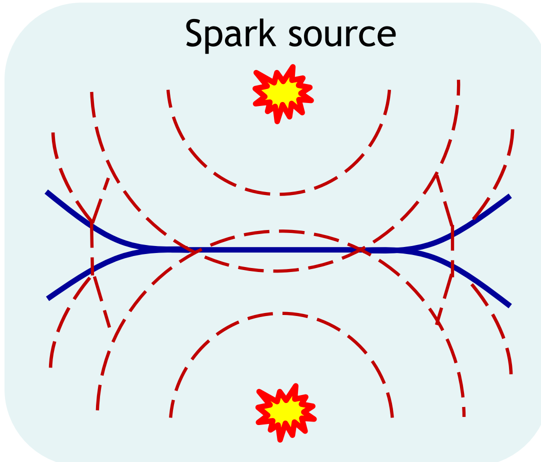

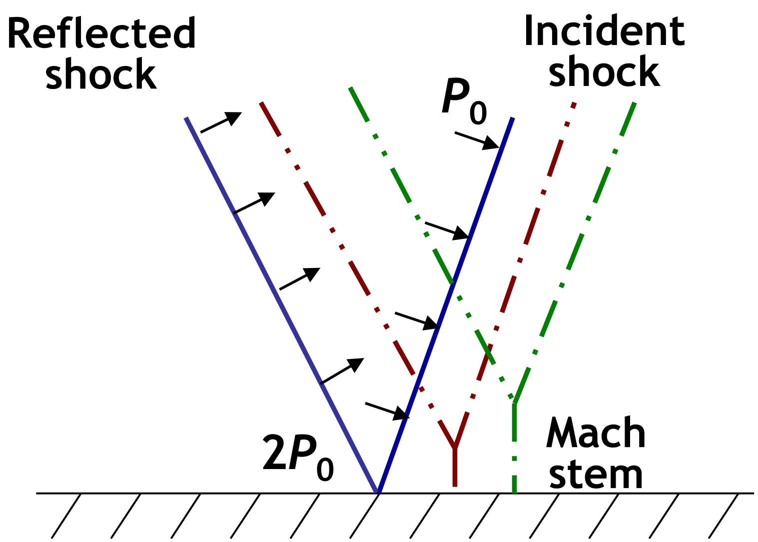

1943: Three-shock theory by von Neumann

Rankine-Hugoniot jump conditions (conservation of mass, momentum and energy) and perpendicularity of the Mach stem to the surface

$$\rho_1 u_1 \sin\theta_1 = \rho_2 u_2 \sin(\theta_1 - \varphi_1)$$

$$p_1 + \rho_1 u_1^2 \sin^2\theta_1 = p_2 + \rho_2 u_2^2 \sin^2(\theta_1 - \varphi_1)$$

$$\frac{\gamma}{\gamma-1}\frac{p_1}{\rho_1} + \frac{1}{2}u_1^2 \sin^2\theta_1 = \frac{\gamma}{\gamma-1}\frac{p_2}{\rho_2} + \frac{1}{2}u_2^2 \sin^2(\theta_1 - \varphi_1)$$

M_a > 0.47 theory is in agreement with experiment

0.1< M_a < 0.47 discrepancy between theory and experiment

M_a < 0.1 theory predicts that **irregular reflection is physically unrealistic**

1950: the von Neumann paradox - discrepancy between the three-shock theory and the experimental studies

Mach stem formation

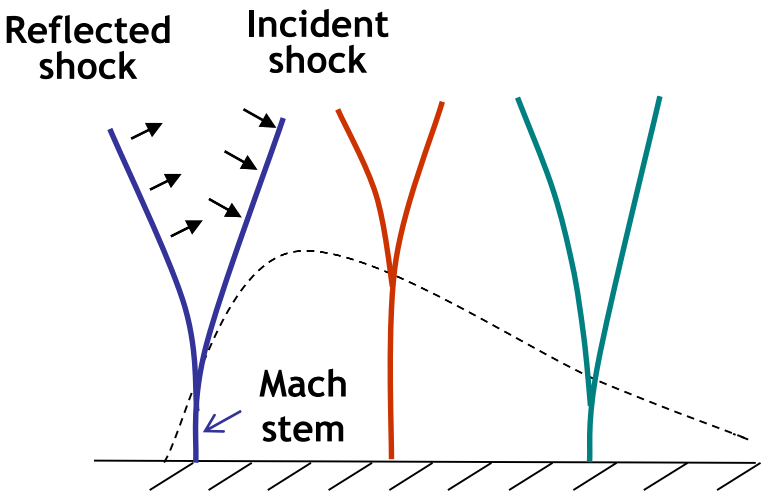

Reflected shock overtakes incident shock

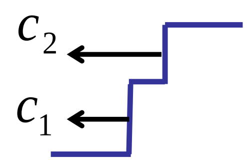

$$c_2 > c_1$$

$$c(p) = c_0 + \frac{\varepsilon p}{\rho_0 c_0}$$

Critical parameter

$$\boxed{a(\theta, M_a) = \frac{\sin(\theta)}{\sqrt{2\varepsilon M_a}}}$$

Types of *N*-wave reflection from the rigid boundary

Linear regular reflection

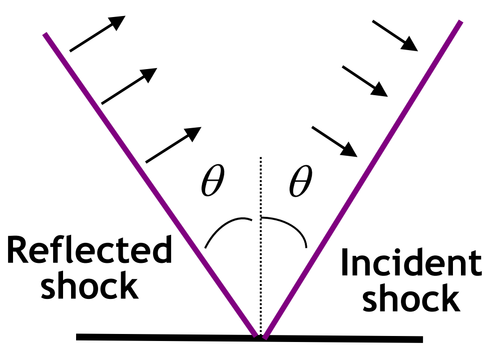

$a \geq 5$

Nonlinear regular reflection

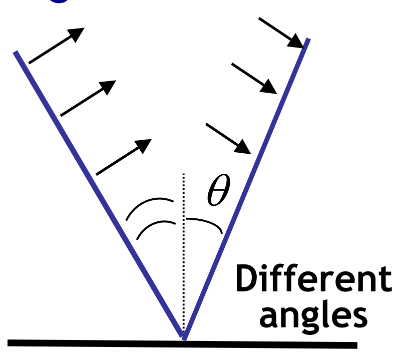

$0.8 \leq a \leq 5$

von Neumann reflection

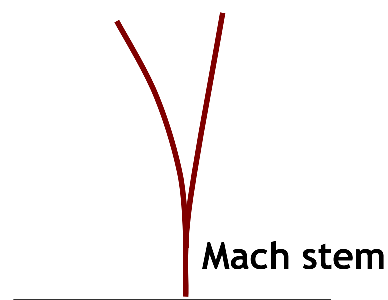

$0.4 \leq a \leq 0.8$

Weak von Neumann regime

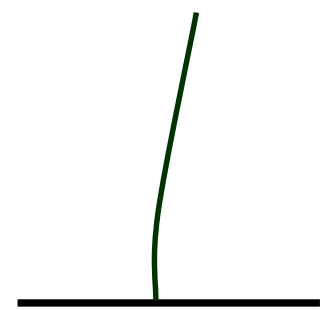

$a \leq 0.4$

S. Baskar, F. Coulouvrat, R. Marchiano, *J. Fluid Mech.*, Vol. 575, 27-55, (2007).

Difficulties in measuring *N*-wave using microphones

High voltage electric spark source (20 kV)

Broadband microphone Brüel&Kjær 1/8”

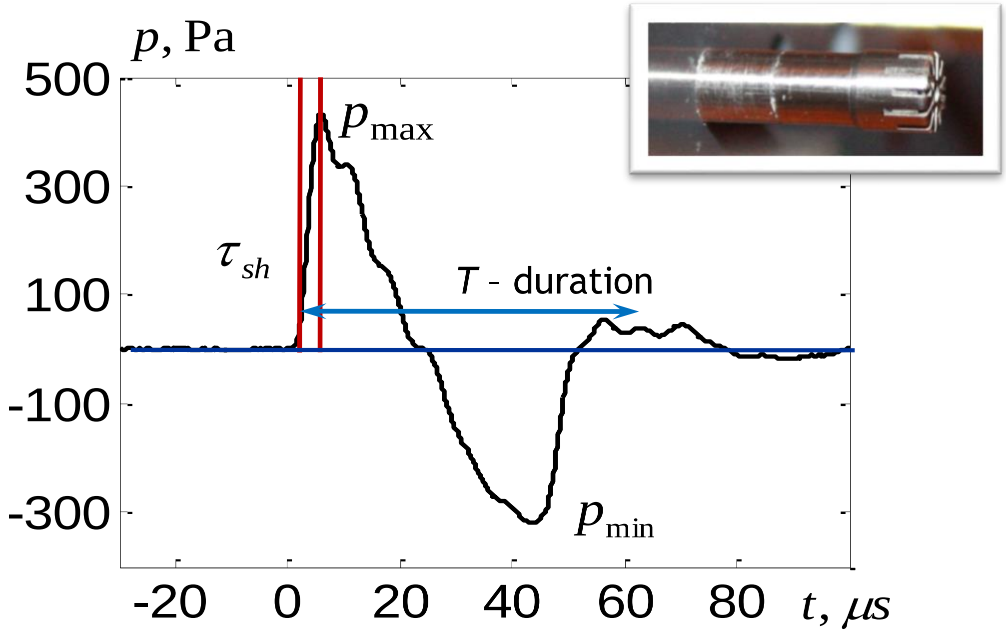

Drawbacks: limited bandwidth, calibration problem, diffraction wave, not possible to measure reflection patterns, *etc*

The optical refractive index is locally modified due to acoustic wave ⇨ **Optical methods are alternative to measure acoustic shocks**

Z-Type Schlieren setup

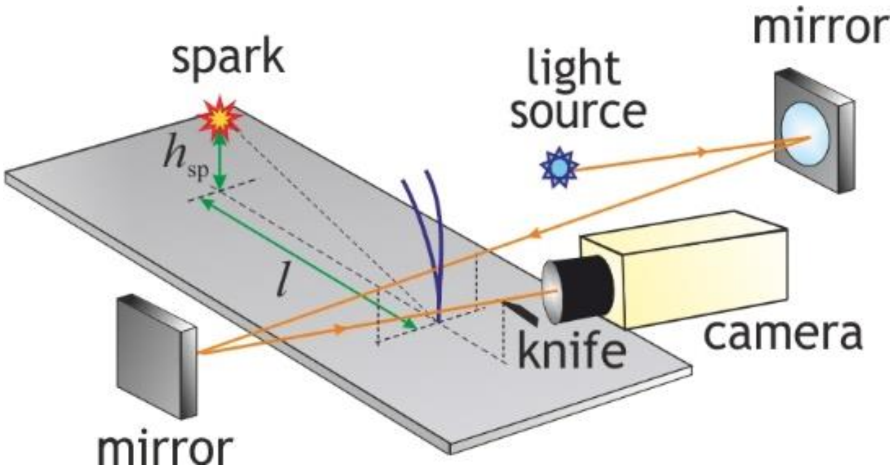

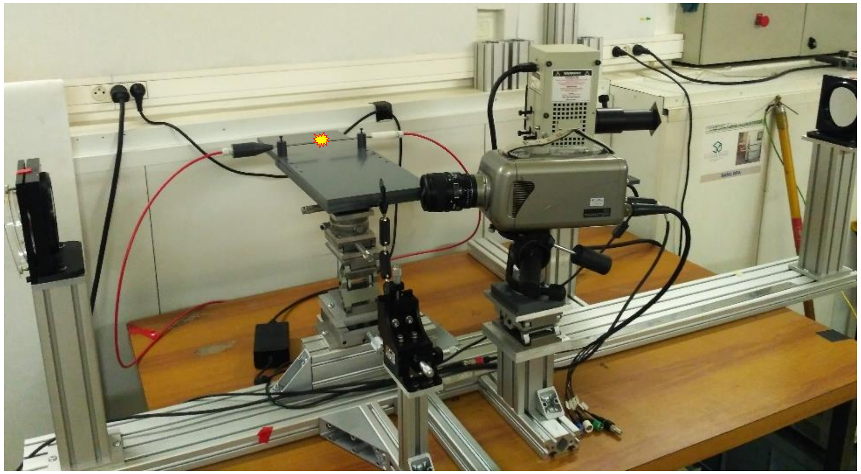

The brightness of schlieren images is proportional to the gradient of acoustic pressure

- Exposure time: 1 µs
- Frame rate: 18000 f/s (55 µs interval)
- Distance l : [100-330] mm
- Source position h_{sp} : [6-41] mm
- Spatial resolution: 0.15 mm/pixel
- Mirrors: D = 108 mm, F = 864 mm

Scheme of the reflection process

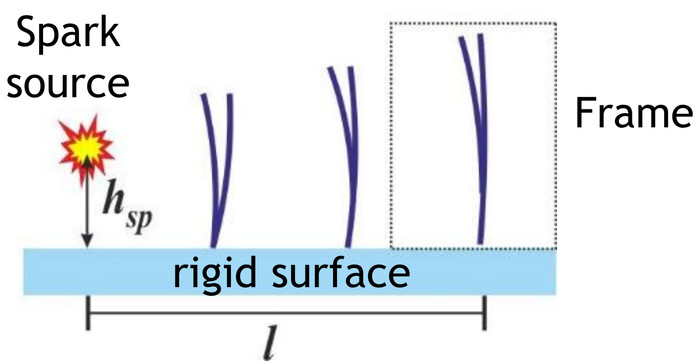

Schlieren visualization of the reflection patterns

Different types of the *N*-wave reflection

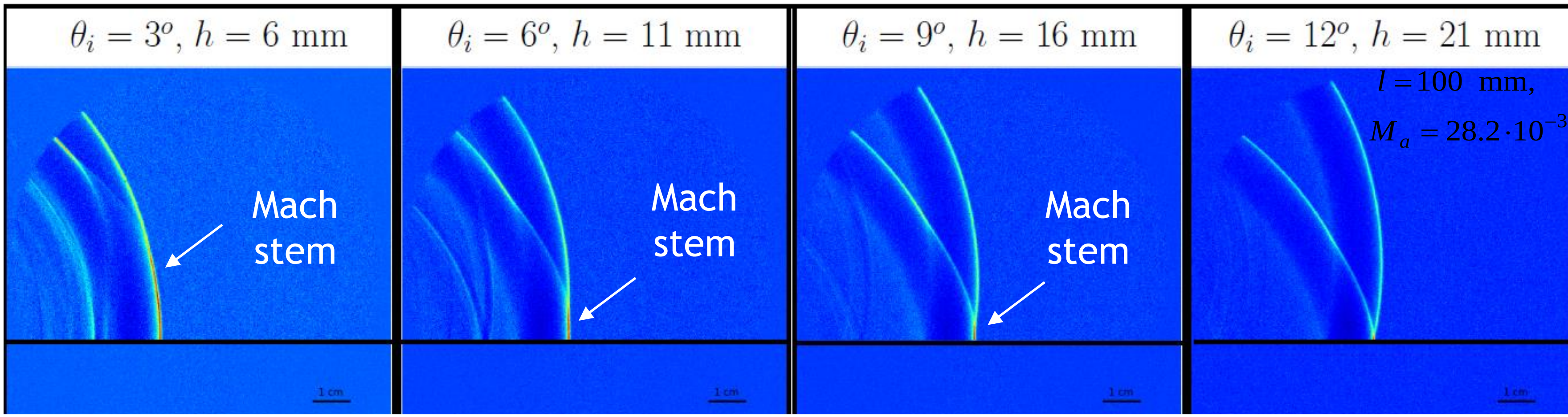

Irregular reflection

Regular reflection

Dynamics of irregular reflection of the front shock

Schlieren method provides only visualization.

How to reconstruct **waveforms ?**

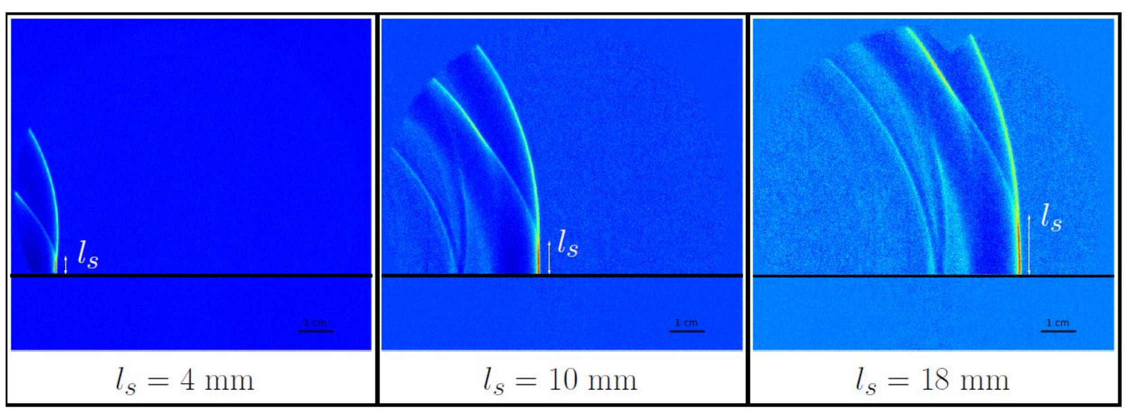

Karzova *et al*, JASA-EL 137(6), (2015).

Desjouy *et al*, Phys. Fluids 28, (2016).

Mach-Zehnder interferometer

Diagram of the experimental setup

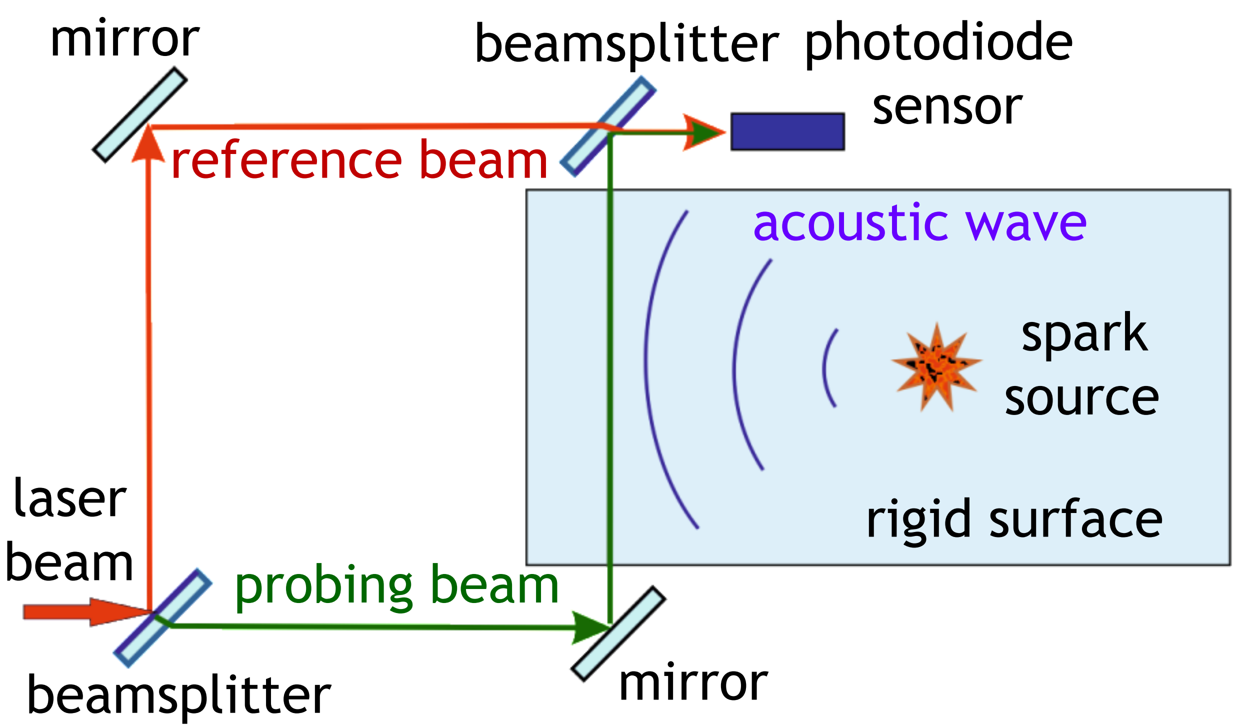

Acoustic wave $\Rightarrow \Delta\varphi$

⇩

optical phase

$$\Delta\varphi = \frac{2\pi}{\lambda}\int \Delta n ds$$

⇩

changing of light intensity on photodiode sensor

Quantitative reconstruction of pressure waveforms from the refractive index inhomogeneities caused by the acoustic wave

Mach-Zehnder interferometer

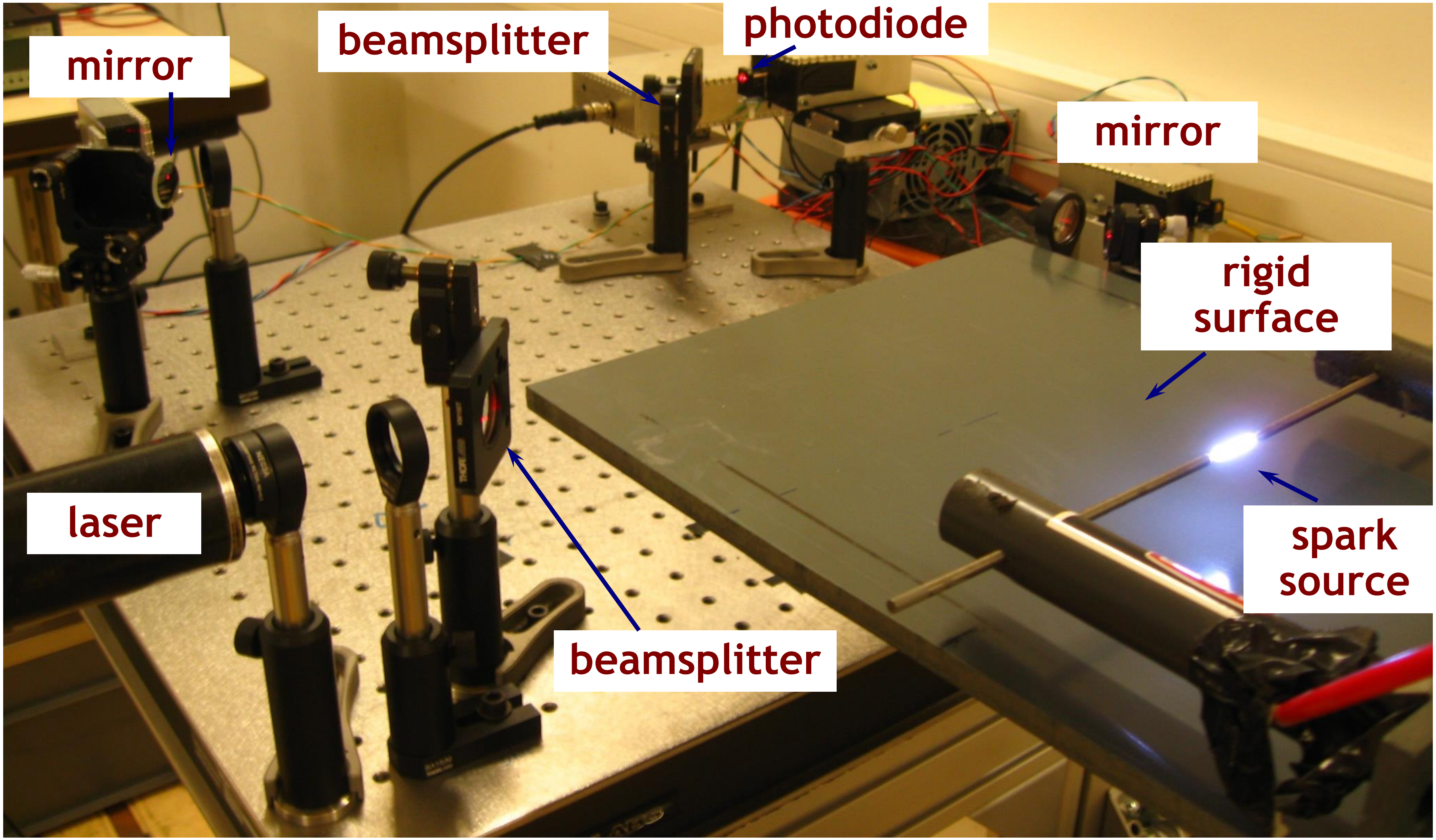

Optical signal processing

Output voltage signal $$u = u_1 + u_2 + 2\sqrt{u_1 u_2}\cos\psi$$ ← the interference of the reference beam and of the probe beam

Phase $$\psi = \pi/2 + \Delta\varphi$$ ← the phase shift $\pi/2$ - the optical path difference of the beams

Output voltage signal ~ sine of the optical phase shift $$u = 2\sqrt{u_1 u_2}\sin(\Delta\varphi)$$

Optical phase difference $$\Delta\varphi = \frac{2\pi}{\lambda}\int \Delta n(x,y)\,dx$$ ← Neglect the refraction of the beam, spherical symmetry

Reconstruction of the pressure waveforms from measurements of the phase shift

$$\Delta\varphi(x) = \frac{4\pi}{\lambda}\int_y^{\infty}\frac{\Delta n(r)\,r\,dr}{\sqrt{r^2 - y^2}}$$ → $$\Delta n(r) = -\frac{\lambda}{2\pi}\frac{1}{\pi}\int_r^{\infty}\frac{d\Delta\varphi(y)}{dy}\frac{dy}{\sqrt{y^2 - r^2}}$$ →

direct Abel transform

inverse Abel transform

calculating the pressure from refractive index (linear approximation) $$p = \frac{n c_0^2}{K}$$ → $$p = -\frac{c_0^2\lambda}{2\pi^2 K}\int_r^{+\infty}\frac{d}{dy}\left(\arcsin\frac{u}{2\sqrt{u_1 u_2}}\right)\frac{dy}{\sqrt{y^2 - r^2}}$$

Karzova *et al*, JASA 137(6), 3244 - 3252, 2015. **Yuldashev *et al*, JASA 137(6), 3314 - 3324, 2015.**

Pressure waveforms reconstructed from optical measurements
at different height *h* from the rigid surface

Scheme of the reflection process

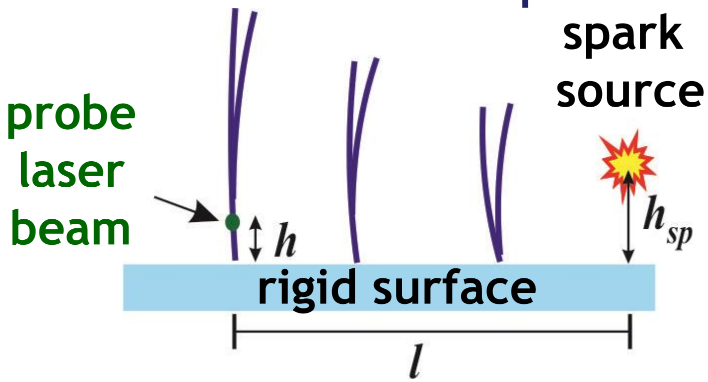

In experiments:

l = 17 cm, 25 cm, 33 cm;

h_{sp} = 2.1 cm,

h changes from 2 mm to 30 mm

Reflection pattern

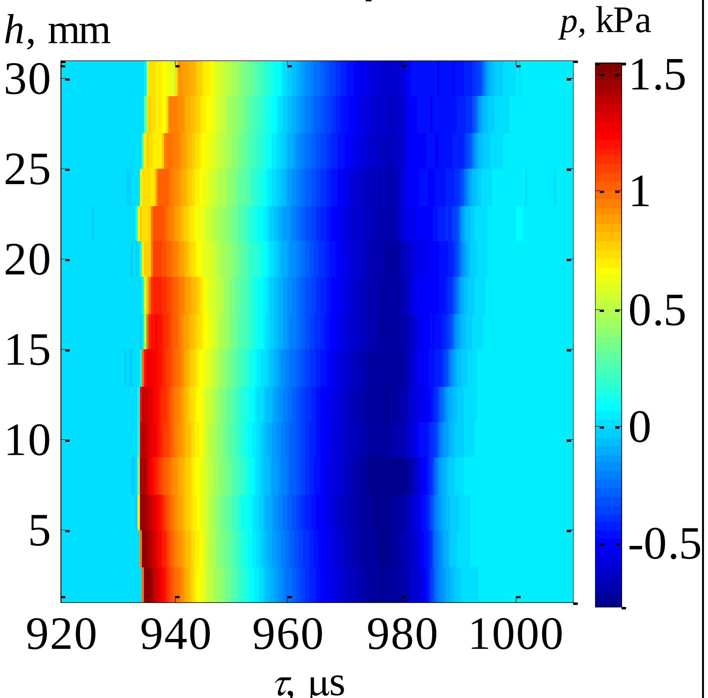

l = 33 cm

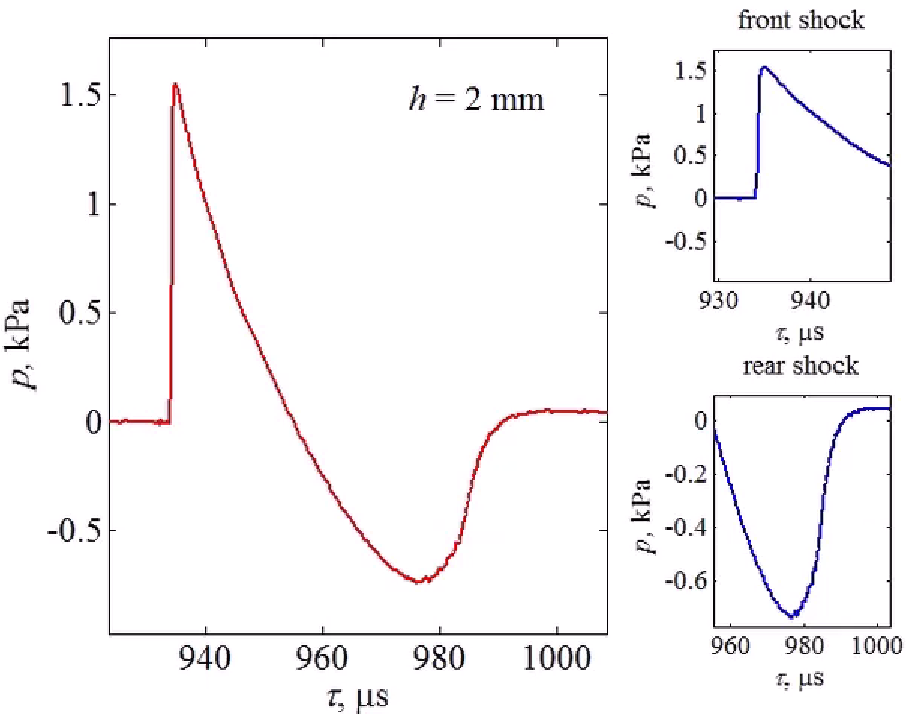

Numerical modeling

Axisymmetric Euler equations (finite-difference time-domain algorithm)

$$
\begin{cases}
\dfrac{\partial \tilde{\rho}}{\partial t} + \dfrac{\partial(\tilde{\rho} v_r)}{\partial r} + \dfrac{\partial(\tilde{\rho} v_z)}{\partial z} + \dfrac{\tilde{\rho} v_r}{r} = 0, \\
\dfrac{\partial(\tilde{\rho} v_r)}{\partial t} + \dfrac{\partial(\tilde{\rho} v_r^2 + \tilde{p})}{\partial r} + \dfrac{\partial(v_r v_z)}{\partial z} + \dfrac{\tilde{\rho} v_r^2}{r} = 0, \\
\dfrac{\partial(\tilde{\rho} v_z)}{\partial t} + \dfrac{\partial(\tilde{\rho} v_r v_z)}{\partial r} + \dfrac{\partial(\tilde{\rho} v_z^2 + \tilde{p})}{\partial z} + \dfrac{\tilde{\rho} v_r v_z}{r} = 0, \\
\dfrac{\partial(\tilde{\rho} E)}{\partial t} + \dfrac{\partial(v_r\{\tilde{\rho} E + \tilde{p}\})}{\partial r} + \dfrac{\partial(v_z\{\tilde{\rho} E + \tilde{p}\})}{\partial z} + \dfrac{v_r\{\tilde{\rho} E + \tilde{p}\}}{r} = 0,
\end{cases}
$$

$\tilde{p}$ - total pressure,
$\tilde{\rho}$ - total density,
v_r, v_z - velocity components,
E - total energy

$$\tilde{\rho} E = \frac{\tilde{p}}{(\gamma - 1)} + \tilde{\rho} \frac{|\vec{v}|^2}{2}$$

Acoustic source: Gaussian-envelope injection of energy

$$
\begin{cases}
\tilde{p}(r,z) = p_0 \exp\left\{-(\ln 2) \dfrac{\sqrt{r^2 + (z - z_0)^2}}{\alpha^2}\right\} + p_{\mathrm{atm}}, \\
\vec{v}(r,z) = 0, \\
\tilde{\rho}(r,z) = \rho_0, \\
E(r,z) = \dfrac{\tilde{p}(r,z)}{\rho_0(\gamma - 1)}.
\end{cases}
$$

p_0 = 0.46 MPa, α = 2.5 mm

- J. Berland *et al*, J. Comput. Phys. 224(2), (2007).
- C. Bogey *et al*, J. Comput. Phys. 228(5), (2009).
- J. Berland *et al*, Computers & Fluids 35(10), (2006).
- C. Bogey and C. Bailly, J. Comput. Phys. 194(1), (2004).

Results: reflection patterns

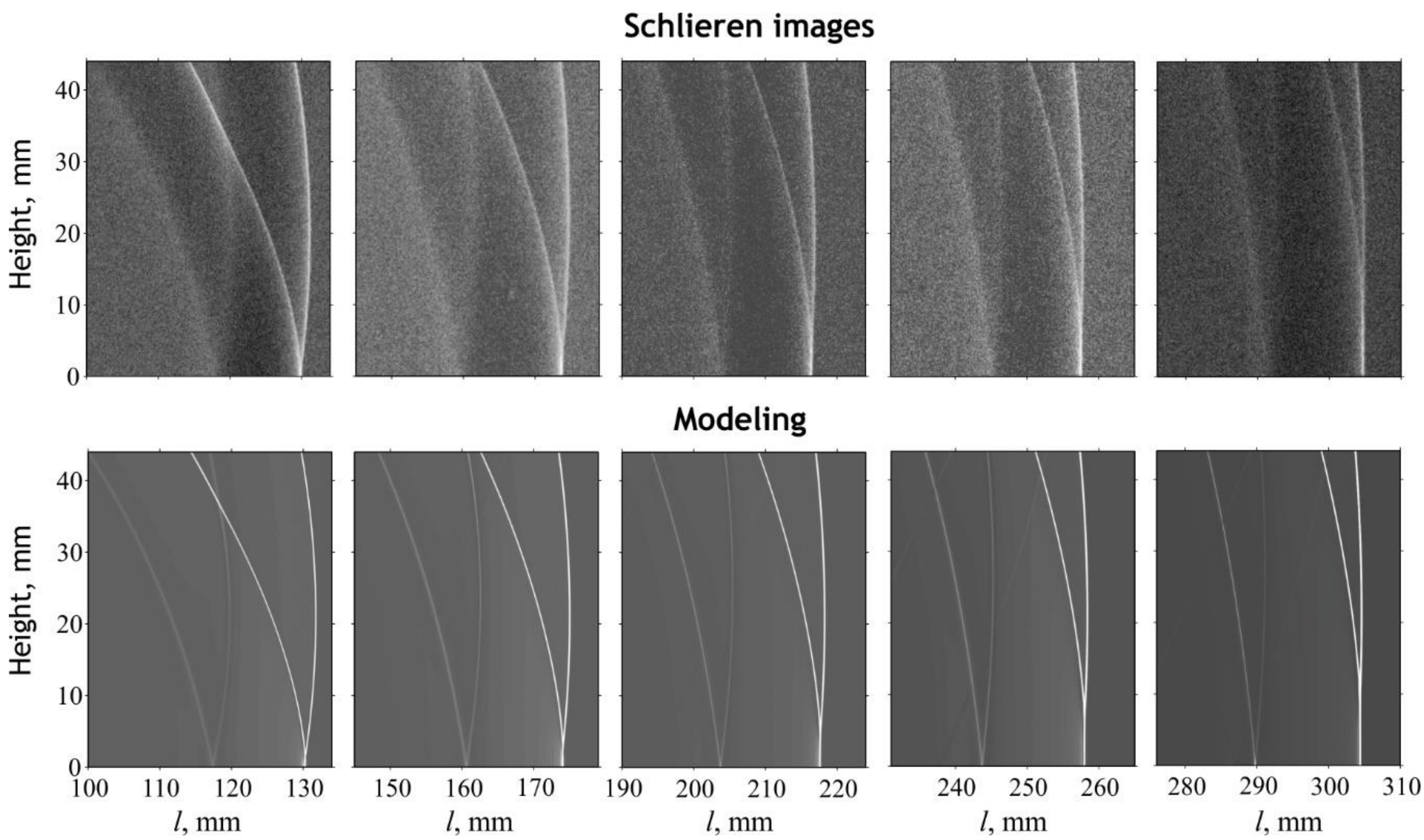

Simulation results are in good agreement with the experimental data

Results: waveforms in reflection pattern

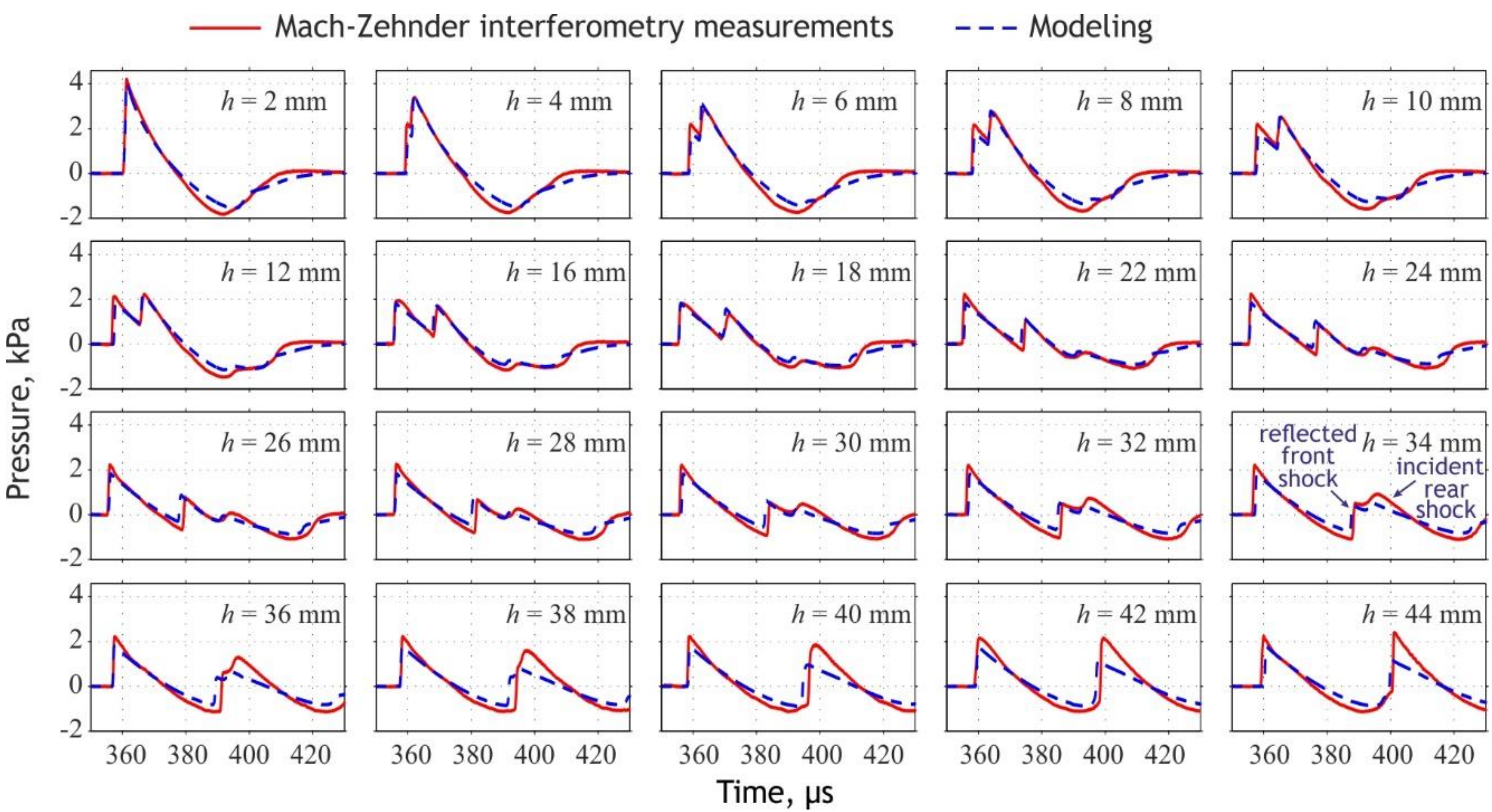

A simplified model of numerical spark as Gaussian-envelope injection of energy is appropriate to study irregular reflection problem

Interaction of the front and rear shocks above the surface

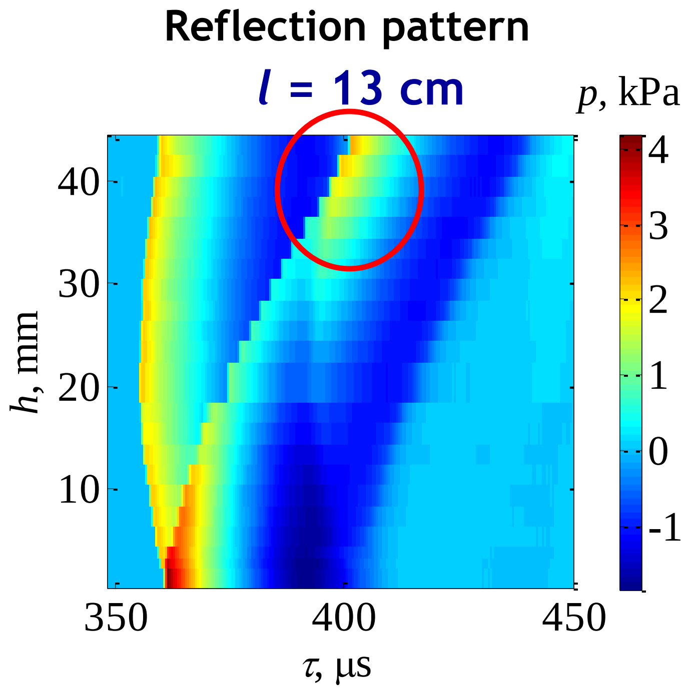

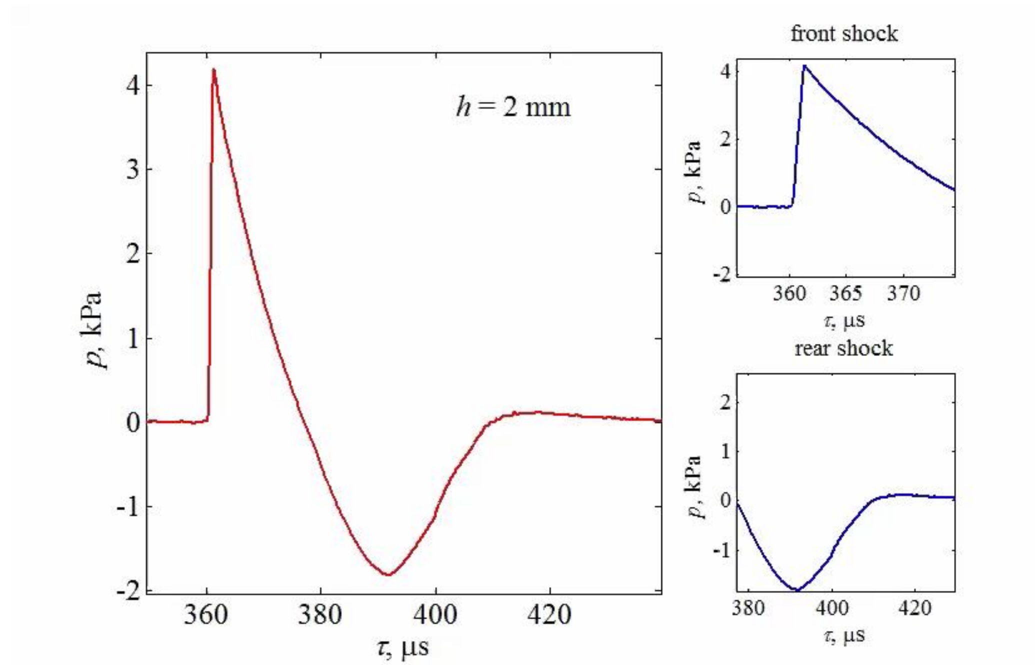

Interaction between the reflected front shock of *N*-wave and its incident rear shock leads to formation of high pressure region above the surface where these fronts intersect

Results: irregular reflection patterns

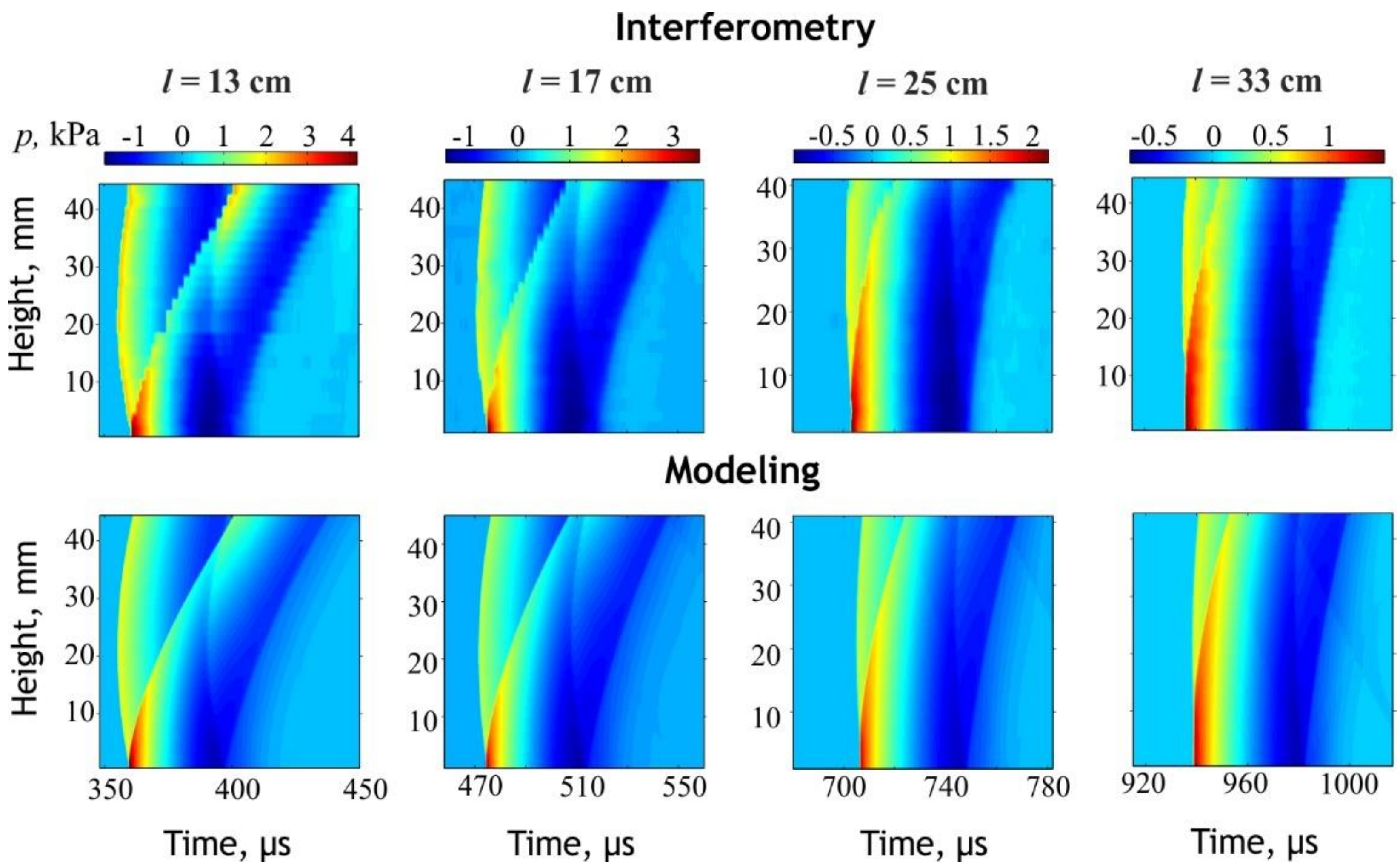

- The length of the Mach stem monotonically increased as the point of *N*-wave reflection moved from the spark source along the surface
- Irregular type of reflection was observed only for the front shock of the pulse; rear shock reflection occurred in a regular regime

Evolution of the Mach stem

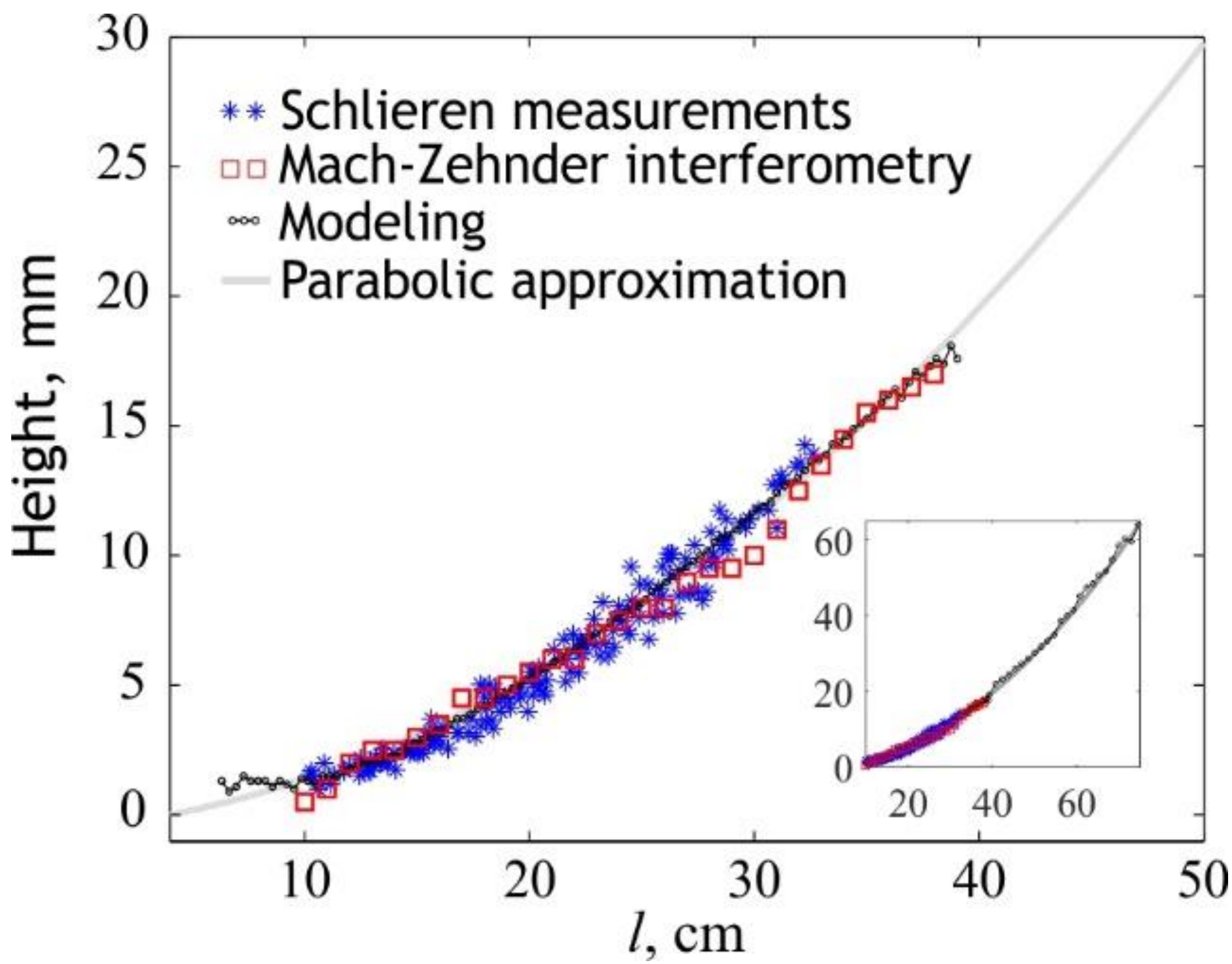

The length of the Mach stem increases on parabolic law until the reflection type turns into the weak von Neumann reflection

Conclusions

- Irregular reflection of spark-generated *N*-waves from the rigid surface was measured in air using the Mach-Zehnder interferometer
- Temporal resolution of the Mach-Zehnder interferometry method is 0.4 μs, which is 6 times better comparing with condenser microphones
- Optical methods provide a possibility for quantitative reconstruction of acoustic pressure signatures with sharp shocks
- Dynamic behavior of the Mach stem length was observed for the front shocks of such reflected *N*-waves
- Interaction between the reflected front shock and its incident rear shock leads to formation of the Mach stem above the surface
- A Gaussian-envelope injection of energy is appropriate model to study numerically irregular reflection problem
- Laboratory scale experiments allow to reproduce irregular reflection of blast wave

Thank you for your attention!

Work supported by RSF-17-72-10277 and by the Labex CeLyA of Université de Lyon, operated by the French National Research Agency (ANR-10-LABX-0060/ ANR-11-IDEX-0007).

The Infasound Signal Generated by the October 2014 Wollaps Island Antares Rocket Failure

Roger Waxler and Claus Hetzer

NCPA at UM

June, 2018

Wallops Island Rocket Explosion Oct 2015

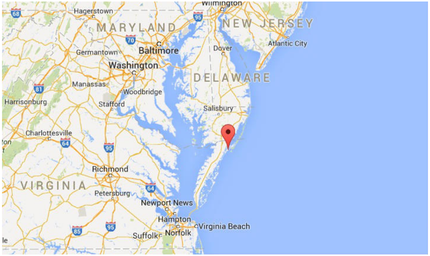

An Antares rocket launch failed on liftoff

- The launch site was Wallops Island on the coast of Northern Virginia
  - This is a populated region of the country
- The rocket was detonated by the ground crew
  - No one was hurt and damage was not extensive

The Static USArray Stations

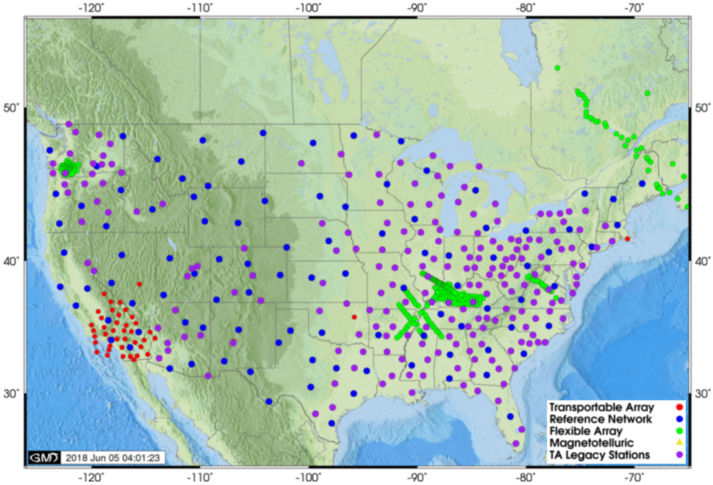

A large number of single-element seismo-acoutic stations

USArray Signal Detection Map

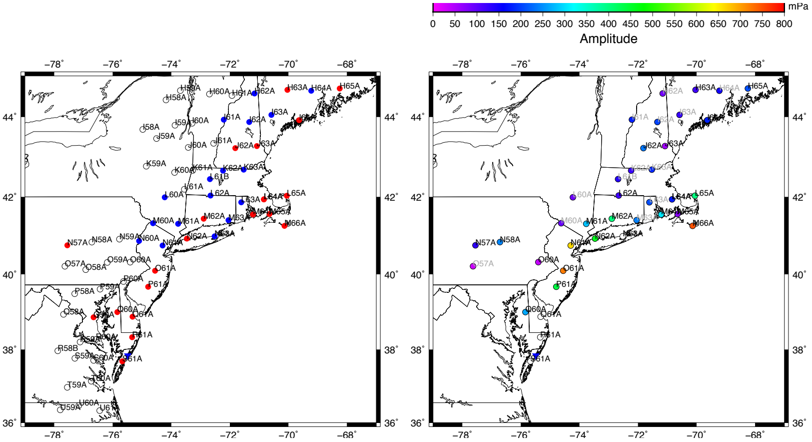

The signal propagaed well up a narrow corridor to the north east

Closest Stations: North versus South

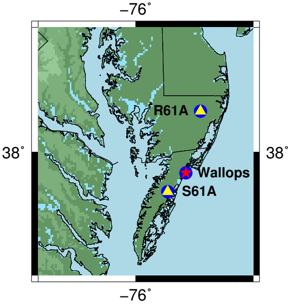

Classic blast wave to the south

- Precursor from intial explosion
- Signal is attenuated somewhat
- No significant dispersion is visible

Narrow band chirp to the north

- Precursor from intial explosion
- Signal is quite large
- Significant dispersion

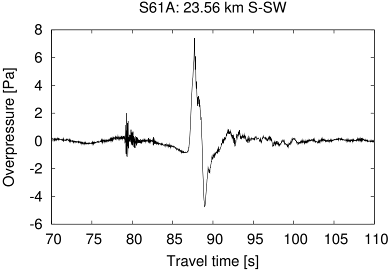

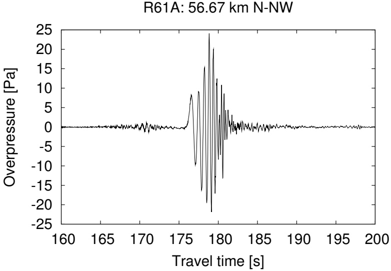

Following the Signal up the East Coast

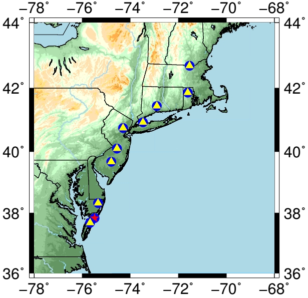

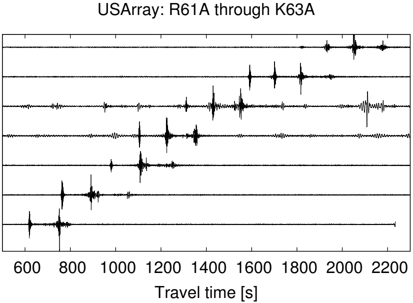

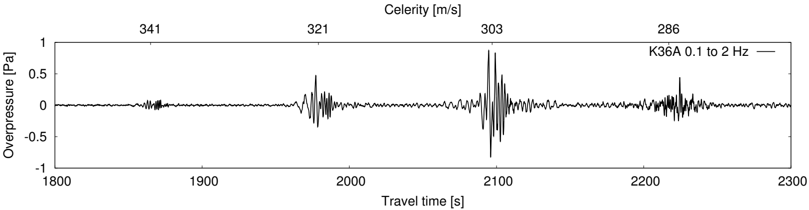

The Nature of the Propagated Signal in the North-Easterly Corridor

The signal was conditioned to a narrow band chirp in the nearfield

Several propagration phases developed:

- A tropospheric phase propagating with sound speed celerity
- Several stratospheric phases
  - The conditioned signal was launched into the far field

Signal captured on a research array in North Boston:

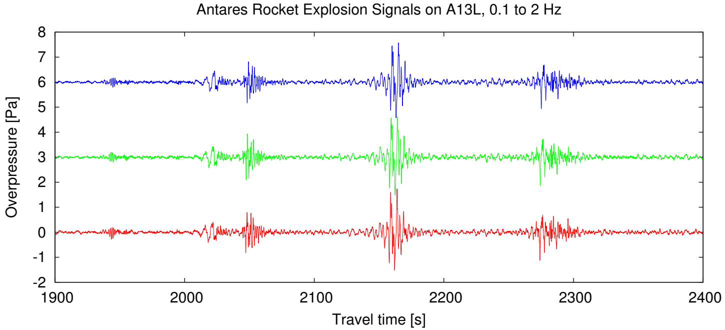

Wavetrain Comparison from two Research Arrays

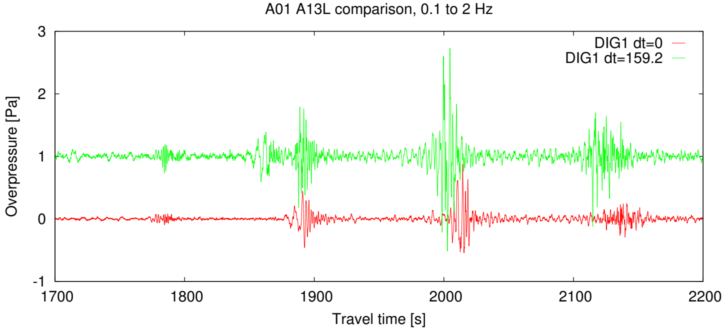

Two research arrays happened to be deployed at the time

- Roughly 60 km apart on the N-NE azimuth
- A01 to the south
- A13L to the north

The tropospheric phase can be used as an onset marker

- The stratospheric phases produce an effective spherical-front trace velocity
- Coherence between the stratospheric phases is not great

Propagation Environment

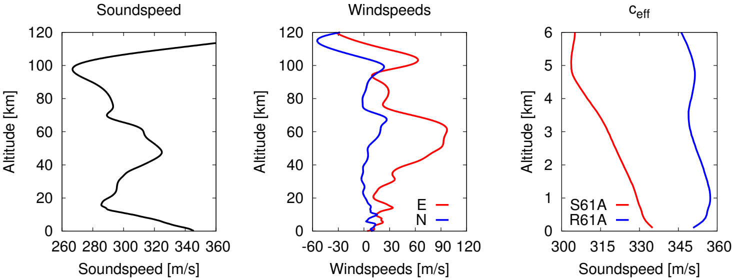

Low altitude tropospheric duct to the N-NE

- Nocturnal temperature inversion
- solid jet stream
- low atitude jet

Upward refraction to the south

Solid stratospheric duct

- stratospheric jet E-NE

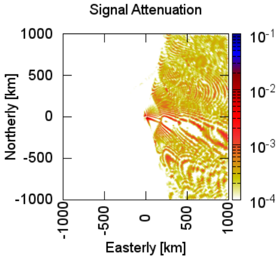

Tropospheric Ducts

Factors controlling tropospheric ducting

Wind speed versus temperature drop

- c at 10 km is $\approx$ 35 m/s less than c on the ground

Wavelength versus wind jet thickness

- long wavelength components penetrate the jet

Wavelength versus upward refraction

- short wavelength components refract away from the ground

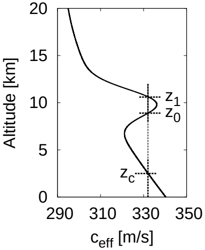

WKB tunnelling factor $e^{-f/F(c)}$, phase speed c, frequency f

Ducting by elevated wind jet

- reduced by tunnelling: high pass filter
- lower phase speeds, more ducting

$$\frac{1}{F(c)} = 2\pi \int_{z_0}^{z_1} \sqrt{\frac{1}{c^2} - \frac{1}{c_{eff}(z)^2}}\, dz$$

Ground contact

- enhanced by tunnelling: low pass filter
- higher phase speeds, better contact

$$\frac{1}{F(c)} = 2\pi \int_{0}^{z_c} \sqrt{\frac{1}{c^2} - \frac{1}{c_{eff}(z)^2}}\, dz$$

Borderline Ducts are Band Pass Filters in both Frequency and Wavenumber.

Stratospheric Arrivals with a Tropospheric Jet

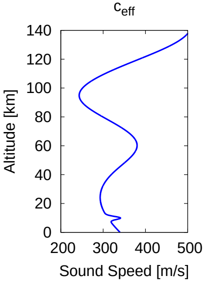

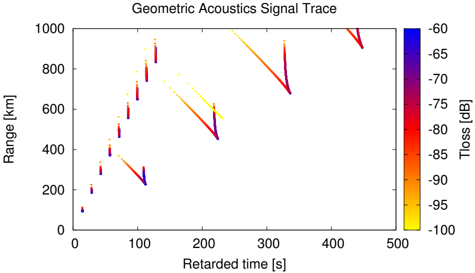

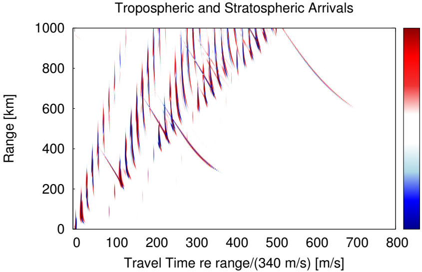

Tropospheric train

- fills the classical shadow
- reverberation

Stratospheric train

- "slow" arrival with echoes
- "fast" arrival without echoes

Thermospheric late arrival

Stratospheric Duct Alone

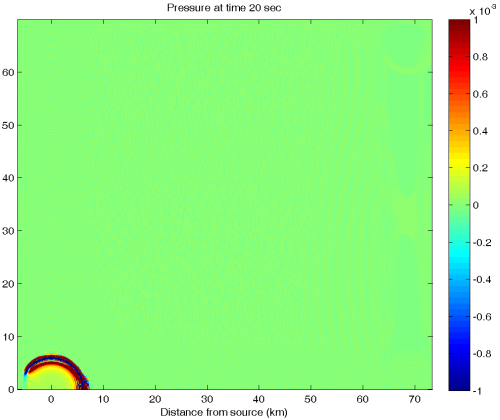

Stratospheric and Tropospheric Duct

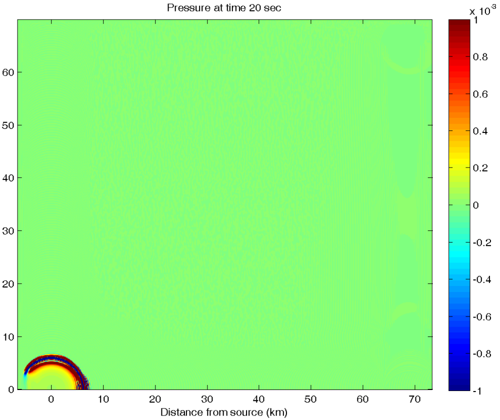

The Influence of a Ground Duct

Becomes a high pass filter

- All frequency components interact with the ground
- Lower frequencies leak into the stratosphere

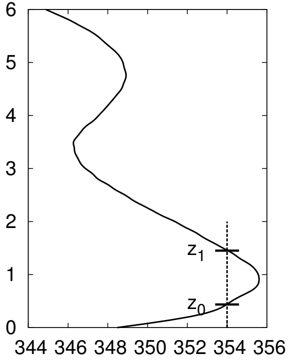

Frequency f and trace velocity c

$$2\pi f \int_{z_0}^{z_1} \sqrt{\frac{1}{c^2} - \frac{1}{c_{eff}(z)^2}}\, dz = \frac{f}{F(c)}$$

$f \gg F(c) \Rightarrow$ trapped

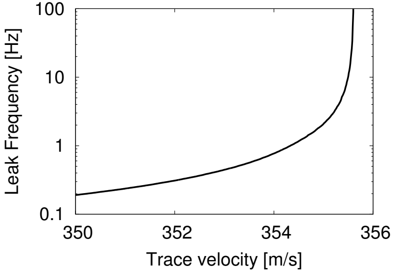

Monotone Propagation up the Coast: Leaky Duct

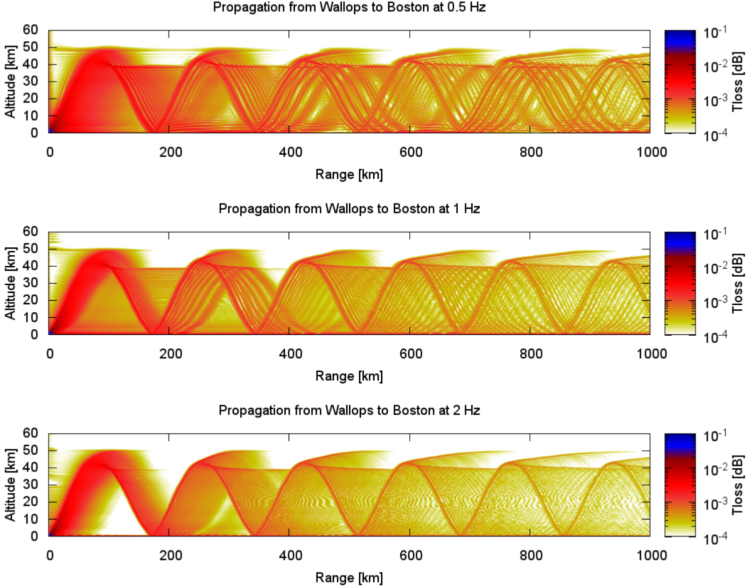

Propagation Model Output Comparison

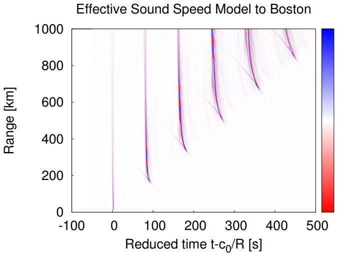

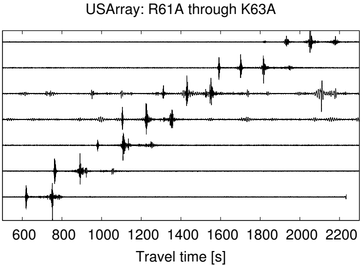

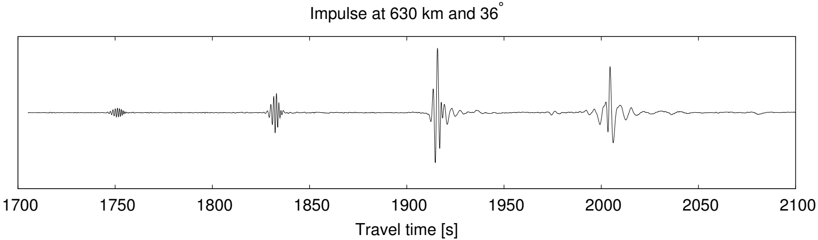

Qualitative features are captured, propagation times are not accurate

Acoustic- gravity waves observed during strong atmospheric storms in Moscow region.

Igor Chunchuzov, Sergey Kulichkov, Oleg Popov, Vitaly Perepelkin

Obukhov Institute of Atmospheric Physics, 119017 Moscow, 3 Pyzhevskii Per., Russia.

Presented at 17th Symposium on Long-Range Sound Propagation , June 12-June 14, Lyon, France, 2018

Content

- Acoustic-gravity waves (AGWs) from atmospheric storms detected by a network of microbarographs near Moscow and by infrasound station IS43 in Dubna.
- Temporal changes in the characteristics of AGWs prior and during a passage of strong storm through the network.
- The differences in the characteristics of AGWs from the warm and cold fronts.
- The possible generation mechanisms for the observed AGWs.
- Detection of the wave precursors of strong atmospheric storms and the possibility to forecast such storms.

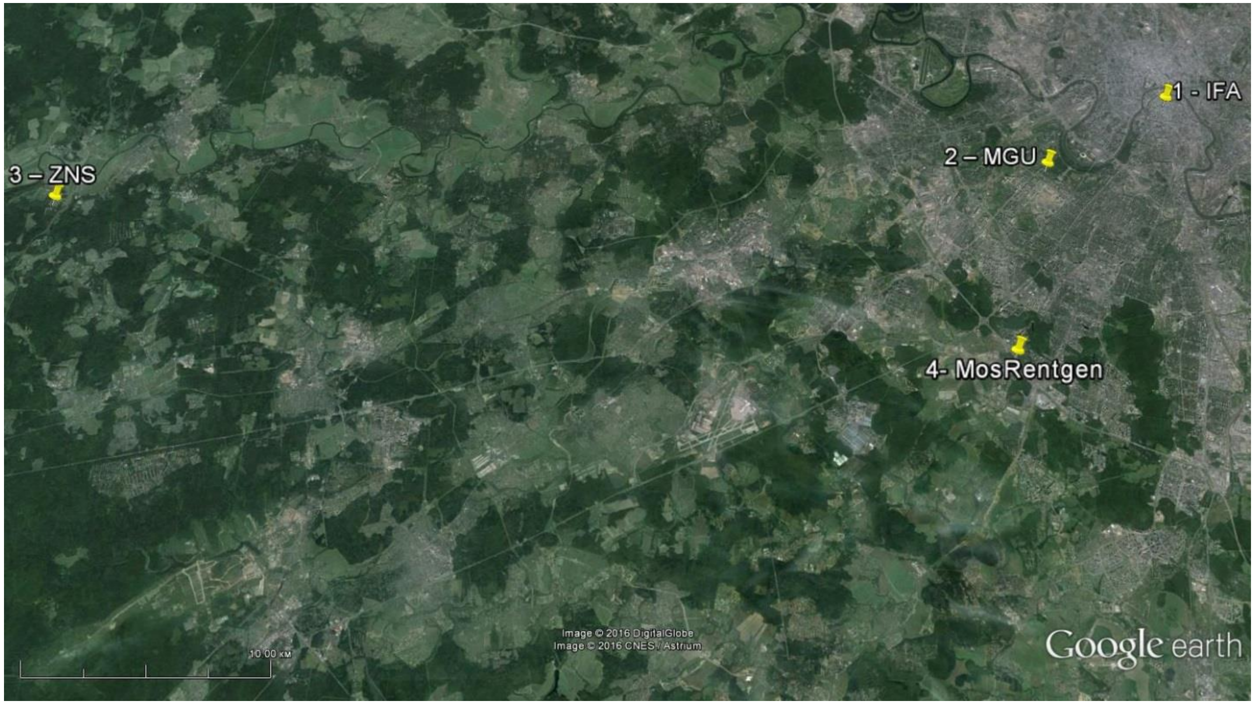

The network of microbarographs MGU-IFA-ZNS-MosRentgen near Moscow.
The distances between MGU and IFA is 7.2 km,
between IFA and ZNS-53 km, between MGU and ZNS-47 km.

MAP OF INFRASOUND STATION IS43 WITH 4 SENSORS, DUBNA

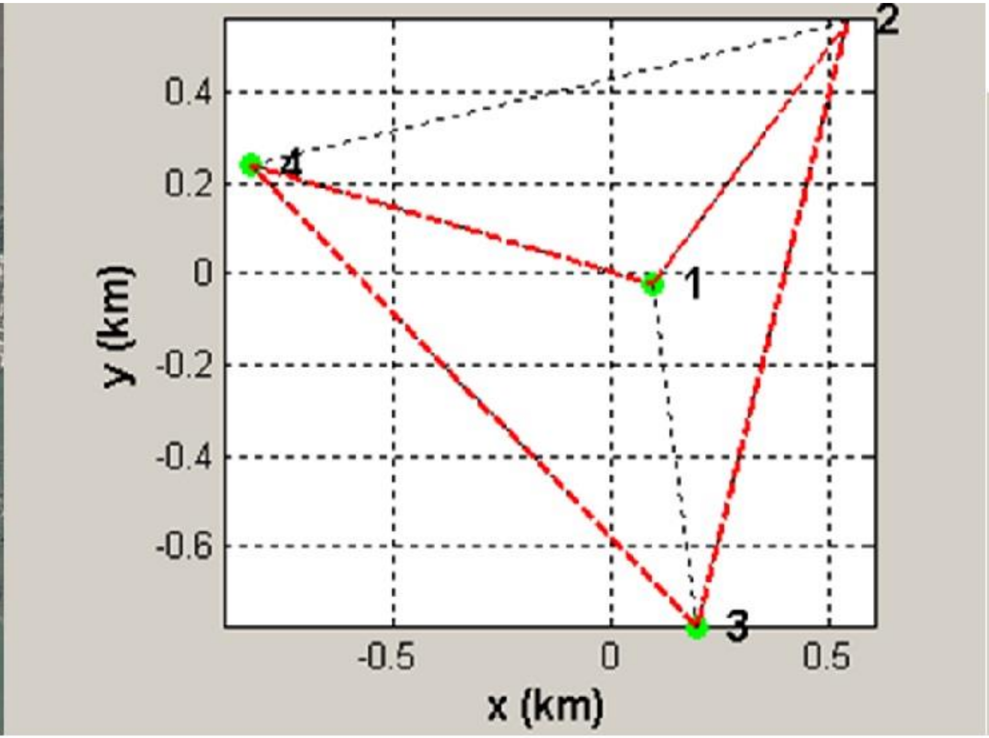

The distance between Moscow and Dubna is 110 km.

Internal gravity waves from atmospheric storm in Moscow, May 28-29, 2017

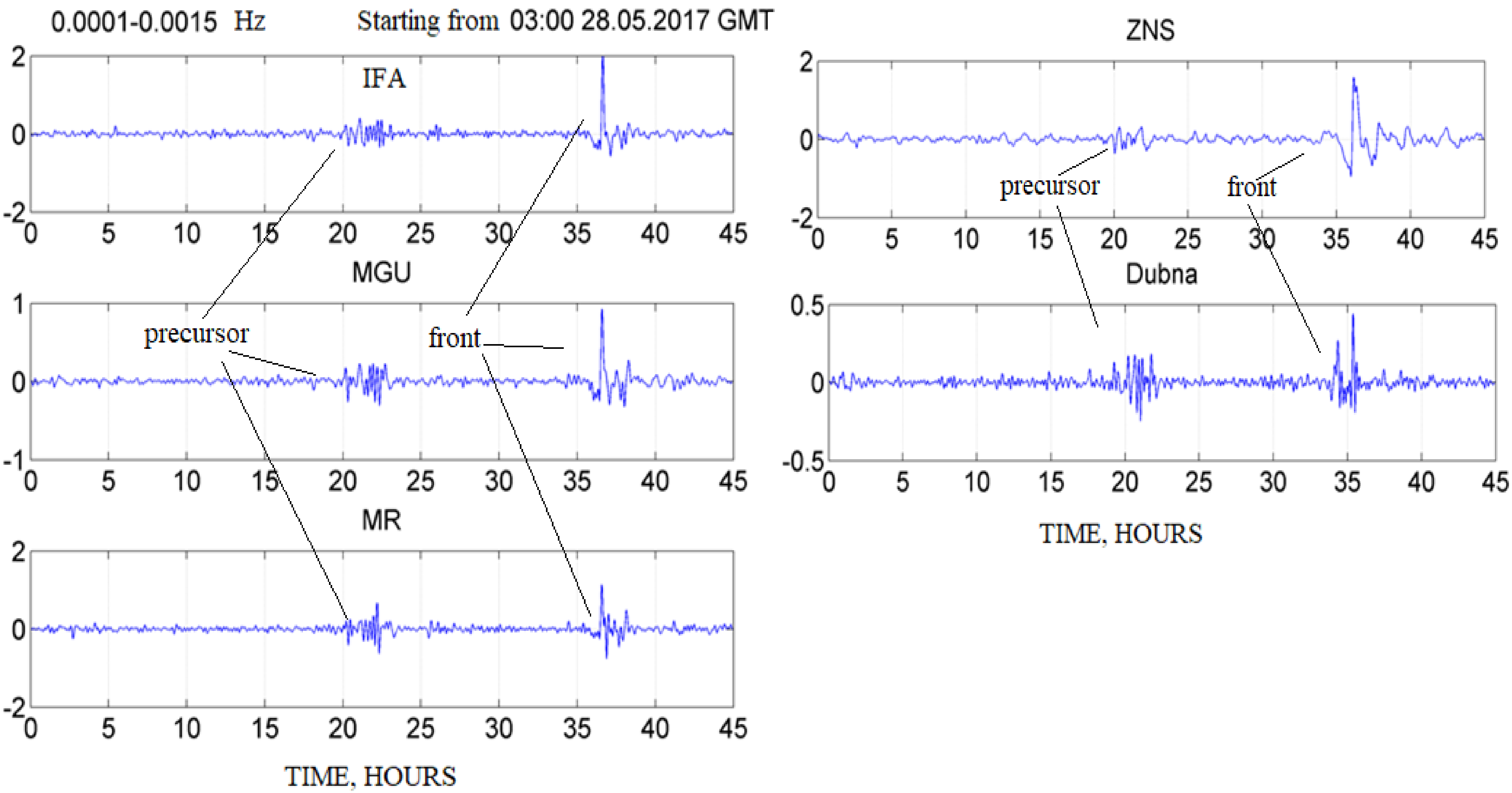

A violent storm that passed through Moscow on May 29, 2017 caused severe destruction in the city and the death of ten people

Coherence analysis of the signals from atmospheric storm recorded in Moscow, May 28-29, 2017

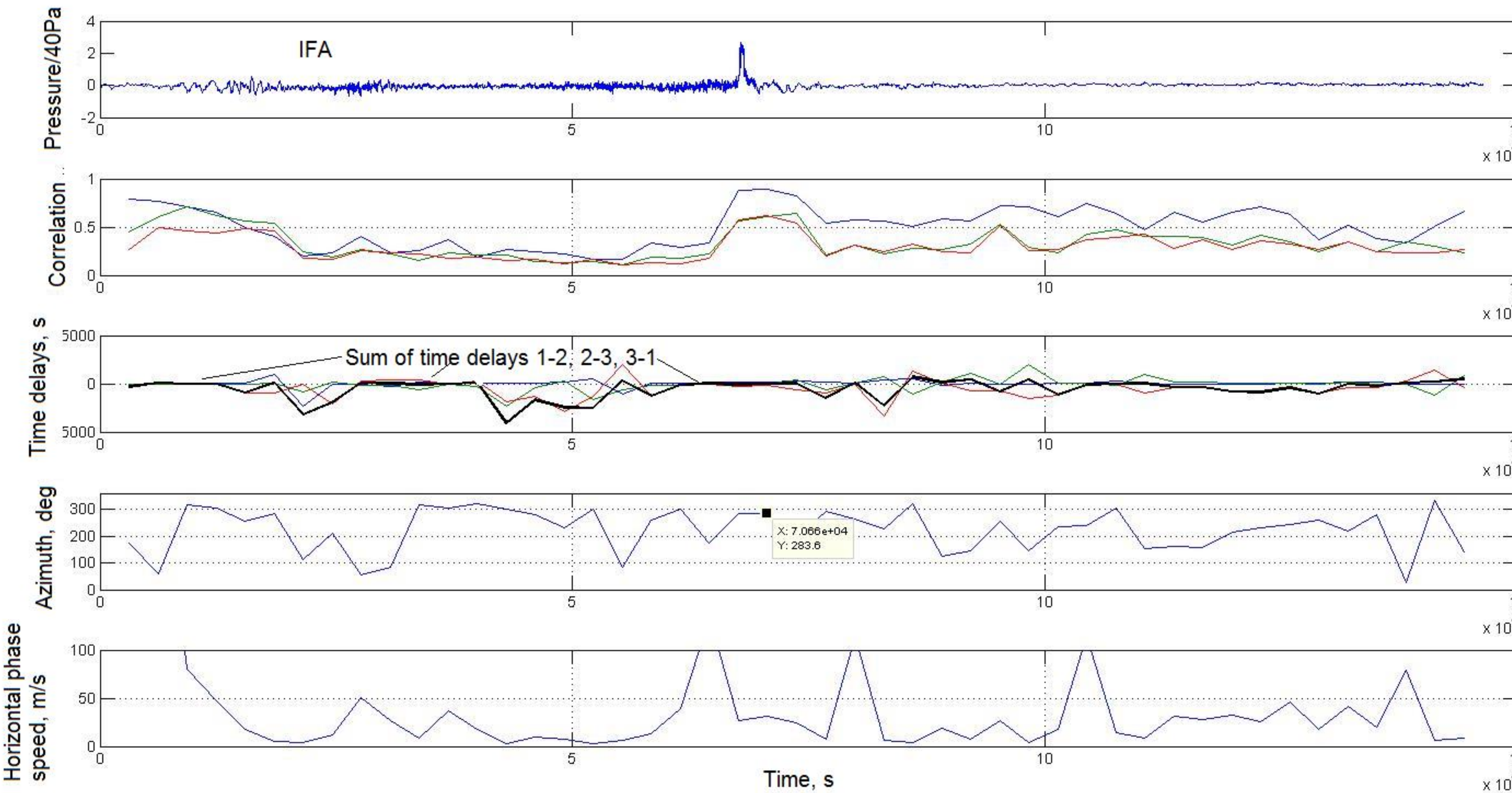

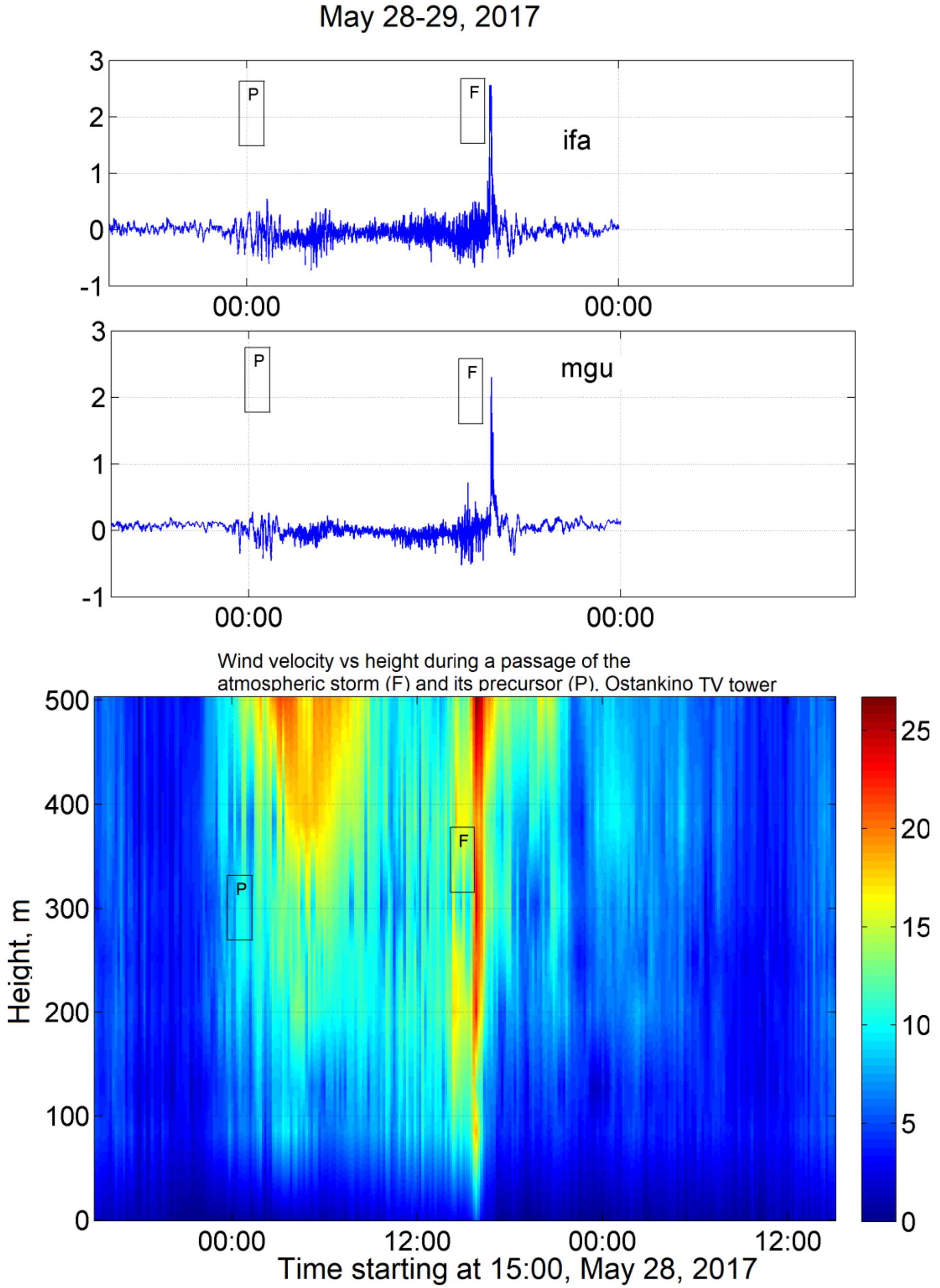
May 28-29, 2017
P
F
ifa
3
2
1
0
-1
00:00
00:00
P
F
mgu
Wind velocity vs height during a passage of the atmospheric storm (F) and its precursor (P). Ostankino TV tower
P
F
500
400
300
200
100
0
Height, m
00:00
12:00
00:00
12:00
Time starting at 15:00, May 28, 2017
25
20
15
10
5
0

Variations of atmospheric pressure, NOx and airborne particulates PM10, 26-28 June, 201 5, ZNS

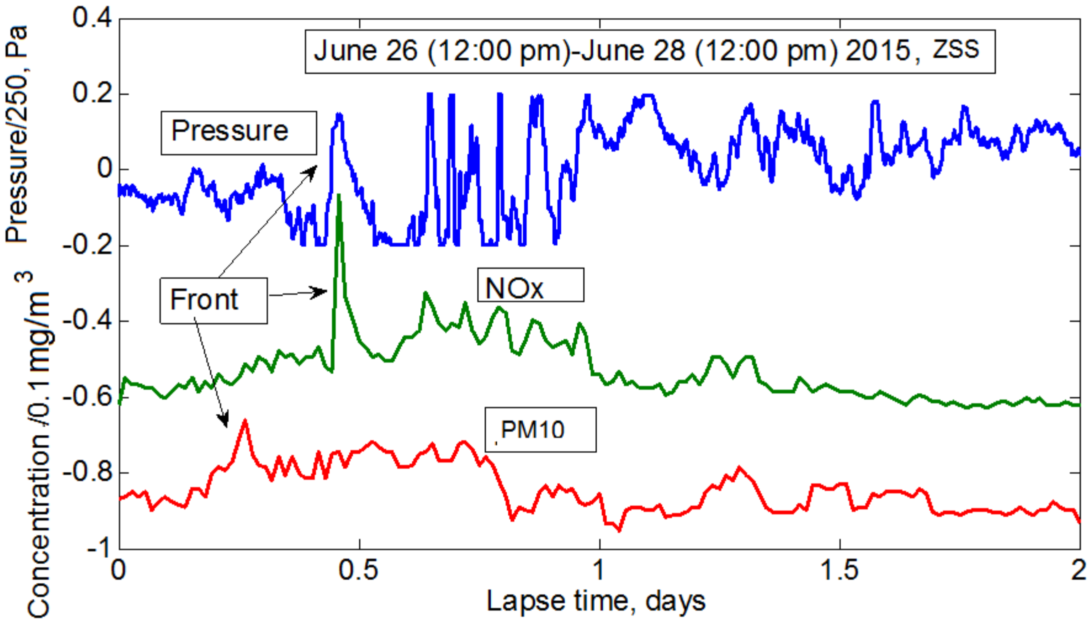

The Application of the Hydraulic Analogy to Certain Atmospheric Flow Problems *by* MORRIS TEPPER. -RESEARCH PAPER NO. 35, US WEATHER BUREAU, 1952

Weather map at 06:00 GMT of May 28, 2017

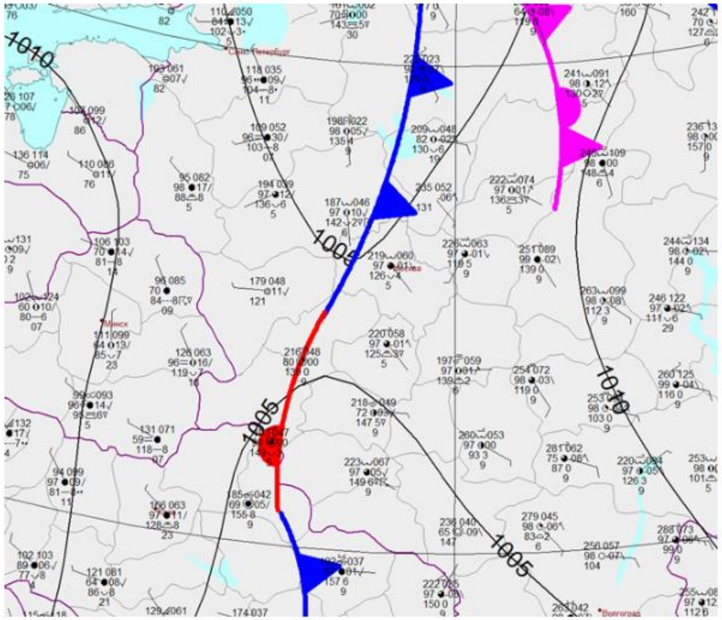

Карта погоды, 06:00 по Гринвичу 28 мая 2015 г. © Гисметео

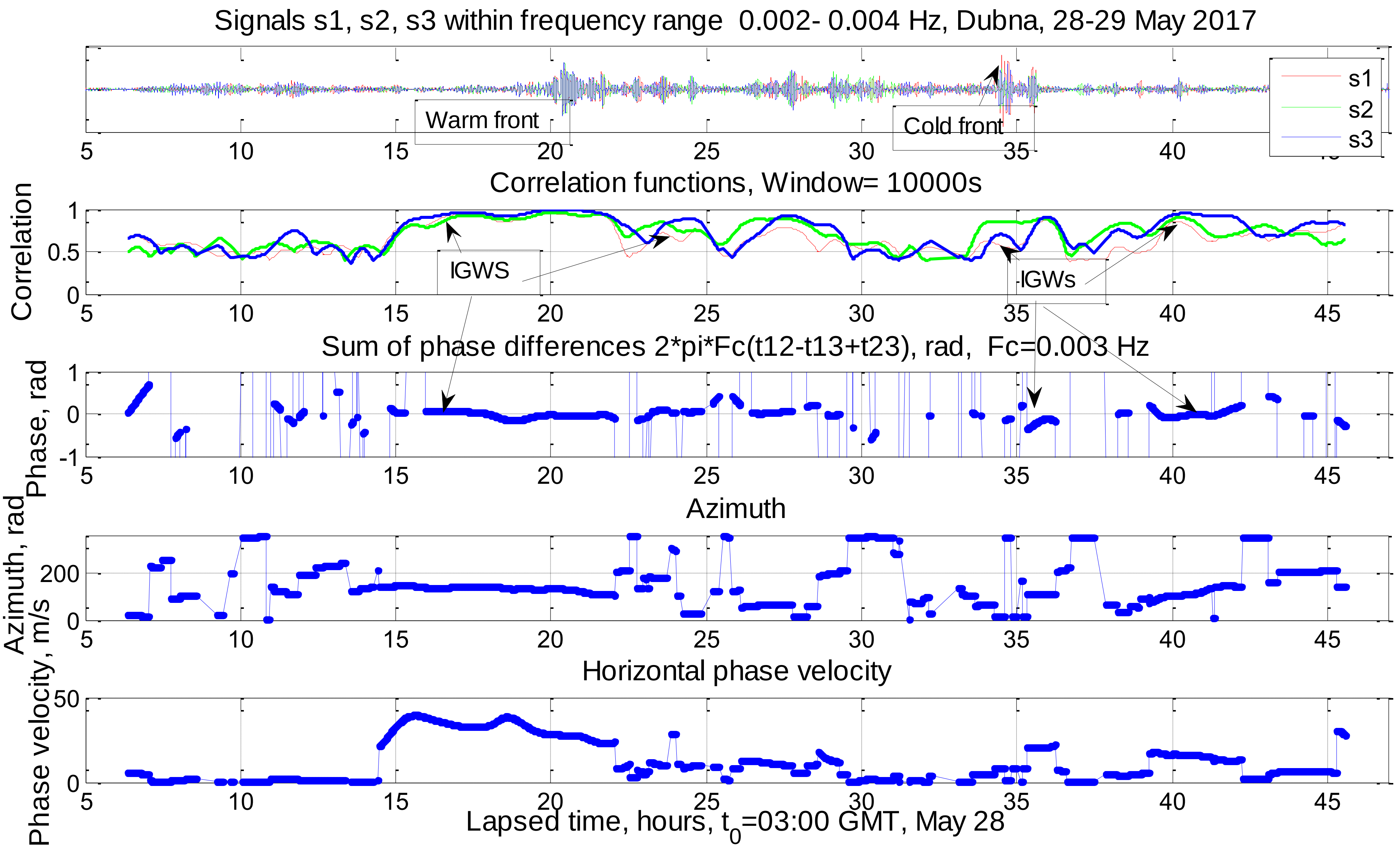

Signals s1, s2, s3 within frequency range 0.002- 0.004 Hz, Dubna, 28-29 May 2017
Warm front
Cold front
s1
s2
s3
Correlation functions, Window= 10000s
Correlation
IGWS
IGWs
Sum of phase differences 2*pi*Fc(t12-t13+t23), rad, Fc=0.003 Hz
Phase, rad
Azimuth
Azimuth, rad
Horizontal phase velocity
Phase velocity, m/s
Lapsed time, hours, t0=03:00 GMT, May 28

Transition from IGWs to infrasound, May 28-29, 2017

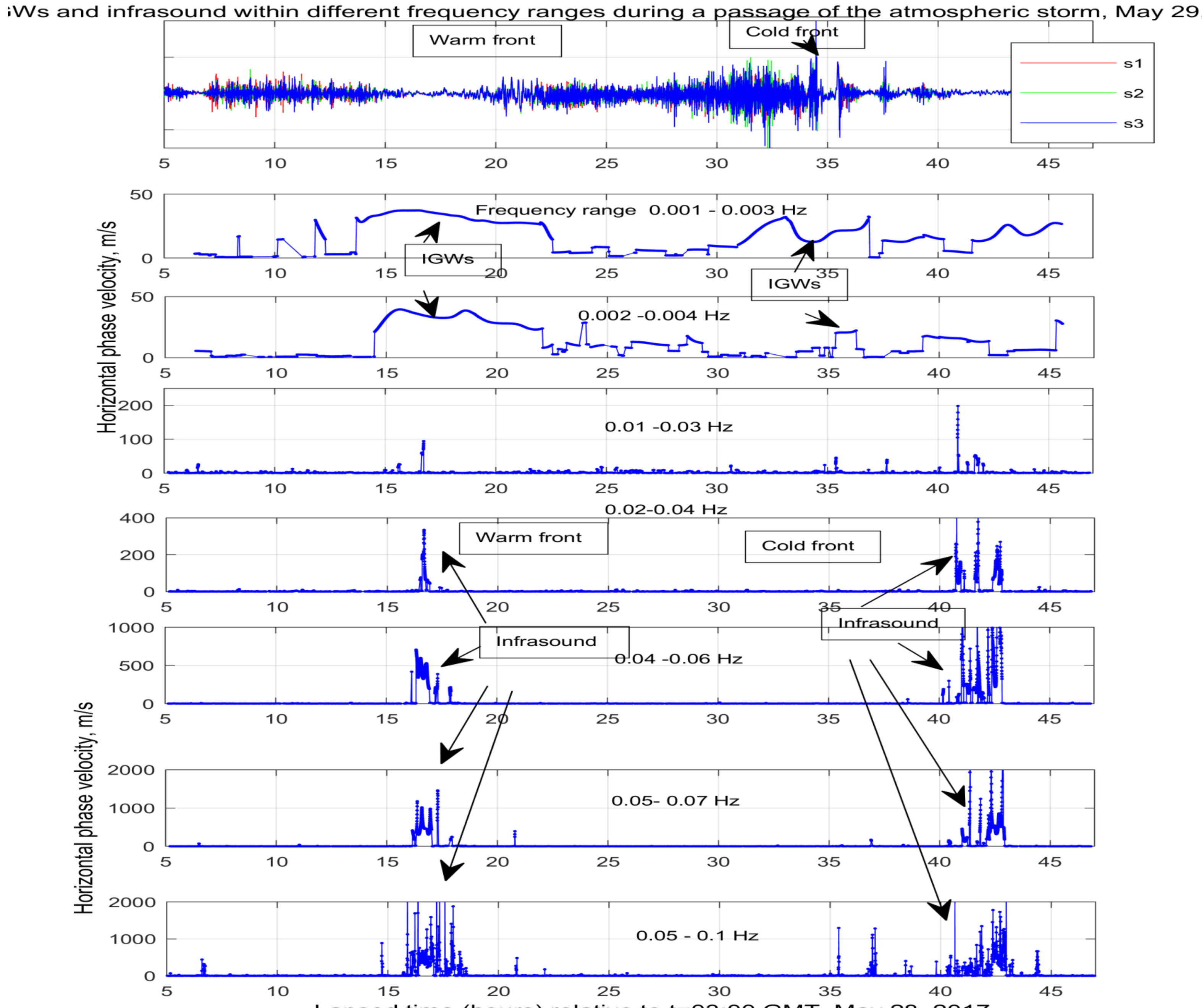

Correlation functions for the infrasound in the range 0.05-0.1 Hz generated by atmospheric storm, May 28-29, 2017

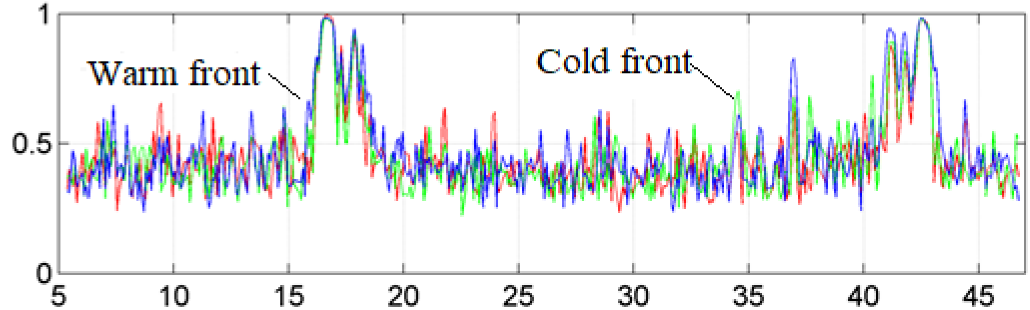

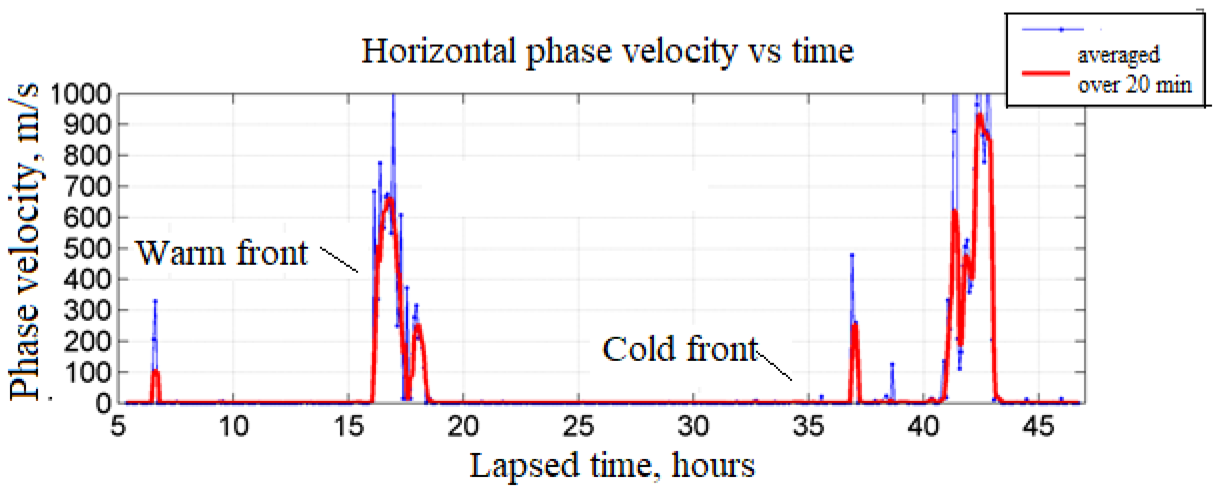

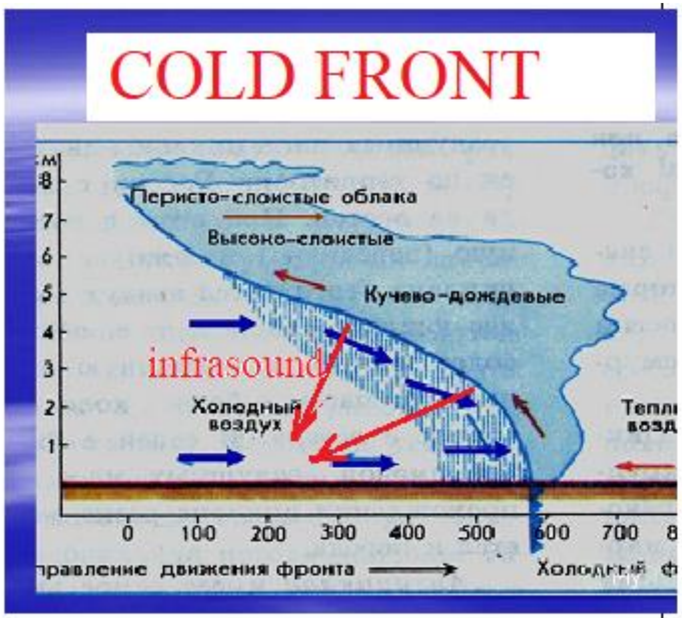
COLD FRONT
Перисто-слоистые облака
Высоко-слоистые
Кучево-дождевые
infrasound
Холодный воздух
0 100 200 300 400 500 600 700
правление движения фронта
Холодный

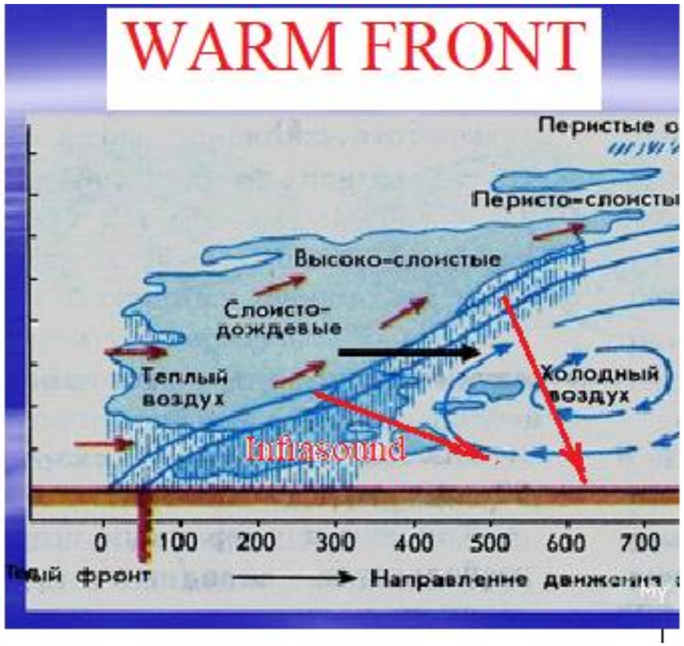
WARM FRONT
Перистые
Перисто-слоисты
Высоко-слоистые
Слоисто-дождевые
Теплый воздух
Холодный воздух
Infrasound
0 100 200 300 400 500 600 700
фронт
Направление движения

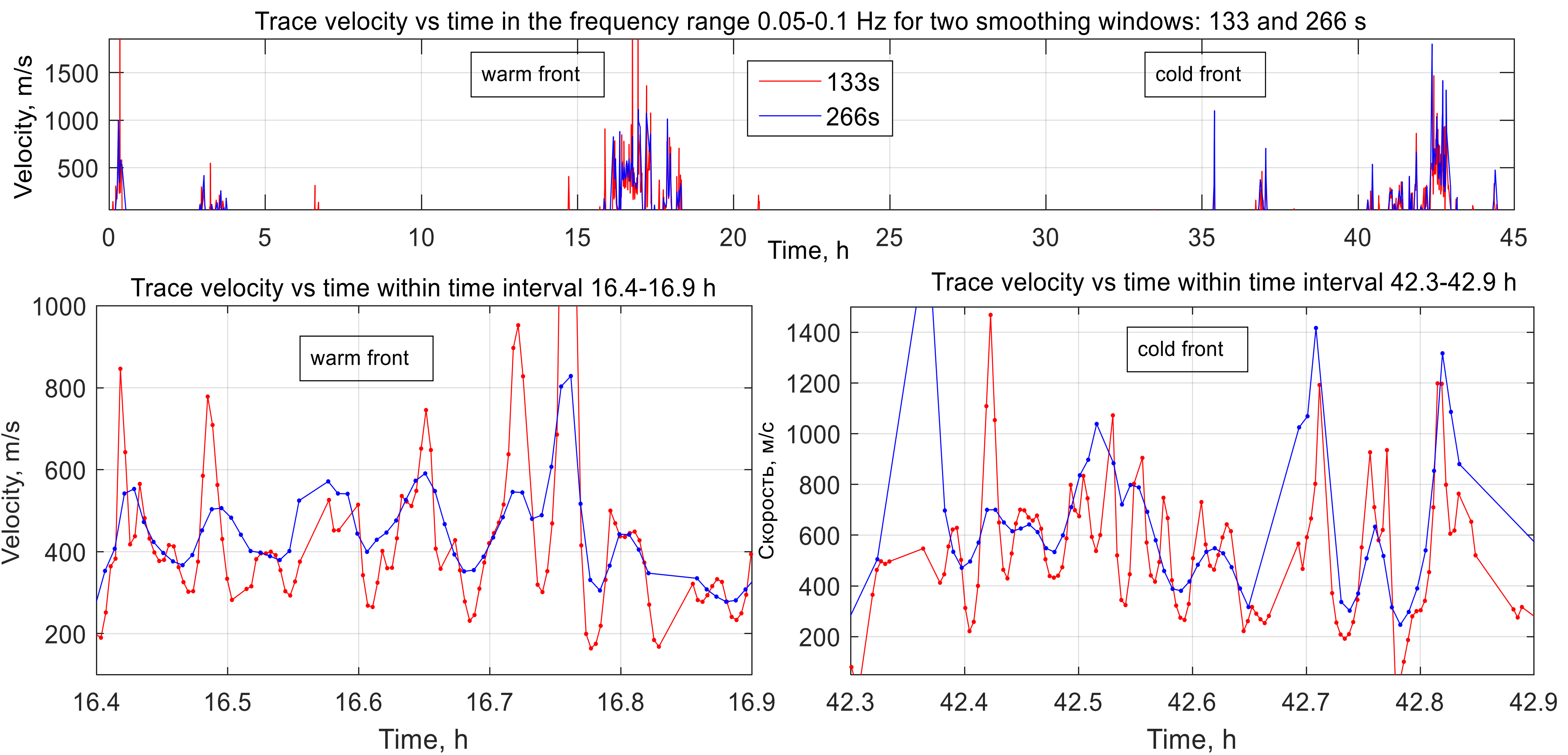

Horizontal phase speed of the infrasound C(t)=C'+V(t) is modulated in time by wind velocity fluctuations induced by internal waves generated by warm and cold fronts. The intrinsic horizontal velocity C'(t) also varies due to periodical vertical displacements of the layers of turbulence that generate infrasound. Such displacements change elevation angle of the infrasound arrival to the receivers and C'

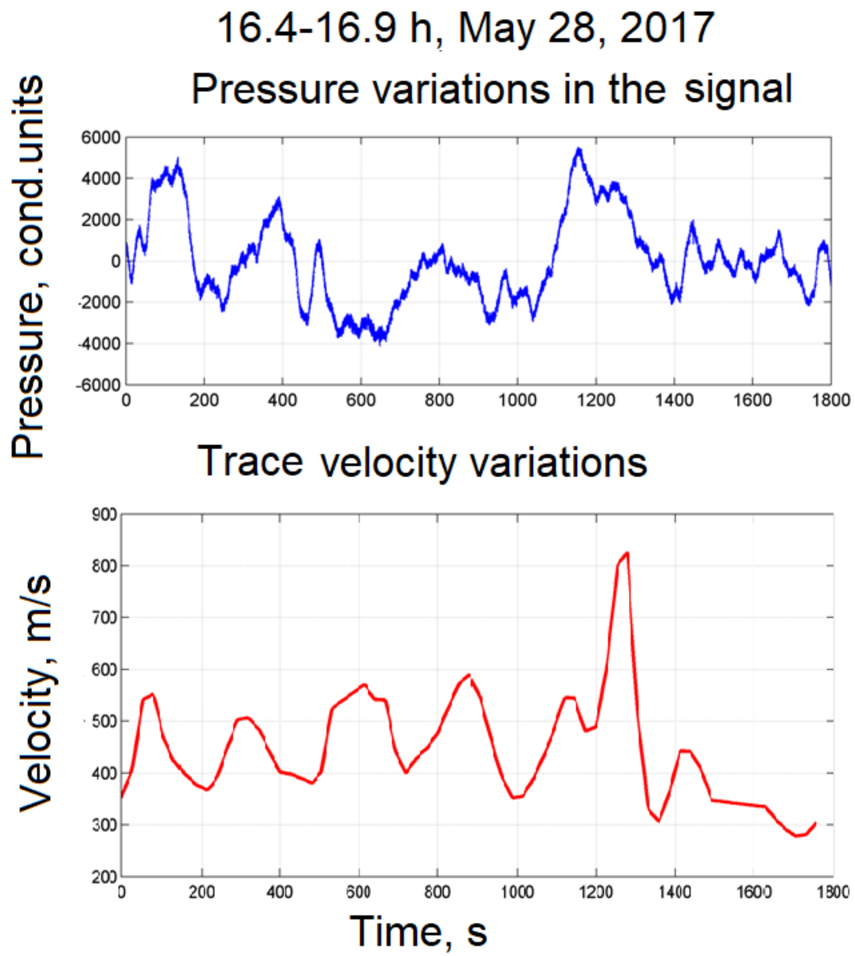
16.4-16.9 h, May 28, 2017
Pressure variations in the signal
Pressure, cond.units
6000
4000
2000
0
-2000
-4000
-6000
0
200
400
600
800
1000
1200
1400
1600
1800
Trace velocity variations
Velocity, m/s
900
800
700
600
500
400
300
200
0
200
400
600
800
1000
1200
1400
1600
1800
Time, s

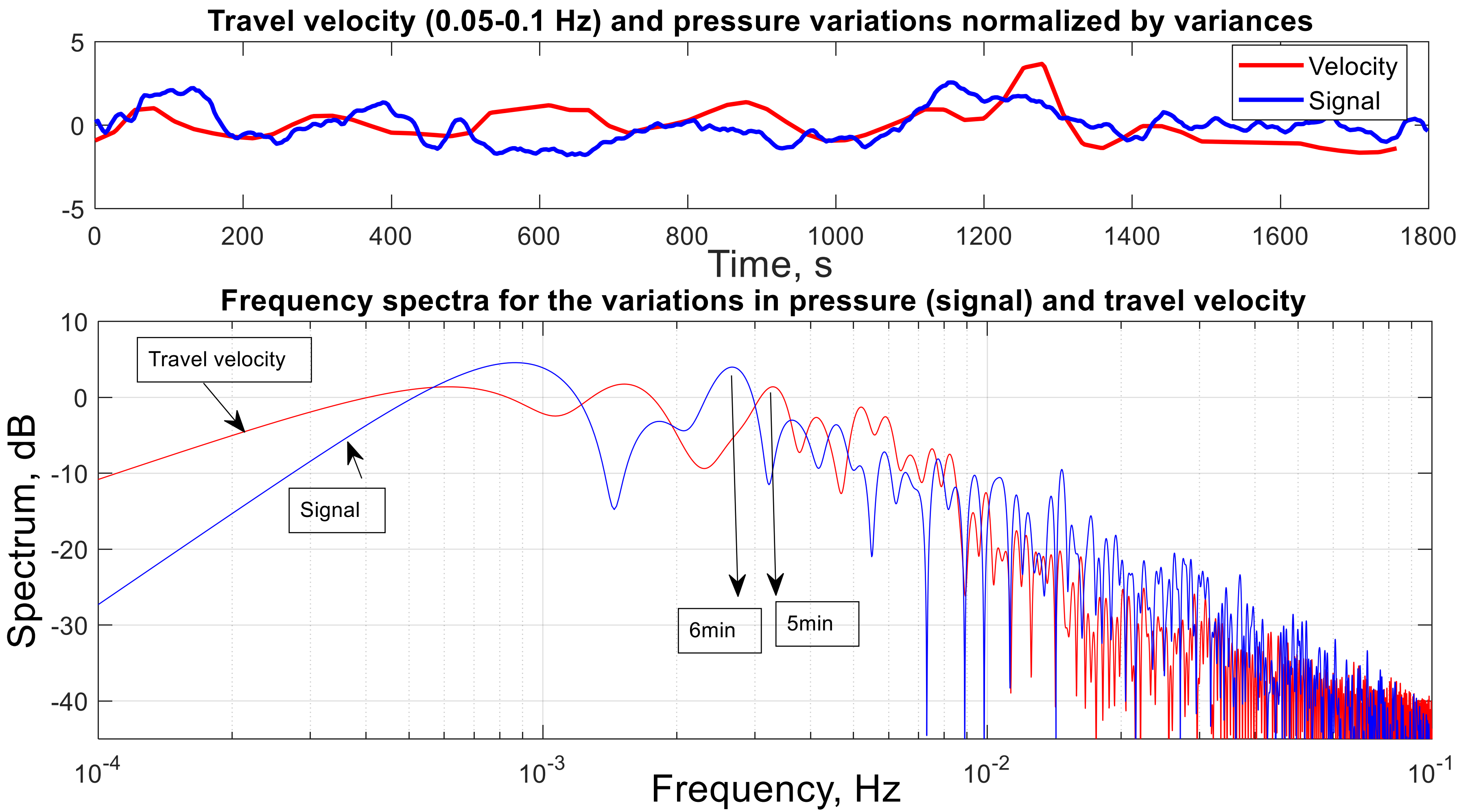
Travel velocity (0.05-0.1 Hz) and pressure variations normalized by variances
Velocity
Signal
Time, s
Frequency spectra for the variations in pressure (signal) and travel velocity
Travel velocity
Signal
6min
5min
Spectrum, dB
Frequency, Hz

CONCLUSIONS

1. The wave precursors (IGWs and infrasound) and signals associated with strong atmospheric storms were detected by a network of microbarographs in Moscow region. The temporal changes in the characteristics of AGWs prior and during a passage of strong storm through the network have been studied.

2. The pressure pulse of IGWs associated with atmospheric storm was found to have a sharp jump similar to the shock front of the intense acoustic pulse. Such a shock front may be formed due to dependence of the local phase velocity of the pressure jump on the local vertical displacement or local pressure caused by the gravity wave perturbation. This causes the steepening of the wave form and appearance of the “shock” wave front.

3. The wave precursor of the storm was found to be generated by the warm front that passed the network about 15 hours before the passage of the storm and cold front. Both the warm front (wave precursor) and the storm generated long-lasting gravity wave trains and infrasound.

4.The filtering of the signals within different frequency ranges showed the transition from gravity waves with low frequencies (0.001-0.005 Hz) and low trace velocities (20-50 m/s) to the infrasound with high frequencies (0.01-0.1 Hz) and high trace velocities (up to 800-1000m/s). Such high trace velocities may be explained by high elevation angles relative to the ground of the infrasound arrivals generated by the layers of turbulence existing at high altitudes (up to 10km) of the upper troposphere

5. The differences in the characteristics of infrasound from the warm and cold fronts were found. The observed oscillations in trace velocity with a period of 5-6 min may be caused by the wind velocity fluctuations and vertical displacements of the layers of turbulence caused by IGWs.
The observed effects of IGWs on infrasound propagation should be taken into account in the long-range sound propagation models.

Modeling the seismo-acoustic events of DPRK's underground nuclear tests

Gil Averbuch [1,2] Jelle D. Assink [2] Pieter S.M. Smets [1,2] Läslo G. Evers [2,1]

[1]Department of Geoscience and Engineering, Faculty of Civil Engineering and Geosciences, Delft University of Technology, Delft, the Netherlands.

[2]R&D Department of Seismology and Acoustics, Royal Netherlands Meteorological Institute, De Bilt, the Netherlands.

June 11, 2018

Outline

Outline

Infrasound signals from DPRK's underground nuclear tests

Seismo-acoustic coupling mechanisms

Results

Conclusions

DPRK's Underground Nuclear Tests

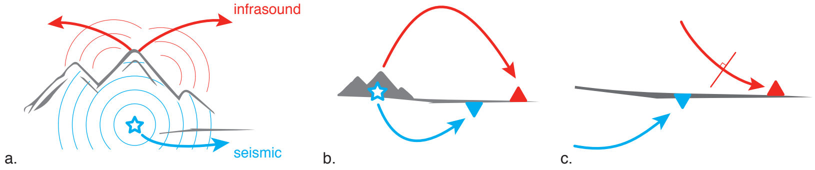

On the infrasound detected from the 2013 and 2016 DPRK's underground nuclear tests

AGU PUBLICATIONS

Geophysical Research Letters

RESEARCH LETTER
10.1002/2016GL068497

On the infrasound detected from the 2013 and 2016 DPRK's underground nuclear tests

J. D. Assink[1], G. Averbuch[2], P. S. M. Smets[1,2], and L. G. Evers[1,2]

[1]R&D Seismology and Acoustics Department, Royal Netherlands Meteorological Institute (KNMI), De Bilt, Netherlands, [2]Department of Geoscience and Engineering, Faculty of Civil Engineering and Geosciences, Delft University of Technology, Delft, Netherlands

All authors contributed equally.

Key Points:
- Underground nuclear tests by the DPRK have generated observable atmospheric infrasound
- During the 2013 and 2016 tests, the stratospheric waveguide was in a very different state
- We hypothesize that the 2016 test took place at least 1.5 times deeper than the 2013 test

Supporting Information:
- Supporting Information S1

Correspondence to:
J. D. Assink,
assink@knmi.nl

Citation:
Assink, J. D., G. Averbuch, P. S. M. Smets, and L. G. Evers (2016), On the infrasound detected from the 2013 and 2016 DPRK's underground nuclear tests, *Geophys. Res. Lett.*, *43*, doi:10.1002/2016GL068497.

Received 2 MAR 2016
Accepted 18 MAR 2016
Accepted article online 22 MAR 2016

Abstract The underground nuclear tests by the Democratic People's Republic of Korea (DPRK) generated atmospheric infrasound both in 2013 and 2016. Clear detections were made in the Russian Federation (I45RU) and Japan (I30JP) in 2013 at stations from the International Monitoring System. Both tropospheric and stratospheric refractions arrived at the stations. In 2016, only a weak return was potentially observed at I45RU. Data analysis and propagation modeling show that the noise level at the stations and the stratospheric circumpolar vortex were different in 2016 compared to 2013. As the seismic magnitude of the 2013 and 2016 nuclear test explosions was comparable, we hypothesize that the 2016 test occurred at least 1.5 times deeper. In such a case, less seismic energy would couple through the lithosphere-atmosphere interface, leading to less observable infrasound. Since explosion depth is difficult to estimate from seismic data alone, this motivates a synergy between seismics and infrasonics.

1. Introduction

Sources of seismic energy in the subsurface can generate low-frequency acoustic waves in the atmosphere, i.e., infrasound. Examples of such sources are earthquakes and explosions [*Donn and Posmentier*, 1964]. There are various mechanisms through which seismic waves in the subsurface can couple to infrasonic waves in the atmosphere at the lithosphere-atmosphere interface. Previous studies with earthquake recordings have shown the following: (1) epicentral infrasound, (2) topographical infrasound, and (3) evanescently coupled infrasound. (1) Epicentral infrasound is the direct coupling of seismic-to-infrasonic energy at the earthquake's epicenter, due to the movement of the Earth's surface [*Mutschlecner and Whitaker*, 2005]. (2) Topographical infrasound can be generated away from the epicentral region by the movement of mountain ranges [*Le Pichon et al.*, 2006] or steep slopes, like a cliff [*Green et al.*, 2009]. Here also, the movement of the Earth's surface due to seismic waves is the source of infrasonic waves [*Walker et al.*, 2013]. (3) Evanescently coupled infrasound has been observed from an earthquake under the ocean. Secondary sources in the water column generated hydroacoustical waves. The ocean-atmosphere interface became anomalously transparent, since the underwater source depths were within one acoustic wavelength, generating infrasound in the atmosphere [*Evers et al.*, 2014].

When a source in the subsurface is capable of generating infrasound, there is no guarantee that the infrasound generated will be detected at a distant station. This strongly depends on the source-receiver distance, the atmospheric winds and temperature, and noise levels at the receiver due to wind and turbulence. In long-range infrasound propagation, i.e., over distances of more than 100 km, the state of the stratosphere [*Assink et al.*, 2014; *Waxler et al.*, 2015] and to a lesser extent the thermosphere determine the (un)favorable conditions for detection.

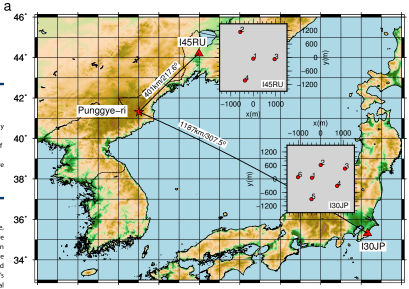

On the infrasound detected from the 2013 and 2016 DPRK's underground nuclear tests

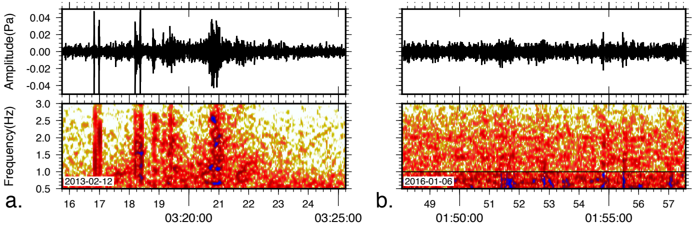

On the infrasound detected from the 2013 and 2016 DPRK's underground nuclear tests

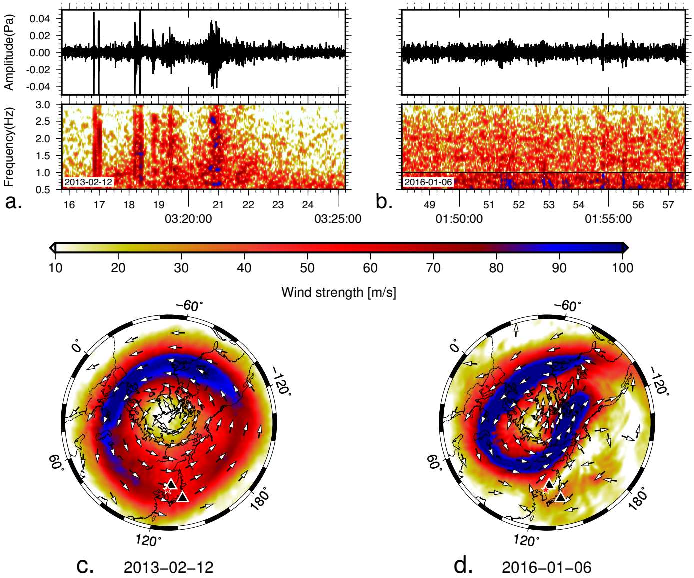

Outline

Infrasound signals from DPRK's underground nuclear tests

Seismo-acoustic coupling mechanisms

Results

Conclusions

Seismo-acoustic coupling mechanisms

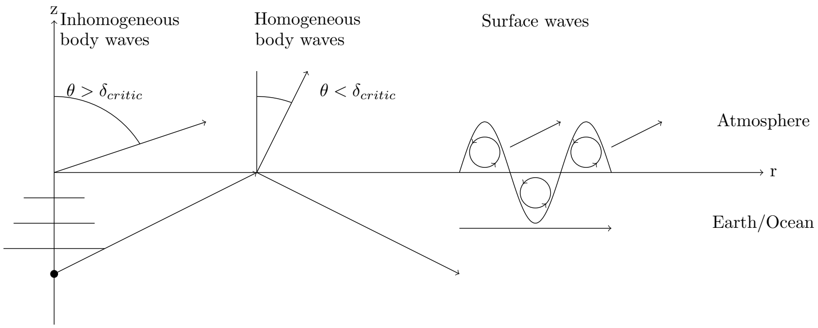

Figure modified from Godin, O. A. (2008). Sound transmission through water-air interfaces: New insights into an old problem. Contemporary Physics 49 (2), 105-123.

Fast Field Program

Solid-fluid

The FFP is a wavenumber integration method. It solves the range independent Helmholtz equation for horizontally stratified medium.

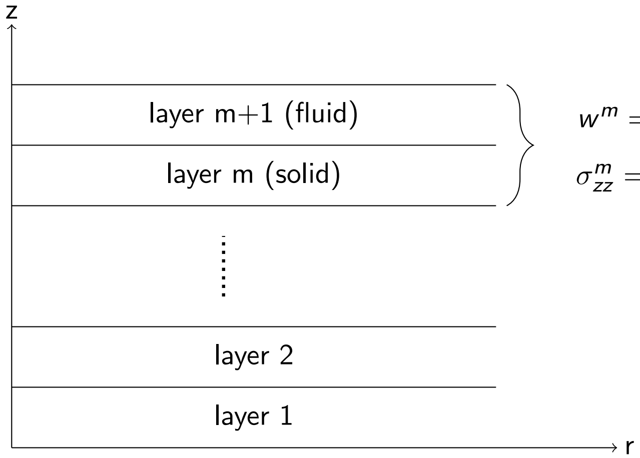

$$w^m = w^{m+1}$$

$$\sigma_{zz}^m = \sigma_{zz}^{m+1} \quad \sigma_{rz}^m = 0$$

Seismo-acoustic coupling

$$V_p = 2000 m/s \quad V_s = 800 m/s \quad V_{atm} = 330 m/s$$

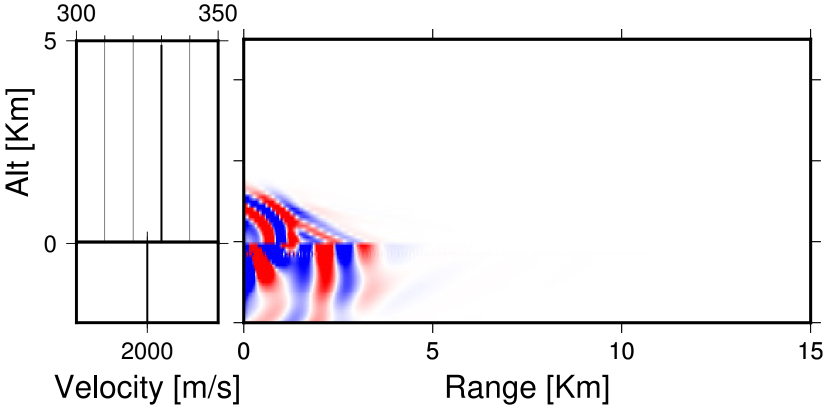

Seismo-acoustic coupling

$$V_p = 2000 m/s \quad V_s = 500 m/s \quad V_{atm} = 330 m/s$$

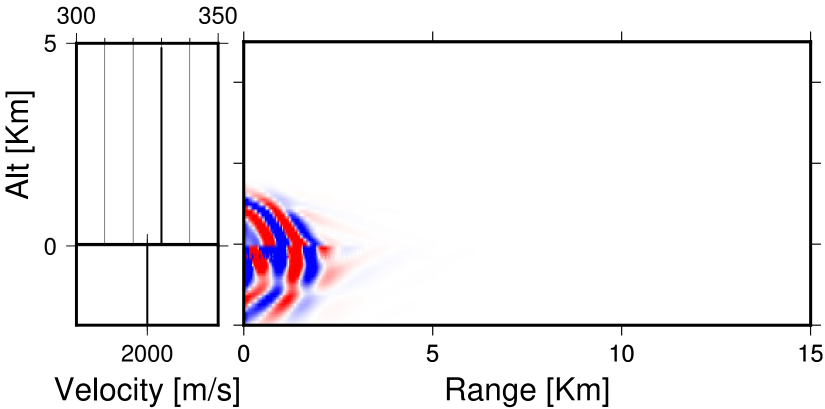

Outline

Seismo-acoustic modeling. DPRK's 2016

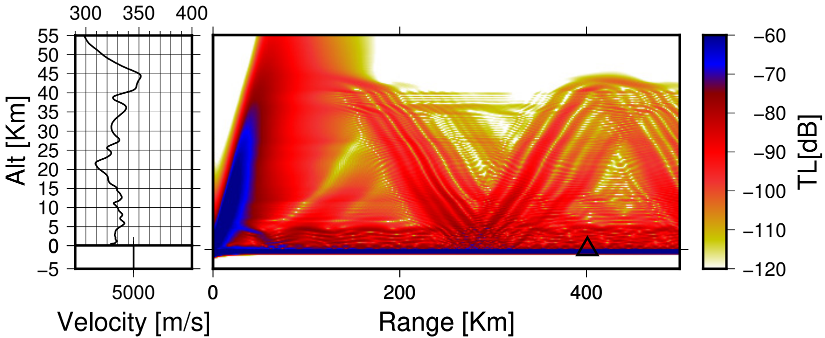

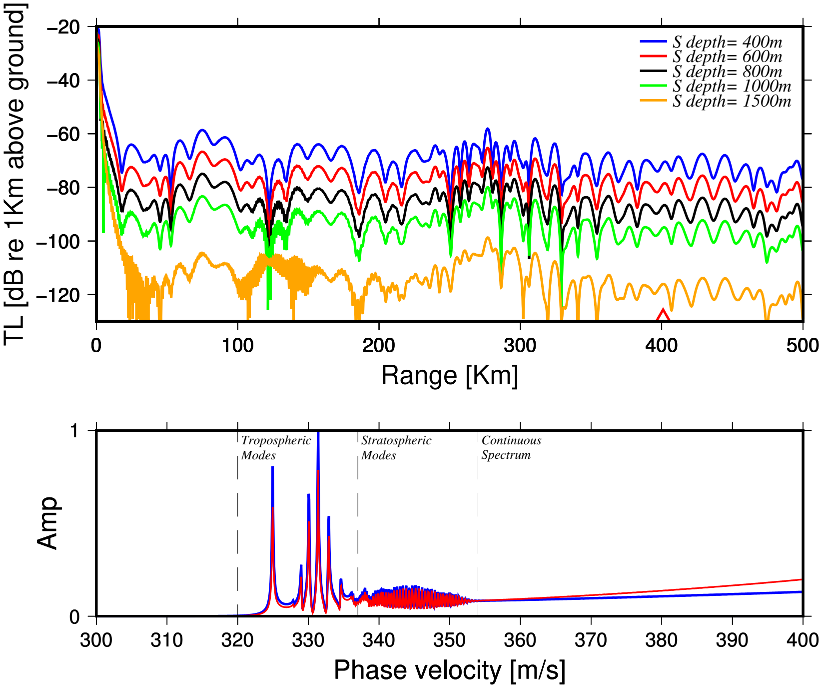

TL [dB re 1Km above ground]
Range [Km]
S depth= 400m
S depth= 600m
S depth= 800m
S depth= 1000m
S depth= 1500m
Amp
Phase velocity [m/s]
Tropospheric Modes
Stratospheric Modes
Continuous Spectrum

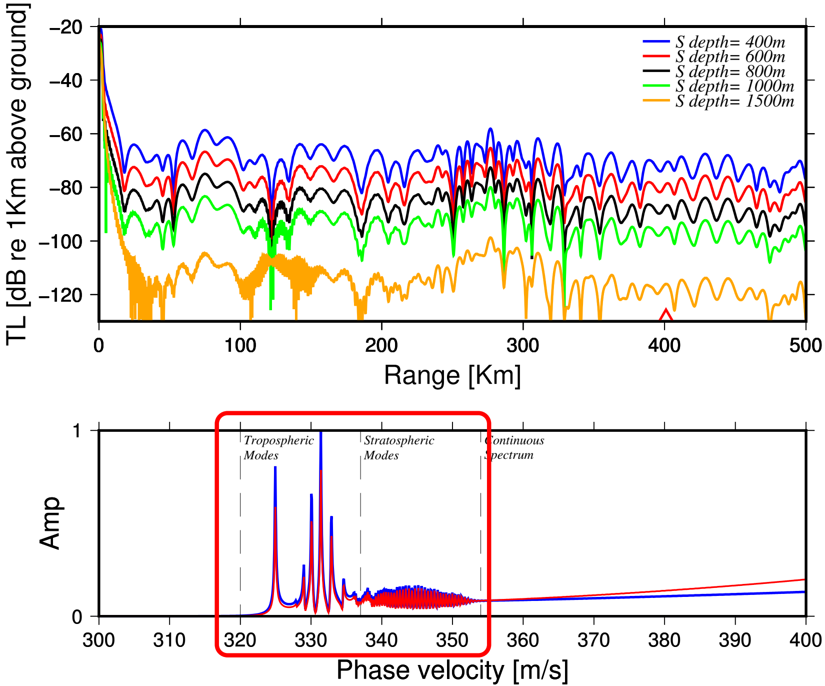
TL [dB re 1Km above ground]
−20
−40
−60
−80
−100
−120
0
100
200
300
400
500
Range [Km]
S depth= 400m
S depth= 600m
S depth= 800m
S depth= 1000m
S depth= 1500m
Amp
1
0
300
310
320
330
340
350
360
370
380
390
400
Phase velocity [m/s]
Tropospheric Modes
Stratospheric Modes
Continuous Spectrum

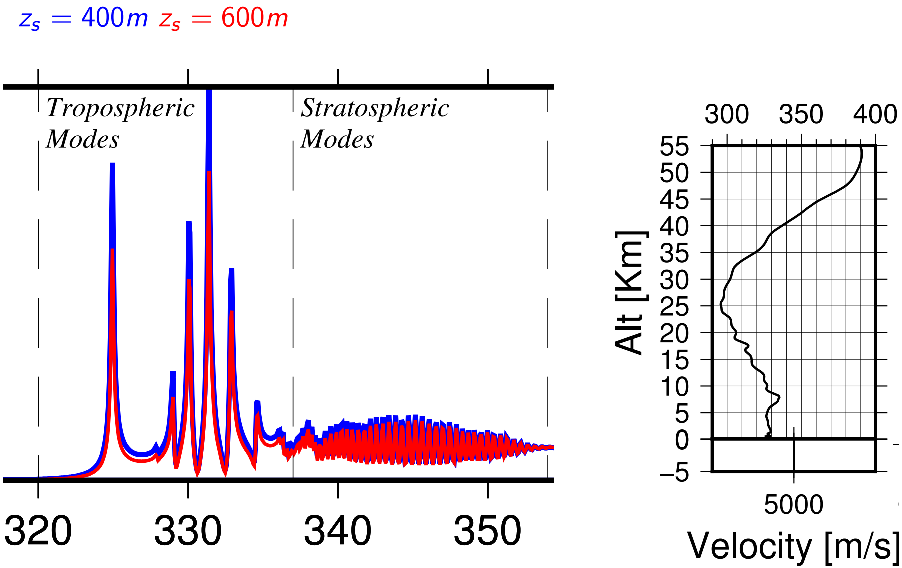
$z_s = 400m$ $z_s = 600m$
Tropospheric Modes
Stratospheric Modes
320
330
340
350
300
350
400
55
50
45
40
35
30
25
20
15
10
5
0
−5
5000
Alt [Km]
Velocity [m/s]

Seismo-acoustic modeling. DPRK's 2013 and 2016

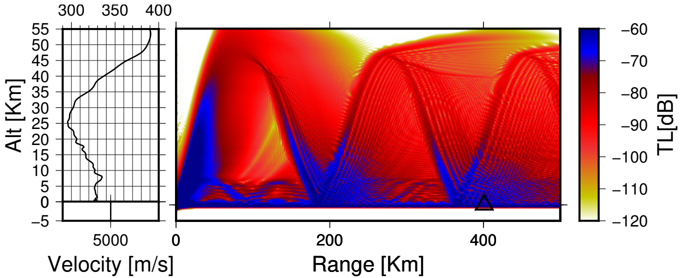

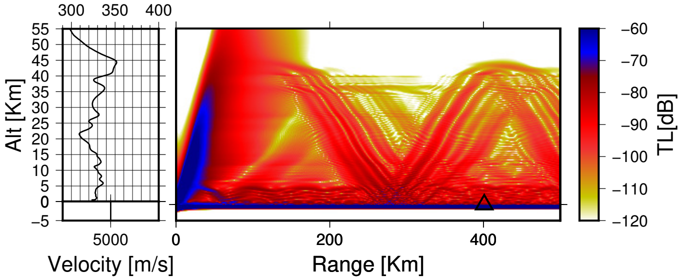

Seismo-acoustic modeling. DPRK's 2013 and 2016

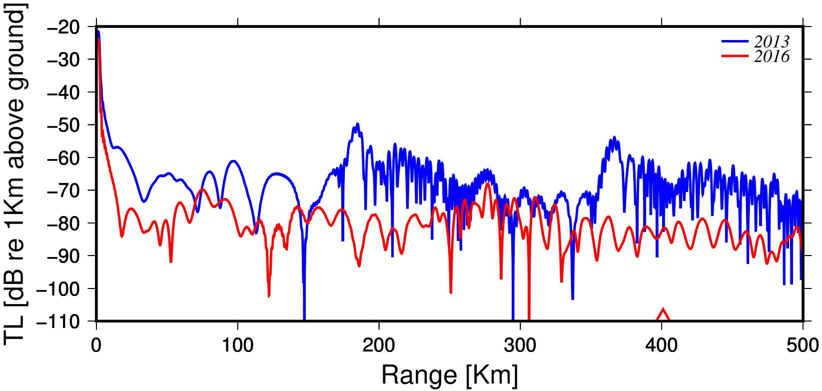

Conclusions

- The results show the important role of evanescent coupling between the Earth and the atmosphere and the ability of such emitted energy to get trapped in the atmospheric waveguides.
- As the source depth increases, less energy will be trapped in the tropospheric waveguide compared to the stratospheric waveguide.
- Surface waves velocity determines whether the emitted acoustic energy will be trapped in the atmospheric waveguids or not.
- As the depth of an explosion is difficult to estimate from seismic data alone infrasound may thus provide useful complementary information.
- The estimated source depths are in agreement with independent observations.
- The effect of topography on coupling mechanism needs to be investigated.
- Future work will investigate seismo-acoustic events in a Earth-ocean-atmosphere system.

DPRK's Underground Nuclear Tests: Infrasound Detections

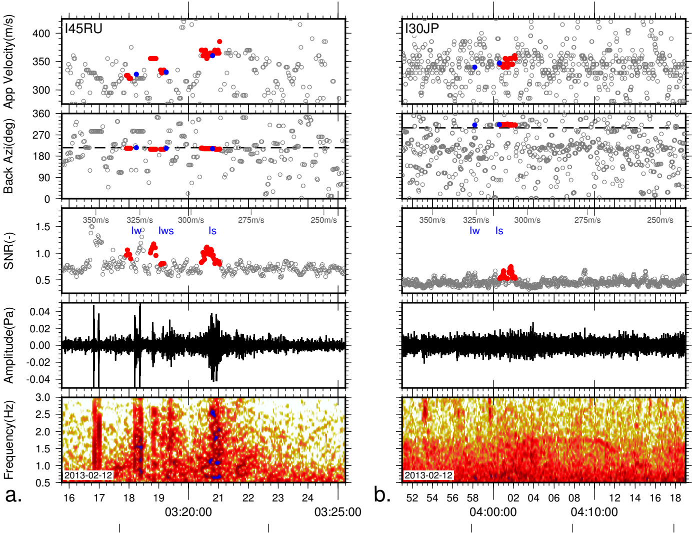

Figure: Red dots indicate detections of interest.

Infrasound Propagation Models

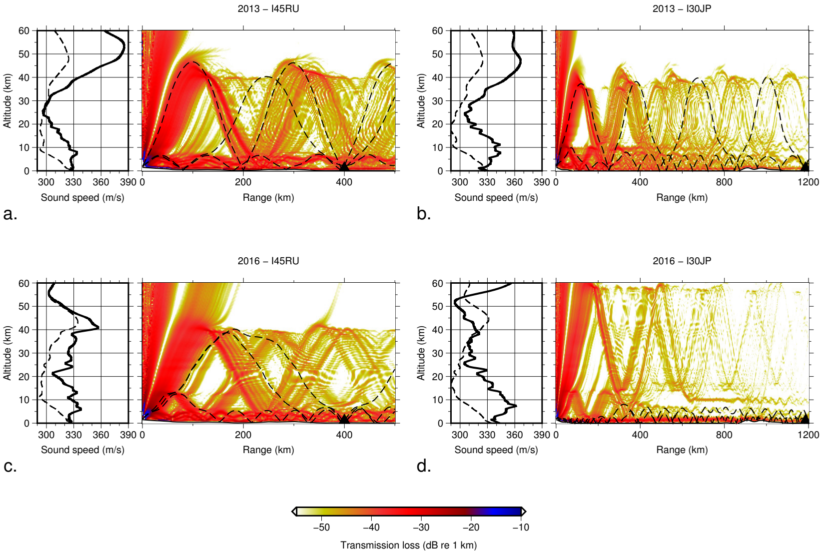

Radiation pattern from evanescent coupling

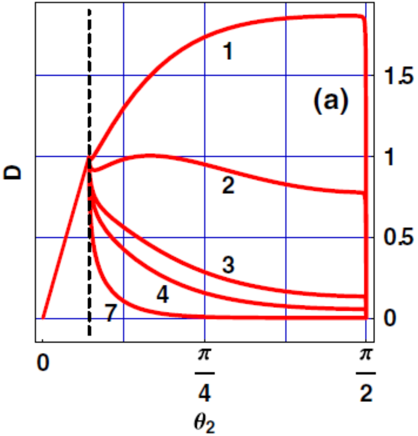

Figure: Nondimentional source depth kz_s is (1) 0.1, (2) 0.2, (3) 0.4, (4) 0.5, and (7) 1.0.

Figure from Godin, O. A. (2006), Anomalous transparency of water-air interface for low-frequency sound, Physical

Fast Field Program

Fluid

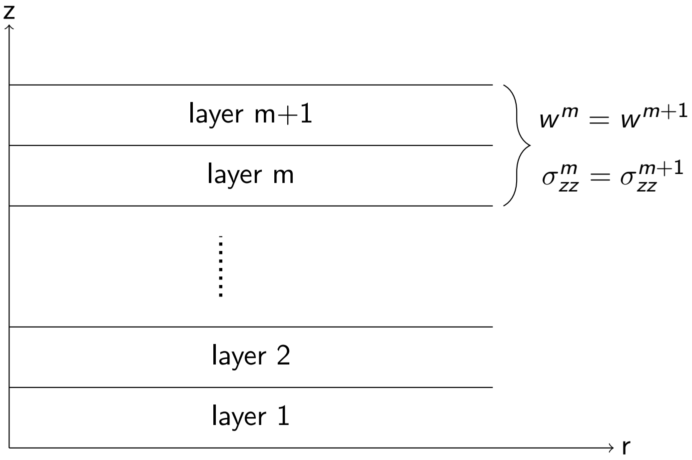

Fast Field Program

Solid

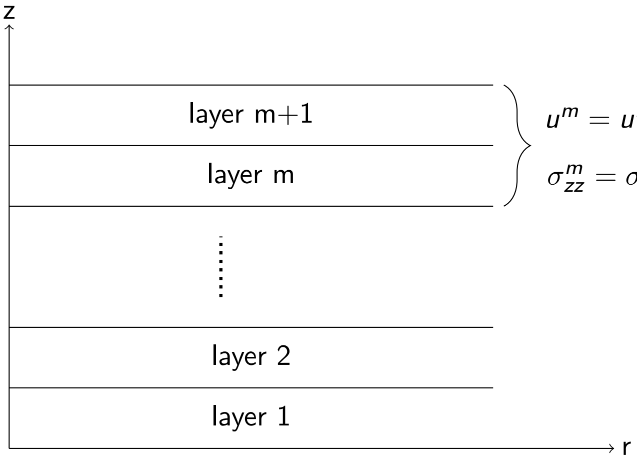

$$u^m = u^{m+1} \qquad w^m = w^{m+1}$$

$$\sigma_{zz}^m = \sigma_{zz}^{m+1} \qquad \sigma_{rz}^m = \sigma_{rz}^{m+1}$$

DE LA RECHERCHE À L'INDUSTRIE

A polynomial chaos-based approach of infrasound propagation

17th International Symposium on Long Range Sound Propagation

A. Goupy [1,3], C. Millet[1,3] & D. Lucor[2]

[1] CEA, DAM, DIF, F-91297 Arpajon, France
[2] LIMSI-CNRS, F-91403 Orsay, France
[3] CMLA, ENS Paris-Saclay, F-94235 Cachan, France

www.cea.fr

- On the use of Atmospheric Specifications (AS).
  - AS are provided by numerical weather forecasts / atmospheric climate reanalysis.
  - AS capture most efficient ducts but fail in representing small-scale fluctuations.
- The impredicable component of AS.
  - Epistemic uncertainty: lack of knowledge that can be reduced... Provided we can improve our physics' knowledge.
  - Aleatoric uncertainty: due to the natural variability of the propagation medium.
- Assessing the impact of those uncertainties:

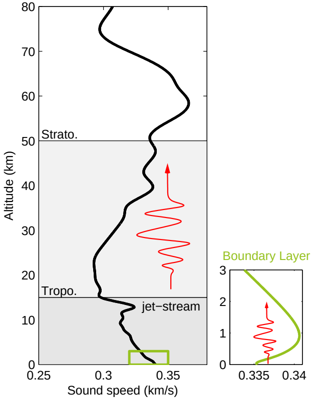

« Knowledge increases by taking into account uncertainty, not by exorcising it. »

Edgar Morin, philosopher

Motivations

- On the use of Atmospheric Specifications (AS).
  - AS are provided by numerical weather forecasts / atmospheric climate reanalysis.
  - AS capture most efficient ducts but fail in representing small-scale fluctuations.
- The impredicable component of AS.
  - Epistemic uncertainty: lack of knowledge that can be reduced... Provided we can improve our physics' knowledge.
  - Aleatoric uncertainty: due to the natural variability of the propagation medium.
- Assessing the impact of those uncertainties:
  - The statistical approaches (Monte Carlo) need a large number of runs.
  - For fixed model's parameters θ, can we reduce the numerical cost by using a metamodel?

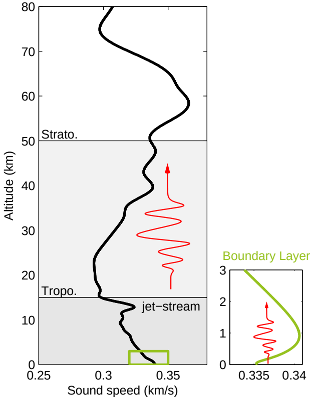

$$\boxed{Y = F(X(\xi);\theta)}$$

Outline

A non-intrusive metamodel of $Y = F(X(\xi);\theta)$ where $\xi \sim \mathcal{N}(0, I_n)$.

- Polynomial chaos decomposition*.

$$Y = \sum_{j \in J} a_j H_j(\xi) \text{ and } a_j = \langle Y, H_j \rangle,$$

  where $(H_j)_{j\in J}$ set of polynomials (up to degree d) that are orthonormal for scalar product $\langle f, g\rangle = \mathbb{E}[fg]$.

- Computation of coefficients $(a_j)_{j \in J}$.

Monte Carlo - Regression $w^{(k)} = 1$

Quadrature - Projection $w^{(k)} \neq 1$

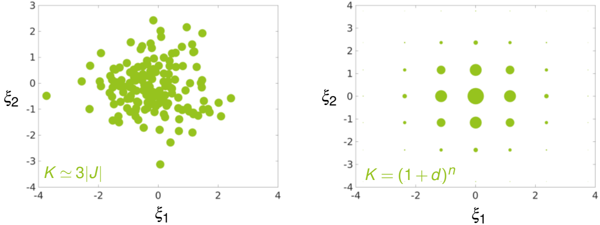

$$a_j = \sum_{k=1}^{K} Y^{(k)} H_j(\xi^{(k)}) w^{(k)}.$$

* Wiener 1938, Cameron & Martin 1947, Ghanem & Spanos 1991.

- A gPC model for $Y = (k_l, \Psi_l)_{l=1,\dots,N}$, where k_l and Ψ_l are eigenvalues and eigenfunctions (at ground level) of the Helmholtz equation.

- Green function at distance R.

$$G(\omega, R, \xi) \sim \sum_{l=1}^{N} \underbrace{\frac{\Psi_l(\omega,\xi)^2 e^{ik_l(\omega,\xi)R}}{\sqrt{k_l(\omega,\xi)R}}}_{G_l(R,\omega,\xi)}$$

The number of modes depends on frequency and ξ: $N = N(\omega, \xi)$.

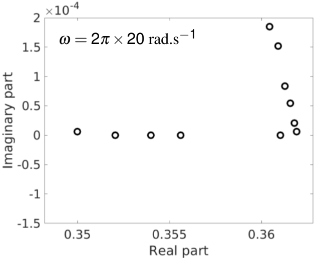

- Signals and wavepackets.

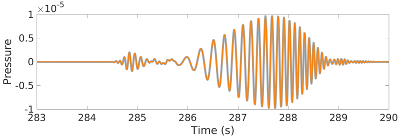

$$\mathscr{F}^{-1}\left[\sum_{l=1}^{N_0} \overline{G_l} s_0\right] = \sum_{l=1}^{N_0} \mathscr{F}^{-1}\left[\overline{G_l} s_0\right]$$

$\overline{G_l} = G_l 1_{\{\omega > \omega_l\}}$, ω_l: cut-off freq.

$N_0 = \max N(\omega; \xi)$

The propagation model

- A gPC model for $Y = (k_l, \Psi_l)_{l=1,\dots,N}$, where k_l and Ψ_l are eigenvalues and eigenfunctions (at ground level) of the Helmholtz equation.

- Green function at distance R.

$$G(\omega, R, \xi) \sim \sum_{l=1}^{N} \underbrace{\frac{\Psi_l(\omega,\xi)^2 e^{ik_l(\omega,\xi)R}}{\sqrt{k_l(\omega,\xi)R}}}_{G_l(R,\omega,\xi)}$$

The number of modes depends on frequency and ξ: $N = N(\omega, \xi)$.

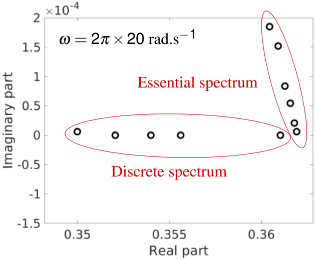

- Signals and wavepackets.

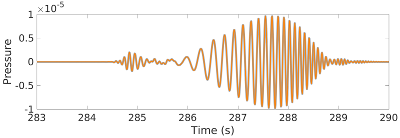

$$\mathscr{F}^{-1}\left[\sum_{l=1}^{N_0} \overline{G_l s_0}\right] = \sum_{l=1}^{N_0} \mathscr{F}^{-1}\left[\overline{G_l s_0}\right]$$

$\overline{G_l} = G_l 1_{\{\omega > \omega_l\}}$, ω_l: cut-off freq.

$N_0 = \max N(\omega; \xi)$

The propagation model

- A gPC model for $Y = (k_l, \Psi_l)_{l=1,\dots,N}$, where k_l and Ψ_l are eigenvalues and eigenfunctions (at ground level) of the Helmholtz equation.

- Green function at distance R.

$$G(\omega, R, \xi) \sim \sum_{l=1}^{N} \underbrace{\frac{\Psi_l(\omega,\xi)^2 e^{ik_l(\omega,\xi)R}}{\sqrt{k_l(\omega,\xi)R}}}_{G_l(R,\omega,\xi)}$$

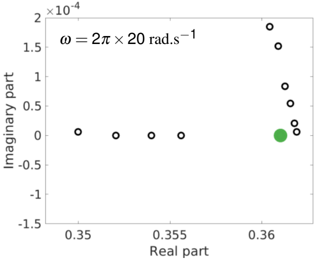

The number of modes depends on frequency and ξ: $N = N(\omega, \xi)$.

- Signals and wavepackets.

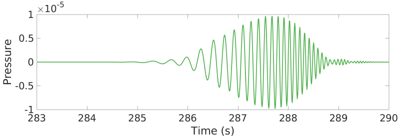

$$\mathscr{F}^{-1}\left[\sum_{l=1}^{N_0} \overline{G_l} s_0\right] = \sum_{l=1}^{N_0} \mathscr{F}^{-1}\left[\overline{G_l} s_0\right]$$

$\overline{G_l} = G_l 1_{\{\omega > \omega_l\}}$, ω_l: cut-off freq.

$N_0 = \max N(\omega; \xi)$

The propagation model

- A gPC model for $Y = (k_l, \Psi_l)_{l=1,\dots,N}$, where k_l and Ψ_l are eigenvalues and eigenfunctions (at ground level) of the Helmholtz equation.
- Green function at distance R.

$$G(\omega, R, \xi) \sim \sum_{l=1}^{N} \underbrace{\frac{\Psi_l(\omega,\xi)^2 e^{ik_l(\omega,\xi)R}}{\sqrt{k_l(\omega,\xi)R}}}_{G_l(R,\omega,\xi)}$$

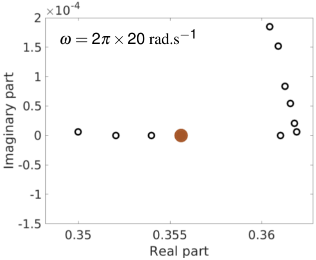

The number of modes depends on frequency and ξ: $N = N(\omega, \xi)$.

- Signals and wavepackets.

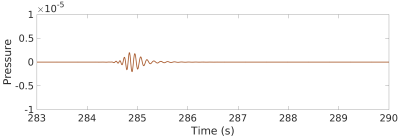

$$\mathscr{F}^{-1}\left[\sum_{l=1}^{N_0} \overline{G_l} s_0\right] = \sum_{l=1}^{N_0} \mathscr{F}^{-1}\left[\overline{G_l} s_0\right]$$

$\overline{G_l} = G_l 1_{\{\omega > \omega_l\}}$, ω_l: cut-off freq.

$N_0 = \max N(\omega; \xi)$

Computation of the gPC coefficients

- For a fixed frequency $\omega_0 = 2\pi \times 20$ rad.s^{-1} we are interested in the variability of a given eigenvalue:

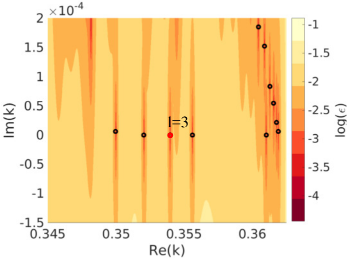

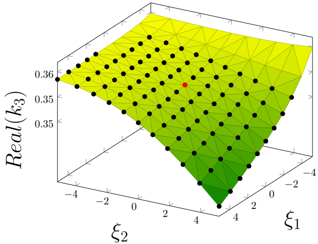

Where pseudospectrum is defined by: $Sp_\varepsilon(A) = \{z \in \mathbb{C} / z \in Sp(A+E) \text{ with } ||E|| < \varepsilon\}$

- The cut-off frequency is also developped on the gPC basis $\tilde{\omega}_l(\xi)$ and used to bound the domain of validity of the metamodel.
- Our metamodel has been computed using a regression on a quadrature grid, the optimal polynomial order is selected using a cross-validation technique.

- For a fixed frequency $\omega_0 = 2\pi \times 20$ rad.s^{-1} we are interested in the variability of a given eigenvalue:

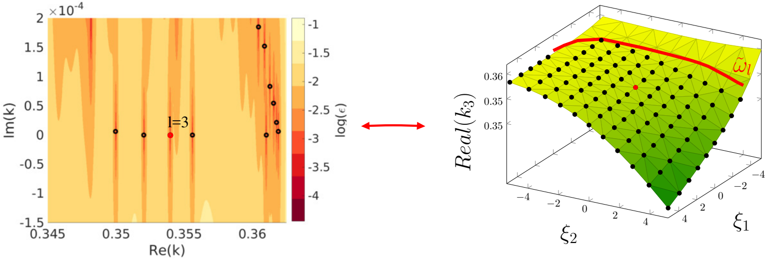

Where pseudospectrum is defined by: $Sp_\varepsilon(A) = \{z \in \mathbb{C} / z \in Sp(A+E) \text{ with } ||E|| < \varepsilon\}$

- The cut-off frequency is also developped on the gPC basis $\tilde{\omega}_l(\xi)$ and used to bound the domain of validity of the metamodel.
- Our metamodel has been computed using a regression on a quadrature grid, the optimal polynomial order is selected using a cross-validation technique.

Numerical illustration

- A toy model: the Planetary Boundary Layer (PBL).
  - PBL + nocturnal jet*:
    PBL model from Waxler 2008
    $u_J(z,\xi) = a \times e^{\frac{z-z_J}{\sigma^2}}$ the nocturnal jet.
    $\Rightarrow$ Effective celerity approximation: $c(z,\xi)$
  - Uncertainties on the jet properties:
    - Jet amplitude: $a \sim N(m_a, s_a)$.
    - Jet spread: $\sigma \sim N(m_\sigma, s_\sigma)$.
    $\Rightarrow \xi = (a, \sigma)$

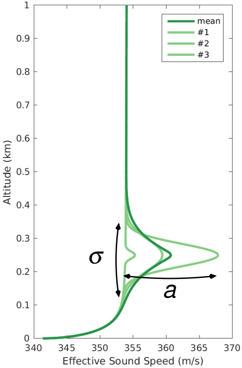

- Numerical setup.
  - Perfectly Matched Layer used as $z \to \infty$.
  - Neumann homogeneous condition at the ground.
  - Variance of the parameters $\to\sim 7\%$ of fluctuation on the profil.

* Waxler *et al.*, JASA, 2008; Chunchuzov *et al.*, JASA, 1990, 2005, Wilson *et al.*, JASA, 2015.

Technical issue: eigenvalue tracking

- With the classical Helmoltz operator:

$$H = \frac{\partial^2 \Psi}{\partial z^2} - \frac{\omega^2}{c(z)^2}\Psi$$

- Spectrum of H:

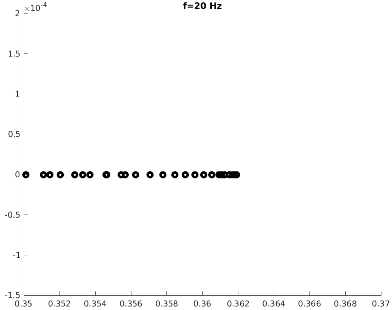

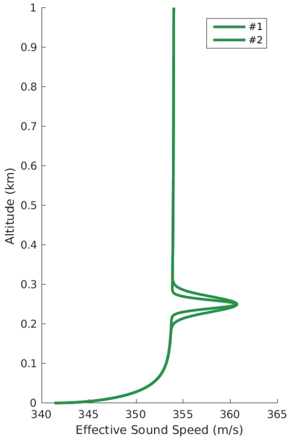

* Boyd 1984, Berenger 1994, Chew et al. 1996.

Technical issue: eigenvalue tracking

- With the classical Helmoltz operator:

$$H = \frac{\partial^2 \Psi}{\partial z^2} - \frac{\omega^2}{c(z)^2}\Psi$$

- Spectrum of H:

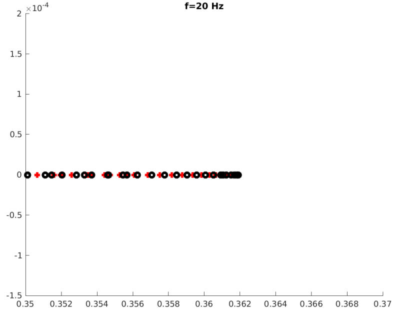

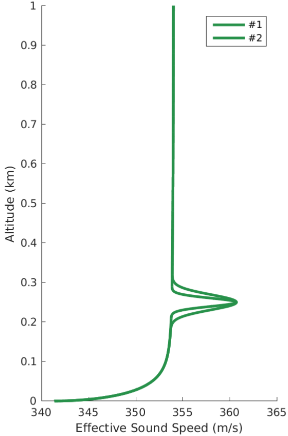

* Boyd 1984, Berenger 1994, Chew et al. 1996.

Technical issue: eigenvalue tracking

- With the classical Helmoltz operator:

$$H = \frac{\partial^2 \Psi}{\partial z^2} - \frac{\omega^2}{c(z)^2}\Psi$$

- Spectrum of H:

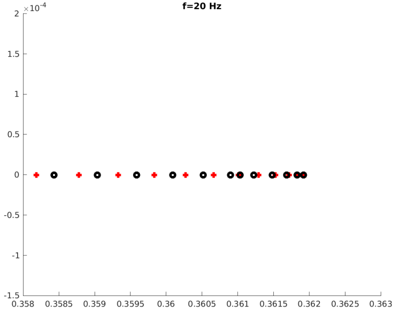

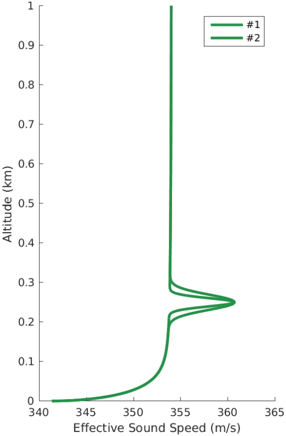

* Boyd 1984, Berenger 1994, Chew et al. 1996.

Technical issue: eigenvalue tracking

- Using a PML* $z \to \tilde{z} = z + if(z)$:

$$H = \frac{\partial^2 \Psi}{\partial \tilde{z}^2} - \frac{\omega^2}{c(\tilde{z})^2}\Psi$$

- Spectrum of H:

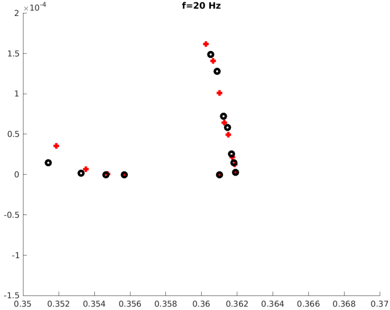

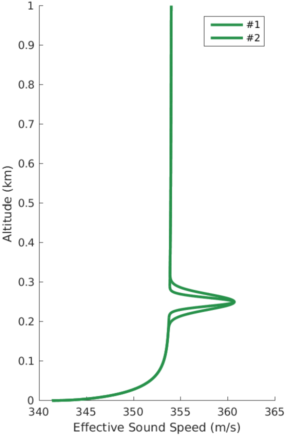

* Boyd 1984, Berenger 1994, Chew et al. 1996.

- About convergence of signals $\tilde{s}(t,\xi)$ produced by the gPC-metamodel.
  - (1) gPC provides convergence* in L^2-norm and (2) G depends continuously on k_l and Ψ_l. Hence $||\tilde{G}-G||_2 \xrightarrow{P\to\infty} 0$.
  - $\mathscr{F}$ is an L^2-isometry and thus, $||\tilde{s}(t,\xi)-s(t,\xi)||_2 \xrightarrow{P\to\infty} 0$.
- Validation through a measure of discrepancy between gPC and QMC (Quasi Monte-Carlo).

$$\varepsilon = ||\tilde{s}(t,\xi)-s(t,\xi)||.$$

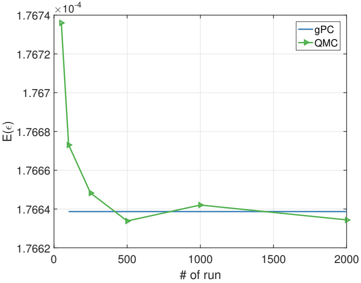

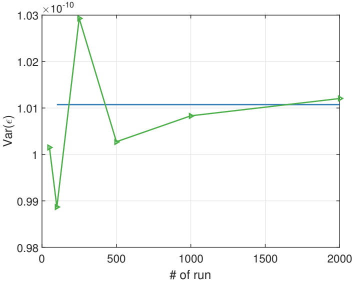

* Cameron Martin theorem.

- The Sobol index $S_r(k_l)$ measures the sensitivity of eigenvalue k_l to the parameter ξ_r:

$$S_r(k_l) = \frac{\mathrm{Var}(\mathbb{E}[k_l|\xi_r])}{\mathrm{Var}(k_l)}$$

- gPC allows direct computation of Sobol indices so as to assess the role of each input (**random**) parameter - here a and σ, onto $\mathrm{Var}(k_l)$ ($l \leq N$).

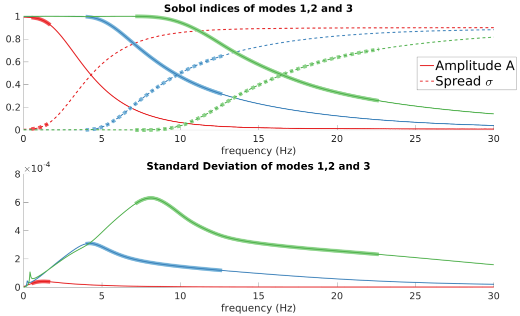

Conclusion

- Efficient way to obtain a metamodel for complex signals, provided the dimension of stochastic inputs ξ is rather small (typically less than 10).
- The metamodel can be used to produce signal statistics and sensitivity indices at low cost, thereby allowing its intensive use in operational-like environments.
- Main limitation comes from the ability to track your random eigenvalues in the complex plane.
- Short-term development: take into account uncertainties on the source (for the next LRSP Symposium ☺!).

Thank you for your attention !

DE LA RECHERCHE À L'INDUSTRIE

Towards the Use of Infrasound Observations for Improving Weather Forecasts

Pierre VANDERBECKEN[1]
Christophe MILLET[1,2]
Jean-François MAHFOUF[3]

———————-

[1] CEA, DAM, DIF, F-91297 Arpajon, France
[2] CMLA, ENS, F-94235 Cachan, France
[3] CNRM, Météo-France, F-31000 Toulouse, France

17th LRSP Symposium

www.cea.fr

How Infrasound Can Improve Weather Forecasts ?

- Generalities:
  - Weather forecast: a prediction of the atmosphere state given by a Numerical Weather Prediction (NWP) model
  - Data assimilation: use of observations to improve the NWP model
- Issue: Lack of relevant observations to assimilate over 35 km

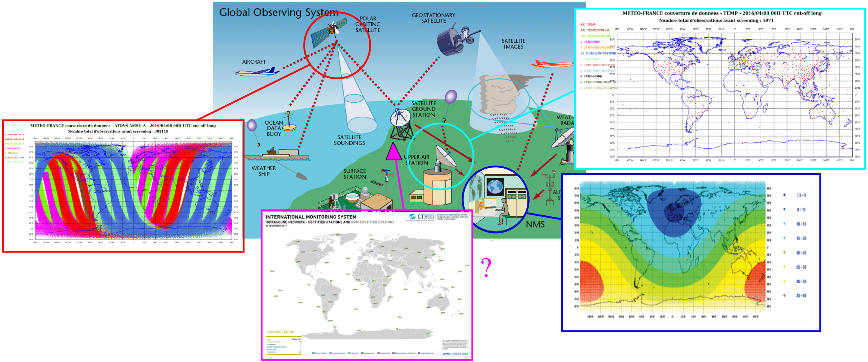

Outline

I. Methodology

II. Case study: Etna Related Detections

III. Synthesis

I. Methodology. Assimilate Infrasound data in NWP

- Our challenge: assimilation of infrasound technology in NWP models
- Infrasound and constraints associated with the data assimilation (DA) process

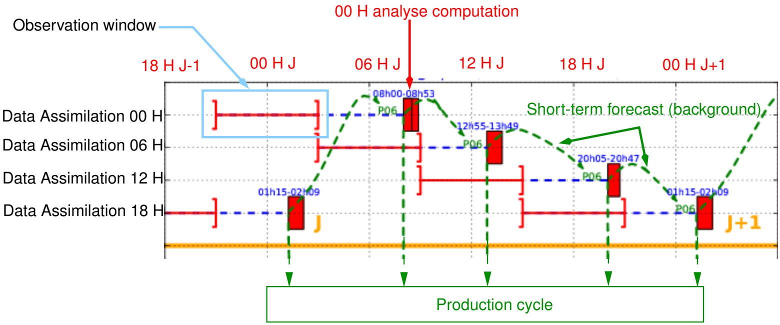

  - Infrasound detections recorded belong to a observation window
  - Infrasound signals have to be post-processed before assimilation
- A simplified approach

Infrasound signals → Updated vertical profiles → NWP models

I. Methodology. A statistical View of Weather Prediction

- An Inverse method not based only on the acoustics measurements: Use of a Meteorological data base
- A data base that sample the uncertainties on weather forecasts

Ensemble assimilation

Inputs	Outputs
several forecasts perturbed observations	perturbed analyses

Input forecasts for the 00 H analyses of the state on the 08/04/2016

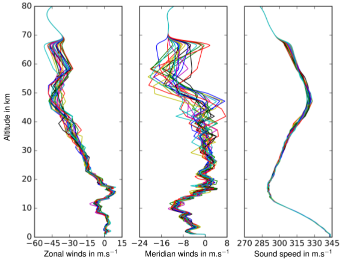

Ensemble analyses of the state on the 08/04/2016

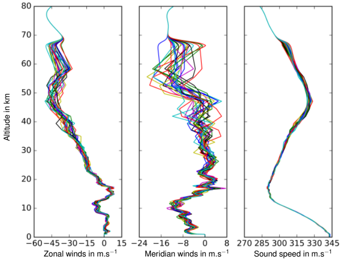

- Significant spread above 25 km on the meteorological state

I. Methodology. Ray-Tracing Methods

- Assumption: Geometrical acoustics (High frequency approximation)
- Propagation model: 3D spherical linear ray-tracing code GeoAc[1]

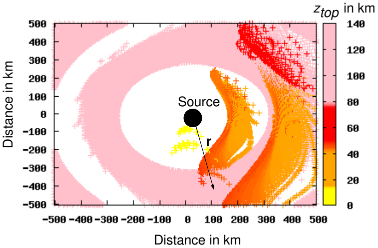

Sound speed: $c=\sqrt{(\gamma r T)}$, where γ=1.4 and r=287 J.kg^{-1}.K^{-1}.

Trace velocity: $v_t = \frac{c(z=0)}{\cos(\theta)}$

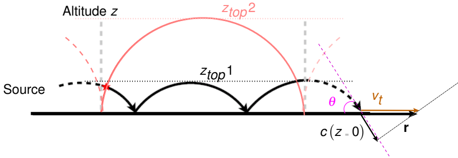

- Inputs: $\mathbf{X} = (U(z), V(z), T(z))$ and source/station locations
- Outputs: $\mathbf{Y} = F(\mathbf{X})$ =(Travel time T_t, back-azimuth ϕ, trace velocity v_t)

[1] Blom & Waxler, *JASA*, 2017.

- Simplification:
  - $\mathbf{X}(z)$ extracted at the source location
  - The station is represented by a Ø20 km disc center
  - Rays refracting in range 25-65 km and reaching the station are considered
- Cost function: Optimal state regarding the measurements $\hat{\mathbf{Y}} = (\hat{T}_t, \hat{\phi}, \hat{v}_t)$

$$\boxed{J(\mathbf{X}) = \|F(\mathbf{X}) - \hat{\mathbf{Y}}\|_{R^{-1}} = \frac{1}{N}\sum_{j=1}^{N}\Big((T_t - \hat{T}_t)^T R_T^{-1}(T_t - \hat{T}_t) + (\phi - \hat{\phi})^T R_\phi^{-1}(\phi - \hat{\phi}) + (v_t - \hat{v}_t)^T R_v^{-1}(v_t - \hat{v}_t)\Big)},$$

where R_T^{-1}, R_ϕ^{-1}, R_v^{-1} are diagonals and N is the number of eigen rays for the propagation with the member $\mathbf{X}$

- First guess: A first estimation of the optimal state

$$\boxed{\mathbf{X}_{\mathbf{Best}} = argmin(J)}$$

- Bayesian approach: $\boxed{\mathscr{P}(\mathbf{X}|\mathbf{Y}) = A\exp(-J)}$, where A is the normalization factor
- For an ensemble data (Ens.)

$$\boxed{\mathbf{X}_{\mathbf{Bay}} = \sum_{\mathbf{X}\in Ens.} \mathscr{P}(\mathbf{X}|\mathbf{Y})\mathbf{X}}$$

I. Methodology

II. Case study: Etna Related Detections

III. Synthesis

II. Case study. Etna Related Detections During Summer 2016.

- Meteorological data

Met. Centre	Type	Member	Vertical grid
ECMWF Météo-France	r0 analyses r0 AEARP analyses	1 25	91 levels; top at 80 km 105 levels; top at 65 km

- Infrasound data from IS48: 15 days of detections during Summer 2016

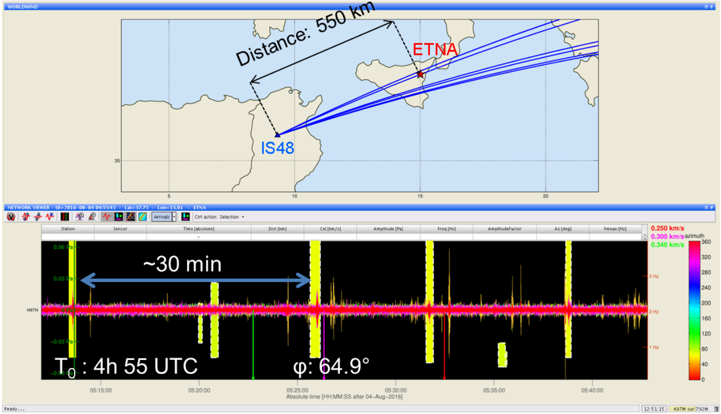

II. Case study. Numerical Strategy

- Rays are computed for
  - A source located at $z = 3350$ m
  - Azimuth in $[245°, 252°]$ by 1 ° step
  - θ in $[-5°, 45°]$ by 0.5 ° step

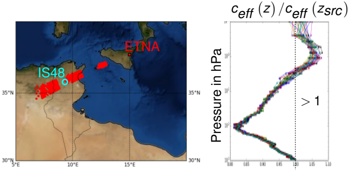

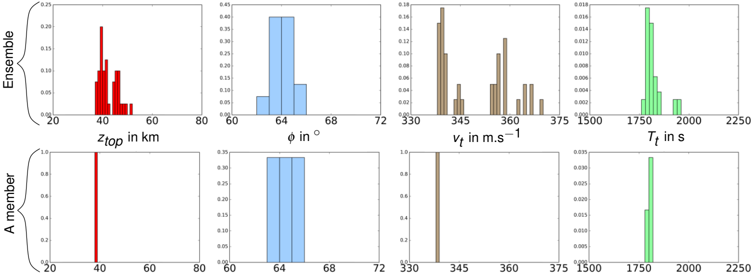

$\Rightarrow$ The spread of the ensemble leads to a significant dispersion of results

II. Case study. Application with Ensemble Analyses

- Source: 05/15/2016, 12h UTC
- Detections at IS48: 6 between 12h16 UTC and 12h39 UTC
- Results are given by the inversion method applied on the 00H ensemble analyses for each of the 6 detections

$\mathscr{P}(X\|Y)$	X_1	X_2	X_3	X_4	X_5	X_6	X_7	X_8	X_9	X_{10}	X_{11}	X_{12}	X_{13}	X_{14}	X_{15}	X_{16}	X_{17}	X_{18}	X_{19}	X_{20}	X_{21}	X_{22}	X_{23}	X_{24}	X_{25}
D. 1	0.	0.	0.	0.	0.	0.	0.	0.	0.	0.	0.	0.	0.	0.	0.	0.	0.	0.	0.	0.	0.	0.	0.	0.	0.
D. 2	0.	0.	0.	0.	0.	0.	0.	0.	0.	0.	0.	**1.**	0.	0.	0.	0.	0.	0.	0.	0.	0.	0.	0.	0.	0.
D. 3	0.	0.	0.	0.	0.	0.	0.	0.	0.	0.	0.	**1.**	0.	0.	0.	0.	0.	0.	0.	0.	0.	0.	0.	0.	0.
D. 4	0.	0.	0.	0.	0.	0.	0.	0.	0.	0.	0.	0.	0.	0.	0.	0.	0.	0.	0.	0.	0.	0.	0.	**1.**	0.
D. 5	0.	0.	0.	0.	0.	0.	0.	0.	0.	0.	0.	0.	0.	0.	0.	0.	0.	0.	0.	0.	0.	0.	0.	0.	**1.**
D. 6	0.	0.	0.	0.	0.	0.	0.	0.	0.	0.	0.	0.	0.	0.	0.	0.	0.	0.	0.	0.	0.	0.	0.	0.	0.

- Remarks: $\mathbf{X_{best}} = \mathbf{X_{bay}}$ and two detections are mute

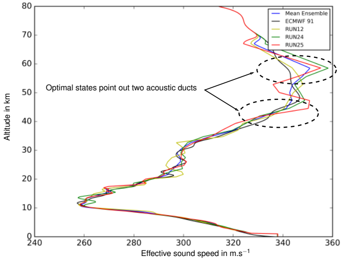

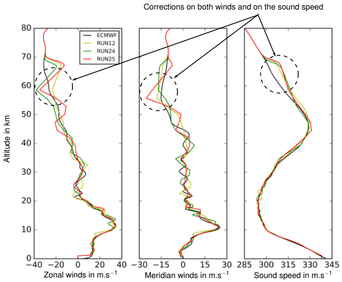

II. Case study: Comparison to the Measurements

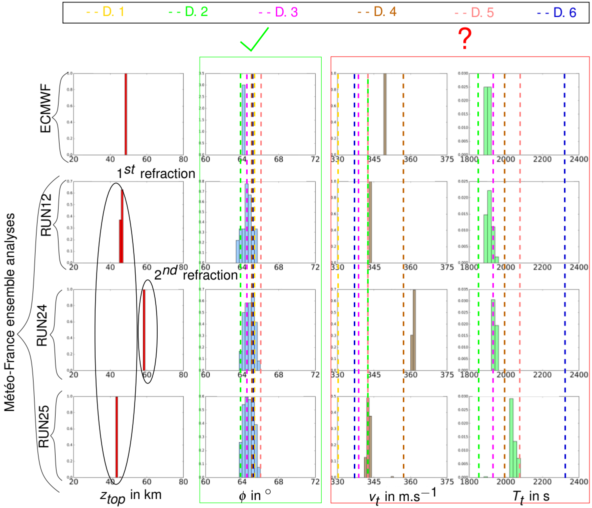

⇒ 4 of these detections are likely due to this event

II. Case study. Application in Operational-like Conditions

- Source: 05/15/2016, 12h00. Detections: 6 (12h16-12h39 UTC)
- Results are given by the inversion method applied to the input forecasts used for the 00 H ensemble assimilation for each of the 6 detections

$\mathscr{P}(\mathbf{X}\vert\mathbf{Y})$	$\mathbf{X}_1$	$\mathbf{X}_2$	$\mathbf{X}_3$	$\mathbf{X}_4$	$\mathbf{X}_5$	$\mathbf{X}_6$	$\mathbf{X}_7$	$\mathbf{X}_8$	$\mathbf{X}_9$	$\mathbf{X}_{10}$	$\mathbf{X}_{11}$	$\mathbf{X}_{12}$	$\mathbf{X}_{13}$	$\mathbf{X}_{14}$	$\mathbf{X}_{15}$	$\mathbf{X}_{16}$	$\mathbf{X}_{17}$	$\mathbf{X}_{18}$	$\mathbf{X}_{19}$	$\mathbf{X}_{20}$	$\mathbf{X}_{21}$	$\mathbf{X}_{22}$	$\mathbf{X}_{23}$	$\mathbf{X}_{24}$	$\mathbf{X}_{25}$
D. 1	0.	0.	0.	0.	0.	0.	0.	0.	0.	0.	0.	0.	0.	0.	0.	0.	0.	0.	0.	0.	0.	0.	0.	0.	0.
D. 2	0.	0.	0.	0.	0.	0.	0.	0.	0.	0.	0.	0.	0.	0.	**1.**	0.	0.	0.	0.	0.	0.	0.	0.	0.	0.
D. 3	0.	0.	0.	0.	0.	0.	0.	0.	0.	0.	0.	0.	0.	0.	0.	0.	0.	**1.**	0.	0.	0.	0.	0.	0.	0.
D. 4	0.	0.	0.	0.	0.	0.	0.	0.	0.	0.	0.	0.	0.	0.	0.	0.	0.	0.	0.	0.	**1.**	0.	0.	0.	0.
D. 5	0.	0.	0.	0.	0.	0.	0.	0.	0.	0.	0.	0.	0.	0.	0.	0.	0.	0.	0.	0.	0.	0.	0.	0.	**1.**
D. 6	0.	0.	0.	0.	0.	0.	0.	0.	0.	0.	0.	0.	0.	0.	0.	0.	0.	0.	0.	0.	0.	0.	0.	0.	0.

- Remarks: the corrections provided by $\mathbf{X}_{\mathbf{best}}$ are smaller.

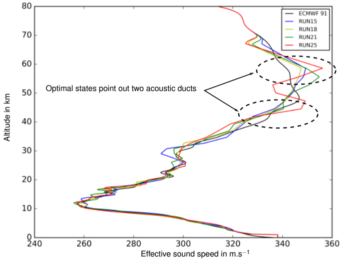

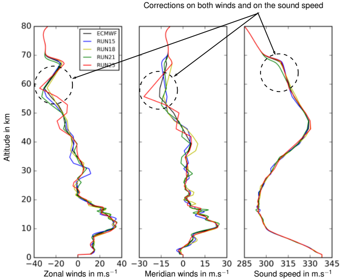

II. Case study. Comparison to measurements

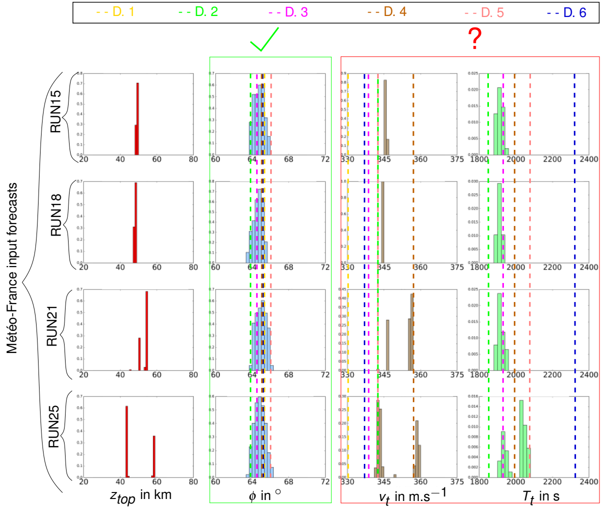

⇒ Member #RUN25 seems to explain most of the 4 detections

III. Synthesis and Perspectives

- Synthesis
  - Analyses and forecasts ensemble from NWP models may provide relevant scenarii for the acoustic propagation
  - The optimal state resulting from inversion is one of the members, provided we consider a single detection. What if we use several detections?
  - The inverse method provides large-scale deviations in temperature and wind profiles

- Perspectives
  - Use of Ensemble prediction data from Météo-France
  - Sensitivity study of the inverse method to smale-scale perturbations
  - Use the waveform in the inverse method
  - Define a methodology to assimilate the updated profiles in ARPEGE
  - Examine the feasability of this method during a SSW

LETMA
MODELLING INFRASONIC PROPAGATION

Inter-comparison of numerical models for propagation of infrasounds

L. Robert, R. Marchiano, O. Gainville, C. Millet, L. Aubry, J. P. Braeuning, D. Dragna and C. Bailly

LRSP, Lyon, June 13th 2018

Context

Numerical platform of the LETMA (Laboratoire Études et Modélisation Acoustiques, Laboratory of studies and modelling in acoustics) : Gathering codes from different laboratories to share expertise.

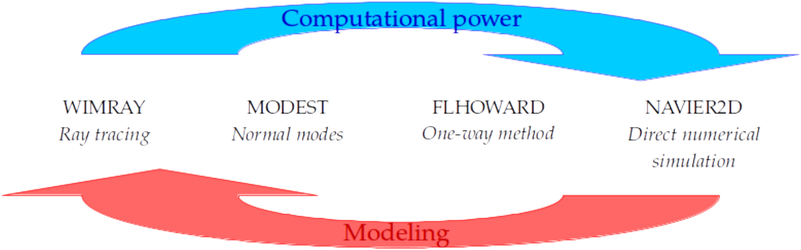

numerical platform content

Outlines

Is it possible to compare these models for similar atmospheric conditions ?

Do they give similar results and how much are they reliable ?

$\Rightarrow$ Intercomparison protocol for 3 of the 4 models :

- WIMRAY : Ray tracing model
- FLHOWARD : One-way method
- NAVIER2D : Direct numerical simulation (DNS)

Numerical models : WIMRAY

WIMRAY : 3D ray tracing method developed to study infrasound caused by explosions and sonic booms.

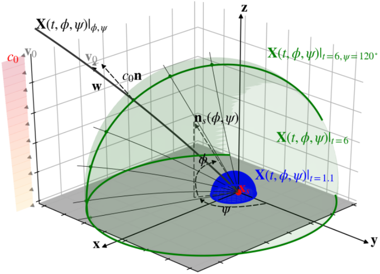

Schematic depiction of WIMRAY configuration for explosions

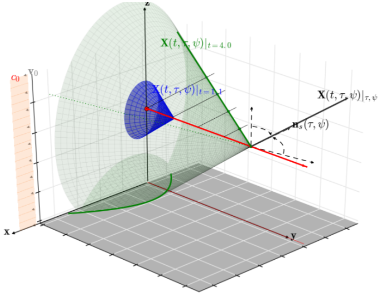

Schematic depiction of WIMRAY configuration for sonic booms

Numerical models : WIMRAY

- based on geometrical acoustics (Eikonal equation)
- full 3D atmospheric condition

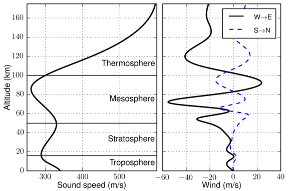

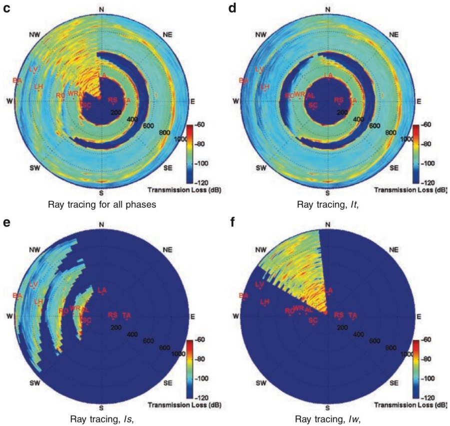

Example of application : Misty Picture benchmark

Gainville O. and coauthors, Misty Picture : A Unique Experiment for the Interpretation of the Infrasound Propagation from Large Explosive Sources, in Infrasound Monitoring for Atmospheric Studies, 2009, ed. Springer, p. 575–598

FLHOWARD : 3D one-way method developed to study propagation of acoustic shock waves through heterogeneous and turbulent media.

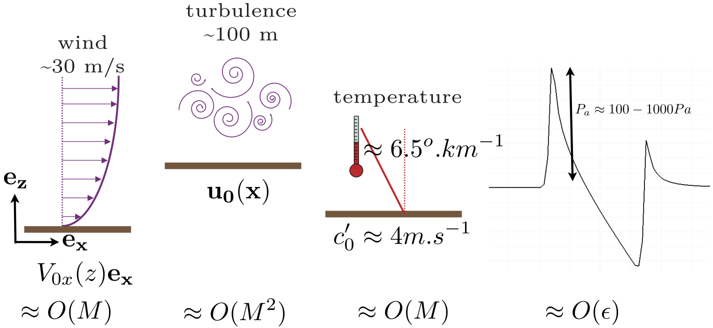

- sound speed : $cv_0(\underline{x}) = \bar{c} + c'(\underline{x})$,
- density : $\rho_0(\underline{x}) = \bar{\rho} + \rho'(\underline{x})$,
- flow velocity : $\underline{V}_0(\underline{x}) = V_{0x}(z)\underline{e}_x + \underline{u}_0(\underline{x})$,
- $V_{0x}(z)\underline{e}_x$ stratified mean flow and $\underline{u}_0(\underline{x})$ the turbulent flow field.

Equation of motion written in retarded time $\tau = t - x/c_0$:

$$
\begin{aligned}
&2\overline{c}_0 \frac{\partial^2 \phi}{\partial x \partial \tau} - \overline{c}_0^2 \frac{\partial^2 \phi}{\partial x^2} - \overline{c}_0^2 \frac{\partial^2 \phi}{\partial z^2} = \frac{\beta}{2\overline{\rho}_0 \overline{c}_0^2} \frac{\partial}{\partial \tau} \left[\left(\frac{\partial \phi}{\partial \tau} \right)^2 \right] \\
&+ 2V_{0x} \frac{\partial}{\partial \tau} \left(\frac{1}{\overline{c}_0} \frac{\partial \phi}{\partial \tau} - \frac{\partial \phi}{\partial x} \right) + 2\overline{c}_0^2 \frac{\mathrm{d}V_{0x}}{\mathrm{d}z} \frac{\partial}{\partial z} \int^{\tau} \left(\frac{1}{\overline{c}_0} \frac{\partial \phi}{\partial \tau} - \frac{\partial \phi}{\partial x} \right) \mathrm{d}\tau' \\
&- V_{0x} V_{0x} \left(\frac{1}{\overline{c}_0^2} \frac{\partial^2 \phi}{\partial \tau^2} - \frac{\partial^2 \phi}{\partial z^2} \right) + 2\overline{c}_0^2 V_{0x} \frac{\mathrm{d}V_{0x}}{\mathrm{d}z} \frac{\partial}{\partial z} \int^{\tau} \int^{\tau'} \left(\frac{1}{\overline{c}_0^2} \frac{\partial^2 \phi}{\partial \tau^2} - \frac{\partial^2 \phi}{\partial z^2} \right) \mathrm{d}\tau'' \mathrm{d}\tau' \\
&+ 2u_{0x} \frac{\partial}{\partial \tau} \left(\frac{1}{\overline{c}_0} \frac{\partial \phi}{\partial \tau} - \frac{\partial \phi}{\partial x} \right) - 2u_{0z} \frac{\partial^2 \phi}{\partial \tau \partial z} - 2\overline{c}_0^2 \frac{\partial u_{0x}}{\partial x} \int^{\tau} \left(\frac{1}{\overline{c}_0^2} \frac{\partial^2 \phi}{\partial \tau^2} - \frac{\partial^2 \phi}{\partial z^2} \right) \mathrm{d}\tau' \\
&+ 2\overline{c}_0^2 \left(\frac{\partial u_{0z}}{\partial x} + \frac{\partial u_{0x}}{\partial z} \right) \frac{\partial}{\partial z} \int^{\tau} \left(\frac{1}{\overline{c}_0} \frac{\partial \phi}{\partial \tau} - \frac{\partial \phi}{\partial x} \right) \mathrm{d}\tau' - 2\overline{c}_0^2 \frac{\partial u_{0z}}{\partial z} \int^{\tau} \frac{\partial^2 \phi}{\partial z^2} \mathrm{d}\tau' \\
&+ 2 \frac{c_0'}{\overline{c}_0} \frac{\partial^2 \phi}{\partial \tau^2} + \frac{\overline{c}_0^2}{\rho_0} \frac{\partial \rho_0}{\partial x} \left(\frac{1}{\overline{c}_0} \frac{\partial \phi}{\partial \tau} - \frac{\partial \phi}{\partial x} \right) - \frac{\overline{c}_0^2}{\rho_0} \frac{\partial \phi}{\partial z} \frac{\partial \rho_0}{\partial z}
\end{aligned}
$$

Numerical models : FLHOWARD

Equation of motion written in retarded time $\tau = t - x/c_0$:

$$2\overline{c}_0\frac{\partial^2\phi}{\partial x\partial\tau} - \overline{c}_0^2\frac{\partial^2\phi}{\partial x^2} - \overline{c}_0^2\frac{\partial^2\phi}{\partial z^2} = \frac{\beta}{2\overline{\rho}_0\overline{c}_0^2}\frac{\partial}{\partial\tau}\left[\left(\frac{\partial\phi}{\partial\tau}\right)^2\right]$$

$$+ 2V_{0x}\frac{\partial}{\partial\tau}\left(\frac{1}{\overline{c}_0}\frac{\partial\phi}{\partial\tau} - \frac{\partial\phi}{\partial x}\right) + 2\overline{c}_0^2\frac{\mathrm{d}V_{0x}}{\mathrm{d}z}\frac{\partial}{\partial z}\int^{\tau}\left(\frac{1}{\overline{c}_0}\frac{\partial\phi}{\partial\tau} - \frac{\partial\phi}{\partial x}\right)\mathrm{d}\tau'$$

$$- V_{0x}V_{0x}\left(\frac{1}{\overline{c}_0^2}\frac{\partial^2\phi}{\partial\tau^2} - \frac{\partial^2\phi}{\partial z^2}\right) + 2\overline{c}_0^2V_{0x}\frac{\mathrm{d}V_{0x}}{\mathrm{d}z}\frac{\partial}{\partial z}\int^{\tau}\int^{\tau'}\left(\frac{1}{\overline{c}_0^2}\frac{\partial^2\phi}{\partial\tau^2} - \frac{\partial^2\phi}{\partial z^2}\right)\mathrm{d}\tau''\mathrm{d}\tau'$$

$$+ 2u_{0x}\frac{\partial}{\partial\tau}\left(\frac{1}{\overline{c}_0}\frac{\partial\phi}{\partial\tau} - \frac{\partial\phi}{\partial x}\right) - 2u_{0z}\frac{\partial^2\phi}{\partial\tau\partial z} - 2\overline{c}_0^2\frac{\partial u_{0x}}{\partial x}\int^{\tau}\left(\frac{1}{\overline{c}_0^2}\frac{\partial^2\phi}{\partial\tau^2} - \frac{\partial^2\phi}{\partial z^2}\right)\mathrm{d}\tau'$$

$$+ 2\overline{c}_0^2\left(\frac{\partial u_{0z}}{\partial x} + \frac{\partial u_{0x}}{\partial z}\right)\frac{\partial}{\partial z}\int^{\tau}\left(\frac{1}{\overline{c}_0}\frac{\partial\phi}{\partial\tau} - \frac{\partial\phi}{\partial x}\right)\mathrm{d}\tau' - 2\overline{c}_0^2\frac{\partial u_{0z}}{\partial z}\int^{\tau}\frac{\partial^2\phi}{\partial z^2}\mathrm{d}\tau'$$

$$+ 2\frac{c_0'}{\overline{c}_0}\frac{\partial^2\phi}{\partial\tau^2} + \frac{\overline{c}_0^2}{\rho_0}\frac{\partial\rho_0}{\partial x}\left(\frac{1}{\overline{c}_0}\frac{\partial\phi}{\partial\tau} - \frac{\partial\phi}{\partial x}\right) - \frac{\overline{c}_0^2}{\rho_0}\frac{\partial\phi}{\partial z}\frac{\partial\rho_0}{\partial z}$$

Diffraction + Nonlinearities + Flows + Heterogeneities $+O(M^3)(\approx (\epsilon^2 M) \approx (\epsilon M^2))$

Numerical models : FLHOWARD

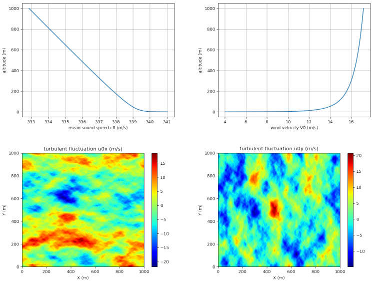

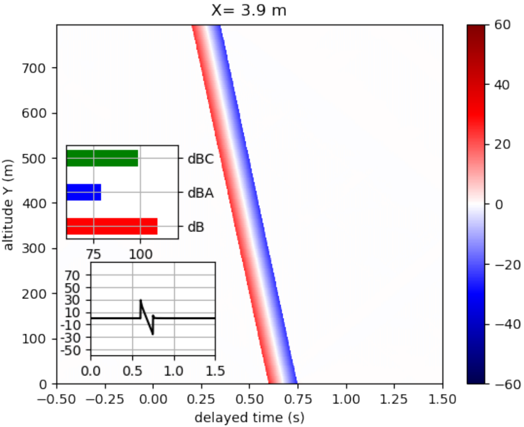

Exemple of application : sonic boom through an heterogeneous atmosphere

Numerical models : NAVIER2D

NAVIER2D : 2D direct numerical simulation based on Navier-Stokes equations and specially designed for long range propagation.

$$\frac{\partial \rho'}{\partial t} + \frac{\partial}{\partial x}(\rho u) + \frac{\partial}{\partial z}(\rho v) = 0, \tag{1}$$

$$\frac{\partial}{\partial t}(\rho u)' + \frac{\partial}{\partial x}(\rho u^2 + p') + \frac{\partial}{\partial z}(\rho u v) = \frac{\partial \tau'_{xx}}{\partial x} + \frac{\partial \tau'_{xz}}{\partial z}, \tag{2}$$

$$\frac{\partial}{\partial t}(\rho v)' + \frac{\partial}{\partial x}(\rho u v) + \frac{\partial}{\partial z}(\rho v^2 + p') + \rho' g = \frac{\partial \tau'_{xz}}{\partial x} + \frac{\partial \tau'_{zz}}{\partial z}, \tag{3}$$

$$\begin{aligned}\frac{\partial}{\partial t}(\rho e)' &+ \frac{\partial}{\partial x}[u(\rho e + p')] + \frac{\partial}{\partial z}[v(\rho e + p')] + \overline{p}\left(\frac{\partial u}{\partial x} + \frac{\partial v}{\partial z}\right) + \rho' g v \\ &= \Lambda_s + \frac{\partial}{\partial x}(u\tau'_{xx} + v\tau'_{xz}) + \frac{\partial}{\partial z}(u\tau'_{xz} + v\tau'_{zz}) - \frac{\partial q'_x}{\partial x} - \frac{\partial q'_z}{\partial z}\end{aligned} \tag{4}$$

Numerical models : NAVIER2D

Simulation of a the infrasound caused by localized source of energy.

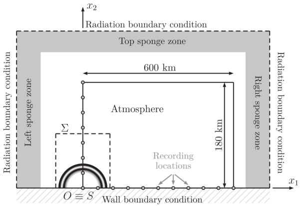

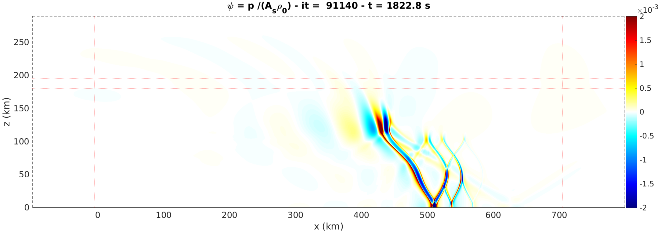

Sabatini, R., Marsden, O. Bailly, C. and Bogey, C.. 2016, *A numerical study of nonlinear infrasound propagation in a windy atmosphere*, J. Acoust. Soc. Am., 140(1), 641–656

Intercomparison : outlines

Intercomparison of models has 3 main challenges :

- Input : develop equivalent source terms
- Medium : ensure similar propagation conditions
- Output : isolate specific quantities which can be compared

Chosen test case : propagation of a spherical wave emited at ground level in a stratified atmosphere (Sabatini et al., 2016)

Input : Source terms

WIMRAY : pressure signature at a blast radius from source point.

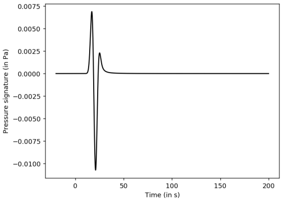

Pressure signal used to initialize WIMRAY

FLHOWARD : initial pressure/potential field.

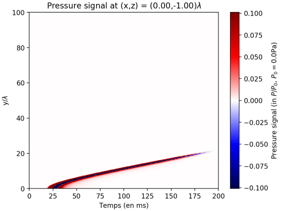

Potential field used to initialize FLHOWARD

NAVIER2D : energy input function $\Lambda_s(r, t)$.

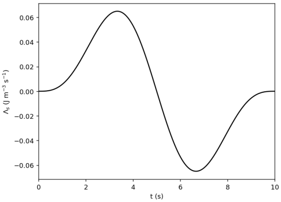

Energy input function $\Lambda_s(0, t)$ used to initialize NAVIER2D

$\Rightarrow$ equivalent formulation derived using homogeneous analytic solution

SORBONNE UNIVERSITÉ CRÉATEURS DE FUTURS DEPUIS 1257 cnrs cea ÉCOLE CENTRALE LYON

Input : Source terms

Reduced equations for an homogeneous atmosphere :

$$\frac{\partial p}{\partial t} + \rho_0 c_0^2 \vec{\nabla} \cdot \vec{v} = \rho_0 c_0^2 Q(r,t)$$
$$Q(r,t) = \frac{(\gamma - 1)}{\rho_0 c_0^2} \Lambda_s(t) = Q_r(r) f(t)$$

Analytic solution far from the source (in the Fourier space) :

$$\varphi(r,\omega) = \widehat{Q}_r(k_0) \frac{H_0^1(k_0 r)}{4i} \widehat{f}(\omega) \tag{5}$$

with $\widehat{Q}_r(k) = TF[Q_r(r)]$, $\widehat{f}(\omega) = TF[f(t)]$, H_0^1 the Hankel function and $k_0 = c_0/\omega_S$ where ω_S is the characteristic pulsation of the f.

Input : comparison to analytic solution

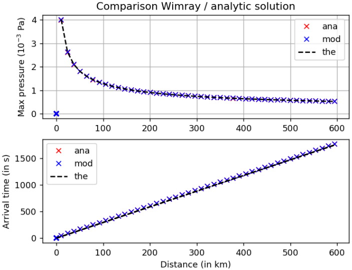

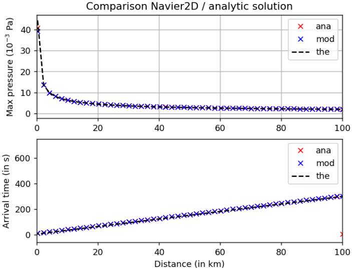

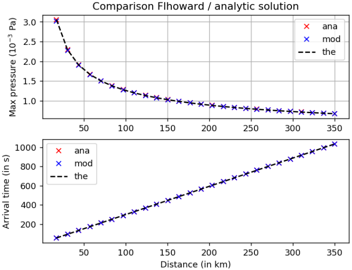

Maximum overpressure and arrival time for model simulation (bleu) and the analytic solution (black)

$\Rightarrow$ Very good agreement between the models and the analytic solution.

Input : comparison to analytic solution

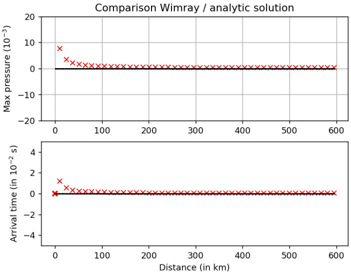

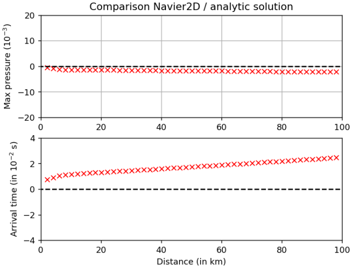

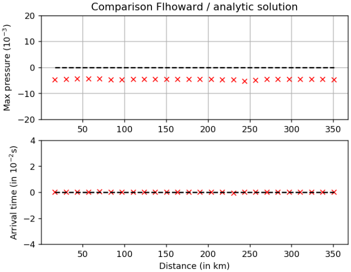

Maximum overpressure and arrival time difference between model simulation and the analytic solution

$\Rightarrow$ Very good agreement between the models and the analytic solution ($< 2\%$ for the overpressure, $< 0.4\%$ for the arrival time).

Stratified atmosphere (Misty Picture) without wind :

- data : celerity value and gradient at given altitude → cubic spline interpolation on each code vertical grid
- Field of interest are derived from the celerity profile ($c_0 \to T \to P \to \rho$)

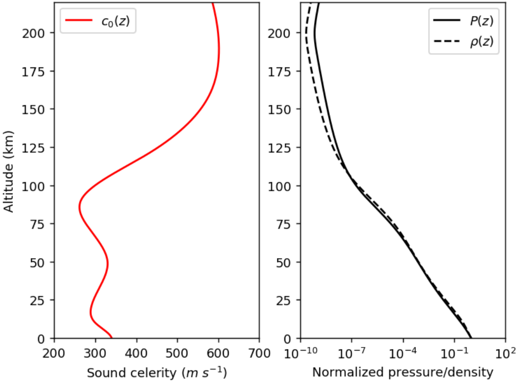

Vertical profiles of celerity, pressure and density

Output : Pressure near the ground

Non-linear runs

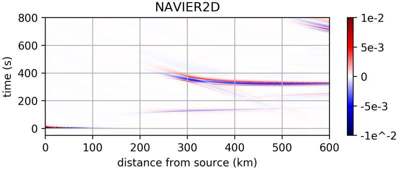

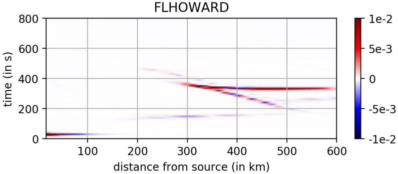

Normalized pressure $\Phi = P/\sqrt{\rho}$ near the ground.

Linear runs

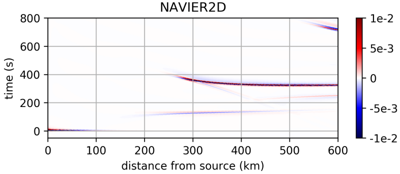

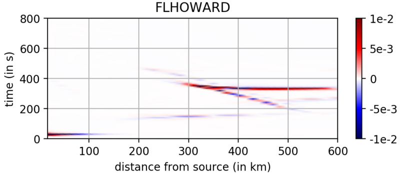

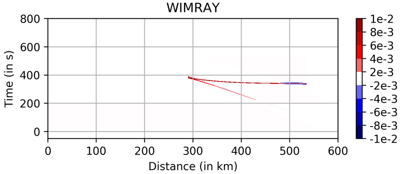

Output : WIMRAY

- No direct phase (due to the method)
- No stratospheric phase (weak stratospheric waveguide)

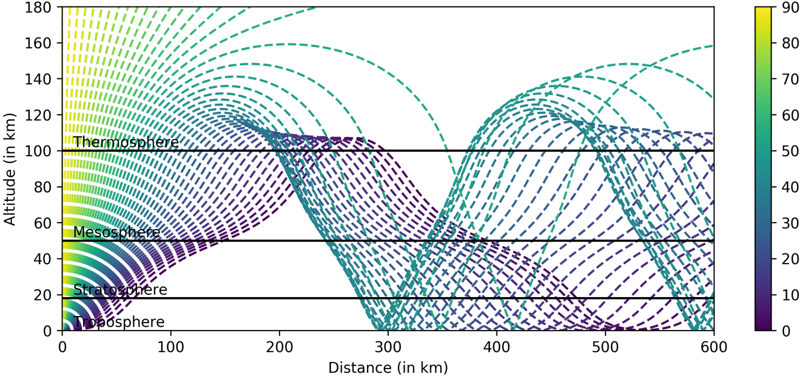

Wimray rays map

Output : FLHOWARD

- No second thermospheric phase (due to filtering)
- False thermospheric phase (due to diffraction)
- No significant non-linear effect (constant density)

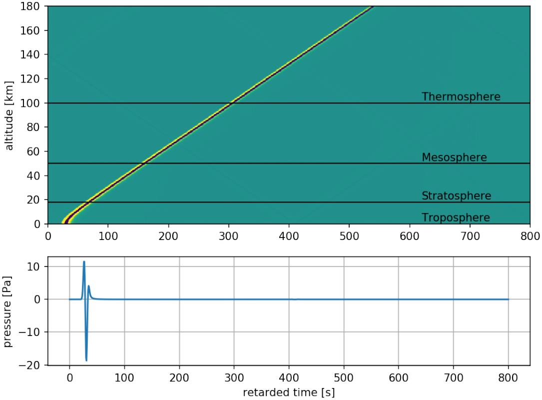

Output : FLHOWARD

- No second thermospheric phase (due to filtering)
- False thermospheric phase (due to diffraction)
- No significant non-linear effect (constant density)

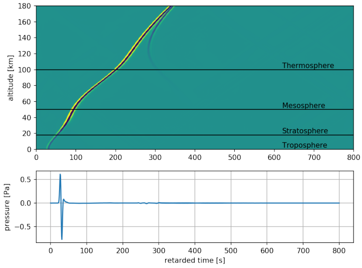

Pressure map at 100km from source

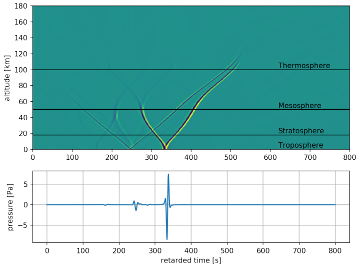

Pressure map at 450km from source

Conclusion

Intercomparison of 3 numerical models from LETMA numerical platform.

WIMRAY : ray-tracing method

- Computational time : 30 s on 1 proc.
- May miss some phases (direct/stratospheric)

FLHOWARD : one-way method

- Computational time : 30min on 1 proc.
- Weak spurious phases and no density effect

NAVIER2D : direct numerical simulation

- Computational time : 30h on 16 proc.
- Very detailed simulation

Test cases data will soon be available for NAVIER2D on LETMA official webpage : www.dalembert.upmc.fr/LETMA/ Data for other models will follow.

Model : FLHOWARD angular opening

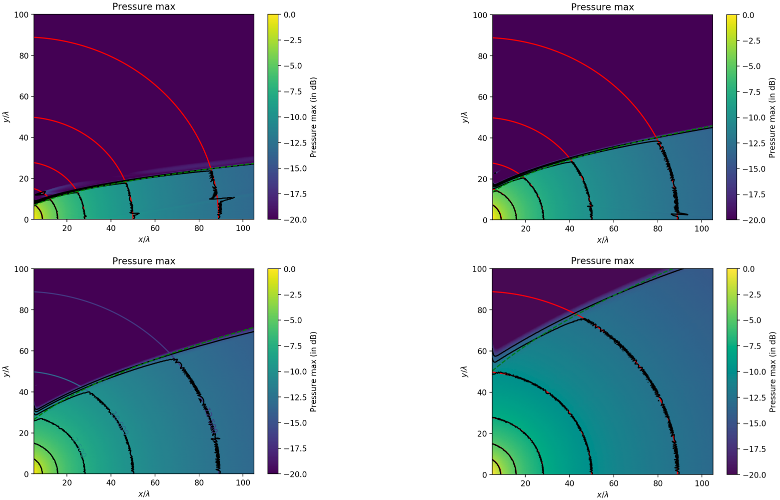

Maximum overpressure for different values of time window : 100s, 200s, 400s and 800s

Model : FLHOWARD angular opening

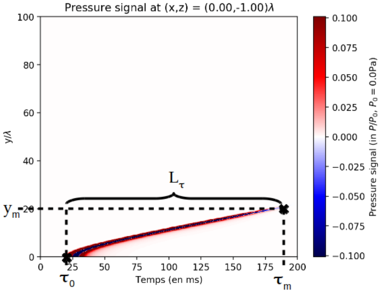

Equation for the angular opening in FLHOWARD as a function of distance x :

$$\theta(x) = \arctan\left(\frac{y_m(x)}{x}\right) = \arctan\left(\sqrt{1 + f\frac{c_0 L_\tau}{x}}\right)$$

with $\Delta\tau = \tau_m - \tau_0$, c_0 is the mean sound speed and $f \in [0, 1]$ a coefficient due to filtering.

Input : Pressure signal

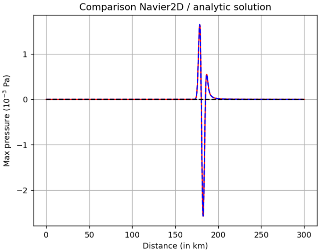

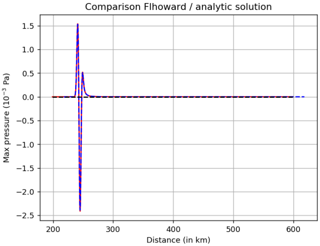

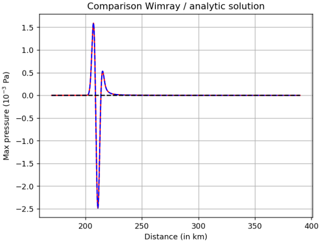

Pressure signal at ground level for each level (in blue) compared to the analytic solution (in dashed red)

A study of tropospheric ducting of Infrasonic Propagation from the Niagara Falls

Max Willis

Roger Waxler, Claus Hetzer

University of Mississippi - National Center for Physical Acoustics

6/12/2018

THE UNIVERSITY OF MISSISSIPPI NCPA

NCPA
Atmospheric Acoustics

Overview

1. Purpose
   - The variations of the Jet Stream directly effects propagation of Infrasonic Signals
2. Jet Stream
   - Atmospheric profiles
   - Generation of ducts
3. Niagara Falls
   - U.S. Array Data
   - Propagation Model
4. Conclusions and Improvements
5. Questions

Jet Stream

- Found at $\sim$10(km)
- Easterly wind jet
  - Northern component varies at least daily
- Magnitude and variations depend upon time of year

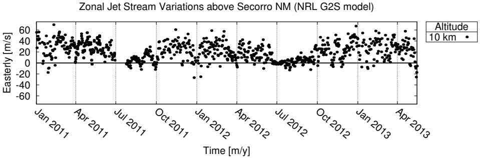

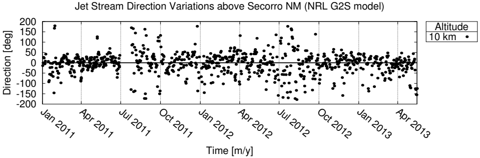

NCPA
Atmospheric Acoustics

Jet Stream

- Calculate wind speed given temperature
- Use desired azimuth to determine Easterly and Northerly wind contributions
- Add in to determine effective sound speed
- Duct created when the effective sound speed exceeds that on the ground

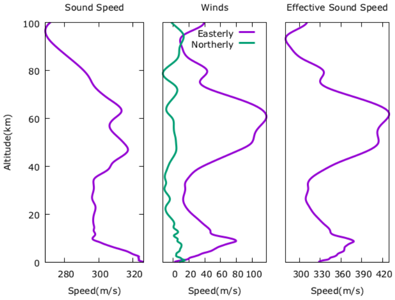

NCPA
Atmospheric Acoustics

U.S. Array

- Noise floor data
- Infrasound is generated by large sources
- Niagara Falls is a large water feature

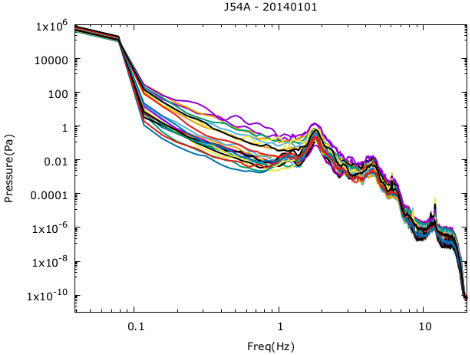

Niagara Falls

- Find sensors near the falls
  - Within 100km for tropospheric returns

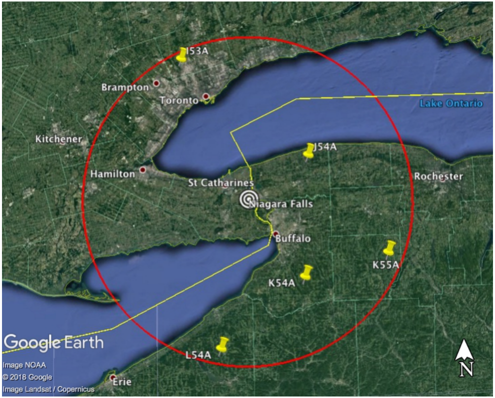

Parabolic Equation Model compared to Winds

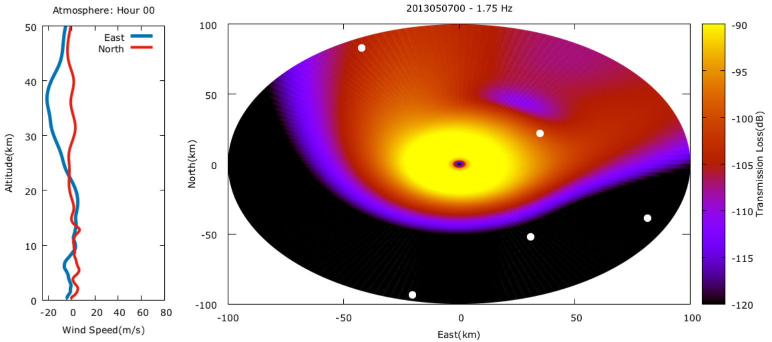

NCPA
Atmospheric Acoustics

Parabolic Equation Model compared to Winds

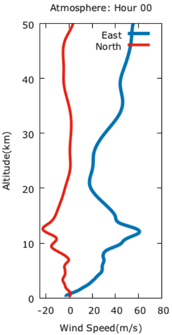

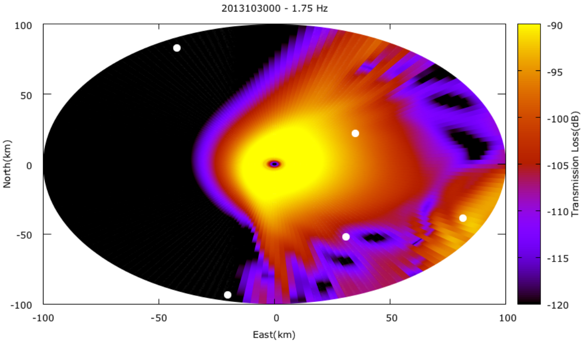

NCPA
Atmospheric Acoustics

Parabolic Equation Model compared to Winds

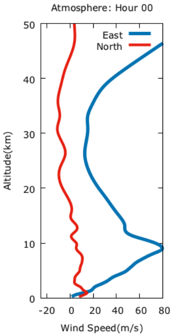

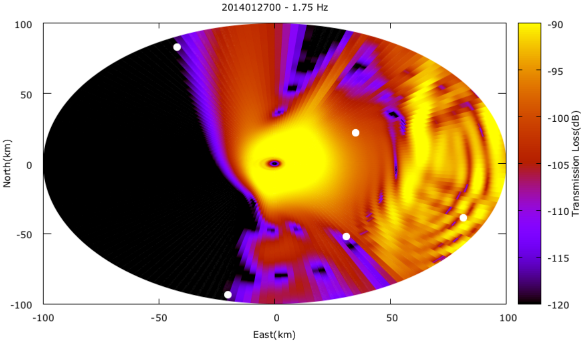

Parabolic Equation Model with PSDs

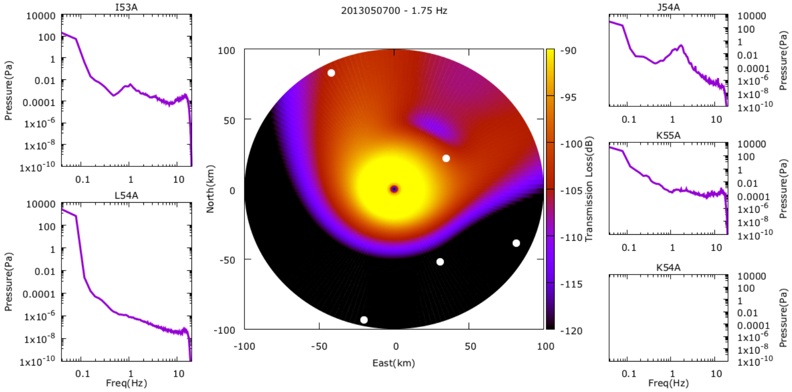

NCPA
Atmospheric Acoustics

Parabolic Equation Model with PSDs

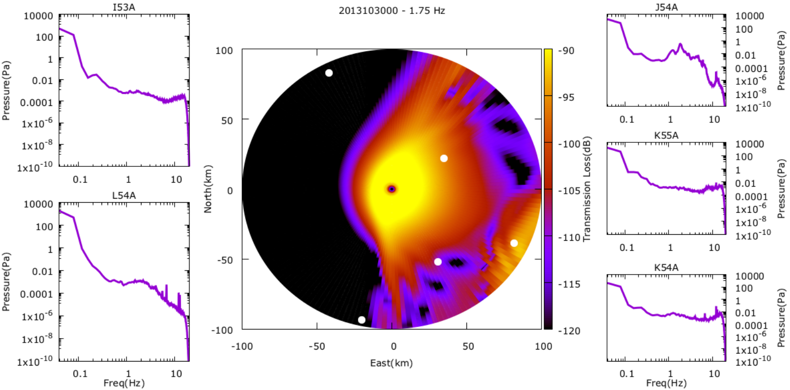

NCPA
Atmospheric Acoustics

Parabolic Equation Model with PSDs

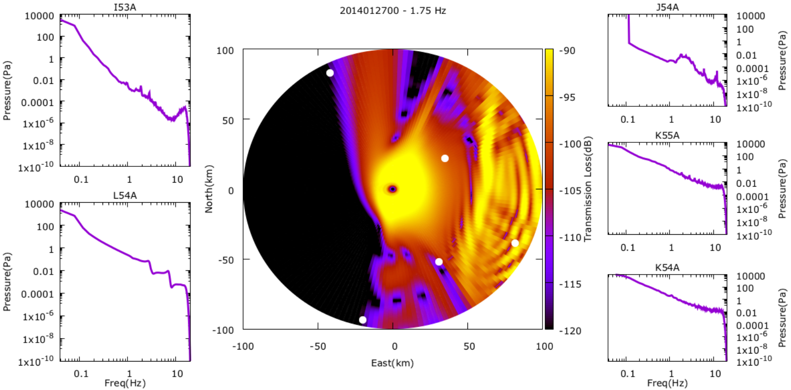

NCPA
Atmospheric Acoustics

Second Look at Niagara Falls

- During the winter, large ice build ups form around the Niagara Falls
- While it does not freeze over, these ice build ups could attenuate sound
- The Niagara Falls is regulated according to time of day as well as time of season

Parabolic Equation Model with PSDs

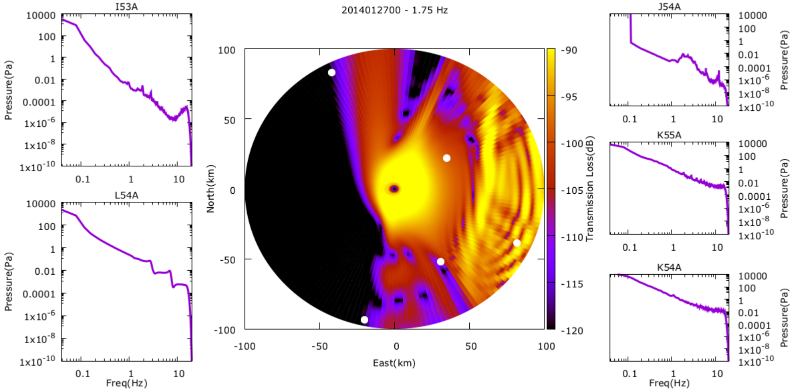

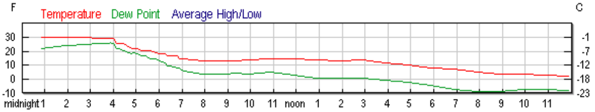

NCPA
Atmospheric Acoustics

Third Look at Niagara Falls

- The Niagara Falls opens in a northerly direction
- This could lead to a directional source
  - $ka = 400 \times \frac{\omega}{c} \approx 12.5 >> 1$
  - When $ka > 1$ we can expect directivity
- It is likely that the Niagara Falls is a directive source orthogonal to the baffle

Third Look at Niagara Falls

- The Niagara Falls opens in a northerly direction
- This could lead to a directional source
  - $ka = 400 \times \frac{\omega}{c} \approx 12.5 >> 1$
  - When $ka > 1$ we can expect directivity
- It is likely that the Niagara Falls is a directive source orthogonal to the baffle

Crude Back Azimuth

- Find back azimuth using 3 axis seismic sensor
- Take the arctan of the East and North components

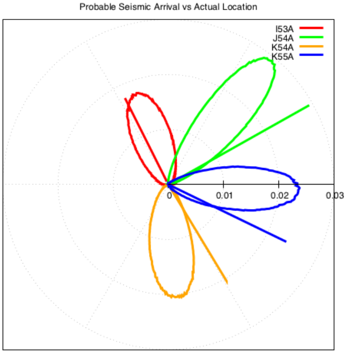

Crude Back Azimuth

- Find back azimuth using 3 axis seismic sensor
- Take the arctan of the East and North components

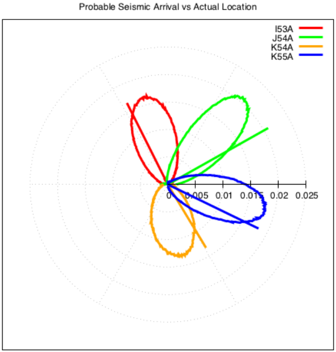

Conclusions and Improvements

- Conclusions
  - The Niagara Falls appears to be generating an infrasonic signal around 1.75Hz
  - Propagation models correlate with signals received at sites near the falls
  - Preliminary back azimuth appears to agree on the direction of the source
- Improvements
  - Find back azimuth during signal arrivals
  - Crude ways of determining back azimuth from 3-axis seismometer
  - Potential use of single infrasound sensor and a 3-axis seismometer to determine accurate back azimuth

Questions

Any Questions?

Thank You

Overview of Acoustic Tomography of the Atmosphere

V. E. Ostashev, S. N. Vecherin, and D. K. Wilson
U.S. Army Engineer Research and Development Center

17th Long Range Sound Propagation Symposium, 12-13 June 2018, Lyon, France

Outline

1. Introduction

2. Acoustic tomography of the atmosphere (ATA) at the Boulder Atmospheric Observatory (BAO)

3. Forward and inverse problems in ATA

4. Numerical simulations and experimental results pertinent to the BAO tomography array

5. Other schematics and techniques for ATA

6. Conclusions

7. References

1. Introduction

Tomography is widely used in medicine, industry, and science. It uses different kinds of waves such as x-rays, laser beams, ultrasound, sound, and seismic waves propagating through a medium to obtain an image of the medium. The word *tomography* is derived from Ancient Greek *tomos*, which means "slice“, and *graphō*, which means "to write“.

An example of tomography is a CT scan which is widely used in medicine. CT stands for “computed tomography”. Next two slides show a medical CT scanner and explain its principal of operation.

CT scanner

A CT scanner.

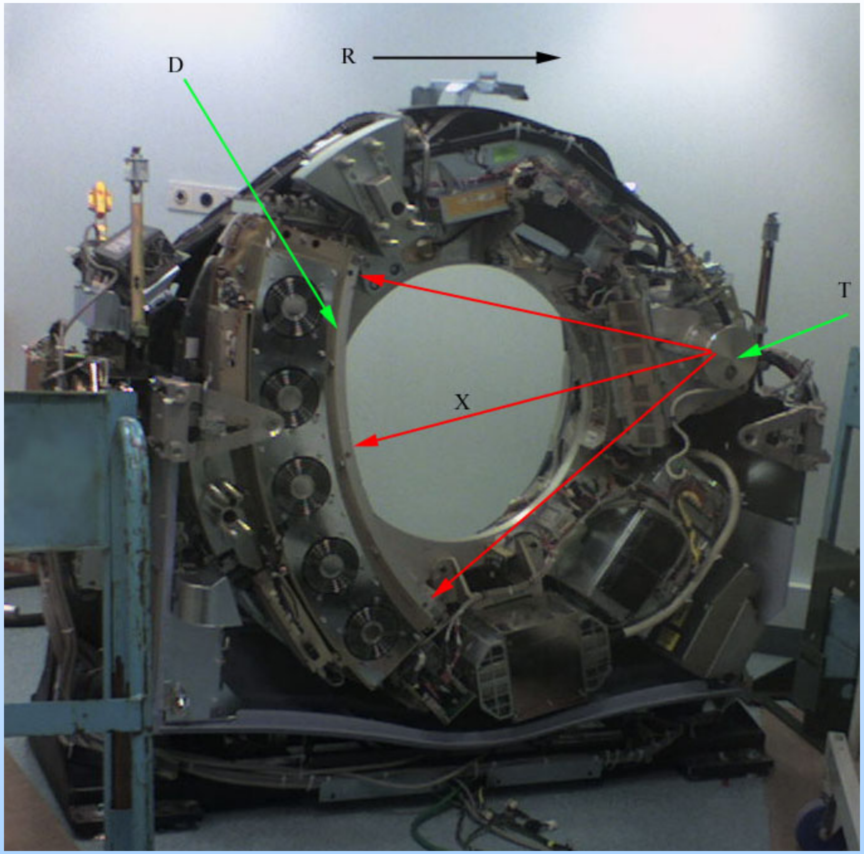

CT scanner with cover removed to show internal components. T: X-ray tube. D: X-ray detectors. X: X-ray beam. R: Gantry rotation

CT scan

Tomography always has two main steps: formulation of a forward problem and a numerical solution of an inverse problem.

1. Forward problem is a formulation of equations describing the effect of a medium on parameters of a propagating wave which are measured experimentally. For a CT scanner, these equations express attenuation of x-rays propagating through a medium with spatially varying properties such as composition and density.

2. Inverse problem is a numerical solution of the equations formulated in the forward problem to infer properties of the medium.

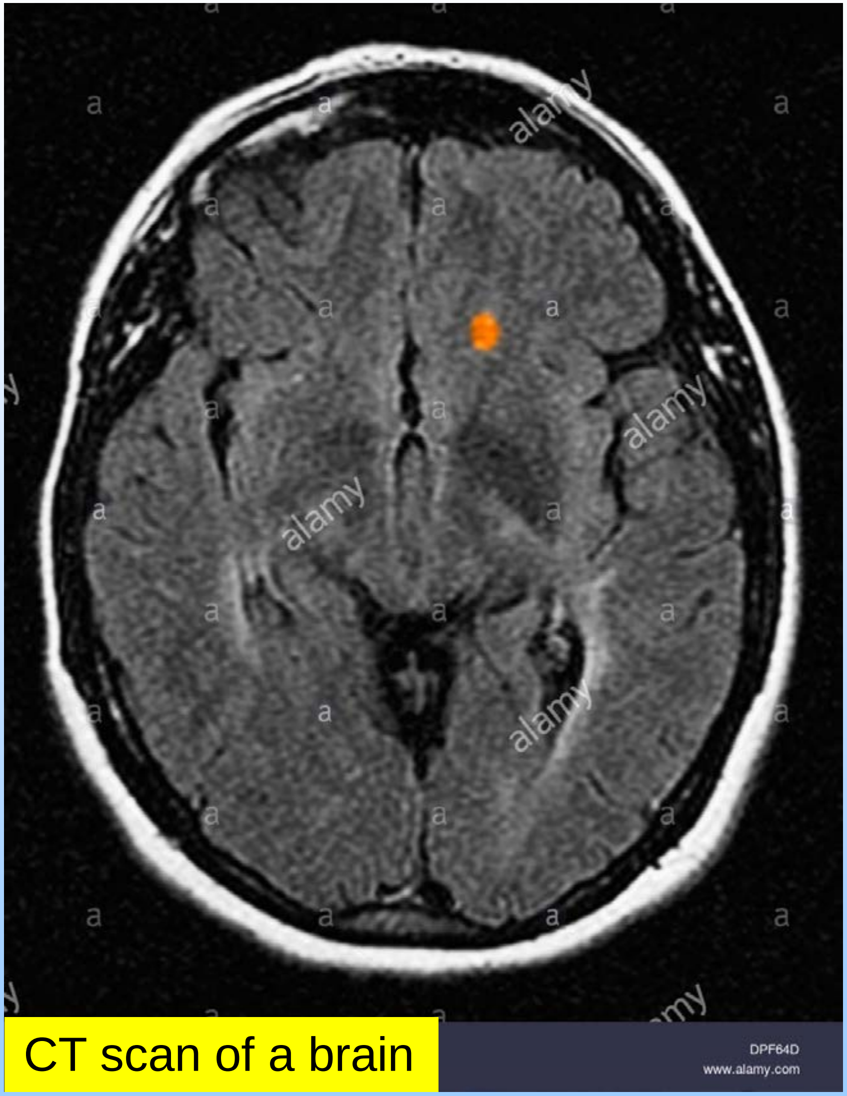

CT scan of a brain

Basics of acoustic tomography of the atmosphere (ATA)

The idea of ATA is similar to that of a CT scanner: using sound waves propagating through the atmosphere, we would like to reconstruct the temperature and wind velocity fields.

Shown is a horizontal slice (80 m x 80 m) of the wind velocity magnitude obtained with Large Eddy Simulations (LES). Arrows indicate the direction of the velocity and colors indicate the magnitude of the velocity. The spatial resolution is 4 m x 4 m with interpolation between grid cells. LES produces realistic temperature and wind velocity fields. The LES solves the Navier-Stocks equations which govern the temporal and spatial evolution of the temperature and wind velocity in the atmospheric boundary layer (ABL). The direct numerical simulation (DNS) of these equations is still computationally prohibitive. In the LES, small scale turbulence is not resolved and its effect on large scales is parameterized.

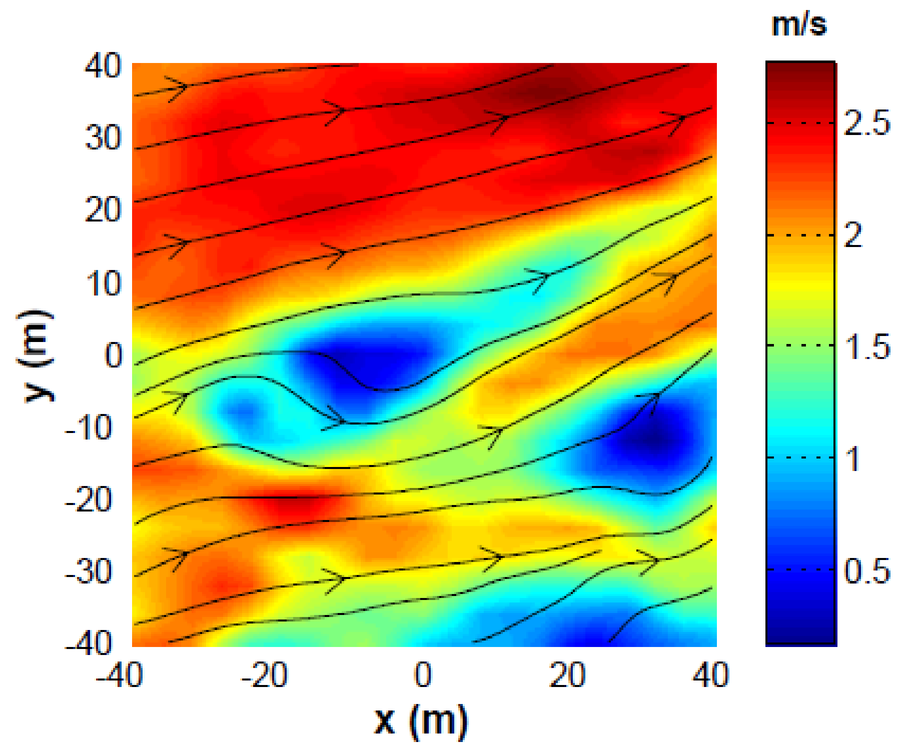

The goal of acoustic tomography of the atmosphere is to obtain experimentally such temperature and velocity fields.

Basics of ATA

A CT scanner is based on attenuation of x rays in a medium. ATA employs the fact that a travel time of sound waves in the atmosphere from a sound source (e.g., a speaker) to a microphone depends on the temperature and wind velocity along the propagation path. Therefore, ATA is also termed as travel-time acoustic tomography. (In principle, other parameters of sound signals such as attenuation can be measured with the goal of reconstructing other properties of the atmosphere, e.g., humidity fluctuations.)

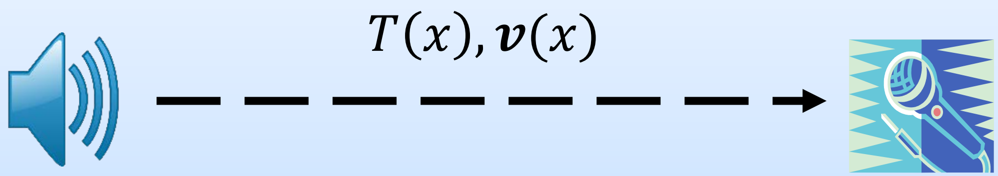

1. Forward problem in ATA: Express the travel time of sound signals in terms of the temperature and wind velocity fields and the coordinates of speakers and microphones.

2. Inverse problem in ATA: Reconstruct the temperature and wind velocity fields from the measured travel times.

Similarly to a CT scanner, in ATA we need many sound propagation paths and, hence, many speakers and microphones. A set of speakers and microphones with pertinent instrumentation is called an acoustic tomography array. As an example of a tomography array, we consider the array for acoustic tomography of the atmosphere built at the Boulder Atmospheric Observatory (BAO), located near Boulder, CO, USA.

2. BAO acoustic tomography array

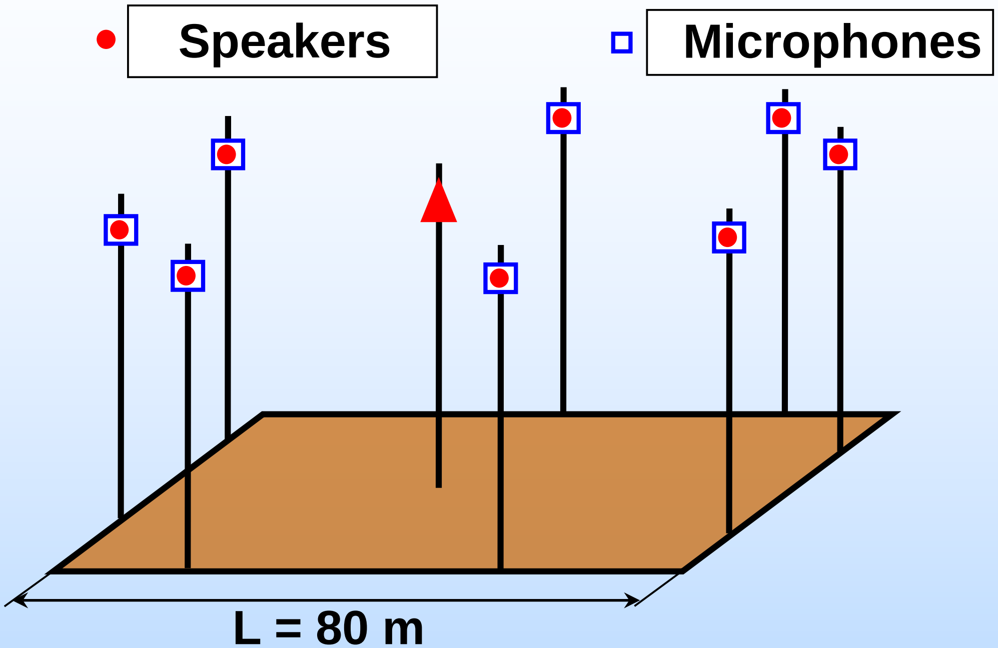

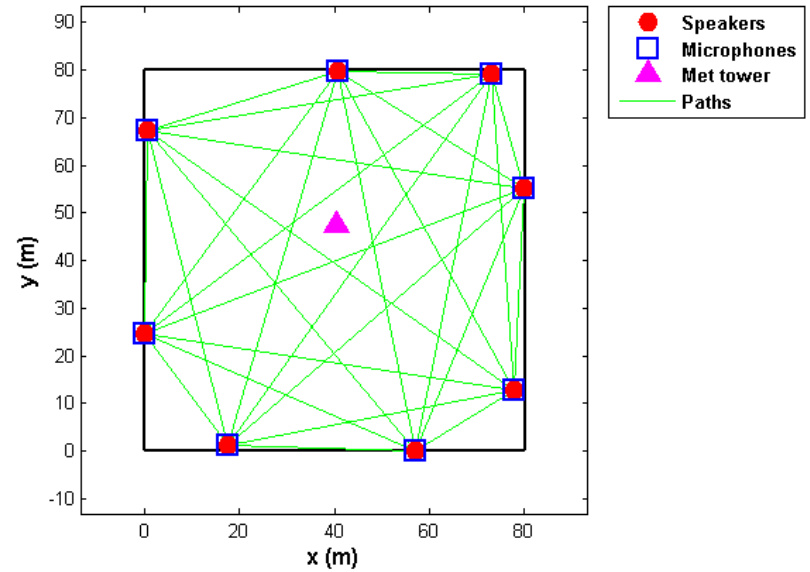

The BAO 2.0 acoustic tomography array consisted of 8 towers located along the perimeter of a square with the size 80 m x 80 m. Each tower carried a speaker and microphone at the height of about 8 m above the ground. The tower #9 in the middle of the array carried a sonic anemometer and a temperature probe. Right plot shows a view from above on the array; speakers and mics are located along the perimeter of a square. Green lines indicate 56 propagation paths. Principle of operation of the BAO 2.0 tomography array: eight speakers were activated in a sequence and transmitted short pulses. Microphones recorded these pulses. One cycle of transmission and recording lasted 0.5 s. This enabled us to determine the travel times of sound propagation along 56 paths every 0.5 s. Then, this cycle was repeated for up to a few hours. (The tomography array was dismantled in 2016 due to decommission of the BAO.) The BAO 1.0 tomography array had the same 8 towers, but 3 towers carried only speakers and the remaining 5 towers carried only mics resulting in 15 paths.

Block diagram of the BAO tomography array

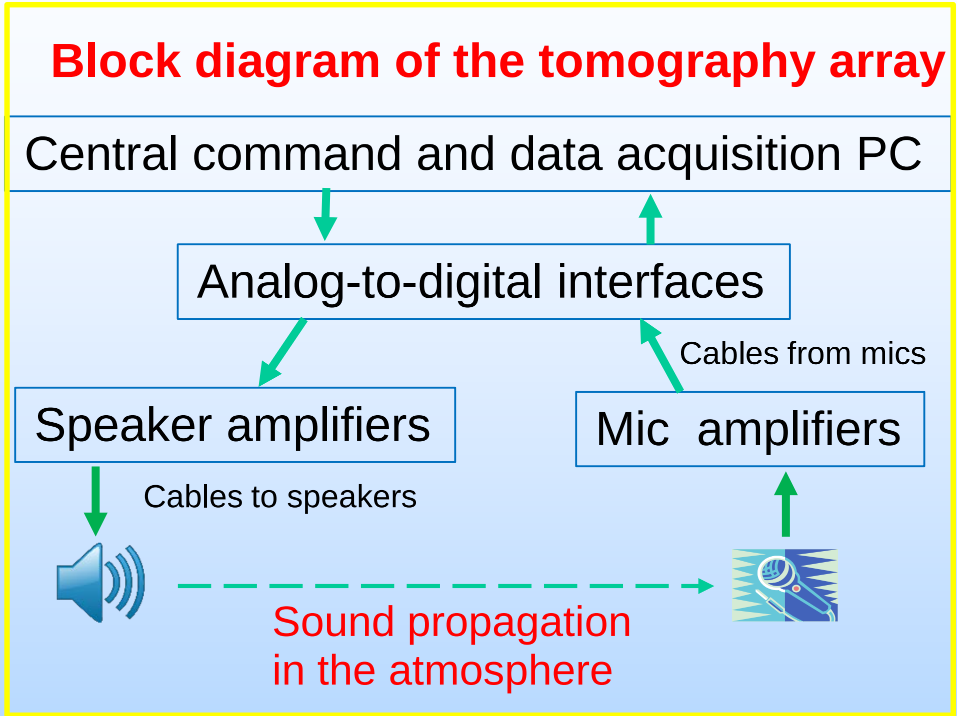

Shown is the block diagram of the BAO tomography array. A LabVIEW program was written to run the tomography array from the central command and data acquisition PC and store all data on the PC. Speakers were activated by this program via A/D interfaces, speaker amplifiers, and cables to the towers. Then, sound pulses propagated in the atmosphere and were recorded by microphones. The microphone signals were amplified and recorded by the PC via A/D interfaces. Simultaneously, the PC recorded the wind velocity and temperature (via a sonic anemometer and temperature probe).

One of the towers of the BAO array

Shown is tower #5 of the BAO tomography array. The tower is 9.1 m high. A speaker and a mic were installed at 8 m above the ground. The instrumentation box carried a mic preamp and power outlet. A building behind the tower is the BAO Visitor Center (VC), where the acoustic tomography operation center was located. Cables in underground conduits connected the towers with the acoustic tomography operation center.

Eight towers of the BAO tomography array and the VC

Acoustic tomography operation center

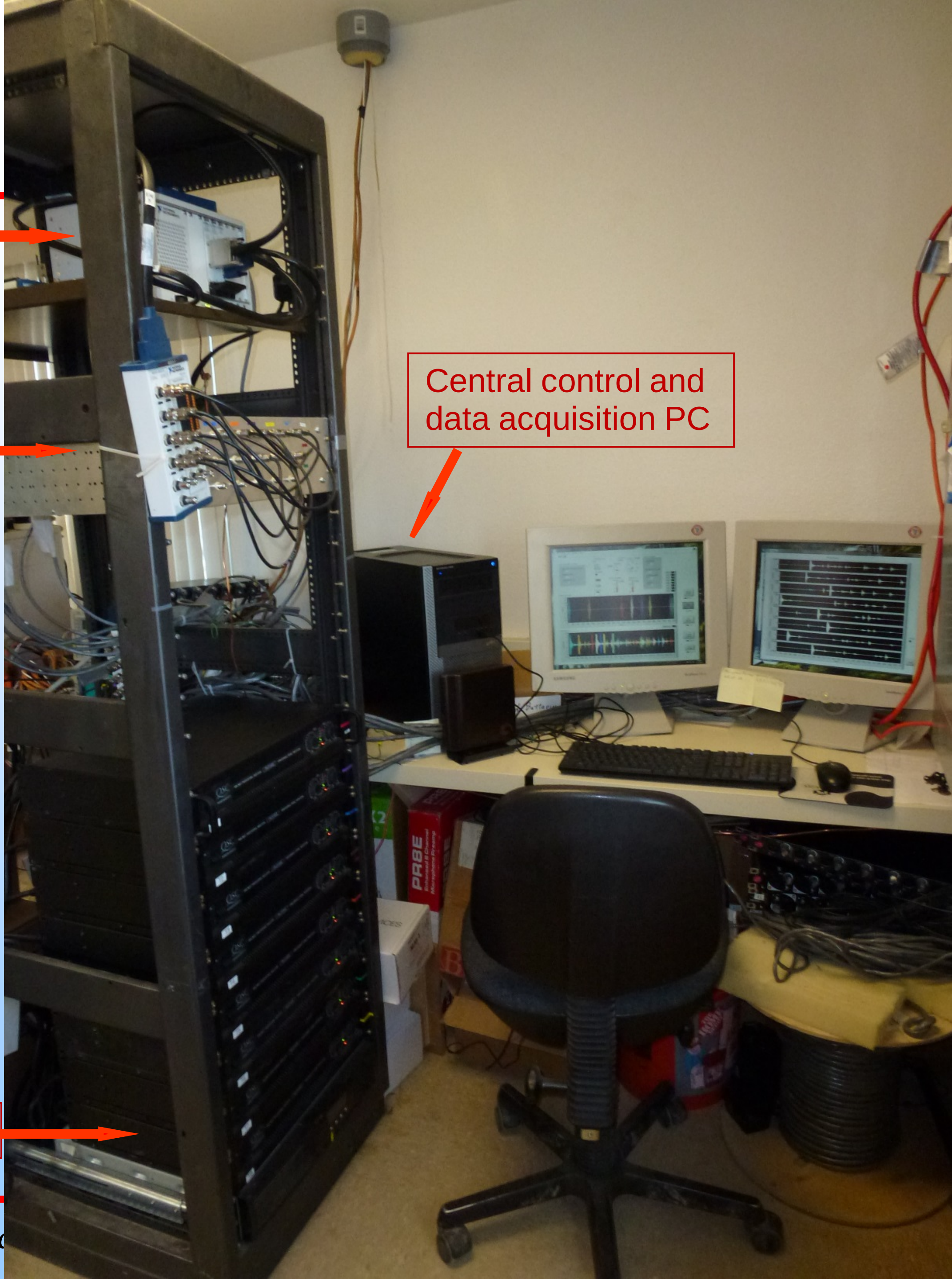

The acoustic tomography operation center inside the Visitor Center. The central command and data acquisition PC is on the desk. Two monitors show 8 transmitted signal and 8 signals recorded by microphones. The rack carries the A/D interfaces, power amplifiers for speakers, and mic filters. Cables to the towers can be seen on the right.

Transmitted signal

Received signal

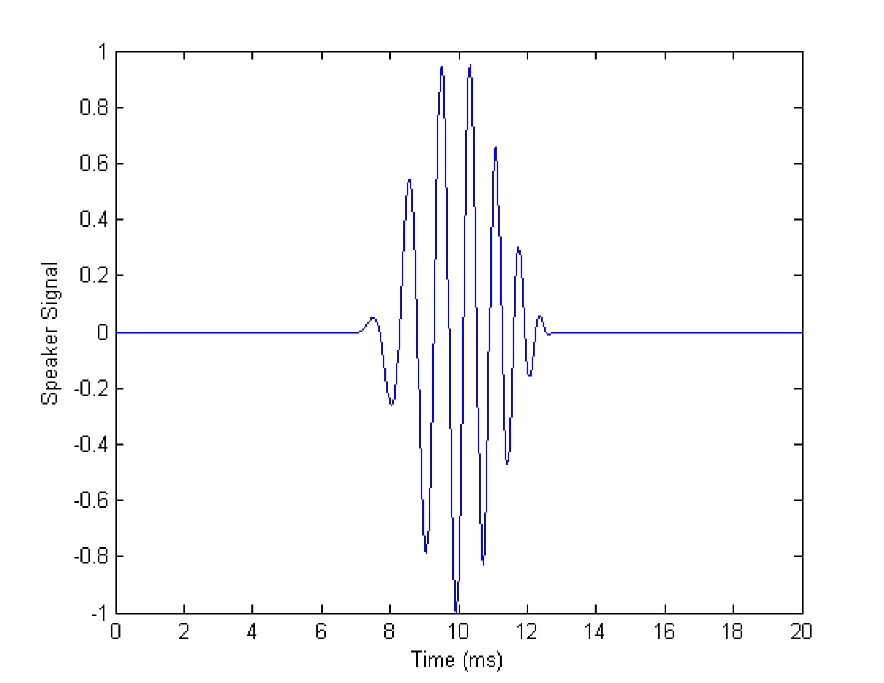

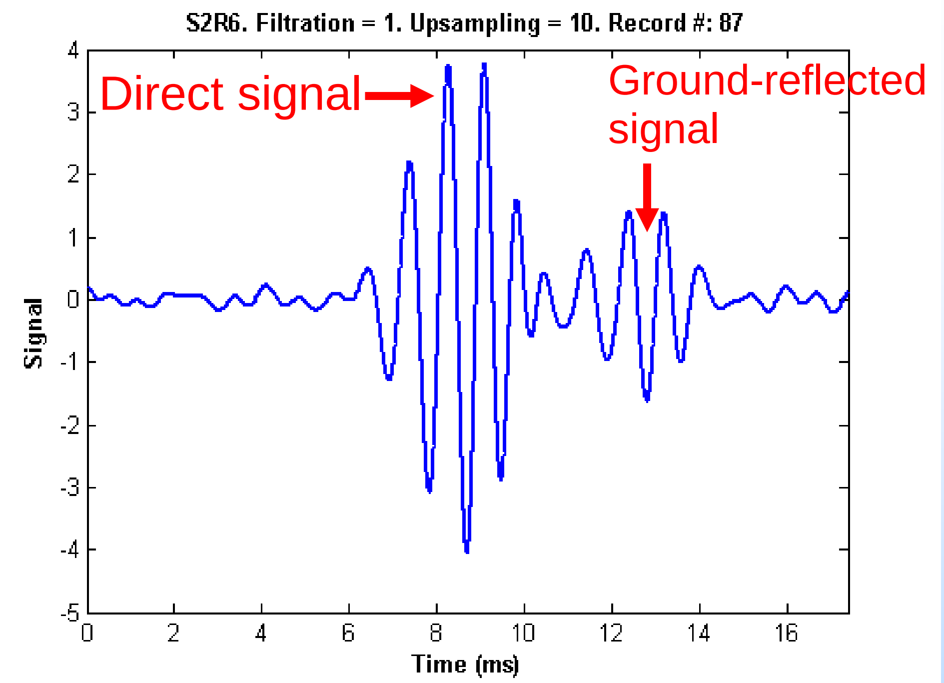

Shown are the transmitted and received signals. Transmitted signal: a chirp with the central frequency 1.2 kHz and duration of 5.8 ms. The received signal consists of the direct signal and that reflected from the ground. Cross-correlation of the transmitted and received signals enables determination of the travel time of sound propagation between a speaker and microphone. The ground reflected signal might be used to reconstruct 3D temperature and velocity fields.

Temporal evolution of the travel time

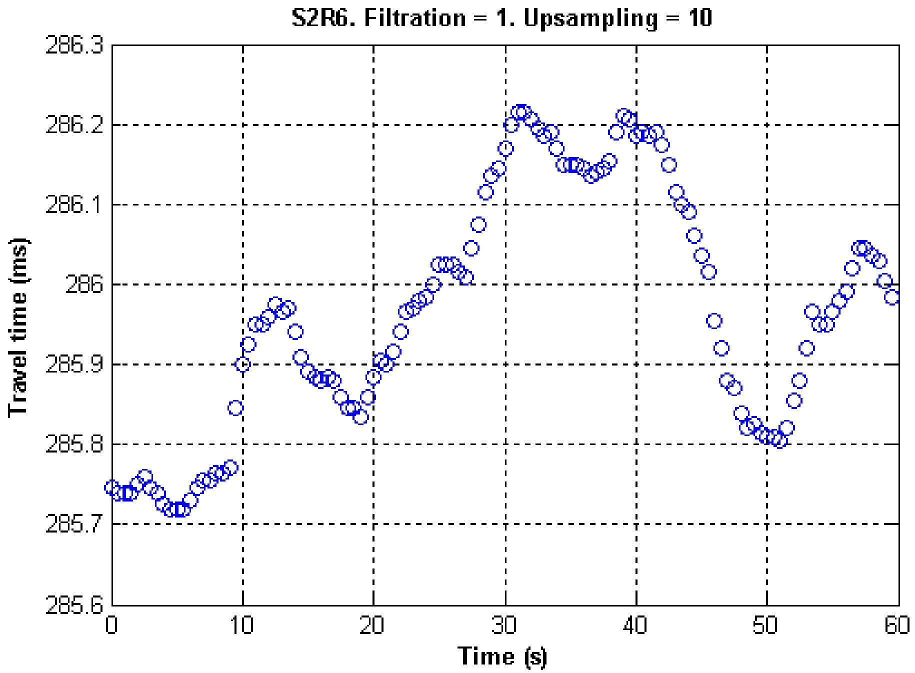

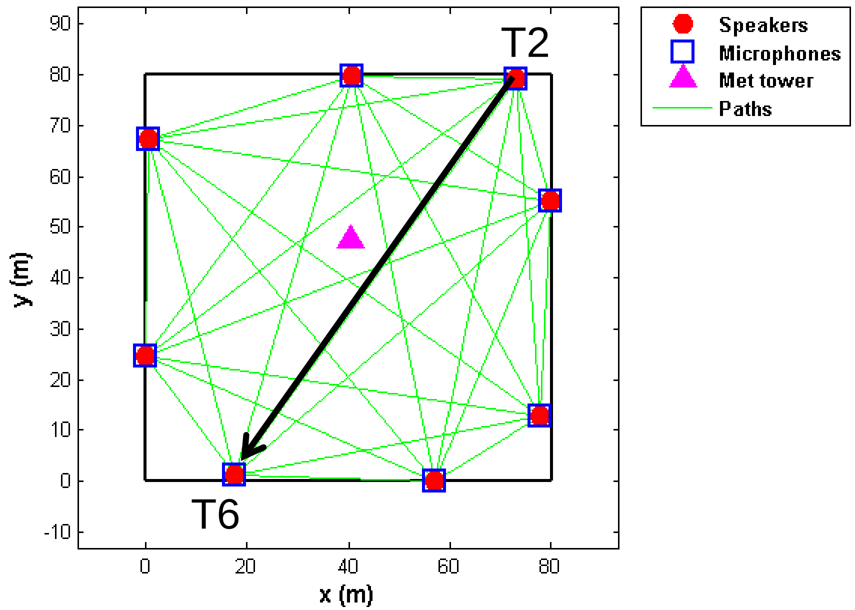

The travel time of sound propagation from speaker T2 to mic T6 during 1 min (120 transmissions). The travel time gradually changes from one measurement to another due to changing temperature and velocity fields along the path. A maximum deviation of the travel time is about 0.5 ms. The travel times for other propagation paths were obtained.

Next step in ATA is reconstruction of the temperature and velocity fields from the travel times.

3. Forward and inverse problems in ATA

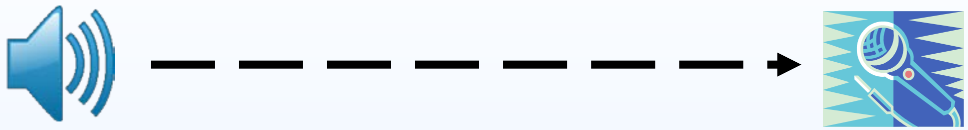

The forward problem in ATA expresses the travel time τ of sound propagation from a speaker to a microphone in terms of the temperature T and wind velocity $\boldsymbol{v}$ along the path:

$$\tau = \int_{l_s}^{l_m} \frac{dl}{u_{\mathrm{gr}}(l)}, \qquad \boldsymbol{u}_{\mathrm{gr}} = c\boldsymbol{n} + \boldsymbol{v}, \qquad c = \sqrt{\gamma R_a T}.$$

Here, the integration is performed along a curved path from a speaker (l_s) to a microphone (l_m), u_{gr} is the magnitude of the group velocity of the sound wave, c is the sound speed, and $\boldsymbol{n}$ is the unit vector normal to the wave front. The sound speed and temperature are related by the well-known equation. The forward problem is formulated rigorously using geometrical acoustics in a moving medium:

Ostashev and Wilson, *Acoustics in Moving Inhomogeneous Media, 2nd Ed.* (CRC Press, 2015).

The temperature, sound speed, and wind velocity are expressed as mean values (averaged over the tomographic area) and fluctuations. The forward problem is linearized assuming that the propagation path is relatively small and that $\tilde{T} \ll T$ and $\tilde{v} \ll c_0$.

$$T(\boldsymbol{r}) = T_0 + \tilde{T}(\boldsymbol{r}), \;\; \mathrm{c}(\boldsymbol{r}) = c_0 + \tilde{c}(\boldsymbol{r}), \;\; \boldsymbol{v}(\boldsymbol{r}) = \boldsymbol{v}_0 + \tilde{\boldsymbol{v}}(\boldsymbol{r}). \;\; \boldsymbol{r} = (x, y).$$

Linearized forward problem in ATA

Linearized forward problem for the travel time of sound propagation along the i propagation path:

$$\tau_i = \frac{L_i}{c_0}\left(1 - \frac{\boldsymbol{s}_i \cdot \boldsymbol{v}_0}{c_0}\right) - \frac{1}{c_0}\int_{L_i}\left[\frac{\tilde{T}(\boldsymbol{r})}{2T_0} + \frac{\boldsymbol{s}_i \cdot \tilde{\boldsymbol{v}}(\boldsymbol{r})}{c_0}\right] dl, \qquad i = 1, 2, \dots, I.$$

Here, the first term is due to the mean temperature and velocity and the second term is due to their fluctuations. Integration is done along the straight line from a speaker to a mic, $\boldsymbol{s}_i$ is the unit vector in the direction of this line, and L_i is the path length. For the BAO tomography array $I = 56$. The mean sound speed and velocity can be measured with a sonic and T-probe or reconstructed using a least square estimation as explained below. This enables us to determine the vector

$$d_i = c_0 L_i\left(1 - \frac{\boldsymbol{s}_i \cdot \boldsymbol{v}_0}{c_0}\right) - c_0^2 \tau_i,$$

which we call the data for reconstruction of the fluctuations. From these equations, we obtain the linearized forward problem for temperature and velocity fluctuations

$$d_i = c_0 \int_{L_i}\left[\frac{\tilde{T}(\boldsymbol{r})}{2T_0} + \frac{\boldsymbol{s}_i \cdot \tilde{\boldsymbol{v}}(\boldsymbol{r})}{c_0}\right] dl.$$

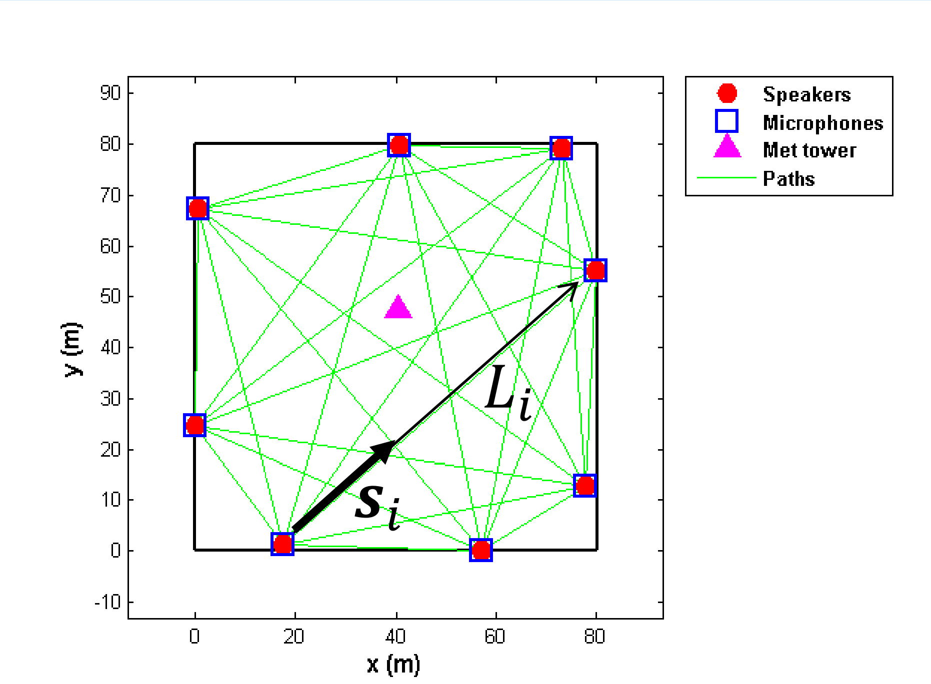

Inverse problem in ATA

The linearized forward problem for T and v fluctuations

$$d_i = c_0 \int_{L_i} \left[\frac{\tilde{T}(\boldsymbol{r})}{2T_0} + \frac{\boldsymbol{s}_i \cdot \tilde{\boldsymbol{v}}(\boldsymbol{r})}{c_0} \right] dl + \varepsilon_i,$$

where ε_i is noise in the data. The column vector of data

$$\boldsymbol{d} = [d_1; d_2; \ldots d_I], \qquad i = 1, 2, \ldots, I.$$

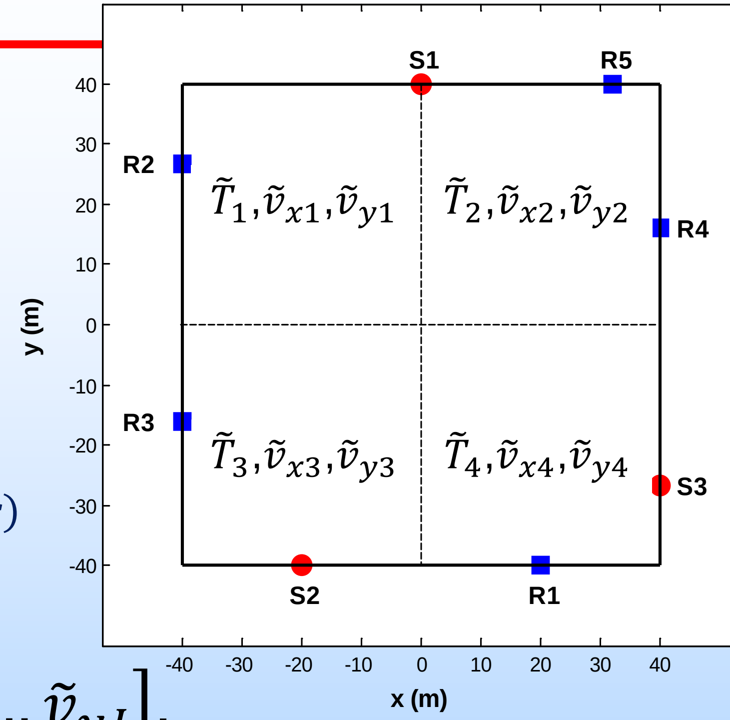

The tomographic area is divided into J grid cells, in which $\tilde{T}(\boldsymbol{r})$ and $\tilde{\boldsymbol{v}}(\boldsymbol{r})$ are assumed constant and termed models. The column vector of models has *3J* components:

$$\mathbf{m} = [\tilde{T}_1; \tilde{T}_2; \ldots \tilde{T}_J; \tilde{v}_{x1}; \tilde{v}_{x2}; \ldots \tilde{v}_{xJ}; \tilde{v}_{y1}; \tilde{v}_{y2}; \ldots \tilde{v}_{yJ}].$$

An inverse problem in ATA is to solve the forward problem for $\boldsymbol{m}$. The solution is termed as an estimation (reconstruction) of models and differs from the models:

$$\hat{\mathbf{m}} = [\hat{T}_1; \hat{T}_2; \ldots \hat{T}_J; \hat{v}_{x1}; \hat{v}_{x2}; \ldots \hat{v}_{xJ}; \hat{v}_{y1}; \hat{v}_{y2}; \ldots \hat{v}_{yJ}].$$

There are many approaches for the inverse problem, e.g., an algebraic reconstruction. For T and v constant in grid cells, the integrals in the forward problem are calculated analytically.

Algebraic reconstruction

The forward problem in the algebraic reconstruction becomes:

$$d_i = \sum_{j=1}^{J} \left(a_{ij}\tilde{T}_j + b_{ij}^{x}\tilde{v}_{xj} + b_{ij}^{y}\tilde{v}_{yj} \right) + \varepsilon_i,$$

The data for path i are expressed in terms of the models (temperature and two velocity components in the grid cells) and the matrices a_{ij}, b_{ij}^{x}, and b_{ij}^{y} which depend on the transducer's coordinates. The forward problem can be written in a matrix form:

$$\boldsymbol{d} = \boldsymbol{M}\boldsymbol{m} + \boldsymbol{\varepsilon}, \qquad \text{where} \qquad \boldsymbol{M} = \left[a_{ij},\, b_{ij}^{x},\, b_{ij}^{y} \right],\;\; \boldsymbol{\varepsilon} = [\varepsilon_1; \varepsilon_2, \ldots \varepsilon_I].$$

In the inverse problem, we solve this equation for $\boldsymbol{m}$. The damped least square (DLS) estimation yields:

$$\hat{\mathbf{m}} = (\boldsymbol{M}^T\boldsymbol{M} + \alpha\boldsymbol{I})^{-1}\, \boldsymbol{M}^T\boldsymbol{d},$$

which expresses $\hat{\mathbf{m}}$ in terms of the column vector of the data $\boldsymbol{d}$. Here, the subscript T indicates the transpose of a matrix, "-1" means the inverse of a matrix, α is the regularization parameter, and $\boldsymbol{I}$ is the identity matrix. The DLS estimation minimizes the difference

$$(\boldsymbol{M}\hat{\mathbf{m}} - \boldsymbol{M}\boldsymbol{m})^2 \;\longmapsto \text{min}.$$

Algebraic reconstruction

$$\hat{\mathbf{m}} = (\boldsymbol{M}^T \boldsymbol{M} + \alpha \boldsymbol{I})^{-1}\, \boldsymbol{M}^T \boldsymbol{d}.$$

The DLS estimation works very well if the number of the data (the length of $\boldsymbol{d}$) is greater than the number of models (the length of $\boldsymbol{m}$): $I > 3J$, i.e., the inverse problem is overdetermined. This is the case for a CT scanner.

In ATA, we would like to reconstruct the T and v fields similar to those obtained with LES, where the spatial resolution is 4 m x 4 m. In this case the number of grid cells is *J = 400* and the number of models is *3J = 1200*! Even for a not very good spatial resolution 16 m x 16 m (right plot), the number of models *3 x J = 3 x 25 = 75* exceeds the number of data *I = 56.* Thus, the inverse problem in ATA is intrinsically underdetermined.

The algebraic reconstruction cannot be used in ATA and we need a good algorithm for solution of undetermined inverse problems.

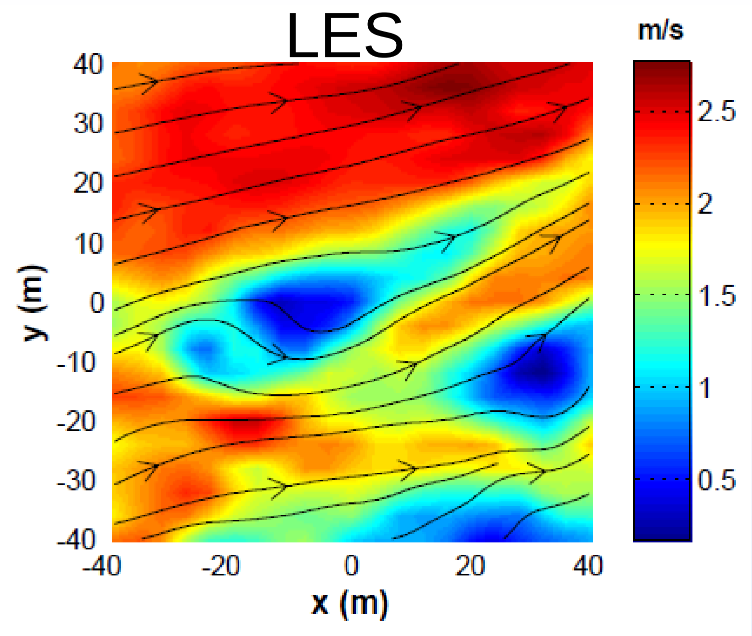

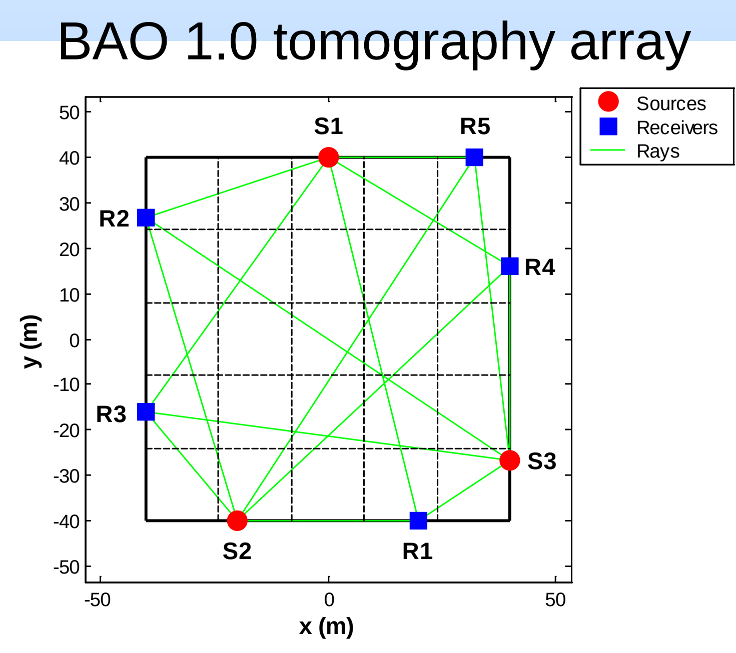

Stochastic inversion (SI)

Another shortcoming of the algebraic reconstruction is that the models within two grid cells are assumed uncorrelated. However, if we measure the temperature fluctuations at two spatial points, $\boldsymbol{r}_1$ and $\boldsymbol{r}_2$, multiply the result, and average over time, we obtain the spatial correlation function of temperature fluctuations:

$$B_T(\boldsymbol{r}_1 - \boldsymbol{r}_2) = \frac{1}{\Delta t}\int_{t_0}^{t_0+\Delta t} \tilde{T}(\boldsymbol{r}_1, t)\tilde{T}(\boldsymbol{r}_2, t)dt.$$

This correlation function is not zero if the two points are located relatively close to each other.

A stochastic inversion employs the fact that the temperature and wind velocity fluctuations are spatially correlated and is used to solve underdetermined inverse problems.

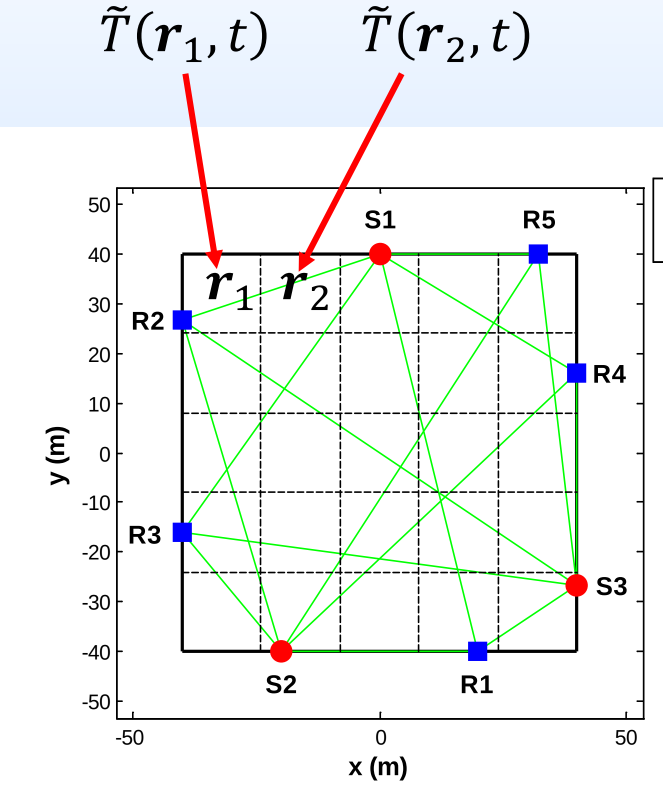

Stochastic inversion

The linearized forward problem for T and v fluctuations is given by the same equations:

$$d_i = c_0 \int_{L_i} \left[\frac{\tilde{T}(\boldsymbol{r})}{2T_0} + \frac{\boldsymbol{s}_i \cdot \tilde{\boldsymbol{v}}(\boldsymbol{r})}{c_0}\right] dl + \varepsilon_i, \quad \boldsymbol{d} = [d_1; d_2; \dots d_I],$$

However, $\tilde{T}(\boldsymbol{r})$ and $\tilde{\boldsymbol{v}}(\boldsymbol{r})$ are now random functions with known spatial correlation functions. The tomographic area is again divided into J grid cells, in which $\tilde{T}(\boldsymbol{r})$ and $\tilde{\boldsymbol{v}}(\boldsymbol{r})$ are constant random values

$$\mathbf{m} = \left[\tilde{T}(\boldsymbol{r}_1); \tilde{T}(\boldsymbol{r}_2); \dots \tilde{T}(\boldsymbol{r}_J); \tilde{v}_x(\boldsymbol{r}_1); \tilde{v}_x(\boldsymbol{r}_2); \dots \tilde{v}_x(\boldsymbol{r}_J); \tilde{v}_y(\boldsymbol{r}_1); \tilde{v}_y(\boldsymbol{r}_2); \dots \tilde{v}_y(\boldsymbol{r}_J)\right].$$

The estimation of the models are not random:

$$\hat{\mathbf{m}} = \left[\hat{T}(\boldsymbol{r}_1); \hat{T}(\boldsymbol{r}_2); \dots \hat{T}(\boldsymbol{r}_J); \hat{v}_x(\boldsymbol{r}_1); \hat{v}_x(\boldsymbol{r}_2); \dots \hat{v}_x(\boldsymbol{r}_J); \hat{v}_y(\boldsymbol{r}_1); \hat{v}_y(\boldsymbol{r}_2); \dots \hat{v}_y(\boldsymbol{r}_J)\right].$$

The stochastic inversion minimizes the deviation of the estimations from the models, where the brackets $\langle \quad \rangle$ indicate averaging over an ensemble of realizations of T and v fluctuations:

$$\left\langle \left(\widehat{m}_j - m_j\right)^2 \right\rangle \mapsto \min, \qquad j = 1, 2, \dots J.$$

Stochastic inversion

Similarly to the algebraic reconstruction, the estimation of the models is expressed in terms of the column vector of the data, but with a different matrix on the right-hand side:

$$\hat{\mathbf{m}} = \boldsymbol{R}_{md}\boldsymbol{R}_{dd}^{-1}\boldsymbol{d}.$$

$$\boldsymbol{R}_{md} = \langle \boldsymbol{m}\boldsymbol{d}^T \rangle = \frac{c_0}{2T_0}\int_{L_i} B_T\big(\boldsymbol{r}_j - \boldsymbol{r}(l_i)\big)dl_i\,,\ j = 1,2,\ldots J, \quad i = 1,2,\ldots I.$$

$$\boldsymbol{R}_{dd} = \langle \boldsymbol{d}\boldsymbol{d}^T \rangle = \frac{c_0^2}{4T_0^2}\int_{L_i} dl_i \int_{L_k} B_T(\boldsymbol{r}(l_i) - \boldsymbol{r}(l_k))\, dl_k\,,\ k = 1,2,\ldots I.$$

Here, $\boldsymbol{R}_{md}$ and $\boldsymbol{R}_{dd}$ are the model-data and data-data covariance matrices which are expressed in terms of $B_T(\boldsymbol{r})$. In $\boldsymbol{R}_{md}$, the integration is done along the *i* path. In $\boldsymbol{R}_{dd}$, the integration is done along the paths *i* and *k*. The velocity fluctuations are accounted similarly. The SI also provides the estimated errors of reconstruction in each grid cell, where $\boldsymbol{R}_{mm} = \langle \boldsymbol{m}\boldsymbol{m}^T \rangle$ is the model-model covariance matrix:

$$\boldsymbol{R}_{ee} = \boldsymbol{R}_{mm} - \boldsymbol{R}_{md}\boldsymbol{R}_{dd}^{-1}\boldsymbol{R}_{md}^T.$$

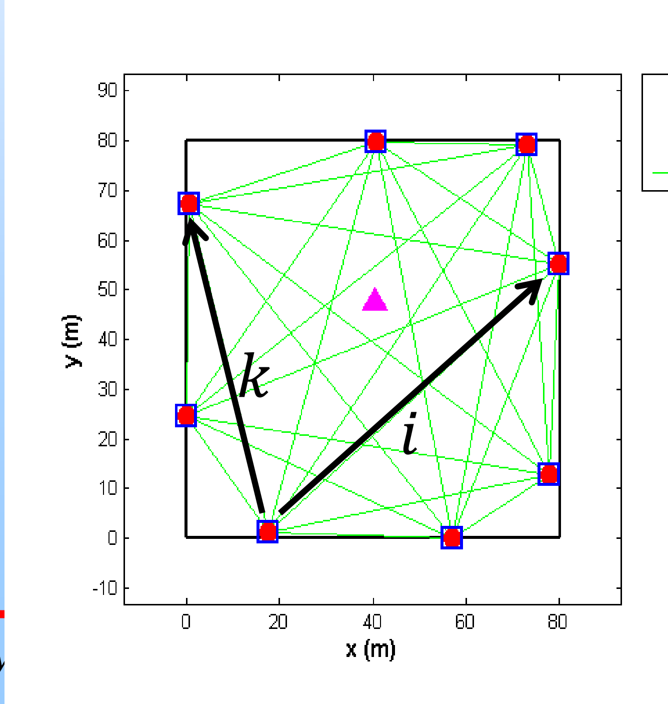

Time-dependent stochastic inversion (TDSI)

The SI had been known in the literature and when applied to ATA, this was a step forward. Vecherin et al. (2006) developed even a better algorithm for the T and v reconstruction, which is termed the time-dependent stochastic inversion (TDSI). In TDSI, we take into account that T and v fluctuations correlate not only in space, but also in time. For frozen turbulence, the T and v fluctuations (such as those in the right plot) move with the mean wind, thus resulting in the spatial-temporal correlations. By repeated measurements of the travel times τ_i at close time moments t_1, t_2, … t_N and accounting for these correlations, we obtain more data for the tomographic reconstruction.

In the BAO tomography array, the travel times were measured every 0.5 s (right plot). In TDSI, N sets of the travel times τ_i are used for the reconstruction of T and v fluctuations:

$$\tau_i(t_1), \tau_i(t_2), \ldots \tau_i(t_N).$$

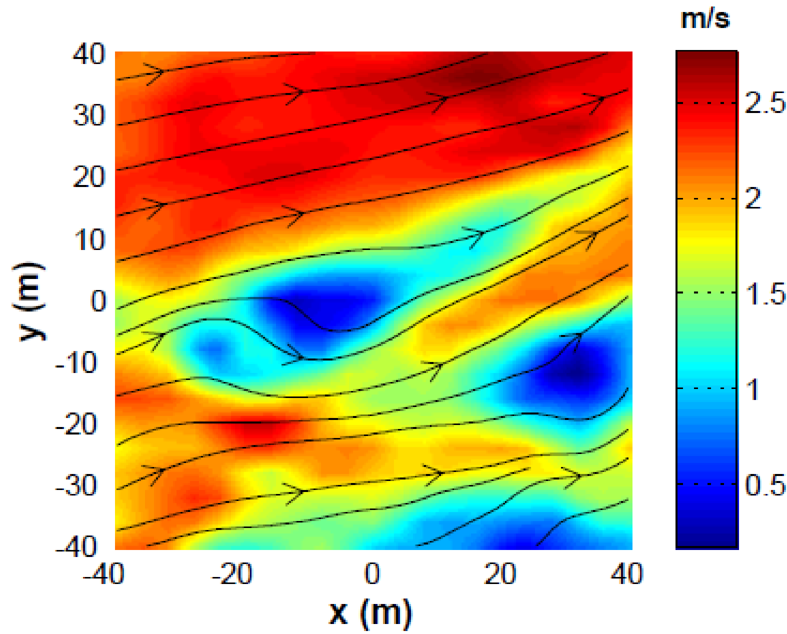

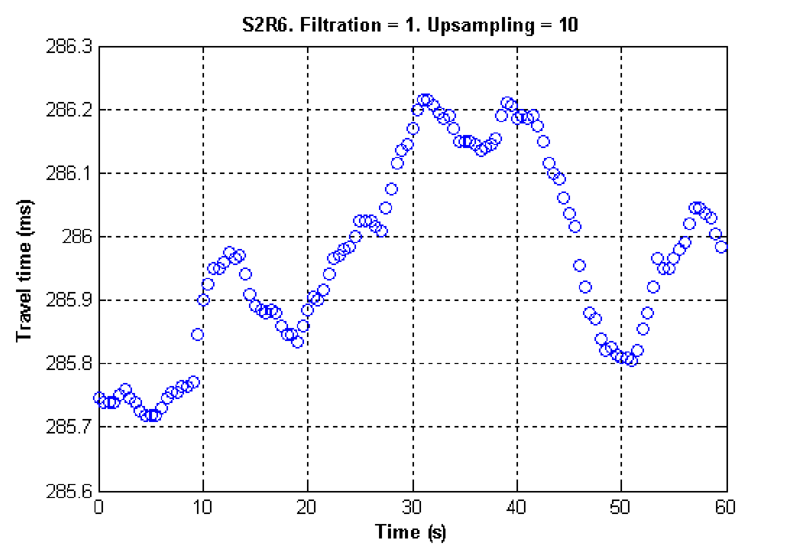

Time-dependent stochastic inversion

This enables to obtain N sets of the data at the time moments $t_1,\ t_2,\ \ldots\ t_N$:

$$\boldsymbol{d} = [\boldsymbol{d}(t_1); \boldsymbol{d}(t_2); \ldots \boldsymbol{d}(t_N)].$$

The models are also specified at the time moments $t_1,\ t_2,\ \ldots\ t_N$:

$$\boldsymbol{m} = [\boldsymbol{m}(t_1); \boldsymbol{m}(t_2); \ldots \boldsymbol{m}(t_N)].$$

The estimation of the models is done at one time moment t_0, for which: $t_1 < t_0 < t_N$,

$$\widehat{\mathbf{m}}(t_0) = \left[\hat{T}(\boldsymbol{r}_1, t_0); \ldots \hat{T}\left(\boldsymbol{r}_J, t_0\right); \hat{v}_x(\boldsymbol{r}_1, t_0); \ldots \hat{v}_x\left(\boldsymbol{r}_J, t_0\right); \hat{v}_y(\boldsymbol{r}_1, t_0); \ldots \hat{v}_y\left(\boldsymbol{r}_J, t_0\right)\right].$$

The solution of the inverse problem is given by the same formula as for the SI. However, the column vector of the data has now many more components.

$$\widehat{\mathbf{m}} = \boldsymbol{R}_{md}\boldsymbol{R}_{dd}^{-1}\boldsymbol{d}; \qquad \boldsymbol{R}_{md} = \langle \boldsymbol{m}\boldsymbol{d}^T \rangle, \quad \boldsymbol{R}_{dd} = \langle \boldsymbol{d}\boldsymbol{d}^T \rangle.$$

Thus, by repeated measurements of the travel times and accounting for the spatial-temporal correlations in the T and v fields, TDSI allows us to increase the amount of data without increasing the number of speakers and microphones. Development of this algorithm was a breakthrough in ATA. TDSI generalizes SI and is similar to the Kalman filter (e.g., Kolouri et al., 2014). In principle, SI and TDSI enable the tomographic reconstruction on a very small grid; there is, however, a tradeoff between the spatial resolution and the errors in reconstruction.

4. Numerical simulations of the BAO tomography array

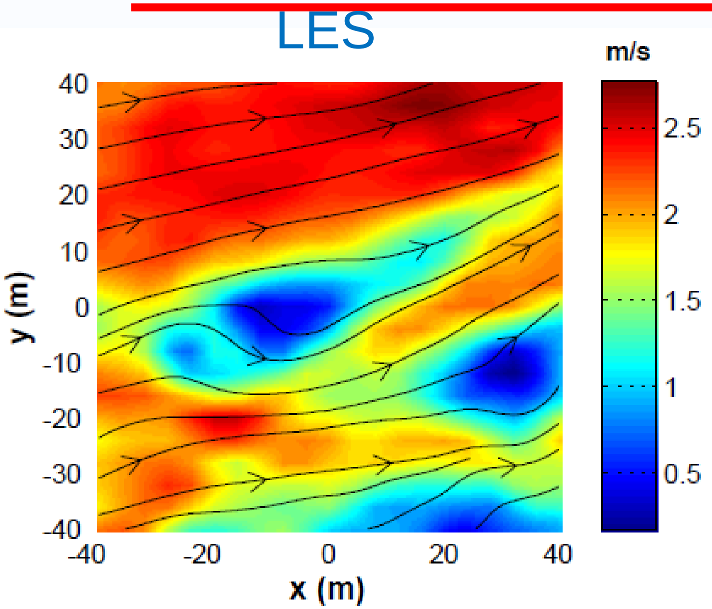

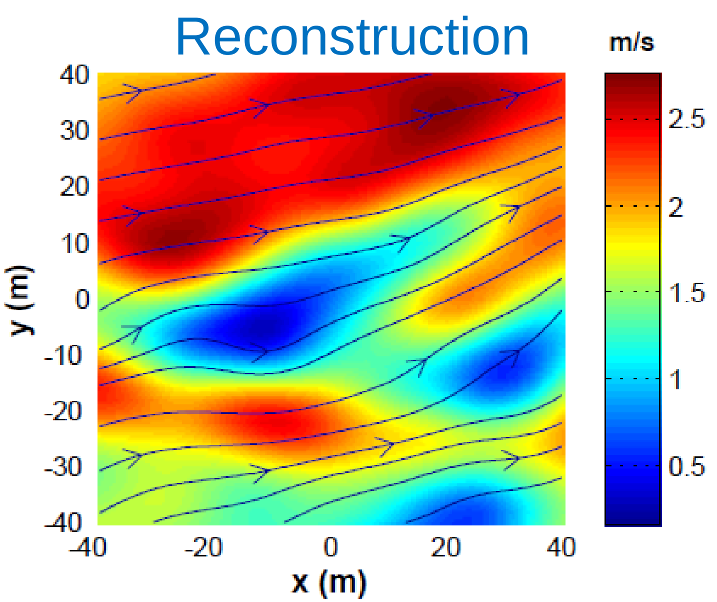

TDSI was used in numerical simulations of the BAO tomography array. The upper plot is the wind velocity magnitude obtained with LES. Arrows indicate the direction of the velocity. This LES field was moving through the tomography array; the travel times of sound pulses were calculated every 0.5 s and corrupted by noise. Five consecutive sets of the travel times were used and the spatial resolution was 4 m x 4 m with interpolation between the grid cells. The lower plot is the tomographic reconstruction of the velocity. The reconstruction reproduces correctly the main features of the LES field: the arrows are pointed in the same direction and fast and slow eddies are reproduced accurately. The results are available as movies.

The accuracy of a tomographic reconstruction of the temperature and velocity depends on many factors such as the number of transducers, the errors in measurements of the travel times and transducers coordinates, location of transducers, and inverse algorithms. In TDSI, it can be as good as 0.1 C for T and 0.1 m/s for **v**. The temporal resolution can be about 0.25 s. An algorithm was developed for finding an optimal location of speakers and microphones of the BAO array.

Calibration of the BAO tomography array

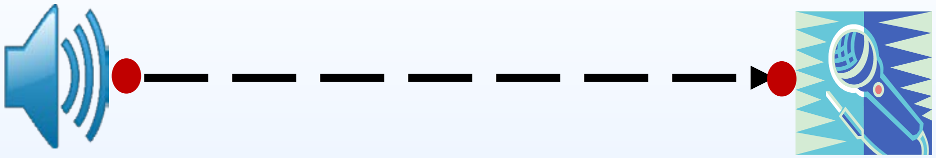

The BAO tomography array was accurately calibrated:

(i) The coordinates of the speakers and microphones were measured with a laser finder.

(ii) The time delays in the hardware and electronic system of the tomography array were determined for every pair of a speaker-microphone.

(iii) The forward problem in ATA is formulated for a point source and receiver. A mic can be considered as a point receiver. But a speaker consists of a driver and horn, and is not a point source. The effective point of emission is different in different azimuthal directions. This was accounted for by special measurements.

Tomography experiment at the BAO on 9 November 2014

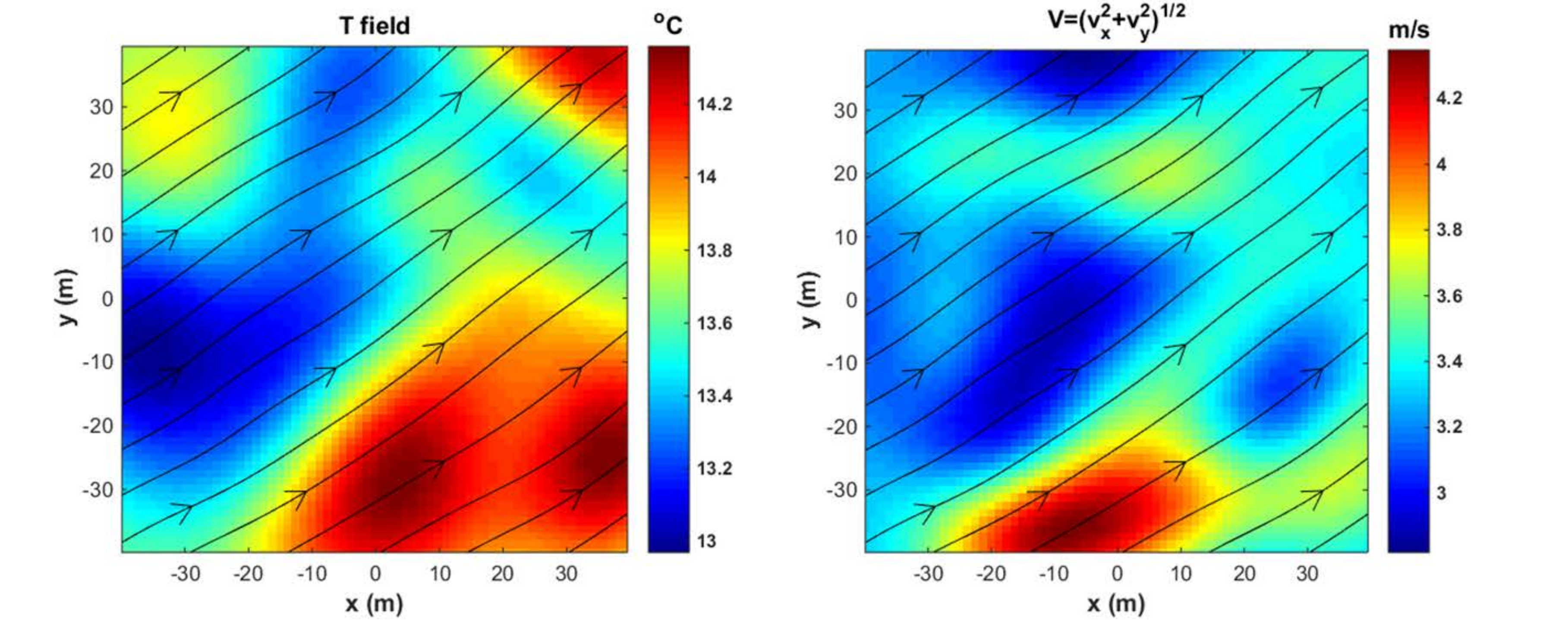

Shown are the temperature and wind velocity fields reconstructed with TDSI from the travel times measured with the BAO tomography array in November 2014. Five sets of the travel times were used and the spatial resolution was 4 m x 4 m. Arrows indicate the wind direction. Several “cold” and “warm” temperature eddies and “slow” and “fast” velocity eddies with different scales are seen in the plots. The eddies are reliably resolved since the expected errors in the reconstruction are less than the difference in temperature and velocity between the eddies. The temperature and velocity reconstructed in the center of the BAO array agree with those measured by a sonic anemometer and T-probe.

ATA for wind energy applications

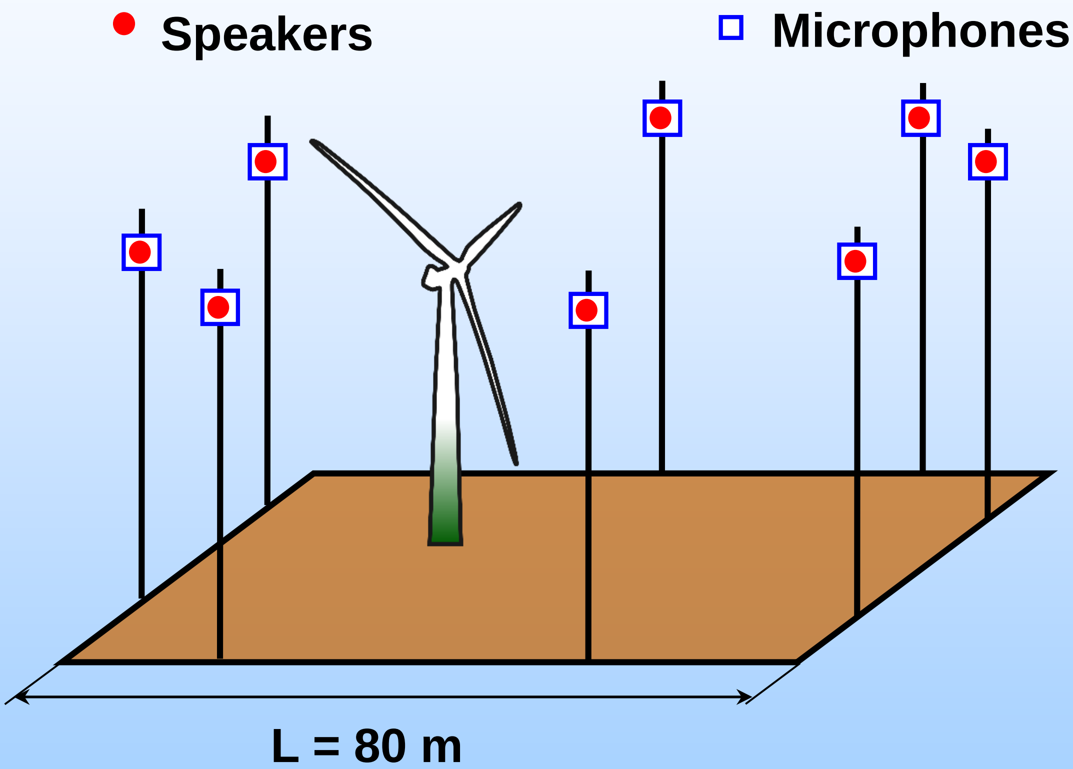

Our tomography array was dismantled in 2016 due to decommission of the BAO. It is now being rebuild at the National Wind Turbine Center (NWTC), located near Boulder, CO. The array will be used to monitor turbulent flows (including a wind turbine wake) near a small wind turbine. Experience gained in this project will allow us to scale acoustic tomography of an incoming turbulent flow and a wind turbine wake to large turbines. This is important for wind energy applications. There is currently no adequate instrumentation for such remote sensing.

Other applications of ATA

- Visualization of 4D dynamic processes in the atmosphere or in a wind tunnel.
- Experimental validation of high-resolution model simulations such as LES. ATA is particularly well suited for this purpose since it enables area-averaged measurements of the temperature and wind velocity fields to be compared with area-averaged results of LES.
- Studies of turbulence over complex topography.
- Input data for atmospheric models and wave propagation codes.
- Advantages of acoustic tomography in comparison with conventional meteorological devices: (i) These devices can perturb the temperature and velocity fields while acoustic tomography does not. (ii) Volume-imaging lidars cannot be used directly for remote sensing of temperature fluctuations. (iii) Acoustic tomography requires fewer sensors per unit of data than do conventional meteorological devices.

5. Other schematics and techniques for ATA

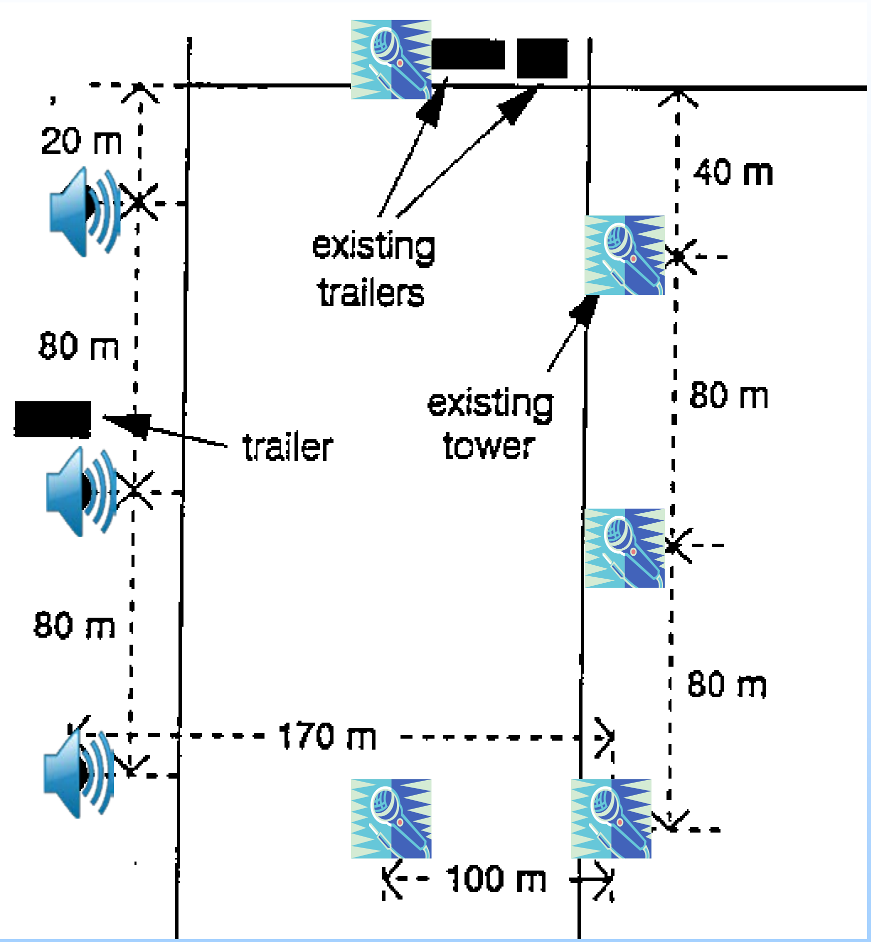

So far, we have considered ATA using the BAO tomography array as an example. In the remaining part of the presentation, we will overview similar tomography arrays and remote sensing techniques which can be termed as ATA.

Application of horizontal-slice tomography to near-ground atmosphere was first suggested by Spiesberger (1990).

First experimental implementation was reported by Wilson and Thomson (1994). Three speakers and five microphones were located 6 m above the ground along the perimeter of a square with the side length of 200 m, resulting in 15 propagation paths. SI was used to reconstruct the T and v fields.

Acoustic tomography array at the University of Leipzig, Germany.

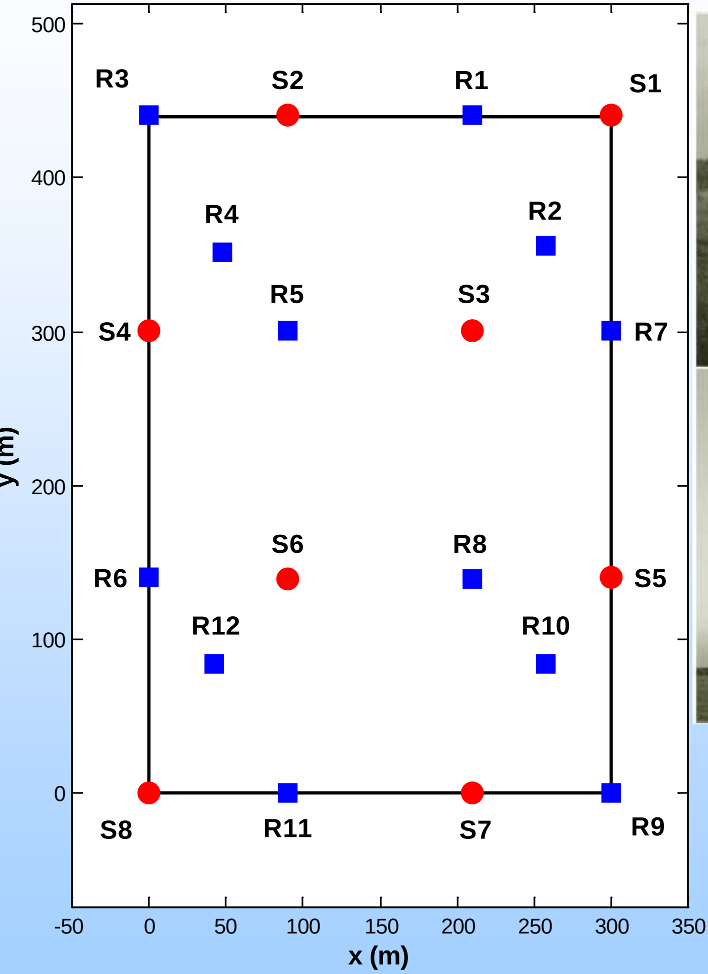

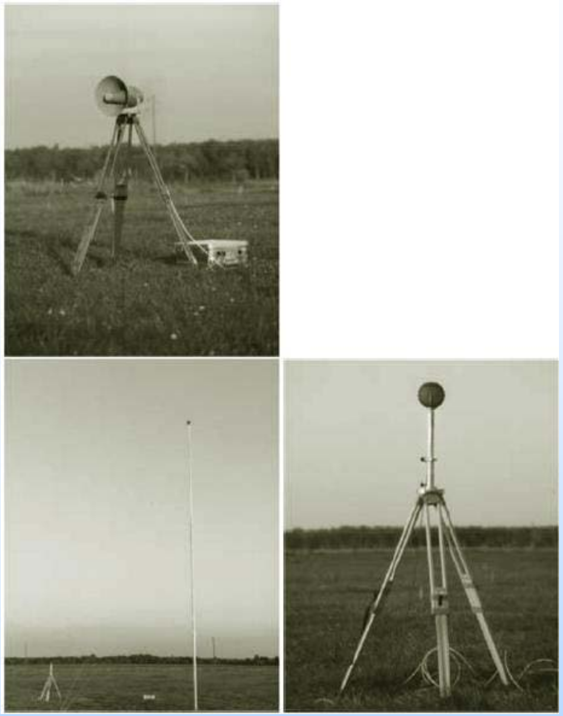

In the mid 1990's, scientists at the University of Leipzig built a portable acoustic tomography array and since then, have used it in many experimental campaigns. Speakers and mics were mounted on tripods 2 m above the ground. The size of the array varied and was of the order of several hundred meters. The German group used the algebraic reconstruction and, later, SI.

The left plot shows locations of 8 speakers and 12 microphones in the acoustic tomography experiment STINHO carried out in July 2002. The size the array was 300 m x 440 m. The travel times were measured every minute.

Site of the STINHO experiment

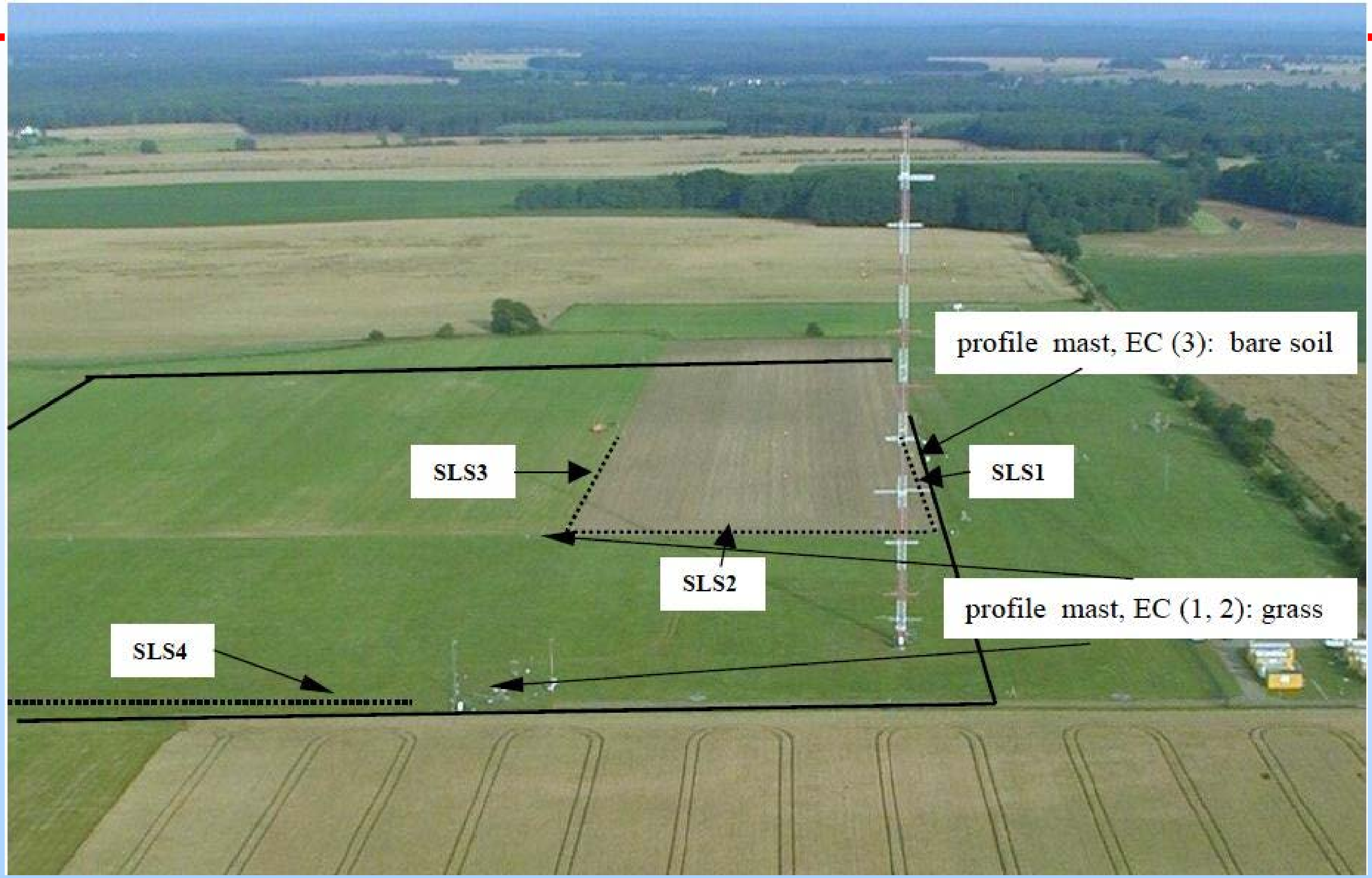

The experimental site consisted of grass and bare soil. The main goal of the experiment was to study the effects of heterogeneous surface on the turbulent heat exchange and horizontal turbulent fluxes. Numerous meteorological equipment including the tomography array was employed to measure parameters of the atmospheric surface layer.

Tomographic reconstruction with TDSI

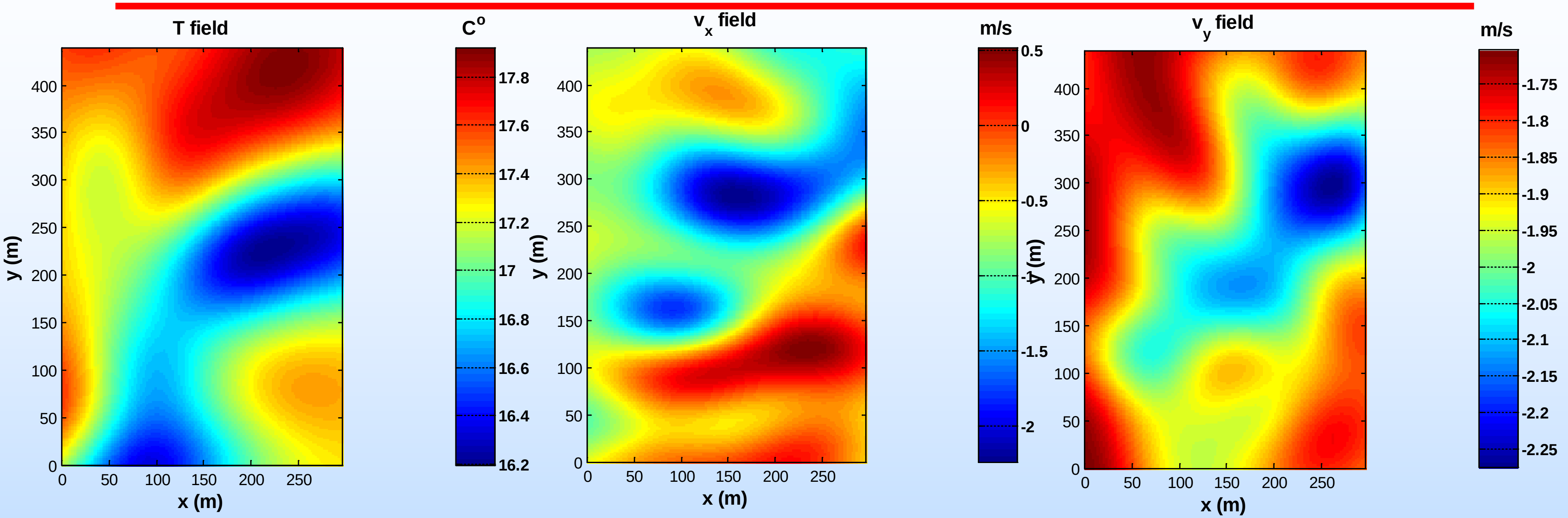

Shown are the temperature and two velocity components reconstructed with TDSI from the travel times provided to us by the German group. Results correspond to 5:30 am on 6 July 2002. Three sets of the travel times were used in TDSI. Expected RMSE in the reconstruction are 0.36 C, 0.35 m/s, and 0.25 m/s. The reconstruction is less detailed than that for the BAO tomography array due to a larger size of the array and less frequent measurements of the travel times. Warm and cold temperature eddies, and fast and slow velocity eddies are seen clearly. The reconstructed values of temperature (at a different time) agree very well with those measured in situ:

In situ, T = 16.24 C; TDSI, 16.14 C.   x = 28 m, y = 138 m.

In situ, T = 15.78 C; TDSI, 15.77 C.   x = 182 m, y = 143 m.

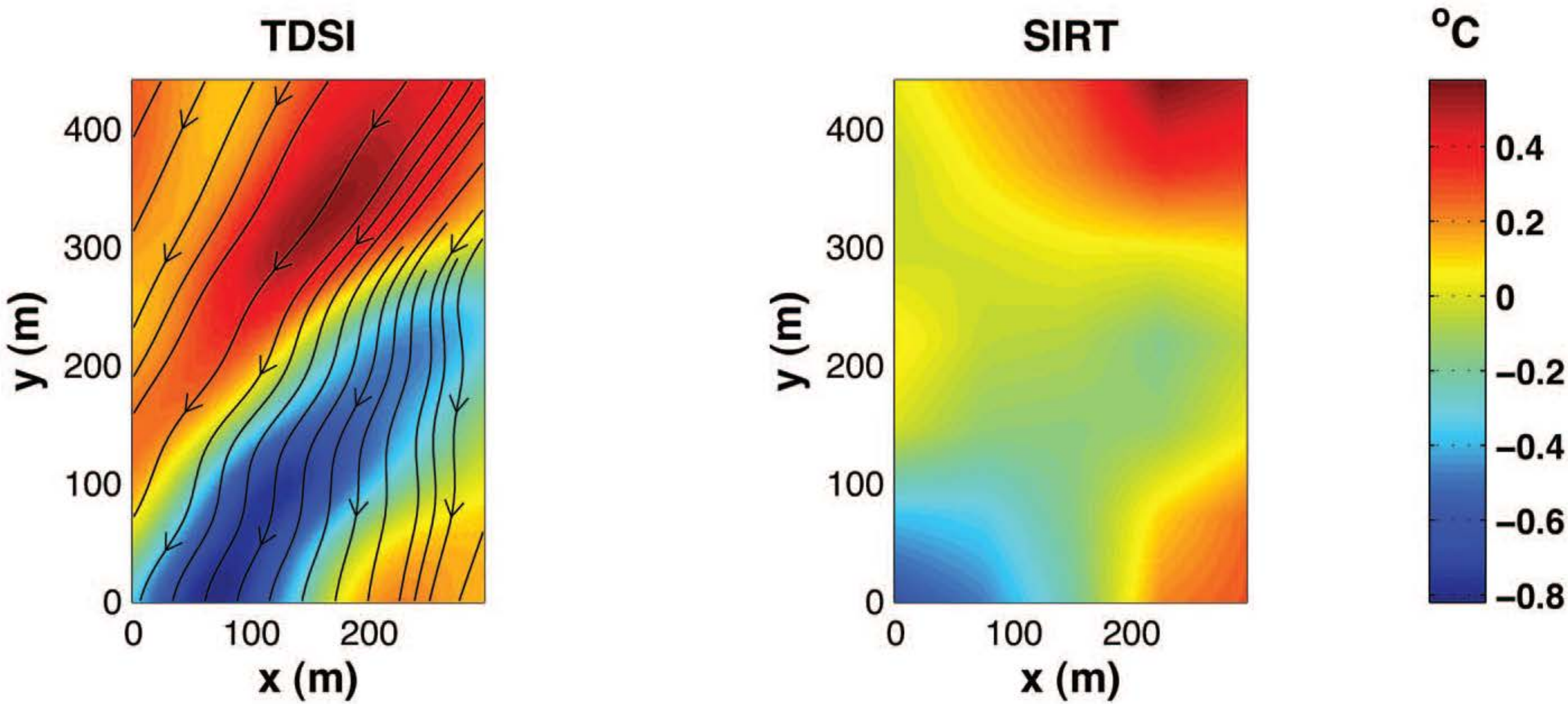

(Left) Temperature field reconstructed with TDSI and averaged over 10 min. Arrows indicate the direction of the averaged wind velocity. Due to heterogeneity of the ground, the temperature has a spatial variation of about 1 C.
(Right) Temperature field reconstructed with an algebraic reconstruction (specifically, Simultaneous Iterative Reconstruction Technique or SIRT). TDSI provides much more detailed reconstruction than SIRT does.

Tomography experiment in a large tank

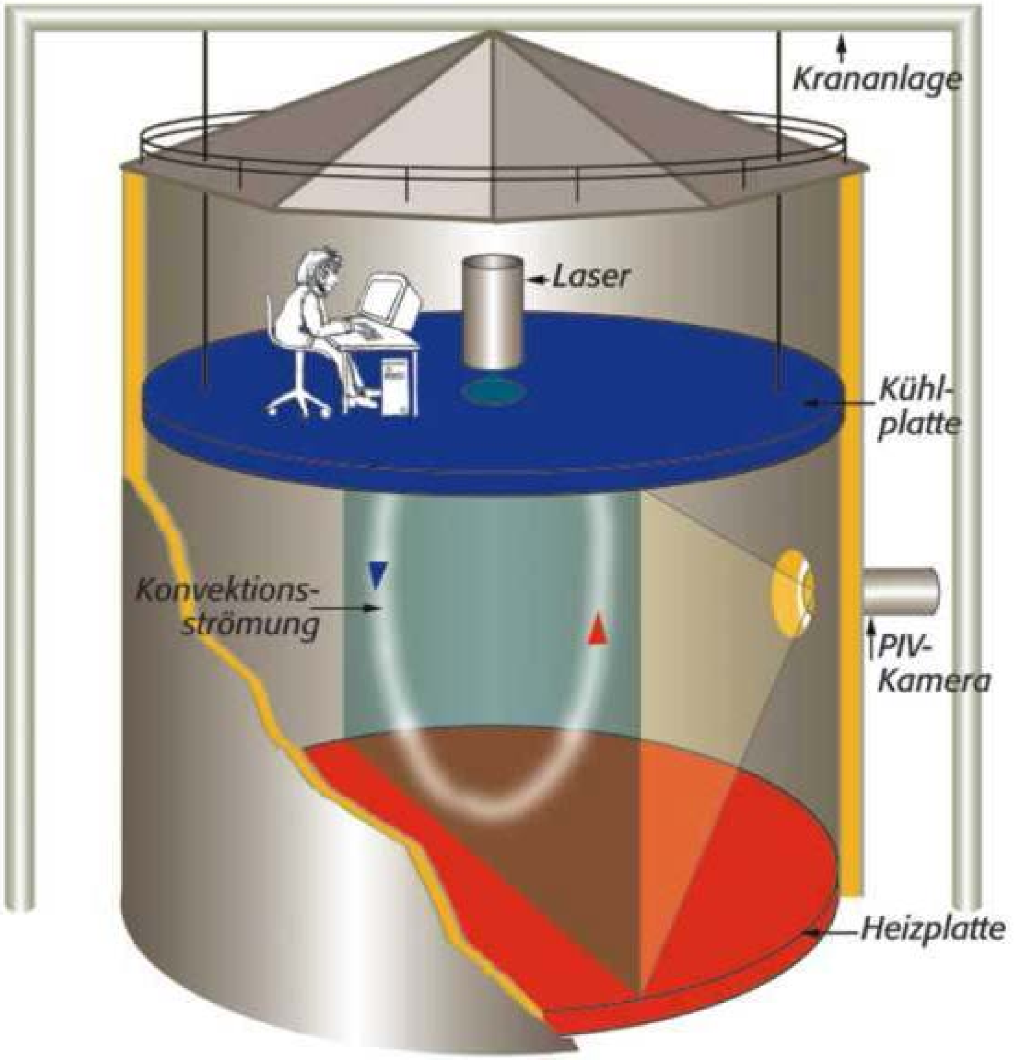

The German group also built a smaller version of the tomography array for indoor applications.

The array was placed between horizontally located heating and cooling plates in a large tank in Ilmenau, Germany to study convection.

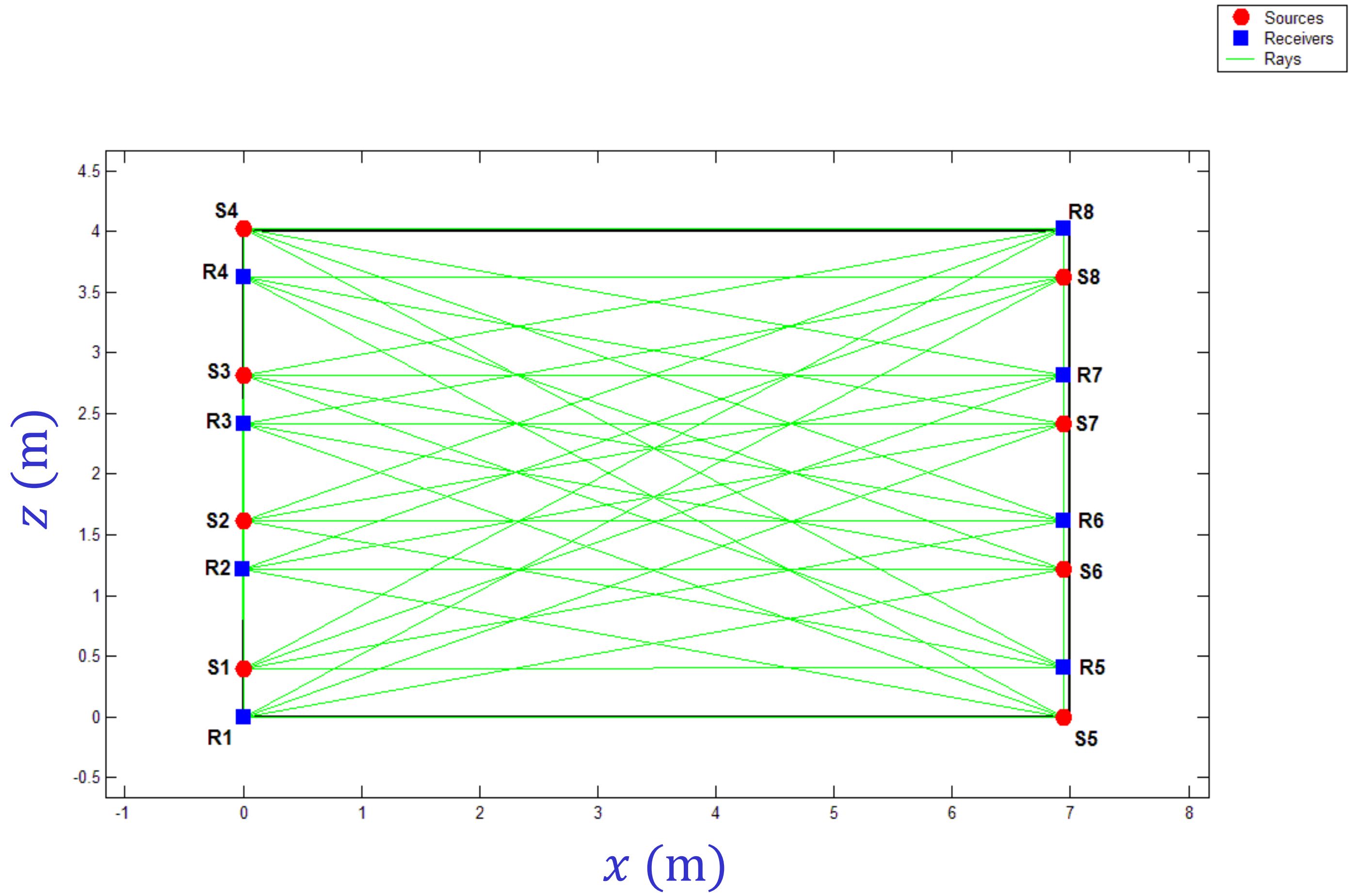

Shown is the schematic of the tomography array with 8 speakers and 8 microphones located in a vertical plane. The size of the array is 7 m x 4 m. Travel times were measured every 20 s.

Reconstruction of the temperature and velocity fields

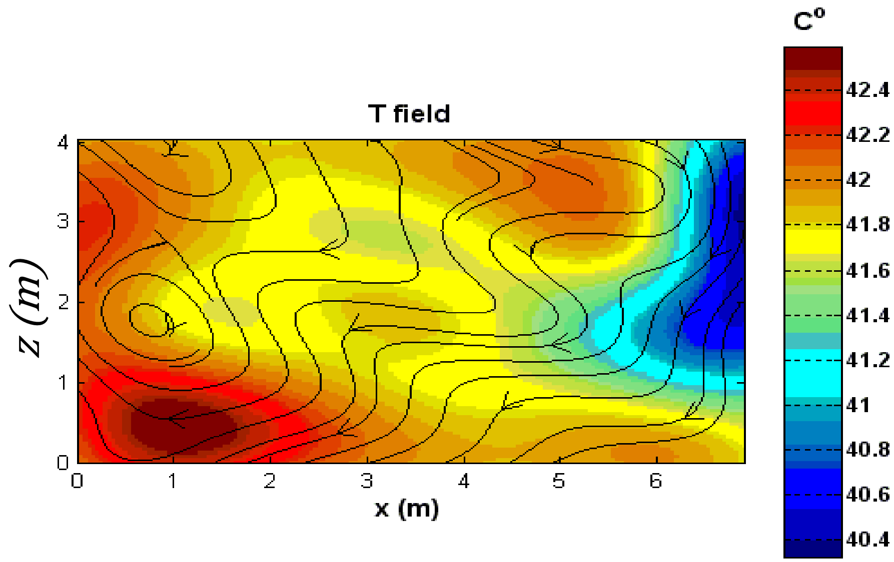

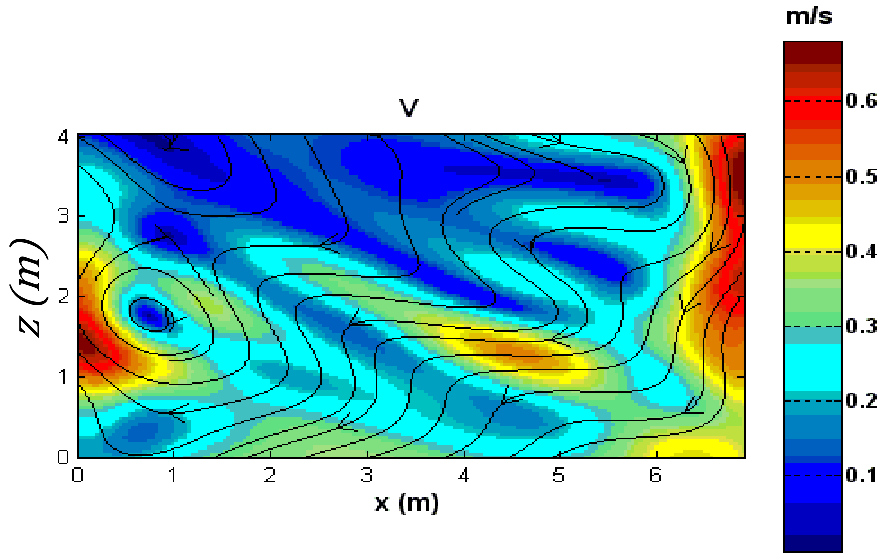

The temperature and the magnitude of the velocity were reconstructed with TDSI from the travel times provided to us by the German group. Five consecutive sets of the travel times were used. The arrows indicate the direction of the velocity. The array was located in the place where the velocity was toward the heating plate.

The temperature varies between 42.6 C at the heating plate and 40 C at the cooling plate. The medium velocity is less than 0.65 m/s which is typical for convection.

The RMSEs in reconstruction are 0.07 C and 0.05 m/s, and are slightly smaller than those for the BAO tomography array due to the smaller size of the array.

Acoustic tomography of the ABL with UAVs

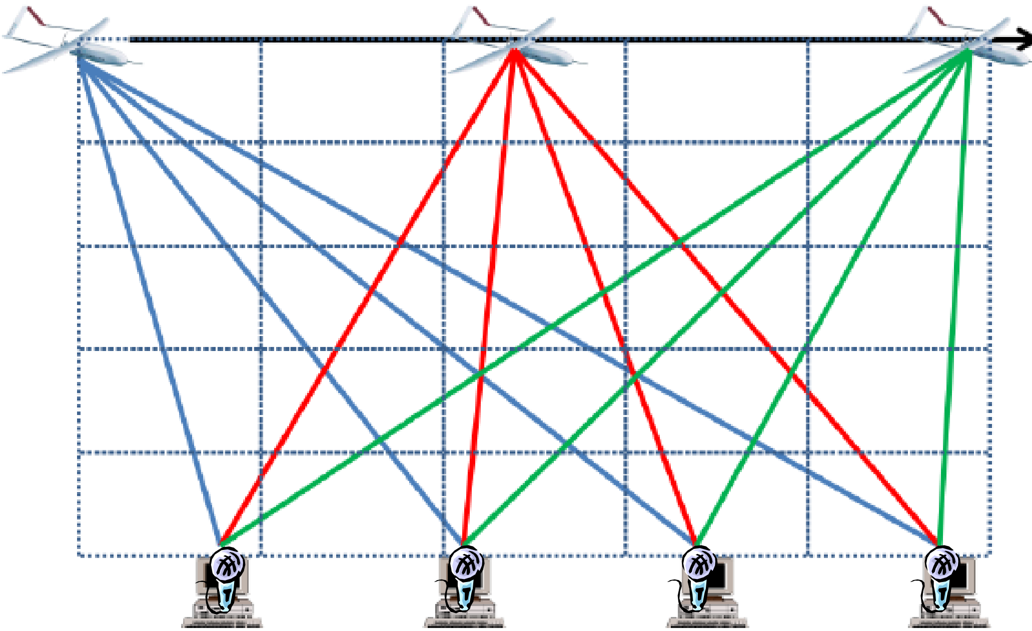

Figure 1: Graphical Depiction of UAV-Based Tomography Concept

Finn and Rogers from the University of South Australia used a small UAV, Aerosonde, to fly at the height of several hundred meters above the ground. It is famous as the first UAV to fly across the Atlantic and in a category 1 cyclone. Propeller noise of the UAV was recorder by microphones on the ground. Using a very elaborate signal processing technique, the travel times of sound propagation from each UAV location to the microphones were determined. The forward problem is similar to that in the BAO tomography array. The reconstruction of the temperature and wind velocity fields is done with a basis function approach. In this approach, the T and v fields are approximated by given functions (e.g., Gaussian envelopes) with parameters to be determined.

Reconstruction of the temperature and wind velocity fields

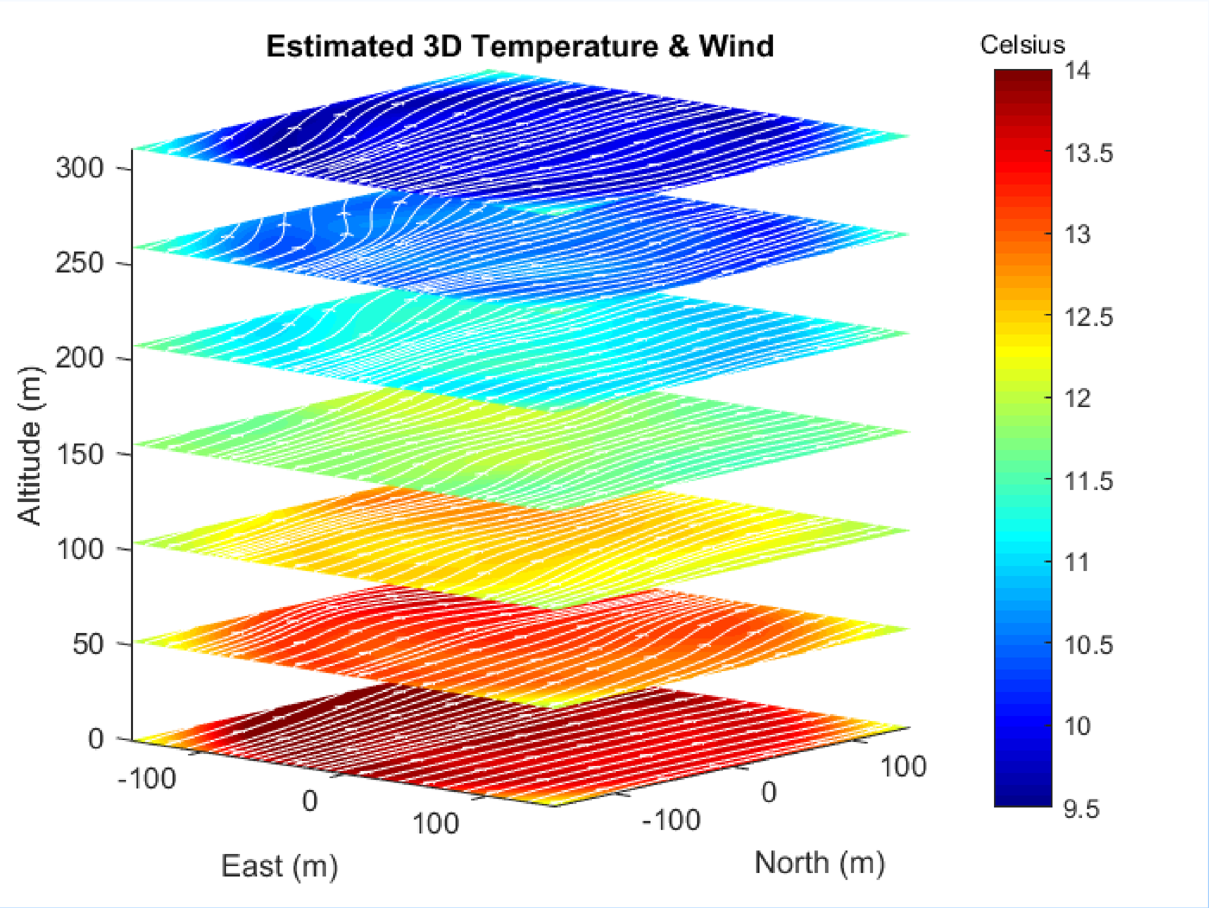

Shown are the reconstructed 3D temperature (colors) and wind velocity (small arrows) fields in a cube with the side length 300 m. The temperature decreases with height by about 5 deg C. The reconstructed temperature field is not very detailed. This is typical for solutions of overdetermined invers problems in ATA such as a basis function approach.

The UAV based ATA can perhaps be improved by using TDSI.

Acoustic tomography of the troposphere

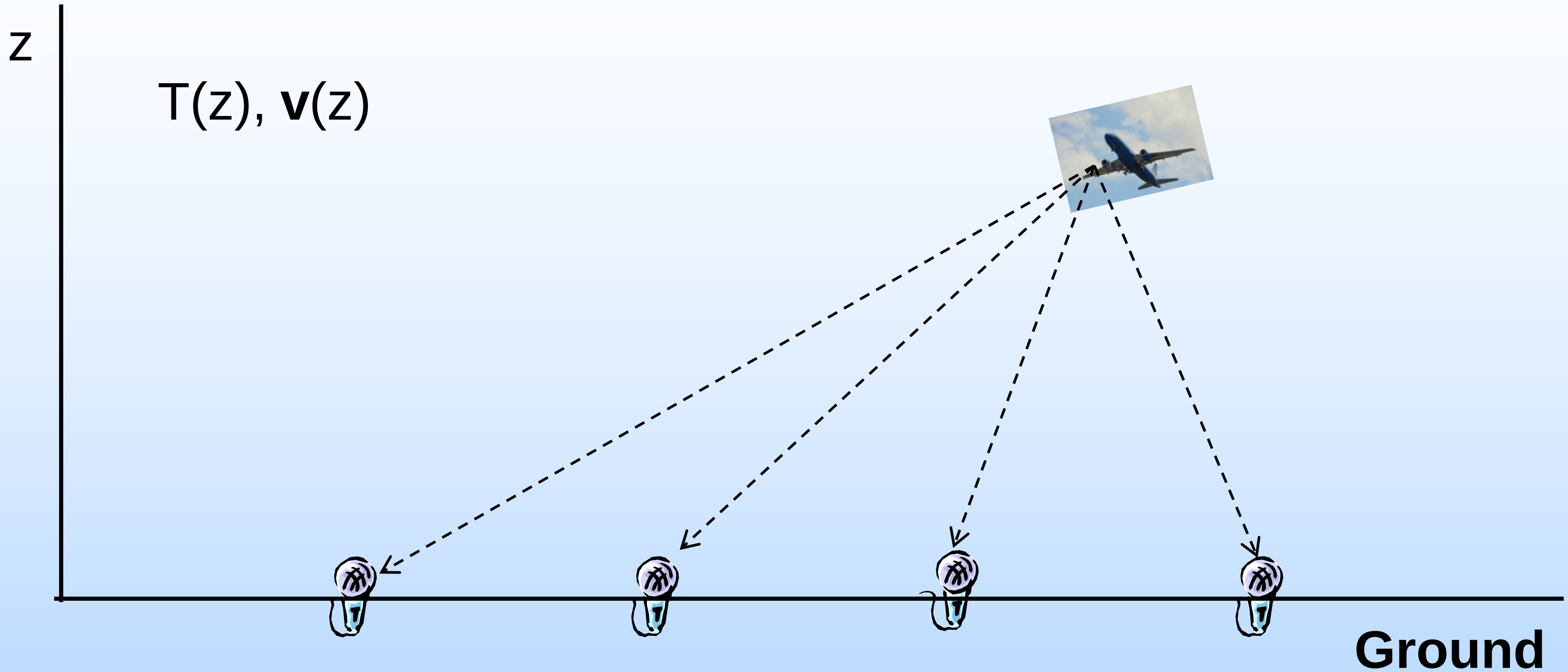

A similar idea was suggested earlier by Wilson et al. (2001). Microphones can be placed on the ground near airports and measure signals from ascending and descending airplanes. By cross-correlating signals at the microphones, the difference in the travel times of sound propagation from an airplane to the microphones can be determined. Then, the vertical profiles of temperature and wind velocity can be reconstructed. This seems as a very inexpensive technique for measuring the vertical profiles. Here, the forward problem is formulated for the vertically stratified atmosphere. The inverse problem can be solved in an analytical form or with a least square estimation.

Acoustic tomography of the upper atmosphere

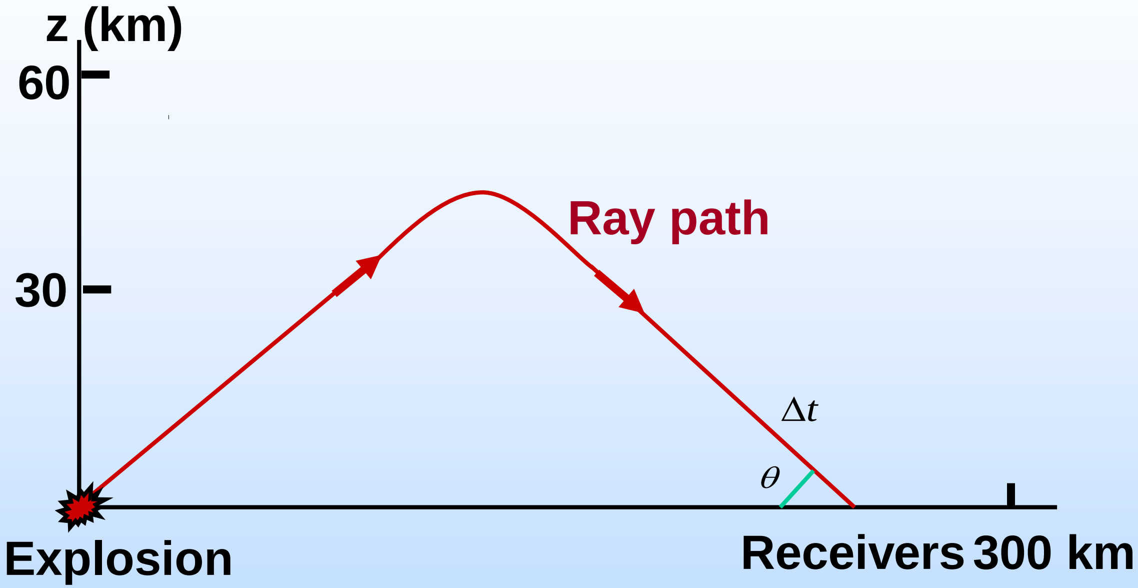

Between the 1900's and 1930's, upper tropospheric and stratospheric wind and temperature profiles were deduced by measuring the travel of sound propagation from large explosions on the ground to receivers also located on the ground. The angles of arrival were also measured.

This technique can be termed as the first acoustic tomography of the atmosphere. The forward problem assumes a vertically stratified atmosphere. Solution of the inverse problem provides the effective sound speed $c_{\mathrm{eff}}(z) = c(z) + v_x(z)$ at the height z of the turning point. Similar remote sensing can be done now with the global infrasound network consisting of several dozens stations of IMS to detect nuclear explosions.

Sonic anemometer as a small tomography array

CSAT3 Sonic anemometer

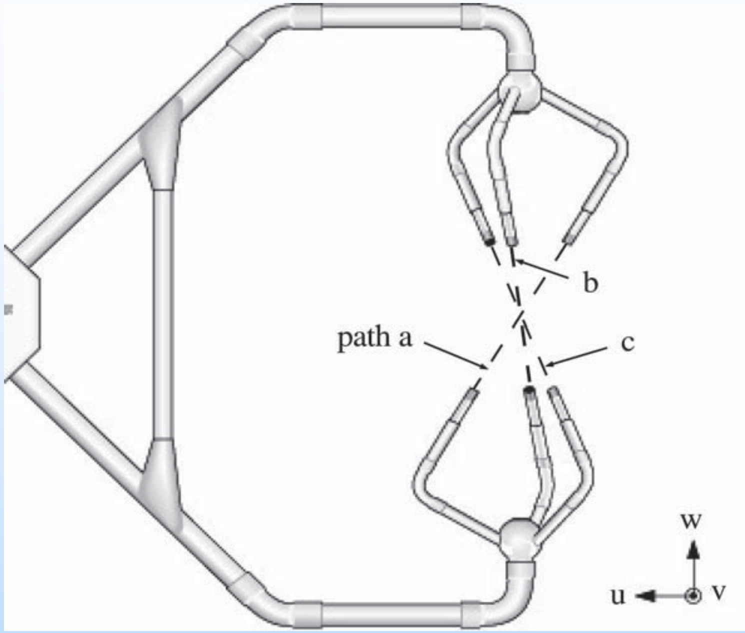

Suggested modification of a sonic

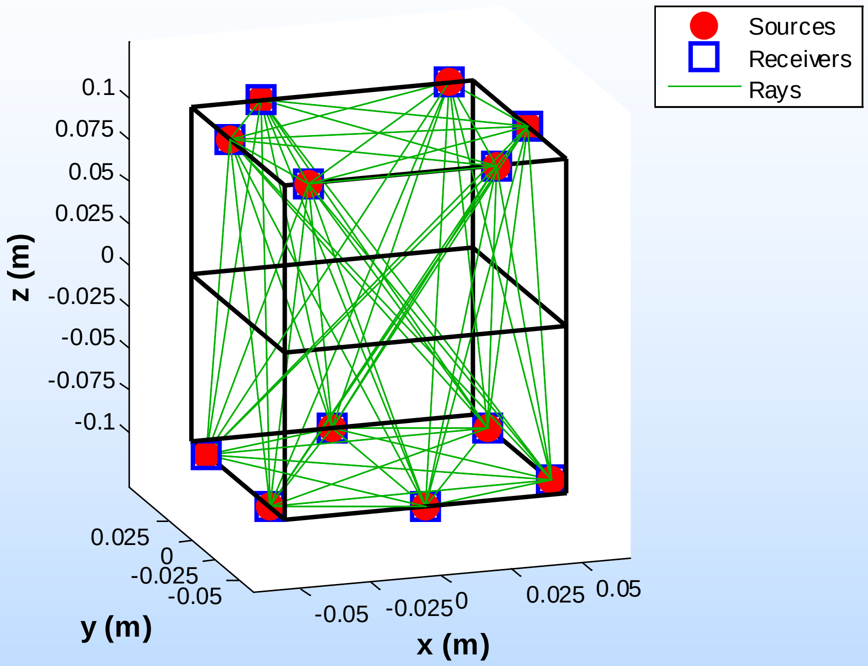

Sonic anemometers are robust instruments for measurements of temperature and wind velocity. Due to concerns about flow distortion, the transducers of a sonic are located at a distance of about 0.2 m thus enabling only path-averaged measurements. Several important applications in boundary-layer physics and turbulence theory require analysis of turbulent fields at smaller scales. To increase the spatial resolution of a sonic anemometer, we suggest considering it as a small acoustic tomography array (Vecherin et al. 2013). A particular modification of the sonic is shown in the right plot. There are 6 transducers at the upper and lower levels. They work as a small tomography array. The forward and inverse problems are formulated similarly to the BAO tomography array, except that this is a 3D acoustic tomography.

Temperature and velocity fields in numerical simulations

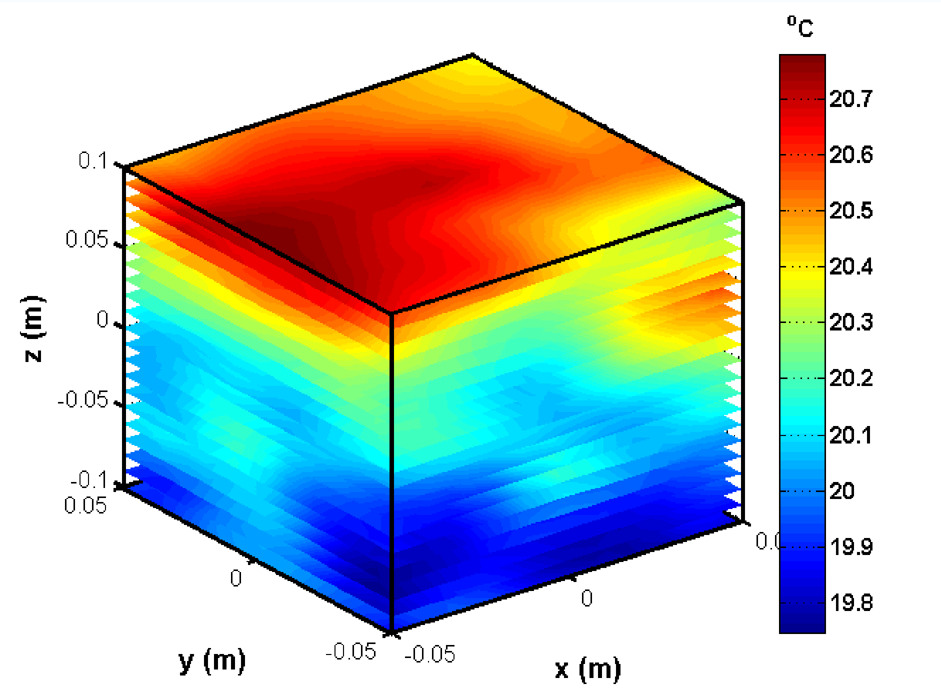

Temperature

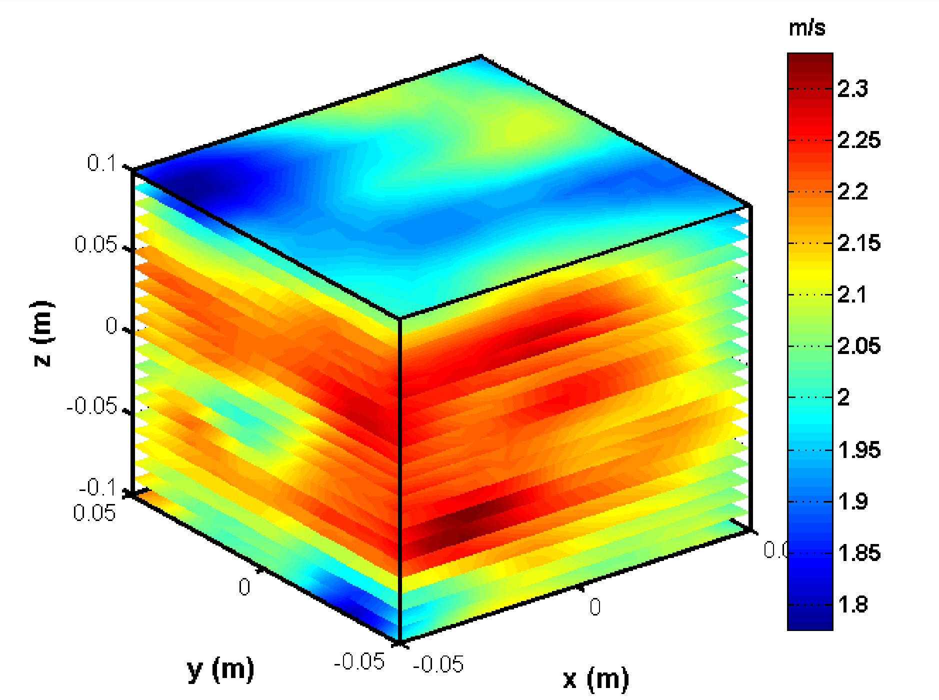

The x-component of velocity

In numerical simulations of the sonic anemometer as a small acoustic tomography array, temperature and velocity fields were modeled with quasi-wavelets (QW), Wilson et al. (2009), Ostashev and Wilson (2015). Using QW fields moving through the sonic, the travel times of sound propagation between 12 transducers were calculated. TDSI was used to reconstruct the temperature and velocity fields.

Results of numerical simulations

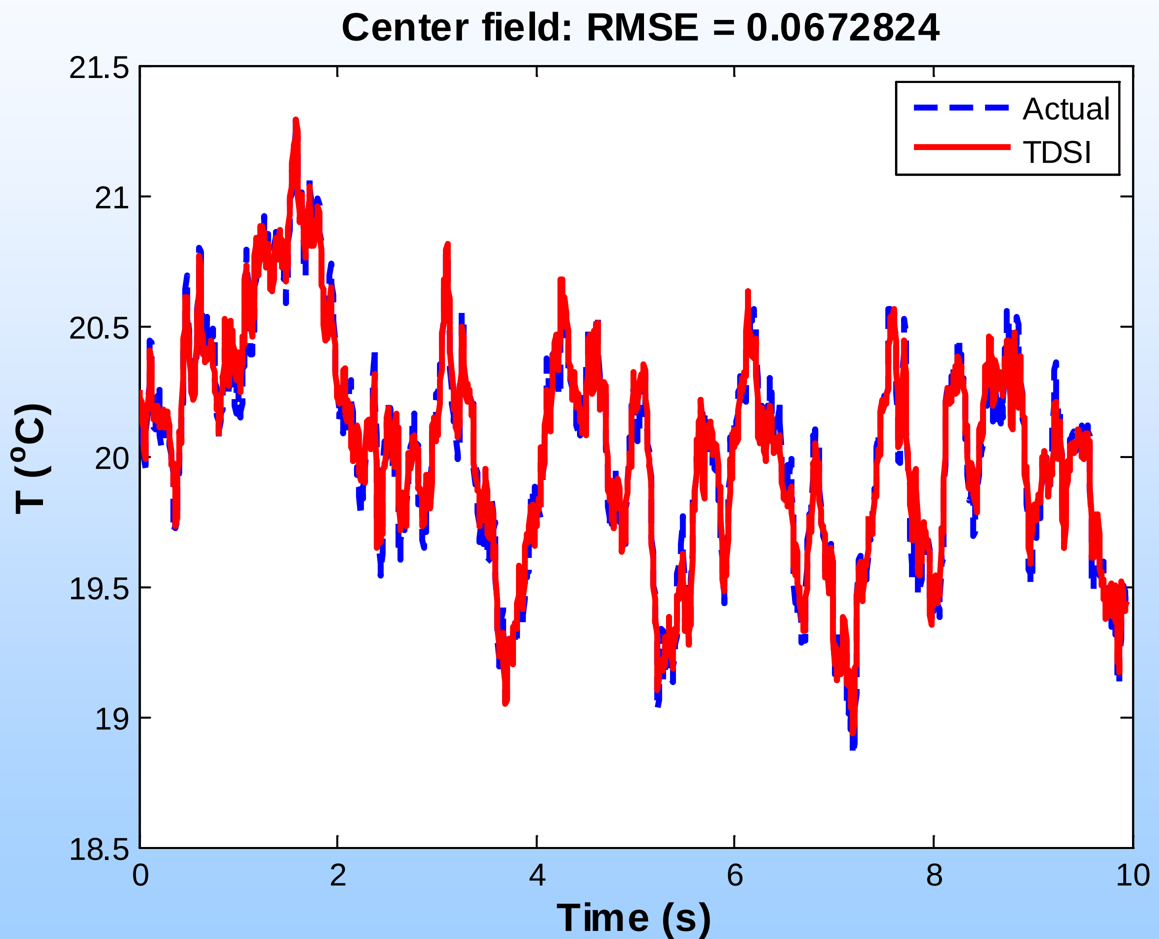

The blue line corresponds to the actual temperature in the center of the sonic anemometer as a small acoustic tomography array. The red line corresponds to that reconstructed with TDSI. The agreement between the actual and reconstructed temperature is very good.

Numerical simulations of a sonic and a sonic as an acoustic tomography array

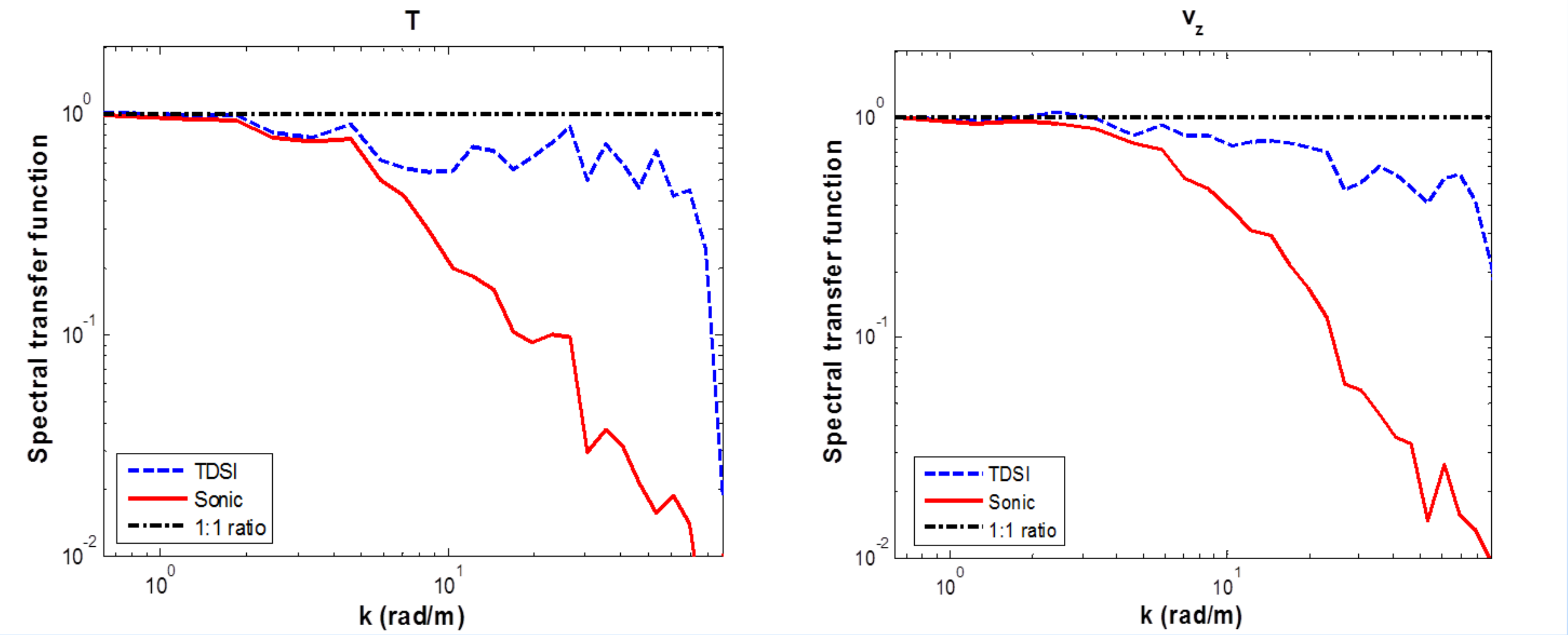

The spectral transfer function is the ratio of the power spectrum of temperature/velocity fluctuations obtained in numerical simulations of a sonic or a sonic as a tomography array and the power spectrum of temperature/velocity fluctuations in the turbulent field moving through the sonic. Solid red lines correspond to numerical simulations of the sonic, while dashed blue lines correspond to the sonic as a tomography array. For a good reconstruction of temperature and velocity, the spectral transfer functions should be close to one. The spectral transfer functions for the sonic drop at much smaller turbulence wavenumbers than those for the sonic as a tomography array. The sonic anemometer as a tomography array enables to increase the spatial resolution by a factor of 10.

6. Conclusions

1. Acoustic tomography of the atmosphere can be done at different scales ranging from a size of a sonic anemometer to the thermospheric heights (about 100 km).

2. By regarding a sonic anemometer as a small acoustic tomography array and applying appropriate inverse algorithms, spatial resolution in reconstruction of the temperature and velocity fields can be increased by a factor of 10 and new atmospheric quantities can be measured. This is important for studies of small-scale turbulence.

3. In the ASL, acoustic tomography is a unique remote sensing technique for simultaneous measurements of the temperature and velocity fields. Acoustic tomography can be used for remote sensing of wind turbine wakes.

4. In the troposphere, acoustic tomography can significantly reduce the cost of remote sensing of the vertical profiles of temperature and wind velocity. Acoustic tomography with UAVs has been demonstrated.

5. Acoustic tomography can also be used to monitor other flows such as those in a wind tunnel.

7. References

Book chapters and journal reviews:

V. E. Ostashev and D. K. Wilson, *Acoustics in Moving Inhomogeneous Media, Second Edition* (CRC Press, 2015), Chapter 3.

V. E. Ostashev, S. N. Vecherin, D. K. Wilson, A. Ziemann, and G. H. Goedecke, “Recent progress in acoustic travel-time tomography of the atmospheric surface layer,” Meteorologische Zeitschrift 18 (2), 125-133 (2009).

D. K. Wilson, A. Ziemann, V. Ostashev, and A. Voronovich, “An overview of acoustic travel-time tomography in the atmosphere and its potential applications,” Acustica-acta acustica 87 (2001).

Selected publications:

S. N. Vecherin, V. E. Ostashev, and D. K.Wilson, “Assessment of systematic errors in acoustic tomography of the atmosphere,” J. Acoust. Soc. Am. 134 (3), 1802-1813 (2013).

S. N. Vecherin, V. E. Ostashev, D. K. Wilson, C. W. Fairall, and L. Bariteau, “Sonic anemometer as a small acoustic tomography array,” Boundary Layer Meteorology 149 (2) 165-178 (2013).

S. N. Vecherin, V. E. Ostashev, and D. K. Wilson, “Three-dimensional acoustic travel-time tomography of the atmosphere,” Acustica-acta acustica 94 (3), 349-358 (2008).

References

S. N. Vecherin, V. E. Ostashev, D. K. Wilson, and A. Ziemann, “Time-dependent stochastic inversion in acoustic tomography of the atmosphere with reciprocal transmission,” Meas. Sci. Technol. 19 (2008).

S. N. Vecherin, V. E. Ostashev, A. Ziemann, D. K. Wilson, K. Arnold, and M. Barth, “Tomographic reconstruction of atmospheric turbulence with the use of time-dependent stochastic inversion,” J. Acoust. Soc. Am. 122 (3), 1416-1425 (2007).

S. N. Vecherin, V. E. Ostashev, G. H. Goedecke, D. K. Wilson, and A. G. Voronovich, “Time dependent stochastic inversion in acoustic travel-time tomography of the atmosphere,” J. Acoust. Soc. Am. 119 (5), 2579-2588 (2006).

S. Kolouri, M. R. Azimi-Sadjadi, and A. Ziemann, “A statistical-based approach for acoustic tomography of the atmosphere,” J. Acoust. Soc. Am. 135 (1), 104-114 (2014).

A. Raabe, K. Arnold, A. Ziemann, M. Schroter, S. Raasch, J. Bange, P. Zittel, Th. Spiess, Th. Foken, M. Gockede, F. Beyrich, J-P. Leps, “STINHO - STructure of turbulent transport under INHOmogeneous conditions - the micro-alpha scale field experiment and LES modeling,” Meteorol. Z. 14, 315-327 (2005).

K. Arnold, A. Ziemann, A. Raabe, G. Spindler, “Acoustic tomography and conventional meteorological measurements over heterogeneous surfaces,” Meteor. Atmos. Phys. 85, 175-186 (2004).

S. Weinbrect, S. Raasch, A. Ziemann, K. Arnold, A. Raabe, “Comparison of large-eddy simulation data with spatially averaged measurements obtained by acoustic tomography – presuppositions and first results,” Boundary Layer Meteorology 111, 441-465 (2004).

References

A. Ziemann, K. Arnold, A. Raabe, “Acoustic tomography as a remote sensing method to investigate the near surface atmospheric boundary layer in comparison with in sit measurements,” J. Atmos. Oceanic Technol. 19, 1208-1215 (2002).

A. Ziemann, K. Arnold, A. Raabe, “Acoustic tomography as a method to identify small-scale land surface characteristics,” Acust. Acta Acust. 87, 731-737 (2001).

A. Finn and K. Rogers, “The Feasibility of Unmanned Aerial Vehicle-Based Acoustic Atmospheric Tomography,” J. Acoust. Soc. Am. 138 (2), 874-889 (2015).

K. J. Rogers and A. Finn, “Three-Dimensional UAV-Based Atmospheric Tomography,” J. Atmos. Oceanic Techn. 30 (2), 336-344 (2013).

K. Rogers and A. Finn, “3D Acoustic Atmospheric Tomography,” Proc. SPIE Conf. Rem. Sens., 2014 (International Society for Optics and Photonics, 2014).

D. K. Wilson and D. W. Thomson, “Acoustic tomographic monitoring of the atmospheric surface layer,” J. Atmos. Ocean. Tech. **11**, 751–769 (1994).

I. Jovanovic, L. Sbaiz, and M. Vetterli. “Acoustic tomography for scalar and vector fields: theory and application to temperature and wind estimation. J. Atmos. Ocean. Tech., 26, 1475-1492 (2009).